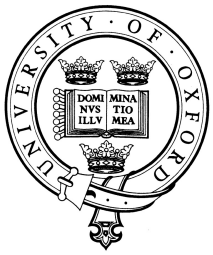
Lower Cretaceous climate records and the correlation between marine and lacustrine settings (Europe and South America)



by

Leonardo Ribeiro Tedeschi

Thesis submitted to University of Oxford for the degree of Doctor of Philosophy

Department of Earth Sciences

Wolfson College

Hilary Term 2017

Supervisors: Dr Hugh C. Jenkyns and Dr Stuart A. Robinson

Abstract

Lower Cretaceous climate records and the correlation between marine and lacustrine settings (Europe and South America)

Leonardo R. Tedeschi, Wolfson College

Thesis submitted to University of Oxford for the degree of Doctor of Philosophy

Hilary Term 2017

Major changes in watermass chemistry during the opening of the central segment of the South Atlantic, and oceanic anoxic events (OAEs 1a to 1d), represent dramatic events that affected the ocean–atmosphere system during the Early Cretaceous. This thesis addresses the chemostratigraphic correlation of Tethyan and South Atlantic sections based on carbon-, sulphur- and strontium-isotopes ($\delta^{13}C$, $\delta^{34}S$ and $^{87}Sr/^{86}Sr$) integrated with other methods to explore the causal links between these phenomena. Firstly, the sedimentation of massive evaporite deposits is discussed and its relationship with the Early Aptian OAE 1a explored. The proposed coincidence in timing between massive evaporite deposition and OAE 1a enhances the understanding of carbon and sulphur cycles in the Early Cretaceous. Secondly, the top of sub-evaporite carbonates in the southern Brazilian basins is identified as having been deposited in a continental environment, and further evidence for its deposition during part of the OAE 1a interval is presented. Thirdly, it is suggested that the formation of the Ontong Java Plateau, already linked to the genesis of OAE 1a, promoted a eustatic sea-level rise responsible for rapid seawater entrance into the southern Brazilian basins during the Early Aptian. Fourthly, the first record of OAE 1a from northeastern Brazil (Sergipe-Alagoas Basin) has been recognized, allowing stratigraphic correlation with southern Brazilian basins. Stratigraphic correlation between the southern Brazilian basins is extended to the Falkland Plateau, where the decrease in the content of organic matter upwards in the stratigraphy of DSDP Site 511 through the Barremian–OAE 1b interval can be related to the evolution of South Atlantic basinal geometry. Finally, in the context of a Tethyan reference section, the record of the Barremian-Aptian boundary and the OAE 1a interval has been characterized in the Tethyan Poggio le Guaine scientific core from Marche–Umbria, Italy.

Extended Abstract

Lower Cretaceous climate records and the correlation between marine and lacustrine settings (Europe and South America)

Leonardo R. Tedeschi, Wolfson College

Thesis submitted to University of Oxford for the degree of Doctor of Philosophy

Hilary Term 2017

The Early Cretaceous represents a time interval that was characterized by dramatic changes in palaeogeography, palaeoceanography, and palaeoclimate of the Earth system. Included in such changes were intervals of time when widespread deposition of organic-rich sediments took place in many mid- to deep-water environments worldwide during oceanic anoxic events (e. g., OAEs 1a to 1d). However, significant changes in ocean chemistry were also promoted by the opening of the central segment of the South Atlantic with massive deposition of sulphate and chloride evaporites (informally termed 'Salt'). The stratigraphic correlation between those two phenomena is, however, poorly constrained, a shortcoming that this thesis attempts to address. Chemostratigraphy based on carbon-, sulphur- and strontium-isotopes ($\delta^{13}C$, $\delta^{34}S$ and $^{87}Sr/^{86}Sr$), integrated with other methods (magneto- and biostratigraphy and Re-Os geochronology), is used to explore possible causal links between these apparently disparate phenomena.

New $\delta^{13}C$ and $^{87}Sr/^{86}Sr$ profiles, constrained by planktonic foraminiferal biostratratigraphy from Petrobras Well CB-3, Campos Basin, allow correlation to $\delta^{13}C$ profiles of a composite carbon-isotope curve from the Campos and Santos Basins as well as an age-calibrated Tethyan reference curve (Chapter 2). The newly obtained stratigraphy of the South Atlantic indicates synchrony between major evaporite deposition and the OAE 1a interval (~125 or ~120 Ma). This correlation implies that the evaporites are significantly older than their former suggested age of 116–111 Ma. The stratigraphic revision suggests that deposition of the South Atlantic evaporites took place after the release of massive amounts of CO_2 and SO_2 during the formation of the Ontong Java Plateau Large Igneous

Province (LIP) and may have removed massive amounts of sulphate from the world ocean, hence fostering important palaeoceanographic changes during and after OAE 1a.

Chapter 3 describes $^{87}Sr/^{86}Sr$ data obtained from ostracods and bulk rock from sub-evaporite (also called pre-Salt) rocks from Petrobras Wells A, B (Santos Basin) and C (Campos Basin), and Re-Os geochronology of a sample at the top of the pre-Salt carbonates from Petrobras Well B. Geochemical evidence suggests that the pre-Salt carbonates in the southern Brazilian basins were deposited in a continental setting until the onset of evaporite precipitation. The fluids that fed the lakes are suggested to have derived from rivers and groundwaters draining felsic and feldspar-bearing siliciclastic rocks exposed on the flanks of the basin. The overall stratigraphy constrains the processes of sea-floor spreading to have taken place after deposition of these dominantly lacustrine carbonates. The new Re-Os age of 117.5 ± 2.5 Ma from an organic-rich carbonate, sampled ~0.3–0.5 m below the base of the evaporites in Petrobras Well B from the Santos Basin, is compatible with the stratigraphic correlation presented in Chapter 2, linking deposition of the upper part of the pre-Salt carbonates, and the evaporites themselves, with OAE 1a.

Chapter 4 presents new $^{87}Sr/^{86}Sr$ ratios and $\delta^{34}S$ values of anhydrites from the Santos Basin and Hg/TOC ratios from pre-Salt carbonates from Petrobras Well A. New $^{87}Sr/^{86}Sr$ measurements of anhydrites from the Santos Basin yield higher values than contemporaneous Aptian seawater but lower than the estimated continental input. This study suggests a rapid entrance of seawater into the South Atlantic basin post-dating deposition of pre-Salt carbonates. However, it was not possible to define whether the development of fully marine conditions corresponded in time to the base or the top of the evaporites. Relatively elevated Hg/TOC ratios within the carbonates ~1.4 m below the evaporite base suggest an input of volcanic Hg and imply a possible link with the main eruption(s) of the Ontong Java Plateau. This event could have triggered a eustatic sea-level rise and the first entrance of seawater into the South Atlantic basin. The cyclic pattern recognized in the evaporites of gypsum/halite/more soluble salts are likely to have been driven by aquifer-eustasy in the (supposedly ice-free) Cretaceous greenhouse climate. $\delta^{34}S$ values at the base of South

Atlantic evaporites have the same values as contemporaneous global Aptian seawater and support an OAE 1a age equivalency with the onset of evaporite deposition.

A new record of OAE 1a based on $\delta^{13}C$ derived from organic matter in the Sergipe-Alagoas Basin, northeast Brazil is presented in Chapter 5. The deposition of siliciclastic rocks in the Sergipe-Alagoas Basin, in the northern part of the central segment of the South Atlantic, is suggested to have been synchronous with evaporite formation in the southern Brazilian basins.

Chapter 6 presents new high-resolution nannofossil zonation, magnetostratigraphy, total inorganic and organic-carbon (TOC and TIC), Rock-Eval pyrolysis, sulphur content of organic matter (S_{OM}), carbon- and oxygen- isotope ratios of carbonate and organic-matter and Re-Os isotope analyses from Deep Sea Drilling Program (DSDP) Site 511, Falkland Plateau. These data from DSDP Site 511 suggest that the deposition of an organic-rich black-shale interval took place from the mid-Jurassic up to the Barremian–Early Aptian interval represented by the hiatus/condensed section. The typical isotopic record of OAE 1a is missing either due to incomplete core recovery or a hiatus, although its latter part (C6 segment) could be represented. Therefore, most black-shale sedimentation on the Falkland Plateau took place before deposition of evaporites in the Campos and Santos Basins during the OAE 1a time interval and before the opening of the central segment of the South Atlantic. Black-shale deposition on the Falkland Plateau was thus likely governed primarily by local forcing factors. Upper Aptian sediments with intermediate TOC values and relatively high terrestrial organic-matter content lie above the hiatus/condensed section at DSDP Site 511 and are partially coeval with shallow- and deep-water post-evaporite carbonates from the Santos and Campos Basins. Local records of OAE 1b, including the Jacob, Kilian and Paquier Levels, are tentatively recognized in DSDP Site 511 based on their carbon-isotope signature but without the organic-rich levels that are typically recognized in the Tethyan realm.

Chapter 7 discusses a new magnetostratigraphic and chemostratigraphic investigation, integrated with biostratigraphy, of the uppermost Barremian–Lower Aptian

Maiolica and Marne a Fucoidi Formations from the PLG core (Northern Apennines, Italy). The data provide the first record of polarity chron M0r and the Early Aptian OAE 1a interval in Poggio le Guaine area, allowing the Barremian–Aptian boundary and the base of the Cretaceous Normal Polarity Superchron (CNPS) to be defined. Above the base of the CNPS, the $\delta^{13}C$ record shows a negative shift and a subsequent positive excursion similar to that documented from elsewhere in the Tethyan realm. OAE1a is lithologically represented by the Selli Level, the origin of which has been linked to volcanic episodes that formed the Ontong Java LIP, which forced the rapid increase of atmospheric pCO_2 triggering a cascade of palaeoenvironmental changes affecting plankton productivity and carbon flux to the sea floor.

These studies expose only a small piece of the possible relationship between the opening of the South Atlantic and other palaeoenviromental changes observed worldwide. In particular, the studies detailed in this thesis open a range of questions as to the role of the Ontong Java Plateau and the opening of central segment of the South Atlantic in palaeoclimatic and palaeoceanographic changes during the Early Cretaceous, especially during the Barremian–Albian interval. Further extensions of these studies are proposed that will expand and refine the conclusions derived from this work.

Acknowledgements

Firslty, I would like to express my sincere gratitude to my supervisors Hugh C. Jenkyns and Stuart A. Robinson, who have supervised this work and contributed to every part of it. Their patience, motivation, and immense knowledge have been sources of inspiration. It is my privilege and honour to learn from them during my DPhil at Oxford.

I also would like to thank Petrobras for all funding and logistic support during my DPhil at Oxford, especially to the Research and Development Centre of Petrobras (CENPES). My sincere thanks to Biostratigraphy and Paleoecology manager Oscar Strohschoen Junior and all group of chemostratigraphy in Petrobras, especially to Joselito C. Vazquez, Milene F. Figueiredo, Raphael Pietzsch, Aline M. Soares, Gabriela M. M. Jacobina and Erik D. Gueiros, who helped me with sampling, analyses, discussion and logistics. My gratitude also goes to geologists and technicians from laboratories from CENPES, UO-BC and UO-SEAL from Petrobras who helped with sampling, Peter Szatmari who supported the Re-Os analyses, Daisy Barbosa Alves who helped with interpretation of diffractograms, Jeanine L. Grilo who made ostracods available, Alexandre de A. Ferreira who made sulphur-isotope analyses available, Rogério da S. Martins da Costa who helped and made available SEM-EDS analyses and the manager Carlos H. L. Bruhn, who gave permission to use Petrobras Wells in this thesis.

I also would like to thank my collaborators – Cecília C. Lana, Marta Claudia Viviers, Antonio E. S. Sanjinés, Isabela de O. Carmo, Claúdia M. S. P. Quintaes, Maria Rosilene F. Menezes and Francisco M. W. Tognoli, Robert A. Creaser, Farid Chemale Jr, Ricardo I. F. Trindade, Jairo F. Savian, Janine A. Carmo, Alex Dickson, Cinzia Bottini, Rodolfo Coccini, Fabrizio Frontalini, Luigi Jovane, Renato Paes de

Almeida, Liliane Janikian, Marianna Sideri – who made samples available, undertook different analyses and made available and contributed thoughts during interpretations.

Special thanks go to Alan Hsieh, Jane Barling, Steve Wyatt, Phil Holdship, Lawrence Percival and Chris Day who offered the time in clean lab and ran or helped to run mass spectrometers, Coulomat and Rock-Eval in the Department of Earth Sciences. Thanks to Micha Rhul, Weimu Xu, Sietske Batenburg, Marisa Storm, Joachim Katchinoff, Rosalind E. M. Rickaby, Tim Sweere, Benjamin Tutolo and John Hooker, who always have been friendly to me, and helpful during discussions of my research. Departmental and Wolfson College staff that offered support during this thesis. Thank you my wife Flávia Bassi Tedeschi, my daughter Júlia Bassi Tedeschi and all the relatives for support and love during this thesis. Thank you my parents Getulio Tedeschi and Olindina Gomes Ribeiro, my parents-in-law Hugo da Silva Bassi and Aparecida de Oliveira Bassi, my aunt Milma Tedeschi de Sá, my sisters, my siblings-in-law and my stepmother for all the support during my thesis. This thesis was examined by Elisabetta Erba and Nicholas Tosca, and I thank them for their attention and suggestions for this work. Finally, thank you God that allowed this to happen in my life.

Contents

Abstract..... i

Extended Abstract..... ii

Acknowledgements..... vi

Chapter 1..... 1

1.1 – Definitions of the Aptian and Albian..... 3

1.2 – Introduction to chemostratigraphy..... 5

1.2.1 – Carbon isotopes..... 5

1.2.2 – Sulphur isotopes..... 9

1.2.3 – Strontium isotopes..... 11

1.3 – Introduction to oceanic anoxic events (OAEs)..... 13

1.4 – The opening of the central segment of the South Atlantic..... 16

1.5 – Aims and description of chapters..... 19

Chapter 2..... 24

2.1 – Introduction..... 24

2.2 – Geological setting of the Santos and Campos Basins..... 25

2.3 – Methods..... 29

2.3.1 – Foraminiferal biostratigraphy..... 29

2.3.2 – Carbon and oxygen isotopes..... 30

2.3.3 – Elemental analyses..... 31

2.3.4 – Scanning electron microscope – energy dispersive spectroscopy (SEM-EDS)..... 32

2.3.5 – Strontium-isotope analyses..... 32

2.3.6 – Campos/Santos composite carbon-isotope curve..... 34

2.4 – Results..... 36

2.4.1 – Foraminiferal biostratigraphy..... 36

2.4.2 – Carbon-isotope stratigraphy..... 36

2.4.2.1 – Diagenesis..... 36

2.4.2.2 – Petrobras Well CB-3..... 37

2.4.2.3 – Campos/Santos Composite carbon-isotope curve..... 40

2.4.3 – Strontium-isotope analyses..... 41

2.4.3.1 – Diagenesis..... 41

2.4.3.2 – Strontium-isotope stratigraphy..... 48

2.5 – Discussion..... 50

2.6 – Conclusions..... 53

Chapter 3..... 54

3.1 – Introduction..... 54

3.2 – Geological setting..... 57

3.3 – Materials and methods..... 61

3.3.1 – Petrobras Well A..... 67

3.3.1.1 – Sampling and separation of ostracods..... 67

3.3.1.2 – $^{87}Sr/^{86}Sr$ analyses..... 68

3.3.1.3 – Elemental content..... 69

3.3.1.4 – Total inorganic carbon and total organic carbon (TIC and TOC)..... 70

3.3.1.5 – X-ray diffractometry (XRD)..... 71

3.3.1.6 – Scanning electron microscope – energy dispersive spectroscopy (SEM-EDS) 71

3.3.2 – Petrobras Wells B and C 71

3.3.2.1 Sampling of Petrobras Well B..... 71

3.3.2.2 Sampling of Petrobras Well C..... 72

3.3.2.3 – $^{87}Sr/^{86}Sr$ analyses..... 73

3.3.2.4 – Elemental content..... 73

3.3.2.5 – Rhenium and Osmium analyses (Re-Os) 74

3.4 – Results..... 74

3.4.1 – Ostracod samples..... 74

3.4.2 – Carbonate samples..... 76

3.4.3 – Rhenium and osmium isotopes..... 86

3.5 – Discussion..... 87

3.5.1 – Diagenetic overprint on $^{87}Sr/^{86}Sr$ ratios..... 87

3.5.1.1 – Dissolution and post-depositional ^{87}Sr..... 87

3.5.1.2 – Fluid–rock interaction..... 91

3.5.2 – Continental origin of pre-Salt carbonates..... 96

3.5.3 – Age constraints of pre-Salt carbonates..... 103

3.5.4 – Consequences for the opening of the CSSA..... 110

3.6 – Conclusions..... 110

Chapter 4..... 112

4.1 – Introduction..... 112

4.2 – Materials and methods..... 116

4.3 – Results..... 119

4.4 – Discussion..... 121

4.4.1 – Strontium isotopes..... 121

4.4.2 – A seawater origin of South Atlantic Salinity Crisis? 126

4.4.3 – Quantifying contribution of seawater entering into the South Atlantic..... 128

4.4.4 – Timing the seawater entrance at the onset of evaporites……..... 132

4.4.5 – New model..... 134

4.4.6 – Cyclic closure of SASC basin or abrupt change in sulphur cycle?..... 137

4.5 – Conclusions..... 138

Chapter 5..... 140

5.1 – Introduction..... 140

5.2 – Geological setting of the Sergipe-Alagoas Basin..... 144

5.3 – Material and methods..... 146

5.4 – Results and discussion..... 154

5.4.1 – The use of bulk $\delta^{13}C_{OM}$ data..... 154

5.4.2 – Carbon-isotope stratigraphy..... 156

5.4.3 – Correlation of the evaporites..... 161

5.5 – Conclusions..... 162

Chapter 6..... 164

6.1 – Introduction..... 164

6.2 – Description of the site..... 169

6.3 – Methods..... 170

6.3.1 – Total inorganic and organic-carbon (TIC, TOC), organic sulphur (S_{OM}) and pyrolysis..... 170

6.3.2 – Carbon and oxygen isotopes from carbonates ($\delta^{13}C_{carb}$ and $\delta^{18}O_{carb}$) 174

6.3.3 – Carbon isotopes from organic matter ($\delta^{13}C_{OM}$) 174

6.3.4 – Calcareous nannofossil biostratigraphy..... 175

6.3.5 – Magnetostratigraphy..... 175

6.3.6 – Re-Os isotope analyses..... 175

6.4 – Results..... 176

6.4.1 – Organic geochemistry (TOC, S_{OM}, HI, OI, Tmax and $\delta^{13}C_{OM}$) 176

6.4.2 – Carbonates (TIC, $\delta^{13}C_{carb}$ and $\delta^{18}O_{carb}$) 178

6.4.3 – Calcareous Nannofossils..... 184

6.4.4 – Magnetostratigraphy..... 188

6.4.5 – Rhenium and osmium isotopes..... 192

6.5 – Stratigraphic revision..... 194

6.5.1 – Sediments deposited in reducing environment 194

6.5.2 – Is the OAE 1a interval recorded in DSDP Site 511? 201

6.5.3 – The transitional environment and the carbon isotope excursion..... 203

6.5.4 – Aptian-Albian transition and the OAE 1b..... 205

6.5.5 – Albian sediments above OAE 1b..... 208

6.5.6 – Late Jurassic–Early Cretaceous environments of deposition on the Falkland Plateau..... 209

6.6 – Conclusions..... 212

Chapter 7..... 215

7.1 – Introduction..... 215

7.2 – Geological setting..... 217

7.3 – Materials and methods..... 219

7.4 – Results..... 221

7.4.1 – Biostratigraphy and Magnetostratigraphy..... 221

7.4.2 – Carbon- and oxygen-isotope stratigraphy..... 222

7.5 – Discussion..... 227

7.6 – Conclusions..... 230

Chapter 8..... 232

8.1 – Summary of the stratigraphic correlations..... 232

8.2 – Environmental evolution of southern Brazilian basins..... 234

8.3 – Relationship between Ontong Java Plateau, absolute ages and evaporite deposits in the southern segment of the South Atlantic..... 235

8.4 – Future directions..... 236

Appendix A..... 239

Appendix B..... 260

Appendix C..... 262

Appendix D..... 272

Appendix E..... 320

Bibliography..... 322

Chapter 1

Introduction

The Cretaceous Period in the Mesozoic Era is divided in the Early Cretaceous and Late Cretaceous, in which the Early Cretaceous (~145–100.5 Ma) has six stages: Berriasian, Valanginian, Hauterivian, Barremian, Aptian and Albian (Ogg et al., 2012) (Figure 1.1). The Aptian and Albian stages are critical time intervals for global palaeoceanography, since fundamental changes took place in the ocean-atmosphere system. These changes include: 1) the opening of the central segment of the South Atlantic with large-scale deposition of gypsum and halite (Torsvik et al., 2009; Moulin et al., 2010; Blaich et al., 2011); 2) periods when unusually large amounts of organic matter were preserved as marine 'black shales' during oceanic anoxic events: OAEs 1a to 1d (Arthur et al., 1990; Jenkyns, 2010); 4) huge events of oxygenation in marine bottom waters generating Cretaceous oceanic red beds (Hu et al., 2012a); 5) high ocean crust production rate (Larson, 1991a); 6) rapid biotic radiations and turnovers (Erba et al., 1999; Leckie et al., 2002; Huber and Leckie, 2011); 7) the beginning of the geomagnetic event with the longest normal-polarity interval called Superchron C34n (Helsley and Steiner, 1968; Ogg, 2012) and; 8) greenhouse conditions punctuated by 'cold snaps' (Föllmi, 2012; McAnena et al., 2013; Bottini et al., 2015).

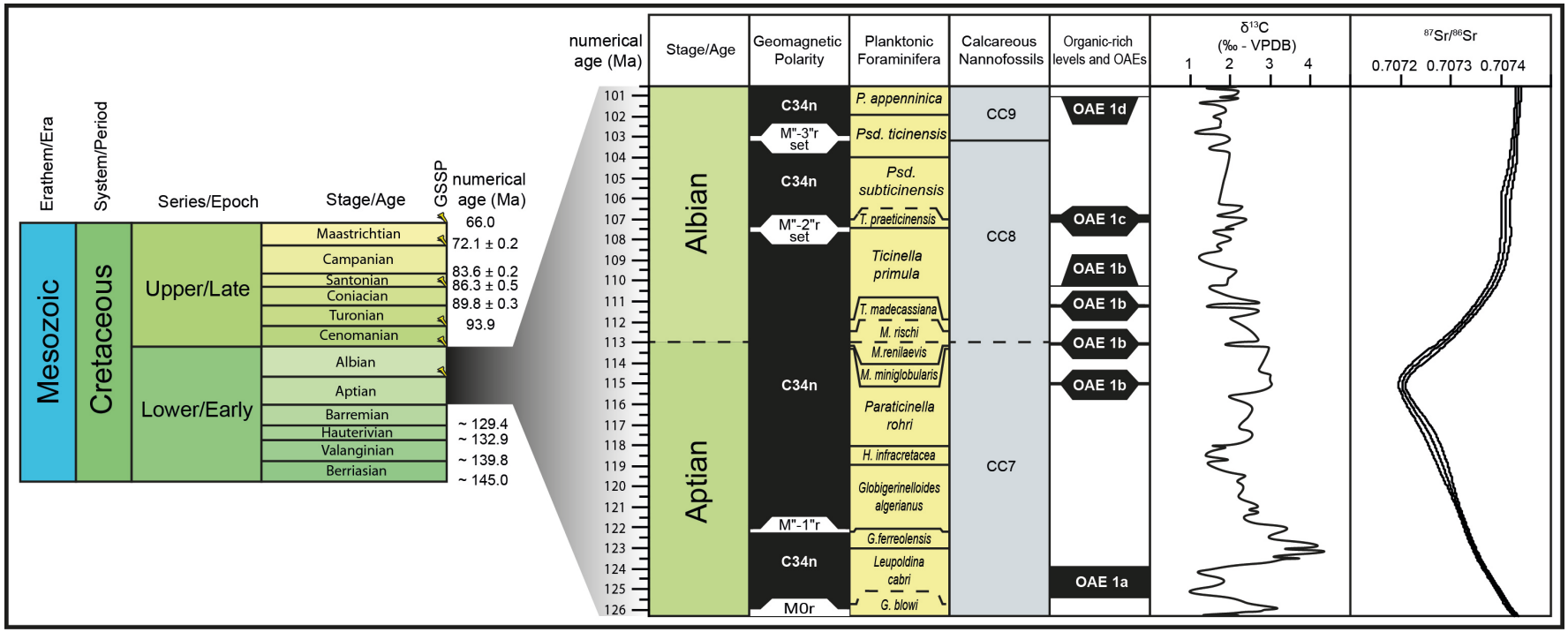


Figure 1 .1 –Aptian and Albian stages of the Lower/Early Cretaceous modified from the latest International Chronostratigraphic Chart (Cohen et al., 2013; updated 2016) and major stratigraphic events. The numerical ages in the left side are from Cohen et al. (2013; updated 2016). The yellow marks in the left-hand table show the limits with Global Boundary Stratotype Sections and Points (GSSPs). Absolute ages from the Aptian and Albian, geomagnetic polarity, Tethyan ammonoids, planktonic foraminifera, calcareous nannofossils, OAEs (oceanic anoxic events) and carbon-isotope curve ($\delta^{13}C$) are from Ogg et al. (2012) and references therein. The planktonic foraminiferal zone *Paraticinella eubejaouaensis* was replaced by *Paraticinella rohri* (Ando et al., 2013). Strontium-isotope curve ($^{87}Sr/^{86}Sr$) is from McArthur et al. (2012). *G.* – *Globigerinelloides*, *H.* – *Hedbergella*, *M.* – *Microhedbergella*, *T.* – *Ticinella*, *Psd.* –*Pseudothamanninella*, *P.* – *Parathalmanninella.*

This thesis mainly considers the significance of the stratigraphic correlation between the opening of the central segment of the South Atlantic and OAEs. Chemostratigraphy based on carbon-, sulphur- and strontium-isotopes ($\delta^{13}C$, $\delta^{34}S$ and $^{87}Sr/^{86}Sr$), integrated with other methods (magneto- and biostratigraphy and Re-Os geochronology), is used to explore possible causal links between these apparently disparate phenomena, specifically to constrain the causal links in the Aptian–Albian interval.

1.1 Definitions of the Aptian and Albian

The base of the Aptian has been defined as the base of the magnetic reversal polarity M0r. However, its absolute age is still a matter of debate (He et al., 2008; Ogg et al., 2012). For example, Malinverno et al. (2012) proposed an age of 121 Ma for the base of M0r assuming uniformly varying spreading rates of oceanic crust, whereas the Geological Time Scale 2012 defines its age as 126.3 ± 0.4 Ma (Ogg et al., 2012) and the International Commission on Stratigraphy put the base of M0r as ~125 Ma (Cohen et al., 2013; updated 2016) based on stratigraphic correlation of radiometric ages from supposed reversal Chron M0r from extrusive rocks, and recognition of Chron M0r in well-defined sedimentary successions calibrated by bio-, magneto- and cyclostratigraphy (Figure 1.2). The divergent time scales of Malinverno et al. (2012) and Ogg et al. (2012) have been used in palaeoenvironmental studies on the Aptian (e. g., Bottini et al., 2015; Erba et al., 2015; Figure 1.2). The base of the Aptian does not have a Global Boundary Stratotype Section and Point (GSSPs, yellow marks in Figure 1.1) and the Gorgo a Cerbara section in Italy is the main candidate at the present time.

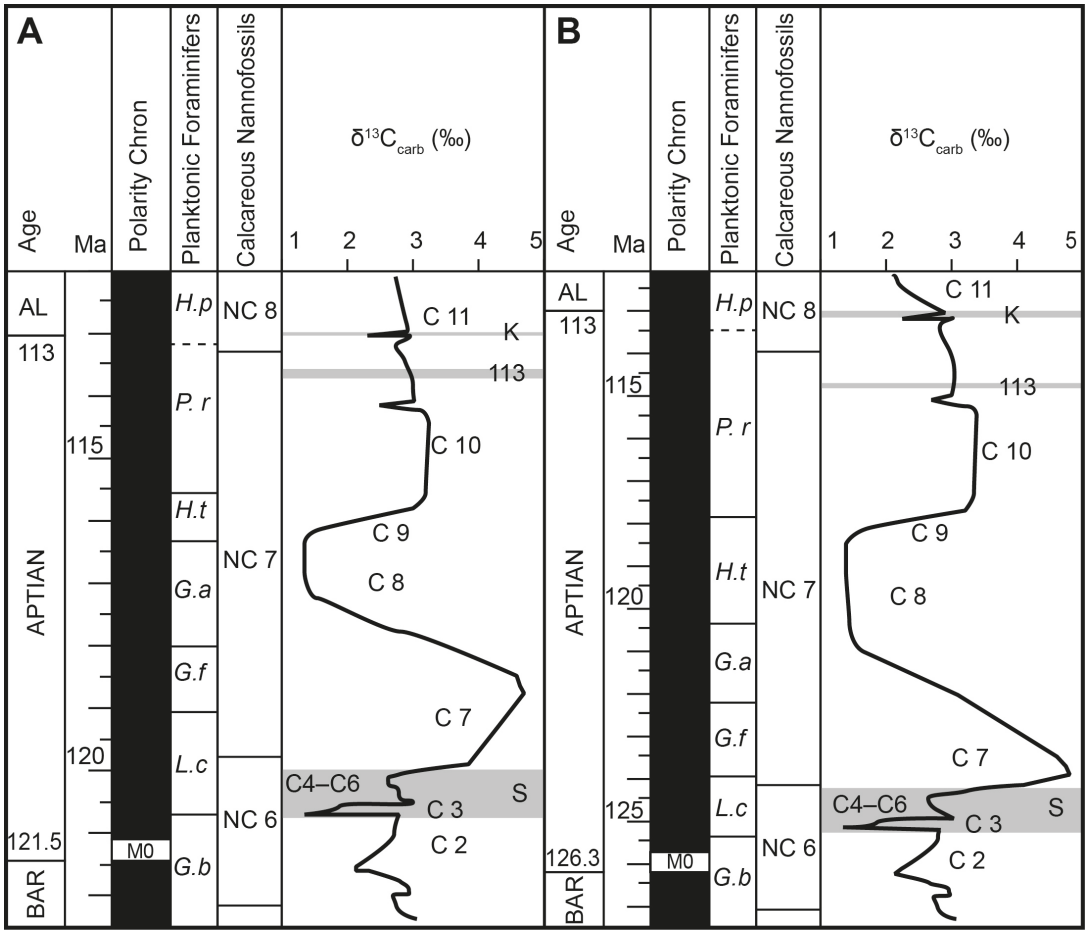


Figure 1 .2 – Latest Barremian (BAR) to earliest Albian (AL) magnetostratigraphy, planktonic foraminifera and calcareous nannofossils biostratigraphy and carbon-isotope stratigraphy on two different time scales: A – Malinverno et al. (2012) and B – Gradstein et al. (2012), according to Erba et al. (2015) and references therein. In both schemes the durations across the latest Barremian to the top of the NC6 nannofossil zone is based on astrochronology of Malinverno et al. (2010). The planktonic foraminiferal zone *Ticinella bejaouaensis* was replaced by *Paraticinella rohri – P. r* (Ando et al., 2013). C-segments are after Menegatti et al. (1998) and Bralower et al. (1999). K – Niveau Kilian; 113 – Livello 113; S – Selli Level (OAE 1a) is indicated by a grey band. *G. b – Globigerinelloides blowi*; *G. a – Globigerinelloides algerianus*; *L. c – Leupoldina cabri*; *G. f – Globigerinelloides ferreolensis*; *H. t – Hedbergella trocoidea*; *H. p – Hedbergella planispira*.

The base of the Albian has been defined by the first appearance datum (FAD) of the planktonic foraminifer *Microhedbergella renilaevis*, in which the Col de Pré-Guitard section, France, is the most recent GSSP candidate (Petrizzo et al., 2012;

Kennedy et al., 2014). The most recent International Commission on Stratigraphy Chart 2016 shows the presence of the GSSP for the base of the Albian (Cohen et al., 2013; updated 2016), although the ratifying paper has not been published. On the other hand, the base of the Cenomanian, which limits the top of the Early Cretaceous, has a GSSP in the Mont Risou, Hautes-Alps, France, where it has been defined as the FAD of the planktonic foraminifer *Thalmanninella globotruncanoides*, at 100.5 ± 0.4 Ma (Kennedy et al., 2004; Ogg et al., 2012).

1.2 Introduction to chemostratigraphy

1.2.1 Carbon isotopes

Carbon-isotope ratios arranged in stratigraphic order can show fluctuations that may be used as a correlation tool between different sections when validated by other stratigraphic methods, such as magneto- and biostratigraphy (Scholle and Arthur, 1980). This method, also called carbon-isotope stratigraphy, has been applied in high resolution in many studies, where the carbon is derived from pelagic sediments, shallow-water marine carbonates, terrestrial organic matter and specific compounds from organic matter. Particularly for the Early Cretaceous, this methodology has been incorporated to the latest geological time scales (e. g., Weissert and Lini, 1991; Jenkyns et al., 1994; Jenkyns, 1995; Menegatti et al., 1998; Gröcke et al., 1999; Méhay et al., 2009; Tiraboschi et al., 2009; Jenkyns, 2010; Saltzman and Thomas, 2012; Erba et al., 2015).

Carbon-isotope data are generally expressed as $\delta^{13}C$, which shows the variation of the ratio $^{13}C/^{12}C$ from one sample compared to a standard, expressed in

per thousand units (‰), where the Vienna Pee Dee Belemnite (VPDB) standard has been widely used for reporting $\delta^{13}C$ values that can be measured in organic matter ($\delta^{13}C_{OM}$) and carbonates ($\delta^{13}C_{carb}$) (Sharp, 2007). $\delta^{13}C_{OM}$ and $\delta^{13}C_{carb}$ profiles usually show parallel trends (e. g., Menegatti et al., 1998). Although the absolute $\delta^{13}C$ values change from place to place, the curves usually have the same trend in specific intervals of time, which allows for inter-continental correlation (Saltzman and Thomas, 2012).

Fluctuations of $\delta^{13}C$ are a function of the carbon cycle as described by Saltzman and Thomas (2012) and references therein. Precipitation of biogenic and inorganic carbonates involves little carbon isotopic fractionation relative to dissolved inorganic carbon (DIC) with $\delta^{13}C$ of ~ 0‰ in deep modern oceans. Hence, $\delta^{13}C$ values from DIC in deep oceans are similar to $\delta^{13}C$ values from carbonates, which are the largest reservoir in the modern ocean-atmosphere system. Carbon is also present in the atmosphere mainly as carbon dioxide with $\delta^{13}C$ of –6.4‰, prior to anthropogenic fossil-fuel burning, which is close to the mantle value ($\delta^{13}C$ = ~ –5/6‰). The atmospheric reservoir was 50 to 60 times smaller than deep oceanic DIC reservoir in pre-industrial times. The lithosphere contains carbonate rocks (limestones and dolomites) and organic matter (e. g., oil, coal, black shales). Photosynthesis is the process responsible for the largest fractionation of carbon isotopes, whereby carbon dioxide is fixed in organic carbon, which is strongly depleted in ^{13}C: C3 and C4 plants, for example, use different photosynthetic pathways have mean $\delta^{13}C$ of –26 and –13‰, respectively. The exchange between lithospheric carbon and the carbon present in the ocean-atmosphere system occurs in time scales of 10^5–10^6 years (long-term cycle), which is much longer than the carbon

cycling between the ocean and the atmosphere of $<10^3$ years (short-term cycle). The $\delta^{13}C$ values from carbonates and organic matter through geological time are a function of the changes in the size and rate of the exchange of fluxes between the Earth-surface carbon reservoirs and the lithosphere in the long-term cycle, specifically storage in the lithosphere of varying amounts of organic carbon and carbonates. Presently, the flux from the oceans into calcium carbonate is about 4 times as large as the flux of carbon into organic matter. However, if relative fluxes change, the $\delta^{13}C$ values of the whole ocean DIC, and consequently $\delta^{13}C$ values from carbonates and organic matter, change also. For example, when there is increased net deposition of organic matter globally, the $\delta^{13}C$ value of DIC in the whole ocean increases, and carbonates and organic matter, deposited under this new atmosphere-ocean system, will have heavier $\delta^{13}C$ values. As the DIC reservoir is much larger than the atmospheric one, the isotopic composition of the atmosphere also changes and can be recorded in terrestrial organic matter, including wood, plant remains and lacustrine materials (e. g., Gröcke et al., 1999; Xu et al., 2017).

Figure 1.1 shows the $\delta^{13}C_{carb}$ curve during the Aptian–Albian interval present in the time scale of Ogg et al. (2012), where there is a negative excursion in the Early Aptian followed by two positive excursions. Small excursions are present around the Aptian-Albian boundary and the carbon-isotope signature of the Middle to Upper Albian shows fluctuations generally less than 1.5‰ (Ogg et al., 2012). This pattern has been recognized in the Tethyan realm, the North Atlantic and the Pacific Oceans (Bralower et al., 1999; Herrle et al., 2004; Giorgioni et al., 2012; Bottini et al., 2015; Erba et al., 2015).

The use of carbon-isotope data has its limitations. $\delta^{13}C_{carb}$ signatures could in part reflect diagenetic rather than depositional signals. For example, the incorporation of isotopically light carbon (^{12}C) from meteoric waters derived from soils developed on shallow-water carbonates or from pore waters derived from marine early diagenetic sulphate reduction or anaerobic methane oxidation, can take place (Hudson, 1977; Raiswell, 1988; Saltzman and Thomas, 2012). Therefore, negative isotope excursions must be examined, case by case, and when multiple sites show the same negative signatures and/or are also corroborated by negative excursions in $\delta^{13}C_{OM}$, the stratigraphic value is reinforced (e. g., Scholle and Arthur, 1980; Menegatti et al., 1998). Cross-plots between carbon and oxygen isotopes can also be used to check whether the samples have been altered by meteoric-water or burial diagenesis because the oxygen isotopic system is more likely to have been affected by such processes (involving water) than are carbon isotopes. The lack of correlation usually indicates that carbon isotopes have not been significantly diagenetic altered (Hudson, 1977; Jenkyns et al., 1994).

Other limitations include the fact that carbon-isotope stratigraphy simply does not always work, as observed in synchronous carbonate deposition involving different quantities of calcite and aragonite (Swart and Eberli, 2005; Swart, 2008). Hence, age-calibrated sections from different regions are necessary to identify carbon-isotope excursions that reflect changes in the Earth system, rather than local watermasses or differential mineralogies (Scholle and Arthur, 1980; Saltzman and Thomas, 2012). The use of $\delta^{13}C_{OM}$ data also can be misinterpreted if changes in the type of organic matter occur. For example, if a stratigraphic section represented by sediments deposited from a drainage area from one area with C3 plants ($\delta^{13}C_{OM}$ of

~ –26‰) is overlain by sediments that include drainage of C4 plants with $\delta^{13}C_{OM}$ of ~ –13‰, the carbon-isotope excursion will show a positive excursion that reflects local conditions rather than changes in the ocean-atmosphere system. Other types of source mixing are possible due to changes over time in the relative contribution of planktonic organisms, that fractionate differently, that go to make up bulk marine organic matter. Under these circumstances, compound-specific carbon-isotope analysis should more faithfully reflect the ocean-atmosphere signal.

1.2.2 Sulphur isotopes

Sulphur-isotope stratigraphy has also been refined over recent decades, as described for carbon isotope stratigraphy. The first age curve for sulphur isotopes from marine sulphates (anhydrite and gypsum) was first published in 1980 (Claypool et al., 1980). After that, records derived from sulphates, barite and carbonate-associated sulphate expanded the understanding of sulphur-isotope stratigraphy, whereas records of pyrite, involving complex microbial transformations are more ambiguous (Paytan et al., 2004, 2011; Paytan and Gray, 2012). Sulphur-isotope data are generally expressed as $\delta^{34}S$ that represents the ratio $^{34}S/^{32}S$ in the sample, similarly to $\delta^{13}C$, and expressed in parts per thousand units (‰) usually relative to the Vienna Canyon Diablo Troilite (VCDT) standard (Sharp, 2007).

Fluctuations of $\delta^{34}S$ are a function of the sulphur cycle as described by Paytan and Gray (2012) and references therein. The method is valid for marine environments, whereas continental environments may have $\delta^{34}S$ values different from seawater. Sulphur is mainly present as sulphate in the modern ocean, which is the second most abundant marine ion with an average concentration of 28 mmol/kg

($\delta^{34}S$ = 21.0 ± 0.2‰). The relative proportion of sulphide and sulphates input and removal from the oceans and their isotopic compositions controls the isotopic composition of sulphates. Sulphur is commonly present in seawater and marine sediments in one of two redox states: dissolved sulphate and sulphate minerals (oxidized form) that have $\delta^{34}S$ values similar to those of sulphate dissolved in seawater, usually equal or < 2‰ heavier than seawater; and H_2S and sulphide minerals (reduced form, typically pyrite) generally depleted that have average $\delta^{34}S$ of ~ –15‰, but with a wide range of values. The latter values are a result of the strong sulphur-isotope fractionation involved in bacterial sulphate reduction, the precursor of sulphide mineral formation. The largest modern input is from river run-off from the continent ($\delta^{34}S$ = 0–10‰) and isotopic ratios depend on relative amount of sulphates and sulphides in the catchment areas. Volcanism and hydrothermal activity input have $\delta^{34}S$ of ~ 0‰. The output flux is via deposition of sulphate minerals and sulphides. The relative rate of burial of reduced and oxidized sulphur is likely to have changed throughout the geological time, consequently affecting $\delta^{34}S$ from dissolved sulphate in seawater and sulphate minerals.

The $\delta^{34}S$ records from sulphates, barite and carbonate-associated sulphate shows an important drop in values in the Early Aptian from ~19‰ to ~15.5‰ (see Figure 2.2 in Chapter 2) (Paytan et al., 2004; DeBond et al., 2012; Paytan and Gray, 2012; Wortmann and Paytan, 2012; Gomes et al., 2016). Consequently, sulphur-isotope stratigraphy is potentially useful for this interval of time.

Complications in using sulphur-isotope stratigraphy arise from diagenetic artefacts that can modify $\delta^{34}S$ values of carbonate-associated sulphate by incorporating isotopically modified sulphur from pore fluids during lithification

and/or recrystallization. Barite can be problematic because, as well as precipitating within the water column in equilibrium with ambient seawater, it can form diagenetically in organic-carbon bearing sediments where sulphate reduction drives dissolution-reprecipitation of barite crystals; this mineral can also be hydrothermal (Turchyn et al., 2009; Paytan and Gray, 2012). The use of sulphate minerals from non-marine environments with $\delta^{34}S$ values different from contemporaneous seawater also can be misinterpreted and misused in sulphur-isotope stratigraphy, although restricted environments connected to seawater are likely to have contemporaneous marine $\delta^{34}S$ values (Denison et al., 1998).

1.2.3 Strontium isotopes

Strontium isotopes are usually represented as the $^{87}Sr/^{86}Sr$ ratios in strontium-isotope stratigraphy, in contrast to carbon and sulphur isotopes that are expressed in parts per thousand. The $^{87}Sr/^{86}Sr$ ratios must be reported with respect to a standard, of which SRM 987 with an agreed value of 0.710248 is recommended (McArthur et al., 2012). Because $^{87}Sr/^{86}Sr$ ratios are obtained in mass spectrometers where isotopic fractionations occur, corrections must be performed by using another isotopic ratio, namely an $^{88}Sr/^{86}Sr$ ratio of 0.1194, which also removes any natural fractionation (Krabbenhöft et al., 2010; McArthur et al., 2012).

The first Phanerozoic $^{87}Sr/^{86}Sr$ isotopic curve used for strontium-isotope stratigraphy was obtained in 1982 (Burke et al., 1982), although earlier studies have shown that $^{87}Sr/^{86}Sr$ ratios of seawater varied throughout geological time (e. g., Peterman et al., 1970; Veizer and Compston, 1974). The amount of $^{87}Sr/^{86}Sr$ data incorporated to a 'standard curve' has increased through time and extended to the

Precambrian (Veizer et al., 1997, 1999; Prokoph et al., 2008; McArthur et al., 2012). The method works only for marine minerals, as described by Allègre et al. (2010) and McArthur et al. (2012) and references therein. It is based on the fact that marine strontium residence time (~10^6 years) is long compared to the mixing time of the oceans (~10^3 years). Consequently, the oceans are well mixed on time scales that are short relative to the rates of gain and loss of strontium and the ratio $^{87}Sr/^{86}Sr$ is globally homogeneous. It is important to note that $^{87}Sr/^{86}Sr$ ratios from modern seawater and shells are uniform and with value of 0.70920 ± 0.00002 (2σ) even considering inland seas such as the Sea of Azov and Black Sea (Kuznetsov et al., 2012). Over geological time scales, this ratio has changed. The main reasons for that is the change in rates of continental weathering, island-arc weathering, and hydrothermal circulation through oceanic crust in the oceans, releasing Sr with different ratios (Burke et al., 1982; Banner, 2004; Allègre et al., 2010; McArthur et al., 2012). A lower $^{87}Sr/^{86}Sr$ ratio (~0.703) is typical of fluids from mantle-derived rocks whereas riverine input comes with higher $^{87}Sr/^{86}Sr$ ratio (~0.7136) from weathering of silicic continental crust (Burke et al., 1982; Banner, 2004; Allègre et al., 2010; McArthur et al., 2012).

Turning to the Aptian and Albian, $^{87}Sr/^{86}Sr$ ratios have been obtained from bulk shallow-marine carbonates, deep-sea carbonates, inoceramids, planktonic foraminifera and belemnites (Jenkyns et al., 1995; Bralower et al., 1997; Yamamoto et al., 2013; Bodin et al., 2015). $^{87}Sr/^{86}Sr$ ratios show a trend of decreasing values through the Aptian from ~0.70745 at its base to ~0.70715 to its top, returning to ~0.70745 in the Early Albian, and relatively constant up to the limit with the Cenomanian (Figure 1.1). Higher $^{87}Sr/^{86}Sr$ ratios than those of contemporaneous

seawater are likely to be diagenetic artifacts (Denison et al., 1994) or represent continental environments dominated by more radiogenic values.

The use of pristine fossils such as calcitic belemnites, brachiopods, inoceramid prisms, aragonitic ammonites, very clay-poor atoll carbonates are recommended, whereas bulk limestones usually contain impurities, mainly clays, that can affected measured $^{87}Sr/^{86}Sr$ ratios (McArthur et al., 2012). However, pre-leaching procedures have been shown to be successful in decreasing contamination (Bailey et al., 2000).

1.3 Introduction to oceanic anoxic events (OAEs)

Oceanic anoxic events (OAEs) are periods when an expanded oxygen-minimum zone characterized many mid- to deep- water environments so that unusually large amounts of organic matter were preserved as marine 'black shales' (Schlanger and Jenkyns, 1976; Jenkyns, 2010). Records of OAEs are recognized by the presence of typical 'black shales' and/or carbon-isotope signatures (Jenkyns, 2010). Firstly they were recognized as OAEs 1 (Aptian–Albian) and 2 (Cenomanian–Turonian) (Schlanger and Jenkyns, 1976). With the advances of improved stratigraphic characterization, OAE 1 was subsequently split into four sub-events called 1a to 1d, and a Jurassic event was recognized also in the Toarcian (T-OAE) (Jenkyns, 1980, 1988; Arthur et al., 1990; Jenkyns, 2010). The three major important OAEs of the Mesozoic are the T-OAE (~183 Ma), the Early Aptian OAE 1a (~120 Ma), and the Cenomanian–Turonian OAE 2 (~93.6 Ma). In addition, there are other significant events such as OAE 1b (~112 Ma) that includes a number of events

around the Aptian-Albian boundary that appear to have a more parochial sedimentary record (Bréhéret, 1994; Leckie et al., 2002; Jenkyns, 2010).

The Early Aptian OAE 1a has been recognized by its characteristic negative carbon-isotope excursion followed by the onset of a positive excursion, originally divided into stratigraphic segments C3–C6 (Menegatti et al., 1998). Isotopic records exist in carbonates and organic matter from pelagic and hemipelagic sediments in several Tethyan locations such as Roter Sattel (Switzerland), Cismon section and core (northern Italy), Calabianca section (Sicily, Italy), Lower Saxony Basin (northwest Germany), Roquefort-La Bédoule (southeast France), Yenicesihlar section (central Turkey) (Menegatti et al., 1998; Erba et al., 1999; Bellanca et al., 2002; Kuhnt et al., 2011; Hu et al., 2012b; Pauly et al., 2013). In addition, similar patterns in $\delta^{13}C$ logs obtained from organic matter and shallow-water carbonates have also been recorded in Pacific deep-sea drilling sites and in an allochthonous terrain in California (Jenkyns and Wilson, 1999; Ando et al., 2002; Robinson et al., 2008). The massive volcanism that formed the Ontong Java Plateau has been suggested as the driving force behind widespread ocean anoxia during OAE 1a, based on palaeoecological evidence from calcareous nannofossils and osmium-isotope ratios of Lower Aptian sediments (Erba, 1994; Larson and Erba, 1999; Tejada et al., 2009; Bottini et al., 2012; Erba et al., 2015). The Ontong Java Plateau forced the rapid increase of atmospheric pCO_2, triggering a cascade of palaeoenvironmental changes affecting plankton productivity and carbon flux to the sea floor (Méhay et al., 2009; Jenkyns, 2010; Erba et al., 2015; Naafs et al., 2016), and increased global temperature (Bottini et al., 2015; Naafs and Pancost, 2016). These changes led to the deposition locally of thick, laminated, organic-rich black

shales to form an interval known as the "Selli Level" and its correlatives (Coccioni et al., 1987).

Significantly, this excursion towards lower $\delta^{34}S$ around the OAE 1a is decoupled from the positive excursion observed in $\delta^{13}C$ worldwide, which is unexpected because large-scale burial of ^{12}C-rich organic matter is usually associated with ^{32}S-rich sulphide burial, as observed in the T-OAE and OAE 2 (Gill et al., 2011; Owens et al., 2013). The extent of preservation of organic matter in the marine environment could have been globally enhanced because of the reduction of dissolved seawater sulphate as a consequence of massive gypsum ($CaSO_4$) burial during evaporite deposition in the South Atlantic (Wortmann and Chernyavsky, 2007).

The records of OAE 1b are a matter of debate, because a cluster of four negative carbon-isotope excursions and/or organic rich-levels, or just one or three of them, has been described as the OAE 1b equivalent (e. g., Leckie et al., 2002; Herrle et al., 2004) (Figure 1.1). The organic-rich levels were originally recognized in the Vocontian Basin, France and named Jacob, Kilian, Paquier and Leenhardt levels in ascending stratigraphic order (Bréhéret, 1994) and are recognized elsewhere in the Tethyan and North Atlantic regions by typical lithological features or carbon-isotope excursions (e. g., Herrle et al., 2004; Trabucho Alexandre et al., 2011; Coccioni et al., 2014) (Figure 1.1). Biostratigraphy indicates that the Jacob level, also called 113 level, is Late Aptian in age, occurring below the lowest occurrence (LO) of the nannofossil *Prediscosphaera columnata* within the planktonic foraminifera *Paraticinella rohri* biozone (Coccioni et al., 2014; Erba et al., 2015). The Kilian level coincides with the LO of the planktonic foraminifera *Microhedbergella*

renilaevis, and stratigraphically above the LO of *P. columnata* (Petrizzo et al., 2012; Kennedy et al., 2014). The Paquier and Leenhardt levels occur above the Kilian level, within the planktonic foraminiferal *Microhedbergella rischi* zone (Herrle et al., 2004; Coccioni et al., 2014). All these four levels show negative carbon-isotope excursions (Herrle et al., 2004; Trabucho Alexandre et al., 2011; Coccioni et al., 2014). OAE 1b has been associated with an increase in surface-water temperatures and runoff that led to decreased bottom-water formation and increased thermohaline stratification and productivity, permitting elevated carbon burial in the restricted basins of the western Tethys and North Atlantic (Erbacher et al., 2001; Herrle et al., 2003).

1.4 The opening of the central segment of the South Atlantic

The emplacement of the first oceanic crust or the break-up of the South Atlantic have been extensively studied to understand an evolution that started during the Jurassic in the Falkland Segment and continued northwards up to the Equatorial Segment throughout the Early Cretaceous (Rabinowitz and LaBrecque, 1979; Torsvik et al., 2009; Moulin et al., 2010) (Figure 1.3). Magnetic lineaments from oceanic crust are used to define the timing of the break-up from the Falkland Plateau up to the northern limit of the Austral/South Segment at the Walvis Ridge, and also in the northern part of the South Atlantic at latitudes to the north of the Demerara Rise/Guinea Plateau. However, the break-up of the central segment of the South Atlantic (CSSA) occurred during the long-lasting normal-polarity interval called the Cretaceous Normal Polarity Superchron (CNPS or C34n) that ranged from the

Aptian to the Santonian and lacks well-documented magnetic anomalies (Rabinowitz and LaBrecque, 1979; Torsvik et al., 2009; Moulin et al., 2010).

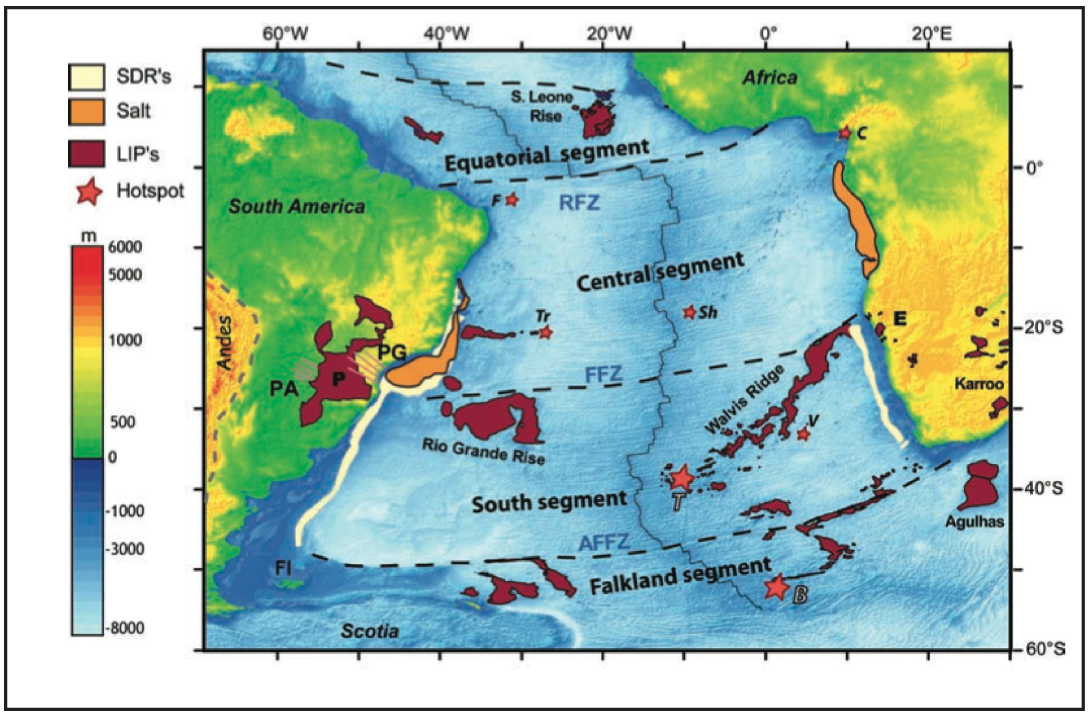


Figure 1 .3 –General structural map of the South Atlantic Ocean draped on a topographic/bathymetric map from GTOPO 30 (Torsvik et al., 2009). Boundaries between the four segments (Equatorial, Central, South and Falkland) are shown by dotted lines (RFZ, Romanche Fracture Zone; FFZ, Florianopolis Fracture Zone; AFFZ, Agulhas – Falkland Fracture Zone). Aptian salt basins (orange), LIPs (P, Parana; E, Etendeka; Karroo, Sierra Leone Rise and Agulhas), Seaward Dipping Reflectors (SDRs, white) and active hotspots (F, Fernando; C, Cameroon; Tr, Trinidade; Sh, St Helena; T, Tristan; V, Vema; B, Bouvet (Meteor) are also shown. PG, Ponta Grossa Dyke System; PA, Paraguay Dyke system; FI, Falkland Islands.

The stratigraphic records are different throughout the South Atlantic. For example, marine environments were established in the Falkland Plateau as early as the mid-Jurassic (Ludwig et al., 1983), whereas the rifting phase of the CSSA, with its continental sediments, started in the Early Cretaceous (~130 Ma) and the first main marine excursion occurred around Aptian–Albian time (Koutsoukos, 1989;

Mizusaki et al., 1992; Koutsoukos et al., 1993; Dias, 1998; Bengston et al., 2007; Moreira et al., 2007; Winter et al., 2007).

One striking feature in the stratigraphy of the CSSA is the presence of evaporites (also informally termed 'Salt') in offshore Brazilian and African basins (e. g., Torsvik et al., 2009; Chaboureau et al., 2012; Chaboureau et al., 2013). The volume of salt in the southern Brazilian basins (Espírito Santo, Campos and Santos Basins) are estimated to be *c.* 4.6×10^{14} m^3, which approximates to 2% of the salt contained in the ocean at the present time (Davison et al., 2012). These figures do not take into account the volumes present in the northern Brazilian basins and African counterparts. The evaporite deposits lie above continental basement and have been interpreted as having formed pre-break-up of the CSSA, based on seismic lines (Torsvik et al., 2009; Moulin et al., 2010; Blaich et al., 2011), although some authors interpret part of the evaporites as having been deposited during the break-up itself (Norton et al., 2016).

The evaporites in Brazilian basins have been interpreted as deposited in a transitional environment following formation of volcanic and siliciclastic/carbonate rocks deposited during the rift and post-rift phases (Dias, 1998; Campos Neto et al., 2007; Moreira et al., 2007; Winter et al., 2007; Chaboureau et al., 2013). Some of the sub-salt carbonates deposited in the southern Brazilian basins, also called pre-Salt carbonates in the literature, have proved controversial in terms of environment: are they marine or continental? (e. g., Dias, 1998; Wright, 2012; Sabato Ceraldi and Green, 2017). These unusual facies have revolutionized the hydrocarbon prospectivity of the region. For example, the Tupi (Lula) and Iara Fields in the

Santos Basin are among the largest oil fields discovered in recent decades with reserves of more than 3 billion of barrels of oil (Mohriak et al., 2012).

The age of the pre-Salt carbonates and evaporites has also been debated. The evaporite deposits are overlain by carbonates with Lower Aptian ammonites and Upper Aptian foraminifera fauna in the Sergipe-Alagoas Basin in the northeast of Brazil (Bengston et al., 2007; Koutsoukos, 1989; Koutsoukos et al., 1993). On the other hand, the evaporite deposits from the southern Brazilian basins are overlain by shallow-marine platform carbonates containing limited planktonic foraminiferal species that are not age-diagnostic (e. g., *Favusella* ex grege *washitensis*; Azevedo, 1987). Following platform drowning, deeper water sediments accumulated, in which calcareous nannofossils (e. g., *Nannoconus truittii*) and planktonic foraminifera (e. g., *Ticinella raynaudi*) are present, and these have been used to constrain these deeper water sediments to be Albian in age (Azevedo et al., 1987). Supposedly extrusive rocks with Ar-Ar ages of 117 Ma (cited in Moreira et al., 2007) and 113.2 ± 0.1 Ma (cited in Dias et al., 1994) stratigraphically below the evaporites led to the view that the South Atlantic evaporites were deposited between 116–111 Ma in the Late Aptian–earliest Albian interval and post-evaporite shallow-marine platform carbonates were deposited in the Albian (Davison, 2007; Chaboureau et al., 2013; Gomes et al., 2016; timescale of Ogg et al., 2012).

1.5 Aims and description of chapters

The first aim of this project is to improve the stratigraphy for selected sections of Lower Cretaceous successions in the South Atlantic and Tethys by using chemostratigraphy based on carbon-, sulphur- and strontium-isotopes integrated with

other stratigraphic methods (magneto- and biostratigraphy, and Re-Os geochronology) and correlate these sections against the relevant age-calibrated curves obtained by previous workers (from biostratigraphically well-characterized sections). The second aim of this project is to explore causal links between the opening of the central segment of the South Atlantic and OAEs.

Chapter 2 presents new $\delta^{13}C$ and $^{87}Sr/^{86}Sr$ profiles, constrained by planktonic foraminiferal biostratratigraphy, from Petrobras Well CB-3, Campos Basin. Correlation is made between $\delta^{13}C$ profiles of a composite carbon-isotope curve from the Campos and Santos Basins as well as an age-calibrated Tethyan reference curve. The newly obtained stratigraphy of the South Atlantic indicates synchrony between major evaporite deposition and the OAE 1a interval (125.51–124.41 or 120.21–119.11 Ma; Erba et al., 2015 and reference therein). This correlation implies that the evaporites are significantly older than their former suggested age of 116–111 Ma. The stratigraphic revision suggests that deposition of the South Atlantic evaporites took place after the release of massive amounts of CO_2 and SO_2 during the formation of the Ontong Java Plateau Large Igneous Province (LIP) and may have removed massive amounts of sulphate from the world ocean, hence fostering important palaeoceanographic changes during and after OAE 1a.

Chapter 3 describes $^{87}Sr/^{86}Sr$ data obtained from ostracods and bulk rock from sub-evaporite (also called pre-Salt) rocks from Petrobras Wells A and B (Santos Basin) and C (Campos Basin), and Re-Os geochronology of a sample at the top of the pre-Salt carbonates from Petrobras Well B. Geochemical evidence suggests that the pre-Salt carbonates in the southern Brazilian basins were deposited in a continental setting until the onset of evaporite precipitation. The fluids that fed

the lakes are suggested to have derived from rivers and groundwaters draining felsic and feldspar-bearing siliciclastic rocks exposed on the flanks of the basin. The overall stratigraphy constrains the processes of sea-floor spreading to have taken place after deposition of these dominantly lacustrine carbonates. The new Re-Os age of 117.5 ± 2.5 Ma from an organic-rich carbonate, sampled ~0.3–0.5 m below the base of the evaporites in Petrobras Well B from the Santos Basin, is compatible with the stratigraphic correlation presented in Chapter 2, linking deposition of the upper part of the pre-Salt carbonates, and the evaporites themselves, with OAE 1a.

Chapter 4 presents new $^{87}Sr/^{86}Sr$ ratios and $\delta^{34}S$ values of anhydrites from the Santos Basin and Hg/TOC ratios from pre-Salt carbonates from Petrobras Well A. New $^{87}Sr/^{86}Sr$ measurements of anhydrites from the Santos Basin yield higher values than contemporaneous Aptian seawater but lower than the estimated continental input. This study suggests a rapid entrance of seawater into the South Atlantic basin post-dating deposition of pre-Salt carbonates. However, it was not possible to decide whether or not the development of fully marine conditions corresponded in time to the base or the top of the evaporites. Relatively elevated Hg/TOC ratios within the carbonates ~1.4 m below the evaporite base suggest an input of volcanic Hg and imply a possible link with the main eruption(s) of the Ontong Java Plateau. This event could have triggered a eustatic sea-level rise and the first entrance of seawater into the South Atlantic basin. The cyclic pattern recognized in the evaporites of gypsum/halite/more soluble salts are likely to have been driven by aquifer-eustasy in the (supposedly ice-free) Cretaceous greenhouse climate. $\delta^{34}S$ values at the base of South Atlantic evaporites have the same values as contemporaneous global Aptian

seawater and support an OAE 1a age equivalency with the onset of evaporite deposition.

A new record of OAE 1a based on $\delta^{13}C$ derived from organic matter in the Sergipe-Alagoas Basin, northeast Brazil is presented in Chapter 5. The deposition of siliciclastic rocks in the Sergipe-Alagoas Basin, in the northern part of the central segment of the South Atlantic, is suggested to have been synchronous with evaporite formation in the southern Brazilian basins.

Chapter 6 presents new high-resolution nannofossil zonation, magnetostratigraphy, total inorganic and organic-carbon (TOC and TIC), Rock-Eval pyrolysis, sulphur content of organic matter (S_{OM}), carbon- and oxygen- isotope ratios of carbonate and organic-matter and Re-Os isotope analyses from Deep Sea Drilling Program (DSDP) Site 511, Falkland Plateau. These data from DSDP Site 511 suggest that the deposition of an organic-rich black-shale interval took place from the mid-Jurassic up to the Barremian–Early Aptian interval represented by the hiatus/condensed section. The typical isotopic record of OAE 1a is missing either due to incomplete core recovery or a hiatus, although its latter part (C6 segment) could be represented. Therefore, most black-shale sedimentation on the Falkland Plateau took place before deposition of evaporites in the Campos and Santos Basins during the OAE 1a time interval and before the opening of the central segment of the South Atlantic. Black-shale deposition on the Falkland Plateau was thus likely governed primarily by local forcing factors. Upper Aptian sediments with intermediate TOC values and relatively high terrestrial organic-matter content lie above the hiatus/condensed section at DSDP Site 511 and are partially coeval with shallow- and deep-water post-evaporite carbonates from the Santos and Campos

Basins. Local records of OAE 1b, including the Jacob, Kilian and Paquier Levels, are tentatively recognized in DSDP Site 511 based on their carbon-isotope signature but without the organic-rich levels that are typically recognized in the Tethyan realm.

Chapter 7 discusses a new magnetostratigraphic and chemostratigraphic investigation, integrated with biostratigraphy, of the uppermost Barremian–Lower Aptian Maiolica and Marne a Fucoidi Formations from the Poggio le Guaine core (PLG core, northern Apennines, Italy). The data provide the first record of polarity chron M0r and the Early Aptian OAE 1a interval, allowing the Barremian–Aptian boundary and the base of the Cretaceous Normal Polarity Superchron (CNPS) to be defined. Above the base of the CNPS, the $\delta^{13}C$ record shows a negative shift and a subsequent positive excursion similar to that documented from elsewhere in the Tethyan realm. OAE1a is lithologically represented by the Selli Level, the origin of which has been linked to volcanic episodes that formed the Ontong Java LIP, which forced the rapid increase of atmospheric pCO_2 triggering a cascade of palaeoenvironmental changes affecting plankton productivity and carbon flux to the sea floor.

Chapter 2

New age constraints on Aptian evaporites and carbonates from the South Atlantic: Implications for OAE 1a

The revised version of this chapter has been accepted in very similar form for publication in Geology co-authored by Leonardo R. Tedeschi, Hugh C. Jenkyns, Stuart A. Robinson, Antonio E. S. Sanjinés, Marta Claudia Viviers, Cláudia M. S. P. Quintães and Joselito C. Vazquez. Leonardo R. Tedeschi is the lead author who has written the majority of the chapter, with comments from all co-authors. He also performed carbon-, oxygen- and strontium-isotope analyses of Petrobras Well CB-3. Geochemical datasets are provided in the appendix A (Tables 2.1 to 2.4). Petrobras geologists Marta Claudia Viviers and Antonio E. S. Sanjinés performed foraminiferal biostratigraphic studies. Petrobras chemist Joselito C. Vazquez obtained elemental analyses.

2.1 Introduction

Oceanic anoxic events (OAEs) are time intervals when oxygen depletion characterized much of the mid- and/or deeper waters of the world's oceans. As a result an unusual amount of organic matter was preserved in marine sediments worldwide (Jenkyns, 2010). OAE 1a is typically identified by an organic-rich sedimentary record and/or characteristic carbon-isotope signature ($\delta^{13}C$) in carbonate or organic matter: phenomena recorded in geographically widespread localities (Menegatti et al., 1998; Erba et al., 2015). Potential causative mechanisms include

massive CO_2 release from extrusion of the Ontong Java Plateau, and/or dissociation of methane hydrate to cause greenhouse warming and an enhanced hydrological cycle, accelerated input of nutrients from basalt-seawater interaction and/or continental weathering, and increased organic productivity (Beerling et al., 2002; Méhay et al., 2009; Erba et al., 2010; Bottini et al., 2012, 2015; Erba et al., 2015).

The evaporites from the central segment of the South Atlantic (CSSA) (Figure 2.1) are conventionally considered to fall in the age range 116–111 Ma based on Ar-Ar ages from the sub-evaporite volcanic sequence (e. g., Davison, 2007; Chaboureau et al., 2013) and to be unrelated to OAE 1a dated at ~125.5–124.4 or 120.2–119.1 Ma (e. g., Malinverno et al., 2010; Ogg et al., 2012; Bottini et al., 2015; Erba et al., 2015) (Figure 1.2 in Chapter 1). However, the stratigraphic evidence for the age of the evaporites is ambiguous, as will be discussed further in the text. The aim of this study, therefore, is to constrain the age of the evaporites in southern Brazilian basins by using new foraminiferal biostratigraphy and $\delta^{13}C$ and $^{87}Sr/^{86}Sr$ data from carbonates above the evaporite deposits from Petrobras-cored Well CB-3 in the Campos Basin and published $\delta^{13}C$ data from Petrobras Wells CP-5 and X, from below and above the evaporites, respectively (Dias, 1998; Quintaes, 2006) (Figures 2.1 and 2.2).

2.2 Geological setting of the Santos and Campos Basins

The Santos and Campos Basins formed during the opening of the CSSA in the Early Cretaceous (Davison, 2007; Chaboureau et al., 2013). Their stratigraphic record, based on offshore wells, divides into three main super-sequences: rift, post-rift and drift, as described by Moreira et al. (2007) and Winter et al. (2007). Above the basement, the rift super-sequence comprises volcanic rocks, continental

siliciclastics, and interbedded lacustrine coquinas and organic-rich shales (Coqueiros/Itapema Formations; Figure 2.2); in distal settings, the overlying post-rift super-sequence comprises interbedded microbial carbonates and shales (Macabu/Barra Velha Formations; Figure 2.2). The evaporites terminate the post-rift super-sequence and comprise cycles of predominantly anhydrite and halite, locally with more soluble salts such as carnallite, sylvite and tachyhydrite (Retiro/Ariri Formations; Figure 2.2). Halite and anhydrite from the Espírito Santo Basin, to the north of the Campos Basin (Figure 2.1), possess Br contents and $^{87}Sr/^{86}Sr$ ratios that indicate derivation from marine waters (Dias, 1998). The anhydrite probably formed from dewatering of gypsum during burial and show textures typical of precipitation in subaqueous settings such as thin laminations and twinned crystals, as well as nodules of likely sabkha facies (Dias, 1998). Above the evaporites, in distal settings, the early drift super-sequence is represented by shallow-marine platform carbonates (Quissamã/Guarujá Formations) (Figure 2.2), containing planktonic foraminiferal species that are not age-diagnostic (e. g., *Favusella* ex grege *washitensis*; Azevedo et al., 1987). Following platform drowning, deeper water sediments accumulated (Outeiro/Itanhaém Formations) (Figure 2.2) in which Aptian and younger calcareous nannofossils (e. g., *Nannoconus truittii*) and planktonic foraminifera are present (e. g., *Globigerinelloides ferreolensis*; *Ticinella raynaudi*: Azevedo et al., 1987; this study).

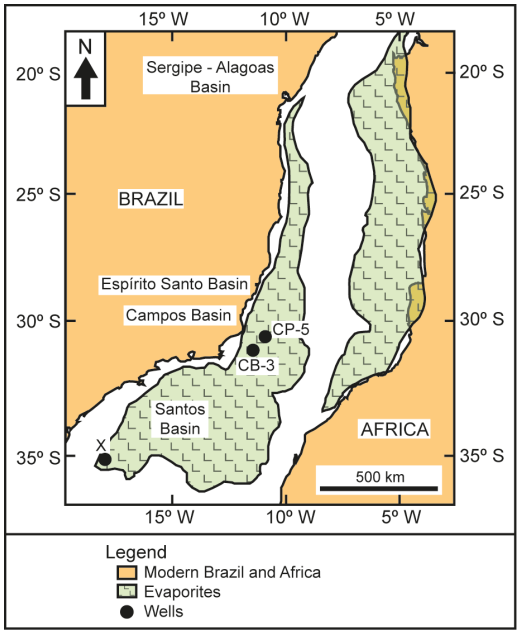
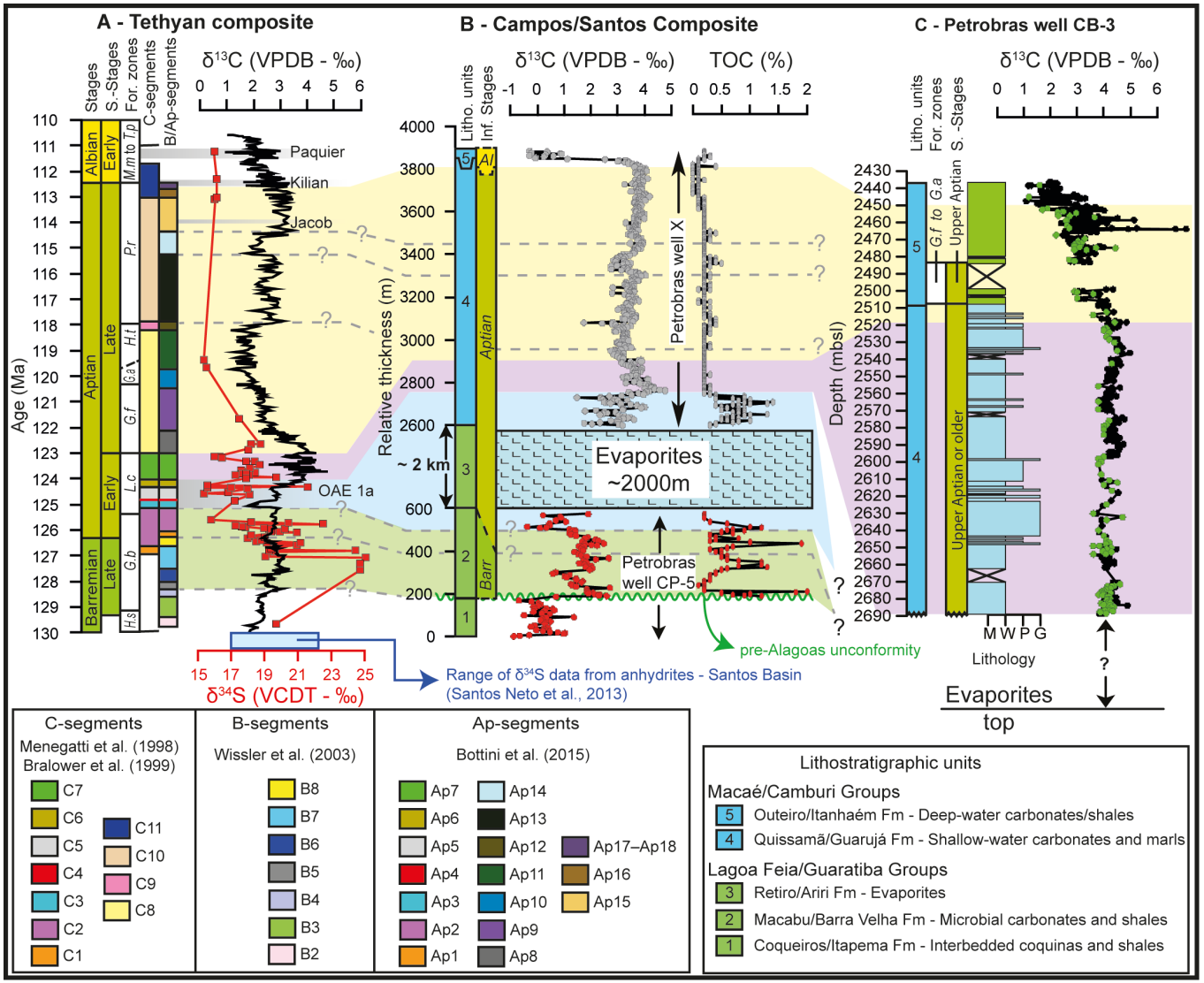


Figure 2 .1 – Location map of offshore Petrobras Wells CB-3 and CP-5 and X, southeast Brazil. Reconstruction between Brazil and Africa to 113 Ma after evaporite deposition and rotated to Tristan da Cunha hotspot (adapted from Norton et al., 2016).

Figure 2 .2 –Chemostratigraphic correlation between A: Tethyan carbonate carbon-isotope composite age-calibrated curve (Ogg et al., 2012): black – carbonate carbon-isotope composite from Herrle et al. (2015), red squares – $\delta^{34}S$ from ODP site 766A, Permanente Section and Cismon core (Paytan et al. 2004; Gomes et al. 2016; numerical age adjusted to time scale of Ogg et al., 2012 after Gomes et al., 2016); grey – organic-rich levels Jacob, Killian, Paquier and oceanic anoxic event 1a (OAE1a). C-segments from Menegatti et al. (1998) and Bralower et al., (1999); B-segments from Wissler et al. (2003); Ap-segments from Bottini et al., 2015; B: Campos/Santos carbonate carbon-isotope and TOC composite curve displayed in relative thicknesses based on Petrobras Wells CP-5 (red circles) and X (grey circles). Note the break in the *y*-axis to include up to 2km of evaporites, as estimated by Davison et al. (2012). TOC values higher than 2 wt % are omitted in this diagram (four samples from Petrobras Well CP-5). C: Petrobras Well CB-3: lithostratigraphic units, foraminiferal zones, Sub-stages, lithology (M – mudstone, W – wackestone, P – packstone, G – grainstone), carbon-isotope data (black – this study, green – Azevedo, 2001). Green, blue, purple and yellow bands and grey dashed lines show suggested correlation between A, B and C. S. -Stages – sub-stages; mbsl – metres below sea level; For. – Foraminiferal; *H.s – Hedbergella similis, G.b – Globigerinelloides blowi, L.c – Leupoldina cabri, G.f – Globigerinelloides ferreolensis, G.a – Globigerinelloides algerianus, H.t – Hedbergella trocoidea, P.r – Paraticinella rohri, M.m – Microhedbergella miniglobularis; T.p – Ticinella primula*. Inf. – Inferred, Barr – Barremian, U. Ap – Upper Aptian, Al – Albian.


A - Tethyan composite
B - Campos/Santos Composite
C - Petrobras well CB-3
Stages
S.-Stages
For. zones
C-segments
B/Ap-segments
δ13C (VPDB - ‰)
Albian
Aptian
Barremian
Early
Late
M.m to T.p
Pr
H.t
G.a
G.f
L.c
G.b
H.s
Paquier
Kilian
Jacob
OAE 1a
Age (Ma)
Litho. units
Inf. Stages
TOC (%)
Relative thickness (m)
~ 2 km
Evaporites
~2000m
Petrobras well X
Petrobras
well CP-5
pre-Alagoas unconformity
Depth (mbsl)
Upper Aptian or older
M W P G
Lithology
Evaporites
top
δ34S (VCDT - ‰)
Range of δ34S data from anhydrites - Santos Basin
(Santos Neto et al., 2013)
C-segments
Menegatti et al. (1998)
Bralower et al. (1999)
B-segments
Wissler et al. (2003)
Ap-segments
Bottini et al. (2015)
Lithostratigraphic units
Macaé/Camburi Groups
Outeiro/Itanhaém Fm - Deep-water carbonates/shales
Quissamã/Guarujá Fm - Shallow-water carbonates and marls
Lagoa Feia/Guaratiba Groups
Retiro/Ariri Fm - Evaporites
Macabu/Barra Velha Fm - Microbial carbonates and shales
Coqueiros/Itapema Fm - Interbedded coquinas and shales

2.3 Methods

This study concerns the stratigraphic interval between 2437 and 2689 metres below sea level (mbsl) of Petrobras Well CB-3, which is located in the offshore Campos Basin (southeastern Brazil) (22°44'S; 40°40'E) (Figure 2.1). The well was drilled in a water depth of 208 m in 1982 and terminated an unknown distance above the evaporites. The studied interval is composed of rocks lying above the evaporites (Figure 2.2): 1) Shallow-water carbonates varying from wackestones to grainstones - Quissamã Formation (2689–2509 mbsl) and; 2) Interbedded marls and wackestones/mudstones deposited in a deeper water environment - Outeiro Formation between (2509–2437 mbsl).

2.3.1 Foraminiferal biostratigraphy

171 samples from depth interval 2484–2689 m were prepared for foraminiferal biostratigraphy in the Research Centre of Petrobras (CENPES). Samples underwent oil extraction in a Soxhlet apparatus, with 30% methanol and 70% chloroform, were crushed in small chips and soaked in hydrogen peroxide (H_2O_2) at 80°C in order to oxidize organic matter and disaggregate the material. After that, residues were washed under running tap water in 1.0 mm and 62 μm sieves. The dried fraction 62μm–1.0 mm was passed through 125 μm and 250 μm sieves. Subsequently, some samples were reacted with acetic acid in order to separate foraminifera from the carbonate matrix and cement. Following this procedure, the specimens of both fractions were picked and analysed for the presence of foraminifera by using a stereomicroscope with reflected light. The biostratigraphic framework used and species concepts adopted in this study follow Caron (1978),

Premoli Silva and Verga (2004), Huber and Leckie (2011), Petrizzo et al. (2012), Ando et al. (2013) and Kennedy et al. (2014).

2.3.2 Carbon and oxygen isotopes

195 samples from depth interval 2437–2689 m were analysed for carbon and oxygen isotopes ($\delta^{13}C$ and $\delta^{18}O$) on bulk rock. 185 samples underwent oil extraction as described above. Thereafter, all samples were ground to less than 0.177 mm at CENPES and analysed at the University of Oxford (UO) and at Universidade do Estado do Rio de Janeiro (UERJ). A VG Isogas Prism II mass spectrometer with an on-line VG Isocarb common acid bath preparation system was used to analyse the samples at UO, whereas a Kiel IV carbonate device coupled to Thermo Delta V Advantage mass spectrometer was used to perform analyses at UERJ. Samples were reacted with purified phosphoric acid (H_3PO_4) at 90°C in both instruments and the gas was analysed on-line. Data are reported in parts per thousand (‰) relative to the Vienna Pee Dee Belemnite (VPDB) scale. The calibration to VPDB was undertaken by using the IAEA CO-1 standard in both laboratories ($\delta^{13}C$ = 2.47‰ and $\delta^{18}O$ = –2.4‰) and its standard deviation (σ) was less than ± 0.07‰ for $\delta^{13}C$ and ± 0.12‰ for $\delta^{18}O$ in both laboratories. All $\delta^{13}C$ and $\delta^{18}O$ values obtained in this study are given in the appendix A (Table 2.1). Figure 2.3 shows a cross-plot of replicates within and between laboratories in order to show the good to excellent reproducibility, in which A-coefficients are close to 1.0, B-coefficients are close to 0.0 and determination coefficients (R^2) are close to 1. Hence, analytical data are hence deemed reliable.

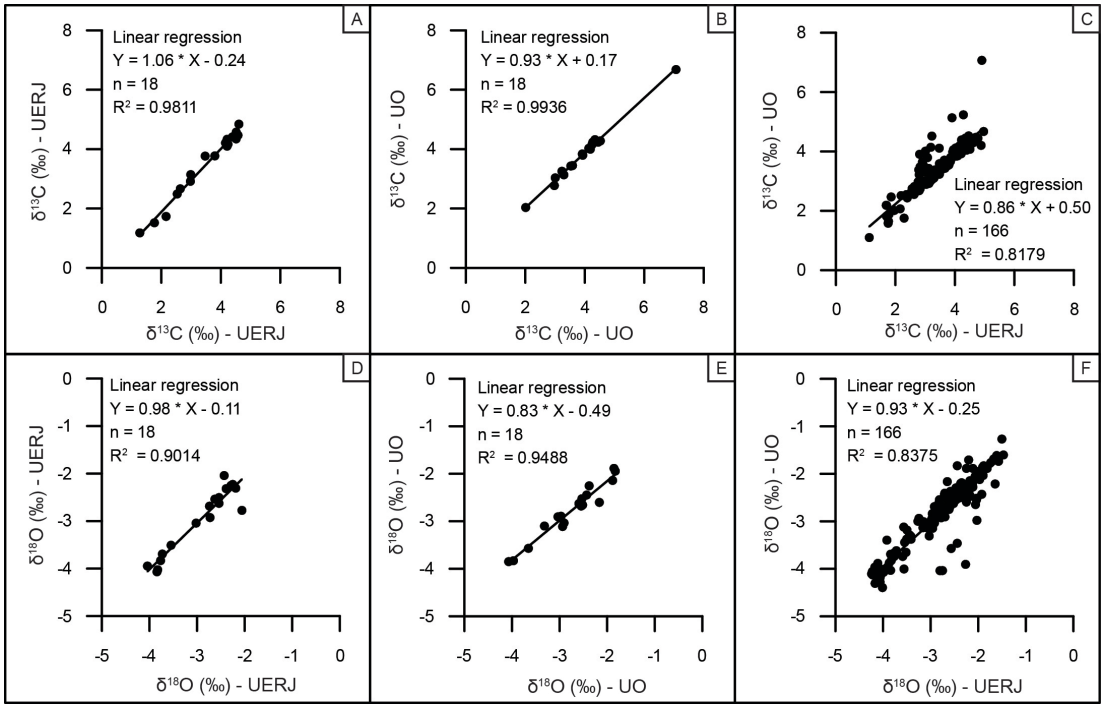


Figure 2 .3 –Cross-plots between replicate analyses of samples from Petrobras Well CB-3. A - $\delta^{13}C$ replicate data obtained at UERJ, B - $\delta^{13}C$ replicate data obtained at UO, C - $\delta^{13}C$ data analysed in both laboratories, D - $\delta^{18}O$ replicate data obtained at UERJ, E - $\delta^{18}O$ replicate data obtained at UO, F - $\delta^{18}O$ data analysed in both laboratories.

2.3.3 Elemental analyses

Al, Ca, Mg, Si, K, Fe, Mn, Rb and Sr contents were analysed in all carbonate samples used for strontium-isotope analyses ($^{87}Sr/^{86}Sr$). Hand-held X-ray fluorescence (XRF Olympus, Delta Premium 6000) was used for analyses on polished surfaces of samples. The equipment employed was an energy dispersive X-ray fluorescence spectrometer with a 40kV tube, 4W Rh excitation source and a Silicon Drift Detector (SDD). Analyses were performed in a workstation for operator protection in air atmosphere in two modes (Mining Plus and Soil) at CENPES. The former was used to analyse Al, Ca, Mg, Si, K and Fe, results being expressed in weight percent (wt %), whereas the latter was used to analyse Mn, Rb and Sr in parts per million (ppm). Only 15 out of 69 samples were analysed without oil extraction.

Each reading lasted 275 seconds with three readings obtained on the same spot. All data showed a coefficient variation of three analyses of each sample, the ratio between the standard deviation and average, of less than 30%, except for one Mn value obtained in the sample from 2661.8 mbsl. The equipment's internal algorithm solved spectral interferences and averaging of all three measurements was performed offline. Reference materials IPT 122 (dolomitic limestone), IPT 28 (Clay), IPT 44 (limestone), NIST 1d (argillaceous limestone), NIST 88b (dolomitic limestone), BRP-1 (basalt) were used to calibrate analyses. All data and detection limits (DL – 3 σ) for each element are in the Appendix A (Table 2.2).

2.3.4 Scanning electron microscope - energy dispersive spectroscopy (SEM-EDS)

Benthic foraminifera used to obtain $^{87}Sr/^{86}Sr$ ratios were screened in a SEM Zeiss model EVO-40 attached to an EDS Oxford INCA at CENPES. Images were obtained in high vacuum with a distance of 12 mm and an energy emission of 20 kV. Samples were imaged to different detectors, after being covered with Au/Pd and carbon by using a Quorum model Q150TES. The detector used in one kind of image was for secondary electrons (SE), which is good for analysing the morphology, while the other was for back-scattered electrons (BSE) for obtaining better analytical data by using an EDS.

2.3.5 Strontium-isotope analyses

69 powdered carbonate and 10 benthic foraminiferal (Lenticulina) samples were analysed for $^{87}Sr/^{86}Sr$ ratios at UO. Carbonates were leached twice by using

0.5M acetic acid (Bailey et al., 2000), in which the first supernatant was discharged after it had dissolved ~40 wt % of carbonate present in the sample and the second was used for analyses after it had dissolved ~30 wt % of the total carbonate originally present in the sample. Consequently ~30 wt % of original carbonate was not leached. Volumes of acid were estimated based on the Ca content obtained from XRF as described above. All samples had more than 70 wt % of $CaCO_3$ based on the XRF data. Foraminifera (Lenticulina) were picked during studies of foraminiferal biostratigraphy as described above. Samples with 7–40 specimens were dissolved in 0.5M acetic acid. All solutions were dried out and dissolved in 2M HNO_3. Strontium was separated by using the automatic prep*Fast* system (procedures adapted from Romaniello et al., 2015). Solutions (1 mL) dissolved in 2M HNO_3 were loaded in prep*Fast*, after at least three blanks (2M HNO_3) had been passed through the supplied Sr-Ca column to avoid a memory effect. Sr was eluted with 5M HNO_3 and Ca with 0.1M HCl. A further wash was performed with 2M HNO_3 and 0.1M HCl to remove any other major and trace elements that remained in the column. Purified Sr in 5M HNO_3 was dried out and re-dissolved in 0.45M HNO_3. Sr isotopic compositions were measured by using a Nu-Plasma HR multi-collector inductively coupled plasma mass spectrometer (MC-ICP-MS, Nu instrument, Wrexham, UK) equipped with B-type sampler and skimmer cones, an Aridus II desolvator (Cetac Technologies) and a PFA microflow nebulizer (100 ml/min) (ESI, USA). Sr samples were introduced at 30–40ppb in order to optimize ^{88}Sr to 7–8V in a matrix of 0.45M HNO_3. Each measurement consisted of fifty 10s cycles, after obtaining a 20s baseline, and samples were run in blank-standard-sample-standard-blank blocks, with SRM 987 as the bracketing standard. Masses 83, 84, 85, 86, 87 and 88 were collected in Faraday cups. All the data were corrected by ^{86}Kr and ^{87}Rb interference

using mass-bias fractionation by taking the ratio $^{86}Sr/^{88}Sr$ of 0.1194 (Ehrlich et al., 2001). ^{83}Kr and ^{85}Rb were calculated by using $^{86}Kr/^{83}Kr$ of 1.5025, $^{85}Rb/^{87}Rb$ of 2.593 (Laeter et al., 2003), and normalizing NIST SRM 987 to 0.710248. All blanks of strontium were less than 9ng, whereas the Sr leached was usually in the range of 3–25μg. The foraminiferal blank was 0.23ng, whereas Sr leached from foraminifera was usually in the range of 0.25–1.81 μg. The external reproducibility of SRM 987 was 0.710249 ± 0.000033 (n=72, 2σ) and an internal standard of Aptian carbonate (PLG 94.66) employed to check all chemical procedures gave a ratio of 0.707464 ± 0.000042 (n=19, 2σ). All the strontium-isotope data are reported in the Appendix A (Table 2.3). Because all standard errors of the mean (2SE) values are lower than the external reproducibility (2σ), we have used 2σ to represent error bars.

2.3.6 Campos/Santos composite carbon-isotope curve

$\delta^{13}C$ and TOC data from Petrobras Wells CP-5 (Campos Basin) and X (Santos Basin) have been used to generate a composite curve, where original samples were not available for further analyses. Because depth intervals (m) are not defined as relative to some reference level (e. g., metres below sea floor or metres below sea level: Dias, 1998, Quintaes, 2006), depth intervals are assumed to correspond to penetrated depth during drilling operations. 106 analyses from Petrobras Well CP-5 (Dias, 1998) derived from the interval 4629–5202 metres penetrated (mp), and represent rocks stratigraphically below the evaporites of the Lagoa Feia Group in the Campos Basin. Sedimentary rocks stratigraphically above 5015 mp are mainly composed of microbial carbonates (Alagoas local stage; Dias, 1998), whereas rocks below this level are from the Coqueiros Formation (Jiquiá local stage) and comprise interbedded coquinas and shales (Dias, 1998; Rodrigues, 2005; Winter et al., 2007).

All analyses of Petrobras Well CP-5 material were performed at the Centro de Energia Nuclear na Agricultura – University of São Paulo (CENA) (Dias, 1998). The sampling interval was usually ~ 6 metres. We also used 428 analyses of material from Petrobras Well X in the interval 4668–5952 mp that represent sediments lying stratigraphically above the evaporites of the Camburi Group in the Santos Basin. This well encountered the top of the evaporites (Ariri Formation) at 5952 mp. Sedimentary rocks stratigraphically lower than 4700 mp are shallow-water carbonates (Guarujá Formation), whereas rocks above this level are mainly deep-water carbonates, marls and shales (Itanhaém Formation) (Quintaes, 2006; Moreira et al., 2007).

The stratigraphic relationship between the wells was calculated by assuming the evaporites to be contemporaneous in both Campos and Santos Basins, based on seismic evidence (Davison et al., 2012). The bottom depth of Petrobras Well CP-5 (4629 mp), below the evaporites, was taken as 0 metres relative thickness (mrt) and the intervals between each sample were summed up to the top of the designated interval (5202 mp = 573 mrt) (Table 2.4 in the Appendix A; Figure 2.2). A gap between relative depths attributed to the top of Petrobras Well CP-5 and the base of Petrobras Well X was used to represent an evaporite thickness of up to ~2km (Davison et al., 2012). The bottom depth (5952 mp) of Petrobras Well X, above the evaporites, was taken as 2600 mrt and the intervals between each sample were summed up to the top of the designated interval (4668 mp = 3884 mrt) (Table 2.4 in the Appendix A; Figure 2.2).

2.4 Results

2.4.1 Foraminiferal biostratigraphy

An assemblage of 11 planktonic foraminifera (*Hedbergella aptiana*, *H. gorbachikae*, *H. infracretacea*, *H. sigali*, *H. luterbacheri*, *H. tuschepsensis*, *H. kuznetsovae*, *H. occulta, Globigerinelloides ferreolensis*, *G. barri* and *Favusella* ex grege *washitensis*) was identified from 2484 to 2508 m from Petrobras well CB-3. This assemblage indicates the Upper Aptian from the *G. ferreolensis* to the *G. algerianus* zones (cf. Premoli Silva and Verga, 2004; Ogg et al., 2012) (Figures 2.2 and 2.4). Samples below 2508 m, deposited in relatively shallow water, contain a low-diversity assemblage with relatively long-ranging species of benthic (e. g., *Lenticulina* ex grege *nodosa*) and planktonic foraminifera (e. g., *Favusella* ex grege *washitensis*) and are interpreted as early Late Aptian or older in age.

2.4.2 Carbon-isotope stratigraphy

2.4.2.1 Diagenesis

With regard to possible significant diagenetic overprint on carbon isotopes, Figure 2.5 shows cross-plots between the $\delta^{18}O$ and $\delta^{13}C$ data. There is little correlation between the different isotopic systems in Petrobras Wells CB-3 and X (coefficient of correlation – R = 0.0309 and 0.1762, respectively), suggesting that diagenetic effects have had little effect on $\delta^{13}C$ values. In general, carbon isotopes in carbonates, particularly of deep-water character, are relatively conservative: unlike oxygen, their concentration in pore waters in initially porous sediment is low, limiting possibilities of diagenetic exchange (e. g., Scholle and Arthur, 1980;

Marshall, 1992; Jenkyns et al., 1994). In addition, $\delta^{13}C$ values do not show different patterns associated with particular carbonate facies. However, the cross-plot between the $\delta^{18}O$ and $\delta^{13}C$ data from Petrobras CP-5 have shown reasonable correlation (R = 0.5741) suggesting that either somewhat modified primary values or that diagenesis has fractionated both isotopic systems in a systematic manner. Because pre-Salt rocks may have been deposited in a lacustrine environment, environmental changes in hydrographically closed lakes could explain these patterns (Sabato Ceraldi and Green, 2017), as well as groundwater-related diagenesis.

2.4.2.2 Petrobras Well CB-3

The carbon-isotope profile from Petrobras Well CB-3 shows a defined pattern (Figure 2.2): a stratigraphically lower section (2689–2517 m) showing relatively high $\delta^{13}C$ values (3.60–4.97‰) and a stratigraphically higher section (2517–2437 m) that shows a trend of decreasing $\delta^{13}C$ values from the bottom (3.0–3.3‰) to top (1.2–1.6‰), interrupted by a positive excursion with values exceeding 4‰. Relatively high $\delta^{13}C$ values, as in the interval 2689–2517 m, characterize part of the so-called C7/Ap7 isotopic segment (latest Early Aptian–earliest Late Aptian interval), as interpreted in the Vocontian Basin used in the Tethyan age calibrated curve, with the highest $\delta^{13}C$ values of the Aptian stage (Menegatti et al., 1998; Herrle et al., 2004; Bottini et al., 2015; Herrle et al., 2015) (purple band; Figure 2.2). Although no biostratigraphic constraints are available stratigraphically above 2484 m, the trend of decreasing $\delta^{13}C$ values and positive excursion, as in the interval 2517–2450 m, is similar to the C8–C10/Ap8–Ap15 segments of the Late Aptian (cf. Bralower et al., 1999; Herrle et al., 2004; Bottini et al., 2015) (yellow band, Figure 2.2). Deeper water sediments stratigraphically above 2450 m do not have biostratigraphic

constraints and do not show diagnostic $\delta^{13}C$ patterns. They are here interpreted as latest Late Aptian or younger in age.

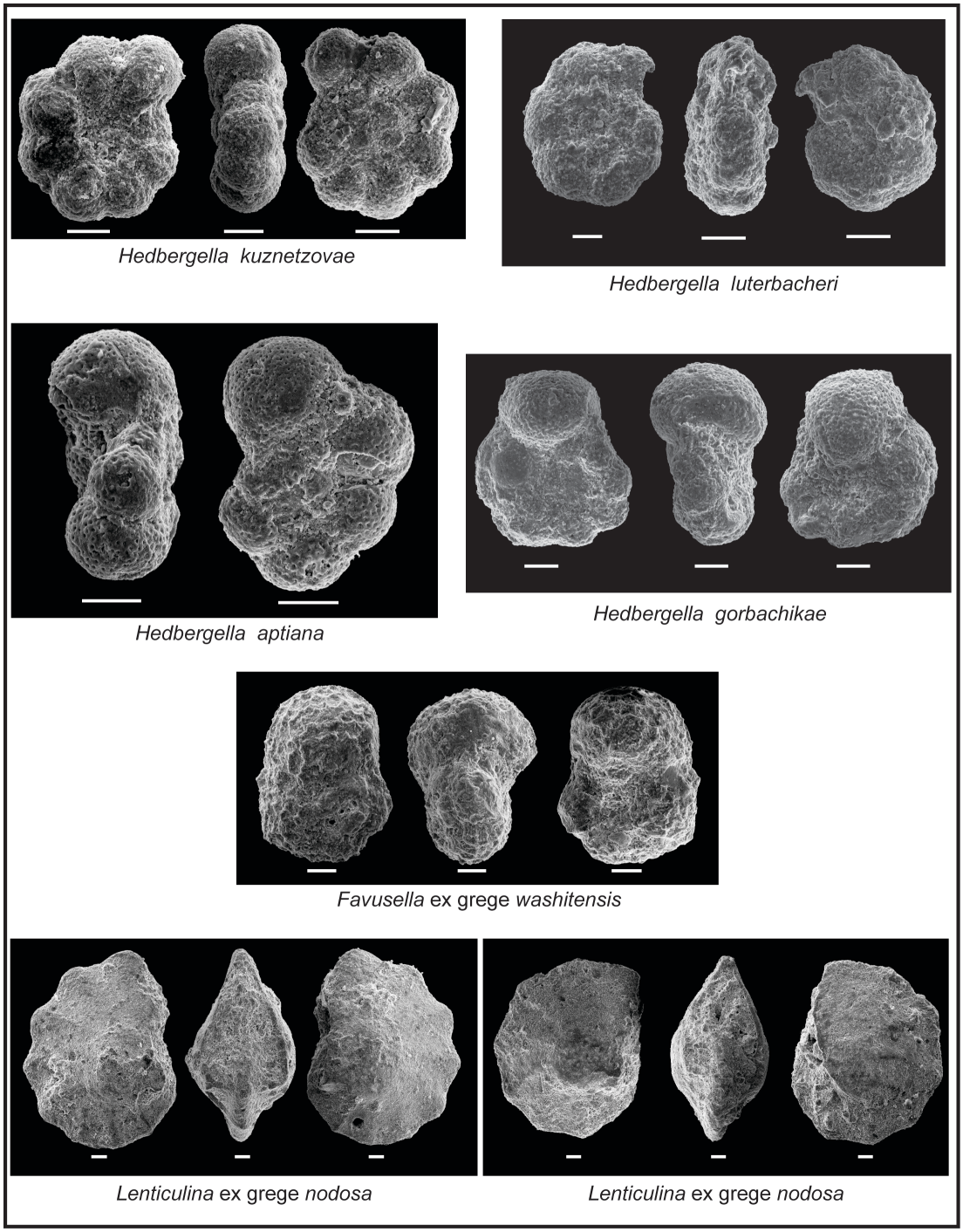


Figure 2 .4 –Examples of Aptian species identified in Petrobras Well CB-3. All planktonic foraminifera are from 2500.3 mbsl and specimens of *Lenticulina* ex grege *nodosa* are from 2505.9m. Scale bars = 50 µm.

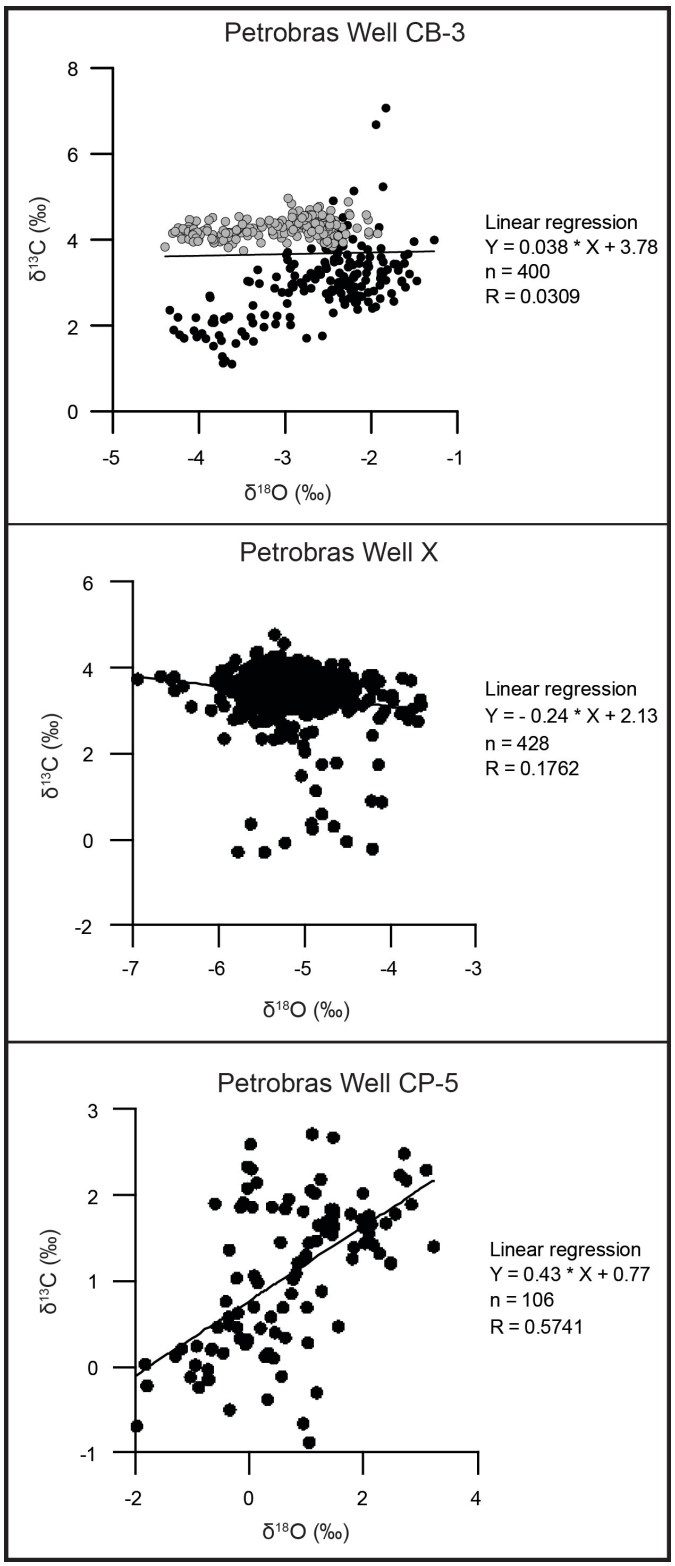


Figure 2 .5 – Cross-plots $\delta^{18}O$ versus $\delta^{13}C$ data from Petrobras Wells CB-3, X and CP-5. Petrobras Well CB-3: Grey – analyses below 2516.50 mbsl. Black – analyses above 2516.50 mbsl.

2.4.2.3 Campos/Santos Composite carbon-isotope curve

The Santos/Campos composite (Figure 2.2) does not have any biostratigraphic constraints from planktonic marine fossils, and this correlation with the Tethyan reference section is based purely on $\delta^{13}C$ values. The basal interval (0–173 m) lacks diagnostic features on the $\delta^{13}C$ curve and it is stratigraphically below an important regional unconformity identified in seismic lines and other oil wells in southern Brazilian basins, named as the 'pre-Alagoas unconformity' (Dias, 1998; Figure 2.2). Hence, it cannot be correlated with the Tethyan reference curve. The stratigraphically higher sub-evaporite interval, 186–501 m, with $\delta^{13}C$ generally in excess of 1.2‰, is tentatively correlated with Upper Barremian B5–B8 segments and Lower Aptian Ap1–Ap2 segments (green band; Figure 2.2; Wissler et al., 2003; Bottini et al. 2015); and the sub-evaporite interval 501–573 m, with $\delta^{13}C$ generally less than 1.2‰, with the C3/Ap3 segment that characterizes the base of the OAE 1a worldwide (cf. Menegatti et al., 1998; Bottini et al., 2015) (blue band; Figure 2.2). However, the correlations of the interval 186–573 m are tentative, especially the lower values found in the interval 501–573 m, because of deposition in continental environments (e. g., Sabato Ceraldi and Green, 2017) and/or diagenetic overprints.

Above the evaporites, the interval 2600–2756 m shows a general trend of increasing $\delta^{13}C$ values typical of the C6/Ap6 segments, with TOC values reaching up to 1.4 wt % (cf. Menegatti et al., 1998; Bottini et al., 2015) (blue band; Figure 2.2): geochemical characters that likely constrain this interval to the latter part of OAE 1a. The highest $\delta^{13}C$ values (3.14–4.77‰) from the Santos/Campos composite (2756–2906 m) are diagnostic of the Aptian immediately post-OAE 1a sediments of the C7/Ap7 segment (cf. Menegatti et al., 1998; Herrle et al., 2004; Bottini et al., 2015)

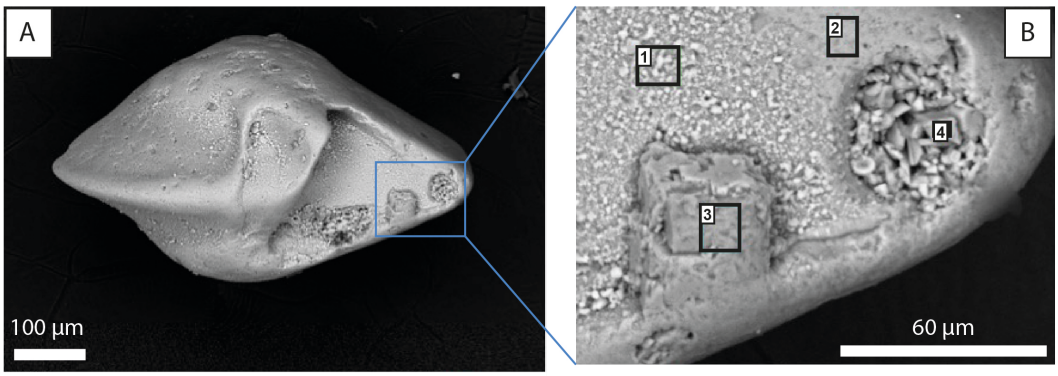
(purple band; Figure 2.2). The interval 2906–2948 m (basal part of yellow band; Figure 2.2) shows a trend of decreasing $\delta^{13}C$ values that may record the lower part of the C8/Ap8 segment (cf. Bralower et al., 1999; Herrle et al., 2004; Bottini et al., 2015). The Campos/Santos composite does not show the lower $\delta^{13}C$ values and subsequent increasing trend of $\delta^{13}C$ values (C8–C9/Ap8–Ap16 segments; Bralower et al., 1999; Bottini et al., 2015) present in the Tethyan reference curve, which could be due to the presence of a condensed section and/or gaps/unconformities (Figure 2.2). Significantly, the Ap8–Ap11 segments are apparently extremely condensed or missing that could be explained by a relative sea level fall. The broad positive excursion in the interval 2948–3803 m has been observed in Upper Aptian sediments worldwide (C10/Ap13–Ap15 segments; Bralower et al., 1999; Bottini et al., 2015) (yellow band; Figure 2.2). Shallow-water and deep-water carbonates above 3803 m, lacking biostratigraphic analyses, are interpreted as latest Late Aptian or younger in age.

2.4.3 Strontium-isotope analyses

2.4.3.1 Diagenesis

All foraminiferal samples used for $^{87}Sr/^{86}Sr$ analyses showed moderate to badly preserved tests, locally with evidence of dissolution. Some tests had overgrowths of calcite and dolomite and all of them showed some degree of infilling, in some instances including potassium aluminosilicates (Figure 2.6). During the leaching process it proved impossible to separate infillings from tests, potentially introducing sources of Sr other than those recording initial seawater values.

Consequently, data from foraminifera may have been affected by a contribution of radiogenic ^{87}Sr from aluminosilicates and diagenetic cement.



Area 1

Element	Weight (%)	Atomic (%)
Mg	0.68	0.78
Ca	70.67	49.22
O	28.66	50.00
Totals	100.00	100.00

Area 2

Element	Weight (%)	Atomic (%)
Mg	0.40	0.46
Ca	70.99	49.54
O	28.60	50.00
Totals	100.00	100.00

Area 3

Element	Weight (%)	Atomic (%)
Mg	19.29	19.81
Si	0.47	0.42
Ca	45.44	28.35
Fe	2.70	1.21
O	32.13	50.21
Totals	100.00	100.00

Area 4

Element	Weight (%)	Atomic (%)
Na	0.46	0.43
Al	9.27	7.32
Si	30.80	23.37
K	12.12	6.61
Ca	0.99	0.52
O	46.36	61.75
Totals	100.00	100.00

Figure 2 .6 –Images and analyses (SEM-EDS) of benthic foraminifera from sample at 2473 mbsl. A – General morphology of benthic foraminifera obtained with BSE, B – Detail of blue area in A, also showing analysed areas 1 to 4 (black rectangles) by using EDS. Image obtained with BSE, Areas 1–4: composition of each area: 1 and 2 – calcite; 3 – dolomite; 4 – potassium aluminosilicate.

Figure 2.7 shows measured elemental concentrations against stratigraphic depth (Table 2.2 in Appendix A). All the carbonates present in the section are represented by low-Mg calcite. The section can be split in two different stratigraphic

levels at 2513 mbsl (red line in Figure 2.7). The lower unit generally shows lower detrital content and higher carbonate content than the upper unit. Sr contents (299–896 ppm) do not show any significant differences when comparing these two stratigraphic levels. Higher Rb contents (>12 ppm) are present in the upper stratigraphic level. Because radiogenic ^{87}Sr ($^{87}Sr_{rad}$) is the product of ^{87}Rb decay, introduction of $^{87}Sr_{rad}$ from detrital minerals rich in K and Rb, such as mica and K-feldspar (e. g., Banner, 2004), to the carbonate fraction is more likely to have happened in this level. Nevertheless, all samples display $^{87}Sr/^{86}Sr$ ratios higher than contemporaneous seawater (Figure 2.8) and they have Rb/Sr ratios higher than 0.005, which suggests that the depositional $^{87}Sr/^{86}Sr$ ratios may have been altered by *in situ* production of $^{87}Sr_{rad}$ (Jacobsen and Kaufman, 1999). In order to test for any effect due to the possible introduction of $^{87}Sr_{rad}$ derived from detrital minerals, the initial $^{87}Sr/^{86}Sr$ ratio ($^{87}Sr/^{86}Sr_i$) is calculated to evaluate possible increase of $^{87}Sr/^{86}Sr$ ratio from $^{87}Sr_{rad}$, using the following equation (Banner, 2004):

$$\left(\frac{^{87}Sr}{^{86}Sr}\right)_i = \left(\frac{^{87}Sr}{^{86}Sr}\right)_n - \left(\frac{^{87}Rb}{^{86}Sr}\right)(e^{\lambda t} - 1) \quad (1)$$

where $(^{87}Sr/^{86}Sr)_n$ is the data from Table 2.3 (Appendix A), ^{87}Rb is the relative abundance of this isotope in the Rb content (27.83% of total Rb content; Laeter et al., 2003) (Table 2.2 in Appendix A), in which all samples with contents <3 ppm were assumed to have Rb content of 3 ppm. The ^{86}Sr abundance was obtained during the analyses in the MC-ICP-MS, corrected by fractionation and assuming the ^{86}Sr abundance of SRM 987 standard of 0.9857 (Moore et al., 1982). λ is the decay constant of the Rb-Sr isotope system (1.42×10^{-11} y^{-1}; Banner, 2004) and t was estimated for two different values: 113 Ma and 124 Ma. The following simplified equation is used (Faure and Mensing, 2005):

$$\left(\frac{^{87}Sr}{^{86}Sr}\right)_{i-s} = \left(\frac{^{87}Sr}{^{86}Sr}\right)_{n} - 2.89\left(\frac{[Rb]}{[Sr]}\right)\lambda t \qquad (2)$$

where $(^{87}Sr/^{86}Sr)_n$ is the data from Table 2.3 (Appendix A), and [Rb] and [Sr] are the Rb and Sr concentrations, respectively (Table 2.2 in Appendix A). This equation has been reported as a good approximation of eq. 1. Therefore, in order to test differences between both equations, $(^{87}Sr/^{86}Sr)_{i-s}$ for t = 124 Ma and using the same λ value has been calculated.

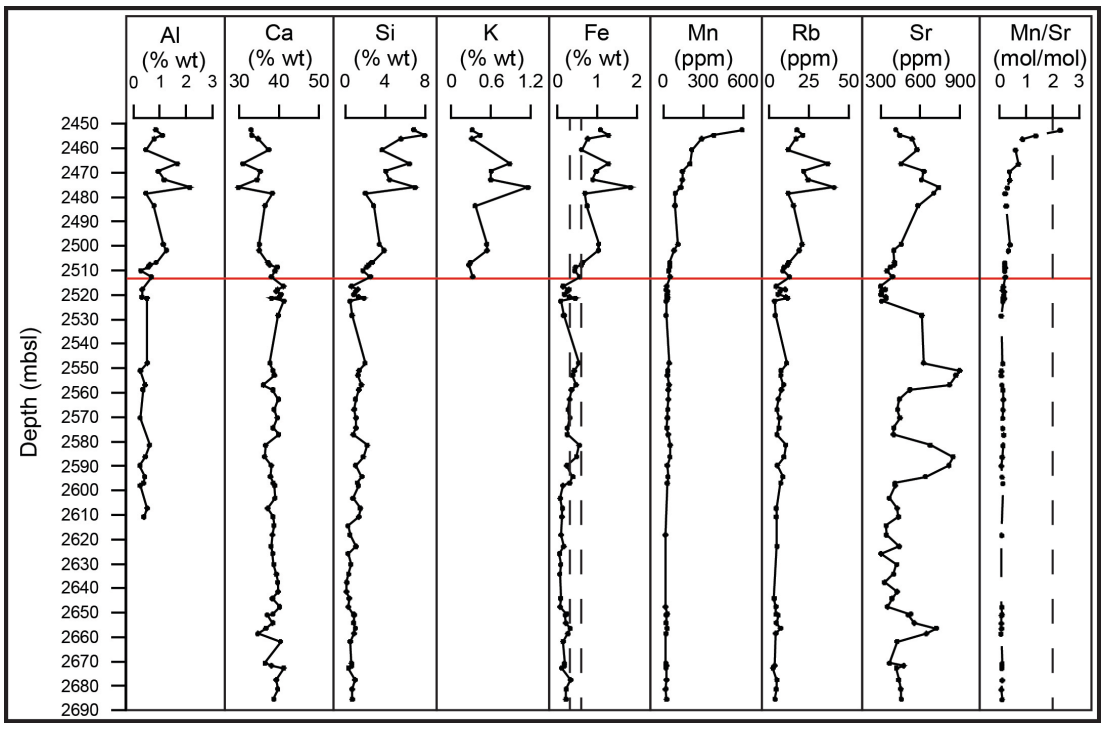


Figure 2 .7 – Al, Ca, Si, K, Fe, Mn, Rb and Sr contents and Mn/Sr ratios from Petrobras Well CB-3 against stratigraphic depth (mbsl – metres below sea level). Red line at 2513 mbsl defines two stratigraphic levels: a lower one with low detrital content and an upper one with higher detrital content. Black dashed lines on Fe content (0.3 an 0.6 wt %) and Mn/Sr ratios (2 mol/mol) show the limits where diagenetic overprint over $^{87}Sr/^{86}Sr$ values is likely to have happened. See text for details.

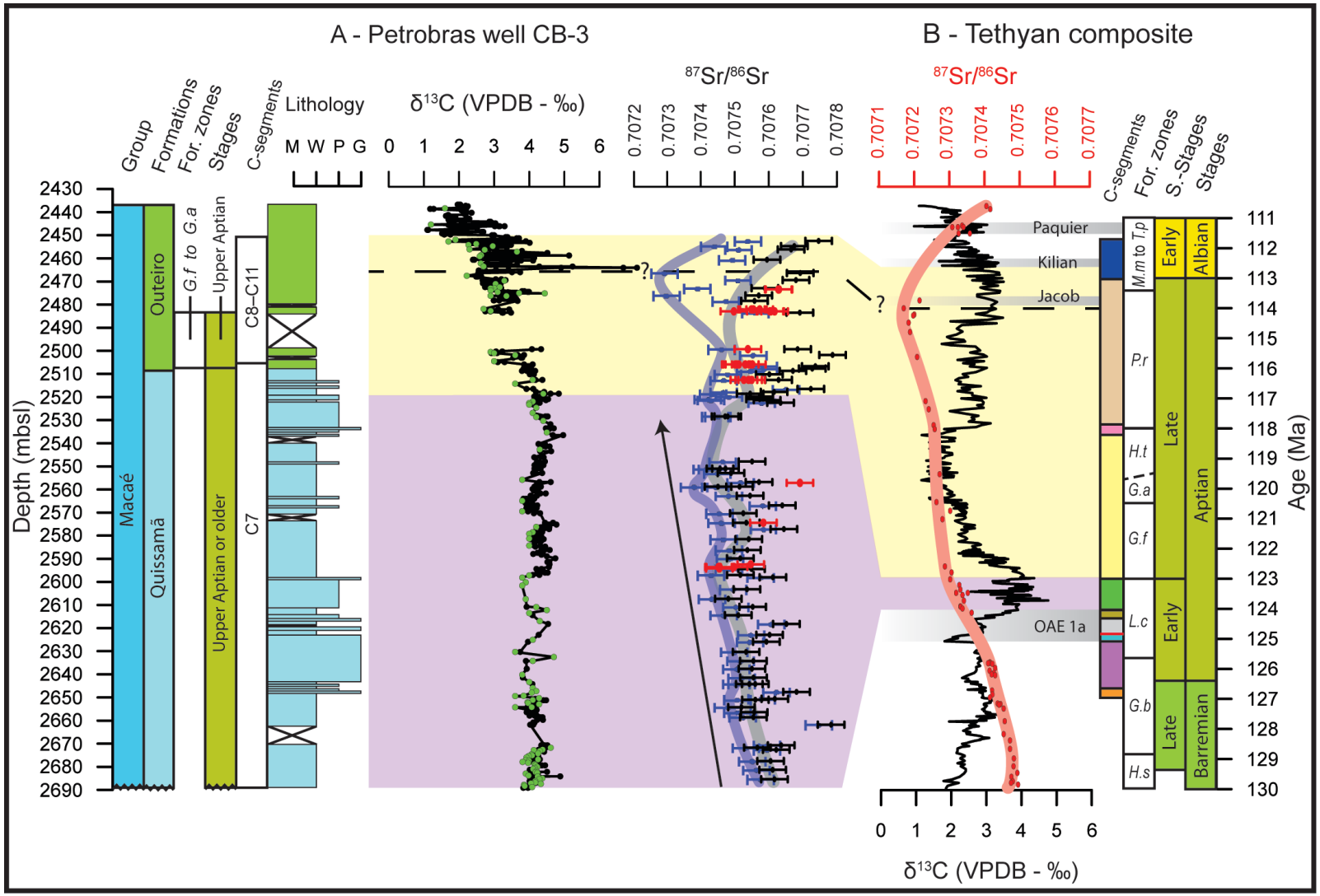

A - Petrobras well CB-3
B - Tethyan composite
Group
Formations
For. zones
Stages
C-segments
Lithology
M W P G
δ13C (VPDB - ‰)
87Sr/86Sr
Depth (mbsl)
Macaé
Outeiro
Quissamã
G.f to G.a
Upper Aptian
Upper Aptian or older
C8–C11
C7
Paquier
Kilian
Jacob
OAE 1a
M.m to T.p
P.r
H.t
G.a
G.f
L.c
G.b
H.s
S.-Stages
Early
Late
Albian
Aptian
Barremian
Age (Ma)

Figure 2.9 shows $(^{87}Sr/^{86}Sr)_n$, $^{87}Sr/^{86}Sr_i$ (113 Ma), $^{87}Sr/^{86}Sr_i$ (124 Ma) and $(^{87}Sr/^{86}Sr)_{i-s}$ (124 Ma) against stratigraphic depth. Rb contributes to an increase of $^{87}Sr_{rad}$ through time. Hence, after subtracting the radiogenic input, $^{87}Sr/^{86}Sr_i$ (113 Ma) and $^{87}Sr/^{86}Sr_i$ (124 Ma) values are lowered and closer to the original seawater composition. The differences between the $^{87}Sr/^{86}Sr_i$ (113 Ma), $^{87}Sr/^{86}Sr_i$ (124 Ma) and $(^{87}Sr/^{86}Sr)_{i-s}$ (124 Ma) profiles are negligible (red, blue and green data in Figure 2.9). Hence $^{87}Sr/^{86}Sr_i$ (124 Ma) is used subsequently in the text. Recalculated $^{87}Sr/^{86}Sr_i$ (124 Ma) do not show significantly lower values than the measured $(^{87}Sr/^{86}Sr)_n$ ratios below a stratigraphic depth of 2520 mbsl. However, they do show differences above 2520 mbsl, where introduction of $^{87}Sr_{rad}$ derived from detrital minerals is likely to have taken place.

Figure 2 .8 –Chemostratigraphic correlation between A: Petrobras Well CB-3 from the Campos Basin: lithostratigraphic units, foraminiferal zones, stages, lithology (see description in Figure 2.2), strontium-isotope data (black – measured values from carbonate leached, blue – $^{87}Sr/^{86}Sr_i$ (124Ma), red – measured values from benthic foraminifera); grey and blue band through lower measured $^{87}Sr/^{86}Sr$ and $^{87}Sr/^{86}Sr_i$ (124Ma) values, respectively and B: Tethyan carbonate strontium- and carbon-isotope composite age-calibrated curve (Ogg et al., 2012): black – carbonate carbon-isotope composite from Herrle et al. (2015), red – strontium-isotope data from Bodin et al. (2015), red band – through lower strontium-isotope data of Bodin et al. (2015); (see description in Figure 2.2). Purple and yellow band shows correlation between A and B based on carbon-isotopes and foraminifera biostratigraphy as in Figure 2.2.

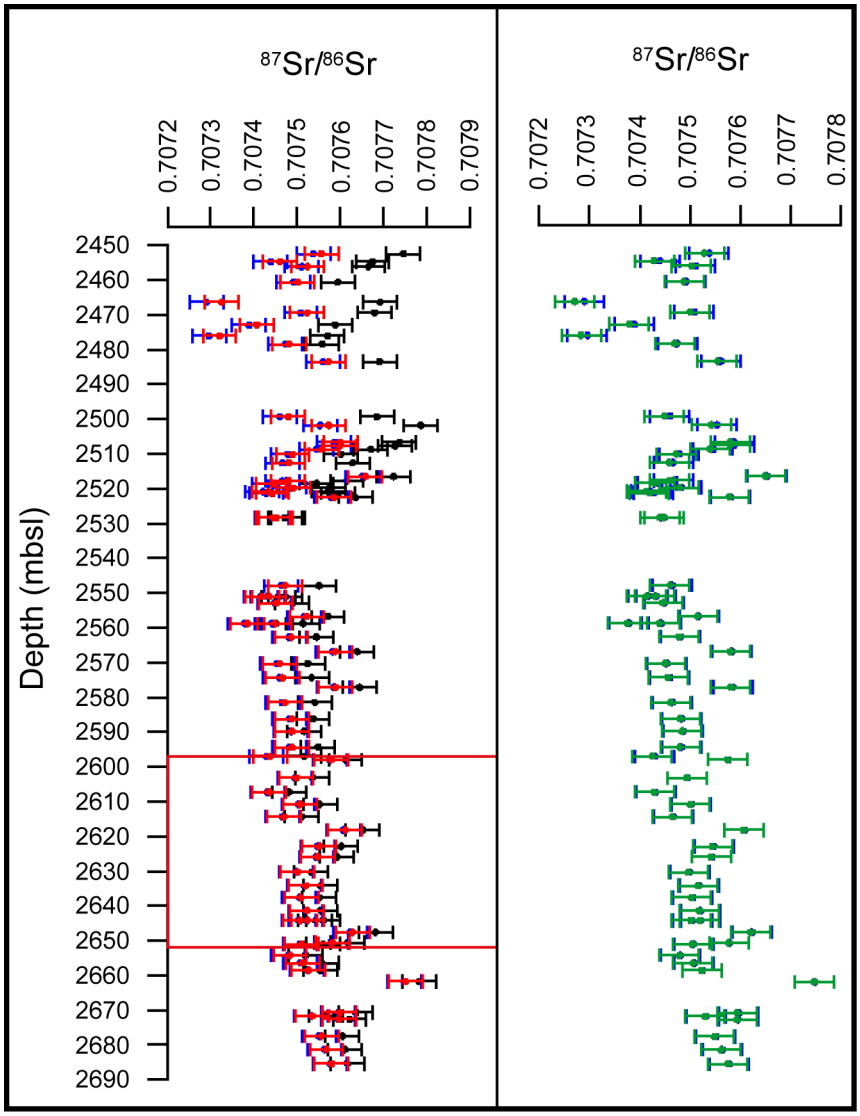


Figure 2 .9 – $^{87}Sr/^{86}Sr$ (black), $^{87}Sr/^{86}Sr_i$ (113 Ma - red), $^{87}Sr/^{86}Sr_i$ (124 Ma - blue) and $^{87}Sr/^{86}Sr_{i\ -\ S}$ (124 Ma - green) from Petrobras Well CB-3 against stratigraphic depth (mbsl). Red rectangle highlights samples that have not underwent oil extraction.

Fe and Mn contents can be used to assess the possible role of diagenetic overprints on carbonate samples (Denison et al., 1994; Jacobsen and Kaufman, 1999; Yamamoto et al., 2013). Fe contents vary between less than 0.1 and 1.8 wt %. All the samples below 2508 mbsl have Fe contents below 0.6 wt % and ~70% of samples

below that level have Fe contents below 0.3 wt % (Figure 2.7). Previous studies have shown that carbonate samples with Fe contents lower than 0.3 wt % usually have $^{87}Sr/^{86}Sr$ ratios derived from seawater, whereas samples with Fe contents higher than 0.6 wt % usually do not (Denison et al., 1994). Mn contents of samples from Petrobras Well CB-3 vary between less than 15 and 594 ppm and have Mn/Sr (mmol/mmol) < 2, except for the sample at 2452.45 mbsl (Figure 2.7). This criterion has been widely used to identify samples with diagenetic overprint affecting $^{87}Sr/^{86}Sr$ ratios in carbonates (Denison et al., 1994; Jacobsen and Kaufman, 1999; Yamamoto et al., 2013). Most samples below 2508 mbsl do not shown evidence of diagenetic alteration of $^{87}Sr/^{86}Sr$ values, whereas above this level some alteration may have taken place. To sum up, carbonates above 2520 mbsl are likely to have suffered diagenetic overprints on $^{87}Sr/^{86}Sr$ values, whereas carbonates below this level largely retain values similar to their depositional $^{87}Sr/^{86}Sr$ ratios.

2.4.3.2 Strontium-isotope stratigraphy

Stratigraphic trends are assessed by drawing a band along the lower limits of the $^{87}Sr/^{86}Sr$ data, assumed to be the least altered (e. g., Burke et al., 1982; Jones and Jenkyns, 2001) (blue and grey bands in the Figure 2.8). A basal interval (2685–2528 mbsl) shows a general trend of decreasing values from ~0.70759 to ~0.70740 on both $^{87}Sr/^{86}Sr$ and $^{87}Sr/^{86}Sr_i$ (124 Ma). The decreasing trend of $^{87}Sr/^{86}Sr_i$ (124 Ma) and $(^{87}Sr/^{86}Sr)_n$ profiles in the interval 2528–2689 mbsl from Petrobras Well CB-3 can be readily correlated to the Barremian–Aptian interval (Jenkyns et al., 1995; Bralower et al., 1997; McArthur et al., 2012; Bodin et al., 2015) (Figure 2.8). However, both $^{87}Sr/^{86}Sr_i$ (124 Ma) and $(^{87}Sr/^{86}Sr)_n$ values from Petrobras Well CB-3 are higher than contemporaneous seawater and the contribution of $^{87}Sr_{rad}$ from detrital input is not

enough to explain the differences in the interval 2685–2528 mbsl. Hence, it is possible that other diagenetic processes not identified by relatively elevated Fe and Mn contents may still have caused some degree of offset of primary $^{87}Sr/^{86}Sr$ ratios.

Alternatively, the $^{87}Sr/^{86}Sr$ values recorded in Petrobras Well CB-3 may be the result of mixing of seawater and groundwater and/or fluids expelled from evaporite dissolution in the depositional environment and/or during early diagenesis. In this model, Sr derived from both groundwaters and/or evaporite dissolution must have had $^{87}Sr/^{86}Sr$ values and/or concentrations considerably higher than contemporaneous seawater. The idealized $^{87}Sr/^{86}Sr$ profile (grey band in Figure 2.8) of the Petrobras Well CB-3 runs roughly parallel to the assumed seawater curve (red band in Figure 2.8) of Bodin et al. (2015), suggesting that the least altered samples carry a primary signature with a roughly constant offset from seawater to more radiogenic values (Figures 2.8 and 2.9).

The correlation to the C7 segment in the reference Tethyan age-calibrated composite based on foraminiferal biostratigraphy and carbon isotopes shows that the trend of decreasing $^{87}Sr/^{86}Sr$ ratios support this correlation, but without totally constraining it (Figure 2.8). Although $^{87}Sr/^{86}Sr$ ratios recorded in the carbonates of the Petrobras Well CB-3 could result from different processes, it is deemed most likely that groundwater and riverine drainage into to the Campos Basin, with relatively radiogenic Sr-isotope values, diluted marine waters in the proto-South Atlantic such that their geochemistry departed somewhat from that of the world ocean (as discussed later in chapter 4).

The upper interval (2528–2452 m) shows different trends in $^{87}Sr/^{86}Sr$ and $^{87}Sr/^{86}Sr_i$ (124 Ma). The former shows a trend of increasing values in the afore-mentioned interval, whereas the latter still shows the decreasing trend in $^{87}Sr/^{86}Sr_i$

(124 Ma) up to ~2465 mbsl and an increasing trend in $^{87}Sr/^{86}Sr_i$ (124 Ma) above this level. Depositional $^{87}Sr/^{86}Sr$ ratios are probably between $^{87}Sr/^{86}Sr$ and $^{87}Sr/^{86}Sr_i$ (124 Ma) values, where the difference between them in the section above 2505 mbsl shows a possible higher contribution of $^{87}Sr_{rad}$ due to detrital input (up to 0.000441). Although $^{87}Sr/^{86}Sr_i$ (124 Ma) values become closer to the lowest contemporaneous seawater values for the interval 2452–2505 mbsl (~0.70715; e. g., McArthur et al., 2012), they are still relatively elevated. A correlation between the lower values encountered in the Late Aptian and $^{87}Sr/^{86}Sr_i$ (124 Ma) values of Petrobras Well CB-3 may be suggested, although ambiguity remains because of possible diagenetic overprint on the carbonates.

2.5 Discussion

The evidence suggests that the top of the evaporites correlates with the upper part of the OAE 1a interval and that most of the post-evaporite shallow-water carbonates are Aptian in age, which constitutes a major stratigraphic revision of southern Brazilian basins. The coincidence in timing of evaporite deposition with OAE 1a was apparently an important factor in fostering palaeoceanographic change during and after this event.

Deposition of the South Atlantic evaporites is estimated to have lasted 400–600 ky based on cyclostratigraphy (Freitas, 2006; Davison et al., 2012), although hiatuses can be present. This estimation is similar to that for deposition of the Miocene Mediterranean evaporites of the Messinian Crisis (~640 ky; Krijgsman et al., 1999). The depositional rate of South Atlantic evaporites is 3.33–5 m/ky, taking 2 km as the depositional thickness (Davison et al., 2012) deposited during 400–600 ky (Freitas, 2006). These figures are comparable with the high observed

depositional rates from modern halite (10–100 m/ky) and sulphates (usually gypsum, 1–40 m/ky) (Schreiber and Hsü, 1980). Therefore, it is likely that duration of evaporite deposition in the South Atlantic is shorter than the estimated duration of OAE 1a (~1.1 my; cf. Malinverno et al., 2010). Hence it is likely that the South Atlantic evaporite body formed during the OAE 1a interval, as also suggested by further evidence present in Chapter 3, although the chemostratigraphic correlation cannot confidently exclude the possibility that the onset of deposition could have been as early as Late Barremian.

The current view is that the South Atlantic evaporites were deposited between 116–111 Ma in the Late Aptian–earliest Albian interval (Davison, 2007; Chaboureau et al., 2013; Gomes et al., 2016; timescale of Ogg et al., 2012), some 4–13 my after OAE 1a (cf. Bottini et al., 2012): an interpretation based upon the stratigraphic relationships between the evaporites and supposedly extrusive rocks with Ar-Ar ages of 117 Ma (cited in Moreira et al., 2007) and 113.2 ± 0.1 Ma (cited in Dias et al., 1994). However, no details are available as to whether the dated samples are from pristine or altered rocks, and detailed analytical methodologies are not reported. In addition, this evidence alone is at odds with the presence of Lower Aptian ammonites (*Dufrenoyia justinae*) described by Bengston et al. (2007) from supra-evaporite sediments in the Sergipe-Alagoas Basin (Figure 2.1), and the record of Lower Aptian planktonic foraminifera (presence of *Leupoldina cabri*) in supra-evaporite sediments from the African side, offshore Angola (Davison, 2007). These associations suggest that evaporite deposition took place, at least locally, before or during the Early Aptian. Significantly, the new stratigraphic correlation for the evaporites from the Campos and Santos Basins with OAE 1a, based on planktonic foraminiferal biostratigraphy and $\delta^{13}C$ profiles, corresponds closely with the well-

dated ages of those from the African margin and Sergipe-Alagoas Basin, onshore northern Brazil (Davison, 2007).

Important evidence for the age of the evaporites is offered by their sulphur-isotope values ($\delta^{34}S$). $\delta^{34}S$ values between ~17 and ~22‰ obtained from anhydrite of the Santos Basin (blue rectangle, Figure 2.2: Santos Neto et al., 2013) can be compared to $\delta^{34}S$ values from barite and carbonate-associated sulphate in sediments worldwide (red data, Figure 2.2). The values from the Santos Basin evaporites are higher than the range of $\delta^{34}S$ values post-dating OAE 1a (14–17‰) and lower than the highest values recorded in the latest Late Barremian (24–25‰; Figure 2.2). Hence, they likely constrain evaporite deposition to the interval latest Late Barremian–Early Aptian, including OAE 1a.

The fall in $\delta^{34}S$ values recorded worldwide (Figure 2.2) coincides with the characteristic pattern in $\delta^{13}C$ profiles during OAE 1a: a negative excursion followed by the onset of a positive excursion (e. g., Gomes et al., 2016). Formation of the Ontong Java Plateau probably released massive amounts of CO_2 and SO_2 during basalt-seawater interaction, both ^{32}S and ^{12}C enriched, which can explain relatively low $\delta^{34}S$ and $\delta^{13}C$ values at the onset of OAE 1a (e. g., Paytan et al., 2004; Meháy et al., 2009). However, it cannot explain the decoupling between $\delta^{34}S$ and $\delta^{13}C$ profiles, whereby the positive excursion in $\delta^{13}C$ occurs with low $\delta^{34}S$ values during and after OAE 1a. This pattern is in marked constrast with positive excursions in both $\delta^{13}C$ and $\delta^{34}S$ profiles of the Toarcian and Cenomanian–Turonian OAEs, when enhanced burial of organic matter and pyrite preferentially sequestered ^{12}C and ^{32}S, respectively (Gill et al. 2011; Owens et al., 2013; Gomes et al., 2016). Geochemical models suggest that burying a huge volume of gypsum and/or anhydrite in the South Atlantic would have led to a reduction of the global concentration of sulphate,

limiting pyrite burial and enhancing organic-matter preservation, which could explain the behaviour of $\delta^{34}S$ and $\delta^{13}C$ profiles during and after OAE 1a (Wortmann and Chernyavsky, 2007). Moreover, although the former suggested age of the evaporites (116–111 Ma) would contradict such a suggestion, the new stratigraphic revision is in perfect agreement with this geochemical model.

2.6 Conclusions

A new stratigraphy of the South Atlantic is presented, whereby evaporites deposited in the early rifting stage are correlated to the OAE 1a interval (125.51–124.41 or 120.21–119.11 Ma; Erba et al., 2015 and references therein) based on foraminiferal biostratigraphy and carbon- and strontium-isotopes. This correlation implies that the evaporites are significant older than their former suggested age of 116–111 Ma. The new stratigraphic revision suggests that deposition of the South Atlantic evaporites took place after the release of massive amount of CO_2 and SO_2 during the formation of Ontong Java Plateau and may have removed massive amounts of sulphate from the world ocean, hence fostering important palaeoceanographic changes during and after OAE 1a.

Chapter 3

New constraints on geochemical origin and age of pre-Salt carbonates in the South Atlantic based upon Re-Os geochronology, $^{187}Os/^{188}Os$ and $^{87}Sr/^{86}Sr$ ratios

This chapter is co-authored by Leonardo R. Tedeschi, Hugh C. Jenkyns, Stuart A. Robinson, Robert A. Creaser, Isabela de O. Carmo, Farid Chemale Jr, Raphael Pietzsch Amora and Joselito C. Vazquez. Leonardo R. Tedeschi is the lead author who has written the majority of the chapter, with comments from all co-authors, and performed all analyses of Petrobras Well A, except for elemental analyses. Leonardo R. Tedeschi also sampled all carbonate samples in collaboration with Petrobras geologists Raphael Pietzsch Amora and Dr Isabela de O. Carmo. Dr Robert A. Creaser obtained the Re-Os dataset. Dr Farid Chemale Jr obtained strontium-isotope analyses of samples derived from Petrobras Wells B and C. Petrobras chemist Joselito C. Vazquez undertook elemental analyses. Petrobras geologist Jeanine L. Grilo sampled, picked and identified ostracods under the stereomicroscope, before sending them to Leonardo R. Tedeschi, who performed other analyses: SEM-EDS, elemental and $^{87}Sr/^{86}Sr$ determinations.

3.1 Introduction

The discovery of sub-salt carbonate reservoirs sealed by Lower Cretaceous (Aptian) evaporites in the South Atlantic, the so-called pre-Salt carbonates, has revolutionized the hydrocarbon exploration of the region. For example, the Tupi (Lula) and Iara Fields in the Santos Basin are among the largest oil fields discovered

in the recent decades with reserves of more than 3 billion of barrels of oil (Mohriak et al., 2012). In addition, other fields have been found in the pre-Salt carbonates in offshore Brazil: the Libra area and Buzios oil field (formerly Franco area) in the Santos Basin and the Whale Park area in the Campos Basin (Sabato Ceraldi and Green, 2017). The depositional context of the pre-Salt carbonates is important not only from the petroleum industry perspective, but also for accurate reconstruction of the opening of the central segment of the South Atlantic (CSSA) during the Early Cretaceous (Davison, 2007; Torsvik et al., 2009; Chaboureau et al., 2013) and its relation to global palaeoceanography. The depositional environment of the upper part of the pre-Salt carbonates in the Campos and Santos Basins is still poorly understood. Deposition in both a continental setting (Wright, 2012) or as part of the initial marine incursion into southern Brazilian basins (Dias, 2005) has been advocated. In the latter case, different models for the entry of seawater into the CSSA have been proposed: either from the south towards the north across the Walvis Ridge (Dias, 1998, 2005) or in the opposite direction as a result of flooding over a large area of other Brazilian Basins (Arai, 2009, 2014). If the upper part of the pre-Salt carbonates records the marine incursion, is it possible to quantify the marine and continental proportions during their deposition? Alternatively, if they record solely a continental environment, such as an evaporative lake (Wright and Barnett, 2015; Sabato Ceraldi and Green, 2017), what exactly is their depositional context?

Another important issue is the precision of the timing related to the deposition of the pre-Salt carbonates, because different age ranges have been proposed for these sedimentary rocks, primarily constrained by two cited Ar-Ar radiometric ages: 113 ± 0.1 Ma from a grey-greenish trachyandesite from Petrobras Well 1-SCS-1 (Florianópolis High, Santos Basin) overlain by evaporites (Dias et al., 1994); and

118–117 Ma from basaltic flows interbedded between carbonates of the Barra Velha Formation (Figure 3.1) stratigraphically below the evaporites in the Santos Basin (Moreira et al., 2007). Neither citations give evidence of stratigraphic relationships from wells or seismic lines that would allow evaluation as to whether or not the basalts represent conformable extrusive rocks, and no petrography given to accompany the original Ar-Ar data. There is also a lack of information provided regarding the methodological and calibration techniques adopted. However, these age determinations have been extensively used to constrain a date for the base of the evaporites (e. g., Davison, 2007) and, consequently, the top of the pre-Salt carbonates, such as the 119–116 Ma assignment to this interval in the Campos and Santos Basins (Figure 3.1) (Chaboureau et al., 2013). These ages are in disagreement with the recent findings of planktonic foraminifera *G. ferreolensis*/*G. algerianus* biozones well above the evaporites in Petrobras Well CB-3 (Chapter 2) dated at 119–123 Ma (time scale of Ogg et al., 2012), and the correlation of the evaporites with the OAE 1a interval dated at ~125.51–124.41 or ~120.21–119.11 Ma (e. g., Erba et al., 2015 and references therein; Figure 1.2 in Chapter 1).

In this chapter, new geochemical data are presented: strontium isotopes ($^{87}Sr/^{86}Sr$) and rhenium-osmium geochronology and isotopes (Re-Os, $^{187}Re/^{188}Os$, and $^{187}Os/^{188}Os$) in order to establish the nature of the aqueous environment (marine versus non-marine) and to help constrain the age of the pre-Salt carbonates.

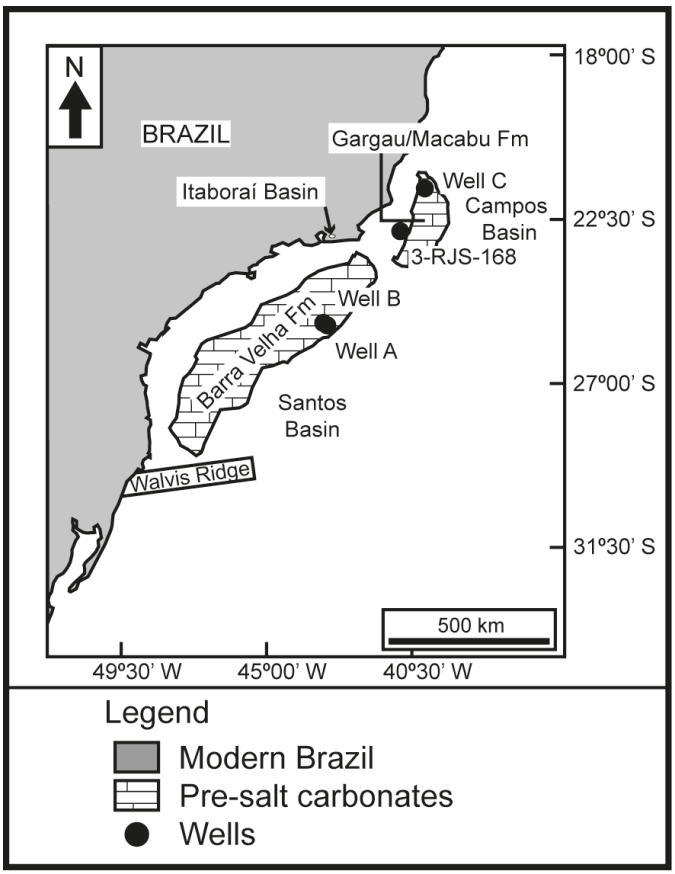


Figure 3 .1 – Location map of Petrobras Wells A, B and C, offshore south-east Brazil. Area of pre-Salt carbonates adapted from palaeogeographic map for 119–116 Ma interval (Chaboureau et al., 2013). Fm – Formation.

3.2 Geological setting

The stratigraphic record of the Campos and Santos Basins, based on offshore wells, can be split into three main super-sequences: rift, post-rift and drift (Moreira et al., 2007; Winter et al., 2007; Chaboureau et al., 2013) (Figure 3.2). Overlying the metamorphic and igneous rocks of the Precambrian basement, the rift super-sequence (<4400 km) is primarily composed of subaqueously and subaerially extruded tholeiitic flood basalts and dolerites that are similar in composition to the inland Paraná basalts (Cabiúnas/Camboriú Formations) (Mizusaki et al., 1992; Moreira et al., 2007; Winter et al., 2007). Most of the K-Ar age of basalts from Campos and Santos Basins lie in the range of 134–122 Ma (cited in Mizusaki et al.,

1992) and published K-Ar ages from offshore Petrobras Wells are in the range of 138–112 Ma (Fodor et al., 1983). Also included in the rift super-sequence are continental siliciclastic and lacustrine volcaniclastic sediments (Itabopoana/Atafona/Piçarras Formations) and interbedded lacustrine coquinas and organic-rich shales (Coqueiros/Itapema Formations), which constitute the lower part of the Lagoa Feia and Guaratiba Groups (Bertani and Carozzi, 1985a, b; Moreira et al., 2007; Winter et al., 2007). In distal settings, the overlying post-rift super-sequence comprises interbedded 'abiotic' and/or microbial carbonates and shales (Gargaú, Macabu and Barra Velha Formations; with a large thickness differences varying between 55 and >500 m) lying stratigraphically below evaporites whose maximum depositional thickness is 2 km (Winter et al., 2007; Davison et al., 2012; Wright and Barnett, 2015). The evaporites terminate the post-rift super-sequence (upper part of Lagoa Feia and Guaratiba Groups) (Figure 3.2) and comprise cycles of anhydrite and halite, locally with more soluble salts such as carnallite, sylvite and tachyhydrite (Freitas, 2006; Moreira et al., 2007; Davison et al., 2012). Halite and anhydrite from onshore wells of the Espírito Santos Basin, which are correlated with evaporites from the Campos and Santos Basins, possess Br contents and $^{87}Sr/^{86}Sr$ ratios that indicate derivation from marine water (Dias, 1998). Above the evaporites, in distal settings, the drift super-sequence (up to 15 km) is composed of shallow- and deep-water carbonates, sandstones, siltstones, marls and shales deposited in a marine setting (Moreira et al., 2007; Winter et al., 2007).

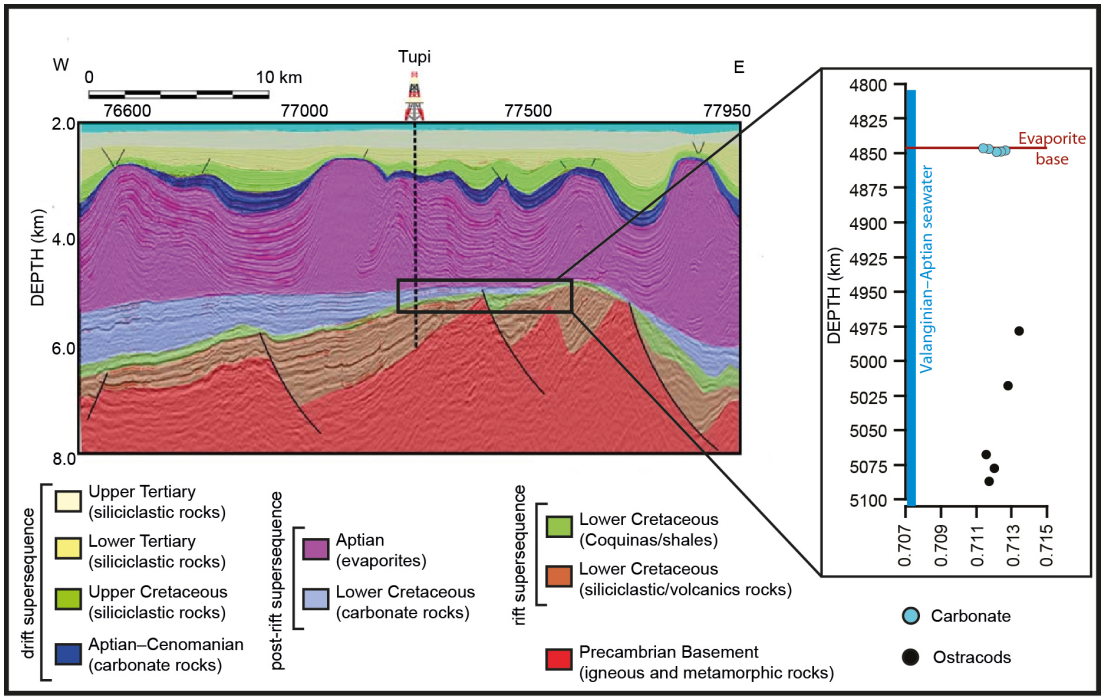


Figure 3 .2 –Seismic section showing stratigraphy with the pre-Salt carbonate reservoir below the massive stratified evaporites in one of the largest oil fields in the western world (Lula oil field: Mohriak et al., 2012). Highlighted is the area where Petrobras Wells A and B were spudded ~10km from the Petrobras Well Tupi. Also shown are the $^{87}Sr/^{86}Sr$ ratios of carbonates and ostracods analysed in this work and $^{87}Sr/^{86}Sr$ ratios of possible contemporaneous seawater (Valanginian–Aptian: McArthur et al., 2012; Bodin et al., 2015). W – West; E – East

The pre-Salt carbonates include coquinas from the rift super-sequence (Coqueiros/Itapema Formations) and 'abiotic' and/or microbial carbonates from the post-rift super-sequence (Gargaú/Macabu/Barra Velha Formations) (Moreira et al., 2007; Winter et al., 2007). The upper part of the coquinas has been described as being deposited in the sag phase (Sabato Ceraldi and Green, 2017) and could be included in the post-rift super-sequence. Coquinas consist of thick packages (300–400 m) dominated by bivalve molluscs, with subordinate ostracods and gastropods (Thompson et al., 2015). They have been interpreted as deposited in lacustrine environment based on several lines of evidence (Bertani and Carozzi, 1985a, b; Abrahão and Warme, 1990; Thompson et al., 2015): 1) lack of typical marine fauna,

including the absence of typical stenohaline marine organisms (i. e., echinoderms, brachiopods, cephalopods, and bryozoans); 2) presence of biogenic components commonly found in lakes, such as lacustrine ostracods; 3) complex facies geometry, distribution, and lateral relationships; 4) occurrence of unusual minerals, such as stevensite, or mineral trace elements that can only form from waters chemically different from normal seawater; 5) indicators of rapid salinity fluctuations compared with marine sequences (based on changing faunal assemblages through time); 6) lack of evidence for typical marine processes, such as tidal currents or strong wave action; 7) complex vertical and lateral lithofacies assemblages (typical of lacustrine settings due to high-frequency climatic oscillations); and 8) comparisons with lithostratigraphic units of similar age, or with recent analogues, that have similar tectono-sedimentary settings and evolution. Because of the occasional presence, in interbedded shales of Petrobras Well 3-RJS-168 (Figure 3.1; Campos Basin), of trochospiral foraminifera and supposed marine ostracods, which are either not age-diagnostic or too badly preserved to permit identification, episodic marine excursions may have taken place during deposition of the coquinas, followed by a return to continental sedimentation (Silva-Telles Jr. et al., 1994; Silva-Telles Jr., 1996).

'Abiotic' and/or microbial carbonates from the post-rift super-sequence (Gargaú/Macabu/Barra Velha Formations) include a variety of facies (Dias, 1998, 2005; Moreira et al., 2007; Winter et al., 2007; Terra et al., 2010; Wright, 2012; Wright and Barnett, 2015; Sabato Ceraldi and Green, 2017): (a) shrubby boundstones/stromatolites, (b) wackestones with spherulites and ostracods, (c) laminites, (d) dolomites, (e) marls, (f) shales, (g) grainstones and packstones with clasts mainly formed by shrubby boundstones/stromatolites, spherulites, laminites and ostracods. The environment associated with these carbonates ('abiotic' and/or

microbial) is still undetermined (marine, brackish or continental), and available evidence supports several distinct environments. Marine to transitional settings have been supported by the similarities between the shrubby boundstone/stromatolite facies and modern shallow-water marine stromatolites, such as those found in Shark Bay, western Australia (Dias, 1998, 2005; Moreira et al., 2007; Winter et al., 2007) and by the tectonic evolution of the basin, whereby subsidence during the sag phase of the basin could have permitted the entrance of the seawater into the CSSA. On the other hand, the lack of marine fauna, the presence of lacustrine ostracods, the presence of Mg-phyllosilicates, such as stevensite, and the similarity of all facies described to those found in continental settings suggest deposition in a lacustrine setting (Wright, 2012; Tosca and Wright, 2015; Wright and Barnett, 2015; Sabato Ceraldi and Green, 2017). In addition, similar facies have been registered and interpreted as lacustrine in the Kwanza Basin, which is the counterpart to the Campos Basin on the African (Angola) side of the South Atlantic (Saller et al., 2016; Sabato Ceraldi and Green, 2017).

3.3 Materials and methods

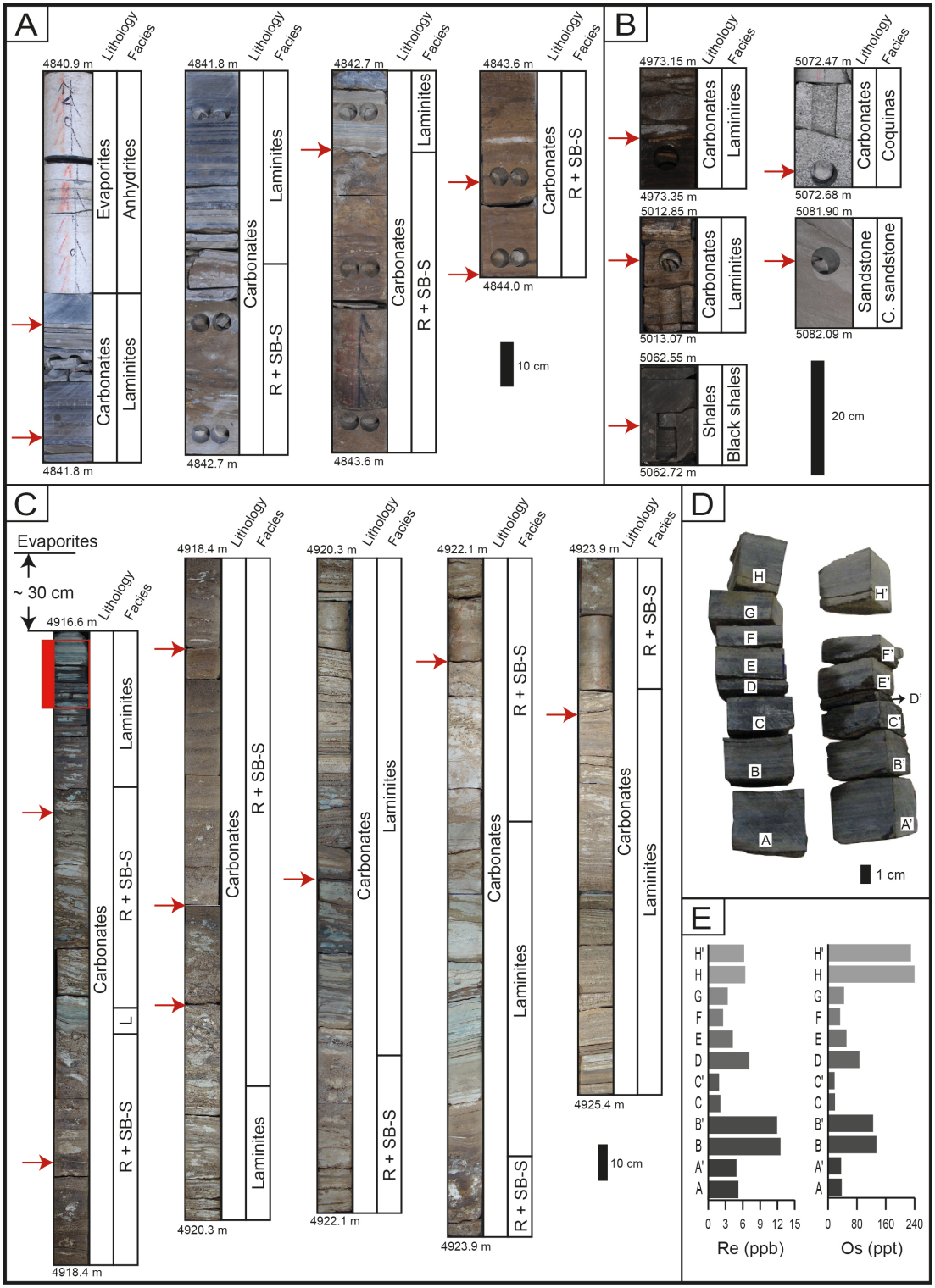
Samples from Petrobras Wells A and B from the Santos Basin and Petrobras Well C from the Campos Basin have been examined (Figure 3.1). Petrobras Wells A and B are less than 10km apart from the Petrobras Well Tupi, which discovered the Lula oil Field (25°33'S; 42°48'E and 25°34'S; 42°50'E, respectively), where a public seismic profile is available to illustrate the stratigraphy (Figure 3.2), whereas the Petrobras Well C (Jubarte oil Field; 21°16'S; 40°00'E) is more than 550km from both Petrobras Wells A and B. All samples are in sub-evaporite parts of the stratigraphy (Table 3.1): (a) 10 samples of cores from Petrobras Well A (5

carbonates and 5 carbonates/sandstone/shales used to separate ostracods from cores; Figures 3.3A and 3.3B); (b) 9 carbonate samples of cores from Petrobras Well B (Figure 3.3C) and; (c) 9 carbonate samples of sidewall cores from Petrobras Well C (Figure 3.4). Therefore, a total of 28 samples have been used in this study (Table 3.1). All samples are related to penetrated depth in metres measured during drilling operations (Figures 3.3 and 3.4). Adjustments made according to confidential logs would change depths in the centimetre- to metre-scale (core depths of Petrobras Well A would be increased by ~4–5 m and core depths of Petrobras Well B would be increased by ~0.3 m). However, the original penetrated depth as described in cores and sidewall core samples has been kept. All depths are expressed with a decimetre resolution, with the exception of the cores where ostracod samples were obtained that are illustrated in Figure 3.3B, whose position is referred to centimetre scale (Table 3.1, Figures 3.3 and 3.4). The base of the evaporite sequence was encountered at 4841.5 m, ~4916.3 m and ~4311 m in Petrobras Wells A, B and C, respectively. The contact between the evaporites and pre-Salt carbonates was cored in Petrobras Well A (Figure 3.3A), but not in Petrobras Wells B and C (Figures 3.3C and 3.4). Consequently, the stratigraphic position of the contact between the evaporites and pre-Salt carbonates in Petrobras Wells B and C has been estimated using confidential logs. The contact was estimated as ~0.3 m above the top of the cored section in Petrobras Well B and ~36 m above the highest sidewall core sample used in this study from Petrobras Well C (Figure 3.3C).

Table 3.1 – Samples used in this study and strontium-isotope analyses. Carb – carbonate, Ostra – ostracods, UO – University of Oxford, UA – University of Alberta, LGI-UFRGS – Laboratório de Geologia Isotópica-Universidade Federal do Rio Grande do Sul, Re-Os – Rhenium-osmium analyses, 2SE – 2 standard error of the mean.

Well	Depth (m)	Material	Laboratory	$^{87}Sr/^{86}Sr$	2SE ($x10^{-6}$)	Counts	$^{87}Sr/^{86}Sr_i$ 113 Ma	$^{87}Sr/^{86}Sr_i$ 130 Ma
A	4841.5	Carb	UO	0.711396	9	47	0.711388	0.711386
				0.711386	9	48	0.711378	0.711377
	4841.8	Carb	UO	0.711704	9	47	0.711690	0.711688
				0.711702	11	48	0.711688	0.711686
	4842.9	Carb	UO	0.712638	9	48	0.712439	0.712409
				0.712630	10	49	0.712431	0.712401
	4843.8	Carb	UO	0.712402	9	48	0.712313	0.712300
				0.712422	9	48	0.712334	0.712320
	4844.0	Carb	UO	0.712155	10	47	0.711912	0.711875
				0.712194	13	49	0.711951	0.711915
	4973.28	Ostra	UO	0.713427	12	49		
				0.713424	10	48		
	5012.93	Ostra	UO	0.712756	13	49		
				0.712791	13	48		
	5062.65	Ostra	UO	0.711558	11	48		
				0.711553	9	46		
	5072.60	Ostra	UO	0.712012	11	49		
	5082.00	Ostra	UO	0.711732	10	47		
				0.711715	10	47		
B	4916.8*	Carb	UA- Re-Os					
	4917.1	Carb	LGI-UFRGS	0.712765	12	117	0.712761	0.712760
	4918.1	Carb	LGI-UFRGS	0.713046	14	117	0.713044	0.713044
	4918.7	Carb	LGI-UFRGS	0.712865	14	114	0.712863	0.712863
	4919.4	Carb	LGI-UFRGS	0.713063	21	90	0.713061	0.713061
	4919.7	Carb	LGI-UFRGS	0.713129	19	57	0.713122	0.713121
	4921.2	Carb	LGI-UFRGS	0.713055	14	115	0.713035	0.713032
	4922.4	Carb	LGI-UFRGS	0.713152	15	117	0.713142	0.713141
	4924.4	Carb	LGI-UFRGS	0.713128	14	116	0.713124	0.713123
C	4347.0	Carb	LGI-UFRGS	0.713061	6	105	0.713042	0.713039
	4348.0	Carb	LGI-UFRGS	0.712991	2	105	0.712970	0.712967
	4348.6	Carb	LGI-UFRGS	0.713044	6	105	0.713034	0.713032
	4350.5	Carb	LGI-UFRGS	0.713180	4	105	0.713172	0.713171
	4351.7	Carb	LGI-UFRGS	0.713217	9	105	0.713205	0.713203
	4352.3	Carb	LGI-UFRGS	0.713365	6	105	0.713354	0.713352
	4363.5	Carb	LGI-UFRGS	0.713344	14	105	0.713334	0.713333
	4366.5	Carb	LGI-UFRGS	0.713125	5	105	0.713089	0.713084
	4369.5	Carb	LGI-UFRGS	0.713365	2	105	0.713350	0.713348

* This depth refers to the mean depth of a whole sample with ~20 cm-thickness. See Figures 3.3C and 3.3D and the text for further explanation.


A
4840.9 m
Lithology
Facies
Evaporites
Anhydrites
Carbonates
Laminites
4841.8 m
4841.8 m
Carbonates
Laminites
R + SB-S
4842.7 m
4842.7 m
Carbonates
Laminites
R + SB-S
4843.6 m
4843.6 m
Carbonates
R + SB-S
4844.0 m
10 cm
B
4973.15 m
Carbonates
Laminires
4973.35 m
5072.47 m
Carbonates
Coquinas
5072.68 m
5012.85 m
Carbonates
Laminites
5013.07 m
5081.90 m
Sandstone
C. sandstone
5082.09 m
5062.55 m
Shales
Black shales
5062.72 m
20 cm
C
Evaporites
~ 30 cm
4916.6 m
Carbonates
R + SB-S
L
Laminites
4918.4 m
4918.4 m
Carbonates
R + SB-S
Laminites
4920.3 m
4920.3 m
Carbonates
Laminites
R + SB-S
4922.1 m
4922.1 m
Carbonates
R + SB-S
Laminites
4923.9 m
4923.9 m
Carbonates
Laminites
R + SB-S
4925.4 m
10 cm
D
H
G
F
E
D
C
B
A
H'
F'
E'
D'
C'
B'
A'
1 cm
E
H'
H
G
F
E
D
C'
C
B'
B
A'
A
0 3 6 9 12 15
Re (ppb)
0 80 160 240
Os (ppt)

Five samples from Petrobras Well A were used to separate ostracods. The lithologies of these samples include carbonates (laminites, coquinas and wackestones with spherulites and ostracods), calcareous sandstone and black shales (Figure 3.3B). These samples will be referred to as "ostracod samples" throughout the text. The other 23 samples presented here are referred to as "carbonate samples" (Table 3.1, Figures 3.3A, 3.3C and 3.4) and the lithologies include laminites, wackestones with spherulites and ostracods, shrubby boundstones/stromatolites and reworked facies (rudstones, grainstones and packstones). Laminites and wackestones with spherulitic calcite and ostracods within a matrix composed mainly of micrite, and dolomite rhombs (<0.1 mm), and locally with Mg-silicates, are displayed in Figure 3.3 and are interpreted as slack-water facies. Shrubby boundstones/stromatolites comprise radiating bundles of fibrous-to-prismatic calcite crystals (up to 5 mm) that in places are entirely dolomitized, with variable amounts of interstitial 'floating' euhedral to subhedral fine-grained dolomite crystals (<0.1 mm) and/or micrite. Such facies have been described and classified both as shrubby boundstones (Wright, 2012; Saller et al., 2016) and stromatolites (Terra et al., 2010), and both names, (SB-S), are used in this study.

Figure 3 .3 –Core images of Petrobras Wells A and B with lithology, facies and sample locations. Red arrows and rectangle show the position of samples used in this study. (3A) Cores from Petrobras Well A show the contact between the evaporites and pre-Salt carbonates and position of five carbonate samples. (3B) Images of cores from Petrobras Well A, where five ostracod samples were obtained. (3C) Cores from Petrobras Well B. Note that the contact between evaporites and pre-Salt evaporites was not cored; it was estimated to be situated ~0.3 m above the top of the cored section based on confidential logs. The rectangle highlights the position of the sample used for Re-Os analyses. (3D) Enlargement of the red rectangle of the sample used for Re-Os analyses, showing letters that represent the subsamples used in Figure 3.10. (3E) Rhenium (Re) and Osmium (Os) concentrations of subsamples are shown in 3D. L – laminites and wackestones with spherulites; R + SB-S – reworked (intraclastic rudstone/grainstone/packstones) and/or shrubby boundstone/stromatolite facies; C. sandstone – calcareous sandstone.

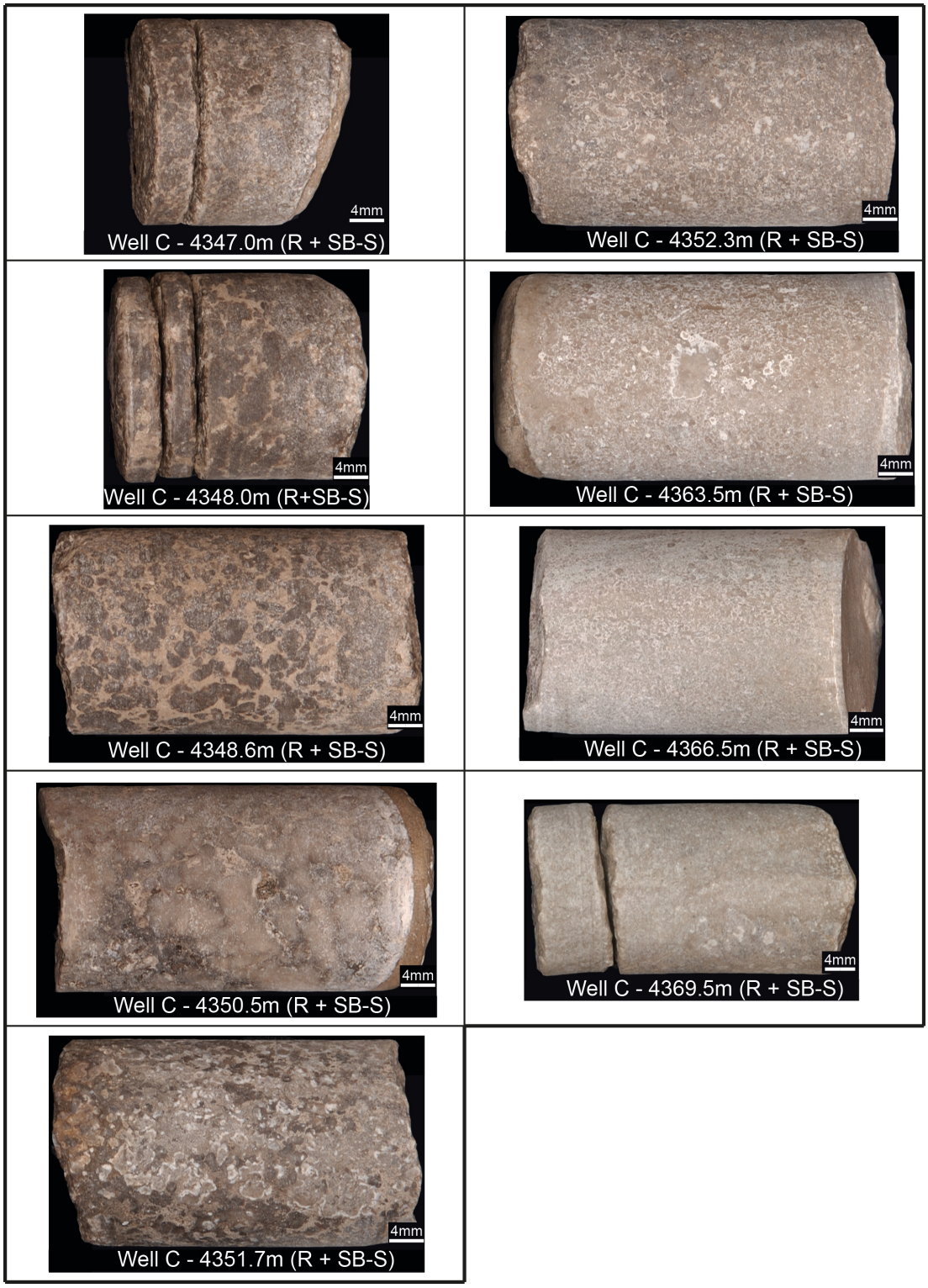


Figure 3 .4 – Sidewall cores from Petrobras Well C used in this study. All of them are reworked (intraclastic rudstone/grainstone/packstones) and/or shrubby boundstone/stromatolite facies (R + SB-S). 'Coins' of 1–2 cm were cut from each sidewall core for this study.

Reworked facies (R) include rudstones, grainstones and packstones with intraclasts of shrubby boundstones/stromatolites, spherulites, laminites and ostracods. Because it is difficult to decide during macroscopic description of some intervals whether shrubby crystals are *in situ* or reworked, and there are rapid lithological changes in core, we represented the samples in question as reworked facies with shrubby boundstones/stromatolites (R + SB-S) in Figures 3.3 and 3.4.

3.3.1 Petrobras Well A

3.3.1.1 Sampling and separation of ostracods

Five carbonate samples and five ostracod samples from Petrobras Well A (Figures 3.3A and 3.3B) were used in this study. Carbonate samples include three samples of laminites and wackestones with spherulites and ostracods (laminites in Figure 3.3A) and two reworked and shrubby boundstone/stromatolite facies (R + SB-S). These five samples (~10g) were powdered at the Petrobras Research Centre (CENPES) using an agate mortar. One aliquot of each powdered sample was sent to Oxford University for strontium-isotope ($^{87}Sr/^{86}Sr$), total inorganic and organic carbon (TIC and TOC), X-ray diffractometry (XRD) analyses, whereas another aliquot remained at CENPES for X-ray fluorescence (XRF).

Five carbonate/sandstone/shale samples from Petrobras Well A (Table 3.1; Figure 3.3B) were used to separate ostracods at CENPES. The procedure includes soaking ~60g of rock in hydrogen peroxide (H_2O_2) at 80°C until complete oxidation of organic matter had taken place and washing in running tap water in 1.0 and 0.125 mm sieves. After drying, ostracod valves were picked under a Discovery V8 stereomicroscope with reflected light at CENPES for taxonomy and geochemical analyses. One specimen of each sample was picked and studied under the scanning

electron microscope by energy-dispersive spectroscopy (SEM-EDS) at CENPES. In addition, four to five valves (138–368 μg) of each sample were analysed at Oxford University, for $^{87}Sr/^{86}Sr$ and major and minor elements.

3.3.1.2 $^{87}Sr/^{86}Sr$ analyses

In the Oxford laboratory, picked ostracods were processed in an ultrasonic bath with deionized water and subsequently dissolved in 0.5M acetic acid for strontium-isotope and elemental analyses. Two different steps of dissolution were performed on powders from carbonate samples as described in item 2.3.5 in Chapter 2, a process that avoids, to some degree, potential contamination of radiogenic $^{87}Sr/^{86}Sr$ ratios present in non-pure (i. e., clay-rich) limestones (Bailey et al., 2000). However, the amount of carbonate present was calculated based on pre-determined total inorganic carbon (TIC) contents for samples from Petrobras Well A in this chapter, unlike the Ca content for samples from Petrobras Well CB-3 used in Chapter 2. These procedures were performed in duplicate for each carbonate sample. Solutions derived from dissolution of ostracod and carbonate samples were dried out in Teflon beakers and dissolved in 2M HNO_3. Sr separation was performed using prep*Fast*, which is an automatic chromatographic column system (Romaniello et al., 2015), and analyses were obtained in a Nu-Plasma HR multi-collector inductively coupled plasma mass spectrometer (MC-ICP-MS, Nu instrument) at Oxford University using the same procedures detailed in section 2.3.5 in Chapter 2. All ostracod samples, bar one (from 5072.6 m), were analysed twice and each duplicate of carbonate samples was analysed once (Table 3.1).

All $^{87}Sr/^{86}Sr$ data were internally corrected for fractionation by assuming $^{88}Sr/^{86}Sr$ ratio = 0.1194. Isotopic ratios were subsequently normalized to the commonly accepted value of the SRM-987 standard ($^{87}Sr/^{86}Sr$ = 0.710248). Data

taken from the literature have also been normalized to this value of SRM-987 for comparative purposes. Blanks were < 10 ng/g and the Sr content of all analysed samples was higher than 1000 ng. External reproducibility of the SRM-987 standard and internal standard of Aptian carbonate PLG9466 obtained throughout this thesis is described in section 2.3.5 in Chapter 2. All mean values, standard errors of the mean and numbers of measurements (counts) are displayed in Table 3.1.

3.3.1.3 Elemental content

All five carbonate samples from Petrobras Well A have been analysed for Al, Ca, Mg, Si, K, Fe Mn, Rb, Sr and S contents. Hand-held X-ray fluorescence equipment (XRF Olympus, Delta Premium 6000) was used for analyses on polished surfaces as described in section 2.3.3 in Chapter 2. The Mining Plus method was used to analyse S, in addition to Al, Ca, Mg, Si, K and Fe, which were expressed in weight percent (wt %), whereas the Soil mode was used to analyse Mn, Rb and Sr in parts per million (ppm). Mn was converted to weight percent (wt %) in order to compare with data from other wells. All data showed a coefficient variation of three analyses of each sample, the ratio between the standard deviation and average, of less than 30% and reference materials used to calibrate analyses are the same as used in section 2.3.3 in Chapter 2.

All five ostracod samples from Petrobras Well A were analysed for Al/Ca, Na/Ca, Mg/Ca, Si/Ca, K/Ca, Fe/Ca, Mn/Ca, Rb/Ca and Sr/Ca ratios at Oxford University. Part of each solution resulting from digestion of each ostracod sample in 0.5M acetic acid for the strontium-isotope analyses was dried out and dissolved in 0.45M HNO_3 (2 wt %). Samples were analysed for their Al, Na, Mg, Ca, Si, K, Fe, Mn, Rb and Sr content on a Thermo Scientific ELEMENT 2 inductively coupled plasma mass spectrometer (ICP-MS) at Oxford University. Matrix-matched

instrument-calibration standards were prepared from NIST SRMs brand-pure, single-element plasma-grade solutions prepared by CPA Chem. Precision of standards was better than ± 3% for all analysed elements, except for K (± 6%), and accuracy was better than ± 2% for all elements.

3.3.1.4 Total inorganic carbon and total inorganic carbon (TIC and TOC)

Five carbonate samples from Petrobras Well A were subjected to TIC and TOC analysis using a Rock-Eval 6 at Oxford University (Lafarge et al., 1998; Behar et al., 2001). Rock-Eval 6 analyses involve temperature-programmed heating (100 to 850°C) of a weighed sample in two micro-ovens in an inert atmosphere. The amount of hydrocarbons released during the pyrolysis are analysed by a flame ionization detector (FID), whereas CO and CO_2 are analysed by an infrared cell during pyrolysis and oxidation of samples. TOC and TIC, as well as many other parameters associated with organic matter not used in this Chapter, are obtained during the analyses. More details of analyses by Rock-Eval 6 are given in section 3 in Chapter 5. TIC and TOC are reported as weight percentage (wt %). The internal reproducibility of parameters obtained in the Rock-Eval 6 was assessed using the in-house standard SAB 134 (Blue Lias organic-rich marl, Lower Jurassic, UK; Hesselbo et al., 2004) and external reproducibility was assessed using the IFP 160000 standard from Institut Français du Pétrole throughout this thesis. SAB 134 has given TIC and TOC average and standard deviation (± 1σ) of 6.10 ± 0.15 wt % and 2.90 ± 0.08 wt % (n = 47), respectively. IFP 160000 standard has given TIC and TOC average and standard deviation (± 1σ) of 3.31 ± 0.04 wt % and 3.36 ± 0.06 wt % (n = 12), respectively. Reported values of IFP 160000 by Vinci Technologies® for TIC and TOC values are 3.26 ± 0.12 wt % and 3.28 ± 0.14 wt %, respectively.

3.3.1.5 X-ray diffractometry (XRD)

Five carbonate samples from Petrobras Well A were also subjected to bulk mineralogical analyses by X-ray diffractometry (XRD). These analyses were performed with a PANalytical Empyrean diffractometer with a Co Ka radiation at 40kV and 40 mA. Randomly oriented samples were analysed from 5–80 degrees per 0.026° step (2θ) in spinning mode. The scan was continuous with a scan step time of 96.4 seconds.

3.3.1.6 Scanning electron microscope - energy dispersive spectroscopy (SEM-EDS)

One specimen of each ostracod sample used to obtain $^{87}Sr/^{86}Sr$ ratios was screened by examination in a SEM Zeiss model EVO-40 attached to an EDS Oxford INCA at CENPES using the same methods described in section 2.3.4 in Chapter 2. Images were obtained in high vacuum with a distance of ~14 mm and an energy emission of 20 kV. An adapted preservation index (PI) was used to assess the effect of dissolution on ostracod valves based on SEM images (Keatings et al., 2002). According to PI, they can be classified from 1 to 4, where 1: presence of generally smooth valve surface; 2: localized pitting and surface etching on valve surface; 3: substantial removal of surface layers of the valve and enlargement of pore canals; 4: extreme surface degradation and cracking.

3.3.2 Petrobras Wells B and C

3.3.2.1 Sampling of Petrobras Well B

Nine carbonate samples from Petrobras Well B (Figures 3.3C and 3.3D) were used in this study. Carbonate samples from cores of Petrobras Well B include

three samples of laminites and wackestones with spherulites and ostracod facies (laminites in Figure 3.3C) and five reworked and shrubby boundstone/stromatolite facies (R + SB-S in Figure 3.3C). Eight out of nine samples from Petrobras Well B were processed for elemental content and $^{87}Sr/^{86}Sr$ ratios. One aliquot (~7g) of each sample from these eight samples underwent oil extraction in a soxhlet apparatus, and powders were obtained by crushing in an agate mortar at CENPES. Subsequently, the powders were sent to the Société Générale de Surveillance - Geosol (SGS-Geosol) laboratory, Brazil, for elemental analyses by ICP-OES and ICP-MS. Other aliquots of the eight samples (~20–30g), unpowdered, were sent to the Laboratório de Geologia Isotópica in the Universidade Federal do Rio Grande do Sul (LGI-UFRGS) for $^{87}Sr/^{86}Sr$ analyses.

The uppermost sample of laminites at the top of the cored section from Petrobras Well B (red rectangle in Figure 3.3C) was processed for Re-Os geochronology at the University of Alberta (UA) (Figures 3.3C and 3.3D). The top of this carbonate sample is ~0.3 m below the base of the evaporites (4916.6–4916.8 m penetrated depth) based on confidential logs. This ~20 cm-thick sample (Figures 3.3C and 3.3D) is visually enriched in organic matter (TOC = 3.59 wt %, confidential data from Petrobras made available for use in this thesis).

3.3.2.2 Sampling of Petrobras Well C

Nine carbonate samples from Petrobras Well C (Figure 4) was used in this study. Carbonate samples from sidewall cores of Petrobras Well C comprise reworked shrubby boundstone/stromatolite facies (R + SB-S in Figure 4). Slices of these sidewall core samples in 1–2 centimetre transversal cuts (coin-shaped) were processed for elemental content and $^{87}Sr/^{86}Sr$ ratios. One aliquot (~5g) of each sample underwent oil extraction in a soxhlet apparatus and powders of samples from

Petrobras Well C were obtained by crushing in an agate mortar at CENPES. Subsequently, the powders were sent to SGS-Geosol laboratory, Brazil for elemental analyses by ICP-OES and ICP-MS. Another aliquot of those samples (~10g), unpowdered, was sent to the LGI-UFRGS for $^{87}Sr/^{86}Sr$ analyses.

3.3.2.3 $^{87}Sr/^{86}Sr$ analyses

At LGI-UFRGS, unpowdered samples (~10–30 g) were cleaned with 0.1M HCl in an ultrasonic bath and then leached using 1M HCl. Sr separation was achieved using a cationic AG-50W-X8 (200-400 mesh) resin. Eight carbonate samples from Petrobras Well B were analysed by using a VG Sector 54 thermal ionization multi-collector mass spectrometer (TIMS, VG Sector 54 instrument) after having been dried in a Ta filament at LGI-UFRGS; and ten carbonate samples from Petrobras Well C were analysed using a Neptune MC-ICP-MS at LGI-UFRGS. Blanks were <30pg/g at LGI-UFRGS. External reproducibility of SRM-987 at LGI-UFRGS was 0.710247±0.000025 (n = 9) for samples from Petrobras Well B and 0.710248±0.000017 (n = 53) for samples from Petrobras Well C. All mean values, standard errors of the mean and numbers of measurements (counts) are displayed in Table 3.1.

3.3.2.4 Elemental content

Al, Ca, Mg, Si, K, Fe and Mn were analysed by ICP-OES model Optima 7300 Perkin Elmer Dupla Vista (method ICP95A) and Rb contents were analysed at SGS-Geosol by using an ICP-MS (minor elements) model Elan DRC II Perkin Elmer (method IMS95A). In both methods, samples underwent lithium metaborate fusion followed by dissolution for bulk-rock analyses.

3.3.2.5 Rhenium and Osmium analyses (Re-Os)

The sample from Petrobras Well B (Figures 3.3C and 3.3D) was split into 8 small samples from slightly different stratigraphic levels (A–H), which were then split in two halves (Figure 3.3D). All samples were broken into chips without metal contact and final powdering was performed using an agate mill. A total of 12 analyses of Re and Os isotopes were performed, including 4 replicates, by using the Carius tube dissolution method followed by solvent extraction, ion exchange and Negative Thermal Ion Mass Spectrometry at the University of Alberta (Selby and Creaser, 2003). For all samples, Os was analysed using an Electron Multiplier detector, and Re was analysed by using a Faraday collector by negative Thermal Ion Mass Spectrometry. During these analyses, determinations of in-house Os and Re standard were carried out to ensure accuracy and all results were within normal tolerance levels. All isochron regressions were calculated using the program *Isoplot* and all uncertainties are quoted at 2σ level. Any ages referred to here use the value of $\lambda = 1.666 \times 10^{-11}\ y^{-1}$ for the decay constant of ^{187}Re (Smoliar et al., 1996).

3.4 Results

3.4.1 Ostracod samples

The identified ostracod genera are Hourcqia sp. (5062.65 m, 5072.60 m, 5082.00 m) and Pattersoncypris ssp. (4973.28 m and 5012.93 m; Figure 3.5). One specimen (5012.93 m) has a PI of 3, whereas the others are more altered with PI = 4, with evidence of intense surface etching, enlarged pits, cracking and locally extreme degradation (Figure 3.5). SEM-EDS analyses permitted identification of Mg-silicates and aluminosilicates covering the valves and overgrowth of calcite and dolomite (Figure 3.5). Nine analyses from other valves of the same samples gave $^{87}Sr/^{86}Sr$

ratios between 0.711553 and 0.713427 (Figure 3.2; Table 3.1). Because most determinations are based on two analyses with differences less than the external reproducibility of the $^{87}Sr/^{86}Sr$ ratios, the mean value has been used in histograms and scatter plots, where five data points represent the samples in question. Valves from samples of Pattersoncypris ssp. (4973.28 m and 5012.93 m) have relatively higher $^{87}Sr/^{86}Sr$ ratios than those from Hourcqia sp. (5062.65 m to 5082.00 m; Table 3.1).

All metal/Ca ratios are in Table 3.2, except for Rb/Ca ratios, which in all cases were lower than the detection limits (0.063–0.49 mmol/mol). Detection limits of all metal/Ca ratios depend upon the Ca concentration in each sample. Mg/Ca ratios vary from 30 to >500 mmol/mol. Therefore, as expected, Ca and Mg are the most abundant elements in the ostracod samples. Al/Ca, Fe/Ca, Mn/Ca, Sr/Ca, Na/Ca and Mn/Sr ratios are above detection limits and reach maximum values of 8.96 mmol/mol, 11.7 mmol/mol, 4.73 mmol/mol, 4.47 mmol/mol, 13.9 mmol/mol and 1.69 mol/mol, respectively. K/Ca and Si/Ca ratios were below the detection limits in three out of five samples. Measured K/Ca ratios are less than 2.16 mmol/mol. However, the detection limit of one sample was 4.98 mmol/mol and the K/Ca ratio could be as high as this figure for this sample at 5072.60 m. Si/Ca ratios are below 17.3 mmol/mol.

Table 3.3 shows a matrix of Pearson-coefficient (R) values for linear regressions between metal/Ca ratios and $^{87}Sr/^{86}Sr$ ratios. Because Rb/Ca, K/Ca and Si/Ca ratios of three or more samples were below the detection limit, they have not been included. Na/Ca and Al/Ca show strong positive correlation ($R = 0.89$). Fe/Ca, Mg/Ca, Mn/Ca and Mn/Sr also show good to strong inter-element positive correlations ($R > 0.85$). All these four ratios exhibit reasonable negative correlations

with $^{87}Sr/^{86}Sr$ ratios (R < –0.55). Mg/Ca and Sr/Ca ratios also exhibit good inter-element positive correlation (R = 0.73).

Table 3.2 – Trace-element data from ostracod samples (mmol/mol).

Depth (m)	Al/Ca	Fe/Ca	K/Ca	Mg/Ca	Si/Ca	Mn/Ca	Sr/Ca	Na/Ca
4973.28	1.31	0.42	0.99	30.27	<1.97	1.09	3.70	3.98
5012.93	0.37	0.79	<0.64	46.01	<1.28	0.85	2.52	1.95
5062.65	2.64	6.75	2.16	195.8	3.93	3.53	4.47	4.00
5072.60	8.96	3.97	<4.98	71.19	17.3	0.33	2.93	13.9
5082.00	1.28	11.7	<1.36	>500	<2.72	4.73	2.80	7.98
Min DL*	0.02	0.003	0.64	0.10	1.28	0.009	0.01	1.11
Max DL*	0.16	0.021	4.98	0.75	9.96	0.073	0.10	8.63

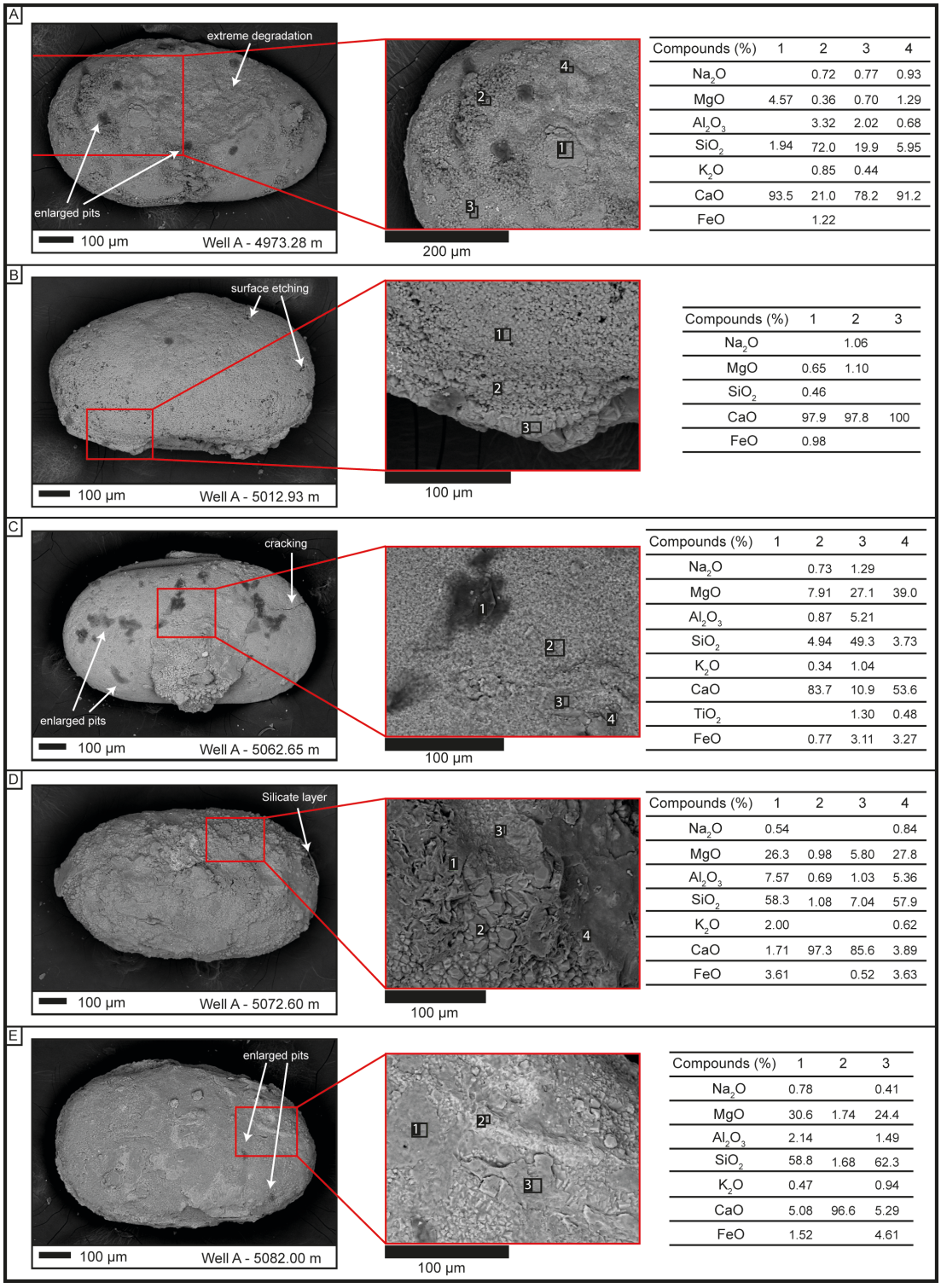
* Min DL and Max DL are the minimum and maximum detection limits, which vary according to the Ca content of samples. All samples below detection limits are shown.

Table 3.3 – Matrix with Pearson coefficient (R) based on linear regression of metal/Ca ratios and $^{87}Sr/^{86}Sr$ ratios derived from ostracod samples. Red values show R higher than 0.5 and blue values show R lower than –0.5.

	Al/Ca	Fe/Ca	Mg/Ca	Mn/Ca	Sr/Ca	Na/Ca	Mn/Sr	$^{87}Sr/^{86}Sr$
Al/Ca	1.00							
Fe/Ca	0.01	1.00						
Mg/Ca	0.08	0.94	1.00					
Mn/Ca	–0.40	0.89	0.90	1.00				
Sr/Ca	–0.03	0.04	0.73	0.26	1.00			
Na/Ca	0.89	0.32	–0.05	–0.12	–0.26	1.00		
Mn/Sr	–0.41	0.90	0.85	0.95	–0.03	–0.03	1.00	
$^{87}Sr/^{86}Sr$	–0.33	–0.82	–0.85	–0.63	–0.16	–0.42	–0.55	1.00

3.4.2 Carbonate samples

All samples exhibit $^{87}Sr/^{86}Sr$ values between 0.711386 and 0.713365 (Table 3.1, Figures 3.6 and 3.7). All values obtained in duplicate from Petrobras Well A are represented by their mean value in histograms (Figures 3.2, 3.6 and 3.7) and scatter plots (Figure 3.8). $^{87}Sr/^{86}Sr$ ratios of carbonates from Petrobras Wells B and C are generally higher than those from Petrobras Well A (Figure 3.6; Table 3.1).



Compounds (%)	1	2	3	4
Na_2O		0.72	0.77	0.93
MgO	4.57	0.36	0.70	1.29
Al_2O_3		3.32	2.02	0.68
SiO_2	1.94	72.0	19.9	5.95
K_2O		0.85	0.44	
CaO	93.5	21.0	78.2	91.2
FeO		1.22		

Compounds (%)	1	2	3
Na_2O		1.06	
MgO	0.65	1.10	
SiO_2	0.46		
CaO	97.9	97.8	100
FeO	0.98		

Compounds (%)	1	2	3	4
Na_2O		0.73	1.29	
MgO		7.91	27.1	39.0
Al_2O_3		0.87	5.21	
SiO_2		4.94	49.3	3.73
K_2O		0.34	1.04	
CaO		83.7	10.9	53.6
TiO_2			1.30	0.48
FeO		0.77	3.11	3.27

Compounds (%)	1	2	3	4
Na_2O	0.54			0.84
MgO	26.3	0.98	5.80	27.8
Al_2O_3	7.57	0.69	1.03	5.36
SiO_2	58.3	1.08	7.04	57.9
K_2O	2.00			0.62
CaO	1.71	97.3	85.6	3.89
FeO	3.61		0.52	3.63

Compounds (%)	1	2	3
Na_2O	0.78		0.41
MgO	30.6	1.74	24.4
Al_2O_3	2.14		1.49
SiO_2	58.8	1.68	62.3
K_2O	0.47		0.94
CaO	5.08	96.6	5.29
FeO	1.52		4.61

Tables 3.4 and 3.5 show the elemental content of 24 carbonate samples of the three wells used in this study. In terms of major elements, the Ca content varies between 15.5 and 38 wt %, Mg contents are less than 9.8 wt % and the Si content varies between 0.80 and 21.7 wt %. The Al, K, Fe and Rb content of all samples are typically lower than 0.37 wt %, 0.45 wt %, 0.38 wt % and 7.4 ppm, respectively (Table 3.4), with the only exception being the sample from 4842.9 m from Petrobras Well A, where elevated Al, K, Fe and Rb concentrations are present (highlighted in Table 3.4). Sr contents generally are higher than 1000 ppm (Table 3.4). Only four samples have Sr contents lower than 1000 ppm (highlighted in Table 3.4); three of them also have Mg contents higher than 7 wt %, and another sample at 4842.9 m from Petrobras Well A has a detrital content. Samples with higher Mg content are likely to contain more dolomite and less Sr, since the lattice of this mineral is too small to readily accommodate Sr (Banner, 1995). The Mn content varies between 0.03 and 0.13 wt % (Table 3.4).

Figure 3 .5 –SEM-EDS images from ostracod samples from Petrobras Well A. (A) Specimen of Pattersoncypris ssp. at 4973.28 m. EDS analyses suggest the presence of aluminosilicates (points 2, 3 and 4), Mg-silicates (points 1 and 4) and calcite (points 1 and 4). (B) Specimen of Pattersoncypris ssp. at 5012.93 m. EDS analyses suggest that all three points are mainly calcite, whereas other non-identified trace minerals containing Na, Mg, Si and Fe may be present. (C) Specimen of Hourcqia sp. at 5062.65 m. Because EDS analyses cannot identify light elements, such as carbon, the absence of metals in enlarged pits, such as Ca and Mg, may suggest the presence of organic matter (point 1); presence of calcite and Mg-silicate (point 2); and dolomite (point 4). There are also other aluminosilicates (points 2 and 3) and a non-identified mineral suggested by the presence of Ti. (D) Specimen of Hourcqia sp. at 5072.60 m. EDS analyses of minerals suggest the presence of calcite (points 2 and 3) and Mg-silicate and aluminosilicates (points 1, 2, 3 and 4). (E) Specimen of Hourcqia sp. at 5082.0 m. EDS analyses of minerals suggest the presence of calcite (point 2) and Mg-silicate and aluminosilicates (points 1, 2 and 3). All samples show evidence of intense dissolution and have been classified with PI = 4, except for one sample at 5012.93 m with PI = 3. See text for further explanations.

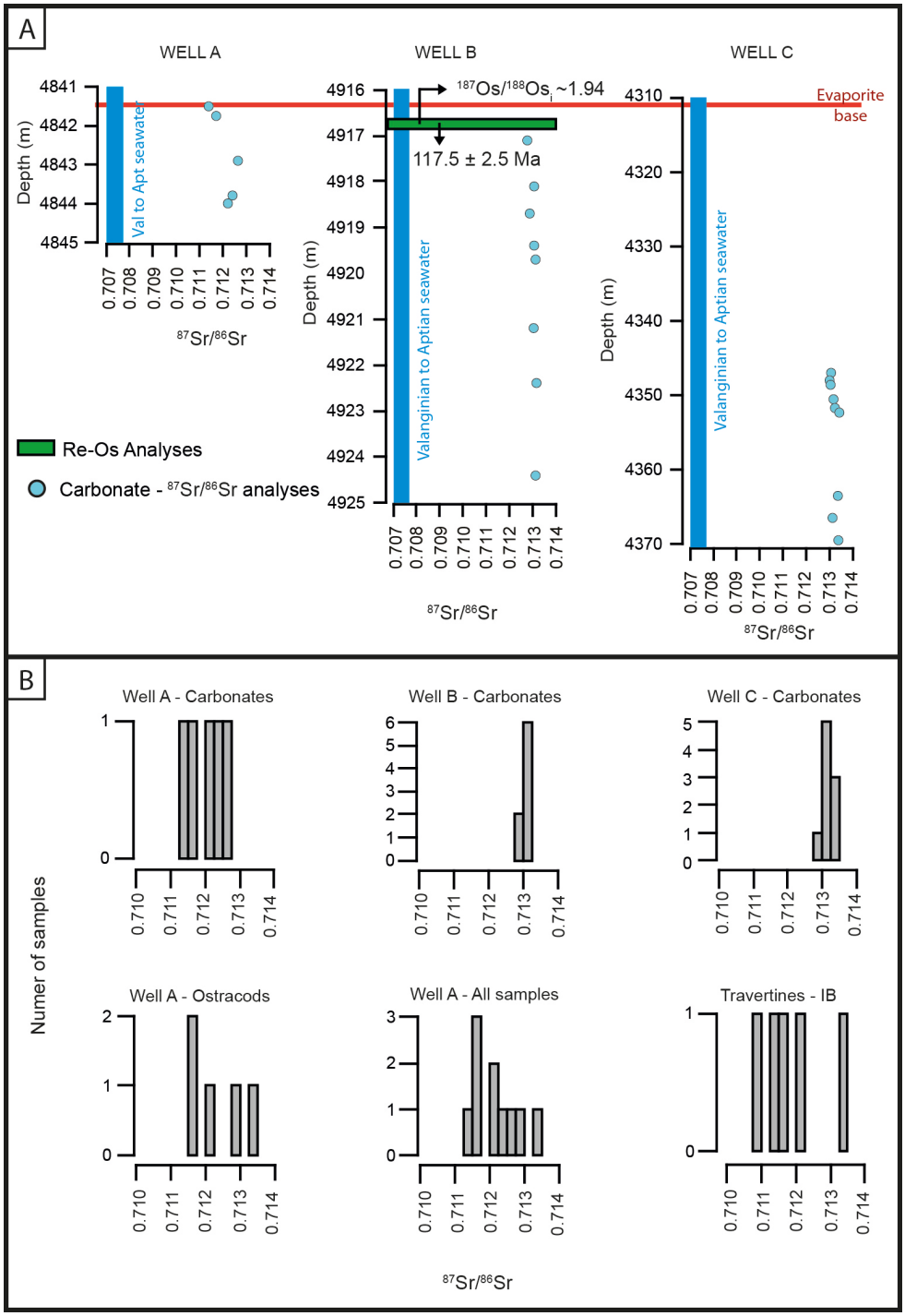


Figure 3 .6 – $^{87}Sr/^{86}Sr$ ratios, $^{187}Os/^{188}Os$ initial ratio ($^{187}Os/^{188}Os_i$) and ages derived from Re-Os geochronology obtained in this study. (A) $^{87}Sr/^{86}Sr$ ratios against depth in Petrobras Wells A, B and C. The red line represents the base of the evaporites that have been used as a datum. The blue rectangle represents possible contemporaneous seawater (Valanginian–Aptian: McArthur et al., 2012; Bodin et al., 2015). The green rectangle represents the sample used for Re-Os geochronology and respective $^{187}Os/^{188}Os_i$ and age. (B) Histograms of $^{87}Sr/^{86}Sr$ ratios. Upper part: carbonate samples from each well. Lower Part: all samples from Petrobras Well A (carbonate and ostracods) and Paleocene travertines from Itaboraí Basin (IB) (Sant'Anna et al., 2004) for comparison.

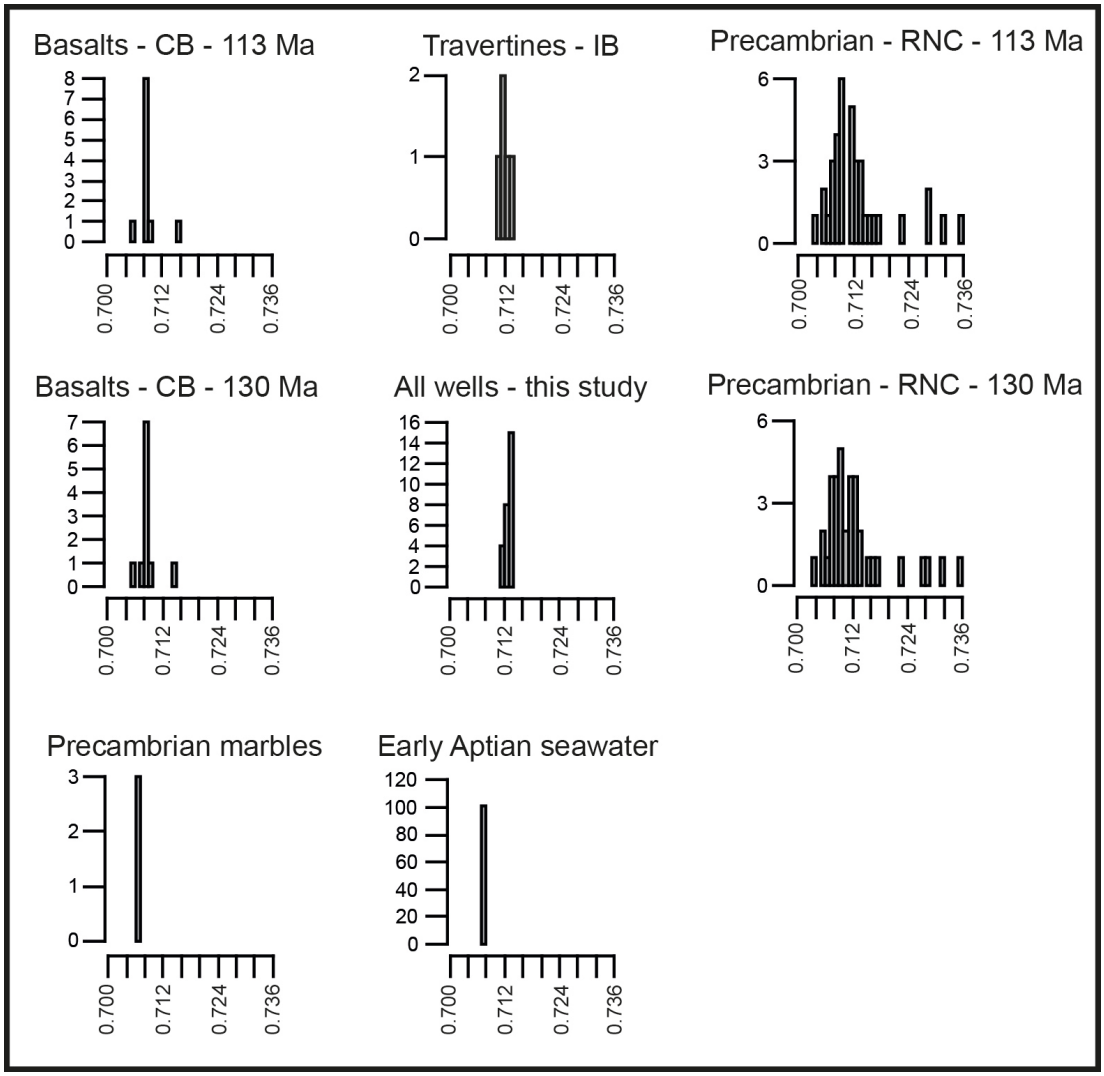


Figure 3 .7 –Histograms of $^{87}Sr/^{86}Sr$ ratios. All carbonate and ostracod samples obtained in this study are represented in the middle histogram for comparison. Basalts – CB are histograms of $^{87}Sr/^{86}Sr$ ratios obtained from basalts of offshore wells from the Campos Basin (Mizusaki et al., 1992), recalculated to ages of 113 Ma and 130 Ma. Precambrian marbles and Travertine – IB (Itaboraí Basin) (Sant'Anna et al., 2004). Early Aptian seawater includes a compilation of belemnites and carbonates of this age (Jenkyns et al., 1995; Yamamoto et al., 2013; Ando, 2015; Bodin et al., 2015). Precambrian – RNC are histograms of $^{87}Sr/^{86}Sr$ ratios of metamorphic rocks of the Rio Negro Complex in the Ribeira Fold Belt (Tupinambá et al., 2012), recalculated to ages of 113 Ma and 130 Ma. See text for further explanation.

Table 3.4 – Elemental content of carbonate samples used for strontium-isotope analyses. Samples in yellow are those that have proxy indications of possible diagenetic overprint on depositional $^{87}Sr/^{86}Sr$ ratios. % – wt %.

Well	Depth (m)	Al (%)	Ca (%)	Fe (%)	K (%)	Mg (%)	Si (%)	Mn (%)	Sr (ppm)	Rb (ppm)
A*	4841.5	<0.3	29.9	0.38	<0.3	<3	5.90	0.05	2043	3.5
	4841.8	<0.3	38.0	0.30	<0.3	<3	1.03	0.08	1781	5.5
	4842.9	1.1	17.6	1.1	0.84	5.6	6.40	0.05	864	37
	4843.8	<0.3	21.2	0.15	<0.3	8.5	1.74	0.03	157	<3
	4844.0	<0.3	21.8	<0.1	<0.3	7.9	0.80	0.04	57.2	<3
B	4917.1	0.08	21.5	0.08	0.06	5.6	8.23	0.07	2577	2.2
	4918.1	0.02	29.9	0.05	0.03	4.3	1.37	0.09	2320	0.8
	4918.7	0.04	31.9	0.06	0.03	3.0	2.01	0.08	2332	0.7
	4919.4	0.06	30.4	0.07	0.03	3.6	3.06	0.13	2751	1.0
	4919.7	0.09	20.6	0.07	0.06	5.2	11.9	0.09	1965	3.0
	4921.2	0.37	15.5	0.12	0.12	2.5	21.7	0.07	1754	7.4
	4922.4	0.05	18.0	0.05	0.02	9.6	7.54	0.12	676	1.4
	4924.4	0.06	27.8	0.07	0.04	4.2	3.34	0.09	2287	1.9
C	4347.0	0.13	34.9	0.11	0.17	1.8	3.72	0.04	1330	5.5
	4348.0	0.12	34.6	0.09	0.17	1.9	3.24	0.04	1410	6.4
	4348.6	0.14	34.3	0.13	0.19	2.7	3.08	0.04	2590	5.6
	4350.5	0.11	35.4	0.21	0.08	1.3	3.41	0.04	1490	2.6
	4351.7	0.06	27.7	0.14	0.12	3.9	8.23	0.04	1590	4.1
	4352.3	0.23	35.3	0.12	0.19	2.2	2.23	0.05	2460	5.8
	4363.5	0.07	31.9	0.14	0.09	3.6	3.98	0.03	1730	3.6
	4366.5	0.37	30.1	0.24	0.45	2.5	6.31	0.03	1960	15
	4369.5	0.13	28.2	0.15	0.16	5.1	4.63	0.03	1530	4.9

*All samples from Well A were analysed using FRX at CENPES; samples from other wells were analysed by using ICP-OES/ICP-MS at SGS-Geosol. See text for further explanation.

Table 3.5 – Sulphur (S), total inorganic and organic carbon (TIC and TOC) and semi-quantitative mineralogy of samples from Well A used in this study.

Depth (m)	S (wt %)	TOC (wt %)	TIC (wt %)	Calcite (wt %)	Dolomite (wt %)	Quartz (wt %)
4841.5	0.49	0.97	8.94	65	6	29
4841.8	0.26	0.56	8.86	96	-	4
4842.9*	0.54	1.42	9.05	-	86	14
4843.8	0.07	1.79	11.5	-	92	8
4844.0	0.05	1.62	12.3	-	97	3

* Peaks were above background and reflect trace amounts of other minerals that were not identified. Semi-quantitative mineralogy must be viewed with caution.

The five samples of carbonates from Petrobras Well A have TIC values between 8.86 and 12.3 wt % (Table 3.5). XRD data from carbonate samples of Petrobras Well A show that all samples contain quartz, four out five contain dolomite and two contain calcite (Figure 3.9; Table 3.5). Hence, three samples are made up

entirely of dolomite in their carbonate phase. In addition, one sample from 4842.9 m from Petrobras Well A contains minerals other than calcite, dolomite and quartz, such as phyllosilicates, probably clay minerals, with reflections above the background (<30° 2Θ, not shown in Figure 3.9), which would need a larger sample for treatment and identification and are beyond the scope of this study. Because of the presence of phyllosilicates, and the dominance of dolomite and quartz, the mineralogy of this sample is clearly different from other samples. The sulphur and TOC values of the five samples from Petrobras Well A are lower than 0.54 wt % and 1.79 wt %, respectively (Table 3.5).

Table 3.6 shows a matrix of Pearson-coefficient (R) values for linear regressions between metal contents, some metal ratios and $^{87}Sr/^{86}Sr$ ratios. Al, K, Fe and Rb show excellent positive correlation ($R > 0.9$) between themselves. Rb/Sr ratios also show positive correlation with Al, K and Fe content ($R > 0.87$). In addition, Rb/Sr ratios show positive correlation with Mn/Sr ratios ($R = 0.79$). Ca has negative correlation with Mg and Si contents ($R < –0.6$). Sr shows strong negative correlation with Mg and Mg/Ca ratios ($R < –0.6$; Table 3.6). Mg also has positive correlation with Mn/Sr ratios ($R > 0.59$). Mg/Ca ratios show fair positive correlation with Rb/Sr ratios ($R = 0.55$). $^{87}Sr/^{86}Sr$ ratios have reasonable negative correlation with Mg and Mg/Ca ratio ($R = –0.52$).

Table 3.6 – Matrix with Pearson coefficient (R) based on linear regression of metal content, $^{87}Sr/^{86}Sr$ and Mn/Sr, Rb/Sr and Mg/Ca ratios from carbonate samples. Mn/Sr, Rb/Sr and Mg/Ca are in mol/mol. Red R values are higher than 0.5 and blue R values are lower than –0.5.

	Al	Ca	Fe	K	Mg	Si	Mn	Sr	Rb	$^{87}Sr/^{86}Sr$	Mn/Sr	Rb/Sr	Mg/Ca
Al	1.00												
Ca	–0.41	1.00											
Fe	0.95	–0.20	1.00										
K	0.94	–0.20	0.92	1.00									
Mg	0.05	–0.71	0.10	–0.01	1.00								
Si	0.24	–0.62	0.02	0.02	–0.05	1.00							
Mn	–0.22	–0.26	–0.21	–0.38	0.29	0.14	1.00						
Sr	–0.39	0.43	–0.33	–0.38	–0.60	0.06	0.28	1.00					
Rb	0.98	–0.32	0.91	0.98	0.05	0.12	–0.29	–0.43	1.00				
$^{87}Sr/^{86}Sr$	–0.49	0.02	–0.37	–0.42	–0.52	0.18	0.00	0.23	–0.11	1.00			
Mn/Sr	0.03	–0.35	0.00	–0.07	0.59	–0.21	–0.03	–0.65	0.01	–0.33	1.00		
Rb/Sr	0.96	–0.43	0.87	0.93	0.46	–0.14	–0.25	–0.70	0.97	–0.34	0.79	1.00	
Mg/Ca	0.21	–0.81	0.20	0.09	0.97	0.13	0.32	–0.64	0.18	–0.52	0.47	0.55	1.00

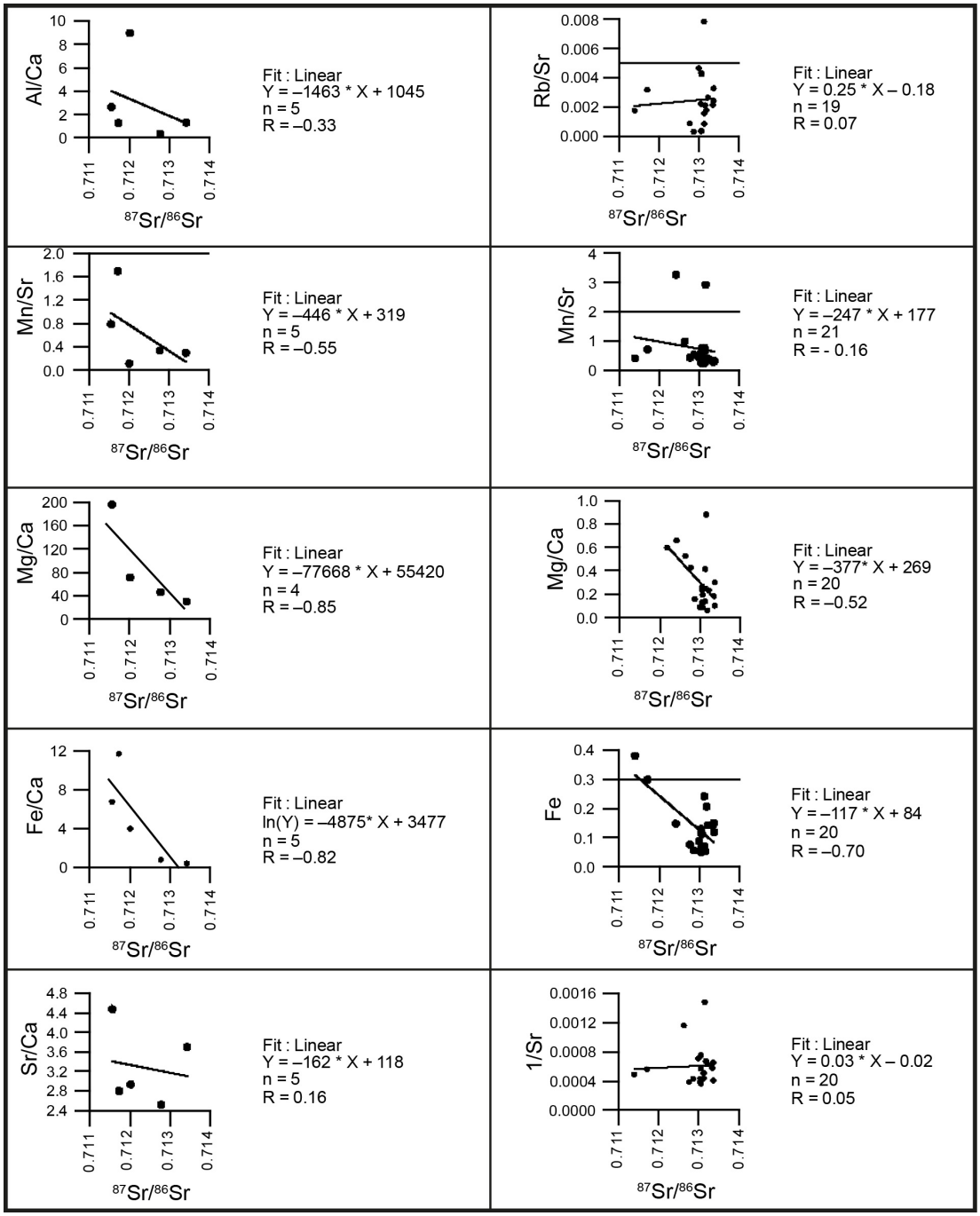


Figure 3 .8 – Scatter plots between metal content or metal ratios and $^{87}Sr/^{86}Sr$ ratios for ostracod samples (left side) and carbonate samples (right side). Horizontal lines, if present, show cut-offs for defining samples with diagenetic overprints on $^{87}Sr/^{86}Sr$ ratios. Lines express the linear fit, whereas the data from the fit is given with each scatter plot showing equation, number of samples used to obtain the fit and R-value. Many of the scatter plots do not include all data due to some values being outside the range of the scale used. See number of samples (n) and text for details. Therefore, R-values may differ from those presented on Table 3.4 and 3.6.

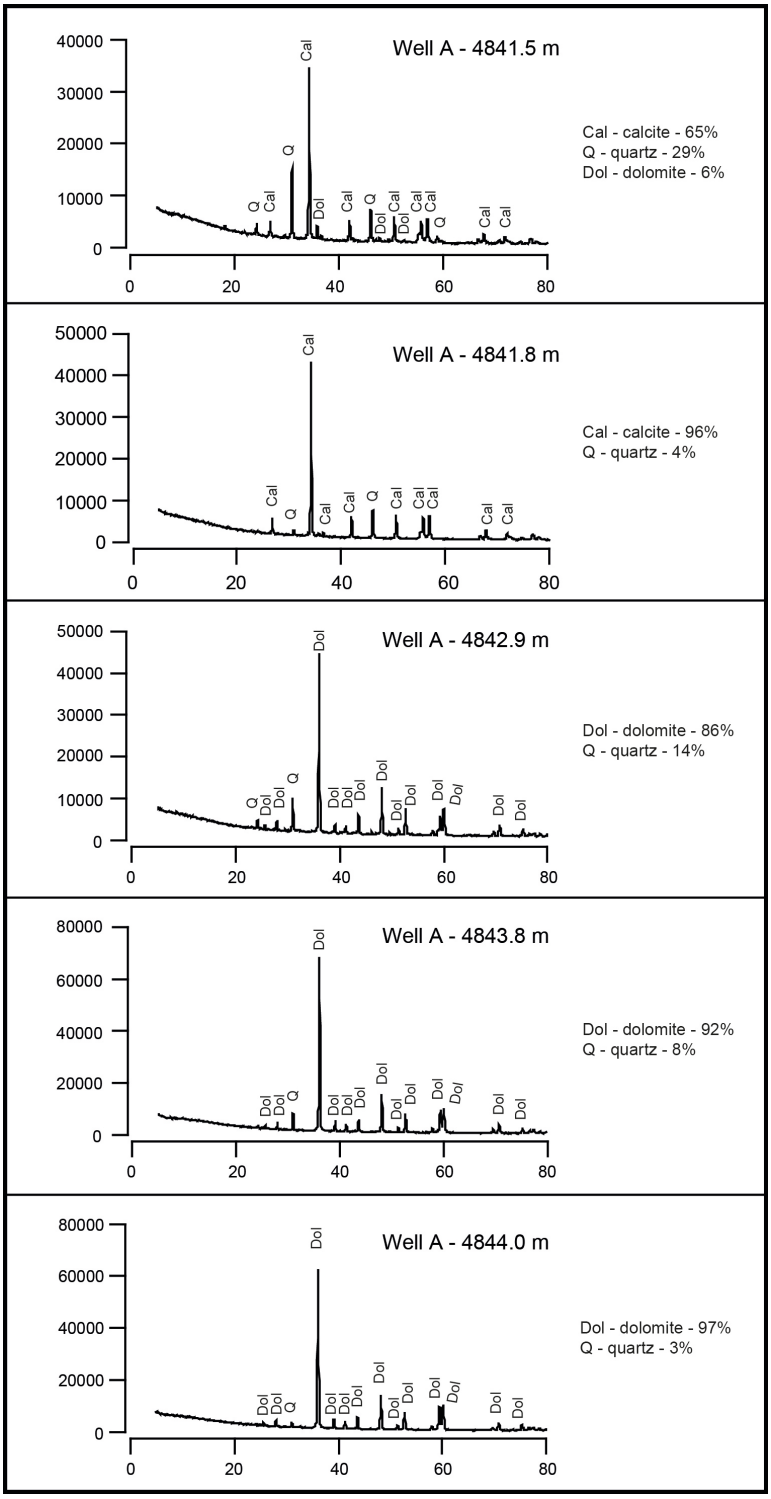


Figure 3 .9 –Diffractograms (XRD data) from five carbonate samples from Petrobras Well A. The *x*-axis expresses the angles of analyses in 2Θ and the *y*-axis is the intensity of peaks in number of counts. The positions of peaks permit the identification of the minerals and the area above the main peaks allow semi-quantification of the proportion of the minerals. The main minerals and their percentages are given in the right-hand side of each diffractogram.

3.4.3 Rhenium and osmium isotopes

The Re contents are low to moderate at 1–13ppb (Figure 3.3E; Table 3.7) but because the analysed samples have low Os abundances (18–240 ppt; Figure 3.3E; Table 3.7), the $^{187}Re/^{188}Os$ ratios are relatively high with a good spread of values from 165–991 (Table 3.7). The data from samples from Petrobras Well B from a level ~0.3–0.5 m below the base of the evaporites, yield an age of 116.4 ± 7.3 Ma, with a very high initial Os ratio ($^{187}Os/^{188}Os_i$) of ~1.96 (Figure 3.10). The scatter of the regression is moderate (MSWD = 12) but is strongly affected by one sample and its replicate (replicate B; Figures 3.3E and 3.10). Without these two analyses, the remaining 10 analyses yield an isochron with an age of 117.5 ± 2.5 Ma with very high $^{187}Os/^{188}Os_i$ of ~1.94 (MSWD = 0.89; Figure 3.10).

Table 3.7 – Rhenium and osmium data from sample at 4916.65–4916.85 m from Well B. Sample names are those in Figures 3.3E and 3.10.

Sample	Re (ppb)	± 2σ	Os (ppt)	± 2σ	$^{187}Re/^{188}Os$	± 2σ	$^{187}Os/^{188}Os$	± 2σ
A	5.239	0.034	37.98	0.71	991.4	37.3	3.895	0.145
A’	4.903	0.026	36.10	0.55	968.3	26.4	3.805	0.103
B	12.53	0.050	134.0	1.1	636.9	6.9	3.300	0.034
B’	11.94	0.050	124.9	0.9	642.3	3.2	3.157	0.024
C	2.118	0.030	19.17	0.55	759.5	52.7	3.399	0.232
C’	1.880	0.020	18.05	0.41	706.9	35.3	3.260	0.163
D	7.113	0.038	87.03	0.89	542.4	8.6	3.018	0.046
E	4.263	0.033	50.89	0.73	558.3	15.0	3.064	0.080
F	2.571	0.029	33.25	0.61	510.4	19.5	2.960	0.109
G	3.376	0.031	44.13	0.69	505.1	15.5	2.964	0.088
H	6.421	0.036	239.7	1.3	165.1	1.3	2.266	0.013
H’	6.219	0.029	229.8	1.2	166.8	1.0	2.267	0.012

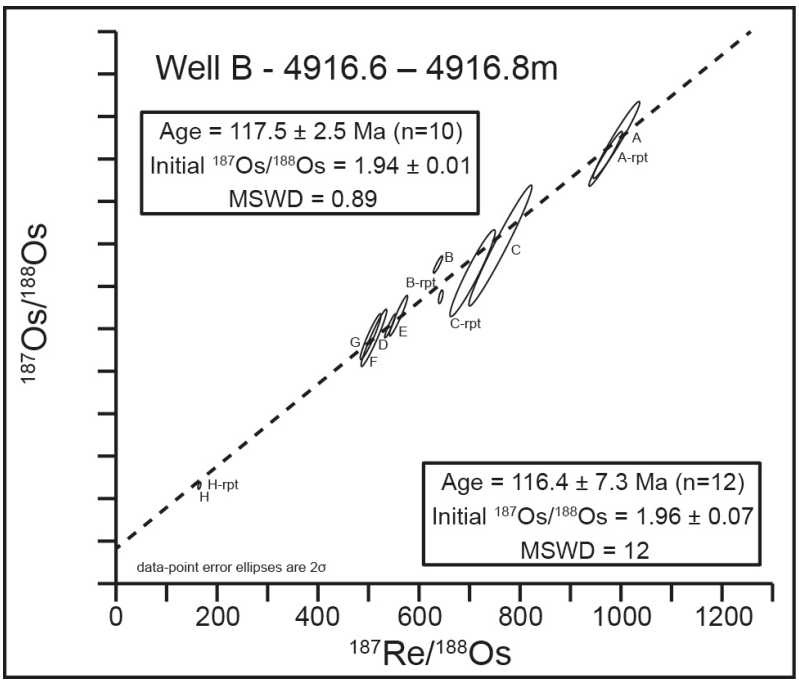


Figure 3 .10 – Re-Os isochron diagrams for sample 4916.6–4916.8 m from Petrobras Well B. Two dates were calculated: one including sample B and its replicates, which yielded a more scattered isochron (MSWD = 12), and another without sample B and its replicates, which yielded a better isochron (MSWD = 0.89). The age assigned for the former isochron is 116.4 ± 7.3 Ma with an $^{187}Os/^{188}Os_i$ of 1.96 ± 0.07, whereas latter yielded an age of 117.5 ± 2.5 Ma and an $^{187}Os/^{188}Os_i$ of 1.94 ± 0.01.

3.5 Discussion

3.5.1 Diagenetic overprint on $^{87}Sr/^{86}Sr$ ratios

3.5.1.1 Dissolution and post-depositional ^{87}Sr

The ostracod samples show evidence for intense dissolution. Significantly, dissolution seems not to impact Mg/Ca and Sr/Ca ratios in Quaternary ostracods (Keatings et al., 2002). Because, in this case, dissolution does not alter Sr/Ca, it is likely that simple removal of shell material would not change $^{87}Sr/^{86}Sr$ ratios. However, diagenetic processes that involve rock-fluid interactions and recrystallization or addition of secondary carbonate will certainly affect original

$^{87}Sr/^{86}Sr$ ratios (Banner, 1995). In addition, the presence of Rb in sedimentary material during deposition that is subsequently incorporated into precipitated carbonate during diagenesis can also play an important role in elevating $^{87}Sr/^{86}Sr$ ratios, due to ^{87}Rb decay to $^{87}Sr - {}^{87}Sr_{rad}$ (Faure and Mensing, 2005). SEM-EDS images from the ostracods show overgrowths of calcite and dolomite, where the ratio of original valve to cement is difficult to estimate. Aluminosilicates in contact with the valves potentially have a higher Rb content and diagenetic fluids derived from their partial dissolution may have interacted with valves during diagenesis. Hence, the measured $^{87}Sr/^{86}Sr$ ratios represent original calcite from ostracods plus additional diagenetic carbonate. The fossils are hence 'non-ideal' as archives of original $^{87}Sr/^{86}Sr$ ratios (Veizer et al., 1997).

To assess the possible significance of post-depositional changes in $^{87}Sr/^{86}Sr$ ratios from carbonate samples, metal/Ca and Mn/Sr ratios have been examined. Considering the similarity of rocks analysed in this study with those from different parts of the Campos, Santos and Kwanza Basins, documented processes, such as recrystallization of shrub crystals, dolomitization, and dissolution of Mg-silicates among others are undoubtedly relevant (Wright and Barnett, 2015; Saller et al., 2016; Sabato Ceraldi and Green, 2017). Hence, a methodology is required to evaluate the extent to which diagenetic overprints on measured isotopic ratios affected the original $^{87}Sr/^{86}Sr$ ratios.

The first issue to address is the impact of Rb on ostracod and carbonate samples since this element substitutes for K in aluminosilicates such as K-feldspars and illite (Faure and Mensing, 2005). Rb/Sr ratios lower than 0.005 were used as a cut-off to identify samples appropriate for $^{87}Sr/^{86}Sr$ analysis on Proterozoic carbonates (Jacobsen and Kaufman, 1999). Unfortunately, the detection limits were

too high to evaluate the proportion of Rb in the ostracod samples themselves. Rb/Sr ratios lower than 0.2–0.17 mol/mol cannot be detected, and these values are much higher than 0.005. Because Al is a proxy for detrital content and is likely associated with Rb in K-bearing silicates, Al/Ca ratios are here used as a proxy for the potential proportion of higher Rb/Ca and probably higher Rb/Sr in the samples. Al and Rb contents of carbonate samples show a strong positive correlation (R = 0.98; Table 3.3) and support the notion that Al/Ca ratios can be used as a proxy for Rb/Ca ratios.

Following this approach, one would expect a positive correlation between $^{87}Sr/^{86}Sr$ ratios and Al/Ca ratios. However, there is no such correlation (R = –0.33; Figure 3.8; Table 3.3). Consequently, it seems that most samples have not been altered significantly by a higher initial Rb content. The ostracod sample at 5072.60 m has a relatively high Al/Ca ratio (8.96 mmol/mol; Figure 3.8; Table 3.3) and $^{87}Sr/^{86}Sr$ ratio (0.712012; Table 3.1), higher than the other samples immediately below at 5082.00 m and above at 5062.65 m (0.711553–0.711732; Table 3.1), and this ~0.0003–0.0005 difference could be related to higher $^{87}Sr_{rad}$ in this fossil material. By contrast, the other two samples with relatively high $^{87}Sr/^{86}Sr$ ratio (4973.28 and 5012.93 m) do not show an elevated Al/Ca ratio. Therefore, this proxy suggests that ingrowth of $^{87}Sr_{rad}$ cannot explain the higher $^{87}Sr/^{86}Sr$ ratios compared to the other three ostracod samples. Indeed, all ostracod samples have $^{87}Sr/^{86}Sr$ ratios similar to those in bulk carbonates analysed in this study (Figure 3.6; Table 3.1).

The evaluation of Rb content on the carbonate samples is straightforward. However, two out of 22 samples (4843.8 and 4844.0 m from Petrobras Well A) do not have Rb/Sr ratios, due to the concentration of Rb being below the detection limit of 3 ppm. Hence, Rb/Sr ratios must be lower than 0.020 and 0.053 mol/mol for these two samples and the cut-off of Rb/Sr ratio of 0.005 mol/mol cannot be used to

determine the veracity of the Sr-isotope data. In addition to this approach, the possible effects of $^{87}Sr_{rad}$ is tested by calculating the initial $^{87}Sr/^{86}Sr$ ratios $(^{87}Sr/^{86}Sr)_i$ to evaluate the possible increase of $^{87}Sr/^{86}Sr$ ratios from addition of $^{87}Sr_{rad}$, by using the following equation (Faure and Mensing, 2005):

$$\left(\frac{^{87}Sr}{^{86}Sr}\right)_i = \left(\frac{^{87}Sr}{^{86}Sr}\right)_m - 2.89\left(\frac{[Rb]}{[Sr]}\right)\lambda t \quad (1)$$

where $(^{87}Sr/^{86}Sr)_m$ is the data measured from Table 3.1, [Rb] and [Sr] are the Rb and Sr contents, respectively in ppm (Table 3.4), in which all samples with contents <3 ppm are assumed to have an Rb content of 3 ppm. λ is the decay constant of the Rb-Sr isotope system (1.42×10^{-11} y^{-1}) (Faure and Mensing, 2005) and t was estimated for two different values: 113 Ma and 130 Ma. These ages are estimated as the maximum and minimum age of pre-Salt carbonates (Mizusaki et al., 1992; Dias et al., 1994) to measure the potential effect of $^{87}Sr_{rad}$. This equation gives a good approximation of the effects of decay of ^{87}Rb on $^{87}Sr/^{86}Sr$ ratios between 0.700 and 0.800 (Faure and Mensing, 2005) and shown in Chapter 2. The results of $(^{87}Sr/^{86}Sr)_i$ for 113 Ma and 130 Ma are displayed in Table 3.1, which indicates that the difference between $(^{87}Sr/^{86}Sr)_i$ (113 Ma) and $(^{87}Sr/^{86}Sr)_i$ (130 Ma) is generally less than 0.000003. The exceptions are three samples from Petrobras Well A whose Sr content is less than 1000 ppm, where this difference in $^{87}Sr/^{86}Sr$ is up to 0.000037, and the sample at 4366.5 m from Petrobras Well C, where the difference is 0.000005. Hence, the differences in age are generally negligible and $^{87}Sr/^{86}Sr_i$ (130 Ma) is thus adopted as representing the maximum possible contribution of $^{87}Sr_{rad}$. This model uses extreme conditions that assume: 1) a greater age than thought likely for the pre-Salt carbonates analysed in this study and; 2) all the Rb present in each sample contributed $^{87}Sr_{rad}$ to the carbonate phase to change the original depositional $^{87}Sr/^{86}Sr$

ratios. Therefore, assuming that decay of ^{87}Rb was the only significant process affecting carbonate phases, depositional $^{87}Sr/^{86}Sr$ ratios should lie between those measured and those calculated.

Two out of 20 samples, with Rb contents higher than 3 ppm, have Rb/Sr ratios higher than 0.005 mol/mol (4842.9 m from Petrobras Well A and 4366.5 m from Petrobras Well C) and are hence likely to have had their depositional $^{87}Sr/^{86}Sr$ ratio changed by ingrowth of $^{87}Sr_{rad}$. The difference between $(^{87}Sr/^{86}Sr)_i$ and $(^{87}Sr/^{86}Sr)_m$ in four samples is higher than 0.000024, similarly suggesting some degree of alteration of the original $^{87}Sr/^{86}Sr$ ratio by addition of $^{87}Sr_{rad}$. Two of these samples are those with Rb/Sr ratios higher than 0.005 mol/mol, and the other two are from Petrobras Well A, which are characterized by relatively low Sr content. The difference between $(^{87}Sr/^{86}Sr)_i$ and $(^{87}Sr/^{86}Sr)_m$ can reach up to 0.000280. To sum up, $^{87}Sr_{rad}$ may have increased the depositional $^{87}Sr/^{86}Sr$ ratios of one ostracod sample (5072.6 m) by ~0.0003–0.0005 and four carbonate samples by 0.000024–0.000280.

3.5.1.2 Fluid–rock interaction

Although it is possible to estimate the effect of $^{87}Sr_{rad}$ on depositional $^{87}Sr/^{86}Sr$, both ostracods and carbonates may have been altered due to fluid–rock interaction involving introduction of fluids with 'exotic' $^{87}Sr/^{86}Sr$, Mn/Sr and Mg/Ca ratios. Sr, Mn and Fe contents have been traditionally used to characterize the extent of such diagenetic overprints on $^{87}Sr/^{86}Sr$ ratios in carbonates (McArthur, 1994; Jacobsen and Kaufman, 1999; Yamamoto et al., 2013). The samples in question are not pristine calcite and, given the common presence of dolomite, may have undergone a range of diagenetic processes involving possible exchange of Sr.

With respect to the Mn/Sr ratio, a cut-off of Mn/Sr (mol/mol) > 2 has been widely used to identify samples with a diagenetic overprint on $^{87}Sr/^{86}Sr$ ratios in carbonates (Jacobsen and Kaufman, 1999; Yamamoto et al., 2013). No ostracod samples have shown Mn/Sr ratios > 2. The ostracod sample with the highest Mn/Sr ratio (1.69 mol/mol) at 5082.00 m would be closest to this cut-off value. All carbonate samples have Mn/Sr ratios < 2, except for three: at 4843.8 m and 4844.0 m from Petrobras Well A and 4922.4 m from Petrobras Well B (Figure 3.8; highlighted on Table 3.4). The sample from 4844.0 m has not been plotted in Figure 3.8, since it has a much higher Mn/Sr ratio (12.45 mol/mol) than other samples.

Mg/Ca has been used as a proxy for the extent of dolomitization in the samples because dolomites usually have a relatively low Sr content and can form from a diagenetic fluid with 'exotic' $^{87}Sr/^{86}Sr$ ratios and hence record a mixing between depositional and non-depositional $^{87}Sr/^{86}Sr$ ratios (Banner, 1995). However, this proxy must be used with caution, because this ratio varies between calcites from different organisms (McArthur, 1994). Mg/Ca ratios from ostracod samples show good negative correlation with $^{87}Sr/^{86}Sr$ ratios ($R = –0.85$; Figure 3.8; Table 3.6). Although dissolution seems not to have altered Mg/Ca ratios in Quaternary ostracods (Keatings et al., 2002), the South Atlantic samples may have experienced precipitation of dolomite in pore spaces, potentially modifying $^{87}Sr/^{86}Sr$ ratios. The presence of dolomite was observed during SEM-EDS analysis of the sample at 5062.7 m, which has an Mg/Ca ratio of 195.8 mmol/mol (Figure 3.5; Table 3.2). In addition, the good correlation between the Mg/Ca ratio and Mn/Ca and Fe/Ca ratios reinforces the notion that dolomitization might have decreased $^{87}Sr/^{86}Sr$ ratios during diagenesis. Complications arise, however, because Mg/Ca and Sr/Ca ratios have been used as proxies for salinity and/or temperature, in Quaternary ostracods (McCulloch

et al., 1989; Holmes, 1996). The ostracod samples from the South Atlantic have shown a reasonable positive correlation between Mg/Ca and Sr/Ca ratios (R = 0.73), which suggest that changes in Mg/Ca ratios could be depositional than diagenetic. Despite these complications, it is deemed more likely that Mg/Ca ratios record diagenetic overprints in ostracod samples rather than depositional features such as palaeosalinity. On this basis, the fact that three ostracod samples at the bottom of Petrobras Well A (at 5062.65, 5072.60 and 5082.00 m) have higher Mg/Ca and lower $^{87}Sr/^{86}Sr$ ratios (Figures 3.2 and 3.8; Tables 3.1 and 3.2) suggests that dolomitization decreased depositional $^{87}Sr/^{86}Sr$. The other two ostracod samples from a stratigraphically higher position in Petrobras Well A (at 4973.28 and 5012.93 m) are more likely to have maintained their depositional $^{87}Sr/^{86}Sr$ ratios.

All carbonate samples contain dolomite and have Mg/Ca ratios with moderate negative correlation with $^{87}Sr/^{86}Sr$ ratios (R = –0.52). However, two samples from Petrobras Well A (at 4841.5 and 4841.8 m) with Mg content lower than the detection limit decrease this correlation. Thus, it seems that lower $^{87}Sr/^{86}Sr$ ratios are associated with higher Mg/Ca ratios. Four out of 22 samples have an Mg/Ca ratio higher than 500 mmol/mol, including the three samples from Petrobras Well A (at 4842.5, 4843.8 and 4844.0 m) that are dominated by dolomite (Figure 3.9; Table 3.5) and the sample at 4922.4 m from Petrobras Well B, which also has Mn/Sr >2 mol/mol. Although the sample from Petrobras Well B does not show different $^{87}Sr/^{86}Sr$ ratios compared with most other samples from Petrobras Wells B and C, the three samples from Petrobras Well A have less radiogenic $^{87}Sr/^{86}Sr$ ratios. Seemingly, therefore, the diagenetic processes that led to significant dolomitization in these samples decreased $^{87}Sr/^{86}Sr$ ratios by introducing less radiogenic Sr. However, the other two samples from Petrobras Well A (at 4841.5 and 4841.8 m)

show lower $^{87}Sr/^{86}Sr$ than samples from Petrobras Wells B and C and Mg contents below detection limits, suggesting that the relationship between $^{87}Sr/^{86}Sr$ ratios and Mg/Ca ratios is complex.

Sr content may also help to identify trends of recrystallization and changes in $^{87}Sr/^{86}Sr$ ratios (Banner, 1995; Jacobsen and Kaufman, 1999). The lack of correlation between Sr/Ca and $^{87}Sr/^{86}Sr$ ratios on ostracod samples does not permit use of this proxy to show trends of diagenetic overprint. With regard to carbonates, four out 22 samples have Sr contents lower than 1000 ppm (highlighted in Table 3.4); three of these four samples also have Mg contents higher than 7 wt % and another is the sample at 4842.9 m from Petrobras Well A, which has relatively high detrital content. The lack of correlation between Sr content and $^{87}Sr/^{86}Sr$ ratios supports the contention that the diagenetic overprints that reduced the Sr contents did not change the $^{87}Sr/^{86}Sr$ ratio. It is possible that the high Sr content found in most samples supports an original aragonitic composition (e. g., Banner, 1995), although petrographic studies of similar facies observed in Kwanza Basin, the African counterpart of the Campos Basin, do not support this contention (Saller et al., 2016). Thus, the elevated Sr content in contemporaneous water was more likely due to high rates of evaporation (Saller et al., 2016).

Previous studies (Denison et al., 1994; Jacobsen and Kaufman, 1999) have shown that carbonate samples with Fe contents lower than 0.3 wt % usually retains original $^{87}Sr/^{86}Sr$ ratios, while samples with Fe contents higher than 0.6 wt % usually do not. Although these cut-offs cannot be used on the ostracod samples, higher Fe/Ca ratios are more likely to signify diagenetic modification of $^{87}Sr/^{86}Sr$ ratios. The good negative correlation between Fe/Ca and $^{87}Sr/^{86}Sr$ ratios ($R = –0.82$; Table 3.6), suggests that three ostracod samples have diagenetically modified depositional

$^{87}Sr/^{86}Sr$ ratios. These three ostracod samples are those whose Mg/Ca ratios also suggest diagenetic overprint.

Only two carbonate samples (from Petrobras Well A at 4841.5 and 4842.9 m) have Fe contents higher than 0.30 wt %, implying alteration of original $^{87}Sr/^{86}Sr$ ratios. Although we cannot rule out a diagenetic overprint on $^{87}Sr/^{86}Sr$ ratios on the sample at 4841.5 m in Petrobras Well A, its Fe content of 0.38 wt % is well below the higher cut-off for identification of well-defined diagenetic overprints (0.6 wt %). Because significant diagenesis is not indicated by other proxies, we assume this sample essentially records depositional $^{87}Sr/^{86}Sr$ ratios.

All ostracods have undergone intense dissolution and, based on Mg/Ca, Fe/Ca and Mn/Ca ratios, the samples at 5082.00 m, 5072.60 m and 5062.65 m have suffered the greatest diagenetic overprint. This process lowered original depositional $^{87}Sr/^{86}Sr$ ratios. Five carbonate samples out of 24 have shown at least one proxy that suggests diagenetic overprint (highlighted in Table 3.4), three of which have lower $^{87}Sr/^{86}Sr$ ratios than those that have not shown any evidence for diagenetic overprints on depositional $^{87}Sr/^{86}Sr$ ratios. Diagenesis, therefore, seems to have lowered $^{87}Sr/^{86}Sr$ ratios, which is a similar pattern to that observed in diagenetically altered deep-sea carbonates from DSDP Site 463, mid-Pacific Moutains, that have lowered $^{87}Sr/^{86}Sr$, possibly recording the transfer of fluids from volcanic ash (Ando, 2015) but the opposite trend to that observed in many ancient marine limestones that tend to acquire more radiogenic values than those of ambient seawater (Burke et al., 1982; Bralower et al., 1999). However, given that all these apparently modified samples all derive from Petrobras Well A, the possibility that Sr-isotope values are associated with a specific local aqueous geochemistry cannot be excluded.

3.5.2 Continental origin of pre-Salt carbonates

The palaeoecology of Hourcqia sp. is interpreted as non-marine with some tolerance to elevated salinity levels (brackish conditions; Poropat and Colin, 2012a, b). This genus is locally found in thin shales containing planktonic and benthic foraminifera suggestive of some degree of marine influence, as reported in the Petrobras Well 3-RJS-168 (Figure 3.1) (Silva-Telles Jr., 1996; Poropat and Colin, 2012a, b). The palaeoecology of Pattersoncypris ssp. is interpreted as saline lacustrine (Poropat and Colin, 2012a, b). The environmental significance of both these genera is based on data from Brazilian and African basins. Hourcqia sp. has been used to identify biozones from the Jiquiá local stage (Barremian/Aptian) and Pattersoncypris ssp. has been used to identify the biozone that characterizes the Alagoas local stage (Aptian) (Poropat and Colin, 2012a). Although the $^{87}Sr/^{86}Sr$ data from three ostracod samples may possibly have been altered by dolomitization, all of them are far too radiogenic (>0.711553) to represent even modified marine values. $^{87}Sr/^{86}Sr$ data from the carbonate samples are similarly too radiogenic to represent ancient seawater (>0.711386). Such values are close to the typical contribution of rivers draining continental landmasses undergoing weathering (~ 0.7116) (Burke et al., 1982; Banner, 2004) and are significantly higher than all Phanerozoic seawater, which has recorded maximum $^{87}Sr/^{86}Sr$ ratios (<0.7095) in Cambrian and Quaternary times (Veizer et al., 1999; Prokoph et al., 2008; McArthur et al., 2012).

Although there are disagreements as to the correlation between the Jiquiá and Alagoas local stages in the Early Cretaceous, it is likely that the deposition of the pre-Salt carbonates probably took place during the Barremian and Aptian, based on correlation between ostracod zonation and other biostratigraphic methods (Regali

and Viana, 1989; Silva-Telles Jr., 1996), radiometric ages (Dias et al., 1994; Moreira et al., 2007), and possible links between eustatic sea-level rises and marine excursions in the Campos Basin (Silva-Telles Jr., 1996; Dias, 1998). Marine $^{87}Sr/^{86}Sr$ ratios for the Valanginian to Albian interval show the highest values in the Lower Barremian (0.707500) and the lowest values in the Upper Aptian (0.707173) (McArthur et al., 2012; Bodin et al., 2015) and therefore the range of 0.707173–0.707500 represents the most extreme contemporaneous seawater values possible for samples analysed in this study (Figures 3.2 and 3.6). A compilation of $^{87}Sr/^{86}Sr$ ratios from Early Aptian seawater (from 0.707074 to 0.707541) based on belemnites and carbonates analysed in four different sites: Vocontian Trough, France (Bodin et al., 2015), Bab Basin, United Arab Emirates (Yamamoto et al., 2013), Ocean Drilling Program Site 866, Resolution Guyot, Pacific Ocean (Jenkyns et al., 1995) and Deep Sea Drilling Program Site 463, Pacific Ocean (Ando, 2015) showed a higher range than other values published for the Valanginian to Aptian interval (McArthur et al., 2012; Bodin et al., 2015). Although the Early Aptian seawater $^{87}Sr/^{86}Sr$ histogram in Figure 3.7 manifestly does not represent values for a large part of the Early Cretaceous, the minimum and maximum figures are likely to represent the largest range possible for the entire Valanginian to Aptian interval and can hence be used as a basis for comparison.

Although $^{87}Sr/^{86}Sr$ ratios of analysed carbonates and ostracods systematically display higher values than Early Cretaceous seawater (Figures 3.2, 3.6 and 3.7) diagenetic processes manifestly cannot explain those differences. Indeed, such processes generally have a tendency to decrease $^{87}Sr/^{86}Sr$ ratios of samples analysed in this study, except for the contribution of $^{87}Sr_{rad}$, which has been evaluated (<0.000280) and found to be of very limited significance. Furthermore, it seems

unlikely that diagenesis alone increased $^{87}Sr/^{86}Sr$ ratios from Valanginian–Aptian seawater values (~0.707) to 0.711–0.713 on material from three separate wells analysed in this study. Hence, $^{87}Sr/^{86}Sr$ ratios clearly show that the pre-Salt carbonates analysed in this study from these basins were deposited in a non-marine setting in agreement with the strontium-isotope values of pre-Salt carbonates from Petrobras Well CP-5 in the Campos Basin that have a range of $^{87}Sr/^{86}Sr$ values of 0.7117–0.7137 (Dias, 1998). Overall, pre-Salt carbonates from four wells from the Campos and Santos Basins, separated by more than 550 km, exhibit high $^{87}Sr/^{86}Sr$ ratios extending over a stratigraphic thickness >100 m in Petrobras Well A (Figures 3.1 and 3.2). Hence, a regional source of continental waters with relatively high $^{87}Sr/^{86}Sr$ ratios, probably due to major contribution of weathering of minerals rich in ^{87}Rb and derived ^{87}Sr (Banner, 2004), must have influenced a large area of both the Campos and Santos Basins.

A similar range of $^{87}Sr/^{86}Sr$ ratios (0.710998–0.713423) has been found in Paleocene travertines of the Itaboraí Basin, close to the Campos/Santos Basin (Figures 3.1, 3.6 and 3.7) (Sant'Anna et al., 2004). These travertines overlie the same basement as the Campos and Santos Basins (Ribeira Fold Belt) and were deposited from terrestrial groundwaters in continental environment (Sant'Anna et al., 2004). They hence represent a Paleocene continental end-member facies whose aqueous geochemistry, in terms of $^{87}Sr/^{86}Sr$ ratios, derived from the basement of the Campos and Santos Basins. This basement may have been the same source as the waters that fed the non-marine environments of the Early Cretaceous pre-Salt carbonates (Wright, 2012) and, this is supported by the fact that the pre-Salt carbonates analysed during this study have similar $^{87}Sr/^{86}Sr$ ratios to the Paleocene continental travertines (Figures 3.6 and 3.7). The large range of $^{87}Sr/^{86}Sr$ ratios in the Cretaceous ostracod

and carbonate samples and the Paleocene travertines (0.002–0.003) is probably related to different sources of Sr to the Campos and Santos Basins.

Although we cannot rule out minor marine excursions, based on the sparse presence of planktonic foraminifera and marine ostracods, during the deposition of pre-Salt carbonates as recorded in Petrobras Well RJS-168 during the Jiquiá local stage (Figure 3.1) (Silva-Telles Jr. et al., 1994), it is probable that environments were dominantly continental and it seems extremely unlikely that seawater contributed to the $^{87}Sr/^{86}Sr$ ratios of pre-Salt rocks. Hence, it is unlikely that there was an aqueous source with even higher $^{87}Sr/^{86}Sr$ ratios that was reduced somewhat by less radiogenic $^{87}Sr/^{86}Sr$ ratios from contemporaneous marine waters. Nevertheless, there is a large range of $^{87}Sr/^{86}Sr$ ratios in the ostracod and carbonate samples (0.002–0.003), which are probably related to different sources of Sr to the Campos and Santos Basin.

The possible continental sources of Sr to the Campos and Santos basins during pre-Salt deposition are: 1) the basement of the Espírito Santo, Campos, Santos and Itaboraí Basins, which are mainly constituted of Precambrian marbles, and felsic to mafic metamorphic and magmatic rocks of the Araçuaí and Ribeira Fold Belts such as gneisses and granites (Sant'Anna et al., 2004; França et al., 2007; Moreira et al., 2007; Winter et al., 2007); 2) Lower Cretaceous volcanic and volcaniclastic rocks from the Camburiú and Cabiúnas Formation and Lower Cretacous post-rift volcanic/volcaniclastic rocks interbedded with pre-Salt Carbonates (Mizusaki et al., 1992; Dias et al., 1994) and; 3) Lower Cretaceous syn-rift immature siliciclastic rocks deposited in alluvial fans and lakes that filled grabens during the rift phase (Bertani and Carozzi, 1985a, b). Such coarse-grained facies from the Campos, Santos

and Kwanza Basins contain lithic grains and feldspars (Bertani and Carozzi, 1985b, a; Dias, 1998; Sabato Ceraldi and Green, 2017).

Tupinambá et al. (2012) have analysed the $^{87}Sr/^{86}Sr$ ratios of Precambrian orthogneisses (ca.790–600 Ma) of plutonic origin from the Rio Negro Complex of the Ribeira Fold Belt from basement outcrops surrounding the Campos and Santos Basins. They have shown a large range of modern $^{87}Sr/^{86}Sr$ ratios (0.70975–0.73335) based on 37 samples of low to medium-K rocks (quartz-diorite, tonalite, granodiorite and trondhjemite) and high-K rocks (quartz monzondiorite, quartz monzonite, granodiorite and granite). These rocks have different Rb/Sr ratios from each other and a correction needs to be made to $^{87}Sr/^{86}Sr$ to represent the time interval when pre-Salt carbonates were being deposited by using the equation (Faure and Mensing, 2005):

$$\left(\frac{^{87}Sr}{^{86}Sr}\right)_i = \left(\frac{^{87}Sr}{^{86}Sr}\right)_m - \frac{^{87}Rb}{^{86}Sr}(e^{\lambda t} - 1) \quad (2)$$

Possible ranges in $^{87}Sr/^{86}Sr$ ratios were calculated using the same λ given in Equation 1 for two possible ages of pre-Salt carbonates analysed in this study: 1) 113 Ma (0.70374–0.73562, median value of 0.71103; Figure 3.7) and; 2) 130 Ma (0.70368–0.73548, median value of 0.71272; Figure 3.7).

The second continental source (Mesozoic volcanic and volcaniclastic rocks) was estimated by using the published data from Mizusaki et al. (1992), who analysed eleven samples from Mesozoic basalts from seven Petrobras Wells in the southern Campos Basin. They have a range in $^{87}Sr/^{86}Sr$ ratios between 0.70586–0.71892. Similarly to rocks of Rio Negro Complex, these rocks also have different Rb/Sr ratios, yielding recalculated $^{87}Sr/^{86}Sr$ ratios for 113 Ma (0.70578–0.71498, median

value of 0.70879; Figure 3.7) and 130 Ma (0.70577–0.71439, median value of 0.70867; Figure 3.7) using Equation 1 and Rb and Sr content given by the authors.

Original $^{87}Sr/^{86}Sr$ ratios for Lower Cretaceous continental facies were not estimated. Nevertheless, it seems reasonable to suggest that the siliciclastic sediments contain a mixture of grains derived from Precambrian metamorphic and magmatic sources as well as volcanic sources. Unfortunately, the proportions of each source are unknown as is the $^{87}Sr/^{86}Sr$ ratios of rivers draining these materials that could have contributed to lake water, but one might expect a relatively radiogenic signature.

Significantly, the median values of calculated $^{87}Sr/^{86}Sr$ ratios for the Rio Negro Complex are close to the values found in the carbonate and ostracod samples. Furthermore, the high variability found in the Precambrian basement could explain the range of values found in the fossils and carbonates. Hence, it seems that the main sources of fluids with high $^{87}Sr/^{86}Sr$ ratios were continental waters mainly derived from the rock-fluid interaction between rainwater/groundwater and Precambrian crystalline rocks like those analysed in the Rio Negro Complex and/or rift sediments with a relatively high proportion of feldspars and lithic fragments derived from Precambrian crystalline basement. Contributions from relatively unradiogenic $^{87}Sr/^{86}Sr$ Precambian marbles (0.706233–0.706468; Figure 3.7) (Sant'Anna et al., 2004), from Mesozoic volcanic and volcaniclastic rocks and from seawater cannot be excluded, but would require a higher relative proportion of weathering products from Precambrian crystalline rocks and/or siliciclastic derivatives with high $^{87}Sr/^{86}Sr$ ratios to match the observed values in the fossils and carbonate. Similarly, it is unlikely that hydrothermal activity, associated with the predominantly mafic volcanic and volcaniclastic rocks characterized by lower $^{87}Sr/^{86}Sr$ ratios (~0.7073; e. g., Burke et

al., 1982; Allègre et al., 2010 or; ~0.708; Mizusaki et al., 1992), acted as a major souce of Sr in the samples analysed.

In addition to $^{87}Sr/^{86}Sr$ ratios, $^{187}Os/^{188}Os_i$ ratios also support the contention that the pre-Salt carbonates were deposited in a continental setting. The $^{187}Os/^{188}Os_i$ range of values (1.94–1.96; Figures 3.6 and 3.10) of carbonates deposited ~0.3–0.5 m below the base of the evaporites from Petrobras Well B from the Santos Basin is probably Early to early Late Aptian because of its Re-Os radiometric age (see discussions below). Because Early to early Late Aptian seawater has $^{187}Os/^{188}Os_i$ between 0.1 and 0.7 (Tejada et al., 2009; Bottini et al., 2012), the $^{187}Os/^{188}Os_i$ range of values (1.94–1.96; Figure 3.6) from this sample is much higher than that of contemporaneous seawater. These high values suggest that Os was similarly derived from continental sources, as argued for the $^{87}Sr/^{86}Sr$ ratios (Peucker-Ehrenbrink and Ravizza, 2000). The $^{187}Os/^{188}Os_i$ (1.94–1.96; Figure 3.6) is also considerably higher than modern continental sources of Os to the oceans ($^{187}Os/^{188}Os$ ~ 1.4). Specifically, there is likely to have been a significant contribution of waters from old rocks where highly radiogenic values have resulted from weathering of ancient shales from Precambrian shields that had an original high content of ^{187}Re followed by a long decay time to produce ^{187}Os (Peucker-Ehrenbrink and Ravizza, 2000). It seems most likely that the meta-sediments present in the Ribeira Fold Belt could be the source of these radiogenic waters, although critical analytical data on the $^{187}Os/^{188}Os$ ratios of basement rocks of the Espírito Santo, Campos and Santos are not available.

Mg-silicates, such as stevensite, have been found within pre-Salt rocks, and the origin of Mg and Si in these carbonates has been linked to volcanic and volcaniclastic rocks (Wright, 2012; Tosca and Wright, 2015; Wright and Barnett, 2015) and also to mantle serpentinization (Tosca and Wright, 2015) that does not

have strong supporting evidence in the Santos Basin (Evain et al., 2015). Another possible source of Mg and Si is rock-fluid interaction between rainwater and/or groundwater, including hydrothermal fluids, and mafic and felsic rocks from the Precambrian basement and siliciclastic derivatives. Therefore, weathering and/or diagenesis of unstable minerals, such as feldspars, resulted in transport of abundant Ca-, Mg- and Si-rich waters to the Campos and Santos Basins. Alternatively, deep faults in a thinned Precambrian crust with high heat flow (Blaich et al., 2011) may also have permitted rock-fluid interaction and promoted the formation of mineral springs in pre-Salt lakes. $^{87}Sr/^{86}Sr$ ratios of authigenic Mg-silicates can help to test this hypothesis.

To sum up, both the $^{87}Sr/^{86}Sr$ and $^{187}Os/^{188}Os_i$ ratios of analysed rocks constitute evidence that the pre-Salt carbonates from the Campos and Santos Basins were deposited from continental waters and this likely happened in a lacustrine environment, as suggested by other authors (Wright, 2012; Wright and Barnett, 2015; Sabato Ceraldi and Green, 2017). Although the possibility of minor marine excursions into the Campos and Santos Basins cannot be ruled out (Silva-Telles Jr. et al., 1994), the main influx of seawater probably took place after deposition of the pre-Salt carbonates and led to major evaporite formation. Similar pre-Salt carbonate facies are present in the Kwanza Basin on the African side of the South Atlantic (Saller et al., 2016), and these are predicted to have similar ranges of $^{87}Sr/^{86}Sr$ and $^{187}Os/^{188}Os_i$ ratios as reported here.

3.5.3 Age constraints of pre-Salt carbonates

Globally, the Early Aptian OAE 1a is recognized by marine black shales and/or by characteristic $\delta^{13}C$ profiles in marine and terrestrial records displaying a

negative carbon-isotope excursion followed by the onset of a positive excursion. The carbon-isotope curve can be broken down into segments classically termed C3–C6 (Figure 3.11A; Menegatti et al., 1998; Erba et al., 1999; Gröcke et al., 1999; Li et al., 2008; Erba et al., 2015; Savian et al., 2016). OAE 1a is estimated as having lasted 1.0–1.4 My (Figure 3.11A; Li et al., 2008; Huang et al., 2010; Malinverno et al., 2010). A composite $\delta^{13}C$ curve based on Petrobras Well X from the Santos Basin and Petrobras Well CP-5 from the Campos Basin records the typical isotopic pattern of OAE 1a and conforms to biostratigraphy based on planktonic foraminifera and $^{87}Sr/^{86}Sr$ profiles (Chapter 2). This stratigraphic assignment indicates that the upper part of the pre-Salt carbonates, evaporites and a significant part of the post-evaporite carbonates were deposited around the OAE 1a interval.

The age of 117.5 ± 2.5 Ma obtained through Re-Os dating from a sample ~0.3–0.5 m below the evaporites in Petrobras Well B from the Santos Basin is within range of a Re-Os date of 120.0 ± 3.4 Ma for the organic-rich shales (Selli Level) determined in the Cismon Apticore, Belluno Basin, Italy (Figure 11B; Bottini et al., 2012), but is slightly younger than an Ar-Ar age for M0r of 122.0 ± 0.5 Ma (2σ; recomputed to the Fish Canyon sanidine standard (FCs) of 28.201 ± 0.046; Kuiper et al., 2008), from lava flows at the Mashenmiao-Zhuanchengzi section in Yixian, Liaoning Province, northeast China (He et al., 2008). If the base of M0r is tied to 122.0 Ma, it would place OAE 1a in the range of 120.11 and 121.21 Ma based on cyclostratigraphy (Malinverno et al., 2010) (Figure 3.11A), but disagrees with an age of OAE 1a in the range of 124.55–123.16 Ma from Huang et al. (2010) or ~125.51–124.41 Ma obtained from calibration of Malinverno et al. (2010) tied to 126.3 Ma as the base of M0r according to Ogg et al. (2012) (Figure 1.1 in Chapter 1; Erba et al., 2015). These two latter absolute-age intervals for OAE 1a were based on

astrochronology of the Piobbico and Cismon cores (central Italy) and assumed the base of M0r as 125 Ma or 126.3 Ma (Huang et al., 2010; Ogg et al., 2012). These ages are based on: 1) an Ar-Ar age of 124.3 ± 3.6 Ma (2σ) for the volcaniclastic sequence of the Ontong Java Plateau (Figure 3.11B); 2) an Ar-Ar age of 125.5 ± 0.9 Ma (2σ) for the reversed-polarity chron of basalts at MIT Guyot in the north Pacific (Figure 3.11B); 3) an U-Pb date of 124.07 ± 0.13 Ma (2σ) from calcareous nannofossil-zoned sediments of Early Aptian age in the McCarty Creek section from the Great Valley of California (Figure 3.11B); and 4) an assumption that the reversed polarity within continental deposits of the Yixian Formation of China mentioned above captured the M"-1r" or ISEA event of mid–Early Aptian age. This latter interpretation assumes that determined absolute ages are reliable and have been correctly matched to biostratigraphy and magnetostratigraphy. Note that all Ar-Ar ages have been recalculated to the FCs of 28.201 ± 0.046 Ma (Kuiper et al., 2008) using the software ArAR – Argon Age Recalculator v1.00.00 (Mercer and Hodges, 2016). The same K-decay constant is assumed here for correction (5.453 ± 0.050 $x10^{-10}$ yr^{-1}), taken from Steiger and Jäger (1977).

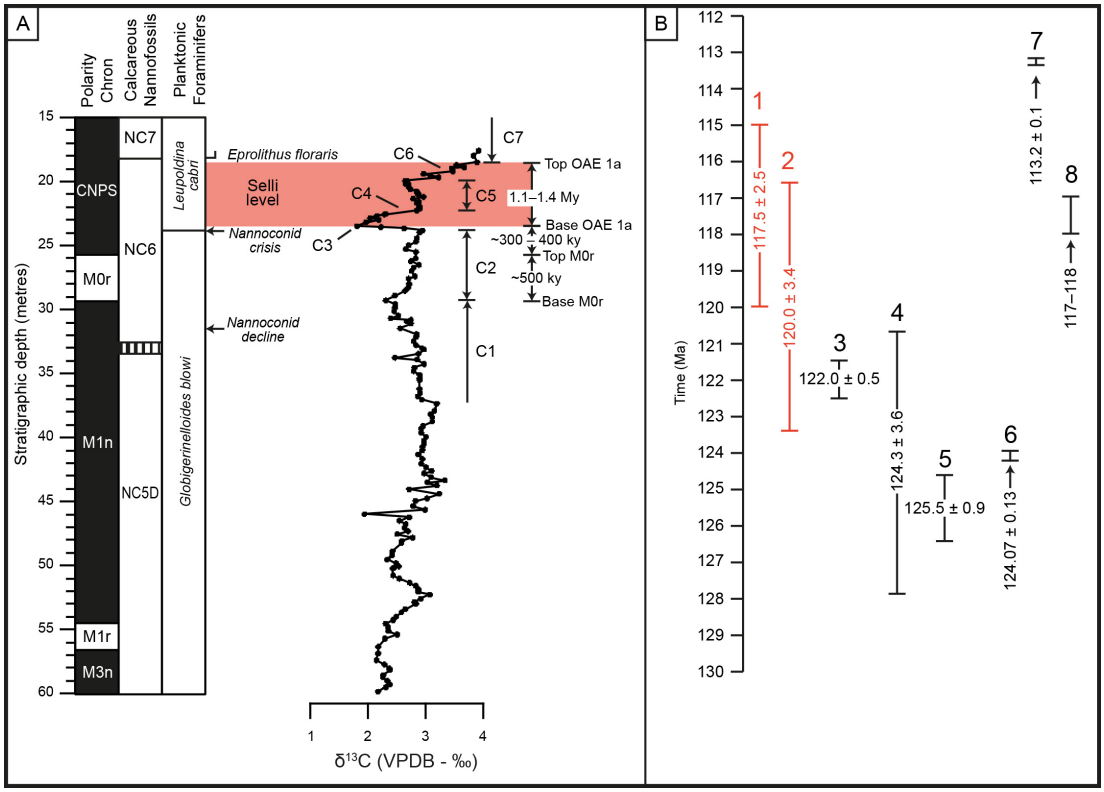


Figure 3 .11 – Main stratigraphic events and radiometric ages. (A) Cismon Apticore with the polarity chrons, calcareous nannofossil, planktonic foraminiferal zones, carbon isotopes with C-segments, some nannofossil events (after Erba et al. 1999, 2010), duration of some events based on cyclostratigraphy (after Li et al., 2008; Malinverno et al., 2010; Huang et al., 2010). The Selli level is in red and it is the record of OAE 1a in the Cismon core. (B) Radiometric ages obtained in this study and from previous works for comparison. 1 – Re-Os age from pre-Salt carbonates ~0.3–0.5 m below the base of the evaporites in the South Atlantic correlated with the OAE 1a interval in this study, 2 – Re-Os age from the Selli level at the Cismon Apticore, Belluno Basin (Bottini et al., 2012), 3 – Ar-Ar age from reversed-polarity chron of basaltic flows at the Mashenmiao-Zhuanchengzi section in Yixian, Liaoning Province, northeast China (He et al., 2008), 4 – Ar-Ar age from the volcaniclastic sequence from ODP Site 1184 at the eastern salient of the Ontong Java Plateau, Pacific Ocean (Chambers et al., 2004), 5 – Ar-Ar age from reversed-polarity chron from ODP Site 878 at MIT Guyot, north Pacific Ocean (Pringle and Duncan, 1995), 6 – U-Pb age from volcanic horizon at the McCarty Creek section from the Great Valley Sequence of California (Shimokawa, 2001), 7 – Ar-Ar age from Petrobras Well SCS-1, south Santos Basin (Dias et al., 1994), 8 – Ar-Ar age from basalt rocks interbedded with carbonate rocks of the Barra Velha Formation, Santos Basin (Moreira et al., 2007). Ages 1 and 2 are in red and are unambiguous links to the Selli level, whereas the others do not show clear stratigraphic relationships to the Selli level.

The age deriving from the volcaniclastic succession of the Ontong Java Plateau (ODP Site 1184), composed mostly of ash- to lapilli-size glass shards, tachylite and crystal fragments, is not a conventional age, because it is a weighted average of six total fusions of plagioclase phenocrystals obtained from different stratigraphic levels, rather than representing step-heating of a single crystal. In addition, the sediments containing these plagioclase crystals are overlain by volcaniclastic deposits with middle Eocene (zone NP16) nannofossils (Bergen, 2004; Chambers et al., 2004) and are clearly not biostratigraphically well constrained. Ogg et al. (2012) indicated that their given age of 124.3 ± 3.6 Ma was obtained in the basaltic basement on the Ontong Java Plateau, which is interbedded and overlain by limestones assigned to the *Leupoldina cabri* foraminiferal zone. They cited biostratigraphic studies of Sikora and Bergen (2004), who studied not only ODP Site 1184, but also other ODP sites on the main Ontong Java Plateau Plateau. Indeed, ODP Sites 1183A and 1186 also have limestones with $\delta^{13}C$ values higher than 3.8‰, assigned to the upper part of the *Leupoldina cabri* foraminiferal zone, just below the lowest occurrence of *Eprolithus floraris,* which constrains the basement age to be older than the positive carbon-isotope excursion that characterizes the post-OAE 1a interval. However, a radiometric age of 118.6 Ma from the basement of ODP Site 1183A in the main plateau was cited by Sikora and Bergen (2004), supposedly from Chambers et al. (2002), where the original data are not available for evaluation. Therefore, the age of 124.3 ± 3.6 Ma from ODP Site 1184 at the eastern salient of the Ontong Java Plateau may not constrain the age of the basaltic basement from ODP Site 1183A on the main part of the plateau.

The reversed-polarity chron recorded in basalts of ODP Site 878 in MIT Guoyot in the Pacific Ocean was interpreted originally as M1r, because it lies

stratigraphically below shallow-water carbonates with levels with relative dominance of nannoconids (below the level of the 'nannoconid crisis') within the *Chiastozigus litterarius* nannofossil zone (Erba et al., 1995; Pringle and Duncan, 1995). However, Pringle et al. (2003) described the possibility that the reversed polarity interval dated at 125.5 ± 0.9 Ma could be interpreted as M0r if there was no 'nannocoid crisis' recorded at MIT Guyot. Hence, ambiguity remains as to whether this reversed-polarity interval should be assigned to the Chron M0r (Aptian) or M1r (Barremian). In addition, it is unclear whether the interval with relative dominance of nannoconids lies below or above the level of the "nannoconid decline" event, below the Chron M0r (Figure 3.11A).

The key interval from the Great Valley Sequence is cited to occur within the *Chiastozygus litterarius* biozone (NC6 biozone) (Shimokawa, 2010). This biozone extends from the Upper Barremian to the Lower Aptian (Bralower et al., 1994; Bischoff and Mutterlose, 1998) and its lower boundary can be used to define the base of the Aptian stage (base of M0r). An integrated study using chemostratigraphy, magnetostratigraphy and biostratigraphy of this section of the Great Valley Sequence is not available for definitive evaluation of the U-Pb age.

Turning to the South Atlantic, cited ages from Ar-Ar determinations on trachyandesite (113.2 ± 0.1 Ma, Figure 3.11B) from Petrobras Well 1-SCS-1, southern Santos Basin (Dias et al., 1994) as the maximum figure for the base of evaporites/top Barra Velha/Macabu/Gargaú Formations disagree with an age range of 120–115 Ma for the top of pre-Salt carbonates based on the Re-Os data presented here. However, petrographic studies and seismic sections are not available for evaluation of these Ar-Ar ages and the ages likely reflect post-extrusion alteration

and/or date intrusive a cross-cutting sills or dykes rather than conformable extrusive rocks.

Our Re-Os age data are within error of the cited Ar-Ar determination on basaltic flows within the post-rift super-sequence in the Santos Basin (117–118 Ma, Figure 3.11B) (Moreira et al., 2007), where the top of the Barra Velha/Macabu/Gargaú Formations would be younger (< 118–117 Ma), and overlaps with the Re-Os age of OAE 1a of 120 ± 3.4 Ma (123.4–116.6 Ma) recorded at the Cismon core, Italy (Bottini et al., 2012). However, as with the age cited by Dias et al. (1994), petrographic studies and seismic sections are not available for evaluation of the age cited by Moreira et al. (2007), and it could reflect post-extrusion alteration and/or date intrusive rather than extrusive rocks.

The planktonic foraminiferal *G. ferreolensis*/*G. algerianus* biozones occur at least 180 metres above the top of the evaporites, stratigraphically above the Barra Velha/Macabu/Gargaú Formations, in Petrobras Well CB-3 (Figure 2.2 in Chapter 2). These biozones correspond to the interval 123–119 Ma according to Ogg et al. (2012). If the new Re-Os date of 117.5 ± 2.5 Ma, at 0.3–0.5 m below the base of the evaporites, represents a reliable age for the OAE 1a interval, the implication is that the age calibration of Ogg et al. (2012) is unlikely. Although evaporite deposition could have begun before the OAE 1a interval, the deposition of the top of the Barra Velha/Macabu/Gargaú Formations is likely to have taken place during the oceanic anoxic event itself, as suggested by carbon-isotope stratigraphy (Chapter 2). The new Re-Os age reinforces the view that the base of the evaporites dates to or just after the OAE 1a interval. If this new Re-Os age of 117.5 ± 2.5 Ma corresponds to the OAE 1a interval, it implies that the OAE 1a interval is younger than most ages ~121.21–120.11 Ma: Malinverno et al., 2010 tied to the base of M0r of 122 Ma) and ~1.1–1.4

My in the interval 125–123 Ma: Huang et al., 2010; Ogg et al., 2012) assigned for OAE 1a.

3.5.4 Consequences for the opening of the CSSA

Because emplacement of oceanic crust in the central segment of the South Atlantic would ultimately have increased the connectivity of a pre-Salt carbonate basin to the World Ocean, allowing entry of seawater, the geochemical data suggest that pre-Salt deposition likely occurred on continental crust prior to significant sea-floor spreading. Such a model agrees with most interpretations of the opening history of the region (Torsvik et al., 2009; Moulin et al., 2010). The source of radiogenic Sr and Os in lake waters was probably basement Precambrian felsic rocks exposed on topographic highs surrounding the 'sag basin' (Blaich et al., 2011). The data constrain the initiation of sea-floor spreading to be younger than 117.5 ± 2.5 Ma without, however, shedding light on whether seawater entered primarily from the north or the south (Dias, 1998; Arai, 2009, 2014).

3.6 Conclusions

Geochemical evidence suggests that the pre-Salt carbonates in the central segment of the South Atlantic were deposited in a continental setting until the onset of evaporite precipitation. The fluids that fed the lakes were predominantly derived from rivers and groundwaters draining felsic and feldspar-bearing siliciclastic rocks exposed on the flanks of the basin. The overall stratigraphy constrains the processes of sea-floor spreading to have taken place after deposition of these dominantly lacustrine carbonates. The new Re-Os age of 117.5 ± 2.5 Ma from an organic-rich carbonate sampled ~0.3–0.5 m below the base of the evaporites in Petrobras Well B

from the Santos Basin, is compatible with the stratigraphy correlation presented in Chapter 2, linking deposition of the upper part of the pre-Salt carbonates, and the evaporites themselves, synchronously with OAE 1a.

Chapter 4

The onset of the South Atlantic Salinity Crisis during OAE 1a

This chapter is co-authored by Leonardo R. Tedeschi, Hugh C. Jenkyns and, Stuart A. Robinson. Leonardo R. Tedeschi is the lead author who has written the majority of the chapter, with comments from all co-authors, and performed all analyses, except for sulphur and elemental analyses. Petrobras chemists Joselito C. Vazquez and Alexandre de A. Ferreira undertook elemental and sulphur-isotope analyses.

4.1 Introduction

During the Aptian (Early Cretaceous, 126.3–113 Ma; time scale of Ogg et al., 2012), extensive evaporites (4.6 x 10^{14} m^3) were deposited in the southern Brazilian basins (Davison et al. 2012; Chapters 2 and 3), which was part of a South Atlantic silled basin with an area of 10^6 km^2 lying below sea-level at the time (Burke and Sengör, 1988). This unusual deposition of evaporites is named here as the South Atlantic Salinity Crisis (SASC), in keeping with the terminology used for the Messinian Salinity Crisis of the Late Miocene (Hsü et al., 1977).

A significant volume of salt deposited during the South Atlantic Salinity Crisis (4.6 x 10^{14} m^3) resides in present-day southern Brazilian basins (Espírito Santo, Campos and Santos Basins; Figure 4.1), and is equivalent to ~2% of salt in the modern ocean (Davison et al., 2012). In these basins, the evaporites comprise cycles

of anhydrite ($CaSO_4$) and halite (NaCl), locally with more soluble salts such as carnallite ($MgKCl_3.6H_2O$), sylvite (KCl) and tachyhydrite ($CaMg_2Cl_6.12H_2O$) (Moreira et al., 2007; Winter et al., 2007). The evaporites mark the end of the post-rift super-sequence above a sedimentary sequence deposited during the rifting of the central segment of the South Atlantic (Figure 4.2) (Torsvik et al., 2009; Chaboureau et al., 2013). The Early Cretaceous-age rift and post-rift super-sequences below the evaporites comprise volcanic rocks, continental siliciclastics, lacustrine coquinas and organic-rich shales and, in distal settings, interbedded carbonates and shales (Figure 4.2 and discussed in Chapters 2 and 3; Moreira et al., 2007; Winter et al., 2007). Above the evaporites, shallow-marine platform carbonates with a marine fauna occur in distal settings (Figure 4.2; Chapter 2).

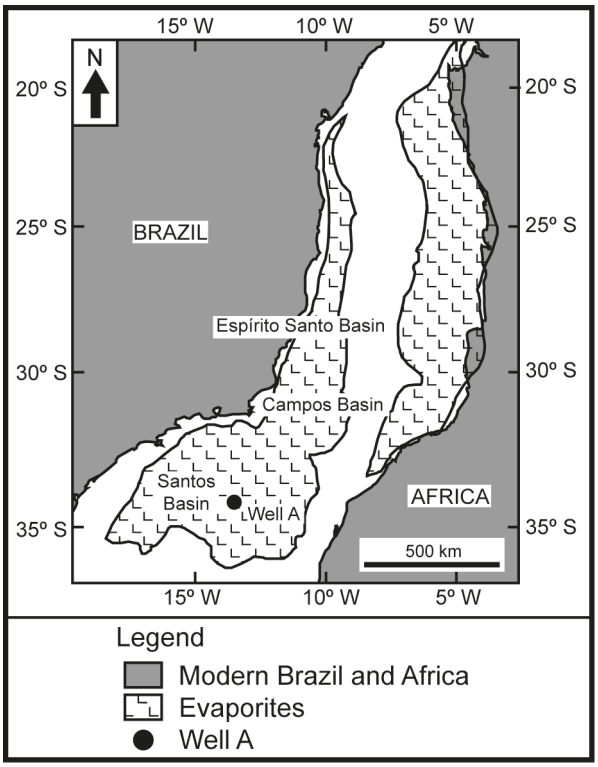


Figure 4 .1 – Location map of Petrobras Well A, offshore southeast Brazil Reconstruction between Brazil and Africa to 113 Ma after evaporite deposition and rotated to Tristan da Cunha hotspot (adapted from Norton et al., 2016).

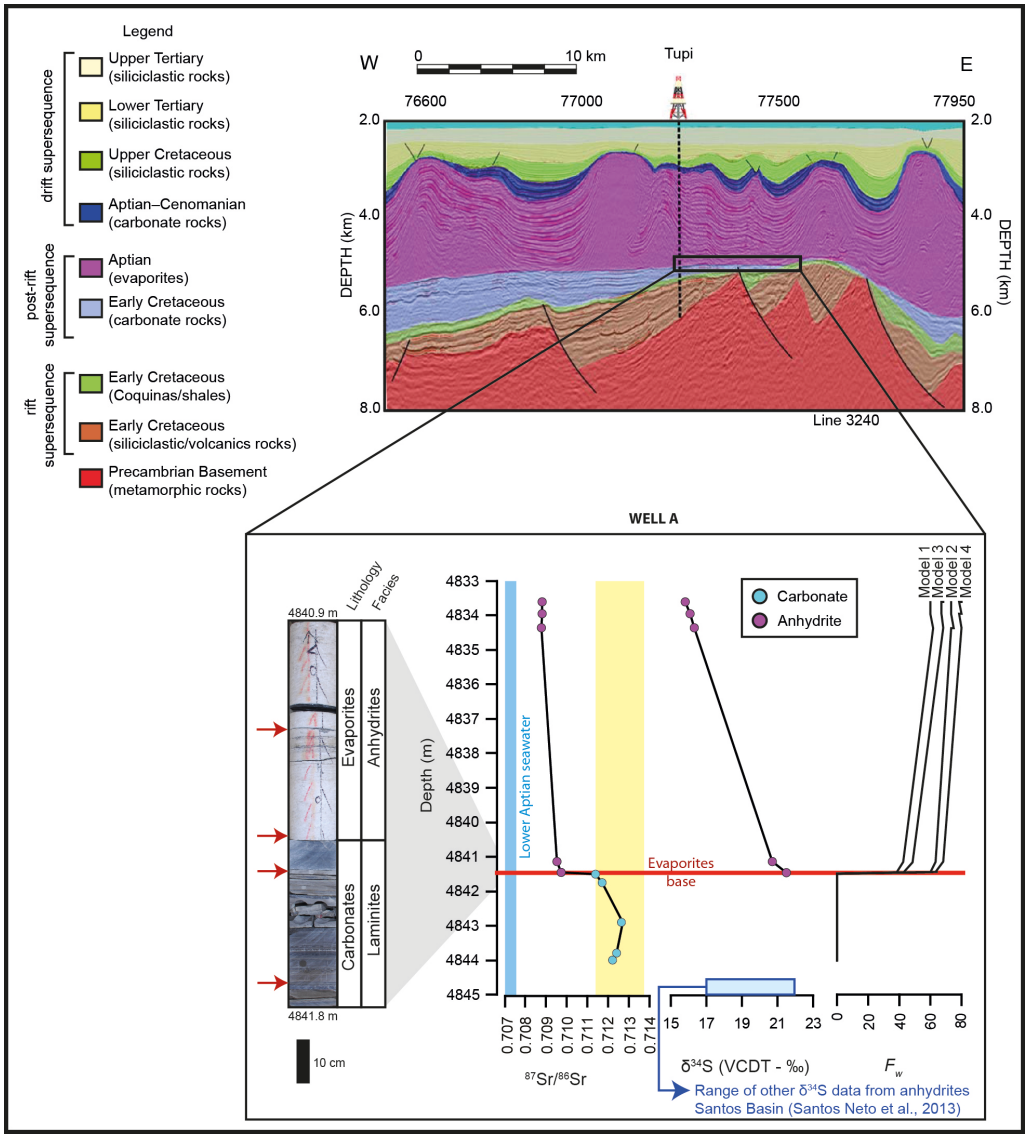


Figure 4 .2 – Seismic section showing stratigraphy with the Petrobras Well Tupi (Mohriak et al., 2012) and geochemical data from Petrobras Well A. Highlighted is the area where Petrobras Well A was spudded ~10km from the Petrobras Well Tupi. The $\delta^{34}S$ values and $^{87}Sr/^{86}Sr$ ratios of anhydrites and carbonates are from this study. F_{sw} values shows minimum and maximum modeled relative fraction of seawater strontium in percentage. See text for further details. Vertical blue rectangle shows the range of $^{87}Sr/^{86}Sr$ ratios of contemporaneous seawater (Lower Aptian) (Jenkyns et al., 1995; Bralower et al., 1997; Jenkyns and Wilson, 1999; Yamamoto et al., 2013; Ando, 2015; Bodin et al., 2015) and vertical yellow rectangle shows the range of $^{87}Sr/^{86}Sr$ ratios from continental pre-Salt carbonates (Chapter 3). Horizontal blue rectangle shows $\delta^{34}S$ values from anhydrites from another Petrobras Well (Santos Neto et al., 2013). It also shows a zoom of the abrupt contact between pre-Salt carbonates and evaporites. Red arrows show sample locations nearby the contact. Note: the uppermost pre-Salt carbonate sample and lowermost anhydrite sample are ~4cm apart. Arrow draw in the cores shows the direction of the top. W – West; E – East.

Although it has long been assumed that the evaporites were deposited during the latest Aptian–earliest Albian, the age of the South Atlantic Salinity Crisis has been redefined and constrained to the Early Aptian recently based on the presence of Upper Aptian planktonic foraminifera in overlying marine sediments, typical stratigraphic signatures of carbon-isotopes above the evaporites (Chapter 2) and Re-Os geochronology of carbonates ~0.3–0.5 m below the evaporites (Chapter 3). Based on these lines of evidence, it has been suggested that the SASC occurred during the Early Aptian oceanic anoxic Event 1a (OAE 1a).

OAE 1a occurred during the Early Cretaceous (125.51–124.41 or 120.21–119.11 Ma; Erba and references therein) and is characterized by widespread deposition of black shales (Arthur et al., 1990; Menegatti et al., 1998). The event occurred during a time of rising sea levels and high pCO_2 (Naafs et al., 2016), which may have led to surface seawater acidification promoting biotic turnover (Erba et al., 2010). The co-occurrence of the SASC with OAE 1a may have influenced global biogeochemical cycles by burying a large amount of sulphur in the oxidized form as calcium sulphate (Wortmann and Chernyavsky, 2007; Wortmann and Paytan, 2012).

Although the importance of South Atlantic Salinity Crisis on the perturbation of the ocean-atmosphere system during OAE 1a has been previously suggested (Wortmann and Chernyavsky, 2007; Wortmann and Paytan, 2012), many questions remain regarding the development of the South Atlantic Salinity Crisis and the role of gateways and sea-level change. The available geochemical and palaeontological evidence (discussed in Chapter 3), suggests that the South Atlantic evolved from a freshwater lake to a hypersaline environment, with a contribution from marine waters (Dias, 1998) at the onset of evaporite deposition. However, three critical questions

remain unaddressed: When did the main incursion of seawater into the southern South Atlantic basins occur and was it during OAE 1a? What mechanism triggered and permitted the South Atlantic Salinity Crisis event? What was the impact of the South Atlantic Salinity Crisis on the global sulphate inventory?

To address these questions, sulphur- and strontium- isotope ($\delta^{34}S$ and $^{87}Sr/^{86}Sr$ ratios) and element concentration data are presented from Petrobras Well A that recovers the transition from the pre-Salt carbonates to the anhydrites deposited in the earliest phases of the South Atlantic Salinity Crisis. These geochemical data are used to constrain a model for the contribution of seawater to the hydrological budget of the South Atlantic during deposition of the pre-Salt carbonates, the evaporites and the post-evaporite carbonates.

4.2 Materials and methods

The samples used here are from Petrobras Well A, which is ~10km from the Petrobras Well Tupi, for where a published seismic line is available to illustrate the stratigraphy (Figures 3.2, 4.1 and 4.2; described in Chapter 3). Petrobras Well A cored a continuous section spanning the contact between the pre-Salt carbonates and evaporites, recovering >8 m of salt. Five anhydrite samples were used in this study: two samples are close to the boundary with pre-Salt carbonates (4841.1 and 4841.5 m) and three are from cores higher in the section (4833.6 m, 4834.0 m and 4834.4 m; Figure 4.2). Unfortunately, cores between those two depth intervals were not made available for sampling. From these five samples sulphur-isotope ($\delta^{34}S$), strontium-isotope ($^{87}Sr/^{86}Sr$), mineralogical, element concentration, total organic and total inorganic carbon (TIC and TOC) data have been generated. Five samples of pre-Salt carbonates from Petrobras Well A were also analysed for all of the same parameters

(discussed in Chapter 3), with the exception of $\delta^{34}S$ values (Figure 4.2). In addition, the mercury (Hg) content of pre-Salt carbonate and evaporite samples was also analysed.

Powdered samples were analysed for $\delta^{34}S$ and element concentrations at CENPES; all other types of data were generated at Oxford University (OU). $\delta^{34}S$ data was obtained by using a Flash EA 1112 Elemental Analyzer coupled to a MAT 253 mass spectrometer with an interface CONFLO II (Thermo Fischer Scientific) (Fry et al., 2002). Sulphur-isotope values are reported in parts per thousand (‰) using the standard delta notation ($\delta^{34}S$) relative to the international standard, Canyon Diablo Troilite (VCDT). The calibration curve was undertaken by using the standards IAEA-S-1 ($\delta^{34}S_{V\text{-}CDT}$ = –0,30‰), IAEA-S-2 ($\delta^{34}S_{V\text{-}CDT}$ = +22,66‰) e IAEA-S-3 ($\delta^{34}S_{V\text{-}CDT}$ = –32,30‰). The long term reproducibitity was acessed using NBS-123 standard and for calibration to VCDT during this study. The standard NBS-123 gave an average of +17.09‰ and standard deviation (σ) less than ±0.6‰ (n = 105). The standard deviation (σ) of each analysed sample was less than ±0.3‰.

Al, Ca, Mg, Si, K, Fe, Mn, Rb, S and Sr contents of all five samples were obtained using a hand-held X-ray fluorescence (XRF Olympus, Delta Premium 6000), using the same method described in section 2.3.3 in Chapter 2 and section 3.3.1.3 in Chapter 3. Mining Plus mode was used to analyse Al, Ca, Mg, Si, K, Fe, and S which were expressed in weight percent (wt %), whereas the Soil mode was used to analyse Mn, Rb, and Sr in parts per million (ppm). All data showed a coefficient of variation of three analyses of each sample less than 30% and reference materials used to calibrate analyses are the same as used in section 2.3.3 in Chapter 2.

In Oxford, $^{87}Sr/^{86}Sr$ ratios were analysed following standard procedures (Ehrlich et al., 2001; Romaniello et al., 2015). Evaporite powders were dissolved in hot deionized water (<18 $m\Omega cm^{-1}$) by using an ultrasonic bath. This procedure was performed twice for each sample in order to generate duplicates. Sample solutions were dried down in Teflon beakers and dissolved in 2M HNO_3. Sr separation was performed using prep*Fast* (Romaniello et al., 2015), and analyses were obtained in a Nu-Plasma HR multi-collector inductively coupled plasma mass spectrometer (MC-ICP-MS, Nu instrument) using the same procedures detailed in section 2.3.5 in Chapter 2. All duplicates of anhydrite samples were analysed providing two $^{87}Sr/^{86}Sr$ values for each evaporite sample (Table 4.1). Blanks were < 10 ng/g and the Sr content of all analysed samples was higher than 1000 ng. External reproducibility of the SRM-987 standard and internal standard of Aptian carbonate PLG9466 obtained throughout this thesis is described in section 2.3.5 in Chapter 2. All mean values, standard errors of the mean and numbers of measurements (counts) are displayed in Table 4.1.

Bulk-rock mineralogy of five anhydrite samples was obtained using X-ray diffractometry (XRD). Those analyses were performed with a PANalytical Empyrean diffractometer with a Co Kα radiation at 40kV and 40 mA using the same method described in section 3.3.1.5 in Chapter 3, in which randomly oriented powdered samples were analysed from 5-80 degrees per 0.026° step (2θ) in spinning mode. The scan was continuous with a scan step time of 96.4 seconds.

Table 4.1 – Sulphur-isotope ($\delta^{34}S$) and strontium-isotope ($^{87}Sr/^{86}Sr$) data of anhydrite samples from Petrobras Well A obtained in this study.

Depth (m)	$\delta^{34}S$ (‰)	$^{87}Sr/^{86}Sr$		
		Mean	2SE (x10^{-6})	Counts
4833.6	+15.8	0.708780	7	45
		0.708815	9	48
4834.0	+16.1	0.708800	11	48
		0.708806	9	47
4834.4	+16.3	0.708772	12	49
		0.708758	11	48
4841.1	+20.7	0.709523	9	48
		0.709522	8	47
4841.5	+21.5	0.709728	10	48
		0.709722	11	50

TIC and TOC were measured using the Rock-Eval 6 and the method is described in section 3.3.1.4 in Chapter 3 and detailed section 5.3 in Chapter 5. Results are expressed in weight % (wt %). External reproducibility of the IFP 160000 standard and internal reproducibility of the in-house standard SAB 134 obtained throughout this thesis is described in section 3.3.1.4 in Chapter 3.

The mercury (Hg) content of five evaporite samples and five pre-Salt carbonates (Chapter 3) was measured using the same procedures of Percival et al. (2015) and a RA-915 Portable Mercury Analyzer with PYRO-915 Pyrolyser, Lumex. 8 samples of peat (NIMT/UOE/FM/001 – Inorganic Elements in Peat) with a known mercury concentration of 169 ± 7 ng/g (ppb) were analysed using masses between 10 and 100 mg, in order to calibrate the instrument. Each measurement was performed in triplicate and samples above the detection limit had coefficient of variation <11%. The mean of triplicates was used as reported Hg content.

4.3 Results

The evaporites have two distinct groups of $\delta^{34}S$ values and $^{87}Sr/^{86}Sr$ ratios. The two samples at the base of the analysed section (4841.1 m and 4841.5 m) have

higher $\delta^{34}S$ values (+21.5‰ and +20.7‰) and $^{87}Sr/^{86}Sr$ ratios (0.709522 and 0.709728) than the three samples from the stratigraphically higher interval (4834.4–4833.6 m), which have $\delta^{34}S$ values between +15.8‰ and +16.3‰ and $^{87}Sr/^{86}Sr$ ratios vary from 0.708758 to 0.708815 (Figures 4.2; Table 4.1). Thus, the $\delta^{34}S$ data show a trend of decreasing values from the deepest sample to the shallowest sample of 5.7‰ over ~7.9 m continuous deposition of anhydrite. There is a slight decrease in $^{87}Sr/^{86}Sr$ values up section.

Semi-quantitative XRD analyses show that each evaporite sample is composed by more than 99 wt % of anhydrite. <1 wt % comprises other minerals, including calcite (4833.6 m), dolomite (4834.0 m) and pyrite (4834.4 m). The XRD data from the sample at 4833.6 m shows the presence of calcite and this sample also has the highest carbonate content based on TIC values. TIC values range between 0.02 and 0.49 wt % (Table 4.2), equating to total calcium carbonate contents lower than 4.1 wt %, if all carbonate is associated with calcium, although the XRD suggests that trace amounts of dolomite might be present. TOC values are also very low, in the range of 0–0.15 wt % (Table 4.2). XRF data show that all the anhydrite samples have Al, Mg, Fe, K, Rb contents below the detection limits of the analyses (Al<0.3 wt %, Mg<3 wt %, Fe<0.1 wt %, K<0.3 wt % and Rb<3 ppm), suggesting that there are almost no detrital materials in these samples. Ca content varies between 26.1 and 27.4 wt % and S content varies between 14.6 and 15.9 wt %, consistent with the high abundance of anhydrite ($CaSO_4$) in the samples (Table 4.2). Si content varies between 0.16 and 0.96 wt % and shows that silicate content is low (Table 4.2). Sr varies between 1633 ppm and 8794 ppm (Table 4.2). High Sr contents are expected in anhydrite ($CaSO_4$), where Sr substitutes for Ca in the lattice sites (Kushnir, 1982).

Table 4.2 – Element content, TIC and TOC values of anhydrite samples from Petrobras Well A obtained in this study.

Depth (m)	Ca (wt %)	S (wt %)	Si (wt %)	TOC (wt %)	TIC (wt %)	Mn (ppm)	Sr (ppm)	Mn/Sr (mol/mol)
4833.6	26.4	14.6	0.96	0.15	0.49	49	4353	0.018
4834.0	26.8	15.7	0.32	0.04	0.05	14	4485	0.005
4834.4	27.3	15.9	0.91	0.07	0.09	20	8795	0.004
4841.1	26.1	15.2	0.23	0.07	0.19	31	1633	0.030
4841.5	26.4	15.4	0.16	0.00	0.02	20	1654	0.019

Hg contents of all anhydrite samples and two of the pre-Salt carbonate samples (4844.0 m and 4841.5 m depth) are below detection limits (Hg < 5 ppb). Two of the pre-Salt carbonate samples have Hg contents of 6.4 and 7.7 ppb (Table 4.3). The pre-Salt carbonate sample from 4842.9 m depth has the highest Hg concentration of 55 ppb. Hg/TOC values were calculated between 4 ppb/wt % and 39 ppb/wt % (Table 4.3).

Table 4.3 – Hg content of carbonate samples analysed in this study. TOC values from Chapter 3 is also present to calculate Hg/TOC ratios.

Depth (m)	Hg (ppb)	TOC (wt %)	Hg/TOC (ppb/wt %)
4841.5	<5	0.97	-
4841.8	7.7	0.56	14
4842.9	55	1.42	39
4843.8	6.4	1.79	4
4844.0	<5	1.62	-

4.4 Discussion

4.4.1 Strontium isotopes

The strontium-isotopic composition of both anhydrites and carbonates can reflect the water from which they formed, but can also be compromised by *in situ* production of Sr (through decay from Rb) and diagenesis, as discussed in Chapters 2

and 3. Because of the low Rb content, Rb/Sr ratios are not quantifiable in the samples presented here. Low Al and K contents suggest that K-bearing aluminossilicates are not present. As Rb substitutes for K in those minerals, such as K-feldspars and illite, this is further evidence that there is negligible Rb in the samples. Mn/Sr ratios > 2 (mol/mol) and Fe content > 0.3 wt % have been widely used to identify carbonate samples with a potential diagenetic overprint on $^{87}Sr/^{86}Sr$ ratios (Jacobsen and Kaufman, 1999; Yamamoto et al., 2013). None of the samples discussed here possesses high ratios of Mn/Sr or high concentrations of Fe and thus the strontium-isotope data probably reflect the depositional $^{87}Sr/^{86}Sr$ ratios.

$^{87}Sr/^{86}Sr$ ratios of the anhydrites (0.708758–0.709728) are lower than $^{87}Sr/^{86}Sr$ ratios of the pre-Salt carbonate samples from Petrobras Well A (0.711386–0.712638) (Figure 3.2 and Table 3.1 in Chapter 3) and are also significantly lower than $^{87}Sr/^{86}Sr$ ratios of pre-Salt carbonates from other wells in the Santos and Campos Basin (Dias, 1998; Chapter 3). Thus, a decrease of $^{87}Sr/^{86}Sr$ ratios occurred during the onset of the South Atlantic Salinity Crisis. In Petrobras Well A this decrease occurs over ~4 cm between the closest carbonate and evaporite samples, where a sharp boundary occurs between these two facies (Figure 4.2). ~6.8 m above this level, $^{87}Sr/^{86}Sr$ ratios of the anhydrites are slightly (~0.0007) lower than they are at the base. The anhydrite $^{87}Sr/^{86}Sr$ ratios reported here are higher than other reported anhydrite values from Campos and Espírito Santo Basin (0.70749 and 0.70849; Table 4.4), although these data are from unknown stratigraphic positions relative to the base of the evaporites (Rodrigues, 1995; Dias, 1998). Therefore, differences between the anhydrite strontium-isotope data from Petrobras Well A and other Petrobras wells may be related to different stratigraphic levels being sampled in the evaporite sequence. All $^{87}Sr/^{86}Sr$ ratios of both pre-Salt carbonates and evaporites

from this study, and previous work, are higher than data from post-evaporite marine carbonates (Chapter 2) and contemporaneous Early Cretaceous seawater (Jenkyns et al., 1995; Bralower et al., 1997; Jenkyns and Wilson, 1999; McArthur et al., 2012; Yamamoto et al., 2013; Ando, 2015; Bodin et al., 2015) (Figure 4.2). Therefore, there is a well-defined stratigraphic trend (Figure 4.3), where $^{87}Sr/^{86}Sr$ ratios decrease from pre-Salt carbonates (0.7113–0.7137) to the evaporites (0.7087–0.7097) and then to marine post-salt carbonates and contemporaneous seawater (0.7071–0.7076).

Those changes are probably associated with input of a less radiogenic source of Sr into southern South Atlantic basins associated to the onset of anhydrite deposition. Possible sources of lower $^{87}Sr/^{86}Sr$ ratios are: (1) Aptian seawater (0.707054 and 0.707541 during OAE 1a; Bralower et al., 1997; Jenkyns and Wilson, 1999; Yamamoto et al., 2013; Ando, 2015; Bodin et al., 2015) (Figure 4.2); (2) Changes in the catchment area of riverine/groundwater waters that fed South Atlantic basins where unradiogenic sources are present, for example the uradiogenic Precambrian marbles (0.706233–0.706468; Sant'Anna et al., 2004) and/or; (3) Hydrothermal alteration and weathering of mafic rocks. $^{87}Sr/^{86}Sr$ ratios of ten out eleven basaltic samples of seven Petrobras wells spudded in the southern Campos Basin have shown values between 0.70586 and 0.70958 (Mizusaki et al., 1992), and may have been exposed on structural highs during the onset of the evaporite deposition.

Table 4.4 – Strontium-isotope ($^{87}Sr/^{86}Sr$) data of anhydrite samples from Espírito Santo (ES) and Campos (C) Basins (Rodrigues, 1995; Dias, 1998) and F_{sw} values of models 1 to 4. See text for details.

Basin	Reference	$^{87}Sr/^{86}Sr$*	F_{sw} values (%)			
			Model 1	Model 2	Model 3	Model 4
ES	Dias (1998)	0.70849	67	79	75	85
ES	Dias (1998)	0.70794	80	87	90	94
ES	Dias (1998)	0.70847	68	79	76	85
ES	Dias (1998)	0.70765	87	91	97	98
ES	Dias (1998)	0.70749	90	94	101	101
ES	Dias (1998)	0.70767	86	91	97	98
ES	Dias (1998)	0.70770	85	91	96	97
ES	Dias (1998)	0.70787	82	88	91	95
ES	Dias (1998)	0.70821	74	83	83	89
ES	Rodrigues (1995)	0.70833	71	81	80	87
ES	Rodrigues (1995)	0.70820	74	83	83	89
ES	Rodrigues (1995)	0.70813	76	84	85	90
ES	Rodrigues (1995)	0.70787	82	88	91	95
C	Rodrigues (1995)	0.70779	83	89	94	96
C	Rodrigues (1995)	0.70788	81	88	91	94
C	Rodrigues (1995)	0.70792	80	87	90	94
C	Rodrigues (1995)	0.70794	80	87	90	94
C	Rodrigues (1995)	0.70809	76	85	86	91
C	Rodrigues (1995)	0.70818	74	83	83	90
C	Rodrigues (1995)	0.70781	83	89	93	96
C	Rodrigues (1995)	0.70766	86	91	97	98
C	Rodrigues (1995)	0.70783	82	89	92	95

* Original values do not show values of SRM-987, standard error of the mean and external reproducibility. Data were used just for comparison with results obtained in this study.

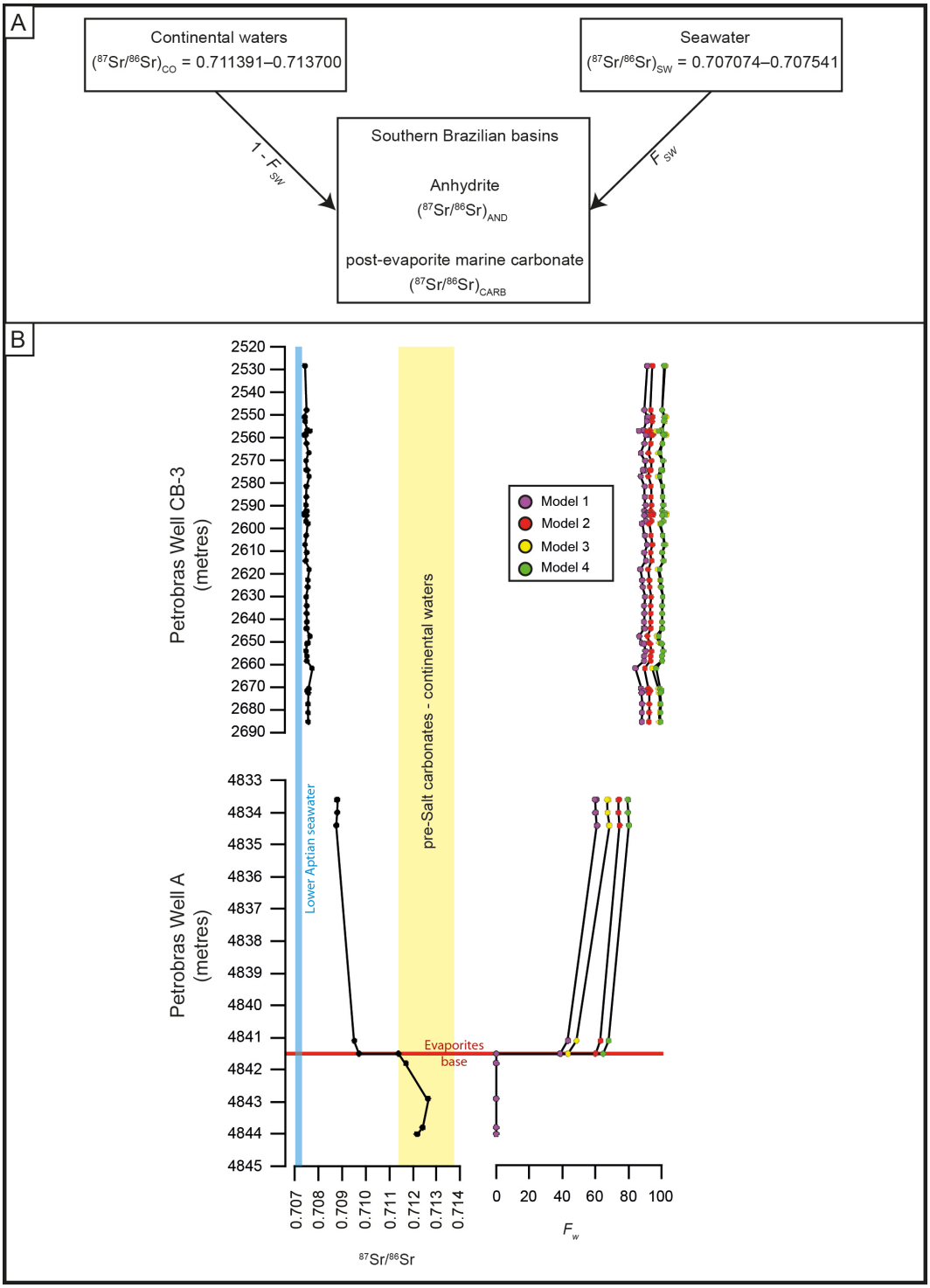


Figure 4 .3 – $^{87}Sr/^{86}Sr$ ratios and calculated F_{sw} from Petrobras Wells A and CB-3. A: Schematic diagram of equation 1 that shows how F_{sw} values are calculated. B: $^{87}Sr/^{86}Sr$ ratios from Petrobras Wells A (pre-Salt carbonates and evaporites) and CB-3 (post-evaporite shallow water carbonates) and calculated F_{sw} values in percentage calculated by using models 1 to 4. The red line shows the stratigraphic position of the evaporites base and the blue and yellow band show the range of $^{87}Sr/^{86}Sr$ ratios of Lower Aptian seawater and pre-Salt continental carbonates.

4.4.2 A seawater origin of South Atlantic Salinity Crisis?

$\delta^{34}S$ values of anhydrites analysed during this study (ranging from +15.8 to +21.5‰) are comparable to anhydrites from another well in the Santos Basin (Santos Neto et al., 2013), where $\delta^{34}S$ values range from +17 to +22‰ (blue rectangle in Figure 4.2). Hence, it seems that the data presented here probably reflect regional $\delta^{34}S$ values.

Evaporites usually have $\delta^{34}S$ values similar to sulphate (SO_4^{2-}) in water (Paytan et al., 2004). Early Aptian global seawater $\delta^{34}S$ values reconstructed from carbonate-associated sulphate and barite show a decrease around OAE 1a from values of +19–23‰ to +15–19‰ (Figure 4.4; Paytan et al., 2004; DeBond et al., 2012; Gomes et al., 2016). The data from the South Atlantic also display the same range of values, with a decreasing trend from +21.5‰ to +15.8‰ (Figure 4.4), suggesting a marine origin for the anhydrites and supporting the contention that its deposition took place in the Early Aptian. However, $^{87}Sr/^{86}Sr$ ratios of the anhydrites are higher than contemporaneous Early Cretaceous seawater values (Figures 4.2 and 4.4), suggesting at least some mixing of marine and terrestrial waters. This apparent contradiction between different geochemical datasets may be explained by the very high sulphate (SO_4^{2-}) concentration in seawater and low concentration in freshwaters, compared to Sr, and thus the relative insensitivity of $\delta^{34}S$ values (compared to $^{87}Sr/^{86}Sr$ ratios) to mixing between marine and continental waters (Denison et al., 1998). The trend to lower $^{87}Sr/^{86}Sr$ ratios in anhydrites could be taken to suggest an increasing influence of waters recording a signature of local hydrothermal alteration and weathering of mafic rocks and changes in catchment areas with unradiogenic rocks from the basement. However, if the former were the sole source of water then

$\delta^{34}S$ would be expected to fall dramatically to values close to volcanic sources of ~ +3‰ (Paytan et al., 2011). The change in the catchment area would require a large area of unradiogenic rocks from the basement to be exposed or as aquifers during the Early Cretaceous. However, the predominance of modern radiogenic metamorphic and igneous Precambrian basement shows that unradiogenic sources are unlikely to have been important during this time interval (e. g., Tupinambá et al., 2012). Consequently, a mixture of seawater and continental waters is the more parsimonious explanation for the sulphur- and strontium-isotope records.

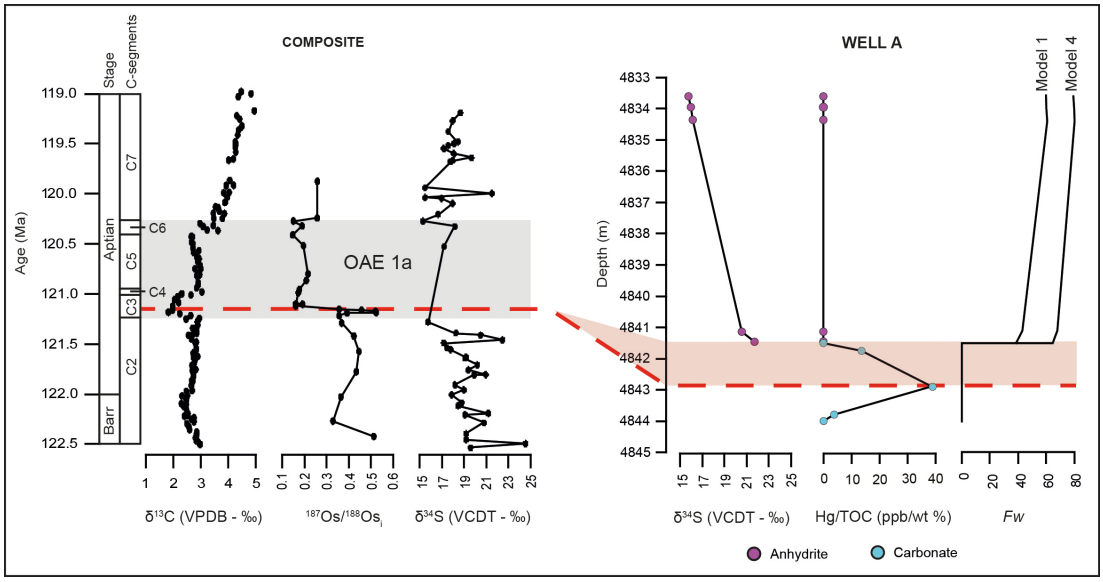


Figure 4 .4 –Correlation between composite curve of carbon- ($\delta^{13}C$) (Erba et al., 1999; Gomes et al., 2016), osmium- ($^{187}Os/^{188}Os_i$) (Bottini et al., 2012) and sulphur-isotopes ($\delta^{34}S$) (Paytan et al., 2004; Gomes et al., 2016) and $\delta^{34}S$ values, Hg/TOC ratios and fluxes of seawater (F_{sw}) of extreme models 1 and 4 of Petrobras Well A obtained during this study. The composite curve was based on time scale developed on Cismon core (Malinverno et al., 2010) with the Barremian-Aptian boundary tied to 122 Ma (see text for details), C-segments based on $\delta^{13}C$ values (Menegatti et al., 1998; Erba et al., 1999). Grey band shows the limits of OAE 1a. Red line shows the coincidence in time between the higher Hg/TOC value and the drop of $\delta^{13}C$ and $\delta^{34}S$ values and $^{187}Os/^{188}Os_i$ ratios related to main eruption(s) of Great Ontong Java Plateau. Red band shows the record of the gap of time between the this event and the contact between pre-Salt carbonates and evaporites, when seawater entered southern South Atlantic basins represented by an abrupt increase of F_{sw}.

Higher $^{87}Sr/^{86}Sr$ ratios than contemporaneous global seawater may be a result of mixing between continental and marine sources of Sr. The decrease of $^{87}Sr/^{86}Sr$ ratios within anhydrites probably reflects changes of the strontium fluxes derived from continental waters and seawater (Dias, 1998), as also occurred during the Messinian Salinity Crisis, although with very different values for riverine and marine sources (Sprovieri et al., 2004).

4.4.3 Quantifying the contribution of seawater entering into the South Atlantic

Because Sr is a conservative element, relative proportions derived from seawater and continental water can be estimated using a of simple mixing of two components (Figure 4.3) (Faure and Mensing, 2005):

$$\left(\frac{Sr^{87}}{Sr^{86}}\right)_{AND} = \left(\frac{Sr^{87}}{Sr^{86}}\right)_{SW} \times F_{sw} + \left(\frac{Sr^{87}}{Sr^{86}}\right)_{CO} \times (1 - F_{sw})$$

where $(^{87}Sr/^{86}Sr)_{AND}$, $(^{87}Sr/^{86}Sr)_{SW}$ and $(^{87}Sr/^{86}Sr)_{CO}$ are the isotopic ratios of anhydrite, seawater and continental inputs and F_{sw} is the relative fraction of seawater Sr within the SASC basin. The minimum and maximum values of $(^{87}Sr/^{86}Sr)_{SW}$ of Lower Aptian contemporaneous seawater are 0.707074 and 0.707541 (Jenkyns and Wilson, 1999; Yamamoto et al., 2013; Ando, 2015; Bodin et al., 2015) and minimum and maximum $^{87}Sr/^{86}Sr$ ratios from pre-Salt carbonates from Chapter 3 and reported by Dias (1998) (0.711391 and 0.713700) were used to estimate $(^{87}Sr/^{86}Sr)_{CO}$. The F_{sw} values were calculated and resulted in four models (Figure 4.3 and Table 4.5 in Appendix B): 1) $(^{87}Sr/^{86}Sr)_{SW}$ = 0.707704 and $(^{87}Sr/^{86}Sr)_{CO}$ = 0.711391; 2) $(^{87}Sr/^{86}Sr)_{SW}$ = 0.707704 and $(^{87}Sr/^{86}Sr)_{CO}$ = 0.713700; 3) $(^{87}Sr/^{86}Sr)_{SW}$ = 0.707541 and $(^{87}Sr/^{86}Sr)_{CO}$ = 0.711391; and 4) $(^{87}Sr/^{86}Sr)_{SW}$ = 0.707541 and $(^{87}Sr/^{86}Sr)_{CO}$ =

0.713700. The same four models for data obtained of post-evaporites carbonates – $(^{87}Sr/^{86}Sr)_{CARB}$ – from the interval 2685–2528 metres below sea level (mbsl) from Petrobras Well CB-3 (Figure 4.3 and Table 4.5 in Appendix B), where $(^{87}Sr/^{86}Sr)_{CARB}$ replaced $(^{87}Sr/^{86}Sr)_{AND}$.

Petrobras Well A shows the highest $^{87}Sr/^{86}Sr$ ratios of pre-Salt carbonates at ~1.4 m below the evaporite base (Figures 4.2), where two samples have relatively lower ratios (0.7113 and 0.7117) than other samples analysed in the same well (0.7121–0.7126) and other Petrobras wells from Santos Basin (0.7127–0.7134) (Chapter 3). Samples at 4841.5 and 4841.8 m from Petrobras Well A could represent minor marine incursions. However, Petrobras Well B, which is less than 10km away, has high $^{187}Os/^{188}Os_i$ ratios ~0.3–0.5 m below the onset level of the evaporites, suggesting that continental waters prevailed almost until the end of pre-Salt carbonate deposition (Chapter 2). For simplicity of modelling, the calculations presented here do not consider the possibility of minor marine incursions during the deposition of the pre-Salt carbonates from Petrobras Well A. By definition, this means that below the contact between the pre-Salt carbonates and evaporites the F_{sw}=0% and the $^{87}Sr/^{86}Sr$ ratios of the pre-Salt carbonates represents continental waters.

The extreme possibilities of F_{sw} values for the anhydrites and post-evaporite shallow marine carbonates are those obtained in models 1 and 4 (Figures 4.2, 4.3 and 4.4). All the models show a trend of increasing F_{sw} values from the base of the anhydrite to the post-evaporite shallow marine carbonates. Model 1 has shown the minimum F_{sw} values throughout the analysed sections, where anhydrite just above the pre-Salt carbonates has F_{sw} = 39%, increase to 60–61% in the highest anhydrite samples, and have F_{sw} of 84–91% in the post-evaporite shallow marine carbonates.

Model 1 implies that the contribution of Sr sourced from the continents decreased from 100% in the pre-Salt carbonates, to 39–61% in the anhydrites and further to 9–16% in the post-evaporite shallow-marine carbonates. Model 4 shows a similar stratigraphic trend but with a sharper change between F_{sw} values of the pre-Salt carbonates (0%) to the anhydrites (64–80%), then a further increase occurs to the post-evaporite shallow-marine carbonates that some depths have F_{sw} values are in the range 96–101%, implying little or no continental contribution of Sr and that Aptian seawater probably had $^{87}Sr/^{86}Sr$ ratio less than 0.707541. Although this approach provides a constraint on the Sr budget of the South Atlantic, it does not constrain the relative proportions of discharge of marine and continental waters into the South Atlantic Basin. The modern strontium concentration – [Sr] – in seawater is 7–8 ppm (Banner, 2004; Faure and Mensing, 2005). However, Aptian seawater had a higher Ca content (32–39 mmol/kg H_2O) than modern waters (11 mmol/kg H_2O) (Timofeeff et al., 2006) and, in general, Cretaceous seawater had lower Sr/Ca ratios (6–11 mmol/mol) than modern seawater (13–14 mmol/mol) (Steuber and Veizer, 2002), suggesting that Aptian [Sr] in seawater was probably in the range of 17–38 ppm. Cretaceous [Sr] of continental waters is difficult to estimate. Modern waters from Precambrian aquifers in the Rio de Janeiro State usually have [Sr] between 0.005 and 0.442 ppm (Barandas et al., 2011). If Cretaceous [Sr] from continental water were the same as groundwaters from Rio de Janeiro, it would imply that the relative influx of seawater would be smaller than continental waters. However, it cannot be ruled out that [Sr] of continental waters could have been much higher than modern groundwaters, because it is not possible to estimate the rock-fluid interaction in aquifers in thinned crystalline continental crust (Blaich et al., 2011) potentially with high heat flux. In such environments, continental waters could have ascended in

springs with higher [Sr], such those found in Yellowstone and Grand Canyon with similar $^{87}Sr/^{86}Sr$ ratios to those found in pre-Salt carbonates (Fouke et al., 2000; Crossey et al., 2006).

The same model applied to $^{87}Sr/^{86}Sr$ ratios from anhydrites of the Campos and Espírito Santo Basins (Rodrigues, 1995; Dias, 1998), yields F_{sw} values between 67% and 101% (Figure 3.3, Table 3.4), higher than the proportions calculated for the Santos Basin. These results are likely to represent temporal changes in the proportion of seawater Sr as the stratigraphic relationships between samples within evaporites are unknown. Alternatively, it could represent geographic trends. However, $^{87}Sr/^{86}Sr$ ratios from Espírito Santo and Santos Basins are higher than from the Campos Basin (Tables 3.1 and 3.4) and do not distinguish whether the entrance of seawater occurred from North to South or in the opposite direction.

The trends defined by F_{sw} values can be interpreted in two different ways: 1) there was a gradual increase in relative contribution of seawater strontium, within the range defined by models 1 and 4, with the discharge of each end-member being inversely proportional to their Sr concentration. Extreme relative high Sr concentration of continental waters implies in larger relative discharge of seawater into the South Atlantic, where the depositional onset of the base of the evaporites would have recorded a more dramatic flooding of the South Atlantic by seawater. On the other hand, extreme low Sr concentration of continental waters would have required a smaller entry of seawater during anhydrite deposition, where a dramatic flooding is expected at the top of the evaporite deposits or; 2) there was an abrupt flooding of the SASC by seawater at the onset of evaporite deposition, with an even higher contribution of seawater strontium than modelled F_{sw} values but with strong chemical stratification of the water body (due to different salinity and/or temperature

of continental waters and seawater), such that the anhydrite did not record fully marine conditions (i. e., seawater and continental waters were incompletely mixed).

The ingress of seawater into the Santos, Campos and Espirito Santo Basins might have been via either over spilling of topographic barriers and/or via seepage through a permeable topographic barrier, as suggested by Nunn and Harris (2007). A total rupture of topographic barriers is unlikely, because it would have decreased the restriction of the South Atlantic basin and the lack of extreme negative hydrological balance would have hindered evaporite deposition (Warren, 2010). A further question to this model is: how fast did F_{sw} increase?

4.4.4 Timing the seawater entrance at the onset of evaporites

Deposition of evaporites during the South Atlantic Salinity Crisis are estimated to have lasted 400–600 ky, as discussed in section 2.5 in Chapter 2 based on comparison with the duration of deposition of Miocene Mediterrean evaporites of the Messinian Crisis (~640 ky; Krigjsman et al., 1999) and similarity between depositional rates estimated for the South Atlantic evaporites (3.33–5 m/ky; Chapter 2) with modern depositional rates of halite (10–100 m/ky) and sulphates (1–40 m/ky) (Schreiber and Hsü, 1980). Significantly, Freitas (2006) identified 22 cycles using spectral analyses on amplitude from seismic traces from Santos Basin, and spectral analyses of gamma-ray, density and sonic logs from two Petrobras Wells from the same basin suggested that they constitute 'brining'-upward/downward cycles of anhydrite/halite/and more soluble salts (carnallite, sylvite). The cycles have average thicknesses of 49–103 m and were interpreted to record precessional forcing (Freitas, 2006).

The base of the SASC is suggested (in Chapters 2 and 3) to have occurred during OAE 1a. Given a duration of OAE 1a of 1.1–1.4 My (Li et al., 2008; Huang et al., 2010; Malinverno et al., 2010; Moullade et al., 2015), the record of the event in the southern South Atlantic basins must include not only the evaporites but also carbonates below and above (Chapter 2). The composite section and correlation presented in Chapter 2 (Figure 2.2) established that, during OAE1a, ~66 m of pre-Salt carbonates, ~2,000 m of evaporites, and ~165 m of post-salt carbonates were deposited in the Santos/Campos Basins. If the evaporites were deposited in 400–600 ky and the duration of OAE 1a is 1.1–1.4 My, ~231 m of carbonates (~66 m of lacustrine pre-Salt carbonates and ~165 m of marine post-salt carbonates) from Santos/Campos composite were likely deposited in 0.5–1.0 My, suggesting a minimum sedimentation rate of 231–462 m/My. Given that these values are very high compared to most accumulation rates observed in carbonate platforms (200 m/My, but values as high as ~230/240 m/My have been recorded in Triassic dolomites; Bosscher and Schlager, 1993), and to lacustrine sedimentation rates found in Green River Formation (169.5 m/My in Wilkins Peak Member; Meyers, 2008), it seems likely that evaporite deposition was shorter in duration (i. e., closer to 400 ky) and it is unlikely that a substantial gap of time exists at the contact between pre-Salt carbonates and evaporites. Otherwise, minimum carbonate sedimentation rates would have to be unreasonably high compared to other carbonate platforms (Bosscher and Schlager, 1993) and lacustrine sediments as found in Green River Formation.

In Petrobras Well A, the proportion of seawater-sourced Sr changed by approximately 14–25% over the 7.9 m of anhydrite studied. This interval represents ~13 kyrs (assuming a depositional rate 0.61–0.64 m/ky in the Santos Basin, Freitas, 2006) and thus a rate of increasing F_{sw} of 1.1–1.9 %/ky. Assuming the higher of

these estimates, the boundary between pre-Salt carbonates and evaporites, which shows a F_{sw} increase of 39–65% would have required ~20–59 ky. Although these numbers are rough estimates they suggest that the gap in time at the base of the evaporites is extremely short, relative to the duration of OAE1a.

Rapid deposition of a thick sequence of evaporites during the South Atlantic Salinity Crisis suggests that the basin must have been deep, prior to the onset of the event (possibly with net accommodation space totalling 1–3km; Davison et al., 2012); otherwise, subsidence of the South Atlantic would have been outpaced by the sedimentation rate of evaporites (Torsvik et al., 2009; Chaboureau et al., 2013). If the southern South Atlantic basins were already sub-sea level during deposition of the pre-Salt carbonates, as suggested by previous models (Sabato Ceraldi and Green, 2017), this would easily provide the opportunity for an ingress of seawater. Hence, the conceptual model for the evolution of the SASC starts with a rapid ingress of seawater into the southern South Atlantic basins (<59,000 yrs as estimated above); the maintenance of conditions suitable for deposition of evaporites with the cyclic variations over 400,000–600,000 kys (Dias, 1998, 2005; Freitas, 2006); and then the final flooding and deposition of post-evaporite shallow-water marine carbonates.

4.4.5 New model

One possible mechanism of introducing seawater into the South Atlantic at the onset of the SASC might have been a eustatic sea level rise during OAE 1a. The KAp1 (>75 m) sea-level rise event followed by a major eustatic sea-level fall has been reported in many localities around the world, and the maximum eustatic sea level is dated at 125.6 Ma (Haq, 2014; time scale of Ogg et al., 2012) close to the onset of OAE1a (125.51–124.41 Ma; according to the time scale of Ogg et al., 2012;

see Figure 1.2 in Chapter 1). Thus, based on the correlations presented here, the maximum sea level was achieved at virtually the same time as the flooding of the South Atlantic basin, assuming that changes between time scales of Ogg et al. (2012) and Malinverno et al. (2012) would not change the temporal relationship between KAp1 and OAE 1a events.

The trigger for the KAp1 sea-level rise might have been a pulse of rapid volcanism and vertical tectonics associated with the Great Ontong Java Plateau (GOJP), which includes the emplacement of Ontong Java, Manihiki, and Hikurangi Plateaus and is the single largest oceanic plateau known (Taylor, 2006; Chandler et al., 2012). It potentially covered ~1% of the Earth's surface (Chandler et al., 2012) and may have resulted in a rise of sea level of 70 m through decreasing the volume of the ocean basin when the large volume of volcanism and thermal rejuvenation of the sea floor uplifted the Pacific and Farallon plates (Schlanger et al., 1981).

The eruption of the GOJP has been linked to the OAE 1a (Tejada et al., 2009; Bottini et al., 2012; Erba et al., 2015) based on metal concentrations and a drop in the initial osmium-isotope ratio ($^{187}Os/^{188}Os_i$) during the OAE 1a, estimated to have occurred in ~6,200–12,400 years (Figure 4.4; Menegatti et al., 1998; Erba et al., 1999; Malinverno et al., 2010; Kuhnt et al., 2011; Moullade et al., 2015). The Re-Os isochron age of 121.5 ± 1.7 Ma (Parkinson et al., 2002) of GOJP is compatible with the idea that it was the main trigger for this drop in global seawater $^{187}Os/^{188}Os_i$ (Tejada et al., 2009; Bottini et al., 2012) during the OAE 1a (120.21–119.11 Ma; according to the time scale of Malinverno et al. 2012; see Figure 1.2 in Chapter 1). Relative enrichment of Hg/TOC ratios recorded in sections from France and Switzerland has also been used to associate the volcanic outgassing from GOJP with the OAE 1a interval (Charbonnier and Föllmi, 2017). In the South Atlantic, elevated

Hg/TOC ratios have been identified close to the base of the SASC (Figure 4.4), that appear to be stratigraphically associated with pre-Salt carbonates containing relatively higher Al and K contents, implying derivation during increased weathering of the local felsic basement rocks. This suggests that the high Hg/TOC ratios may be the result of the emplacement of GOJP. If correct then the formation of the GOJP occurred corresponding to a depositional level ~1.4 m below the base of the evaporites in the South Atlantic basin. This model would fit with a rising eustatic sea level that, eventually, overcame the topographic barriers or permeability constraints and entered into the South Atlantic, leading to the deposition of the evaporites. Therefore, the contact pre-Salt carbonates/evaporites could record the entrance of seawater, although the relative volume of seawater could initially have been smaller than the volume of continental waters.

The topographic barriers surrounding the South Atlantic basin must have played an important role in determining the onset of seawater flux. Although it is not possible to estimate the elevation of the barriers, isolation of the South Atlantic was necessary to promote desiccation because of the presence of high soluble salts such as carnallite ($MgKCl_3.6H_2O$), sylvite (KCl) and tachyhydrite ($CaMg_2Cl_6.12H_2O$) in southern Brazilian basins (Moreira et al., 2007; Winter et al., 2007) and cycles of 'brining'-upwards/downwards that were probably of 22kyr duration (Freitas, 2006). The volume present in the South Atlantic sub-sea level basin are estimated to have been 2×10^6 km^3, taking 2 km as the depositional thickness of the evaporites (Davison et al., 2012) and 10^6 km^2 in area (Burke and Sengör, 1983). In a most dramatic scenario, if each cycle corresponded to the desiccation of all the volume in the South Atlantic, the volume of water (~2×10^6 km^3) would have returned to the world ocean, which in turn would have allowed return to the South Atlantic basin

and attained equilibrium between the SASC basin and the world ocean. Following this scenario, a delay between the evaporation of water from the South Atlantic and the return to world ocean is necessary to explain the presence of cycles present in the South Atlantic evaporates. Because OAE 1a took place in a greenhouse period, virtually without ice (Bottini et al., 2015), it is proposed that aquifer-eustasy was the main driver, where evaporated water from the SASC was stored as groundwaters and promoted 10^4–10^5-year changes in eustatic sea-level (Hay and Leslie, 1990; Sames et al., 2016; Wendler and Wendler, 2016). Modern aquifers above sea level can potentially store ~25 x 10^6 km^3 and Cretaceous aquifers may have potentially stored ~40 x 10^6 km^3 (Hay and Leslie, 1990).

The final entrance of seawater could have occurred as a catastrophic flood at the end of the South Atlantic Salinity Crisis, as suggested for the Black Sea in the Holocene (Ryan et al., 2003) and the end of Messinian Salinity Crisis in the Plioceone (Hilgen and Langereis, 1993), although it is difficulty to estimate strontium concentration from continental waters and define whether or not this catastrophic event took place.

4.4.6 Cyclic closure of SASC basin or abrupt change in sulphur cycle?

The drop of $\delta^{34}S$ values (5.72‰) in ~7.9 m occurred over ~13 kyrs using a depositional rate of 0.61 m/kyrs for the anhydrites (Freitas, 2006). This is a rapid change of $\delta^{34}S$ values ($\frac{d\delta^{34}S_{SO_4}}{dt} = -0.44$‰/ky) within the South Atlantic basin. Two possible mechanisms can explain this dramatic change: 1) the drop of $\delta^{34}S$ values of anhydrites represents contemporaneous seawater. Considering the residence time of

sulphur in the modern seawater of 10^7 years, such rate of change in $\delta^{34}S$ values would require anomalous changes of fluxes of sulphur during 13 kyrs. If this mechanism is correct, $\delta^{34}S$ values can be used as a chemostratigraphic tool (Paytan et al., 2011; DeBond et al., 2012) to constrain the correlation of evaporite base to the Early Aptian (Figure 4.4); 2) the trend of descreasing $\delta^{34}S$ values from Petrobras Well A is not a record of changes of sulphur cycle worldwide. South Atlantic basins became more restricted just after a rapid seawater input to SASC because halite lies stratigraphically above gypsum, suggesting a 'brining' upward. $\delta^{34}S$ values measured in gypsum from the Messinian Mediterranean evaporites vary considerably compared to contemporaneous seawater and were interpreted as changes of sulphur supply from riverine influx and/or redox reactions in stratified brines within the Mediterranean Basin (Lu et al., 2001). Therefore, $\delta^{34}S$ values from Petrobras Well A could be different from contemporaneous seawater, where the closest ones to contemporaneous seawater would be those at the base of the evaporites, whereas $\delta^{34}S$ values stratigraphically above are different from contemporaneous seawater. In this scenario, just $\delta^{34}S$ values at the base of the evaporites are likely to be valid as a chemostratigraphic tool (DeBond et al., 2012) and could be used to constrain the evaporite base to around the Early Aptian OAE 1a interval.

4.5 Conclusions

New $^{87}Sr/^{86}Sr$ measurements of anhydrites of Santos Basin yield higher values than contemporaneous Aptian seawater but lower than continental input. This study suggests a rapid seawater flux to the South Atlantic basin (<59 ky). However, it was not possible to define whether the development of fully marine conditions occurred synchronously with deposition of the base or the top of the evaporites.

Elevated Hg/TOC ratios within the carbonates ~1.4 m below the evaporite base suggest the input of volcanic Hg and suggest a possible link with the main eruption(s) of the Great Ontong Java Plateau. This event would have triggered a eustatic sea-level rise and the first entrance of seawater into the South Atlantic basin. Afterwards, the cyclic pattern of SASC was likely driven by aquifer-eustasy. Lowermost $\delta^{34}S$ values at the base of South Atlantic salinity crisis have the same values of contemporaneous Aptian seawater and support an Early Aptian age equivalency for the evaporite base around OAE 1a.

Chapter 5

Aptian carbon isotope record from Sergipe-Alagoas Basin: New insights about OAE 1a and the entrance of seawater in the South Atlantic

This chapter is co-authored by Leonardo R. Tedeschi, Hugh C. Jenkyns, Stuart A. Robinson and, Cecília C. Lana, Maria Rosilene F. Menezes and Francisco M. W. Tognoli. Leonardo R. Tedeschi is the lead author who has written the majority of the chapter, with comments from all co-authors, and performed all geochemical analyses. Petrobras geologists Cecília C. Lana and Paulo R. S. Santos and biologist Renata G. Netto undertook palynological analyses. Petrobras geologists Maria Rosilene F. Menezes, Paulo R. S. Santos, Francisco M. W. Tognoli and biologist Renata G. Netto performed detailed lithological description and interpretation of depositional environment.

5.1 Introduction

During the last decade, major progress has been made in understanding the palaeoclimatic and palaeoceanographic changes that occurred during Early Aptian OAE 1a (e. g., Méhay et al., 2009; Erba et al., 2010; Bottini et al., 2015; Erba et al., 2015). However, environmental changes at low-latitudes, associated with the entrance of seawater into the northern part of the central segment of the South Atlantic (CSSA), have not been studied. Due to the results presented in earlier Chapters, understanding the relative timing and geographic origin of

palaeoenvironmental changes in this northern region is important to constrain the origin of environmental changes in the south and their relationship to OAE1a.

Planktonic foraminiferal, calcareous nannofossil and palynological studies have demonstrated that many Petrobras Wells from the Sergipe-Alagoas Basin, northeast Brazil pass through sediments of Early Cretaceous age (Koutsoukos, 1989; Regali and Viana, 1989; Koutsoukos et al., 1991; Koutsoukos et al., 1993). However, there is, to date, no definitive record of OAE 1a in this basin. Importantly, the evaporites in the southern Brazilian basins (Espírito Santo, Campos and Santos Basins) have been correlated to the OAE 1a interval (Chapters 2, 3 and 4) and are traditionally correlated to the evaporites from the Ibura Member, which is present onshore in the Sergipe-Alagoas Basin, more than 900 km away (Figures 5.1 and 5.2) (e. g., Dias, 1998; Chaboureau et al., 2012; Chaboureau et al., 2013). However, evaporites are present in the Sergipe-Alagoas Basin within at least three different stratigraphic units – the Horizonte, Paripuera and Ibura (Campos Neto et al., 2007). The deposition of these units in continental to shallow-water marine environments means that biostratigraphic constraints are rather coarse and, consequently (and despite the traditional view), there is considerable uncertainty over the correlation between evaporites in the northern and southern Brazilian basins.

Here, new palynological and chemostratgraphic ($\delta^{13}C_{OM}$, Rock-Eval) data are presented from the cored Petrobras Well D (~10°S), northeast Brazil (Figure 5.1). These new proxy records provide a unique view of Aptian palaeoenvironmental history of the low-latitude equatorial region and record the transition from continental to shallow-water marine setting. The $\delta^{13}C_{OM}$ record is compared to the composite carbon-isotope record from the Campos-Santos Basins discussed in Chapter 2 and to an age-calibrated Tethyan reference curve. This comparison allows

construction of a detailed chemostratigraphic framework for Petrobras Well D. The evidence suggests that the record of OAE 1a was dominated by deposition of coarse immature clastic sediments of Carmópolis Member and shales from the base of the Ibura Member, both part of Muribeca Group and deposited in continental environments. It is also suggested that most of Ibura Member is Aptian in age and was deposited mainly during the deposition of post-evaporite shallow-water carbonates was taking place in the southern Brazilian basins. This stratigraphic arrangement does not shed light about the stratigraphic relationship between evaporites within the Ibura Member deposited elsewhere in Sergipe-Alagoas Basin and those evaporites present in the Campos and Santos Basins (Retiro and Ariri Formations).

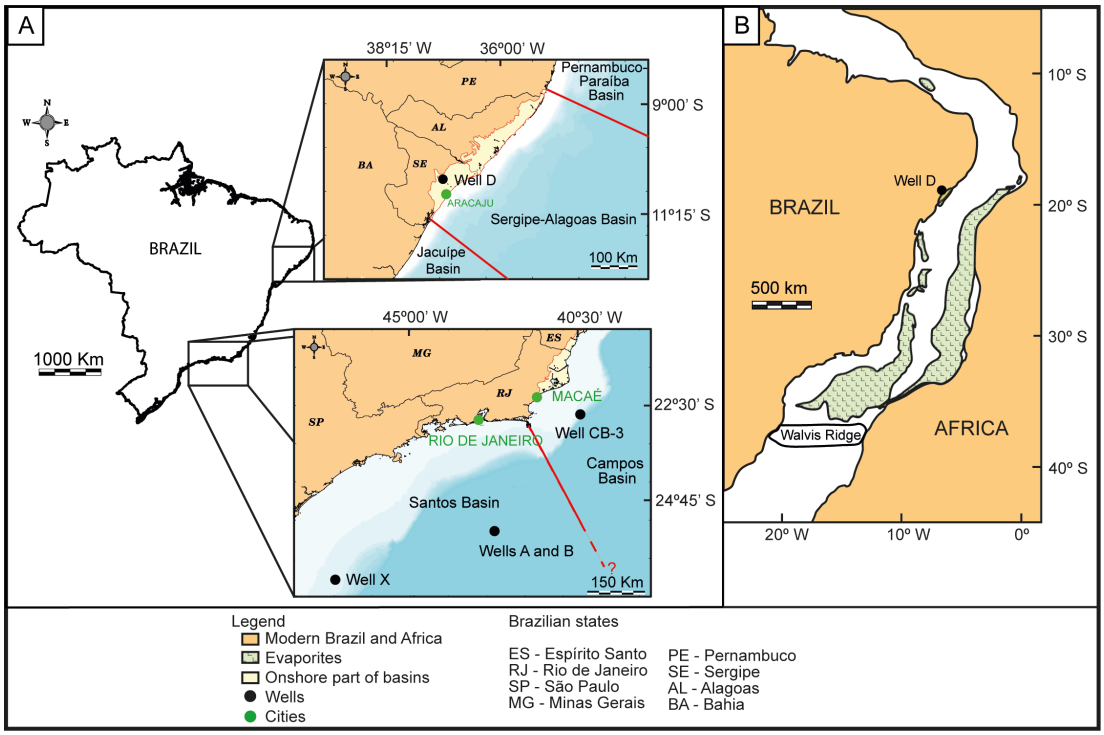


Figure 5 .1 – Location map of offshore Petrobras Wells D, northeast Brazil. Petrobras Wells A, B, X and CB-3 are also shown (A). Reconstruction between Brazil and Africa to 113 Ma after evaporite deposition (adapted from Davison, 2007, where latitude and longitude were adapted after rotation to Tristan da Cunha hotspot as defined by Norton et al., 2016).

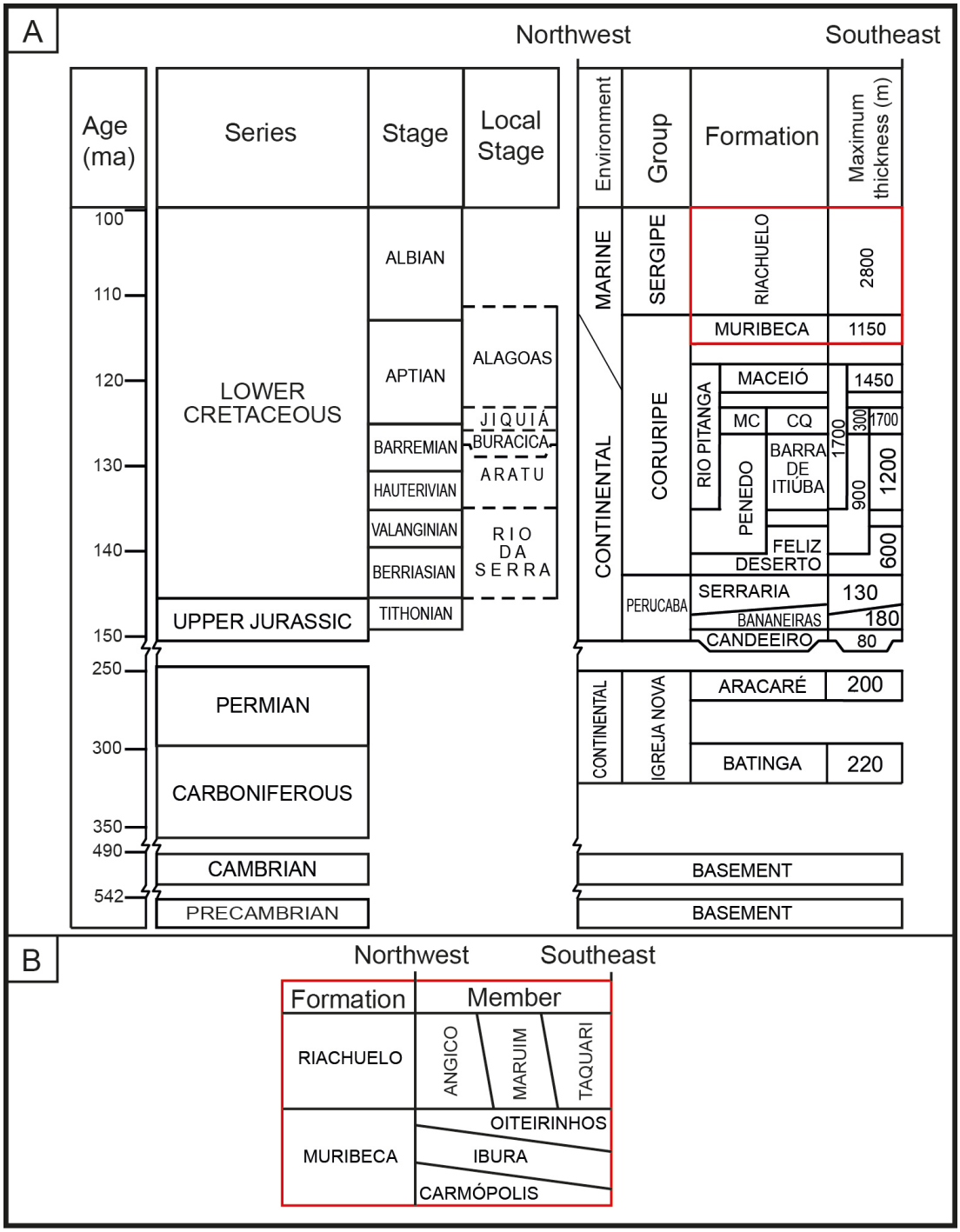


Figure 5 .2 –Stratigraphic chart of from the basement up to Albian sediments of Riachuelo Formation from the Sergipe-Alagoas sub-Basin, with local stages and maximum thickness of each formation (A) adapted from (Campos Neto et al., 2007). The members of the Muribeca and Riachuelo Formations are shown in detail (B).

5.2 Geological setting of the Sergipe-Alagoas Basin

The Sergipe-Alagoas Basin formed during the opening of the CSSA in the Early Cretaceous (Davison, 2007; Chaboureau et al., 2013). Onshore, a structural high (the Japoatã-Penedo High) separates the Sergipe and Alagoas sub-basins (Campos Neto et al. 2007). However, offshore this structural high seems to not be present in the sub-surface and hence the basins are termed the Sergipe-Alagoas Basin. Some differences exist in the lithostratigraphic records onshore of the Sergipe and Alagoas sub-basins, and hence there are two stratigraphic charts with small differences. This Chapter uses samples from one well located in the Sergipe sub-basin and, so, the lithostratigraphy of this basin is used here to describe the general geological setting. The Sergipe sub-basin stratigraphy is divided into five main super-sequences (Figure 5.2): Paleozoic, pre-rift, rift, post-rift and drift, as described by Campos Neto et al. (2007). Lying above the Precambrian to Cambrian igneous and metamorphic basement, there are a variety of Carboniferous–Permian siliciclastic rocks (Batinga and Aracaré Formations). Above this, there are lacustrine red shales (Bananeiras Formation), fluvial-deltaic sandstones (Candeeiro Formation) and braided fluvial/aeolic sandstones (Serraria Formation) that are Late Jurassic–Early Cretaceous age. These sediments constitute the Pre-rift super-sequence and are up to 390 m thick. The rift super-sequence can reach more than 4 km thick and is Early Cretaceous in age. This super-sequence comprises interbedded lacustrine greenish shales and sandstones (Feliz Deserto Formation), alluvial-deltaic conglomerates (Rio Pitanga and Poção Formations), alluvial-fluvial sandstones (Penedo Formation), deltaic-lacustrine siltstones and shales (Barra de Itiúba Formation), interbedded lacustrine coquinas and organic-rich shales (Morro do

Chaves Formation), deltaic-lacustrine sandstones and shales (Coqueiro Seco Formation), sandstones, calcareous mudstones, shales, and evaporites (Maceió Formation).

Two evaporite levels were identified in the rift super-sequence: 'Horizonte' and 'Paripuera'. The former is interpreted as the first marine incursion in the Sergipe-Alagoas Basin (Campos Neto et al., 2007) and occurs within the Coqueiro Seco Formation, whereas the latter occurs within the Maceió Formation and shows 'sabkha' facies and Br content in halite, interpreted as marine excursions with continental influence (Florencio and Evaristo Filho, 1998; Campos Neto et al., 2007). The main marine incursion occurred during the deposition of the post-rift super-sequence during the deposition of the Muribeca Formation, which comprises conglomerates (Carmópolis Member), and evaporites, microbial carbonates, and shales (Ibura Member) and interbedded shales and calcareous mudstones (Oiterinhos Member) (Figure 5.2). The Ibura Member includes anhydrite, halite and more soluble salts such as sylvinite and carnallite, and has been exploited in the Taquari-Vassouras mine (Mohriak et al., 2012).

Above the post-marine super-sequence, the drift super-sequence started with the 'truly' marine sedimentary record in the Late Aptian–Albian. The base of this sequence is the Riachuelo Formation, which can reach up to 2.8 km in thickness. It is a carbonate-siliciclastic unit composed of three members: 1) Angico Member: conglomerate, sandstone, siltstone, and/or shale, and rare thin beds of grainstone or packstone containing mollusks; 2) Taquari Member: rhythmically bedded, organic-rich, calcareous black shale and carbonate mudstone; and 3) Maruim Member: bioclastic and oolitic–oncolitic–peloidal grainstone or packstone, and local red algal patch reefs, with subordinate intercalations of calcareous mudstone and mudstone

(Koutsoukos et al., 1991; Koutsoukos, 1992; Koutsoukos et al., 1993; Campos Neto et al., 2007;). Upper Aptian planktonic foraminifera (e. g., *Globigerinelloides barri*, *Hedbergella gorbachikae*, *H. trocoidea*, *H. similis*) have been identified in the Riachuelo Formation (Koutsoukos, 1989; Koutsoukos, 1992; Koutsoukos et al., 1993). In addition, the presence of the ammonite *Dufrenoyia justinae* at some localities of the Sergipe-Alagoas Basin suggests an Early Aptian age (Bengston et al., 2007), although it is unclear in which lithostratigraphic unit they occur. Therefore, part of the Riachuelo Formation and super-sequences stratigraphically below are Late Aptian or older in age. The Riachuelo Formation continues into the Cenomanian and is overlain by sediments of Late Cenomanian to Recent age, which reach more than 4 km in thickness and are not discussed any further here.

5.3 Material and methods

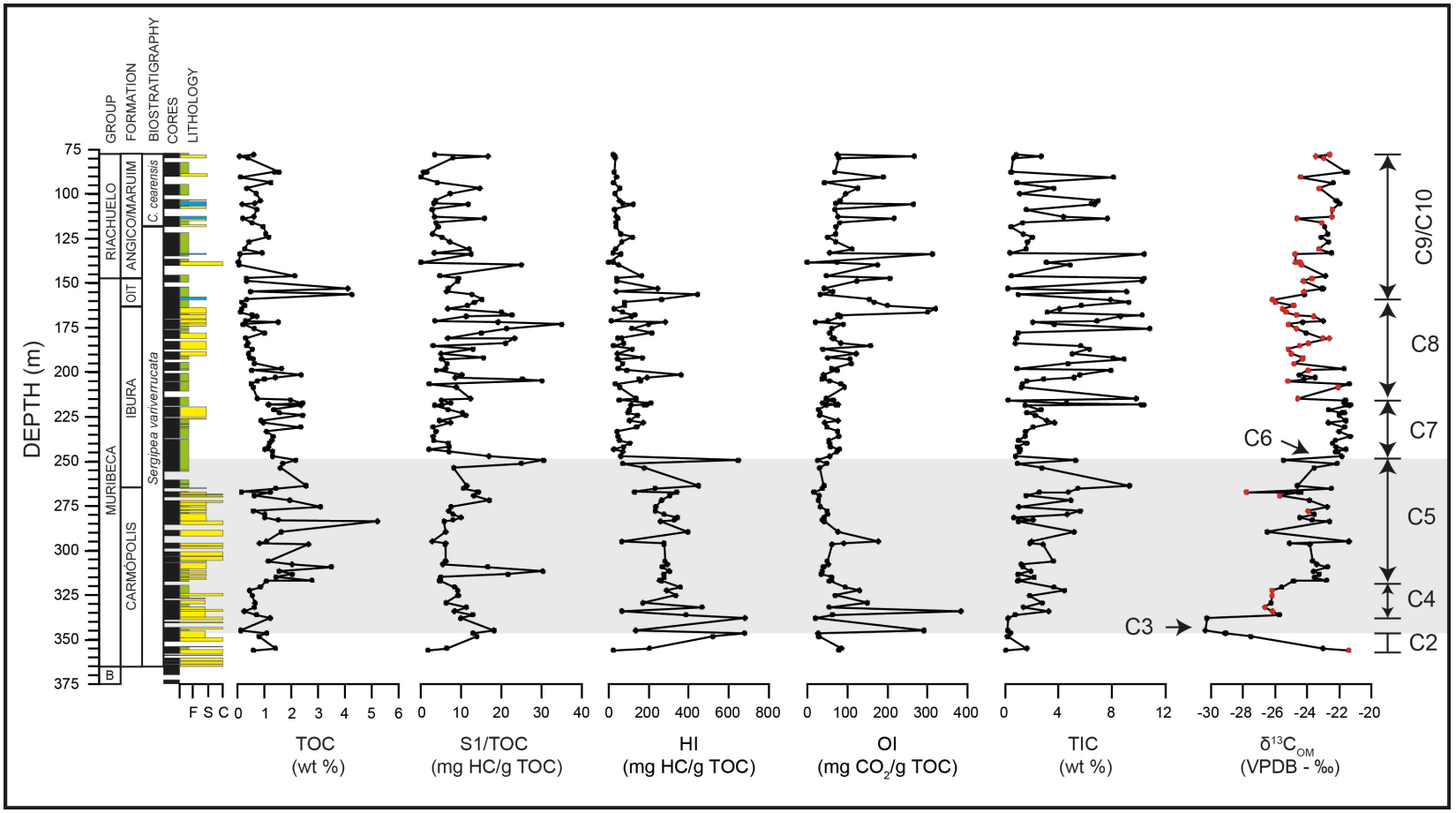
The work presented here was performed using samples from the Petrobras Well D (10°35' S; 37°05'W), which was spudded onshore at 92 metres above sea level (Figure 5.1). All data are referred as metres penetrated (m) throughout the text. Petrobras Well D was drilled in the Castanhal oil field of the Sergipe-Alagoas Basin and has been extensively cored in the interval 77.0–376.30 m (Figure 5.3). The sequence cored from the base towards the top comprises (Figure 5.3): basement (376.30–365.34 m); Muribeca Formation (365.34–147.20 m), and Riachuelo Formation (147.20–77.0 m). The basement includes metamorphic rocks, mainly phyllite and schist. All the members from the Muribeca Formation were cored and present in the Petrobras Well D (Carmópolis Member; 365.34–264.90 m; Ibura Member; 264.88–163.70 m; and Oiteirinhos Member; 163.70–147.20 m) In contrast only the Angico and Maruim Members (147.20–77.0 m) of the Riachuelo Formation

are recovered. The Carmópolis Member consists of conglomerates, sandstones (mostly immature lithic sandstones), and few layers of fine-grained rocks (siltstones/shales) and is interpreted as being deposited by alluvial fans and deltaic-fluvial systems. The Ibura Member consists mainly by siltstones and shales, although calcareous mudstones and sandstones are also present. This Member has been interpreted as being deposited in a lagoon/gulf, where sandstones represent rare episodes of fluvial-deltaic influence. The Oiteirinhos Member consists interbedded shales and calcareous mudstones, interpreted as deposited in a coastal lagoon. The Angico Member is represented by interbedded siliciclastic rocks (shales, siltstones, and sandstones) that are interpreted as deposited in coastal lagoon or lagoon at the base and grades upwards to a fluvial-deltaic environment. The Maruim Member is represented by carbonate rocks (oolitic/oncolitic/bioclastic grainstones, packstones, and calcareous mudstones), which locally interrupts facies from Angico Member. The lower energy facies (calcareous mudstones) have been interpreted as deposited in coastal lagoon or lagoon and higher energy facies (grainstones and packstones) have been interpreted as deposited in bars under turbulent waters.

Samples for palynological biostratigraphy were prepared at Universidade Vale do Rio dos Sinos (Unisinos), São Leopoldo, Brazil and the Geological Laboratory (GL) of Petrobras at Sergipe (UO-SEAL), Aracaju, Brazil. Both laboratories used the standard Petrobras method of palynological preparation compiled by Uesugui (1979), and described by Carvalho et al. (2016). The biostratigraphic framework is based mainly on pollen zones defined by Regali and Viana (1989), which does not use lowest occurrence of pollens. This pollen biostratigraphic framework was correlated to standard foraminiferal zones by Carvalho et al. (2016) and references therein (Figure 5.4). According to this

biostratigraphic framework, the pollen zone *Sergipea veriverrucata* is defined between the acme zone of the pollen *Inaperturopollenites turbatus* and the HO of pollen *Sergipea veriverrucata* (Müller, 1966, Regali and Viana, 1989). The latter was found at 117.32 m in Petrobras Well D and the acme zone *I. turbatus* has not been found. Therefore, the interval 365.34–117.32m is attributed to the *Sergipea veriverrucata* pollen Zone (Figure 5.3). This pollen zone is correlated the Upper Aptian foraminiferal zone *Globigerinelloides algerianus* or older (Figure 5.4). Regali and Viana (1989) also defined the pollen zone *Complicatisaccus cearensis* between the HO of the pollen *C. cearensis* and the HO of the *S. veriverrucata* which is broadly correlated to foraminiferal zones *G. algerianus*, *Hedbergella infracretacea* and *Paraticinella rohri* that are Aptian in age (Figure 5.4; Carvalho et al., 2016) and to the Albian according to Regali Viana (1989), albeit these authors did not show the correlation to ammonoides, nannofossil calcareous and planktonic foraminifera zones. The pollen zone *C. cearensis* is identified because of the presence of species *Uesuguipollenites callousus* and *Sergipea tenuiverrucata* at 96.7 m and 78.0 m, respectively (Regali, 1989).

Figure 5 .3 –Rock-Eval and $\delta^{13}C_{OM}$ data against stratigraphy. It includes total organic carbon (TOC), S1/TOC ratios, hydrogen and oxygen indexes (HI an OI), total inorganic carbon (TIC), $\delta^{13}C_{OM}$ data obtained in UERJ (black) and Open University (red). Also shown the group, formation, and pollen zones, cores in black and lithology described during this study. Green – fine-grained lithology (F), which include shales, calcareous mudstones and siltstones; blue – packstones; yellow – clastic sediments, where S is related to sandstones and C is related to coarse clastic sediments (sandstones with expressive amount of gravels) and conglomerates. C-segments interpreted in this study according to Menegatti et al. (1998) and Bralower et al. (1999). Grey shaded is the record of the OAE 1a interval.


GROUP
FORMATION
BIOSTRATIGRAPHY
CORES
LITHOLOGY
DEPTH (m)
RIACHUELO
MURIBECA
CARMÓPOLIS
IBURA
OIT
ANGICO/MARUIM
C. cearensis
Sergipea variverrucata
B
F S C
TOC (wt %)
S1/TOC (mg HC/g TOC)
HI (mg HC/g TOC)
OI (mg CO2/g TOC)
TIC (wt %)
δ13COM (VPDB - ‰)
C9/C10
C8
C7
C6
C5
C4
C3
C2

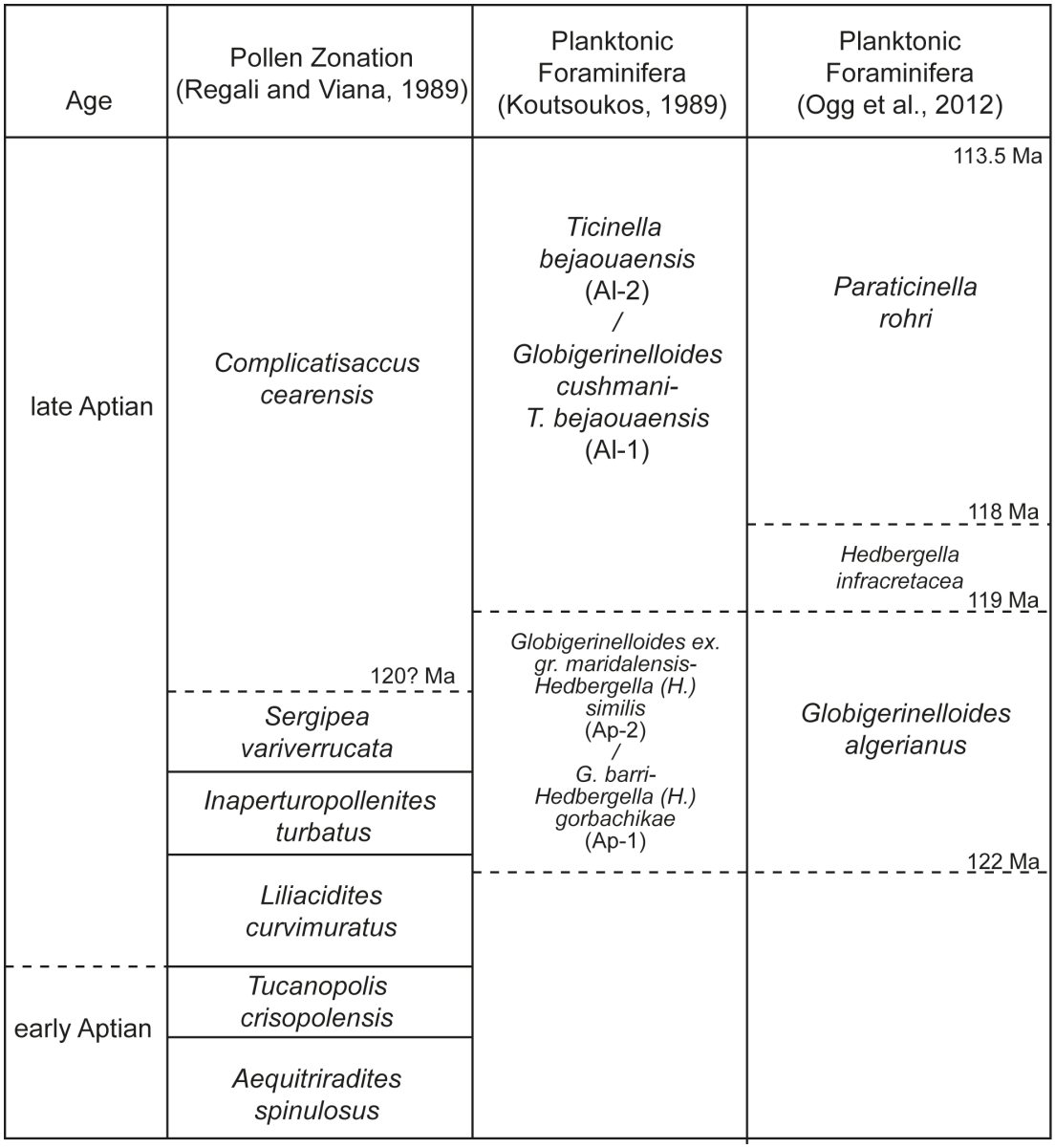


Figure 5 .4 –Biochronostratigraphic framework for the Aptian of the Sergipe-Alagoas Basin (adapted from Carvalho et al. (2016) with the relationship between pollen zones (Regali and Viana, 1989), local planktonic foraminiferal zones (Koutsoukos, 1989) and planktonic foraminiferal zones in the geological time scale 2012 (Ogg et al., 2012). The planktonic biozone *Paraticinella eubejaouaensis* was replaced by *Paraticinella rohri* according to Ando et al. (2013). *T.* –*Ticinella*.

Samples for geochemical analyses are from the interval 77.8–354.9 m. Samples underwent oil extraction in a Soxhlet apparatus, with 30% methanol and 70% chloroform, were crushed in small chips by using harmer and ground in an agate pestle and mortar at CENPES. Total organic and inorganic carbon (TOC and

TIC), S1, S2 and S3 parameters were obtained in a Rock-Eval 6 at the University of Oxford and $\delta^{13}C_{OM}$ values were obtained at Stable Isotope Laboratory of the Open University (Milton Keynes, UK) and Universidade do Estado do Rio de Janeiro (UERJ) (Tables 5.1–5.3 in the Appendix C).

The Rock-Eval 6 method consists of temperature-programmed heating of a weighed sample (~30–60mg) present in crucibles (Lafargue et al., 1998; Behar et al., 2001). Each crucible was analysed in programed heating in two different micro-ovens in an inert atmosphere as mentioned in section 3.3.1.4 in Chapter 3. The amount of hydrocarbons released during the pyrolysis are analysed by a flame ionization detector (FID), where temperature reaches up to 550–600°C, which permits analysis of the parameters S1 and S2 and the temperature of peak S2 maximum (Tmax). The amount of CO and CO_2 in the same oven is analysed by an infrared cell, which permits analysis of the parameters S3 and S3CO. Afterwards the sample is heated in an oxidation oven where the programed heating reaches up to 850°C and analyses, in an infrared cell, the quantity (mg) of CO and/or CO_2 released by residual organic matter and/or carbonates present in the sample, which permits analysis of the parameters S4CO, $S4CO_2$ and S5. All those parameters allow determination of TOC, TIC, hydrogen index (HI) and oxygen index (OI). The parameters S1 and S2 are reported in milligrams of hydrocarbons per gram of rock (mg HC/g rock) and the parameter S3 in milligrams of CO_2 per gram of rock (mg CO_2/g rock). The parameter S1, which is the amount of free HCs in the sample, was used to constrain the effectiveness of the oil extraction from the samples because some intervals are oil reservoirs. The S2 parameter is the amount of HCs released by the sample during the heating in the pyrolysis oven and it corresponds to the amount of HCs that could be released by the sample were it to reach thermal maturity in the

subsurface. The Tmax parameter is the peak of temperature obtained during the S2 measurement. It is a proxy that indicates whether the sample has reached maturity in the subsurface. A Tmax value higher than 435°C indicates mature rocks that have gone through oil window during burial; a lower Tmax suggests that the rock is immature and did not reach the temperature and pressure conditions necessary to be a source of liquid oil (Tissot et al., 1987). The HI is the ratio between S2 and TOC (reported in mg HC/ g TOC) an OI is the ratio between S3 and TOC (reported in mg CO_2/ g TOC).

The in-house SAB134 standard and the IFP160000 standard were used to check internal and external reproducibility of parameters obtained in the Rock-Eval 6 in addition to TOC and TIC values as described in section 3.3.1.4 in Chapter 3. The SAB134 standard gave S1, S2, S3 and Tmax average and standard deviation (± 1σ) of 0.38 ± 0.03 mg HC/ g rock, 18.27 ± 0.57 mg HC/ g rock, 0.23 ± 0.10 mg CO_2/ g rock and 420 ± 2°C (n = 47), respectively. The IFP160000 standard gave S1, S2, S3 and Tmax average and standard deviation (± 1σ) of 0.13 ± 0.03 mg HC/ g rock, 12.25 ± 0.50 mg HC/ g rock, 0.72 ± 0.15 mg CO_2/ g rock and 417 ± 4°C (n = 12), respectively. Reported values of IFP 160000 by Vinci Technologies® for S1, S2, S3 and Tmax parameters are 0.14 ± 0.07 mg HC/g rock, 12.43 ± 0.50 mg HC/g rock, 0.79 ± 0.20 mg CO_2/g rock and 416 ± 2°C, 3.28 ± 0.14 wt %, respectively. Results of TIC and TOC of SAB 134 and IFP 160000 are described in section 3.3.1.4 in Chapter 3.

The $\delta^{13}C_{OM}$ values are measured after carbonate fraction was removed from samples. At UERJ, carbonate fraction of samples were removed by acidifying them in porous ceramic boats, that were submerged in 50% volume HCl at room temperature for 24hs, where acid ascends through capillary action and reacts with the

sample. Samples analysed at Open University were acidified at the University of Oxford by using 3M HCl in one gram of sample powder in 50 mL centrifuge tubes. Samples dissolved in 3M HCl were reacted cold or on a hot plate for 2 hours at 60°C until no more bubbles were released by the reaction between acid and carbonate. Samples were subsequently rinsed 4–5 times with distilled water to reach neutral pH and dried at 40°C in an oven. The dried residue was weighed into 8×5-mm tin capsules (1–15mg) for $\delta^{13}C_{OM}$ analyses at UERJ and University of Oxford. A Flash Elemental Analyzer (EA) 1112 device attached to a Thermo Delta V Advantage isotope ratio mass spectrometer was used at UERJ, whereas a Thermo Scientific Flash 2000 HT EA coupled to a Thermo Scientific MAT253 isotope-ratio mass spectrometer via a Conflo IV open split interface was used at Open University. In both EA, combustion in an oxidizing environment within a furnace at 900–1000 °C converts organic carbon from the sample into CO_2 gas, which is analysed on-line in the mass spectrometer. Data are reported in parts per thousand (‰) relative to the Vienna Pee Dee Belemnite (VPDB) scale in both laboratories. At UERJ, the in-house Carbonífera and IAEA 600 standards were used to monitor internal and external reproducibility. The in-house Carbonífera standard is an oil sample obtained from Palaeozoic sandstones of Rio Bonito Formation at the Carbonífera Mine, Criciúma, Brazil gave an average and standard deviation (± 1σ) of –23.24 ± 0.14 (n = 24). The pure caffeine IAEA 600 standard gave an average and standard deviation (± 1σ) of –27.698‰ ± 0.107 (n = 24), which compares well with reported values of caffeine IAEA 600 standard ($\delta^{13}C_{OM}$ = –27.771 ± 0.043‰; Coplen et al., 2006). The differences between $\delta^{13}C_{OM}$ values from duplicate samples were <0.16‰ (n = 8) at UERJ. At Open University, the external reproducibility was monitored by using the L-alanine IR-R041, L-glutamic acid NIST 8573, and sucrose IAEA-CH-6 standards,

which has given an average and standard deviation (± σ) of –23.37 ± 0.13‰ (n = 55), –26.34 ± 0.11‰ (n = 53) and –10.26 ± 0.56‰ (n = 62), respectively. The standards IR-R041, NIST 8573, and IAEA-CH-6, have reported $\delta^{13}C_{OM}$ of -23.33 ± 0.10‰, -26.39 ± 0.09‰ -10.449 ± 0.033‰, respectively (Brookes and Belanger, 2005; Coplen et al., 2006; Wise and Watters Jr., 2007).

5.4 Results and discussion

5.4.1 The use of bulk $\delta^{13}C_{OM}$ data

Many authors have shown the reliability of using $\delta^{13}C_{OM}$ data from bulk organic matter, terrestrial organic matter (including discrete wood fragments) and specific organic compounds as chemostratigraphic tools in the Early Cretaceous (Menegatti et al., 1998; Bralower et al., 1999; Gröcke et al., 1999; Ando et al., 2002; Heimhofer et al., 2003; Robinson and Hesselbo, 2004; Naafs et al., 2016). $\delta^{13}C$ data from Petrobras Well D were generated from bulk organic matter, so there are some potential limitations, which must be addressed before the data can be used for chemostratigraphy. The data are derived from known oil reservoirs and, consequently, $\delta^{13}C_{OM}$ could be partially derived from migrated oil. Additionally, the data span changes in facies that may have led to changes in the source of organic matter present.

To address the first of these issues, all samples were submitted to oil extraction prior to analysis in order to remove any oil present in the samples. The impact of any oil remaining in the samples was evaluated using the S1 parameter and TOC data obtained from the Rock-Eval. The S1 value is the amount of free hydrocarbons (HCs) present in the sample (Lafargue et al., 1998; Behar et al., 2001).

The ratio S1/TOC was calculated in milligrams of hydrocarbons per gram of organic matter (mg HC/ g TOC), similar to the HI and OI indices, to show the amount of free HCs present in the organic matter evaluated in the sample. Figure 5.3 shows that S1/TOC values do not show any significant stratigraphic trend and that all values are below 35 mg HC/g TOC. Therefore, this strongly suggests that any oil present in the Carmópolis Member was effectively removed during oil extraction. Significantly, the cross-plot of S1/TOC versus $\delta^{13}C_{OM}$ (Figure 5.5) does not show significant correlation (R = 0.3561); reinforcing the view that free HCs present do not contribute to changes in bulk $\delta^{13}C_{OM}$ data obtained from the studied samples.

The many trends present in the bulk $\delta^{13}C_{OM}$ curve are generally not associated to with changes in HI and OI profiles (Figure 5.3). Furthermore, the HI values show a poor negative correlation with bulk $\delta^{13}C_{OM}$ data (R = 0.5273), whereas OI values seems to not have any relationship to bulk $\delta^{13}C_{OM}$ data based on the lack of correlation (R = 0.2733) (Figure 5.5). Hence $\delta^{13}C_{OM}$ data partially reflect partially changes in HI values, but it does not related to changes of HI and OI simultaneously (Figure 5.3), which would suggest potentially could reflect changes in the abundance flux of terrestrial organic matter to the basin, which could be responsible for changes on $\delta^{13}C_{OM}$ curve. Therefore, although changes in organic matter source cannot be totally discounted, it is likely that bulk $\delta^{13}C_{OM}$ data reflect changes in the carbon-isotope composition of the ocean-atmosphere carbon reservoir**.**

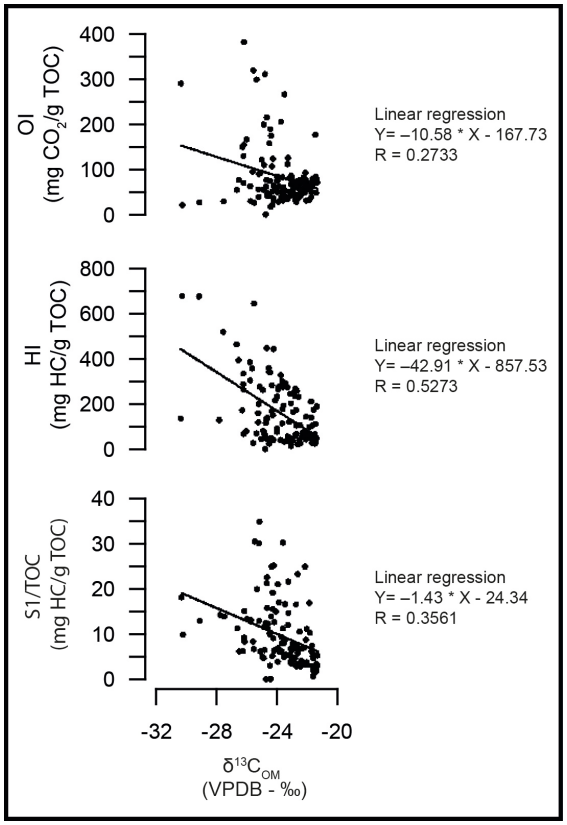
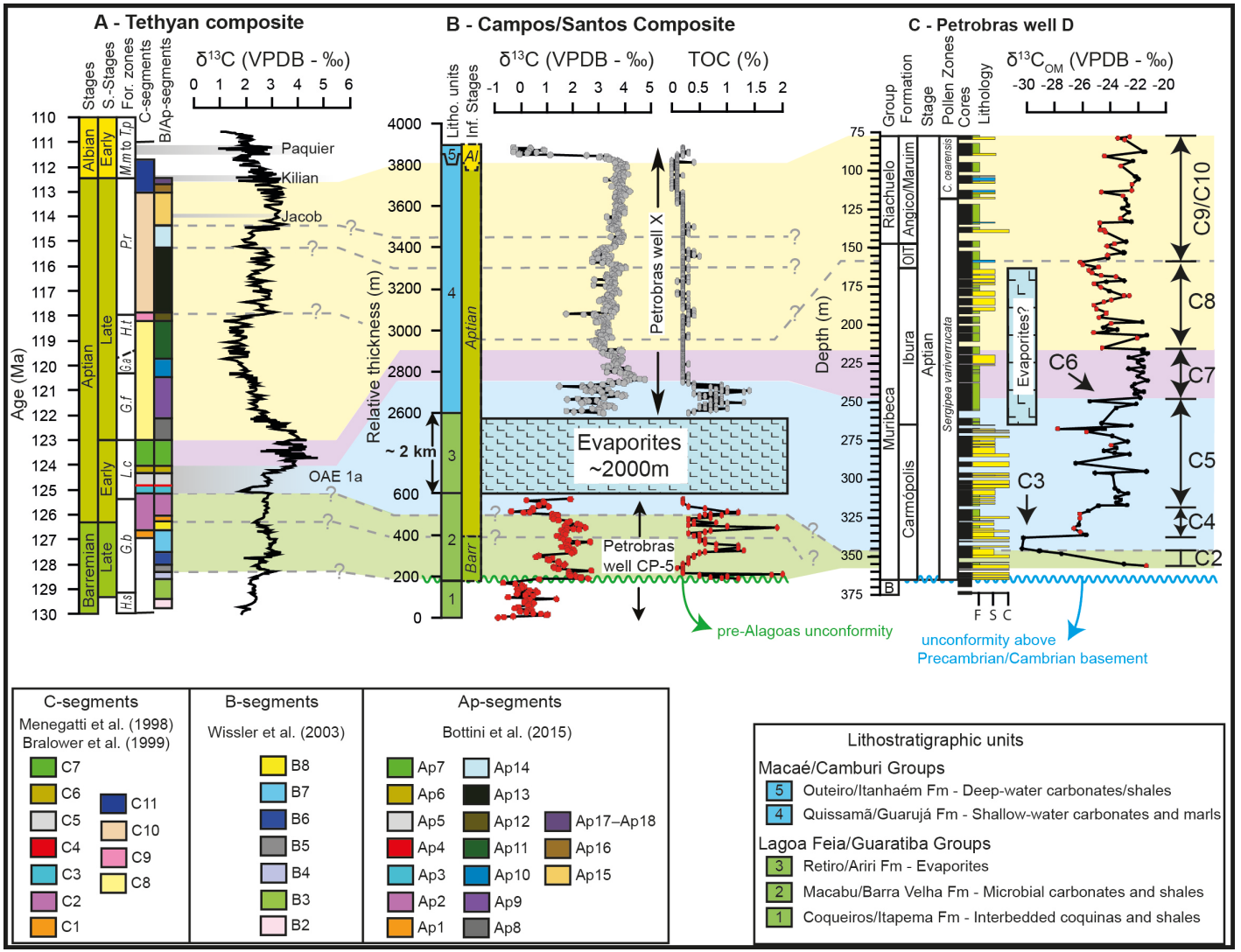


Figure 5 .5 –Cross-plots S1/TOC ratios and Hydrogen and Oxygen indexes (HI and OI) versus $\delta^{13}C_{OM}$ data. Also shown linear regressions, and its equations and coefficient of correlation (R).

5.4.2 Carbon-isotope stratigraphy

All $\delta^{13}C_{OM}$ data presented in Figure 5.3 were obtained either at UERJ (black) or the Open University (red). Both datasets show good agreement when plotted in stratigraphic order. Significantly, the stratigraphic $\delta^{13}C_{OM}$ curve obtained from Petrobras Well D shows the typical trends present in Aptian records from other sites and this allows stratigraphic correlation to reference sections (Figures 5.3 and 5.6). Data obtained in the coarse clastic section (Carmópolis Member) just above the Precambrian/Cambrian metamorphic rocks show a negative excursion from ~ –21‰ to ~ –30‰ typical of the Ap2/C2 segment (Menegatti et al., 1998; Bottini et al., 2015). The minimum values defined by three samples in the interval 346.35–337.92

m are typical of the Ap3/C3 segment (Menegatti et al., 1998; Bottini et al., 2015). The interval 337.32–313.13m has a positive excursion from ~ –30‰ to ~ –23‰ that is characteristic from Ap4/C4 segment. The pattern of $\delta^{13}C_{OM}$ values in the interval 313.13–251.08 m is not clear, where most of samples are in the range of –25.5 to –22.5‰. This interval is correlated to the Ap5/C5 segment. An abrupt shift towards higher $\delta^{13}C_{OM}$ values occurs between the sample at 251.08 m (–24.6‰) and the sample at 247.09 m (–22.1‰), where after relatively higher $\delta^{13}C_{OM}$ values > –22.7 ‰ occur in the interval up to 208.32 m. Hence the abrupt shift is correlated with the Ap6/C6 segment and the interval of relatively high $\delta^{13}C$ values is correlated to the Ap7/C7 segment. Upwards, the interval 208.32–154.63 m is characterized by a trend of decreasing $\delta^{13}C_{OM}$ values from ~ –22 to ~ –26‰, which is typical of the C8/ Ap8–Ap10 (Bralower et al., 1999; Bottini et al., 2015), where the minimum $\delta^{13}C_{OM}$ values (–26‰) of the C8/Ap11 segment are suggested to be correlated to the interval 159–160 m based on two samples. From 159.12 m up to 77.80 m there is a trend of increasing $\delta^{13}C_{OM}$ values, but there is no well-defined shift towards higher $\delta^{13}C$ values that would allow a definitive correlation to the C9/Ap12 segment. Nevertheless, relatively higher $\delta^{13}C_{OM}$ values are typical of the Upper Aptian C10/Ap13–Ap15 segments. Therefore, the interval 159.12–77.80m is correlated to the C9/C10 segments, without a well-defined boundary between those two segments.


A - Tethyan composite
B - Campos/Santos Composite
C - Petrobras well D
Stages
S.-Stages
For. zones
C-segments
B/Ap-segments
δ13C (VPDB - ‰)
Albian
Aptian
Barremian
Early
Late
M.m to Tp
Pr
H.t
G.á
G.f
L.c
G.b
H.s
Paquier
Kilian
Jacob
OAE 1a
Age (Ma)
Litho. units
Inf. Stages
TOC (%)
Relative thickness (m)
~ 2 km
Aptian
Barr.
Petrobras well X
Evaporites
~2000m
Petrobras
well CP-5
pre-Alagoas unconformity
unconformity above
Precambrian/Cambrian basement
Group
Formation
Stage
Pollen Zones
Cores
Lithology
δ13COM (VPDB - ‰)
Depth (m)
Riachuelo
Angico/Maruim
Muribeca
Ibura
Carmópolis
OIT
Sergipea variverrucata
C. cearensis
Evaporites?
C3
C6
C9/C10
C8
C7
C5
C4
C2
F S C
C-segments
Menegatti et al. (1998)
Bralower et al. (1999)
B-segments
Wissler et al. (2003)
Ap-segments
Bottini et al. (2015)
Lithostratigraphic units
Macaé/Camburi Groups
Outeiro/Itanhaém Fm - Deep-water carbonates/shales
Quissamã/Guarujá Fm - Shallow-water carbonates and marls
Lagoa Feia/Guaratiba Groups
Retiro/Ariri Fm - Evaporites
Macabu/Barra Velha Fm - Microbial carbonates and shales
Coqueiros/Itapema Fm - Interbedded coquinas and shales

The lithostratigraphic record of the first part of the OAE 1a interval (C3/Ap3–C5/Ap5 segments) consists mainly of immature coarse clastic sediments (conglomarates and sandstones) of the Carmópolis Member, which also has a few thinner beds of fine-grained sediments (siltstone/shales) (Figures 5.3 and 5.6). Shales at the base of the overlying Ibura Member include the uppermost part of C5/Ap5 and the C6/A6 segment. Shales of the Ibura Member were deposited during the C7/Ap7 segment. The upper part of the section (above the base of the C8/Ap8 segment) (Figure 5.3 and 5.6) consists mainly of fine-grained mudstones and shales from the upper part of Ibura Member and Oiterinho Member (Muribeca Formation) and Angico/Maruim Members from Riachuelo Formation, where beds of packstones/grainstones and siltstones/sandstones are also present.

Figure 5 .6 –Chemostratigraphic correlation between A: Tethyan carbonate carbon-isotope composite age-calibrated curve (Ogg et al., 2012): black – carbonate carbon-isotope composite from Herrle et al. (2015); grey – organic-rich levels Jacob, Killian, Paquier and Oceanic Anoxic Event 1a (OAE1a). C-segments from Menegatti et al. (1998) and Bralower et al., (1999); B-segments from Wissler et al. (2003); Ap-segments from Bottini et al., 2015; B: Campos/Santos carbonate carbon-isotope and TOC composite curve displayed in relative thicknesses based on Petrobras Wells CP-5 (red circles) and X (grey circles). Note the break in the *y*-axis to include up to 2km of evaporites, as estimated by Davison et al. (2012). TOC values higher than 2% are omitted in this diagram (four samples from Petrobras Well CP-5). C: Petrobras Well D: lithostratigraphic units, pollen zones, lithology (see description in Fig. 5.3), carbon-isotope data (black – data obtained at UERJ, red – data obtained at Open University). All profile suggested to be Aptian in age. Green, blue, purple and yellow bands and grey dashed lines show suggested correlation between A, B and C. S. -Stages – sub-stages; mbsl – metres below sea level; For. –Foraminiferal; *H.s – Hedbergella similis, G.b – Globigerinelloides blowi, L.c – Leupoldina cabri, G.f – Globigerinelloides ferreolensis, G.a – Globigerinelloides algerianus, H.t – Hedbergella trocoidea, P.r – Paraticinella rohri, M.m – Microhedbergella miniglobularis; T.p – Ticinella primula*. Inf. – Inferred, Barr – Barremian, U. Ap – Upper Aptian, Al –Albian.

The carbon-isotope correlation agrees with the inferred Aptian age for the *Sergipea veriverrucata* and the *Complicatisaccus cearensis* pollen Zones (Figure 5.4) (Regali and Viana, 1989; Carvalho et al., 2016). The top of the *Tucanopollis crisopolensis* pollen zone has traditionally been used to define the boundary between the Early and Late Aptian in northern Brazilian basins (Regali and Viana, 1989; Fig. 4). However, the studied section has shown that the C7/Ap7 segment which usually is associated to the boundary between the Early and the Late Aptian, is within the *Sergipea veriverrucata* pollen zone (e. g., Bottini et al., 2015; Herrle et al., 2015). Therefore, the base of the *Sergipea veriverrucata* pollen Zone is older than the Late Aptian and the top of *Tucanopollis crisopolensis* pollen zone are likely to be older than the Aptian in contrast with previous works (Regali and Viana, 1989; Carvalho et al., 2016).

The HI curve shows two stratigraphic interval with characteristic values: the basal one extends from the base of the analysed section up to 263.63 m with HI values that are generally higher than 200 mg HC/g TOC. The overlying interval has HI values generally lower than 200 mg HC/g TOC (Figure 5.3). The lower interval is correlated to the record of OAE 1a, where a higher detrital organic matter content is expected because of the presence of coarse clastic facies. Therefore, higher HI values could reflect the presence of cuticles, spores, bacterial anaerobic transformation of tracheids (phytoclasts), and/or autochthonous amorphous organic matter as found in Upanema Members and Ponta do Tubarão Beds in Potiguar Basin, northeast Brazil, as pointed out by Spigolon (2003).

The OI values can be divided in three levels: a basal one up to 325.20 m with variable values, that can reach up to 383 mg CO_2/g TOC; and intermediate one (325.20–167.74 m) with relatively constant OI values below 100 mg CO_2/g TOC;

and the upper interval (167.74–77.80 m) where OI values are variable and can reach up to 312 mg CO_2/g TOC. The basal and upper stratigraphic levels show a relatively higher content of oxidized organic matter, probably reflecting higher input of terrestrial organic matter. The basal level correlates to the interval represented by C2/Ap2–C4/Ap4 segments and upper interval is younger than the uppermost part of C8/Ap8–Ap10 segments.

5.4.3 Correlation of the evaporites

Unusual deposits of evaporites are present in the Sergipe-Alagoas Basin above the conglomerates and shales of the Muribeca Formation (Wardlaw, 1972). Br in halite and Br and Rb in carnallite indicate that these evaporites were crystallized from marine brines (Wardlaw, 1972) and, thus, could record marine incursions into the Sergipe-Alagoas Basin. The limited record of the carbon-isotope record from just Petrobras Well D does not permit to define whether lithologies from Carmópolis and Ibura Members present in Petrobras Well D are equivalent in time to evaporites from Ibura Member present elsewhere in the basin, although both occur within the *Sergipea variverrucata* pollen Zone (Uesugui, 1987).

The Ibura Member recorded in Petrobras Well D is Aptian in age and the carbon-isotope stratigraphy presented here suggests that this lithological unit were deposited within the interval represented by the C5/Ap5–C8/Ap8 segments. The deposition of the evaporites in the southern Brazilian basins likely occurred during the C4 to C6 segments. If evaporites present elsewhere in the Sergipe-Alagoas Basin are equivalent in time to the Ibura Member present in the Petrobras Well D, they may have overlapped in time with deposition of the evaporites in the southern Brazilian basins or may have post-dated deposition in the south (Figure 5.6). Simultaneous

deposition of evaporites in the north and south would suggest the presence of seawater over 20˚ of latitude. Synchronous deposition would suggest a highly anomalous climate state in order to permit evaporation across a 20˚ low latitudinal belt (Chaboureau et al. 2012). Indeed, climate models suggest that there was a humid climate in the area of Sergipe-Alagoas Basin when the southern Brazilian basins were under semi-arid/arid climate. Diachronous deposition of salt between the south and north is easier to reconcile if the entrance of the seawater occurred from the south towards the north in the CSSA. The deposition of large volumes of sulphate minerals in the southern Brazilian basins in the Aptian likely lowered the concentration of sulphate in global seawater. Thus, diachronous deposition of salt from south to north would also account for the low sulphate concentrations observed in the evaporites of the northern basins.

The stratigraphic position of the Ibura Member is important not only for the understanding of the entrance of the seawater in the CSSA, but also to comprehend the chemical composition of global seawater in the Aptian. Fluid inclusions and calcium isotopes from evaporite deposits of the Ibura Member have been widely used to corroborate the contention that Cretaceous seawater was Ca-rich and sulphate-poor, in contrast to modern seawater (Timofeeff et al., 2006; Blättler and Higgins, 2014; Lowenstein et al., 2014). Here the ages of these deposits are more closely determined for the first time.

5.5 Conclusions

A new record of OAE 1a based on $\delta^{13}C$ derived from organic matter in the Sergipe-Alagoas Basin, northeast Brazil is presented. The deposition of coarse clastic rocks from the Carmópolis Member and shales at the base of the Ibura Member are

the lithological expression of OAE 1a in Petrobras Well D in the Sergipe-Alagoas Basin, in the northern part of the central segment of the South Atlantic. Organic matter deposited during OAE 1a has relatively higher HI values than sediments deposited above this this interval. It is suggested that these lithologies were deposited synchronously with evaporite formation in the southern Brazilian basins. However, this study is unable to define whether or not the thick evaporites from the southern basins of the CSSA were deposited synchronously with, or before, the thinner evaporite deposits of the Ibura Member.

Chapter 6

New stratigraphy of DSDP Site 511, Falkland Plateau: Aptian–Albian OAEs and changes in ocean circulation in the South Atlantic

This chapter is co-authored by Leonardo R. Tedeschi, Hugh C. Jenkyns, Stuart A. Robinson, Alex Dickson, Cinzia Bottini, Elisabetta Erba, Ricardo I. F. Trindade, Janine A. Carmo and Robert A. Creaser. Leonardo R. Tedeschi is the lead author who has written the majority of the chapter, with comments from the majority of co-authors, and performed all geochemical analyses. Dr Cinzia Bottini and Elisabetta Erba undertook nannofossil calcareous analyses. Janine A. Carmo and Dr Ricardo I. F. Trindade performed magnetostratigraphic analyses and Dr Robert A. Creaser undertook Re-Os analyses.

6.1 Introduction

The opening of the South Atlantic started in the Falkland segment in the Jurassic and continued through the Early Cretaceous, when the final break-up of the central segment of the South Atlantic took place in the Aptian–Albian interval (Torsvik et al., 2009; Moulin et al., 2010). Another important feature of the Early Cretaceous was the presence of mid- to deep-waters characterized by enhanced production and preservation of organic matter worldwide, the so-called oceanic anoxic events (OAEs), of which the Early Aptian OAE 1a and the Aptian–Albian OAE 1b cluster are important examples (Schlanger and Jenkyns, 1976; Leckie et al.,

2002; Jenkyns, 2010). These important OAEs are recorded not only by organic rich-sediments but also by typical carbon-isotope signatures in carbonates and marine and terrestrial organic matter (Menegatti et al., 1998; Gröcke et al., 1999; Herrle et al., 2004; Trabucho Alexandre et al., 2011; Bottini et al., 2015; Erba et al., 2015).

Jurassic and Lower Cretaceous palaeoclimate records from the high-latitude South Hemisphere are limited, one exception being the Deep Sea Drilling Program (DSDP) Site 511 from the Falkland Plateau in the South Atlantic (Figure 6.1). DSDP Site 511 shows a well-defined trend in organic matter content from its base towards the top (Deroo et al., 1983; Ludwig et al., 1983) (Figure 6.2): 1) basal levels comprise organic-rich black mudstone and nannofossil mudstone (black shales) from the bottom of the cored interval up to 513.75 metres below sea floor (mbsf), with the highest total organic carbon (TOC) values, generally in the range of 2–6 wt %, and hydrogen indexes (HI) usually between 200 and 600 mg HC/ g TOC, and the lowest oxygen indexes (OI) usually lower than <100 mg CO_2/g TOC; 2) a ~20 m stratigraphic level in the interval 513.57–494.04 mbsf that includes organic-rich black shales and greenish grey muddy nannofossil chalks lying stratigraphically above the basal organic rich-sediments, where organic carbon content is minor, with lower TOC values (usually <1 wt %) and HI (0–100 mg HC/ g TOC and higher OI (usually >100 mg CO_2/ g TOC) and; 3) an upper part above 493.95 mbsf made up of reddish-brown and grey to greenish grey claystones and muddy nannofossil chalks with low TOC values (<0.5 wt %). This stratigraphic pattern can be recognized in the core pictures (Figure 6.2) and has been recorded not only in DSDP Site 511, but also in DSDP Sites 327A and 330 in the Falkland Plateau, where suggestions have been made that ‘barriers broke’ allowing the entrance of oxygenated waters into the Falkland Plateau area. The influx of marine waters is suggested to have taken place

when the deposition of the intermediate stratigraphic level occurred (Early Aptian–Early Albian), separating the basal levels interpreted as deposited in a reducing environment (Jurassic–Early Aptian) from the upper part deposited after the Early Albian interpreted as deposited in an oxidizing environment (Deroo et al., 1983). In addition, a stratigraphic compilation of organic-rich sediments present in the South Atlantic led Zimmerman et al. (1987) to propose that their formation was a consequence of watermass restriction during the separation of Africa from South America, whereas subsequent decrease in organic matter would primarily have been a consequence of the tectonic evolution of the South Atlantic, whose opening promoted a decrease in its preservation of organic matter in the Falkland Plateau areas throughout the Early Cretaceous.

However, a stratigraphic compilation of Lower Cretaceous sediments worldwide, including calcareous nannofossil data from DSDP Site 511, suggested that most of the organic-rich sediments on the Falkland Plateau were deposited during intermittent oceanic dysoxia–anoxia in the Late Barremian–Early Aptian interval (Wise et al., 1983; Mutterlose, 1989; Bralower et al., 1994). Subsequently, the interval 513–540 mbsf from DSDP Site 511 (Figure 6.2) was interpreted as a record of part of the OAE 1a interval, based not only on biostratigraphic evidence, but also on organic-carbon isotopes ($\delta^{13}C_{org} < -30‰$) and relatively high TOC values (Jenkyns et al., 2012). Hence, organic-rich sediments cored at DSDP Site 511 could have recorded global dysoxia/anoxia rather than changes in basinal geometry during the opening of the South Atlantic.

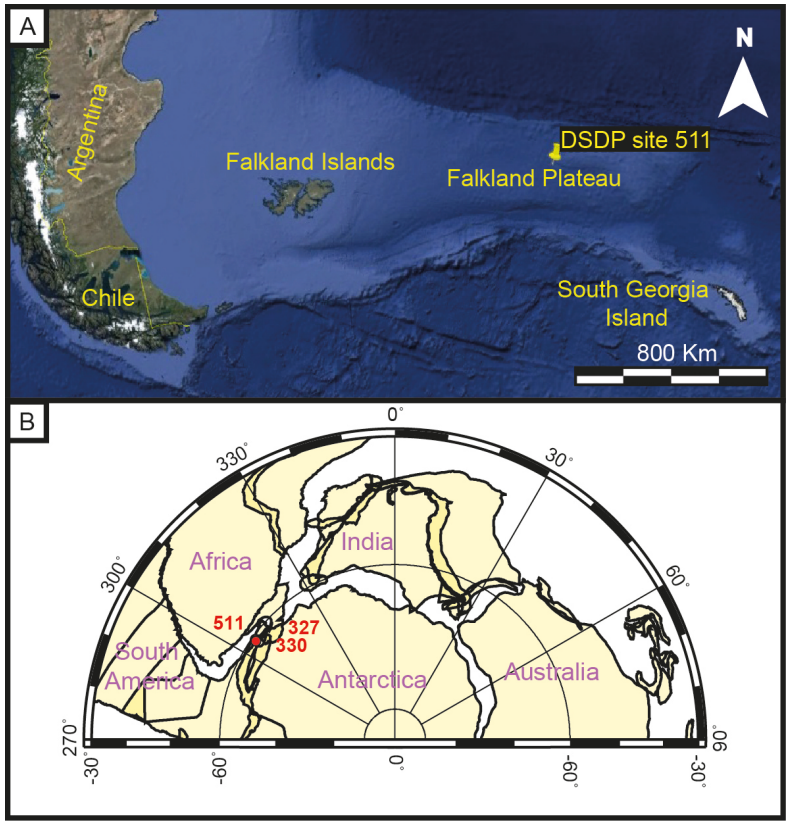
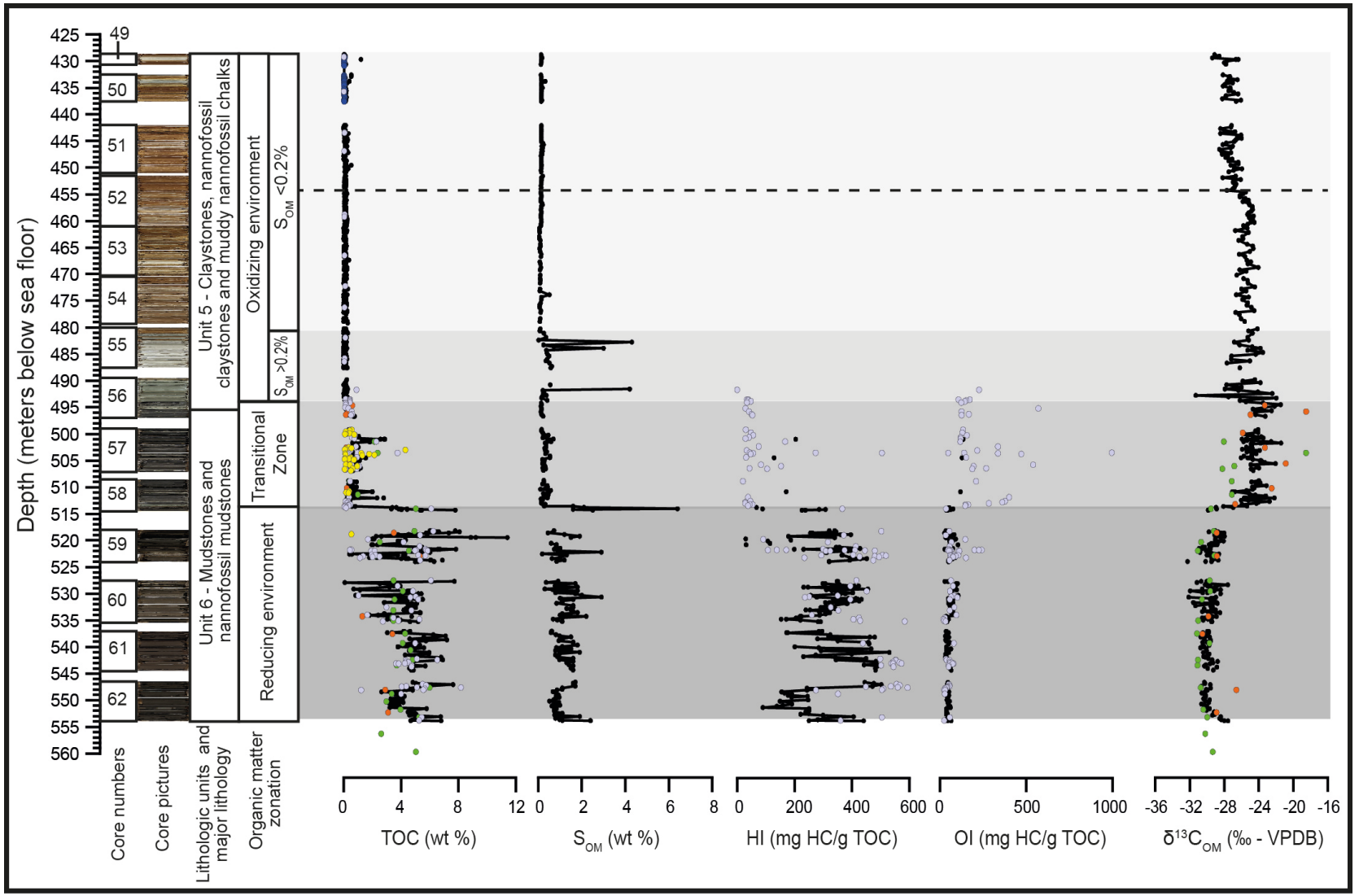


Figure 6 .1 –Location map of the DSDP Site 511 (51°00.28'S, 46°58.30'W) on the Falkland Plateau (Wise, 1983) (A). Image adapted from Google Earth® available on 06/June/2016. Palaeogeographic reconstruction at 130Ma (B). DSDP Sites 327A, 330 and 511 are shown in red. Name of plates in purple (generated from the GEOMAR website http://www.odsn.de/odsn/services/paleomap/paleomap.html, Kiel, Germany).

Figure 6 .2 –High-resolution organic parameters from DSDP Site 511: total organic carbon (TOC), total organic sulfur (S_{OM}), hydrogen and oxygen indexes (HI and OI) and carbon-isotope from organic matter ($\delta^{13}C_{OM}$). Numbers and pictures of the cores, lithological units and major lithology after Ludwig et al. (1983) and Deroo et al. (1983) and organic matter zonation defined by Deroo et al. (1983) and this study. Black data – this study; purple data – Deroo et al. (1983); yellow data – Parker et al. (1983); green data – Dias (1998); blue data – Azevedo (2001); orange data – Jenkyns et al. (2012). Grey bands show organic matter zonation based on all analysed parameters.


Depth (meters below sea floor)
425
430
435
440
445
450
455
460
465
470
475
480
485
490
495
500
505
510
515
520
525
530
535
540
545
550
555
560
49
50
51
52
53
54
55
56
57
58
59
60
61
62
Unit 5 - Claystones, nannofossil claystones and muddy nannofossil chalks
Unit 6 - Mudstones and nannofossil mudstones
Oxidizing environment
S_OM <0.2%
S_OM >0.2%
Transitional Zone
Reducing environment
Core numbers
Core pictures
Lithologic units and major lithology
Organic matter zonation
0 4 8 12
TOC (wt %)
0 2 4 6 8
S_OM (wt %)
0 200 400 600
HI (mg HC/g TOC)
0 500 1000
OI (mg HC/g TOC)
-36 -32 -28 -24 -20 -16
δ13C_OM (‰ - VPDB)

The main aim of this study is to revaluate the stratigraphic framework for the Lower Cretaceous sediments deposited at DSDP Site 511, in order to test whether the timing of organic-matter deposition bears any relation to global oceanic anoxic events, or whether more regional restriction imposed by tectonic configuration exerted a dominant control on organic-matter burial at this time. The interval 560–429 mbsf (cores 49 to 62) was studied, with emphasis on the sediments between 524 and 509 mbsf (cores 58 and 59) (Figure 6.2). Stratigraphic data derive from high-resolution nannofossil zonation, magnetostratigraphy, total inorganic and organic-carbon, Rock-Eval pyrolysis, sulphur content of organic matter, carbon- and oxygen-isotope ratios of carbonate and organic-matter and Re-Os isotope analyses. In addition, planktonic foraminiferal and strontium-isotope ($^{87}Sr/^{86}Sr$) data already published were used to characterize further the record obtained in this work (Bralower et al., 1997; Price and Gröcke, 2002; Huber and Leckie, 2011).

6.2 Description of the site

Site 511 was drilled during the Deep Sea Drilling Project (DSDP) Leg 71 at the eastern end of Falkland Plateau between January 15th and 21th, 1980 (Ludwig et al., 1983). The site is at Latitude 51°00.28'S and Longitude 46°58.30'W (Figure 6.1) and was drilled in 2589 metres water depth. The section was drilled to a depth of 632m, of which 385.62 metres were recovered (61% recovery). The section was divided into lithological units 1 to 6 from the top to the bottom (Ludwig et al., 1983). The studied interval consist of the uppermost part of Unit 6 (56 m) and the lowermost part of Unit 5 (63 m), where the limit between units is at the base of core 56 at 495.80 mbsf (Figure 6.2) (Deroo et al., 1983; Ludwig et al., 1983). All of Unit 6 is represented by ~134 metres of organic-rich mudstone and calcareous nannofossil

mudstone (black shales) of Callovian–Oxfordian (Late Jurassic) to earliest Albian age, whereas Unit 5 consists of ~80 metres of claystone, nannofossil claystone and nannofossil chalk pertaining to the Early Albian–Turonian (Ludwig et al., 1983).

6.3 Methods

6.3.1 Total inorganic and organic-carbon (TIC, TOC), organic sulphur (S_{OM}) and pyrolysis

TIC and TOC analyses and pyrolysis from samples in the interval 554–429 mbsf were obtained by using the Coulomat and Rock-Eval 6 at the University of Oxford (UO), the LECO at Universidade do Estado do Rio de Janeiro (UERJ) and Rock-Eval 6 at the Research Centre of Petrobras (CENPES). All powders were obtained by using agate pestle and mortar at UO, which were also used for carbon- and oxygen-isotope analyses. Total carbon (TC) and total inorganic carbon (TIC) were analysed by using a Ströhlein Coulomat 702 (manufactured by Firma Ströhlein Gmbh, Kaarst, Germany). The Coulomat method used consists of weighing each sample in pairs. One sub-sample (~60–120mg) is put into a furnace at 420°C overnight in order to eliminate organic carbon and measure TIC, while the other (~30–60mg) is reserved for measurement of TC. Each sub-sample of the pair is introduced to the system, which consists of a high-temperature furnace (1350°C) in an oxygen stream attached to a titration cell in closed system. The CO_2 released by total breakdown of the sub-samples in the furnace is measured by the change of pH in the titration cell, which results from the dissolution of the CO_2. Then, a simple stoichiometric computation enables calculation of the weight percentage (% wt) of carbon in the sample. The sub-samples are analysed in sequence, TOC being the

difference between TC and TIC. A total of 248 samples were analysed in pairs in the Coulomat and have both TIC and TOC values, whereas 94 samples were analysed after being roasted and have just TIC values. TIC values are reported as wt %. The internal and external reproducibility of TOC and TIC values were accessed using the in-house SAB134 standard and the IFP 160000 standard that were used to monitor Rock-Eval analyses throughout this thesis (Chapters 3, 4, 5 and this Chapter). The in-house SAB 134 standard gave TOC and TIC average and standard deviation (± 1σ) of 2.94 ± 0.07 wt % and 6.05 ± 0.07 wt % (n = 59), respectively. The IFP 160000 standard gave average and standard deviation (± 1σ) of 3.39 ± 0.06 wt % (n = 59) and 3.16 ± 0.06 wt % (n = 10), respectively. Reported TOC and TIC values of IFP 160000 by Vinci Technologies® are 3.28 ± 0.14 wt % and 3.26 ± 0.12 wt %, respectively.

Differences between replicate samples were lower than 0.20 wt % (n =22) and 0.13 wt % (n = 18) for TIC and TOC values, respectively. TIC values can be converted to $CaCO_3$ assuming that all inorganic carbon is combined with Ca by multiplying by a factor of 8.33, where TIC = 12 wt % is equivalent to 100 wt % $CaCO_3$. The respective values of wt % $CaCO_3$ is given in the results and discussion sections.

A total of 326 samples were analysed by using the LECO® CS 632 at UERJ. The method consists in weighing each sample (~35–40mg) in porous ceramic boats, which are submerged in 50 % volume HCl at room temperature for 24hs. The acid ascends through capillarity and reacts with the sample, in order to remove the carbonate fraction. After drying, samples are weighed again. The difference between the weights before and after acid leaching is the insoluble residue (IR). Following this procedure, each sample is introduced to the LECO® device for combustion of

residual organic matter at temperatures that can reach up to 1550°C. The carbon and sulphur (S) liberated during combustion is analysed in an infrared cell and reported in wt %. Sulfur content is here reported as present in organic matter (S_{OM}). However, sulphides and sulphates that were not dissolved and/or leached during submersion in the 50% volume HCl could be a fraction of the sulphur content analysed. The standard LECO-COT reference standard 502-308 Lot number 1016 gave TOC average and standard deviation (± σ) of 2.38 ± 0.14 wt % (n = 13), whereas reported values are 2.35 ± 0.07 wt % (Lawrenz, 2012). An in-house standard of Permian organic-rich shale from São Matheus do Sul Mine, southern Brazil gave TOC average and standard deviation (± 1σ) of 4.01 ± 0.24 wt % and S content of 0.19 ± 0.06 wt %. The differences of replicate samples were lower than 0.19 wt % (n =11) and 0.06 wt % (n = 11) for TOC and S values, respectively.

Fifty samples and 114 samples were analysed in a Rock-Eval 6 at UO and CENPES, respectively. The Rock-Eval 6 method used at UO is described in section 5.3 in Chapter 5, where the sample is analysed in programed heating in two different micro-ovens in an inert atmosphere at UO (pyrolysis and oxidation ovens, Standard Rock-Eval 6), whereas just one micro-oven was used at CENPES (pyrolysis oven, Classic Rock-Eval 6) (Behar et al., 2001). Hence, the Classic Rock-Eval 6 at CENPES lacks a oxidation oven where the programed heating reaches up to 850°C and analyses in an infrared cell the quantity (mg) of CO and/or CO_2 released by residual organic matter and/or carbonates present in the sample, which permits analysis of the parameters S4CO, S4CO_2 and S5. These parameters obtained at OU allow determination of TOC, TIC, hydrogen index (HI) and oxygen index (OI). Internal and external reproducibility of all parameters obtained in the Standard Rock-

Eval 6 during this thesis is reported in the section 3.3.1.4 in Chapter 3 and section 5.3 in Chapter 5.

The parameters S1 and S2 are reported in milligrams of hydrocarbons per gram of rock (mg HC/g rock) and the parameter S3 in milligrams of CO_2 per gram of rock (mg CO_2/g rock). Although the parameter S1 has been measured, which is the amount of free HCs in the sample, these data are not used in this study. The HI is the ratio between S2 and TOC (reported in mg HC/ g TOC), where HI was calculated by using S2 values from CENPES and TOC values from UERJ, whereas HI values derived from the Rock-Eval 6 at OU were calculated automatically using S2 and TOC. Similarly, OI is the ratio between S3 and TOC (reported in mg CO_2/ g TOC), by using the same sources of data as indicated for HI. The analyses of fourteen aliquots of the IFP 160000 standard at CENPES gave average and standard deviation (± σ) of S1, S2, S3 and Tmax parameters of 0.13 ± 0.01 mg HC/g rock, 12.40 ± 0.30 mg HC/g rock, 0.78 ± 0.10 mg CO_2/g rock and 416 ± 1°C, respectively. Reported values of IFP 160000 by Vinci Technologies® for S1, S2, S3 and Tmax parameters are 0.14 ± 0.07 mg HC/g rock, 12.43 ± 0.50 mg HC/g rock, 0.79 ± 0.20 mg CO_2/g rock and 416 ± 2°C, respectively. In addition, replicate samples analysed at CENPES and UO were generally lower than 1.00 mg HC/g rock for the S2 parameter (39 out of 44 samples) and 0.60 mg CO_2/g rock for the S3 parameter where values were usually less than 2.5 mg CO_2/g rock (40 out of 44 samples). Therefore, good inter-laboratory reproducibility has been achieved.

6.3.2 Carbon and oxygen isotopes from carbonates ($\delta^{13}C_{carb}$ and $\delta^{18}O_{carb}$)

253 samples from the interval 554–429 mbsf were analysed for carbon and oxygen isotopes ($\delta^{13}C$ and $\delta^{18}O$) on bulk rock at UERJ. A Kiel IV carbonate device coupled to Thermo Delta V Advantage mass spectrometer was used to perform analyses. Samples were reacted with purified phosphoric acid (H_3PO_4) at 90°C and the gas was analysed online. Data are reported in parts per thousand (‰) relative to the Vienna Pee Dee Belemnite (VPDB) standard. The reproducibility of the IAEA CO-1 standard has given an average and standard deviation (± σ) of 2.48 ± 0.05‰ for $\delta^{13}C$ and $\delta^{18}O$ = –2.46 ± 0.10‰ ‰, for $\delta^{18}O$ (n = 53) during the analyses of samples from DSDP Site 511. The IAEA CO-1 standard has reported values of $\delta^{13}C$ = 2.492 ± 0.030 ‰ and of $\delta^{18}O$ = –2.437 ± 0.073 ‰ (Stichler, 1995; Coplen et al., 2006).

6.3.3 Carbon isotopes from organic matter ($\delta^{13}C_{OM}$)

121 samples from the interval 554–501 mbsf with TOC higher than 1 wt % were analysed for carbon isotopes from organic matter at UERJ and 274 samples from the interval 540–429 mbsf were analysed at the Open University (Milton Keynes, UK), after acidification at UO. Data are reported in parts per thousand (‰) relative to the Vienna Pee Dee Belemnite (VPDB) scale. Procedures and standards used to monitor internal and external reproducibility are detailed in section 5.3 in Chapter 5.

6.3.4 Calcareous nannofossil biostratigraphy

A total of 132 samples were used to investigate the nannofossil biostratigraphy of DSDP Site 511 in the interval 560–490 mbsf. Calcareous nannofossils were investigated in standard smear slides, with a polarizing light microscope (cross-polarized, transmitted light and quartz lamina), at 1250× magnification.

6.3.5 Magnetostratigraphy

Magnetic susceptibility (χ) and natural remanent magnetization (NRM) were determined from 41 samples from the interval 509–524 mbsf (cores 58 and 59) in the Palaeomagnetic Laboratory of the University of São Paulo, Brazil. Each sample was plastic film covered and weighed. Measurements of magnetic susceptibility (χ) were made on an MFK1-FA Multi-Function Kappabridge (Savian et al., 2016) at 976 Hz in a field of 200 A/m. All data were normalized by mass and are expressed as m^3/kg. NRM measurements were obtained by applying alternating field (AF) demagnetization over 16 steps (2, 4, 7, 10, 15, 20, 25, 30, 35, 40, 50, 60, 70, 80, 90, 100 mT), where a u-channel pass-through 2G-Enterprises model 755 SQUID magnetometer was used. Interpretation of vector end-point demagnetization (Zijderveld, 1967) and magnetic components based on principal component analyses were calculated to define all components of NRM directions.

6.3.6 Re-Os isotope analyses

Two sets of 9 samples from the intervals 513.61–514.06 m (section 4, core 58) and 519.01–519.40 m (section 1, core 59) were sent to the University of Alberta

for Re-Os analysis. Powdering was performed using an agate mill. A total of 18 analyses were performed using the Carius tube dissolution method, followed by solvent extraction, ion exchange and Negative Thermal Ion Mass Spectrometry at the University of Alberta (Selby and Creaser, 2003). For all samples, Os was analysed using an Electron Multiplier detector, and Re was analysed using a Faraday collector by negative Thermal Ion Mass Spectrometry. During these analyses, determinations of in-house Os and Re standards were carried out to ensure accuracy and all results were within normal tolerance levels. All isochron regressions were calculated using the program *Isoplot* and all uncertainties are quoted at the 2σ level. Any ages referred to here use the value of 1.666×10^{-11} y^{-1} for the decay constant of ^{187}Re (Smoliar et al., 1996). All analytical procedures are the same described in section 3.3.2.5 in Chapter 3.

6.4 Results

6.4.1 Organic geochemistry (TOC, S_{OM}, HI, OI, Tmax and $\delta^{13}C_{OM}$)

New high-resolution TOC, HI, OI, S and $\delta^{13}C_{OM}$ logs can be split into four distinct intervals (Figure 6.2; Tables 1–3 in Appendix D): 1) 553.87–513.61 mbsf; 2) 513.54–494.22 mbsf; 3) 493.71–481.09 mbsf and; 4) 480.67–428.81 mbsf. The basal interval (553.87–513.61 mbsf) comprises organic-rich black mudstone and nannofossil mudstone with the highest TOC and S_{OM} values of all studied interval (553.87– 428.81 mbsf). TOC values are generally between 2.0 and 7.0 wt %, with one sample reaching up to 9.0–11.0 wt %. The S_{OM} content is generally between 0.6 and 2.0 wt %, with one sample attaining a value of 6.4 wt %. This interval is also

characterized by the highest HI values, generally between 200 and 500 mg HC/g TOC, and low OI values (usually < 100 mg CO_2/g TOC). The $\delta^{13}C_{OM}$ values of this interval are the lowest of the analysed section, mostly lying between –32 and –28‰.

The interval 513.54–494.22 mbsf has intermediated TOC and S_{OM} values. TOC values are usually between 0.3 and 2.0 wt % and S_{OM} values are usually in the range of 0.15–0.60 wt %. HI and OI were obtained in just three samples, because the other samples analysed at the Rock-Eval did not yield HCs, CO and CO_2 above the detection limit during pyrolysis. The results are 171, 128, and 204 mg HC/g TOC, and 118, 127 and 134 mg CO_2/g TOC for samples at 510.85, 504.47 and 500.99 mbsf, respectively. This interval shows the highest $\delta^{13}C_{OM}$ values (generally > –25‰).

The interval 493.97–428.81 mbsf has TOC values usually lower than 0.3 wt %, with eight samples that have TOC values between 0.30 and 0.54 wt % and another sample with a TOC value of 1.21 wt % at 429.69 mbsf. This interval was divided in two, based on S_{OM} values: a basal unit (493.71–481.09 mbsf), where S_{OM} values usually exceed 0.20 wt % with a few samples with values higher than 3.0 wt %; and an upper unit (480.67–428.81 mbsf), where S_{OM} values usually are less than 0.20 wt %. Because of these low TOC values, determinations of HI and OI values were not reliable. This upper interval has intermediate $\delta^{13}C_{OM}$ values usually between –28 and –24‰. A marked shift from –25‰ to –27‰ occurs at ~454.5 mbsf, such that $\delta^{13}C_{OM}$ values are generally lower than –26‰ above this level and higher than –26‰ below this level (dashed line in Figure 6.2).

All Tmax values are lower than 433°C, which suggest that all analysed section is immature (Table 6.2 in Appendix D), as indicated by the organic geochemistry and the fact that TEX_{86} values can be readily determined (Jenkyns et

al., 2012). Our TOC, HI, OI and Tmax values are similar to those published by Deroo et al. (1983), Parker et al. (1983), Dias (1998), Azevedo (2001) and Jenkyns et al. (2012) (Figure 6.2). Because original data are present in Brazilian theses, Tables 6.4 and 6.5 in Appendix D show compilations from Dias (1998) and Azevedo (2001), respectively. Two boundaries of the four intervals described correspond roughly to those defined in terms of organic- matter zonation described by Deroo et al. (1983): their limit between sediments of the so-called reducing environment and transitional zone was fixed at 513.76–513.58 mbsf, whereas our profiles tighten this interval to 513.61–513.54 mbsf; similarly the limit between the sediments of the transitional zone and the oxidizing environment was defined at 494.04– 493.95 mbsf, whereas it is defined here at 494.22–493.97 mbsf (Figure 6.2). The low-resolution $\delta^{13}C_{OM}$ profiles from Dias (1998) and Jenkyns et al. (2012) illustrate relatively low $\delta^{13}C_{OM}$ values between –32 and –28‰ below 514.05 mbsf, which are in the same range obtained in the interval 553.87–513.61 mbsf in this study. Dias (1998) and Jenkyns et al. (2012) described a irregular positive excursion on $\delta^{13}C_{OM}$ values in the interval 514.05–494.65 mbsf, where the profiles reach up to –18.5‰, which are in agreement with the broad positive excursion on $\delta^{13}C_{OM}$, characterized by values > –25‰ obtained from the interval 513.54–494.22 mbsf in this study. However, the maximum $\delta^{13}C_{OM}$ value obtained in this study is –21.4‰, which is lower than –18.5‰ reported by Dias (1998) and Jenkyns et al. (2012) (Figure 6.2).

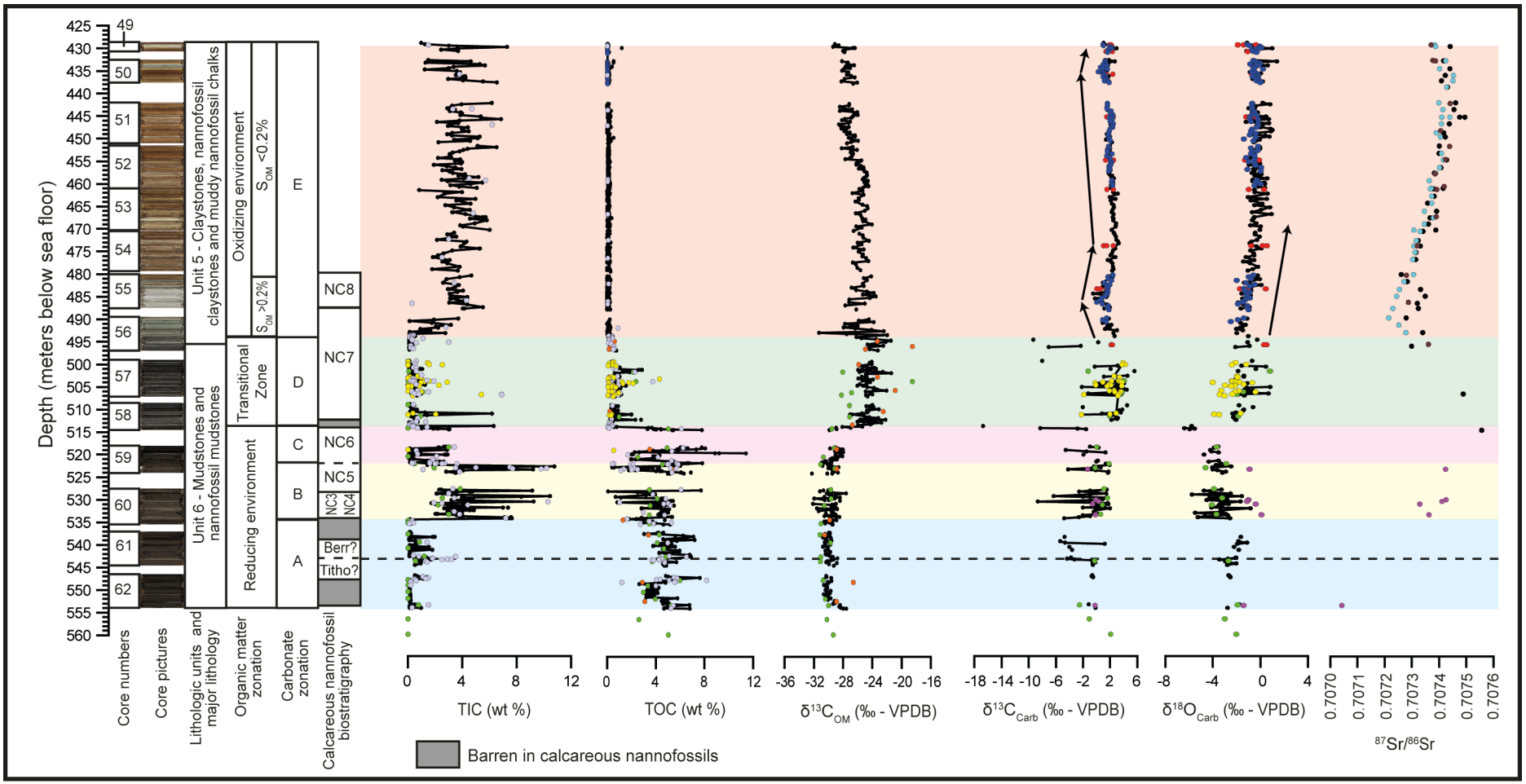
6.4.2 Carbonates (TIC, $\delta^{13}C_{carb}$ and $\delta^{18}O_{carb}$)

The TIC profile shows that the carbonate content defines five stratigraphic levels (carbonate zonation), named A to E from the base towards the top (Figure 6.3; Table 6.6 in Appendix D). Three basal stratigraphic levels A to C are correlated to

the basal organic-rich level at 553.87–513.61 mbsf. The intermediate level B from 534.04 to 522.56 mbsf generally has TIC values of 2–7 wt % (17–58 wt % $CaCO_3$) (yellow band in Figure 6.3). It is relatively enriched in carbonate compared to the stratigraphic level A (583.57–534.28 mbsf), which is almost devoid of carbonate (TIC values < 2 wt % or < 17 wt % $CaCO_3$; blue band in Figure 6.3) and stratigraphic level C (522.23–513.61 mbsf), where TIC values are usually less than 4 wt % (< 34 wt % $CaCO_3$; pink band in Figure 6.3), but have some layers with higher carbonate content (TIC values as high as 10.8 wt %; 90 wt % $CaCO_3$). Higher in the section, stratigraphic level D (interval 513.57 to 493.97 mbsf) has almost no carbonate (TIC values usually < 1.0 wt %; < 8.33 wt % $CaCO_3$; green band in Figure 6.3) and is broadly correlated with the transition zone of organic-matter zonation (513.54–494.22 mbsf). Stratigraphic level D has just eight samples with TIC values higher than 1 wt % (8.33 wt % $CaCO_3$), six of which have less than 2.74 wt % (< 23 wt % $CaCO_3$) and one has 6.18 wt % (51 wt % $CaCO_3$). The upper stratigraphic level E (493.71–429.41 mbsf) has higher TIC values (2.0–7.3 wt %; 17–61 wt % $CaCO_3$), except for ten samples with values lower than 2.0 wt % (< 17 wt % $CaCO_3$; orange band in Figure 6.3). It correlates roughly with the upper stratigraphic level where low TOC values predominate. Our dataset shows the same range of values as obtained by Deroo et al. (1983), Parker et al. (1983) and Dias (1998) (Figure 6.3), except for the relatively higher TIC values reported within the stratigraphic level A at ~543 mbsf, where TIC values extend up to 3.2 wt % (27 wt % $CaCO_3$; Deroo et al., 1983), and some samples in stratigraphic level D with TIC values higher than 1.0 wt % (8.3 wt % $CaCO_3$) that can reach up to 6.9 wt % (57 wt % $CaCO_3$; Deroo et al., 1983) and 5.4 wt % (45 wt % $CaCO_3$; Parker et al., 1983).

$\delta^{13}C_{carb}$ values are usually between –2.0 and 5.6‰ in the stratigraphic levels A to D (below 494.04 mbsf), although extremely negative $\delta^{13}C_{carb}$ values as low as –16.7‰ occur locally (Figure 6.3; Table 6.7 in Appedix D). Similarly, most $\delta^{18}O_{carb}$ values lie between –3.0 and 1.0‰ below 494.04 mbsf, although negative $\delta^{18}O_{carb}$ values as low as –5.9‰ do occur (Figure 6.3; Table 6.7 in Appedix D). The $\delta^{13}C_{carb}$ and $\delta^{18}O_{carb}$ profiles show distinct trends from the base towards the top: 1) the interval 553.87–543.35 mbsf has ten samples with slightly negative $\delta^{13}C_{carb}$ values (between –1.2 and –0.2‰) and negative $\delta^{18}O_{carb}$ values (between –2.9 and –1.8‰). The top of this interval is marked by an abrupt shift towards more negative $\delta^{13}C_{carb}$ values (dashed line within the blue band in Figure 6.3); 2) the interval 543.14–534.04 mbsf is the stratigraphic level where the most consistent group of samples with relatively negative $\delta^{13}C_{carb}$ values occur (typically from –5.4 to –3.7‰). These data are likely to record diagenetic overprints on $\delta^{13}C_{carb}$ values. On the other hand, this stratigraphic interval has relatively higher $\delta^{18}O_{carb}$ values than the overlying stratigraphic level. Because most of the samples at the top of zone B did not have enough carbonate to allow carbon- and oxygen- isotope analyses, we defined the abrupt shift in $\delta^{13}C_{carb}$ profiles towards higher values and abrupt shift on $\delta^{18}O_{carb}$ values towards lower values at ~534.0–533.0 mbsf (boundary between blue and yellow bands in Figure 6.3); 3) the interval 533.06–513.61 mbsf shows a trend of decreasing $\delta^{13}C_{carb}$ and $\delta^{18}O_{carb}$ values from the bottom towards the top. Its top shows the lowest $\delta^{13}C_{carb}$ value (–16.7‰) and $\delta^{18}O_{carb}$ values (~ –6‰) of all analysed samples; and 4) the interval 512.22–494.50 mbsf has the highest $\delta^{13}C_{carb}$ values, with 27 samples lying between 2.0 and 5.6‰ and only 11 samples with $\delta^{13}C_{carb}$ values less than 2.0‰ (green band in Figure 6.3). The $\delta^{18}O_{carb}$ values lie between –2.3 and 0.0‰, with the exception of three values that are greater than 0.0‰. All $\delta^{13}C_{carb}$ data are

between –0.5 and 3.2‰ and all $\delta^{18}O_{carb}$ data are between –2.0 and 1.4‰ in the stratigraphic level E (above 493.71 mbsf). The $\delta^{13}C_{carb}$ profile shows two trends of decreasing values from the base towards the top in the intervals 493.71–484.30 mbsf and 472.80–435.30 mbsf, whereas the intervals 484.30–472.80 mbsf and 435.30–432.60 mbsf shows the trend of increasing $\delta^{13}C_{carb}$ values (see black arrows in Figure 6.3). The $\delta^{18}O_{carb}$ profile shows a trend of increasing values from 493.71 mbsf up to ~469 mbsf (see black arrow in Figure 6.3) and the interval from ~469 mbsf to the top of the analysed section is characterized by values mostly between –1.0 and 1.0 ‰ (Figure 6.3). Significantly, $\delta^{13}C_{carb}$ and $\delta^{18}O_{carb}$ values from foraminifera in the Aptian–Maastrichtian interval (195–495.63 mbsf) from DSDP Site 511 are usually between –1 and +4‰ and –4.0 and 0.0‰, respectively (Huber et al., 1995; Bice et al., 2003). The lowest $\delta^{13}C_{carb}$ values are from benthic foraminifera, where the lowest value is –1.81‰ at 412.14 mbsf from the Upper Turonian, whereas the lowest $\delta^{18}O_{carb}$ are from planktonic foraminifera, where the minimum is –4.66‰ from pristine examples from the Upper Turonian (Huber et al., 1995; Bice et al., 2003). This study overlaps with previous studies on foraminifera in the interval 428.81–495.63 mbsf and extends the record down to 553.87 mbsf, where data from belemnites from Price and Gröcke (2002) and bulk carbonate rock from Parker et al., (1983), Dias (1998), Azevedo (2001) and foraminifera from Huber et al. (1995) generally agrees with those obtained in this study. The only exception is that $\delta^{18}O_{carb}$ values of these molluscs are usually higher than those obtained from bulk rock in this study (Price and Gröcke, 2002), suggesting that these lighter $\delta^{18}O_{carb}$ values imply diagenetic overprint. However, $\delta^{13}C_{carb}$ values > –2.0‰ in the interval 543.14–534.04 mbsf are in the same range as observed in belemnites.


Depth (meters below sea floor)
425
430
435
440
445
450
455
460
465
470
475
480
485
490
495
500
505
510
515
520
525
530
535
540
545
550
555
560
49
50
51
52
53
54
55
56
57
58
59
60
61
62
Unit 5 - Claystones, nannofossil claystones and muddy nannofossil chalks
Unit 6 - Mudstones and nannofossil mudstones
Oxidizing environment
Transitional Zone
Reducing environment
S_{OM} >0.2%
S_{OM} <0.2%
E
D
C
B
A
NC8
NC7
NC6
NC5
NC3
NC4
Berr?
Titho?
Core numbers
Core pictures
Lithologic units and major lithology
Organic matter zonation
Carbonate zonation
Calcareous nannofossil biostratigraphy
0 4 8 12
TIC (wt %)
0 4 8 12
TOC (wt %)
-36 -32 -28 -24 -20 -16
$\delta^{13}C_{OM}$ (‰ - VPDB)
-18 -14 -10 -6 -2 2 6
$\delta^{13}C_{Carb}$ (‰ - VPDB)
-8 -4 0 4
$\delta^{18}O_{Carb}$ (‰ - VPDB)
0.7070 0.7071 0.7072 0.7073 0.7074 0.7075 0.7076
$^{87}Sr/^{86}Sr$
Barren in calcareous nannofossils

It is worth mentioning that those samples that have low TIC values from stratigraphic levels A, C and D and high TOC values in stratigraphic levels A to D, $\delta^{13}C_{carb}$ and $\delta^{18}O_{carb}$ values are most likely to record the presence of carbonate cement formed during diagenesis (Hudson, 1977). However, $\delta^{13}C_{carb}$ and $\delta^{18}O_{carb}$ values do not show covariance, which suggests that $\delta^{13}C_{carb}$ values do not record a diagenetic overprint, because oxygen isotopes in marine carbonates are more prone to diagenetic alteration than carbon isotopes (Scholle and Arthur, 1980; Jenkyns et al., 1994. It is suggested that extremely negative $\delta^{13}C_{carb}$ values (< –6‰) in organic-rich sediments record an early diagenetic overprint that may in some circumstances be associated with negative $\delta^{18}O_{carb}$ values (Irwin et al., 1977; Raiswell, 1988; Sass et al., 1991; Raiswell and Fisher, 2000).

Figure 6 .3 –High-resolution carbonate parameters from DSDP Site 511: total inorganic and organic carbon (TIC and TOC), carbon isotope from organic matter ($\delta^{13}C_{OM}$), carbon and oxygen isotope from bulk carbonate ($\delta^{13}C_{carb}$ and $\delta^{18}O_{carb}$) and strontium-isotope ratios ($^{87}Sr/^{86}Sr$). Numbers and pictures of the cores, lithologic units and major lithology after Ludwig et al. (1983) and Deroo et al. (1983), organic matter zonation defined by Deroo et al. (1983) and this study, carbonate zonation and calcareous nannofossil biostratigraphy obtained in this study. Black data – this study (except $^{87}Sr/^{86}Sr$ ratios); light purple data – Deroo et al. (1983); yellow data – Parker et al. (1983); red data – Huber et al. (1995); green data – Dias (1998); dark blue data – Azevedo (2001); orange data – Jenkyns et al. (2012); light blue, black and brown data – $^{87}Sr/^{86}Sr$ ratios from inoceramids, foraminifera and other fossils, respectively (Bralower et al. 1997); dark blue data – $^{87}Sr/^{86}Sr$ ratios from belemnites from Price and Gröcke (2002). Blue, yellow, pink, green and orange bands show carbonate zonation, named A to E, based on TIC values. Arrows show the main trends in $\delta^{13}C_{carb}$ and $\delta^{18}O_{carb}$.

6.4.3 Calcareous Nannofossils

Preservation of nannofossils is moderate to good throughout the entire studied interval between 560 and 490 mbsf. A total of 61 barren samples out of 132 samples analysed were encountered. In particular, three intervals characterized by absence of nannofossils are identified: 1) between 547.73 and 553.65 mbsf; 2) between 538.85 and 534.28 mbsf and; 3) between 514.08 and 512.83 mbsf. The results are compared with previous nannofossil studies on DSDP Site 511 by Wise (1983), Mutterlose (1989) and Bralower et al. (1994), and a revised age assignment of the studied interval is provided (Figure 6.4).

Because a biozonation scheme for the Early Cretaceous of the high southern latitudes does not exist and some of the biostratigraphic markers commonly used for the Boreal Realm are not observed at DSDP Site 511, seven age-assigned intervals from the interval 560–480 mbsf are proposed (Figures 6.3 and 6.4). The basal interval (interval 560–542.98 mbsf) was probably deposited during the latest Jurassic, probably middle to Late Tithonian based on the presence of Late Jurassic species (e. g., *Biscutum dorsetensis*; *Ethmorhabdus gallicus*; *Axopodorhabdus cylindratus*) above and below a barren interval (547.73–553.65 mbsf). The lowest occurrence (LO) of *Cretarhabdus surirellus* at 544.02 mbsf is suggestive of a latest Tithonian age (following Casellato, 2010) and the LO of *Braarudosphaera regularis* indicates an early Late Tithonian age (Erba and Quadrio, 1987; Casellato, 2010). The LO of *B. regularis* was found above the LO of *C. surirellus*, at 543.14 mbsf, which is stratigraphically higher in the section than its presence reported in sample 62-3, 114-115 cm (ca. 550.50 mbsf) by Bralower et al. (1994). Samples analysed in this work just above and below sample 62-3, 114-115

cm (550.64 mbsf) are barren, as also found by Wise (1983).

The interval 542.73–534.28 mbsf can be ascribed to the Berriasian based on the LO of *Grantarhabdus meddii,* which appears in the lower part of the stage (Bown et al., 1998). The nannofossil assemblages also include *Crucibiscutum salebrosum* and *Conusphaera rothii*, which are species characteristic of the Lower Cretaceous. No marker species indicative of ages younger than Berriasian were found, which could in part be related to the presence of many barren samples. One peculiar feature of this interval is the presence of some Jurassic species (e. g., *B. dorsetensis; E. gallicus*), as observed by Wise (1983) and Bralower et al. (1994), who suggested that they are reworked specimens in a Lower Cretaceous assemblage. Following this interpretation, this interval is depicted as deposited during the Berriasian.

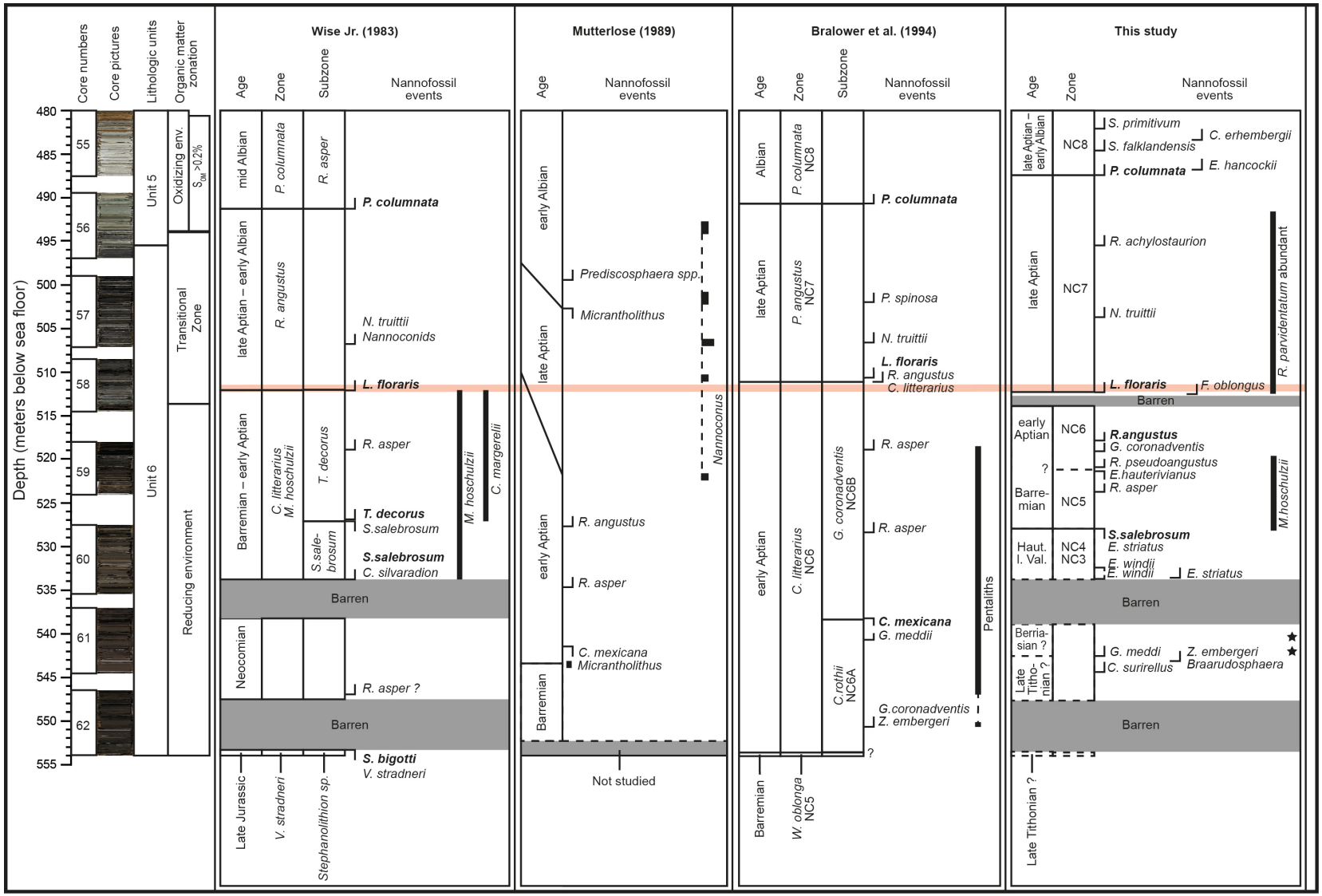
The interval 534.04–528.33 mbsf shows the LOs of *Eiffellithus windii* and *Eiffelithus striatus* at 534.04 mbsf, which indicates a Late Valanginian–Hauterivian age. The presence of *C. salebrosum* and *E. hauterivianus* are compatible with this age assignment (following Bown et al., 1998 and Jeremiah, 2001). Hence the interval was interpreted as deposited during the Late Valanginian–Hauterivian. The highest occurrences (HOs) of *C. salebrosum* and *E. striatus* at 528.33 mbsf are approximately associated with the Hauterivian–Barremian boundary (following Bown et al., 1998 and Jeremiah, 2001). Therefore, the interval 528.11–521.94 mbsf is interpreted as deposited during the Barremian**.**

The absence of cosmopolitan species does not permit definition of the Barremian–Aptian boundary. However, the interval 521.65–514.08 mbsf is close to this boundary as suggested by the HO of *E. hauterivianus* at 521.65 mbsf, followed by the LO of *Rhagodoscus angustus* and *Rucinolithus irregularis* (519.46 mbsf) and

Grantarhabdus coronadventis (518.39 mbsf), which are indicative of an Early Aptian age (following Bown et al., 1998; Jeremiah, 2001; Bischoff and Mutterlose, 1998). The interval 514.08–512.83 mbsf is barren in nannofossils.

The LO *E. floralis* (at 512.22 msbf) in core 58 is an unambiguous datum in the calcareous nannofossil biostratigraphy. It marks the base of Zone NC7 and occurs soon after the OAE 1a interval. This bioevent is cosmopolitan and dated as latest Early Aptian, and has been recorded at essentially the same stratigraphic level by previous studies of DSDP Site 511 (Figure 6.4). Because of the presence of the *N. truittii* acme (*sensu* Mutterlose, 1989) at 506.50 mbsf and abundant *Repagulum parvidentatum* above 512.22 msbf, the interval 512.22–487.50 mbsf is likely to be Late Aptian in age.

Figure 6 .4 –High-resolution nannofossil calcareous biostratigraphy: interpreted age assignment, zones, subzones and main calcareous nannofossil events. The same data from previous studies are shown for comparison (Wise, 1983; Mutterlose, 1989; Bralower et al., 1994). Numbers and pictures of the cores, lithologic units and major lithology after Ludwig et al. (1983) and Deroo et al. (1983), organic matter zonation defined by Deroo et al. (1983) and this study are also shown. Orange band shows the firm-point: LO *E. floralis* (at 512.22 msbf) in the core 58, which marks the base of Zone NC7. Stars – *C. rothii*.


Depth (meters below sea floor)
480
485
490
495
500
505
510
515
520
525
530
535
540
545
550
555
Core numbers
55
56
57
58
59
60
61
62
Core pictures
Lithologic units
Unit 5
Unit 6
Organic matter zonation
Oxidizing env. S_{OM} >0.2%
Transitional Zone
Reducing environment
Wise Jr. (1983)
Age
Zone
Subzone
Nannofossil events
mid Albian
late Aptian – early Albian
Barremian – early Aptian
Neocomian
P. columnata
R. angustus
C. litterarius
M. hoschulzii
T. decorus
S.sale-brosum
R. asper
P. columnata
N. truittii
Nannoconids
L. floraris
R. asper
T. decorus
S.salebrosum
S.salebrosum
C. silvaradion
M. hoschulzii
C. margerelii
Barren
R. asper ?
Barren
S. bigotti
V. stradneri
Late Jurassic
V. stradneri
Stephanolithion sp.
Mutterlose (1989)
Age
Nannofossil events
early Albian
late Aptian
early Aptian
Barremian
Prediscosphaera spp.
Micrantholithus
R. angustus
R. asper
C. mexicana
Micrantholithus
Nannoconus
Not studied
Bralower et al. (1994)
Age
Zone
Subzone
Nannofossil events
Albian
late Aptian
early Aptian
Barremian
P. columnata NC8
P. angustus NC7
C. litterarius NC6
W. oblonga NC5
G. coronadventis NC6B
C.rothii NC6A
P. columnata
P. spinosa
N. truittii
L. floraris
R. angustus
C. litterarius
R. asper
R. asper
C. mexicana
G. meddii
G.coronadventis
Z. embergeri
?
Pentaliths
This study
Age
Zone
Nannofossil events
late Aptian – early Albian
late Aptian
early Aptian
?
Barre-mian
Haut. l. Val.
Berria-sian ?
Late Titho-nian ?
NC8
NC7
NC6
NC5
NC4
NC3
S. primitivum
S. falklandensis
P. columnata
C. erhembergii
E. hancockii
R. achylostaurion
N. truittii
L. floraris
F. oblongus
R. parvidentatum abundant
Barren
R.angustus
G. coronadventis
R. pseudoangustus
E.hauterivianus
R. asper
M.hoschulzii
S.salebrosum
E. striatus
E. windii
E. windii
E. striatus
Barren
G. meddi
C. surirellus
Z. embergeri
Braarudosphaera
Barren
Late Tithonian ?

The LO of *Prediscosphaera columnata* at 487.52 mbsf approximates to the base of the Albian. The LOs of several species (*E. hancockii* 485.97 mbsf*; S. falklandensis* 484.7 mbsf; *C. erhembergii* 483.3 mbsf; *S. primitivum* 481.89 mbsf) also support are compatible with the presence the latest Late Aptian–earliest Early Albian interval. Therefore, the interval 487.52–480.28 mbsf is latest Late Aptian–earliest Early Albian interval in age (Figure 6.4).

6.4.4 Magnetostratigraphy

The magnetic susceptibility (χ) varied between 2.00×10^{-8} m^3/kg and 1.13×10^{-7} m^3/kg in the studied interval (523.94–508.77 mbsf) (Figure 6.5; Table 6.8 in Appendix D). The highest value was found at 520.81 mbsf is anomalous as all other data were less than 7.42×10^{-8} m^3/kg. With regards to natural remanent magnetization (NRM), most of the samples have shown reliable inclination; exemplified by the two samples shown in Figure 6.6 (Table 6.8 in Appendix D). Two out 41 samples, from at 518.60 and 523.70 mbsf, do not show vectors during demagnetization process (Figure 6.6; Table 6.8 in Appendix D). Therefore, interpretation of NRM inclination was not performed in those samples. Eleven samples have maximum angular deviation values (MAD) higher than 18° (Figure 6.6) (Savian et al., 2016), and two of them have vectors that are not reliable and were not plotted in Figure 6.5: 511.48 and 520.54 mbsf (Table 6.8 in Appendix D). Three polarity zones are interpreted based on 28 samples; inclinations and virtual geomagnetic pole latitudes are plotted in Figure 6.5. The interval 518.9–518.16 mbsf has three samples that show positive inclination and are interpreted as a reversed-polarity interval. The intervals 523.94–519.23 mbsf and 514.28–508.77 mbsf have the majority of samples with negative inclination that are interpreted as normal-

polarity intervals, although the samples at 511.48 and 509.20 mbsf do have positive inclination, which may affect this interpretation. The sample at 511.48 mbsf has a MAD of 32.6°, so inclination does not seem to be reliable in this case. The sample at 509.20 mbsf has a MAD of 7.3° so could represent either a reversed polarity or, more likely, a discrepant sample given that samples less than 20 cm above and below show normal polarity (question mark at Figure 6.5). In addition, this depth is within the planktonic foraminifera *Hedbergella trocoidea* zone (Huber and Leckie, 2011), where no reversal has been recorded in the literature (Ogg, 2012; Ogg et al., 2012). The results given here partially agree with those from Salloway (1983), where a reversed-polarity interval was identified between samples 59-2, 140–142cm and 58-4, 129–131cm (ca. 520.90–514.00 mbsf), based on three samples, interpreted as reversed chron M3r (grey color Figure 6.5). However, our new high-resolution data constrained the reversed interval to be at 518.0–518.16 mbsf, whereby the top of the reversal was defined at the top of core 59 (sample at 518.16 mbsf) but reversed-polarity samples were not found at the base of the core 58 (sample at 514.28 mbsf).

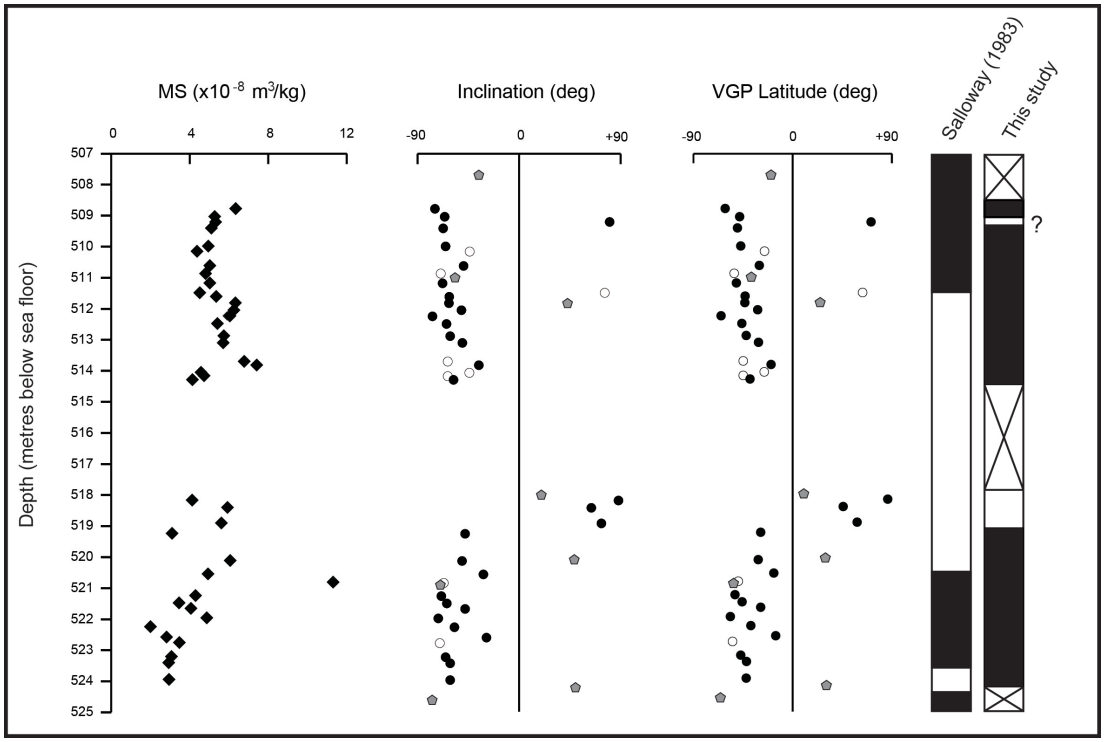


Figure 6 .5 – Magnetic data of the DSDP Site 511. The left plot shows the magnetic susceptibility (MS) obtained at the frequency 976 Hz (black diamonds). The middle and right plots show the characteristic component inclination and the VGP Latitude respectively, black circle – reliable inclination; white circle – not reliable inclination with MAD higher than 18° and; grey pentagon – data from Salloway (1983). A comparison of reversal scales is shown, grey scale – data from Salloway (1983) and black scale – data obtained in this study.

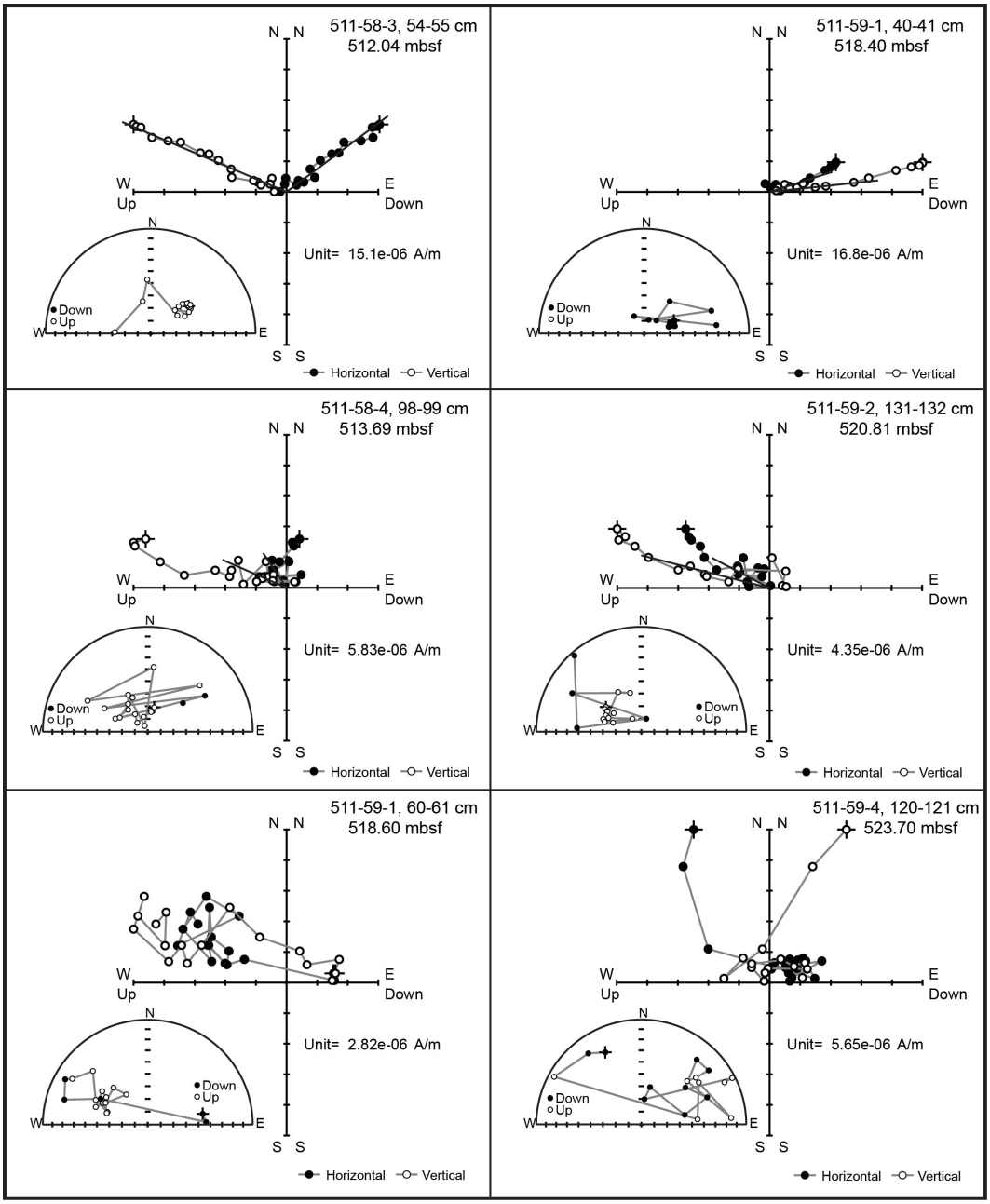


Figure 6 .6 – AF demagnetization results for 6 discrete samples. For each sample are shown the NRM vector measured on an orthogonal projection and on an equal area projection. In the orthogonal projection, close circles = horizontal components and open circles = vertical components. In the equal area projection, close circles = positive inclinations and open circles = negative inclinations. The samples 511-58-3, 54-55 cm (512.04 mbsf) and 511-59-1, 40-41 cm (518.40 mbsf) are examples of reliable inclination; samples 511-58-4, 98-99 cm (513.69 mbsf) and 511-59-1, 123-124 cm (520.81 mbsf) are examples of not reliable inclination with maximum angular deviation values (MAD) higher than 18°; and samples 511-59-1, 60-61 cm (518.60 mbsf) and 511-59-4, 120-121 cm (523.70 mbsf) do not show a well-defined vector.

6.4.5 Rhenium and osmium isotopes

The Re and Os contents are moderate at 28–536ppb and at 746–1765ppt, respectively (Table 6.9 in Appendix D). The $^{187}Re/^{188}Os$ ratios are relatively high with a good spread of values in both groups of samples: 154–1489 (core 59) and 284–2583 (core 58). The data from core 58 yield an age of 128 ± 10 Ma, where the scattered regression is high (MSWD = 4571), but is strongly affected by one sample at 513.86 mbsf (Figure 6.7A). Without this analysis, the remaining eight samples yield an isochron with an age of 129.7 ± 4.9 Ma, where the scattered regression is still high (MSWD = 1329). The initial Os ratios ($^{187}Os/^{188}Os_i$) obtained for the two isochrons from core 58 are 0.54 ± 0.21 and 0.48 ± 0.10 with and without taking into account the sample at 513.86 mbsf (Figure 6.7A). The data from core 59 yield an age of 125.3 ± 2.2 Ma, where scattered regression is moderate to high (MSWD = 311) and an $^{187}Os/^{188}Os_i$ of 0.53 ± 0.03 (Figure 6.7B). All samples combined from both cores, with the exception of one from core 58, yield an age of 128.2 ± 2.5 Ma, where scattered regression is high (MSWD = 873) and an $^{187}Os/^{188}Os_i$ of 0.50 ± 0.04 (Figure 6.7C). Although the scatter of isochrons is higher than ideal (MSWD < 1), the lowest value (MSWD = 311) was obtained by using samples from core 59. Hence, this is the most reliable age obtained is of 125.3 ± 2.2 Ma.

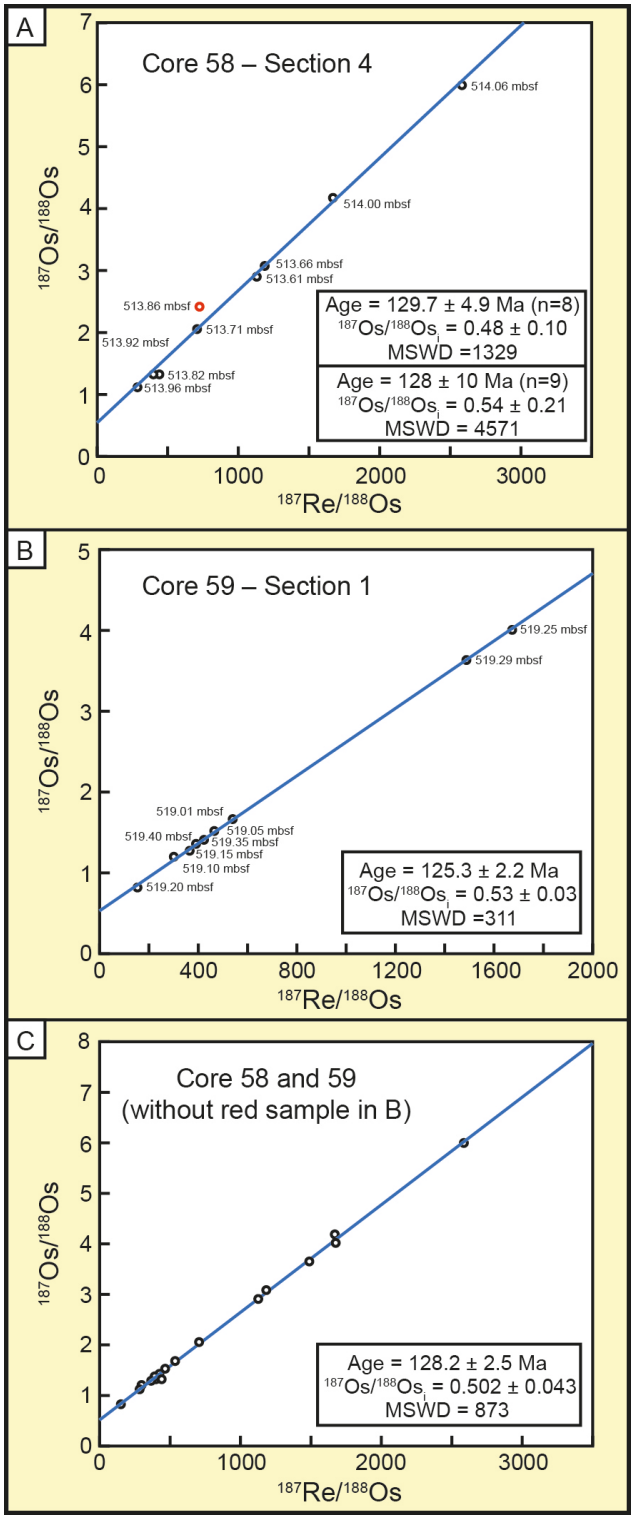


Figure 6 .7 –Re-Os isochrones obtained during this study. A: Data from the interval 519.01–519.40 mbsf (section 1, core 59). B: Data from the interval 513.61–514.06 mbsf (section 4, core 58), where two dates were obtained, with and without the sample in red. C: All the data from A and B, but the red sample displayed in B.

6.5 Stratigraphic revision

6.5.1 Sediments deposited in reducing environment

The stratigraphy proposed here for the 512.22–553.87 mbsf depth interval is at odds with some previous schemes (Figure 6.4; Mutterlose, 1989; Bralower et al., 1994; Jenkyns et al., 2012). The first results from the initial reports of DSDP Site 511 reported that those sediments were deposited from the Late Jurassic to Barremian/Early Aptian (Wise, 1983), in broad agreement with our findings (Figure 6.4). However, two subsequent studies suggested that those sediments are Barremian–Aptian in age (Mutterlose, 1989; Bralower et al., 1994). More bioevents were identified in this research than previous studies, likely because higher resolution sampling was undertaken.

It is difficult to assign an age to the lower part of the studied interval due to the presence of an interval (560 – 543.35 mbsf) with a paucity of marker species and many barren samples, overlain by an interval (542.73 to 534.28 mbsf) containing reworked Jurassic species. These characteristics partly explain the large differences between the interpretations given by different authors. It is assigned a Late Tithonian age up to 542.98 mbsf and tentatively place the Jurassic/Cretaceous boundary at the LO of *G. meddii* (542.73 mbsf) (Figure 6.4). It is possible that a hiatus occurs at this level, because the abundance and composition of nannofossil assemblages abruptly change between samples 542.98 and 542.73 mbsf, suggesting that the uppermost Jurassic and the lowest Cretaceous are missing. The presence of a hiatus is supported not only on changes of nannofossil assemblages, but also by abrupt changes of TIC and $\delta^{13}C_{carb}$ values at 543.45–542.50 mbsf (Figure 6.3; Deroo et al., 1983). In this

interval, TIC values are generally higher than 1.3 wt % (<11 wt % $CaCO_3$) and attain 3.5 wt % (29 wt % $CaCO_3$), whereas samples immediately lower and higher in the section usually display values below 1.3 wt % (>11 wt % $CaCO_3$). In addition, $\delta^{13}C_{carb}$ values show a sharp negative excursion towards more negative values (~ –4‰) in the interval 543.14–534.04 mbsf (Figure 6.4). This abrupt change in $\delta^{13}C_{carb}$ values without corresponding changes in $\delta^{18}O_{carb}$ values has been related to incorporation of ^{12}C in carbonate cement as a result of sulphate reduction of organic matter during early diagenesis (Hudson, 1977). Hence, it is most likely that changes in $\delta^{13}C_{carb}$ values from bulk carbonate in the interval 543.14–534.04 mbsf are related to early diagenesis. Although the relationship between early diagenetic changes in $\delta^{13}C_{carb}$ values and the increase in carbonate content in this interval is not obvious, an episode of non-deposition, represented by an unconformity and/or condensed section probably favoured both phenomena. Studies on diagenetic carbonate concretions in organic-rich mudrocks with $\delta^{13}C_{carb}$ values (< –6 ‰) derived from anaerobic methane oxidation and/or sulphate reduction during early diagenesis are likely to occur during persistent reduced sedimentation rate or a depositional hiatus that could also be associated with lower $\delta^{18}O_{carb}$ values (Irwin et al., 1977; Raiswell, 1988; Sass et al., 1991; Raiswell and Fisher, 2000).

The intervals 542.73–534.28 mbsf, 534.04–528.33 mbsf and 528.11–521.94 mbsf have been interpreted as deposited during the Berriasian, Late Valanginian–Hauterivian and Barremian based on the calcareous nannofossil biostratigraphy performed in this study, rather than solely in the Barremian–Early Aptian interval as suggested by both Mutterlose (1989) and Bralower et al. (1994) (Figure 6.4). Significantly, strontium-isotope ratios ($^{87}Sr/^{86}Sr$) from belemnites, foraminifera, inoceramids and other macrofossils show the same trends from

Tithonian to Albian observed in the international fit based on $^{87}Sr/^{86}Sr$ ratios worldwide (Figure 6.8) (Bralower et al., 1997; Price and Gröcke, 2002; McArthur et al., 2012). Although absolute $^{87}Sr/^{86}Sr$ ratios from belemnites and foraminifers are higher than those expected from the age based on calcareous nannofossil biostratigraphy, the general trend of increasing and decreasing $^{87}Sr/^{86}Sr$ ratios from sediments deposited in the interval 553–490 mbsf finds better correspondence with the new calcareous nannofossil age assignment than those suggested by both Mutterlose (1989) and Bralower et al. (1994). The latter authors suggest the presence of Barremian–Lower Aptian down to core 62. If those sediments were Barremian–Early Aptian in age, they should displayed a subtle trend of increasing $^{87}Sr/^{86}Sr$ ratios from 0.70747 to 0.70749 (difference of ~0.00002) followed by a decrease down to ~ 0.7072 (difference of ~0.00029) in the interval Barremian–Upper Aptian (McArthur et al., 2012; Figure 6.8). However, $^{87}Sr/^{86}Sr$ ratios from belemnites and foraminifera show an increasing trend from 0.707044 to 0.707557 (difference of 0.000513) in the interval 553–515mbsf (Figure 6.8), which is a greater difference than expected for the Barremian interval, but similar to that found in the interval Tithonian–Barremian from ~0.7070 to ~0.7075 (difference of ~0.0005) (McArthur et al., 2012). In addition, the trend of decreasing $^{87}Sr/^{86}Sr$ ratios from 0.707577 to 0.707252 (difference of 0.000325) in the interval 515–491 mbsf from DSDP Site 511 is similar to the trend of decrease in the interval Barremian–Upper Aptian from ~0.7075 to ~0.7072 (difference of ~0.0003; McArthur et al., 2012). The higher absolute $^{87}Sr/^{86}Sr$ ratios from the interval 553–506 mbsf than those recorded worldwide can be explained by a shorter Early Cretaceous residence time of Sr than exists in the modern oceans and/or a higher mixing time of

Cretaceous oceans whereby the South Atlantic would not be homogenised compared to other oceans (Fig. 8). The homogeneity of modern marine $^{87}Sr/^{86}Sr$ ratios has generally been assumed for the geological past based on the higher residence time of Sr in the oceans today ($\approx 10^6$ years) compared to the time it takes currents to mix the oceans ($\approx 10^3$ years) (e. g., McArthur et al., 2012).

The sediments from the interval 528.11–512.22 mbsf at the top of core 59 have been assigned an age of Barremian–Early Aptian based on calcareous nannofossil biostratigraphy, although the boundary Barremian/Aptian cannot be defined due to the absence of marker species (Figure 6.4). The boundary Barremian-Aptian is defined at the base of the reversed polarity chron M0r, which precedes the Cretaceous Normal Polarity Superchron (CNPS) that extends from the Aptian to the Santonian (Ogg, 2012; Ogg et al., 2012). A reversed-polarity interval, named ISEA or M'-1r', have been reported in the NC7 calcareous nannofossil zone and the *Globigerinelloides ferreolensis* planktonic foraminifera zone in the Upper Aptian (Ogg, 2012; Ogg et al., 2012). A reversed-polarity interval has been recognized from the section 518.90–518.16 mbsf in the NC6 calcareous nannofossil zone in DSDP Site 511 (Figures 6.5 and 6.9) and could be assigned to Chron M0r or a reversed-polarity Chron older than Aptian (e. g., M1r), but not the reversed-polarity ISEA. Therefore, all sediments below 528.11–518.90 mbsl are assigned to a Barremian age (Figure 6.9).

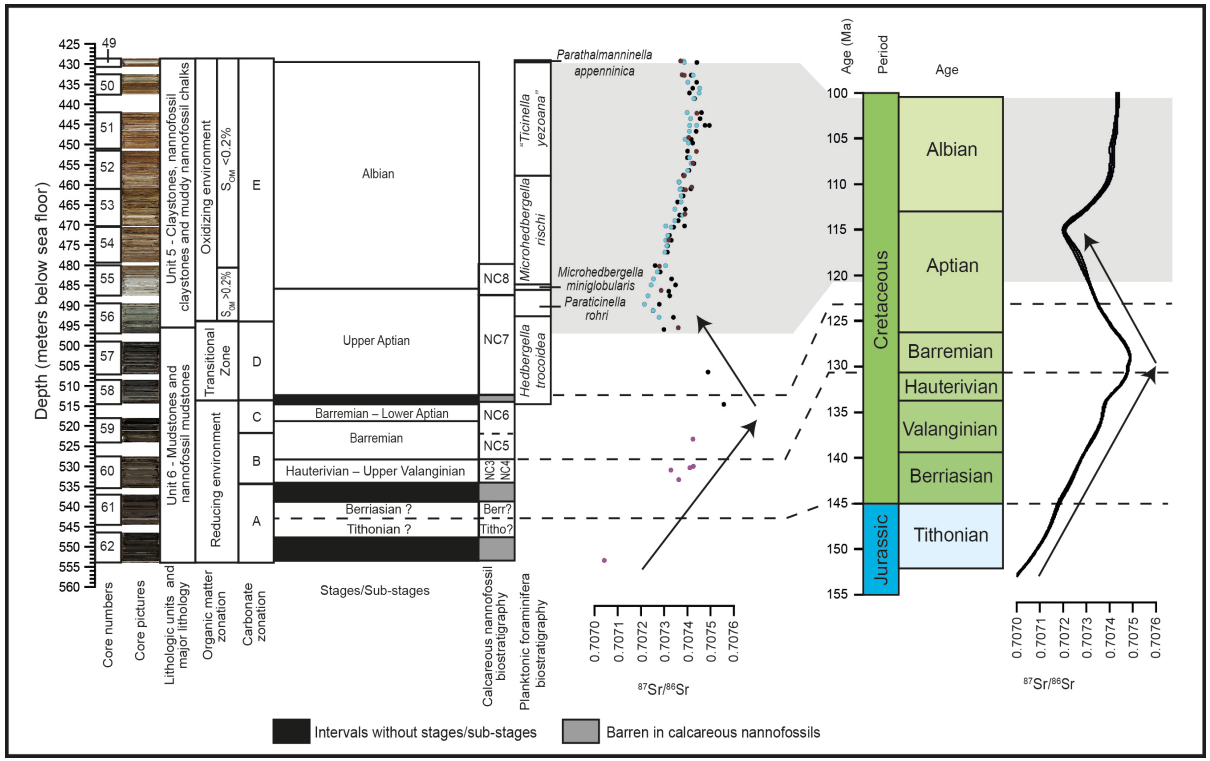


Figure 6 .8 –Correlation between $^{87}Sr/^{86}Sr$ ratios of samples from DSDP Site 511 and the best fit of $^{87}Sr/^{86}Sr$ ratios from data worldwide (McArthur et al., 2012). Purple – belemnites (Price and Gröcke, 2002); blue – inoceramids, black – foraminifera, brown – other macrofossils not identified (Bralower et al., 1997). Numbers and pictures of the cores, lithologic units and major lithology after Ludwig et al. (1983) and Deroo et al. (1983), organic matter zonation defined by Deroo et al. (1983) and this study, carbonate zonation and calcareous nannofossil biostratigraphy obtained in this study. Planktonic foraminifera biostratigraphy from Huber and Leckie (2011) and after Ando et al. (2013). Stages/sub-stages interpreted based on magnetostratigraphy, nannofossil calcareous and planktonic foraminifera biostratigraphy. Grey band – correlation of $^{87}Sr/^{86}Sr$ ratios. Dashed lines – limits of age assignments based on calcareous nannofossil biostratigraphy. Arrows – main trends on $^{87}Sr/^{86}Sr$ ratios. Titho – Tithonian; Berr –Berriasian.

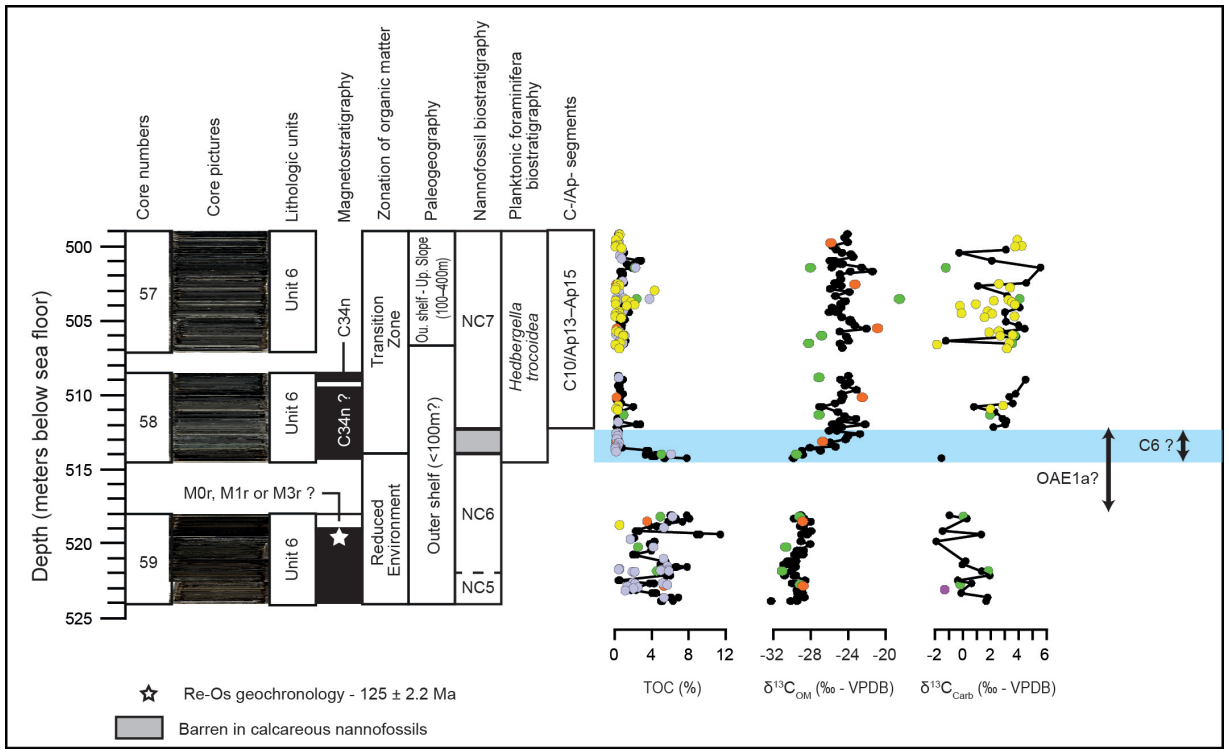


Figure 6 .9 –High-resolution data from the cores 57–59 from the DSDP Site 511. TOC, $\delta^{13}C_{OM}$, and $\delta^{13}C_{carb}$ (> –2 ‰) values plotted against stratigraphy. All legend is similar to those shown in Figures 6.2 and 6.3. It also shows the magnetostratigraphy from Figure 6.5, palaeogeography based on benthic foraminifera from Basov and Krasheninnikov (1983), planktonic foraminifera biostratigraphy from Huber and Leckie (2011) and after Ando et al. (2013), stratigraphic position of samples from core 59 where Re-Os geochronology was performed. C-/Ap-segments interpreted in this study (see text for details). Possible records of C6 segment and the OAE 1a interval are shown in the blue rectangle.

The most reliable Re-Os age of 125.3 ± 2.2 Ma (section 6.4.4) was obtained from the samples in the interval 519.01–519.40 mbsf (Figures 6.7 and 6.9). This radiometric age obtained from a level just below the reversed-polarity zone indicates that this reversal could represent one of three chronozones: M3r (126.05–124.58 Ma; time scale of Malinverno et al., 2012), M1r (123.92–123.51 Ma; time scale of Malinverno et al., 2012) from the Barremian or M0r (126.3–125.8 Ma; time scale of Ogg et al., 2012) from the Early Aptian. The divergences between age assignments of those reversal polarities have important implications for identification of the rates of environmental changes during the Barremian–Early Aptian (Bottini et al., 2015; Erba et al., 2015). However, there is no consensus as to the applicability of these ages. The LO of the nannofossil *R. irregulars* suggests that the reversed-polarity interval is M0r, because its first occurrence (FO) predates the chron M0r and is younger than reversed-polarity chrons M3r or M1r. The assignment of M0r is important for locating the Barremian-Aptian boundary at DSDP Site 511 as is the use of Re-Os geochronology to constrain its absolute age, as discussed in Chapter 3. The age assignment of M0r of 125.3 ± 2.2 Ma overlaps 126.3–125.8 Ma (time scale of Ogg et al., 2012), which is in agreement with the U-Pb age of 124.07 ± 0.17 Ma obtained from in the Great Valley Sequence of California (Shimokawa, 2010) where *Chiastozygus litterarius* biozone (NC6) was identified and therefore supposedly Early Aptian in age. On the other hand, this date disagrees with an Ar-Ar age for M0r of 122 ± 0.5 Ma, corrected to Fish Canyon Sanidine standard of 28.201 ± 0.046 (Kuiper et al., 2008), from lava flows at the Mashenmiao-Zhuanchengzi section in Yixian, Liaoning Province, northeast China (He et al., 2008; Malinverno et al., 2012). The Re-Os age of 125.3 ± 2.2 Ma at 519.01–519.40 mbsf just below the reversed-polarity interval at 518.90–518.16 mbsf identified in DSDP Site 511

implies that this interval is M0r and agrees better with the time scale of Ogg et al. (2012) than that of Malinverno et al. (2012). Alternatively, the reversed-polarity interval identified in this study could be older than reversed-polarity Chron M0r and the base of *Chiastozygus litterarius* biozone (NC6), as defined in the DSDP Site 511, could be older than Chron M1r or M3r (Figure 6.9). Significantly, the reversal polarity that we have found constrains the possible records of the Early Aptian OAE 1a to lie above the top of core 59 (518.16 mbsf), which disagrees with the interpretation of the presence of a partial record in the interval ~540–518 mbsf (Jenkyns et al., 2012).

6.5.2 Is the OAE 1a interval recorded in DSDP Site 511?

The LO of *E. floralis* (at 512.22 msbf) in core 58 is a firm bioevent that is cosmopolitan and dated as latest Early Aptian. This LO has been recorded essentially at the same stratigraphic level by previous studies performed on DSDP Site 511 (Figure 6.4). Compared to Tethyan carbon-isotope profiles, the FO of *E. floralis* always postdates OAE 1a occurring at the beginning of C7 (Menegatti et al 1998; Erba et al., 1999). Therefore, OAE 1a could be recorded in the interval between 518.16–512.22 mbsf, although a core gap between 518–514.46 mbsf limits the record available (Figure 6.9). The interval 514.46–512.22 mbsf shows an unusual positive excursion on $\delta^{13}C_{OM}$ values and a drop in TOC and $\delta^{13}C_{carb}$ values (Figure 6.9). One possible interpretation is that the upper part of the OAE 1a interval (C6 segment) is recorded in this excursion, whereas the other segments C3–C5 were not recovered in the gap between the cores 58 and 59. However, this interval could also record a hiatus as suggested by changes in the type of organic matter, from higher HI and lower OI values

below this interval to low HI and higher OI values with terrestrial organic matter above it (Deroo et al., 1983). In addition, changes in both $\delta^{13}C_{carb}$ and $\delta^{18}O_{carb}$ values, which are negative and have suffered intense diagenetic overprint (Figures 6.3 and 6.9). In addition, this interval also shows an overlap of the *Hedbergella trocoidea* planktonic foraminifera zone and the NC6 nannofossil calcareous zone (Figures 6.3 and 6.8). The former occurs in the Late Aptian whereas the latter is typical from the Early Aptian. It suggests the presence of a condensed layer and/or reworking of older calcareous nannofossils. Therefore, this interval could represent a condensed section, a hiatus with reworking and/or the latter part of the OAE 1a interval (C6 segment).

The positive carbon positive excursion observed in the $\delta^{13}C_{carb}$ and $\delta^{13}C_{OM}$ profiles from the interval 512.22–494.22 mbsf of DSDP Site 511 in the Late Aptian could be correlated to the Ap7/C7 segments and/or the Ap13–Ap15/C10 segments (Menegatti et al., 1998; Bralower et al., 1999; Bottini et al., 2015). Because the base of the increase of the relative high abundance of *R. parvidentatum* from 512.22 mbsf occurs as well as the "acme of *N. truittii*" (sensu Mutterlose 1989), it is more likely that sediments above this level record the Ap13–Ap15/C10 segments in the Late Aptian (Figure 6.9). This interpretation agrees with the presence of the planktonic foraminifera biozones *Hedbergella trocoidea* and *Paraticinella rohri* (Figures 6.9 and 6.10; Huber and Leckie, 2011; Ando et al., 2013; Bottini et al., 2015; Erba et al., 2015). Therefore, if the interval 514.46–512.22 mbsf records the C6 segment, there must be a hiatus at 512.22 mbsf between Early Aptian C6 segment and Late Aptian C10 segment.

Significantly, the interval 513–540 mbsf was previously interpreted as a record of OAE 1a, during which sea-surface temperature (SST), based on TEX_{86}, dropped by up to 3°C (Jenkyns et al., 2012). However, this interpretation is at odds with records of rises in SST in the Tethyan realm (Cismon, Piobbico and PLG cores, Italy), proto-North Atlantic (DSDP Site 398 and Djebel Serdj Formation, Tunisia), Boreal Realm (Alstätte 1 section, Germany, and Ulyanovsk area, Russia) and Pacific Ocean (DSDP Site 463), based on TEX_{86}, oxygen isotopes ($\delta^{18}O$) and nannofossil temperature index (NTI) (Schouten et al., 2003; Ando et al., 2008; Zakharov et al., 2013; Mutterlose et al., 2014; Bottini et al., 2015; Naafs and Pancost, 2016; Savian et al., 2016). Our new integrated stratigraphy suggests that the only TEX_{86} value analysed by Jenkyns et al. (2012) possibly from OAE 1a is that at 513.19 mbsf, where SST was calculated to be 28.0–28.8°C. This temperature is similar to those found below and above this level (Jenkyns et al., 2012). The significant drop in SSTs to 25–27°C recorded in the interval 522.93–519.79 mbsf is dated here as Barremian and has similar values and trends to data observed in the Upper Hauterivian–Lower Barremian of the Moorberg and Goot sections, Germany and Speeton section, northeast England (Mutterlose et al., 2012).

6.5.3 The transitional environment and the carbon isotope excursion

The interval from 512.22–494.22 mbsf of DSDP Site 511 was deposited during the Late Aptian and likely was synchronous with the Ap13–Ap15/C10 carbon-isotope segments based on the planktonic foraminifera and calcareous nannofossil biostratigraphy (Bralower et al., 1999; Huber and Leckie, 2011; Bottini

et al., 2015; this study, Figure 6.9). Elsewhere the AP13–Ap15/C10 carbon-isotope excursion is characterized by a positive shift in both carbonate and organic matter (Bralower et al., 1999; Price, 2003; Herrle et al., 2004; Bottini et al., 2015; Herrle et al., 2015). Although higher $\delta^{13}C_{carb}$ and $\delta^{13}C_{OM}$ values were already published from Site 511 (Parker et al., 1983; Dias, 1998; Jenkyns et al., 2012), the new stratigraphic revision allows identification of the Ap13–Ap15/C10 segments in the high-latitude South Atlantic for the first time. Therefore, this stratigraphic level is the oldest time when both $\delta^{13}C_{carb}$ and $\delta^{13}C_{OM}$ logs seem to represent the global carbon cycle. Because terrestrial organic matter is likely to record the global carbon cycle acquired from atmospheric carbon dioxide (e. g., Gröcke et al., 1999, Ando et al., 2002), higher input of terrestrial organic matter in the interval 512.22–494.22 mbsf could explain why the $\delta^{13}C_{OM}$ values illustrate the global carbon cycle.

The transitional environment between reducing and oxidizing recorded by the interval 512.22–494.22 mbsf, as interpreted by Derro et al. (1983), is characterized by higher quantities of detrital/terrestrial organic matter with higher OI values, lower HI and lower TOC, than the stratigraphically lower interval. The interval 512.22–494.22 mbsf has also been interpreted to show a rise in relative sea level, as suggested by benthic foraminifera (Basov and Krasheninnikov, 1983). Therefore, a rise in relative sea level and increase in oxygenation as recorded in the interval 512.22–494.22 mbsf can be used to suggest enhanced water exchange between the South Atlantic in the Falkland Plateau areas and oceans worldwide, consequently permitting $\delta^{13}C_{carb}$ values to also record the global carbon cycle.

The Late Aptian Ap13–Ap15/C10 segments have been associated with a ‘cold snap’ in the Tethyan realm (Piobbico core, Italy), proto-North Atlantic (DSDP Site 545), Pacific (DSDP Site 463), based on TEX_{86} and NTI (McAnena et

al., 2013; Bottini et al., 2015). Five TEX_{86} data points recording SSTs during this time interval from DSDP Site 511 show temperatures of 26.8–29.3°C (Jenkyns et al., 2012). Because of the condensed layer and/or unconformity below 512.22 mbsf and the absence of TEX_{86} data just above the Ap13–Ap15/C10 interval, it is not possible to say whether or not these temperatures are lower than those immediately before or after the Ap13–Ap15/C10 interval and define a 'cold snap' in this interval of time.

6.5.4 Aptian-Albian transition and the OAE 1b

DSDP Site 511 is one of the few places where a complete planktonic foraminifera zonation of the Aptian-Albian boundary is present (Huber and Leckie, 2011). Hence it potentially records the carbon-isotope excursions and/or organic rich-levels that define the OAE 1b cluster, which has been recognized in the Tethyan and North Atlantic regions (e. g., Herrle et al., 2004; Trabucho Alexandre et al., 2011; Coccioni et al., 2014). In the Vocontian Basin, France, four organic-rich levels that are named Jacob, Kilian, Paquier and Leenhardt levels (Bréhéret, 1994) have been considered records of OAE1b, although some studies include just three levels (Jacob, Kilian and Paquier; e. g., Trabucho Alexandre et al., 2011) or just the Paquier (e. g., Herrle et al., 2004). At the proposed GSSP for the Aptian-Albian boundary of Col de Pré-Guitard, the Jacob level is Late Aptian in age, occurring below the LO of the nannofossil *P. columnata* within the planktonic foraminifera *Paraticinella rohri* biozone (Petrizzo et al., 2012; Kennedy et al., 2014). The Kilian level coincides with the LO of the planktonic foraminifera *Microhedbergella renilaevis*, and stratigraphically above the LO of *P. columnata.* The Paquier and Leenhardt levels occur above the Kilian level, within the planktonic foraminifera *Microhedbergella*

rischi zone. All four levels show negative carbon-isotope excursions (Herrle et al., 2004; Trabucho Alexandre et al., 2011; Coccioni et al., 2014).

At DSDP Site 511, the LO of the planktonic foraminifera *M. renilaevis* is at 485.11 mbsf (Huber and Leckie, 2011) and LO of the calcareous nannofossil *P. columnata*, which defines the base of the NC8 calcareous nannofosssil zone, is at 487.52 mbsf based in this study (Figure 6.10). Although a relative organic-rich level has not been found, the Jacob Level equivalent is interpreted as the negative excursion observed in both $\delta^{13}C_{carb}$ and $\delta^{13}C_{OM}$ in the interval 492.42–490.78 mbsf, (~2.0 ‰ and ~5.0 ‰, respectively) below the LO of both *M. renilaevis* and *P. columnata* (Fig. 10). Negative excursions in $\delta^{13}C_{carb}$ and $\delta^{13}C_{OM}$ were recognized in the 487.32–485.39 mbsf interval of ~2.4 ‰ and ~1.0–1.5 ‰, respectively. The negative excursion for $\delta^{13}C_{OM}$ values is not as evident as the one observed in $\delta^{13}C_{carb}$; nevertheless, there is a decrease from –26 ‰ to –27 ‰. Although those excursions occur ~28cm below the LO of the planktonic foraminifera *M. renilaevis*, it is suggested that they are correlated to the Kilian Level rather than Jacob Level because it is the closest negative excursion to the LO of the *M. renilaevis* and occurs stratigraphically above the LO of the *P. columnata* (Herrle et al., 2004; Petrizzo et al., 2012; Coccioni et al., 2014).

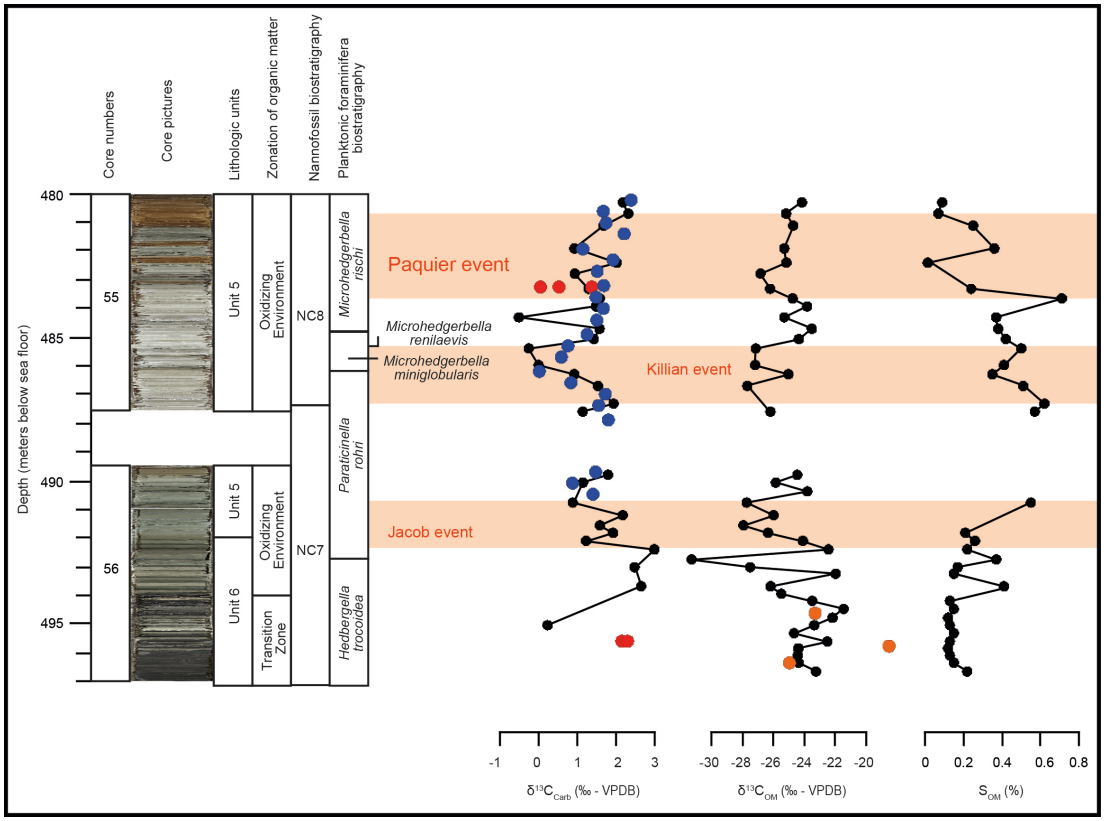


Figure 6 .10 – High-resolution data from the cores 55–56 from the DSDP Site 511. $\delta^{13}C_{carb}$, $\delta^{13}C_{OM}$, and S_{OM} (< 3 wt %) values plotted against stratigraphy. All data and legend similar to those shown in Figures 6.2 and 6.3. It also shows the planktonic foraminifera biostratigraphy from Huber and Leckie (2011) and after Ando et al. (2013). Orange bands highlight the interpreted Jacob, Kilian and Paquier events from the OAE 1b interval. The LO of the planktonic foraminifera *Microhedbergella renialevis* at 485.11 mbsf is shown, which is used to define the limit Aptian-Albian (Kennedy et al., 2014).

However, there is not a single organic-rich level that could be used to identify the Kilian Level equivalent. Similarly, the Paquier Level equivalent is suggested to be in the interval 485.06–483.64 mbsl, where dark grey levels occur interbedded with red claystones (Figure 6.10), although it is not possible to rule out the possibility that this interval could be equivalent to Leenhardt Level. The interval between the Jacob and the Paquier Level equivalents has relatively higher S_{OM} values (>0.2 wt %) than sections immediately above or below (usually <0.2 wt %) (Figures 6.2 and 6.9). The Jacob and Paquier level equivalent horizons have three samples with S_{OM} content of

3.0–4.3 wt % (Figure 6.2). All three negative carbon-isotope excursions are within the onset interval of the oxidizing environment where the sediments lying stratigraphically between the Jacob level and the Paquier level are formed by cycles of white/grey/dark grey claystones/chalks. Red claystones are predominant stratigraphically above the Paquier Level. It is possible that OAE 1b in this area was characterized by sulphide-rich bottom waters, which favoured the relatively higher S_{OM} values, which are likely to represent sulphides rather than sulphur present in organic matter, because of the low TOC values found in this interval (Figure 6.2). Hence, both enhanced productivity in surface waters and stratification of the water column likely favoured formation of the interval between Jacob and Paquier Levels. The balance between the increasing oxygenation of the South Atlantic due to its expanding geometry and the relatively higher productivity and stratification during OAE 1b may have influenced the deposition of the cycles of white/grey/dark grey claystones/chalks and prevented the full oxygenation between Jacob and Paquier Levels, in clear contrast with the oxygenated bottom waters recorded as red claystones above the Paquier level.

6.5.5 Albian sediments above OAE 1b

Albian sediments from Tethyan and Pacific Ocean sites show a trend of decreasing $\delta^{13}C_{carb}$ values throughout the Albian, without the relatively high positive values that characterize the Aptian (Price, 2003; Tiraboschi et al., 2009; Giorgioni et al., 2012). Carbon-isotope values derived from organic matter in the Santa Rosa Section, Mexico also show the same trend of decreasing values, with a shift on $\delta^{13}C_{OM}$ profiles towards lower values (1.5 ‰). The carbon-isotope profiles from DSDP Site 511 show the same trends of decreasing values, with a negative shift at

~454.6 mbsf of ~ 1.5‰. Hence, the carbon-isotope data show the same pattern as other localities and reinforce the supposition that the Albian trends seem to be global.

The oxygen-isotope profiles show the differences between well-preserved planktonic and benthic foraminifera recorded in DSDP Site 511 to be 1.0–1.2‰. The bulk-rock oxygen isotopes generally agree with the data obtained from benthic and planktonic foraminifera (Huber et al., 2002). However, the bulk-carbonate data from these study show a range of up to 2‰ between neighbouring samples, which is higher than the differences of 1.0–1.2‰ between benthic and planktonic foraminifera. The larger difference found in this study can be interpreted as relative difference between surface and bottom environments, changes in sea-surface temperature and/or salinity through time or early diagenetic processes (Pearson et al., 2001; Bice et al., 2003).

6.5.6 Late Jurassic–Early Cretaceous environments of deposition on the Falkland Plateau

The changes in the environment based on the organic matter present in the DSDP Site 511 shows the following pattern: a) reducing environment from Jurassic to the Barremian–Early Aptian; b) an intermediate transitional environment from reducing to oxidizing during the Late Aptian–Early Albian and; c) well-oxygenated environment during the Albian. This pattern has similarities to other locations in the South Atlantic and seems to be associated with a relative sea-level rise that ultimately may be related to the changes of the changing geometry of the opening South Atlantic.

Reducing environments were suggested by the presence of pre-Aptian organic-rich sediments with TOC values higher than 1 wt %, as recorded at DSDP sites 327A and 330 on the Falkland Plateau (Deroo et al., 1983). Organic-rich sediments have also been recognized in supra-evaporite Upper Aptian sediments that are older than the top of planktonic foraminifera *Hedbergella trocoidea* zone in DSDP Site 364, off-shore Angola, suggesting regional dysoxia. (Deroo et al., 1983; Zimmerman et al. 1987, Naafs and Pancost, 2014). The data from DSDP Site 511 suggest that reducing environments existed from the mid-Jurassic (Callovian–Oxfordian) up to Barremian/Early Aptian; confirming the hypothesis of regional dysoxia. The high S_{OM} content in DSDP Site 511 could reflect euxinic environments, although direct evidence, such as characterization of pyrite framboids or biomarkers, has not be obtained in this study. Notably, euxinic conditions were described in DSDP Site 364 based on the presence of thiophenic compounds and high TOC and S content. This site would likely reflect the same restricted environment as DSDP Site 511, despite a palaeodistance of more than 1500 km between these localities (Zimmerman et al., 1987; Naafs and Pancost, 2014). The reducing environments recorded in both DSDP Sites 364 and 511 are interpreted as relatively shallow (shelf/neritic environments) based on benthic foraminifera (Basov and Krasheninnikov, 1983; Kochhann et al., 2014; Naafs and Pancost, 2014). The lower $\delta^{13}C_{OM}$ values (–32 to –28‰) observed in the bulk rock from DSDP Site 511 are atypical, because they do not show any correspondence with $\delta^{13}C$ profiles recorded in the Tethyan sections of Jurassic to Barremian age, but they are similar to $\delta^{13}C_{OM}$ values obtained in C16–C18 n-alkanes, pristine, phytane and norpristane recorded in the DSDP Site 364 (–33 to –28‰) (Naafs and Pancost, 2014). Those lower $\delta^{13}C_{OM}$ values suggest therefore an atypical fractionation, which may reflect the composition

of local organism(s) that lived in the widespread shallow-marine poorly oxygenated environment rather than recording global carbon-cycle changes from the Early Cretaceous (e. g., Sprovieri et al., 2006),

The unconformity/condensed layer present in the interval 514.70–512.22 mbsf from the DSDP Site 511 (Barremian/Early Aptian to Late Aptian) shows a shift in environment conditions. Above the condensed layer/unconformity observed in core 58, the transitional environment up to core 55 is represented, where higher $\delta^{13}C_{carb}$ and $\delta^{13}C_{OM}$ values that potentially record the global carbon cycle from the Late Aptian are present (Figures 6.9 and 6.10). This interval displays relative enrichment of residual/terrestrial organic matter and changes in the lithology from black shales to claystones, nannofossil claystones and muddy nannofossil chalks that are white to grey. The decrease in TOC values have also been recorded in DSDP Sites 327A and 330 on the Falkland Plateau (Deroo et al., 1983). DSDP Site 364, Angola, records a drop in TOC values, and evidence for a decrease in salinity and euxinia, in the interval 1034–1025 mbsf supposedly Aptian in age (Bralower et al., 1994; Kochhann et al., 2013; Naafs and Pancost, 2014). In addition, benthic foraminifera also support the notion of a relative sea-level rise recorded by Upper Aptian sediments of DSDP Sites 511 in the Falkland Plateau (Basov and Krasheninnikov, 1983) and at DSDP Site 364, Angola (Kochhann et al., 2014). It is herewith suggested that the regional transitional environment in the interval Barremian/Early Aptian–Late Aptian in the Falkland Plateau area correlates with the lacustrine carbonates, evaporites and post-evaporite carbonates deposited in the southern Brazilian basins (Chapters 2, 3 and 4), and that both were associated with relative sea-level rise and increased exchange of waters between the South Atlantic with other oceans.

This gradual increase in ocean connectivity and relative sea-level rise from the mid-Jurassic to the Albian seems to be related to the opening of the South Atlantic, where the opening of the central segment of the South Atlantic and the Mozambique Rift were the main events. Zimmerman et al. (1987) have proposed a link between decrease of preservation and/or production of organic matter and the decrease of restriction promoted by the opening of the South Atlantic. The records presented here agree with this model. Significantly, one of the main phases of oxygenation/decrease of restriction is coincident in time with the OAE 1b interval. The other important phase of tectonic activity was related to formation of the major unconformity/condensed section before or around OAE 1a that confines the occurrence of the bulk of the organic-rich sediments to the Jurassic–Barremian/Early Aptian interval.

6.6 Conclusions

The main conclusions of this high-resolution record on DSDP Site 511 are:

1. Four main stratigraphic intervals were recognized: a) a basal interval older than Barremian–Early Aptian age composed of black shales deposited under anoxic conditions. This interval has the highest TOC, S_{OM} and HI values and the lowest $\delta^{13}C_{OM}$ and OI values; b) an intermediate Upper Aptian section comprising grey to green claystones and black shales representing a transition from anoxic to oxygenated environments. This unit has intermediate TOC and S_{OM} values and the highest $\delta^{13}C_{OM}$ and OI values; 3) an intermediate Aptian–earliest Albian section with low TOC and relatively higher S_{OM} than the stratigraphic level above and; 4) an upper interval comprising reddish to brownish claystones and ‘coquinas’ throughout

the Albian, suggesting a well-oxygenated environment, which displays the lowest TOC values and intermediate $\delta^{13}C_{OM}$ values.

2. It is suggested that the Jurassic–Cretaceous boundary is higher in the section than suggested by Wise (1983), Mutterlose (1989) and Bralower et al. (1994). The reversed chron at the top of core 59 was confirmed during this study and has an age of 125.3 ± 2.2 Ma based on Re-Os geochronlogy at its base. However, it is not clear whether the chron correlates to M3r (126.05–124.58 Ma; time scale of Malinverno et al., 2012), M1r (123.92–123.51 Ma; time scale of Malinverno et al., 2012) or M0r (126.3–125.8 Ma; time scale of Ogg et al., 2012).

3. The major episode of organic-rich black-shale deposition, which took place up to the Barremian–Early Aptian interval, as also recorded in DSDP Sites 327 and 330 (Falkland Plateau) and 364 (Angola Basin), indicates that local forcing functions governed deposition and preservation of organic matter in this part of the South Atlantic up to the Early Aptian.

4. The typical isotopic record of OAE 1a is missing either due to incomplete core recovery or a hiatus. However, its latter part (C6 segment) could be represented in the interval 512–514m, where a hiatus and/or condensed section also occurs. This interval represents an episode of vigorous bottom-current activity that may be related to the opening of the central segment of the South Atlantic and/or Mozambique Rift.

5. The transition between the intermediate and the upper interval is gradual and encompasses the Aptian–Albian boundary, where the typical isotopic records of the Jacob, Kilian and Paquier events, also called OAE 1b, are tentatively recognized. Although OAE 1b is characterized by black shales in the Tethyan–Atlantic area, at DSDP Site 511 a transition to more oxygenated environments is recorded, with deposition of grey claystones and marls. The Aptian–Albian boundary is marked by

the presence of red claystones and ‘coquinas’ just above the OAE 1b, which likely represent an increase in bottom-current activity.

6. Most black-shale sedimentation on the Falkland Plateau took place before deposition of evaporites in the Campos and Santos Basins that formed during the Early Aptian OAE 1a time interval and before the opening of the central segment of the South Atlantic. It is also shown that Upper Aptian sediments with intermediate TOC values and relatively high terrestrial organic-matter content lie above the hiatus/condensed section at DSDP Site 511 and, thus, are partially coeval with shallow- and deep-water post-evaporite carbonates from the Santos and Campos Basins.

Chapter 7

The Barremian-Aptian boundary in the Poggio le Guaine core (central Italy): evidence for magnetic polarity Chron M0r and oceanic anoxic event 1a

The expanded version of this chapter has been published in very similar form in the Geological Society of America Special Paper 524 (Savian et al., 2016) co-authored by Jairo F. Savian, Ricardo Trindade, Liliane Janikian, Luigi Jovane, Renato Paes de Almeida, Rodolfo Coccioni, Fabrizio Frontalini, Mariana Sideri, Milene Figueiredo, Leonardo R. Tedeschi and Hugh C. Jenkyns. Leonardo R. Tedeschi performed the carbon- and oxygen-isotope analyses, and wrote parts of the chapter on geochemical analyses and chemostratigraphy with comments from all co-authors. All other components presented here are taken directly from Savian et al. (2016). Dr Jairo Savian, Luigi Jovane and Ricardo Trindade obtained palaeomagnetic measurements. Dr Liliane Janikian and Renato Paes de Almeida described macroscopic features in detail. Dr Rodolfo Coccioni and Dr Fabrizio Frontalini undertook biostratigraphic correlation between Poggio le Guaine section and core. Geochemical datasets are provided in the appendix E (Table 7.1).

7.1 Introduction

The Cretaceous Period was characterized by an increase in ocean-crust production rate, a warm but unstable climate related to changes in pCO_2, rapid biotic turnovers, pronounced carbon-isotope excursions, and abrupt changes in redox

conditions in the ocean (e. g., Schlanger and Jenkyns, 1976; Larson, 1991b; Ando et al., 2002; Leckie et al., 2002; Wang et al., 2009; Jenkyns, 2010; Li et al., 2014). In addition, the Earth's magnetic field during the Cretaceous also shows a remarkable feature: long-standing normal polarity of the Cretaceous Normal Polarity Superchron (CNPS) (Helsley and Steiner, 1968). The CNPS also represents a major change, since it occurs following a period of time characterized by a high frequency of reversals. The last reversed chron before the CNPS is the M0r, the base of which has been used to define the Barremian-Aptian boundary (He et al., 2008; Ogg, 2012). Consequently, identification of M0r is the best tool to stratigraphically calibrate a section encompassing this boundary. In the early part of CNPS, short reversed-polarity intervals, such as the ISEA event, have been registered. The ISEA event was recognized for the first time in a bed of reddish Aptian limestone in the Umbrian Apennines, Italy (Vandenberg et al., 1978). Tarduno (1990) documented a similar event in two samples of the middle Aptian at Deep Sea Drilling Project (DSDP) Site 463 in the mid-Pacific Mountains.

The development of a high-quality age model is the first step in establishing the sequence of events and the rates of palaeoenvironmental change. Magnetostratigraphy provides a record of changing magnetic polarity, but it must be integrated with other methods, such as biostratigraphy and chemostratigraphy, in order to allow identification of specific reversal events.

The Poggio le Guaine (PLG) core was drilled to provide a high-resolution magnetic and palaeoenvironmental record of the upper Barremian, Aptian, and Albian stages in order to refine the understanding of the interconnections among geological, biogeochemical, oceanographic and climatic events in the Tethyan realm (Coccioni et al., 2012). This scientific core was drilled in the Poggio le Guaine site, 6

km to the west of the city of Cagli, in the Northern Apennines (central Italy) in 2010 (Figure 7.1A). A considerable amount of work has been performed in the PLG section without, however, recognition of the reversed interval (M0r) in the outcrop. In addition, although the Selli Level is the lithological record of OAE 1a in the Umbria-Marche Basin at several locations (Coccioni et al., 1987), the typical carbon-isotope excursions from the records of the OAE 1a interval have not been reported from the PLG section.

The aim of this chapter is to report, for the first time, carbon- and oxygen-isotope records around the OAE 1a interval in the basal section of the PLG core (from 86 to 96 m) that are integrated with new magnetostratigraphy and constraint with the available biostratigraphic data.

7.2 Geological setting

A complete and well-preserved Aptian–Albian section is exposed at Poggio le Guaine, in the Umbria–Marche Basin (UMB), Northern Apennines, Italy (Figures 7.1A and 7.1B). The section represents a continuous record of fossiliferous pelagic sediments extending from the uppermost Barremian to the Albian–Cenomanian boundary (126–99.6 Ma) (Coccioni et al., 2012; Ogg et al., 2012).

After the opening of the Tethys Ocean, during the Late Triassic–Early Jurassic, evaporitic precipitation was followed by carbonate-platform limestone deposition during the Early Jurassic. Throughout the Early–Middle Jurassic, the opening of the Alpine Tethys (Stampfli et al., 2003) led to the installation of a carbonate platform in the Central Apennines (Latium–Abruzzi region) and a pelagic domain in the Northern Apennines (Umbria–Marche region), divided by a slope-to-basin transitional domain (Santantonio, 1993, and references therein). The pelagic

domain comprised structural highs and deeper basinal areas, bounded by Jurassic faults, whose submarine relief was effectively eliminated during the deposition of the Maiolica Formation in the Early Cretaceous (Figure 7.1C). The sedimentation became homogeneous in thickness in the Umbria-Marche area starting from the Early Aptian with the deposition of the Marne (or Scisti) a Fucoidi Formation and pelagic lithotypes of the Scaglia Formations, characterized by Cretaceous–Paleogene foraminiferal-nannofossil carbonates and marls locally containing abundant biogenic chert (e. g., Bernoulli, 1972; Bernoulli and Jenkyns, 1974, 2009). The collision of Africa and Europe during the Neogene brought orogenesis affecting Triassic to Miocene deposits along the Adrian palaeomargin (Channell et al., 1979).

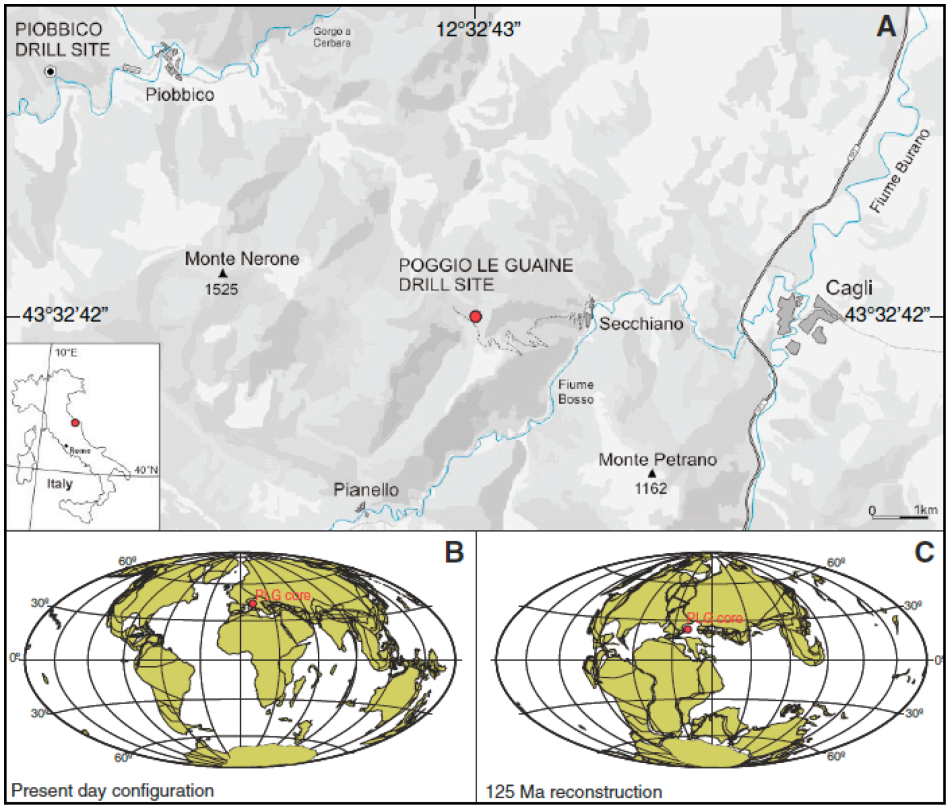


Figure 7 .1 – (A) Location of the Poggio le Guaine (PLG) drill site in the Northern Apennines, central Italy (Coccioni et al., 2012). (B) Present-day location of the PLG core (generated from the GEOMAR Web site, http://www.odsn.de/odsn/services/paleomap/paleomap.html, Kiel, Germany). (C) Palaeogeographic reconstruction showing location of PLG core at 125 Ma (generated from the GEOMAR website, Kiel, Germany).

7.3 Materials and methods

The drilling operation at Poggio le Guaine produced a 98.72-m-long record with 100% recovery of undisturbed drill cores 8 cm in diameter. At the drilling site, outcropping beds strike 310° with a dip of 0–40° to the northeast (Coccioni et al., 2012). After tilting correction, the complete stratigraphic thickness of the PLG core is 96.02 m. For palaeomagnetic purposes, the core was split into two halves along the dip line of the strata (Figures 7.2A and 7.2B). The left side (archived) of the core (Figure 7.2B) was plastic-coated, packed and housed at the University of Urbino, Italy. The right side (working half) of the core (Figure 7.2B) was cut into four parts, comprising two lateral sections, a bottom section and the centre of the split-core (Figure 7.2C). The two lateral sections were sent to Petrobras (Rio de Janeiro, Brazil) for geochemistry and petrology analyses. The centre of the split core and bottom sections were sent to University of São Paulo (São Paulo, Brazil) for palaeomagnetic analyses. Discrete cubic samples were cut from the centre of the split core sections in cubes of ~8 cm^3 (Figure 7.2D) for alternating field (AF) and environmental magnetism analyses. The bottom section was cut to give sister specimens for thermal demagnetization (Figure 7.2D).

After palaeomagnetic measurements were performed at the Palaeomagnetic Laboratory of the University of São Paulo, carbon- and oxygen-isotope analyses of the carbonate fraction ($\delta^{13}C$ and $\delta^{18}O$) were performed at the University of Oxford (UK); 75 bulk rock samples from the interval 86–96 m of PLG core were used in this study. A rotary drill was used in order to sample powder from the cubes used for magnetostratigraphic measurements (Figure 7.2E). Although the sample interval was defined as 10 cm, the mean interval sampled was 16 cm, since some lithologies could

not be cut into cubes; furthermore, some samples did not contain enough carbonate for isotopic analyses. During sampling, veins likely containing diagenetic carbonate were avoided. However, veins from two samples were analysed in order to illustrate the differences between their isotopic composition and that of the matrix. A total of 13 triplicates and 1 quadruplicate of the same powder were used in order to evaluate the variability in isotopic determinations.

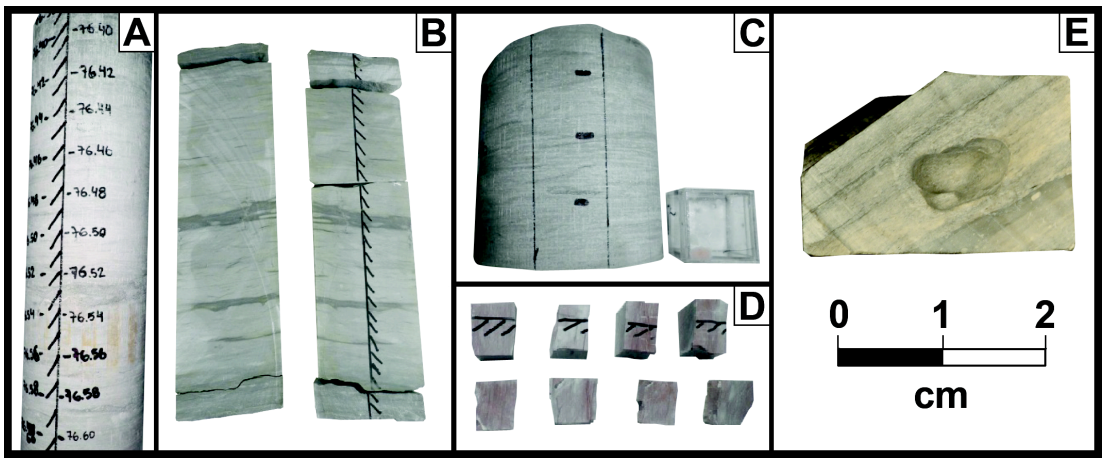


Figure 7 .2 – Photographs of the core and palaeomagnetic samples collected during the drilling of the Poggio le Guaine (PLG) core. (A) Part of the core recovered at Poggio le Guaine; (B) Photo of the whole core cut in two halves: left side is the archive and the right side is the working half; (C) Detail of the right side used for obtaining palaeomagnetic samples with the middle of split core; (D) Palaeomagnetic samples with dimensions of ~2 cm × 2 cm × 2 cm. (E) Detail of the hole in one of the samples, where a rotary drill was used to sample powder for isotope analysis.

The powders were analysed using a VG Isogas Prism II mass spectrometer with an online VG Isocarb common acid-bath preparation system. All samples were cleaned using acetone [$(CH_3)_2CO$] and dried at 60°C for at least 30 min. In the instrument, they were reacted with purified phosphoric acid (H_3PO_4) at 90°C. The calibration was undertaken using the Oxford in-house Carrara marble standard (NOCZ). Data are reported relative to the Vienna Pee Dee Belemnite (VPDB) scale.

The reproducibilities of replicated standards (1σ) were <0.06‰ for $\delta^{13}C$ and <0.09‰ for $\delta^{18}O$.

7.4 Results

7.4.1 Biostratigraphy and Magnetostratigraphy

All the planktonic foraminiferal zones from the uppermost Barremian to the Lower Aptian have been recognized in this core (Savian et al., 2016 and references therein). The following main biostratigraphic events (bioevents) were identified and correlated with the planktonic foraminiferal biozones (from bottom to top). The interval from the base of the core up to 91.50 m falls within the planktonic foraminiferal *Hedbergella excelsa* Zone (latest Barremian to Early Aptian) (Figure 7.3). This interval zone is defined by ranges from the first occurrence (FO) of the nominal taxon to the FO of the planktonic foraminifera *Leupoldina cabri* (Coccioni et al., 2007). The interval between 91.50 and 87.28 m represents the total range zone of the planktonic foraminifera *L. cabri* spanning an interval from early to Late Aptian (Fig. 7.3). In terms of calcareous nannofossils the studied interval of the Poggio le Guaine section spans the interval from the *Chiastozygus litterarius* (NC6; from the base of the core to 88.53 m) to the *Rhagodiscus angustus* (NC7; from 88.53 m to the top) Zones (Fig. 7.3).

Characteristic remanent magnetization allowed recognition of seven samples with reversed directions between 92.7 and 95.1 m in the PLG core, whereas all other samples have normal directions. Therefore, the three intervals are recognized (Figure 7.3): a basal one with normal-polarity chronozone (96.0–95.1 m); an intermediate

one with a reversed-polarity chronozone (95.1–92.7 m) and; an upper interval (92.7–87.3 m) with normal-polarity chronozone.

7.4.2 Carbon- and oxygen-isotope stratigraphy

The $\delta^{13}C$ and $\delta^{18}O$ values are shown in Figure 7.3. Of 75 samples used in this study, 7 did not yield gas for analyses, since they did not have enough carbonate content. All these samples come from the interval between 91 and 89 m where the black shales of the Selli Level are present. Of the 68 samples analysed, two were sampled twice. These samples have millimetric veins of carbonate, which it was possible to analyse (red points in Figure 7.3). In addition, 14 powders were analysed more than once, one in quadruplicate and 13 in triplicate (green points in Figure 7.3); 99 analyses with results were obtained (Table 7.1 in Appendix E).

The $\delta^{13}C$ values varied between 0.59‰ and 4.64‰ and $\delta^{18}O$ values range from –3.47‰ to 0.16‰ (Figure 7.3). However, the veins showed atypical values compared to the matrix by having higher $\delta^{18}O$ values and lower $\delta^{13}C$ values (Table 7.2). So, if these samples are considered as diagenetic artifacts, the values for primary lithologies vary between 1.69‰ and 4.64‰ for $\delta^{13}C$ and –3.47‰ and –1.52‰ for $\delta^{18}O$. These results reinforce the supposition that veinlets should be avoided during the sampling in this section, since they have compositions different from the matrix.

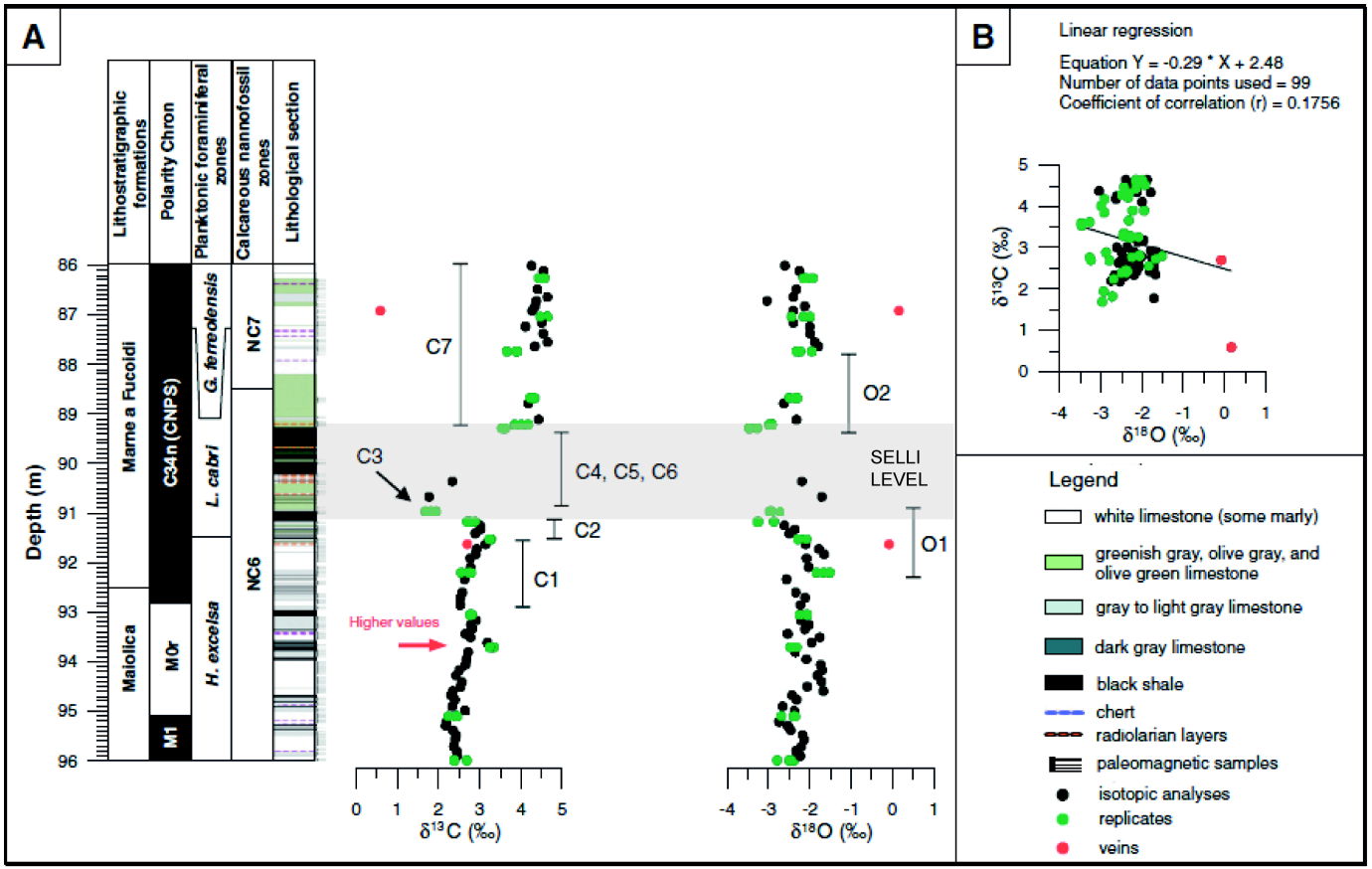


Figure 7 .3 – (A) Magnetostratigraphy, biostratigraphy, and lithostratigraphy of the Poggio le Guaine core showing the $\delta^{13}C$ and $\delta^{18}O$ of the bulk carbonate matrix (black circles), replicates (green circles), and veins (red circles). Labels C1–C7 and O1–O2 are the patterns defined by Menegatti et al. (1998) based on $\delta^{13}C$ and $\delta^{18}O$ curves discussed in the text. CNPS–Cretaceous Normal Polarity Superchron; *H.–Hedbergella*; *L.–Leupoldina*; *G.–Globigerinelloides*. (B) Cross-plot of mean oxygen and carbon isotope ratios.

Table 7.2 – Carbon- and oxygen-isotope composition of matrix and vein at the same depth.

Depth (m)	Subsample	$\delta^{13}C$ (‰)	$\delta^{18}O$ (‰)
86.92	Matrix	4.27	–2.41
	Vein	0.59	0.16
91.63	Matrix	3.14	–2.10
	Vein	2.70	–0.08

The 14 powders analysed more than once (one in quadruplicate and 13 in triplicate) showed a maximum difference between $\delta^{13}C$ values of 0.32‰ and a maximum difference between $\delta^{18}O$ values of 0.45‰ (Table 7.3). These results suggest an analytical variability of ±0.16‰ for $\delta^{13}C$ and ±0.23‰ for $\delta^{18}O$. All replicate measurements are given in Figure 7.3 (green points) in order to show this impact on the stratigraphic variability of the samples analysed. It is apparent that these values are an order magnitude lower than the stratigraphic range (~3‰ for $\delta^{13}C$ and ~2‰ for $\delta^{18}O$).

A cross-plot of $\delta^{13}C$ versus $\delta^{18}O$ shows weak correlation (Figure 7.3) with a coefficient of correlation (R) equal to 0.1756. This relationship implies that the processes by which carbon isotopes were fractionated are different from the processes that fractionated oxygen isotopes. As is typically the case with pelagic carbonates, $\delta^{13}C$ values are probably only little changed by diagenesis whereas $\delta^{18}O$ values can show considerable modification because the ratio of oxygen in pore waters to oxygen in initially porous carbonate sediment is high, unlike the situation with carbon (Scholle and Arthur, 1980; Marshall, 1992; Jenkyns et al., 1994).

Table 7.3 – $\delta^{13}C$ and $\delta^{18}O$ values of quadruplicate and triplicate analyses obtained and the maximum difference between values obtained

Depth (m)	Max $\delta^{13}C$ (‰)	Min $\delta^{13}C$ (‰)	Range $\delta^{13}C$ (‰)	Max $\delta^{18}O$ (‰)	Min $\delta^{18}O$ (‰)	Range $\delta^{18}O$ (‰)
86.26*	4.57	4.43	0.14	–1.93	–2.15	0.22
87.04	4.64	4.47	0.17	–1.99	–2.44	0.45
87.74	3.90	3.66	0.24	–1.95	–2.32	0.37
88.68	4.33	4.22	0.11	–2.31	–2.50	0.20
89.22	4.17	3.85	0.32	–2.92	–2.98	0.07
89.29	3.62	3.54	0.08	–3.27	–3.47	0.20
90.97	1.94	1.69	0.25	–2.72	–2.97	0.24
91.17	2.88	2.70	0.19	–2.87	–3.27	0.40
91.53	3.28	3.23	0.04	–2.09	–2.29	0.20
92.20	2.79	2.55	0.24	–1.52	–1.84	0.32
93.05	2.82	2.77	0.05	–2.06	–2.25	0.19
93.71	3.34	3.24	0.10	–2.32	–2.47	0.15
95.10	2.46	2.24	0.22	–2.35	–2.69	0.34
95.99	2.69	2.38	0.31	–2.38	–2.79	0.41
Maximum difference			0.32			0.45

Note: Max – maximum value obtained for that sample; Min – minimum value obtained for that sample; Range – difference between maximum and minimum value obtained in each sample.

* Sample analysed in quadruplicate. The others just have triplicate analyses.

Although there are sparse data between 91 and 87.73 m, the $\delta^{13}C$ log shows almost the same pattern observed in deep-sea pelagic sections from the same interval of time (e. g., Menegatti et al., 1998). The basal part of the section shows a trend of decreasing $\delta^{13}C$ from 96m (~2.5‰) to 95.29m (2.18‰) followed by increasing $\delta^{13}C$ values from 95.29m up to 93.05m (~2.80‰). The latter trend is interrupted by an interval ~93.61–93.70m, where there are higher values (~3.18–3.30‰) in a dark marl. Given the objectives of this chapter, it is possible to recognize almost all the isotopic patterns defined by Menegatti et al. (1998) for the Early Aptian. Segment C1 is recognized where values increase from ~2.50‰ (92.85 m) to ~3.25‰ (91.53 m). Stratigraphically higher, $\delta^{13}C$ values decrease to 90.97 m, where they reach ~1.8‰. This decrease corresponds to the C2 segment and these minimum values at 90.97 m

and 90.67 m define the C3 segment. Upward, $\delta^{13}C$ values increase up to 89.11 m (~4.43‰). At this depth is the base of the C7 segment, which continues up to 86 m. It is difficult to define the limits of segments C4, C5 and C6 in this study, because the stable values of C5 were not recognized. However, the negative excursion of the C3 segment followed by the increase of values to the C6 segment is the interval where the black shales occur in other sections.

Isotopic signatures similar to C1 to C7 obtained in carbonates and organic matter from pelagic and hemipelagic sediments and platform carbonate sediments have been identified in several northern and southern European (Tethyan) locations such as Roter Sattel section (Switzerland), Cismon section and core, Gorgo a Cerbara section (northern and central Italy), Calabianca section (Sicily, Italy), Gargano (southern Italy), Vocontian Basin (southeast France), Lower Saxony Basin (northwest Germany), Yenicesihlar section (central Turkey), the Prebetic (southern Spain), and sections in Mexico and Atlantic deep-sea drilling sites (Menegatti et al., 1998; Bralower et al., 1999; Erba et al., 1999; Hochuli et al., 1999; Luciani et al., 2001; Bellanca et al., 2002; de Gea et al., 2003; Wissler et al., 2003; Erba, 2004; Heimhofer et al., 2004; Herrle et al., 2004; Méhay et al., 2009; Stein et al., 2011; Bottini and Mutterlose, 2012; Hu et al., 2012b; Westermann et al., 2013; Pauly et al., 2013). In addition, similar profiles have been obtained from terrestrial organic matter in both English and Japanese sections and in shallow-water and pelagic carbonates cored in deep-sea drilling sites from the central Pacific and exposed at outcrop in accreted terrains (Jenkyns, 1995; Gröcke et al., 1999; Jenkyns and Wilson, 1999; Ando et al., 2002; Dumitrescu and Brassell, 2006; Robinson et al., 2008; Bottini et al., 2015; Erba et al., 2015). Hence, the isotopic signatures associated with

the black shales indicate that the interval between 90.97 m and 89.11 m (1.86m) unambiguously records OAE 1a in this section.

With respect to oxygen isotope values, there is a small decrease followed by an increase between 96.00 m and 94.50 m over the range –3.0 to –1.5‰; values then decrease gradually to ~–2.5‰ up to 92.20 m. Higher in the section, the O1 and O2 segments defined by Menegatti et al. (1998) can also be recognized. The O1 segment displays a decrease of $\delta^{18}O$ values between 92.20m (~–1.7‰) and 91.17m (~–3.0‰), whereas the O2 segment shows an increase of $\delta^{18}O$ values between 89.28m (~–3.4‰) and 87.63m (~–1.80‰). However, there are two samples (at 90.35 and 90.37m) that display higher values (–1.71‰ and –2.19‰) between the segments O1 and O2. Above the segment O2, the values do not show any significant trend, albeit varying between –3.04 and –1.88‰. The broad O1 and O2 signatures were interpreted as related to sea-surface temperature by Menegatti et al. (1998).

7.5 Discussion

The ISEA event systematically coincides with the *Globigerinelloides algerianus* biostratigraphical zone of Late Aptian age (Tarduno, 1990). In the PLG drill core, the *G. algerianus* zone lies at 85–80 m, thus well above the interval 95.1–92.7 m where the reversed polarity has been found. The reversed interval described here coincides instead with the *H. excelsa* Zone of Barremian–Aptian age (Coccioni et al., 2012). The biostratigraphy and magnetostratigraphy combined allow us confidently to exclude the possibility of a misinterpretation of the M0r as being the ISEA event in the PLG drill core.

The age of the magnetic polarity interval M0r, and consequently, the OAE 1a interval, has been much debated; estimates vary from 125 to 114 Ma (e. g., Cande

and Kent, 1995; Gradstein et al., 2004; Fiet et al., 2006; He et al., 2008). The top of the M0r chron has been calibrated at 125.93 Ma, and its duration has been estimated as 0.4 my, from magnetostratigraphy and cyclostratigraphy (Ogg et al., 2012, and references therein). The age of M0r is a key point for constructing the M-sequence magnetic polarity time scale and one of the most important stage boundaries in the Cretaceous because of its close relationship with intriguing geological events (e. g., CNPS and the OAE 1a; e. g., Helsley and Steiner, 1969; Larson and Erba, 1999; Ogg, 2012). The massive volcanism that formed the Ontong Java Plateau has been suggested as the driving force for widespread ocean anoxia, based on palaeoecological evidence from calcareous nannofossils, trace-element patterns, and osmium-isotope ratios of Lower Aptian sediments (Erba, 1994; Larson and Erba, 1999; Tejada et al., 2009; Bottini et al., 2012; Erba et al., 2015). These changes led to the deposition of thick, laminated, organic-rich black shales to form an interval known as the Selli Level and its correlatives (Coccioni et al., 1987). The ages of Ontong Java Plateau basalt flows have been determined by ^{40}Ar-^{39}Ar and ^{187}Re-^{186}Re; the Ar-Ar ages range from 124 to 121 Ma (Tejada et al., 1996, 2002; Chambers et al., 2004), close to the estimated age of the Selli Level and compatible with a causative link between ocean anoxia and massive volcanism (Mahoney et al., 1993; Tejada et al., 2002, 2009). An Re-Os date for the Selli Level itself is given as 120 ± 3.4 Ma (Bottini et al., 2012), in agreement with the age of M0r at the base (122.0 ± 0.5 Ma) given by He et al. (2008). This result matches better with the timescale of Malinverno et al. (2012), who fix the base of the Aptian at 121.54 Ma, than with the timescale of Ogg et al. (2012). The Selli Level black shale is the sedimentary expression of OAE 1a (Schlanger and Jenkyns, 1976; Jenkyns, 1980; Arthur et al., 1990). In the PLG drill-core, this characteristic lithology is 195 cm

thick, ranging from 91.19 to 89.24 m and occurs just above the M0r chron, which spans the 95.1–92.7 m interval (Figures 7.4).

The Early Aptian OAE 1a is marked by a negative excursion followed by a positive excursion in marine and terrestrial $\delta^{13}C$ records worldwide. In the PLG core, the $\delta^{13}C$ curve shows similar characteristics to the OAE 1a as recognized at other sites in the Tethyan realm (Figures 7.3 and 7.4). The negative shift in $\delta^{13}C$ at 90.97–90.67 m and the onset of the positive excursion at 90.36–89.11 m in the PLG core correspond to the pattern found between 896.0 and 897.7 m at the Gorgo a Cerbara section (Lowrie and Alvarez, 1984; Coccioni et al., 1992; Channell et al., 2000; Stein et al., 2011) and between 18.77 and 23.68 m in the Cismon core (Erba et al., 1999) (Figure 7.4).

The tie-lines represented by M0r and the records of OAE 1a interval correlates the PLG core with the Gorgo a Cerbara section and the Cismon core (Figure 7.4). The M0r interval corresponds to the 893.4–895.1 m interval at Gorgo a Cerbara section, and 25.75–29.17 m in the Cismon core (Figure 7.4). In summary, it has been demonstrated the presence of the Chron M0r in the Poggio le Guaine core that provides a magnetostratigraphic and the carbon isotope excursions that define OAE 1a. These results offer two tie points at the base of the PLG core for dating respectively the Barremian-Aptian boundary and OAE 1a.

The Selli Level recognized in the PLG core is a regional feature in the Tethyan realm, especially in deep waters where lithological contrast between black shales from Selli Level and pelagic carbonates. This chapter adds data for a well-studied expression of the OAE 1a, which has been identified in the transition from continental to shallow-water marine environment in the central segment of the South

Atlantic (Chapters 2 to 5). It highlights how the records from the South Atlantic are different from the Tethyan realm.

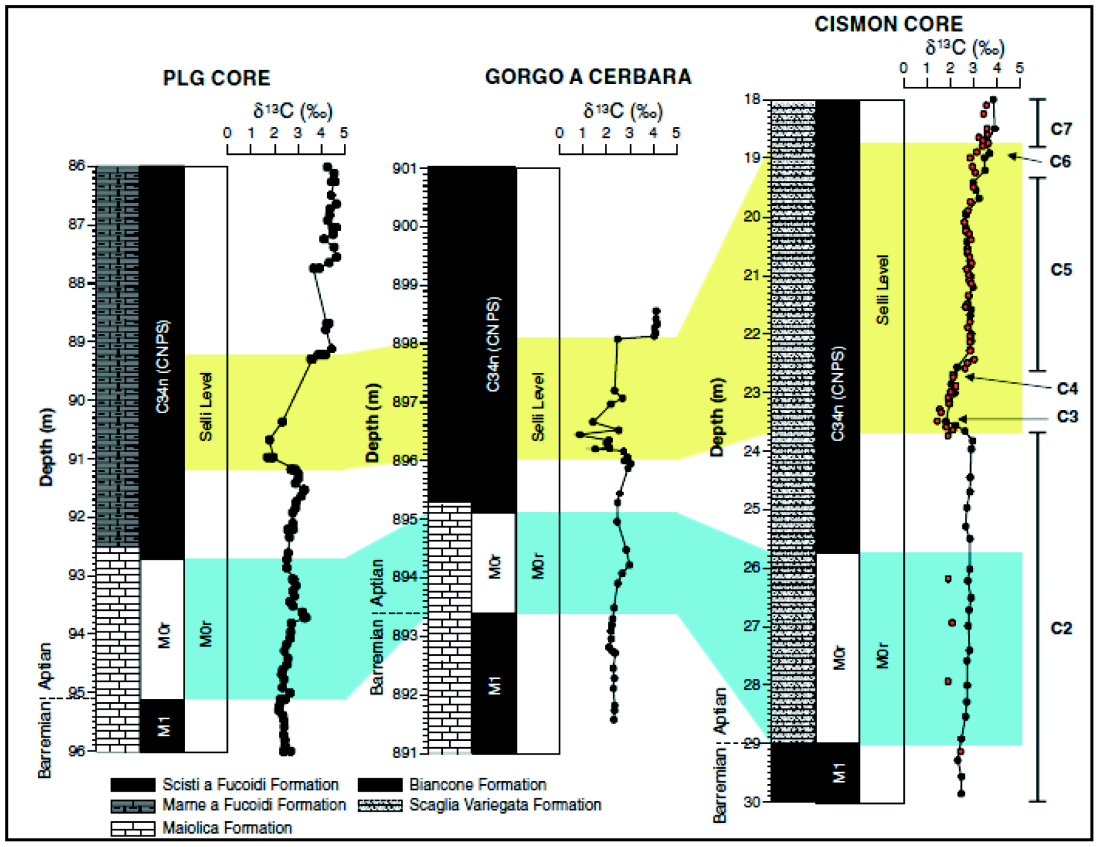


Figure 7 .4 – The correlation of the Selli Level event to polarity chrons for the Poggio le Guaine (PLG) and Cismon cores, and the Gorgo a Cerbara section from the Umbria–Marche Basin. The area shaded in yellow is the entire interval of the Selli Level. The blue area represents the magnetic polarity Chron M0r in the different sections. The lithostratigraphy, magnetostratigraphy and chemostratigraphy are after several sources (Lowrie and Alvarez, 1984; Menegatti et al., 1998; Coccioni et al., 1992; Erba et al., 1999; Channell et al., 2000; Satolli et al., 2007, 2008; Stein et al., 2011).

7.6 Conclusions

The investigation of the uppermost Barremian–Lower Aptian Maiolica and Marne a Fucoidi Formations from the PLG core (Northern Apennines, Italy) has provided the carbon-isotope records of the OAE 1a and the polarity chron M0r in this

locality. This result, integrated with biostratigraphic data, documents the Barremian-Aptian boundary. Above the Barremian-Aptian boundary, the $\delta^{13}C$ record shows a negative shift and a subsequent positive excursion similar to that documented from elsewhere in the Tethyan realm. OAE 1a is lithologically represented by the Selli Level, the origin of which has been linked to volcanic episodes that formed the Ontong Java large igneous province, which forced the rapid increase of atmospheric pCO_2 triggering a cascade of palaeoenvironmental changes affecting plankton productivity and carbon flux to the sea floor (Jenkyns, 2010; Erba et al., 2015). Further insights into these events and related regional climate changes in the Tethyan realm will be gained through future palaeoenvironmental studies of the PLG core.

Chapter 8

Summary and outlook

8.1 Summary of the stratigraphic correlations

A new stratigraphic correlation of the South Atlantic indicates synchrony between major evaporite deposition in the southern Brazilian basins and the OAE 1a interval based on carbon, sulphur and strontium isotopes ($\delta^{13}C$, $\delta^{34}S$ and $^{87}Sr/^{86}Sr$), integrated with other methods (biostratigraphy and Re-Os geochronology). The new $\delta^{13}C$ and $^{87}Sr/^{86}Sr$ curves are integrated with new planktonic foraminiferal biostratigraphy from Petrobras Well CB-3 and correlated with a $\delta^{13}C$ Santos/Campos composite curve and age-calibrated Tethyan composite carbon-isotope curve. This stratigraphic correlation, presented in Chapter 2, has constrained evaporite deposition in southern Brazilian basins to be significantly older (~125 or ~120 Ma) than their former suggested age of 116–111 Ma. In addition, most of post-evaporite carbonates described and discussed in Chapter 2 are Aptian in age rather than Early Albian, as currently suggested in the literature. A new Re-Os age of 117.5 ± 2.5 Ma from an organic-rich carbonate, sampled ~0.3–0.5 m below the base of the evaporites in Petrobras Well B from the Santos Basin, described in Chapter 3, is compatible with the stratigraphic correlation presented in Chapter 2, linking deposition of the upper part of the pre-Salt carbonates, and the evaporites themselves, with OAE 1a. Further evidence is presented by $\delta^{34}S$ values at the base of South Atlantic evaporites, as described in Chapter 4, which have the same values as contemporaneous global

Aptian seawater, and support an OAE 1a age equivalency with the time of onset of evaporite deposition.

Chapter 5 presents a new stratigraphic correlation of the northern part of the central segment of the South Atlantic with recognition of OAE 1a based on $\delta^{13}C$ derived from organic matter integrated with pollen biostratigraphy. The deposition of siliciclastic rocks in the Sergipe-Alagoas Basin, northeast Brazil, in the northern part of the central segment of the South Atlantic, is suggested to have been synchronous with evaporite formation in the southern Brazilian basins and OAE 1a. However, the relationship between the evaporite deposits from the northern and southern Brazilian basins remains ambiguous, because the evaporites from the Sergipe-Alagoas Basin could be either synchronous or younger than those from the southern Brazilian basins.

The stratigraphic correlation is extended to DSDP Site 511 on the Falkland Plateau in Chapter 6 based on integration of different methods: nannofossil calcareous biostratigraphy, magnetostratigraphy, total inorganic and organic-carbon (TOC and TIC), Rock-Eval pyrolysis, sulphur content of organic matter (S_{OM}), carbon-isotope ratios of carbonate and organic matter, strontium- and oxygen-isotope ratios of carbonate, and Re-Os geochronology. Data suggest that deposition of an organic-rich black shale took place from the mid-Jurassic up to the Barremian–Early Aptian interval, which is represented by a hiatus/condensed section. The typical isotopic record of OAE 1a is missing either due to incomplete core recovery and/or a hiatus, although its latter part (C6 segment) could be represented. Therefore, most black-shale sedimentation on the Falkland Plateau took place before deposition of evaporites in the Campos and Santos Basins that formed during the Early Aptian OAE 1a time interval and before the opening of the central segment of the South

Atlantic. It is also shown that Upper Aptian sediments with intermediate TOC values and relatively high terrestrial organic-matter content lie above the hiatus/condensed section at DSDP Site 511 and, thus, are partially coeval with shallow- and deep-water post-evaporite carbonates from the Santos and Campos Basins. Local records of OAE 1b, including the Jacob, Kilian and Paquier Levels, are tentatively recognized in DSDP Site 511 based on their carbon-isotope signature but without the organic-rich levels that are typically recognized in the Tethyan realm.

Finally, Chapter 7 reinforces the stratigraphic correlation between South Atlantic and Tethyan realm by the identification of the reversed-polarity Chron M0r and the Early Aptian OAE 1a interval, based on carbon and oxygen isotopes, integrated with planktonic biostratigraphy, in the Selli Level at the base of the Poggio le Guaine core, Umbria-Marche Basin, northern Apennines, Italy.

8.2 Environmental evolution of southern Brazilian basins

The new $^{87}Sr/^{86}Sr$ data provided in Chapters 2, 3 and 4 reveal new insights into the environmental evolution of southern Brazilin basins in the southern part of the central segment of South Atlantic. The data from pre-Salt carbonates from three different Petrobras Wells A and B (Santos Basin) and C (Campos Basin) presented in Chapter 3 suggest that they were deposited in a continental setting until the onset of evaporite precipitation. The fluids that fed the lakes, where pre-Salt carbonates were deposited, are suggested to have derived from rivers and groundwaters draining felsic and feldspar-bearing siliciclastic rocks exposed on the flanks of the basin. New $^{87}Sr/^{86}Sr$ measurements of anhydrites from the Santos Basin presented in Chapter 4 yield higher values than contemporaneous Aptian seawater but lower than the estimated continental input. These data suggest a rapid entrance of seawater into the

South Atlantic basin post-dating deposition of pre-Salt carbonates. However, it was not possible to define whether or not the development of fully marine conditions corresponded in time to the base or the top of the evaporites. The $^{87}Sr/^{86}Sr$ data from post-evaporite carbonates from Petrobras Well CB-3 presented in Chapter 2 are somewhat higher than contemporaneous seawater values, even though they derive from typical shallow-marine facies. The atypical $^{87}Sr/^{86}Sr$ ratios in this well could be explained by relatively high input of continental water into southern Brazilian basins whose $^{87}Sr/^{86}Sr$ ratios were similar to those found in pre-Salt carbonates, as described in Chapter 4. To sum up: the pre-Salt carbonates were likely to have been deposited in a continental environment; the evaporites mark the first main entrance of marine waters into the central segment of the South Atlantic; and post-evaporite carbonates are the expression of typical shallow-marine environments.

8.3 Relationship between Ontong Java Plateau, absolute ages and evaporite deposits in the southern segment of the South Atlantic

OAE1a is lithologically represented by the Selli Level, the origin of which has been linked to volcanic episodes that formed the Ontong Java Plateau Large Igneous Province (LIP), which released massive amounts of CO_2 and SO_2, thereby triggering a cascade of palaeoenvironmental changes affecting plankton productivity and carbon flux to the sea floor, as discussed throughout the thesis. The absolute ages of the Early Aptian OAE 1a and reversal Chron M0r are still a matter of disagreement in the literature because of different time scales currently in play, as discussed in Chapters 3, 6 and 7. The new Re-Os age of 117.5 ± 2.5 Ma from pre-Salt carbonates correlated with OAE 1a is in agreement with time scale of

Malinverno (2012). On the other hand, the reversed-polarity chron at the top of core 59 from DSDP Site 511, just above sediments with the new Re-Os age of 125.3 ± 2.2 Ma within the calcareous nannofossil *Chiastozygus litterarius* biozone (NC6), could imply that this interval is M0r, which agrees better with the time scale of Ogg et al. (2012) than that of Malinverno et al. (2012). Alternatively, the reversed-polarity interval identified in this study could be reversed-polarity Chrons M1r or M3r, and imply that the base of *Chiastozygus litterarius* biozone (NC6), as defined in DSDP Site 511, could be older than Chron M1r or M3r.

Relatively elevated Hg/TOC ratios within the carbonates ~1.4 m below the evaporite base (Chapter 4) suggest an input of volcanic Hg and imply a possible link with the main eruption(s) of the Ontong Java Plateau. This event could have triggered a eustatic sea-level rise and the first entrance of seawater into the South Atlantic basin at the onset of evaporite formation. It is also suggested that the cyclic pattern recognized in the evaporites of gypsum/halite/more soluble salts are likely to have been driven by aquifer-eustasy in the (supposedly ice-free) Cretaceous greenhouse climate. Significantly, deposition of the South Atlantic evaporites led to a parallel decrease in the global sulphate inventory, hence lessening overall sulphate reduction in the world ocean during and after OAE 1a, allowing enhanced preservation of organic matter at many globally distributed localites.

8.4 Future directions

The results of this thesis open doors to many possible directions for future research. The first concerns the duration of the Aptian Stage itself and the disagreement between time scales must be pursued. Detailed integration of Aptian sections worldwide with different stratigraphic methods, considering all possible

pitfalls, could help in this regard. Integrated stratigraphic studies of Aptian sections together with new radiometric ages and cyclo-, magneto-, planktonic bio- and chemostratigraphy of the most complete records are required. Unfortunately, the absence of one or more of these key elements results in a fragmentary picture, in which stratigraphic mis-correlation can lead to misinterpretation. These difficulties affect not only the time scale but also the dating of the reversed-polarity Chrons of the M-sequence down to the Jurassic, which is tied to M0r.

The impact of evaporite deposition on palaeoceonagraphy during and after OAE 1a is also a new avenue for future research. The data presented are limited to few locations and new stratigraphic records of OAE 1a in the South Atlantic would be extremely helpful. The stratigraphic correlation between the southern and northern Brazilian basins and with African evaporites needs further refinement to constrain the timing of their deposition in different locations in order to estimate the volumes of gypsum, anhydrite and halite present in the central segment of the South Atlantic. Furthermore, new models involving the geochemical elements buried in the evaporites could be useful to constrain the impact on ocean chemistry. For example, the amount of strontium buried in evaporites, and consequently its impact on its global inventory, is unknown. What might be the impact on the residence time of this element in the world ocean after deposition of the South Atlantic evaporites?

Turning to the South Atlantic, the entrance of the seawater from south to the north or in the opposite direction needs better stratigraphic constraints in both regions. The correlation between local stages defined by ostracod and pollen biostratigraphy in continental environments of the South Atlantic with international stratigraphic charts needs to be re-evaluated by studying other sections with detailed integrated stratigraphy (bio-, magneto- and chemostratigraphy and radiometric ages).

An improved stratigraphy could potentially be used to revaluate the changing palaeoreconstruction and palaeoceanography during the opening of the South Atlantic. Wider investigation of black-shale stratigraphy in locations south of the Brazilian Basins, as recorded in the DSDP Site 511 on the Falkland Plateau, could help evaluate the relative roles of local basin geometry, as opposed to globally forced productivity changes, in the Cretaceous South Atlantic.

Appendix A

Table 2.1 (Chapter 2)

$\delta^{13}C_{carb}$ and $\delta^{18}O_{carb}$ data from Petrobras Well CB-3. Samples that have not undergone to oil extraction are shown in red. Lab –laboratory, mbsl – metres below sea level, UO – University of Oxford, UERJ – Universidade do Estado do Rio de Janeiro.

Depth (mbsl)	$\delta^{13}C_{carb}$ (‰)	$\delta^{18}O_{carb}$ (‰)	Lab
2436.75	1.96	–3.25	UERJ
2437.25	2.19	–4.25	UERJ
2437.45	2.25	–3.24	UERJ
2438.00	2.22	–3.09	UERJ
2438.10	2.06	–3.37	UERJ
2438.60	1.18	–3.69	UERJ
2438.60	1.28	–3.73	UERJ
2439.25	2.07	–3.85	UERJ
2439.85	2.21	–3.65	UERJ
2440.26	2.36	–4.34	UERJ
2440.70	2.14	–3.71	UERJ
2441.20	1.69	–3.92	UERJ
2441.65	1.63	–3.37	UERJ
2442.00	1.89	–4.29	UERJ
2442.87	2.29	–2.44	UERJ
2443.35	1.70	–2.75	UERJ
2443.83	1.73	–4.03	UERJ
2443.83	2.16	–3.83	UERJ
2444.14	2.87	–2.70	UERJ
2444.85	3.04	–3.44	UERJ
2445.15	1.86	–3.50	UERJ
2445.55	1.70	–4.17	UERJ
2446.10	3.02	–3.41	UERJ
2446.60	1.78	–4.23	UERJ
2447.20	2.19	–2.94	UERJ
2447.70	1.12	–3.72	UERJ
2448.55	2.65	–3.87	UERJ
2449.23	1.52	–3.83	UERJ
2449.23	1.77	–3.77	UERJ
2449.70	1.76	–2.57	UERJ
2450.00	2.94	–2.79	UERJ
2450.80	3.33	–2.94	UERJ
2451.30	3.65	–2.99	UERJ
2452.00	2.94	–2.92	UERJ
2452.45	2.37	–2.16	UERJ

Depth (mbsl)	$\delta^{13}C_{carb}$ (‰)	$\delta^{18}O_{carb}$ (‰)	Lab
2436.75	2.03	–3.11	UO
2436.75	2.01	–2.94	UO
2441.20	2.19	–3.40	UO
2442.87	1.75	–3.46	UO
2443.35	2.18	–4.04	UO
2443.83	2.07	–3.82	UO
2444.14	2.89	–2.91	UO
2444.85	2.98	–3.30	UO
2445.15	2.47	–3.37	UO
2445.55	1.81	–3.96	UO
2446.10	3.13	–3.10	UO
2446.10	3.16	–2.89	UO
2446.10	3.30	–3.32	UO
2446.60	1.88	–4.06	UO
2447.20	2.51	–2.98	UO
2447.70	1.10	–3.62	UO
2448.55	2.69	–3.88	UO
2449.23	1.65	–3.74	UO
2449.70	1.58	–3.57	UO
2450.00	3.00	–2.82	UO
2450.80	3.38	–2.93	UO
2451.30	3.71	–2.97	UO
2452.00	3.43	–2.89	UO
2452.00	3.53	–2.97	UO
2452.45	2.55	–2.17	UO
2452.60	3.90	–2.54	UO
2453.27	4.01	–2.21	UO
2454.20	3.48	–2.43	UO
2454.70	2.82	–2.24	UO
2455.30	3.36	–2.27	UO
2456.15	2.69	–2.15	UO
2456.80	3.79	–2.70	UO
2457.65	4.52	–2.33	UO
2458.17	2.77	–3.04	UO
2458.17	2.87	–3.12	UO

Depth (mbsl)	$\delta^{13}C_{carb}$ (‰)	$\delta^{18}O_{carb}$ (‰)	Lab
2452.60	2.81	–2.46	UERJ
2453.27	3.01	–1.65	UERJ
2454.20	2.83	–2.42	UERJ
2454.70	2.66	–2.23	UERJ
2454.70	2.64	–2.25	UERJ
2455.30	2.84	–2.39	UERJ
2456.15	2.70	–2.18	UERJ
2456.80	3.08	–2.65	UERJ
2457.65	3.23	–2.37	UERJ
2458.17	2.76	–2.96	UERJ
2458.77	3.90	–2.37	UERJ
2459.75	3.19	–2.59	UERJ
2460.20	2.79	–2.45	UERJ
2460.60	2.40	–1.99	UERJ
2460.95	3.77	–2.51	UERJ
2460.95	3.48	–2.54	UERJ
2461.90	2.80	–2.78	UERJ
2462.80	2.91	–2.11	UERJ
2463.55	4.29	–1.91	UERJ
2464.07	4.91	–2.44	UERJ
2464.98	3.05	–2.07	UERJ
2465.25	2.56	–1.74	UERJ
2466.00	3.74	–2.38	UERJ
2466.35	2.63	–1.90	UERJ
2466.60	2.61	–2.33	UERJ
2467.90	2.49	–2.31	UERJ
2467.90	2.53	–2.19	UERJ
2469.05	3.21	–2.16	UERJ
2469.40	3.32	–2.52	UERJ
2469.50	2.77	–2.04	UERJ
2470.78	2.80	–1.97	UERJ
2471.05	3.18	–2.19	UERJ
2471.75	3.04	–1.47	UERJ
2472.15	3.13	–2.21	UERJ
2472.45	2.83	–2.46	UERJ
2472.90	3.20	–1.56	UERJ
2473.45	2.92	–2.25	UERJ
2473.45	2.98	–2.29	UERJ
2474.20	3.86	–2.11	UERJ
2474.50	3.96	–1.50	UERJ
2474.65	3.39	–1.67	UERJ
2475.15	3.60	–2.02	UERJ

Depth (mbsl)	$\delta^{13}C_{carb}$ (‰)	$\delta^{18}O_{carb}$ (‰)	Lab
2458.17	2.98	–2.91	UO
2458.77	5.13	–2.20	UO
2459.75	4.14	–2.37	UO
2460.20	3.38	–2.53	UO
2460.60	2.44	–1.95	UO
2460.95	4.11	–2.37	UO
2461.90	3.22	–2.70	UO
2462.80	3.65	–2.28	UO
2463.55	5.23	–1.86	UO
2464.07	6.68	–1.94	UO
2464.07	7.07	–1.83	UO
2464.98	3.41	–2.05	UO
2465.25	2.75	–1.76	UO
2466.00	3.51	–2.37	UO
2466.35	2.55	–2.03	UO
2466.60	2.61	–2.49	UO
2467.90	2.63	–2.17	UO
2469.05	3.05	–2.47	UO
2469.40	3.18	–2.62	UO
2469.50	2.67	–2.11	UO
2470.78	2.68	–2.12	UO
2471.05	3.03	–2.25	UO
2471.05	3.00	–2.35	UO
2471.05	3.01	–2.38	UO
2471.75	2.89	–1.60	UO
2472.15	2.92	–2.22	UO
2472.45	2.74	–2.52	UO
2472.90	3.04	–1.65	UO
2473.45	2.90	–2.36	UO
2474.20	3.80	–1.89	UO
2474.50	3.99	–1.27	UO
2474.65	3.28	–1.69	UO
2475.15	3.43	–2.04	UO
2475.40	3.45	–2.14	UO
2475.40	3.59	–1.89	UO
2476.05	3.23	–2.06	UO
2476.15	3.41	–2.21	UO
2477.15	3.16	–1.89	UO
2477.60	3.45	–1.61	UO
2478.20	3.00	–2.35	UO
2478.40	3.43	–1.74	UO
2482.10	3.43	–1.71	UO

Depth (mbsl)	$\delta^{13}C_{carb}$ (‰)	$\delta^{18}O_{carb}$ (‰)	Lab
2475.40	3.48	–2.25	UERJ
2476.05	3.37	–2.03	UERJ
2476.15	3.59	–2.12	UERJ
2477.15	3.30	–1.81	UERJ
2477.60	3.63	–1.61	UERJ
2478.20	3.14	–2.32	UERJ
2478.20	2.99	–2.39	UERJ
2478.40	3.67	–1.57	UERJ
2482.10	3.12	–2.20	UERJ
2482.60	3.10	–1.89	UERJ
2482.95	2.75	–2.35	UERJ
2483.50	3.48	–1.86	UERJ
2499.30	4.34	–2.28	UERJ
2500.30	3.23	–1.89	UERJ
2501.00	3.08	–2.32	UERJ
2501.80	3.85	–2.33	UERJ
2503.00	3.77	–2.04	UERJ
2503.00	3.80	–2.43	UERJ
2504.90	3.30	–2.61	UERJ
2505.90	4.10	–2.37	UERJ
2506.70	3.97	–2.36	UERJ
2507.70	4.06	–2.37	UERJ
2508.70	4.17	–2.47	UERJ
2510.15	4.13	–2.52	UERJ
2512.60	4.37	–2.60	UERJ
2516.50	4.12	–2.03	UERJ
2517.80	4.43	–2.61	UERJ
2518.55	4.84	–2.93	UERJ
2518.55	4.61	–2.73	UERJ
2519.80	4.40	–3.06	UERJ
2520.90	4.54	–2.73	UERJ
2521.35	4.48	–2.57	UERJ
2522.50	4.30	–3.27	UERJ
2528.40	4.46	–2.04	UERJ
2531.80	4.60	–2.73	UERJ
2533.55	4.70	–2.71	UERJ
2536.50	4.97	–2.97	UERJ
2540.32	4.44	–2.42	UERJ
2541.40	4.47	–2.78	UERJ
2541.40	4.58	–2.06	UERJ
2543.45	4.62	–2.91	UERJ
2546.08	4.41	–2.82	UERJ

Depth (mbsl)	$\delta^{13}C_{carb}$ (‰)	$\delta^{18}O_{carb}$ (‰)	Lab
2482.60	2.94	–1.90	UO
2482.95	2.89	–2.19	UO
2483.50	3.25	–1.89	UO
2483.50	3.23	–1.86	UO
2499.30	4.08	–2.33	UO
2500.30	3.05	–1.83	UO
2501.00	2.92	–2.28	UO
2501.80	3.67	–2.39	UO
2503.00	3.54	–2.43	UO
2504.90	3.10	–2.75	UO
2505.90	3.85	–2.37	UO
2506.70	3.87	–2.34	UO
2507.70	3.84	–2.49	UO
2508.70	3.79	–2.53	UO
2508.70	3.93	–2.53	UO
2510.15	4.02	–2.53	UO
2512.60	4.18	–2.69	UO
2516.50	3.92	–2.98	UO
2517.80	4.19	–2.63	UO
2518.55	4.44	–2.84	UO
2519.80	4.14	–3.14	UO
2520.90	4.28	–2.81	UO
2521.35	4.22	–2.63	UO
2522.50	4.19	–3.00	UO
2528.40	4.28	–2.68	UO
2528.40	4.52	–2.55	UO
2533.55	4.47	–2.72	UO
2536.50	4.67	–2.84	UO
2540.32	4.26	–2.47	UO
2541.40	4.35	–2.65	UO
2543.45	4.31	–2.88	UO
2546.08	4.14	–2.54	UO
2547.90	4.22	–2.61	UO
2549.16	4.19	–2.66	UO
2549.50	4.15	–2.66	UO
2549.50	4.24	–2.52	UO
2551.00	4.15	–2.43	UO
2552.90	4.11	–2.51	UO
2556.80	4.29	–2.34	UO
2557.90	4.21	–2.55	UO
2558.80	4.15	–2.44	UO
2559.80	4.10	–2.43	UO

Depth (mbsl)	$\delta^{13}C_{carb}$ (‰)	$\delta^{18}O_{carb}$ (‰)	Lab
2547.90	4.45	–2.83	UERJ
2549.16	4.36	–2.79	UERJ
2549.50	4.40	–2.65	UERJ
2551.00	4.32	–2.71	UERJ
2552.90	4.37	–2.56	UERJ
2556.80	4.61	–2.26	UERJ
2557.90	4.25	–2.64	UERJ
2558.80	4.33	–2.54	UERJ
2558.80	4.21	–2.63	UERJ
2559.80	4.25	–2.50	UERJ
2560.50	4.25	–2.47	UERJ
2561.73	4.47	–2.83	UERJ
2562.70	4.22	–2.75	UERJ
2564.00	4.14	–1.93	UERJ
2564.60	4.08	–2.39	UERJ
2566.00	4.09	–2.39	UERJ
2566.90	4.23	–2.54	UERJ
2567.30	4.21	–2.50	UERJ
2568.00	4.10	–2.63	UERJ
2568.00	4.21	–2.54	UERJ
2569.50	4.18	–2.03	UERJ
2570.30	4.31	–2.49	UERJ
2574.40	4.68	–2.47	UERJ
2575.20	4.77	–2.60	UERJ
2576.40	4.57	–2.25	UERJ
2577.15	4.57	–2.74	UERJ
2578.40	4.37	–2.73	UERJ
2579.10	4.32	–2.75	UERJ
2580.35	4.34	–2.92	UERJ
2581.50	4.41	–3.04	UERJ
2581.50	4.39	–3.02	UERJ
2582.30	4.34	–3.01	UERJ
2584.33	4.32	–3.15	UERJ
2584.75	4.45	–2.78	UERJ
2586.20	4.58	–2.70	UERJ
2587.42	4.38	–2.65	UERJ
2587.90	4.34	–3.16	UERJ
2588.25	4.35	–2.48	UERJ
2588.90	4.50	–2.48	UERJ
2589.80	4.74	–2.62	UERJ
2591.40	4.57	–2.69	UERJ
2591.40	4.52	–2.74	UERJ

Depth (mbsl)	$\delta^{13}C_{carb}$ (‰)	$\delta^{18}O_{carb}$ (‰)	Lab
2560.50	4.13	–2.30	UO
2561.73	4.32	–2.78	UO
2562.70	4.04	–2.72	UO
2564.00	3.84	–2.45	UO
2564.00	3.92	–2.43	UO
2564.60	3.93	–2.33	UO
2566.00	3.90	–2.50	UO
2566.90	4.00	–2.58	UO
2567.30	3.95	–2.54	UO
2568.00	3.92	–2.54	UO
2569.50	3.96	–2.51	UO
2570.30	4.13	–2.55	UO
2574.40	4.45	–2.47	UO
2575.20	4.45	–2.69	UO
2576.40	4.32	–2.63	UO
2576.40	4.34	–2.59	UO
2577.15	4.36	–2.79	UO
2578.40	4.14	–2.73	UO
2579.10	4.08	–2.86	UO
2580.35	4.19	–2.69	UO
2581.50	4.04	–3.04	UO
2582.30	4.14	–3.07	UO
2584.33	4.14	–3.01	UO
2584.75	4.18	–2.93	UO
2586.20	4.35	–2.41	UO
2587.42	4.24	–2.60	UO
2587.42	4.27	–2.16	UO
2587.90	4.11	–3.13	UO
2594.40	4.20	–3.15	UO
2595.40	4.38	–2.84	UO
2596.00	4.23	–2.91	UO
2596.00	4.45	–3.03	UO
2597.00	4.10	–3.31	UO
2610.80	3.93	–3.28	UO
2614.40	4.09	–3.43	UO
2618.20	4.54	–3.54	UO
2622.90	4.27	–3.37	UO
2625.90	3.97	–3.64	UO
2630.30	3.74	–3.48	UO
2634.20	3.91	–3.61	UO
2637.60	3.93	–3.83	UO
2641.40	3.82	–3.66	UO

Depth (mbsl)	$\delta^{13}C_{carb}$ (‰)	$\delta^{18}O_{carb}$ (‰)	Lab
2592.40	4.58	–2.57	UERJ
2593.55	4.56	–2.78	UERJ
2594.40	4.35	–2.96	UERJ
2595.40	4.40	–2.86	UERJ
2596.00	4.52	–2.92	UERJ
2597.00	4.29	–3.03	UERJ
2650.60	4.23	–3.52	UERJ
2651.20	4.48	–3.44	UERJ
2652.60	4.27	–3.41	UERJ
2653.10	4.16	–3.51	UERJ
2653.10	4.24	–3.55	UERJ
2654.20	3.95	–3.76	UERJ
2655.40	4.21	–3.56	UERJ
2656.00	4.18	–3.59	UERJ
2656.40	3.93	–3.83	UERJ
2657.85	4.22	–3.72	UERJ
2658.55	4.38	–3.07	UERJ
2659.70	4.22	–3.57	UERJ
2660.80	4.12	–3.84	UERJ
2661.80	4.03	–4.02	UERJ
2670.70	4.34	–4.07	UERJ
2670.70	4.52	–3.84	UERJ
2671.70	4.47	–4.11	UERJ
2672.65	4.28	–4.24	UERJ
2674.55	4.14	–4.22	UERJ
2675.40	4.26	–3.91	UERJ
2676.80	4.30	–4.12	UERJ
2677.50	4.22	–4.17	UERJ
2678.60	4.26	–4.19	UERJ
2679.40	4.36	–3.50	UERJ
2680.00	4.21	–3.95	UERJ
2680.00	4.16	–4.04	UERJ
2681.30	4.10	–4.07	UERJ
2682.20	4.51	–2.80	UERJ
2682.95	4.25	–4.06	UERJ
2684.15	4.88	–2.27	UERJ
2685.40	4.11	–3.99	UERJ
2686.25	4.16	–4.05	UERJ
2687.00	4.18	–4.02	UERJ
2688.50	4.04	–4.03	UERJ
2689.10	3.96	–4.01	UERJ

Depth (mbsl)	$\delta^{13}C_{carb}$ (‰)	$\delta^{18}O_{carb}$ (‰)	Lab
2644.20	4.09	–3.69	UO
2650.60	4.17	–3.65	UO
2651.20	4.41	–3.29	UO
2652.60	4.18	–3.38	UO
2653.10	4.18	–3.44	UO
2654.20	4.06	–3.66	UO
2655.40	3.99	–4.00	UO
2656.00	4.12	–3.74	UO
2656.40	3.98	–3.72	UO
2657.85	4.01	–3.57	UO
2657.85	4.15	–3.65	UO
2658.55	4.32	–3.09	UO
2659.70	4.39	–3.12	UO
2660.80	4.15	–3.69	UO
2661.80	4.12	–4.01	UO
2670.70	4.43	–4.03	UO
2671.70	4.46	–3.88	UO
2672.65	4.27	–4.11	UO
2673.50	4.42	–3.69	UO
2674.55	4.13	–4.13	UO
2675.40	4.00	–3.83	UO
2675.40	4.19	–3.97	UO
2676.80	4.23	–4.12	UO
2677.50	4.15	–4.31	UO
2678.60	4.18	–4.11	UO
2679.40	4.45	–3.18	UO
2680.00	4.19	–4.12	UO
2681.30	4.01	–4.20	UO
2682.20	4.07	–4.04	UO
2682.95	4.19	–4.28	UO
2684.15	4.20	–3.91	UO
2685.40	4.03	–3.85	UO
2685.40	4.13	–4.07	UO
2686.25	4.01	–4.12	UO
2687.00	4.11	–4.07	UO
2688.50	3.95	–4.07	UO
2689.10	3.83	–4.39	UO

Table 2.2 (Chapter 2)

Element content (Al, Ca, Mg, Si, K, Fe, Mn, Rb and Sr) from Petrobras Well CB–3. Samples that have not undergone to oil extraction are shown in red. DL – detection limit, mbsl – metres below sea level.

Depth (mbsl)	Al % wt DL=0.2	Ca % wt DL=0.2	Mg % wt DL=3	Si % wt DL=0.2	K % wt DL=0.3	Fe % wt DL=0.1	Mn ppm DL=15	Rb ppm DL=3	Sr ppm DL=21
2452.45	0.8	33.0	<3	6.9	0.3	1.1	594	17	415
2454.70	1.1	33.1	<3	8.0	0.4	1.3	379	21	445
2456.15	0.8	34.7	<3	5.6	0.3	0.8	289	17	538
2460.60	0.5	37.4	<3	3.7	<0.3	0.6	214	12	575
2466.35	1.7	30.9	<3	6.4	0.9	1.3	200	37	455
2469.40	0.9	35.2	<3	4.1	0.6	1.0	144	22	626
2472.90	1.2	34.5	<3	4.4	0.6	0.9	144	24	609
2476.05	2.1	29.7	<3	7.0	1.2	1.8	130	41	737
2478.40	0.5	38.3	<3	2.0	<0.3	0.7	90	12	700
2483.50	0.8	36.5	<3	2.8	0.4	0.7	88	15	581
2499.30	1.1	35.0	<3	3.4	0.5	1.0	110	21	456
2501.80	1.2	35.0	<3	3.9	0.5	1.0	80	19	400
2506.70	0.9	37.2	<3	2.7	0.3	0.6	48	12	405
2507.70	0.6	37.6	<3	2.4	0.3	0.6	48	11	403
2508.70	0.6	39.5	<3	2.1	<0.3	0.5	47	9.4	374
2510.15	0.3	39.0	<3	1.8	<0.3	0.4	40	8.6	347
2512.60	0.7	38.1	<3	2.5	0.3	0.6	51	13	390
2516.50	<0.3	41.1	<3	0.6	<0.3	0.1	25	4.3	299
2517.80	0.3	39.6	<3	1.2	<0.3	0.3	22	10	334
2518.55	<0.3	39.3	<3	1.0	<0.3	0.2	31	6.8	305
2519.80	<0.3	40.5	<3	0.8	<0.3	0.2	29	5.5	302
2520.90	0.3	40.0	<3	1.3	<0.3	0.3	27	10	340
2521.35	0.5	38.1	<3	1.9	<0.3	0.5	36	12	343
2522.50	<0.3	41.2	<3	0.5	<0.3	0.1	22	3.4	308
2528.40	<0.3	39.8	<3	0.7	<0.3	0.2	20	3.7	609
2547.90	0.5	37.7	<3	2.0	<0.3	0.5	44	11	625
2551.00	0.3	38.5	<3	1.4	<0.3	0.4	34	7.4	896
2552.90	<0.3	38.8	<3	1.3	<0.3	0.4	31	7.2	867
2556.80	0.4	36.0	<3	1.6	<0.3	0.5	44	9.0	819
2558.80	0.4	38.4	<3	1.3	<0.3	0.4	38	7.5	520
2562.70	<0.3	39.9	<3	1.0	<0.3	0.3	38	5.7	441
2566.90	<0.3	38.7	<3	0.9	<0.3	0.3	33	4.9	427
2570.30	0.3	39.5	<3	1.1	<0.3	0.3	31	6.4	446
2574.40	<0.3	38.5	<3	1.1	<0.3	0.3	27	6.0	400
2577.15	<0.3	39.9	<3	0.8	<0.3	0.3	37	4.8	397

Depth (mbsl)	Al % wt DL=0.2	Ca % wt DL=0.2	Mg % wt DL=3	Si % wt DL=0.2	K % wt DL=0.3	Fe % wt DL=0.1	Mn ppm DL=15	Rb ppm DL=3	Sr ppm DL=21
2581.50	0.6	36.6	<3	2.2	<0.3	0.6	51	10	674
2586.20	0.4	36.4	<3	1.8	<0.3	0.5	49	9.1	845
2589.80	0.2	38.0	<3	1.0	<0.3	0.2	29	5.0	814
2594.40	0.4	37.8	<3	1.7	<0.3	0.4	35	8.6	638
2597.00	0.4	38.5	<3	1.2	<0.3	0.3	29	7.1	407
2598.00	0.3	38.9	<3	1.3	<0.3	0.1	<15	<3	411
2603.20	<0.3	38.9	<3	0.8	<0.3	0.1	<15	<3	364
2607.30	0.5	37.1	<3	1.5	<0.3	0.1	<15	4.3	425
2610.80	0.4	38.5	<3	1.4	<0.3	0.1	<15	4.4	435
2614.40	<0.3	38.7	<3	0.3	<0.3	<0.1	<15	<3	342
2618.20	<0.3	38.3	<3	0.5	<0.3	0.1	15	<3	343
2622.90	<0.3	38.0	<3	1.1	<0.3	0.2	<15	4.9	439
2625.90	<0.3	38.4	<3	0.3	<0.3	0.1	<15	<3	302
2630.30	<0.3	38.7	<3	0.5	<0.3	0.1	<15	<3	421
2634.20	<0.3	39.3	<3	0.3	<0.3	0.1	<15	<3	398
2637.60	<0.3	39.7	<3	0.1	<0.3	<0.1	<15	<3	330
2641.40	<0.3	39.7	<3	0.1	<0.3	<0.1	<15	<3	425
2644.20	<0.3	38.3	<3	0.4	<0.3	0.1	<15	3.1	387
2647.60	<0.3	40.1	<3	0.3	<0.3	0.1	16	4.1	351
2650.60	<0.3	38.4	<3	0.8	<0.3	0.2	29	4.2	528
2651.00	<0.3	37.0	<3	0.9	<0.3	0.2	21	5.5	509
2654.20	<0.3	38.4	<3	0.8	<0.3	0.2	20	4.4	552
2656.40	<0.3	36.7	<3	1.0	<0.3	0.3	28	7.1	720
2658.55	<0.3	34.7	<3	0.9	<0.3	0.3	19	4.0	646
2661.80	<0.3	40.3	<3	0.5	<0.3	0.1	<15	<3	423
2670.70	<0.3	36.5	<3	0.6	<0.3	0.2	19	<3	367
2671.70	<0.3	38.1	<3	0.6	<0.3	0.2	24	3.3	473
2672.65	<0.3	41.1	<3	0.3	<0.3	0.1	20	2.3	420
2677.50	<0.3	39.3	<3	1.0	<0.3	0.3	24	4.7	437
2681.30	<0.3	39.7	<3	0.7	<0.3	0.2	17	4.3	452
2685.40	<0.3	38.7	<3	0.7	<0.3	0.2	25	3.6	456

Table 2.3 (Chapter 2)

Strontium-isotope ratios obtained during this study ($^{87}Sr/^{86}Sr_n$) and calculated $^{87}Sr/^{86}Sr_i$ (113 Ma), $^{87}Sr/^{86}Sr_i$ (124 Ma) and $(^{87}Sr/^{86}Sr)_{i-s}$ from Petrobras Well CB–3. Samples that have not undergone to oil extraction are shown in red. SE – standard error of the mean, mbsl – metres below sea level.

Depth (mbsl)	Material	$^{87}Sr/^{86}Sr_n$	2SE	Count	$^{87}Sr/^{86}Sr_i$ (113 Ma)	$^{87}Sr/^{86}Sr_i$ (124 Ma)	$^{87}Sr/^{86}Sr_{i-S}$ (124 Ma)
2452.45	Limestone	0.707746	0.000014	48	0.707556	0.707538	0.707528
2454.70	Limestone	0.707675	0.000009	47	0.707460	0.707439	0.707428
2456.15	Limestone	0.707665	0.000011	49	0.707524	0.707511	0.707503
2460.60	Limestone	0.707595	0.000009	47	0.707501	0.707492	0.707487
2466.35	Limestone	0.707692	0.000009	46	0.707326	0.707290	0.707271
2469.40	Limestone	0.707680	0.000011	48	0.707524	0.707508	0.707500
2472.90	Limestone	0.707588	0.000010	47	0.707407	0.707389	0.707380
2473.45	*Lenticulina*	0.707630	0.000009	48			
2473.45	*Lenticulina*	0.707628	0.000011	50			
2476.05	Limestone	0.707571	0.000009	46	0.707320	0.707296	0.707283
2478.40	Limestone	0.707558	0.000014	49	0.707481	0.707474	0.707470
2482.10	*Lenticulina*	0.707549	0.000009	48			
2482.10	*Lenticulina*	0.707573	0.000010	47			
2482.10	*Lenticulina*	0.707555	0.000010	48			
2482.94A	*Lenticulina*	0.707497	0.000011	46			
2482.94B	*Lenticulina*	0.707606	0.000009	48			
2482.94B	*Lenticulina*	0.707604	0.000010	48			
2482.94B	*Lenticulina*	0.707617	0.000010	48			
2483.50	Limestone	0.707691	0.000012	48	0.707572	0.707561	0.707554
2499.30	Limestone	0.707685	0.000011	48	0.707480	0.707460	0.707449
2499.30	*Lenticulina*	0.707539	0.000011	48			
2501.80	Limestone	0.707787	0.000010	47	0.707574	0.707553	0.707542
2506.70	Limestone	0.707737	0.000019	47	0.707600	0.707587	0.707579
2505.90A	*Lenticulina*	0.707506	0.000014	41			
2505.90A	*Lenticulina*	0.707502	0.000010	48			
2505.90A	*Lenticulina*	0.707512	0.000010	48			
2505.90B	*Lenticulina*	0.707552	0.000010	49			
2505.90B	*Lenticulina*	0.707531	0.000011	47			
2507.70	Limestone	0.707728	0.000013	47	0.707599	0.707587	0.707580
2508.70	Limestone	0.707671	0.000014	47	0.707557	0.707546	0.707540
2510.15	Limestone	0.707602	0.000012	48	0.707490	0.707479	0.707473
2512.60	Limestone	0.707629	0.000013	48	0.707481	0.707466	0.707458
2512.60	*Lenticulina*	0.707550	0.000012	49			
2512.60	*Lenticulina*	0.707541	0.000011	48			
2512.60	*Lenticulina*	0.707527	0.000009	47			
2516.50	Limestone	0.707723	0.000026	47	0.707659	0.707652	0.707649

Depth (mbsl)	Material	$^{87}Sr/^{86}Sr_n$	2SE	Count	$^{87}Sr/^{86}Sr_i$ (113 Ma)	$^{87}Sr/^{86}Sr_i$ (124 Ma)	$^{87}Sr/^{86}Sr_{i-S}$ (124 Ma)
2517.80	Limestone	0.707615	0.000015	48	0.707479	0.707466	0.707459
2518.55	Limestone	0.707545	0.000011	47	0.707444	0.707434	0.707429
2519.80	Limestone	0.707573	0.000010	48	0.707491	0.707483	0.707478
2520.90	Limestone	0.707573	0.000008	46	0.707434	0.707421	0.707413
2521.35	Limestone	0.707595	0.000014	48	0.707443	0.707428	0.707420
2522.50	Limestone	0.707635	0.000017	46	0.707585	0.707580	0.707578
2528.40	Limestone	0.707479	0.000017	49	0.707452	0.707449	0.707447
2528.40	Limestone	0.707472	0.000008	48	0.707444	0.707441	0.707440
2547.90	Limestone	0.707551	0.000011	47	0.707472	0.707464	0.707460
2551.00	Limestone	0.707473	0.000013	48	0.707436	0.707432	0.707430
2551.00	Limestone	0.707457	0.000011	48	0.707420	0.707416	0.707414
2552.90	Limestone	0.707489	0.000013	47	0.707452	0.707448	0.707446
2556.80	Limestone	0.707571	0.000015	46	0.707522	0.707517	0.707514
2557.15	*Lenticulina*	0.707691	0.000013	31			
2558.80	Limestone	0.707451	0.000010	48	0.707386	0.707379	0.707376
2558.80	Limestone	0.707514	0.000009	46	0.707449	0.707442	0.707439
2562.70	Limestone	0.707545	0.000012	49	0.707487	0.707481	0.707478
2566.90	Limestone	0.707639	0.000012	48	0.707588	0.707583	0.707580
2570.30	Limestone	0.707525	0.000009	46	0.707460	0.707454	0.707450
2574.40	Limestone	0.707534	0.000013	49	0.707466	0.707459	0.707456
2574.40	*Lenticulina*	0.707584	0.000010	47			
2577.15	Limestone	0.707644	0.000011	48	0.707589	0.707584	0.707581
2581.50	Limestone	0.707541	0.000009	48	0.707472	0.707465	0.707461
2586.20	Limestone	0.707537	0.000009	45	0.707488	0.707483	0.707481
2589.80	Limestone	0.707516	0.000011	48	0.707488	0.707486	0.707484
2592.40	*Lenticulina*	0.707547	0.000012	49			
2593.55	*Lenticulina*	0.707456	0.000012	40			
2593.55	*Lenticulina*	0.707498	0.000011	45			
2593.55	*Lenticulina*	0.707452	0.000011	47			
2594.20	*Lenticulina*	0.707455	0.000009	48			
2594.40	Limestone	0.707549	0.000013	49	0.707488	0.707482	0.707479
2597.00	Limestone	0.707516	0.000009	49	0.707437	0.707429	0.707425
2598.00	Limestone	0.707612	0.000008	44	0.707579	0.707576	0.707574
2603.20	Limestone	0.707536	0.000009	38	0.707498	0.707495	0.707493
2607.30	Limestone	0.707481	0.000011	48	0.707435	0.707431	0.707428
2610.80	Limestone	0.707553	0.000012	49	0.707507	0.707502	0.707500
2614.40	Limestone	0.707510	0.000009	39	0.707470	0.707467	0.707464
2618.20	Limestone	0.707652	0.000009	47	0.707612	0.707608	0.707606
2622.90	Limestone	0.707602	0.000008	48	0.707552	0.707547	0.707545
2625.90	Limestone	0.707593	0.000009	48	0.707548	0.707543	0.707541
2630.30	Limestone	0.707533	0.000011	49	0.707501	0.707498	0.707496
2634.20	Limestone	0.707555	0.000008	47	0.707521	0.707517	0.707515

Depth (mbsl)	Material	$^{87}Sr/^{86}Sr_n$	2SE	Count	$^{87}Sr/^{86}Sr_i$ (113 Ma)	$^{87}Sr/^{86}Sr_i$ (124 Ma)	$^{87}Sr/^{86}Sr_{i-S}$ (124 Ma)
2637.60	Limestone	0.707550	0.000011	47	0.707509	0.707505	0.707503
2641.40	Limestone	0.707555	0.000011	48	0.707523	0.707520	0.707518
2644.20	Limestone	0.707560	0.000011	48	0.707524	0.707521	0.707519
2644.20	Limestone	0.707543	0.000010	48	0.707507	0.707503	0.707501
2647.60	Limestone	0.707681	0.000011	49	0.707628	0.707623	0.707620
2650.60	Limestone	0.707618	0.000011	49	0.707582	0.707578	0.707576
2651.00	Limestone	0.707561	0.000011	47	0.707511	0.707506	0.707504
2654.20	Limestone	0.707520	0.000010	47	0.707484	0.707480	0.707478
2656.40	Limestone	0.707557	0.000012	47	0.707512	0.707508	0.707506
2658.55	Limestone	0.707555	0.000012	48	0.707527	0.707524	0.707522
2661.80	Limestone	0.707783	0.000014	49	0.707751	0.707748	0.707746
2670.70	Limestone	0.707636	0.000011	49	0.707599	0.707596	0.707594
2671.70	Limestone	0.707567	0.000010	47	0.707535	0.707531	0.707530
2672.65	Limestone	0.707622	0.000013	48	0.707597	0.707595	0.707594
2677.50	Limestone	0.707605	0.000014	48	0.707556	0.707551	0.707549
2681.30	Limestone	0.707611	0.000011	49	0.707568	0.707564	0.707562
2685.40	Limestone	0.707617	0.000008	48	0.707581	0.707577	0.707575

Table 2.4 (Chapter 2)

Compilation of $\delta^{13}C_{carb}$ and $\delta^{18}O_{carb}$ and TOC from Petrobras Wells CP–5 and X (Dias, 1998; Quintaes, 2006).

Well	Penetrated depth (m)	Relative thickness (m)	$\delta^{13}C_{carb}$ (‰)	$\delta^{18}O_{carb}$ (‰)	TOC (wt %)	Formation
X	4668	3884	–0.29	–5.78	0.2	Itanhaém
X	4671	3881	0.37	–4.92	0.2	Itanhaém
X	4674	3878	0.36	–5.63	0.2	Itanhaém
X	4677	3875	–0.22	–4.21	0.2	Itanhaém
X	4680	3872	0.87	–4.10	0.2	Itanhaém
X	4683	3869	0.90	–4.22	0.2	Itanhaém
X	4686	3866	0.30	–4.66	0.2	Itanhaém
X	4689	3863	–0.30	–5.47	0.3	Itanhaém
X	4692	3860	0.59	–4.80	0.3	Itanhaém
X	4695	3857	0.24	–4.91	0.3	Itanhaém
X	4698	3854	–0.05	–4.51	0.2	Itanhaém
X	4701	3851	–0.08	–5.23	0.2	Guarujá
X	4704	3848	1.13	–4.87	0.1	Guarujá
X	4707	3845	2.52	–5.28	0.2	Guarujá
X	4710	3842	3.30	–5.08	0.1	Guarujá
X	4713	3839	3.06	–5.10	0.1	Guarujá
X	4716	3836	3.00	–5.00	0.1	Guarujá
X	4719	3833	3.42	–4.72	0.1	Guarujá
X	4722	3830	3.27	–5.37	0.1	Guarujá
X	4725	3827	3.40	–5.79	0.1	Guarujá
X	4728	3824	3.56	–6.42	0.1	Guarujá
X	4731	3821	3.72	–6.56	0.0	Guarujá
X	4734	3818	3.73	–6.95	0.1	Guarujá
X	4737	3815	3.80	–6.68	0.1	Guarujá
X	4740	3812	3.78	–6.52	0.4	Guarujá
X	4743	3809	3.63	–5.03	0.1	Guarujá
X	4746	3806	3.89	–5.58	0.0	Guarujá
X	4749	3803	4.03	–5.84	0.1	Guarujá
X	4752	3800	3.97	–5.33	0.1	Guarujá
X	4755	3797	3.84	–4.54	0.1	Guarujá
X	4758	3794	4.02	–5.47	0.1	Guarujá
X	4761	3791	4.08	–4.54	0.0	Guarujá
X	4764	3788	3.79	–4.83	0.1	Guarujá
X	4767	3785	3.68	–4.55	0.1	Guarujá
X	4770	3782	3.66	–5.16	0.1	Guarujá
X	4773	3779	3.90	–5.33	0.0	Guarujá
X	4776	3776	3.75	–5.03	0.1	Guarujá
X	4779	3773	3.89	–5.52	0.1	Guarujá
X	4782	3770	3.76	–3.86	0.1	Guarujá
X	4785	3767	3.92	–5.50	0.1	Guarujá
X	4788	3764	3.91	–5.20	0.1	Guarujá
X	4791	3761	3.95	–5.11	0.1	Guarujá
X	4794	3758	4.00	–5.32	0.1	Guarujá
X	4797	3755	4.11	–5.18	0.0	Guarujá

Well	Penetrated depth (m)	Relative thickness (m)	$\delta^{13}C_{carb}$ (‰)	$\delta^{18}O_{carb}$ (‰)	TOC (wt %)	Formation
X	4800	3752	3.81	–5.16	0.1	Guarujá
X	4803	3749	3.65	–5.39	0.2	Guarujá
X	4806	3746	3.90	–4.54	0.1	Guarujá
X	4809	3743	3.77	–4.62	0.1	Guarujá
X	4812	3740	3.95	–5.20	0.1	Guarujá
X	4815	3737	3.76	–4.78	0.1	Guarujá
X	4818	3734	3.76	–4.72	0.1	Guarujá
X	4821	3731	3.54	–4.72	0.1	Guarujá
X	4824	3728	3.26	–3.65	0.0	Guarujá
X	4827	3725	3.68	–4.92	0.1	Guarujá
X	4830	3722	3.91	–4.55	0.1	Guarujá
X	4833	3719	3.83	–4.89	0.1	Guarujá
X	4836	3716	3.82	–4.20	0.1	Guarujá
X	4839	3713	3.84	–5.06	0.0	Guarujá
X	4842	3710	3.71	–4.81	0.1	Guarujá
X	4845	3707	3.87	–5.10	0.1	Guarujá
X	4848	3704	3.76	–4.44	0.1	Guarujá
X	4851	3701	3.90	–4.80	0.0	Guarujá
X	4854	3698	3.76	–4.63	0.1	Guarujá
X	4857	3695	3.50	–4.67	0.1	Guarujá
X	4860	3692	3.81	–4.26	0.1	Guarujá
X	4863	3689	3.73	–4.93	0.1	Guarujá
X	4866	3686	3.82	–5.10	0.0	Guarujá
X	4869	3683	4.05	–5.00	0.1	Guarujá
X	4872	3680	4.03	–5.62	0.1	Guarujá
X	4875	3677	3.93	–5.52	0.1	Guarujá
X	4878	3674	3.80	–5.37	0.1	Guarujá
X	4881	3671	4.19	–5.08	0.1	Guarujá
X	4884	3668	3.83	–4.90	0.1	Guarujá
X	4887	3665	3.66	–5.18	0.2	Guarujá
X	4890	3662	3.89	–5.16	0.1	Guarujá
X	4893	3659	3.79	–5.02	0.1	Guarujá
X	4896	3656	3.96	–4.70	0.1	Guarujá
X	4899	3653	4.02	–4.90	0.1	Guarujá
X	4902	3650	3.76	–5.24	0.2	Guarujá
X	4905	3647	3.80	–5.42	0.2	Guarujá
X	4908	3644	3.62	–5.64	0.2	Guarujá
X	4911	3641	3.64	–5.63	0.1	Guarujá
X	4914	3638	3.77	–5.26	0.2	Guarujá
X	4917	3635	3.80	–5.42	0.2	Guarujá
X	4920	3632	3.74	–5.56	0.1	Guarujá
X	4923	3629	3.88	–4.92	0.1	Guarujá
X	4926	3626	3.71	–5.46	0.1	Guarujá
X	4929	3623	3.71	–4.96	0.1	Guarujá
X	4932	3620	3.76	–5.33	0.2	Guarujá
X	4935	3617	3.79	–5.24	0.1	Guarujá
X	4938	3614	3.70	–5.32	0.1	Guarujá
X	4941	3611	3.74	–5.05	0.2	Guarujá
X	4944	3608	3.64	–5.52	0.2	Guarujá
X	4947	3605	3.81	–5.40	0.2	Guarujá
X	4950	3602	3.70	–5.58	0.2	Guarujá
X	4953	3599	3.70	–5.55	0.2	Guarujá

Well	Penetrated depth (m)	Relative thickness (m)	$\delta^{13}C_{carb}$ (‰)	$\delta^{18}O_{carb}$ (‰)	TOC (wt %)	Formation
X	4956	3596	3.91	–5.23	0.2	Guarujá
X	4959	3593	3.84	–4.85	0.2	Guarujá
X	4962	3590	4.00	–5.58	0.2	Guarujá
X	4965	3587	3.90	–5.47	0.2	Guarujá
X	4968	3584	3.82	–5.29	0.2	Guarujá
X	4971	3581	3.88	–5.35	0.2	Guarujá
X	4974	3578	3.82	–5.35	0.2	Guarujá
X	4977	3575	3.61	–5.60	0.2	Guarujá
X	4980	3572	3.72	–5.30	0.2	Guarujá
X	4983	3569	3.99	–5.10	0.2	Guarujá
X	4986	3566	3.60	–5.32	0.2	Guarujá
X	4989	3563	3.74	–5.40	0.2	Guarujá
X	4992	3560	3.74	–5.38	0.2	Guarujá
X	4995	3557	3.74	–5.30	0.2	Guarujá
X	4998	3554	3.75	–5.53	0.2	Guarujá
X	5001	3551	3.76	–5.38	0.2	Guarujá
X	5004	3548	3.30	–5.55	0.2	Guarujá
X	5007	3545	3.60	–5.76	0.2	Guarujá
X	5010	3542	3.70	–5.86	0.2	Guarujá
X	5013	3539	3.69	–5.94	0.2	Guarujá
X	5016	3536	3.74	–6.02	0.2	Guarujá
X	5019	3533	3.68	–6.00	0.2	Guarujá
X	5022	3530	3.66	–5.69	0.2	Guarujá
X	5025	3527	3.62	–5.95	0.2	Guarujá
X	5028	3524	3.43	–5.85	0.2	Guarujá
X	5031	3521	3.62	–5.70	0.2	Guarujá
X	5034	3518	3.56	–5.72	0.2	Guarujá
X	5037	3515	3.57	–5.85	0.2	Guarujá
X	5040	3512	3.76	–5.45	0.2	Guarujá
X	5043	3509	3.55	–5.64	0.3	Guarujá
X	5046	3506	3.53	–5.78	0.2	Guarujá
X	5049	3503	3.51	–5.93	0.3	Guarujá
X	5052	3500	3.59	–5.66	0.4	Guarujá
X	5055	3497	3.68	–5.41	0.2	Guarujá
X	5058	3494	3.40	–5.54	0.2	Guarujá
X	5061	3491	3.49	–5.77	0.2	Guarujá
X	5064	3488	3.53	–5.74	0.2	Guarujá
X	5067	3485	3.74	–5.74	0.2	Guarujá
X	5070	3482	3.69	–6.04	0.3	Guarujá
X	5073	3479	3.74	–5.94	0.2	Guarujá
X	5076	3476	3.87	–5.59	0.3	Guarujá
X	5079	3473	3.77	–5.65	0.3	Guarujá
X	5082	3470	3.79	–5.50	0.2	Guarujá
X	5085	3467	3.74	–5.49	0.3	Guarujá
X	5088	3464	3.76	–5.58	0.2	Guarujá
X	5094	3458	3.95	–5.70	0.2	Guarujá
X	5097	3455	3.90	–5.49	0.2	Guarujá
X	5100	3452	3.46	–6.52	0.2	Guarujá
X	5103	3449	3.93	–5.97	0.2	Guarujá
X	5106	3446	3.85	–5.95	0.2	Guarujá
X	5109	3443	3.82	–5.70	0.2	Guarujá
X	5112	3440	3.72	–5.76	0.2	Guarujá

Well	Penetrated depth (m)	Relative thickness (m)	$\delta^{13}C_{carb}$ (‰)	$\delta^{18}O_{carb}$ (‰)	TOC (wt %)	Formation
X	5115	3437	3.83	–5.59	0.2	Guarujá
X	5118	3434	3.70	–5.68	0.2	Guarujá
X	5121	3431	3.66	–5.60	0.2	Guarujá
X	5124	3428	3.87	–5.30	0.2	Guarujá
X	5127	3425	3.75	–5.47	0.2	Guarujá
X	5130	3422	3.60	–5.65	0.2	Guarujá
X	5133	3419	3.60	–5.76	0.2	Guarujá
X	5136	3416	3.62	–6.00	0.2	Guarujá
X	5139	3413	3.58	–5.99	0.2	Guarujá
X	5142	3410	3.65	–5.65	0.2	Guarujá
X	5145	3407	3.58	–5.87	0.2	Guarujá
X	5148	3404	3.59	–5.61	0.2	Guarujá
X	5151	3401	3.35	–5.62	0.2	Guarujá
X	5154	3398	3.18	–5.64	0.2	Guarujá
X	5157	3395	3.44	–5.52	0.2	Guarujá
X	5160	3392	3.10	–5.94	0.2	Guarujá
X	5163	3389	3.09	–6.32	0.3	Guarujá
X	5166	3386	3.28	–5.99	0.2	Guarujá
X	5169	3383	2.98	–5.48	0.4	Guarujá
X	5172	3380	2.98	–5.41	0.2	Guarujá
X	5175	3377	3.21	–5.05	0.2	Guarujá
X	5178	3374	2.95	–5.42	0.3	Guarujá
X	5181	3371	2.85	–5.72	0.4	Guarujá
X	5184	3368	3.24	–5.32	0.3	Guarujá
X	5187	3365	2.91	–5.32	0.4	Guarujá
X	5190	3362	3.32	–5.28	0.3	Guarujá
X	5193	3359	3.48	–4.88	0.5	Guarujá
X	5196	3356	3.35	–4.09	0.3	Guarujá
X	5199	3353	3.19	–4.98	0.2	Guarujá
X	5202	3350	2.98	–4.49	0.2	Guarujá
X	5205	3347	2.97	–3.86	0.3	Guarujá
X	5208	3344	2.75	–3.68	0.3	Guarujá
X	5211	3341	3.41	–5.24	0.2	Guarujá
X	5214	3338	3.28	–4.96	0.2	Guarujá
X	5217	3335	3.22	–5.17	0.2	Guarujá
X	5220	3332	3.37	–4.54	0.2	Guarujá
X	5223	3329	2.76	–5.48	0.2	Guarujá
X	5226	3326	3.13	–4.99	0.2	Guarujá
X	5229	3323	3.40	–5.04	0.2	Guarujá
X	5232	3320	3.67	–4.60	0.2	Guarujá
X	5235	3317	3.51	–4.64	0.2	Guarujá
X	5238	3314	3.70	–3.76	0.2	Guarujá
X	5241	3311	3.80	–5.68	0.2	Guarujá
X	5244	3308	3.83	–5.34	0.3	Guarujá
X	5247	3305	4.01	–5.52	0.2	Guarujá
X	5250	3302	4.04	–4.87	0.2	Guarujá
X	5253	3299	3.86	–4.75	0.2	Guarujá
X	5256	3296	3.70	–4.48	0.2	Guarujá
X	5259	3293	3.53	–5.00	0.3	Guarujá
X	5262	3290	3.57	–5.19	0.2	Guarujá
X	5265	3287	3.65	–5.12	0.2	Guarujá
X	5268	3284	3.61	–4.79	0.2	Guarujá

Well	Penetrated depth (m)	Relative thickness (m)	$\delta^{13}C_{carb}$ (‰)	$\delta^{18}O_{carb}$ (‰)	TOC (wt %)	Formation
X	5271	3281	3.65	–5.35	0.2	Guarujá
X	5274	3278	3.78	–4.23	0.2	Guarujá
X	5277	3275	3.75	–4.23	0.2	Guarujá
X	5280	3272	3.53	–4.79	0.2	Guarujá
X	5283	3269	3.31	–4.67	0.2	Guarujá
X	5286	3266	3.32	–4.75	0.2	Guarujá
X	5289	3263	3.62	–4.22	0.2	Guarujá
X	5292	3260	3.57	–4.93	0.3	Guarujá
X	5295	3257	3.27	–5.02	0.3	Guarujá
X	5298	3254	3.33	–5.18	0.2	Guarujá
X	5301	3251	3.61	–4.86	0.3	Guarujá
X	5304	3248	3.35	–4.66	0.2	Guarujá
X	5307	3245	2.82	–5.76	0.2	Guarujá
X	5310	3242	3.56	–5.00	0.2	Guarujá
X	5313	3239	3.36	–5.09	0.1	Guarujá
X	5316	3236	3.50	–5.43	0.1	Guarujá
X	5319	3233	3.52	–4.97	0.3	Guarujá
X	5322	3230	3.59	–5.12	0.2	Guarujá
X	5325	3227	3.62	–5.07	0.2	Guarujá
X	5328	3224	3.61	–4.96	0.2	Guarujá
X	5331	3221	3.42	–4.48	0.2	Guarujá
X	5334	3218	2.79	–5.83	0.2	Guarujá
X	5337	3215	3.46	–4.46	0.2	Guarujá
X	5340	3212	3.26	–4.66	0.2	Guarujá
X	5343	3209	3.50	–4.77	0.2	Guarujá
X	5346	3206	3.57	–4.62	0.2	Guarujá
X	5349	3203	3.41	–5.08	0.2	Guarujá
X	5352	3200	3.42	–5.51	0.2	Guarujá
X	5355	3197	3.54	–5.25	0.2	Guarujá
X	5358	3194	3.71	–5.23	0.2	Guarujá
X	5361	3191	3.68	–5.32	0.2	Guarujá
X	5364	3188	3.44	–5.15	0.2	Guarujá
X	5367	3185	3.57	–5.07	0.1	Guarujá
X	5370	3182	3.79	–4.50	0.1	Guarujá
X	5373	3179	3.61	–4.84	0.3	Guarujá
X	5376	3176	3.52	–4.70	0.2	Guarujá
X	5379	3173	3.34	–4.95	0.1	Guarujá
X	5382	3170	3.37	–5.05	0.2	Guarujá
X	5385	3167	3.33	–4.95	0.2	Guarujá
X	5388	3164	3.49	–4.92	0.2	Guarujá
X	5391	3161	3.49	–5.22	0.2	Guarujá
X	5394	3158	3.48	–5.07	0.2	Guarujá
X	5397	3155	3.41	–5.06	0.2	Guarujá
X	5400	3152	3.18	–5.27	0.3	Guarujá
X	5403	3149	3.15	–4.90	0.2	Guarujá
X	5406	3146	3.09	–5.25	0.2	Guarujá
X	5409	3143	3.02	–4.76	0.2	Guarujá
X	5412	3140	3.36	–5.00	0.2	Guarujá
X	5415	3137	3.35	–4.73	0.2	Guarujá
X	5418	3134	3.54	–4.90	0.2	Guarujá
X	5421	3131	3.35	–4.96	0.2	Guarujá
X	5424	3128	3.29	–4.73	0.2	Guarujá

Well	Penetrated depth (m)	Relative thickness (m)	$\delta^{13}C_{carb}$ (‰)	$\delta^{18}O_{carb}$ (‰)	TOC (wt %)	Formation
X	5427	3125	3.25	–4.85	0.3	Guarujá
X	5430	3122	3.46	–4.81	0.3	Guarujá
X	5433	3119	3.54	–4.49	0.2	Guarujá
X	5436	3116	3.33	–5.21	0.2	Guarujá
X	5439	3113	3.69	–4.67	0.2	Guarujá
X	5442	3110	3.60	–4.40	0.3	Guarujá
X	5445	3107	3.61	–4.20	0.3	Guarujá
X	5448	3104	3.68	–4.13	0.2	Guarujá
X	5451	3101	3.66	–4.28	0.3	Guarujá
X	5454	3098	3.17	–4.46	0.4	Guarujá
X	5457	3095	3.27	–4.24	0.3	Guarujá
X	5460	3092	3.47	–4.41	0.3	Guarujá
X	5463	3089	3.47	–4.41	0.3	Guarujá
X	5466	3086	3.56	–4.44	0.3	Guarujá
X	5469	3083	2.82	–4.13	0.4	Guarujá
X	5472	3080	1.74	–4.14	0.3	Guarujá
X	5475	3077	2.42	–4.21	0.3	Guarujá
X	5478	3074	2.79	–3.79	0.3	Guarujá
X	5481	3071	2.92	–3.88	0.4	Guarujá
X	5484	3068	3.22	–3.97	0.2	Guarujá
X	5487	3065	3.49	–4.20	0.2	Guarujá
X	5490	3062	3.12	–4.33	0.2	Guarujá
X	5493	3059	3.36	–3.98	0.2	Guarujá
X	5496	3056	2.99	–4.07	0.3	Guarujá
X	5499	3053	3.06	–4.68	0.2	Guarujá
X	5502	3050	3.22	–4.43	0.3	Guarujá
X	5505	3047	3.11	–4.76	0.3	Guarujá
X	5508	3044	3.01	–4.49	0.2	Guarujá
X	5511	3041	2.87	–4.11	0.2	Guarujá
X	5514	3038	2.93	–4.82	0.2	Guarujá
X	5517	3035	3.22	–4.27	0.2	Guarujá
X	5520	3032	3.34	–4.98	0.2	Guarujá
X	5523	3029	3.24	–4.75	0.3	Guarujá
X	5526	3026	3.34	–4.97	0.2	Guarujá
X	5529	3023	3.29	–4.94	0.2	Guarujá
X	5532	3020	3.20	–4.58	0.2	Guarujá
X	5535	3017	3.20	–4.95	0.2	Guarujá
X	5538	3014	3.23	–4.93	0.2	Guarujá
X	5541	3011	3.34	–5.17	0.2	Guarujá
X	5544	3008	3.20	–5.30	0.2	Guarujá
X	5547	3005	3.31	–4.76	0.2	Guarujá
X	5550	3002	3.22	–5.07	0.2	Guarujá
X	5553	2999	3.34	–5.01	0.2	Guarujá
X	5556	2996	3.40	–5.01	0.2	Guarujá
X	5559	2993	3.13	–3.64	0.2	Guarujá
X	5562	2990	3.06	–4.46	0.2	Guarujá
X	5565	2987	2.97	–4.85	0.2	Guarujá
X	5568	2984	3.02	–4.74	0.2	Guarujá
X	5571	2981	3.14	–5.15	0.2	Guarujá
X	5574	2978	3.08	–5.06	0.3	Guarujá
X	5577	2975	3.09	–5.22	0.2	Guarujá
X	5580	2972	3.26	–5.49	0.2	Guarujá

Well	Penetrated depth (m)	Relative thickness (m)	$\delta^{13}C_{carb}$ (‰)	$\delta^{18}O_{carb}$ (‰)	TOC (wt %)	Formation
X	5583	2969	3.44	–5.10	0.3	Guarujá
X	5586	2966	3.40	–5.10	0.3	Guarujá
X	5589	2963	3.50	–4.67	0.2	Guarujá
X	5592	2960	3.28	–5.15	0.2	Guarujá
X	5595	2957	3.04	–3.74	0.2	Guarujá
X	5598	2954	3.12	–5.47	0.2	Guarujá
X	5601	2951	2.87	–5.30	0.2	Guarujá
X	5604	2948	2.76	–5.43	0.2	Guarujá
X	5607	2945	2.92	–5.63	0.2	Guarujá
X	5610	2942	2.99	–5.77	0.2	Guarujá
X	5613	2939	3.04	–5.74	0.2	Guarujá
X	5616	2936	3.23	–5.74	0.2	Guarujá
X	5619	2933	3.02	–5.45	0.2	Guarujá
X	5622	2930	2.86	–5.34	0.2	Guarujá
X	5625	2927	3.12	–5.68	0.2	Guarujá
X	5628	2924	3.00	–5.41	0.2	Guarujá
X	5631	2921	3.23	–5.02	0.2	Guarujá
X	5634	2918	3.13	–5.20	0.2	Guarujá
X	5637	2915	3.09	–5.11	0.2	Guarujá
X	5640	2912	3.21	–4.86	0.2	Guarujá
X	5643	2909	3.20	–5.06	0.2	Guarujá
X	5646	2906	3.88	–5.22	0.2	Guarujá
X	5649	2903	3.80	–5.05	0.2	Guarujá
X	5652	2900	3.89	–5.43	0.2	Guarujá
X	5655	2897	3.48	–5.12	0.2	Guarujá
X	5658	2894	3.14	–4.95	0.2	Guarujá
X	5661	2891	3.16	–5.26	0.2	Guarujá
X	5664	2888	3.58	–5.34	0.2	Guarujá
X	5667	2885	3.62	–5.49	0.2	Guarujá
X	5670	2882	3.33	–4.93	0.2	Guarujá
X	5673	2879	3.39	–5.13	0.2	Guarujá
X	5676	2876	3.52	–5.51	0.2	Guarujá
X	5679	2873	3.60	–5.59	0.2	Guarujá
X	5682	2870	3.88	–5.44	0.2	Guarujá
X	5685	2867	3.62	–5.68	0.2	Guarujá
X	5688	2864	3.91	–5.61	0.2	Guarujá
X	5691	2861	3.69	–5.61	0.2	Guarujá
X	5694	2858	3.58	–5.46	0.2	Guarujá
X	5697	2855	3.85	–5.36	0.2	Guarujá
X	5700	2852	3.67	–5.59	0.2	Guarujá
X	5703	2849	3.83	–5.38	0.2	Guarujá
X	5706	2846	3.74	–5.24	0.2	Guarujá
X	5709	2843	3.61	–5.52	0.2	Guarujá
X	5712	2840	3.71	–5.21	0.2	Guarujá
X	5715	2837	3.58	–5.86	0.3	Guarujá
X	5718	2834	3.69	–5.53	0.2	Guarujá
X	5721	2831	3.48	–5.69	0.2	Guarujá
X	5724	2828	3.33	–5.64	0.2	Guarujá
X	5727	2825	3.20	–5.31	0.2	Guarujá
X	5730	2822	3.36	–5.62	0.2	Guarujá
X	5733	2819	3.74	–5.47	0.2	Guarujá
X	5736	2816	4.11	–5.07	0.2	Guarujá

Well	Penetrated depth (m)	Relative thickness (m)	$\delta^{13}C_{carb}$ (‰)	$\delta^{18}O_{carb}$ (‰)	TOC (wt %)	Formation
X	5739	2813	4.13	–4.96	0.2	Guarujá
X	5742	2810	3.80	–5.26	0.2	Guarujá
X	5745	2807	3.68	–4.73	0.2	Guarujá
X	5748	2804	3.61	–5.02	0.2	Guarujá
X	5751	2801	3.31	–5.09	0.2	Guarujá
X	5754	2798	3.32	–4.88	0.2	Guarujá
X	5757	2795	3.83	–5.28	0.2	Guarujá
X	5760	2792	4.10	–5.24	0.2	Guarujá
X	5763	2789	4.03	–5.08	0.2	Guarujá
X	5766	2786	4.18	–5.43	0.3	Guarujá
X	5769	2783	4.26	–5.56	0.2	Guarujá
X	5772	2780	4.34	–5.57	0.3	Guarujá
X	5775	2777	4.26	–5.37	0.2	Guarujá
X	5778	2774	4.27	–5.28	0.2	Guarujá
X	5781	2771	4.02	–5.31	0.3	Guarujá
X	5784	2768	4.37	–5.55	0.3	Guarujá
X	5787	2765	4.56	–5.24	0.2	Guarujá
X	5790	2762	4.77	–5.35	0.2	Guarujá
X	5793	2759	4.17	–5.81	0.2	Guarujá
X	5796	2756	4.08	–4.69	0.2	Guarujá
X	5799	2753	3.42	–5.66	0.2	Guarujá
X	5802	2750	3.77	–5.30	0.2	Guarujá
X	5805	2747	3.98	–5.54	0.3	Guarujá
X	5808	2744	3.97	–5.88	0.3	Guarujá
X	5811	2741	3.53	–5.67	0.4	Guarujá
X	5814	2738	3.15	–5.57	0.4	Guarujá
X	5817	2735	2.69	–5.28	0.9	Guarujá
X	5820	2732	2.36	–5.28	0.4	Guarujá
X	5823	2729	1.48	–5.04	0.9	Guarujá
X	5826	2726	2.36	–5.14	0.7	Guarujá
X	5829	2723	2.89	–4.97	0.4	Guarujá
X	5832	2720	2.46	–5.22	1.0	Guarujá
X	5835	2717	3.36	–5.30	0.8	Guarujá
X	5838	2714	3.02	–5.23	0.8	Guarujá
X	5841	2711	2.80	–5.32	0.9	Guarujá
X	5844	2708	2.50	–5.25	1.4	Guarujá
X	5847	2705	2.66	–5.23	0.9	Guarujá
X	5850	2702	2.73	–5.58	1.3	Guarujá
X	5853	2699	3.12	–5.59	1.0	Guarujá
X	5856	2696	3.48	–5.63	0.7	Guarujá
X	5859	2693	3.72	–5.29	0.4	Guarujá
X	5862	2690	3.72	–5.23	0.8	Guarujá
X	5865	2687	3.94	–5.42	0.5	Guarujá
X	5868	2684	4.01	–5.60	0.5	Guarujá
X	5871	2681	3.88	–5.33	0.6	Guarujá
X	5874	2678	3.19	–5.22	0.9	Guarujá
X	5877	2675	3.22	–5.24	0.8	Guarujá
X	5880	2672	3.19	–5.15	0.5	Guarujá
X	5883	2669	2.19	–5.02	0.8	Guarujá
X	5886	2666	1.78	–4.63	0.9	Guarujá
X	5889	2663	2.51	–4.91	0.8	Guarujá
X	5892	2660	2.92	–5.00	0.7	Guarujá

Well	Penetrated depth (m)	Relative thickness (m)	$\delta^{13}C_{carb}$ (‰)	$\delta^{18}O_{carb}$ (‰)	TOC (wt %)	Formation
X	5895	2657	2.62	–5.13	0.8	Guarujá
X	5898	2654	2.45	–4.99	0.9	Guarujá
X	5901	2651	2.33	–5.36	1.3	Guarujá
X	5904	2648	2.34	–5.50	1.0	Guarujá
X	5907	2645	3.05	–5.50	0.9	Guarujá
X	5910	2642	3.18	–5.42	0.6	Guarujá
X	5913	2639	3.26	–5.39	0.7	Guarujá
X	5916	2636	3.47	–5.15	0.5	Guarujá
X	5919	2633	3.38	–5.48	0.8	Guarujá
X	5922	2630	3.21	–5.22	0.6	Guarujá
X	5925	2627	3.60	–5.20	0.5	Guarujá
X	5928	2624	3.03	–5.12	0.6	Guarujá
X	5931	2621	2.74	–5.52	1.0	Guarujá
X	5934	2618	2.98	–5.48	0.8	Guarujá
X	5937	2615	3.01	–6.09	0.7	Guarujá
X	5940	2612	2.34	–5.94	0.7	Guarujá
X	5943	2609	1.75	–4.80	0.4	Guarujá
X	5946	2606	2.04	–5.00	0.4	Guarujá
X	5949	2603	3.04	–5.17	0.3	Guarujá
X	5952	2600	3.17	–5.28	0.3	Guarujá
CP–5	4629	573	1.90	–0.60	0.2	Macabu
CP–5	4635	567	0.21	–1.18	0.2	Macabu
CP–5	4641	561	0.85	0.74	0.2	Macabu
CP–5	4647	555	0.88	1.27	0.2	Macabu
CP–5	4659	543	0.69	1.01	–	Macabu
CP–5	4665	537	1.06	0.09	0.3	Macabu
CP–5	4674	528	0.45	0.20	0.6	Macabu
CP–5	4683	519	0.47	1.56	3.3	Macabu
CP–5	4689	513	–0.38	0.32	1.0	Macabu
CP–5	4692	510	0.34	0.63	1.2	Macabu
CP–5	4695	507	0.10	0.43	1.2	Macabu
CP–5	4701	501	1.20	2.48	0.7	Macabu
CP–5	4704	498	1.40	3.23	0.6	Macabu
CP–5	4707	495	1.32	2.28	0.9	Macabu
CP–5	4713	489	1.42	2.17	0.5	Macabu
CP–5	4719	483	1.21	2.48	0.7	Macabu
CP–5	4725	477	1.26	1.81	0.3	Macabu
CP–5	4731	471	1.44	2.02	0.3	Macabu
CP–5	4737	465	1.89	2.84	0.4	Macabu
CP–5	4743	459	1.78	2.56	0.8	Macabu
CP–5	4749	453	2.17	2.75	0.4	Macabu
CP–5	4755	447	2.29	3.10	0.3	Macabu
CP–5	4761	441	1.67	2.39	1.0	Macabu
CP–5	4767	435	2.48	2.71	1.9	Macabu
CP–5	4770	432	1.78	1.78	5.4	Macabu
CP–5	4773	429	2.02	1.99	3.9	Macabu
CP–5	4776	426	2.23	2.64	3.7	Macabu
CP–5	4779	423	1.55	2.09	3.0	Macabu
CP–5	4782	420	1.76	2.10	0.7	Macabu
CP–5	4788	414	1.66	2.14	0.6	Macabu
CP–5	4794	408	1.62	2.00	0.3	Macabu
CP–5	4800	402	1.72	1.97	0.5	Macabu

Well	Penetrated depth (m)	Relative thickness (m)	$\delta^{13}C_{carb}$ (‰)	$\delta^{18}O_{carb}$ (‰)	TOC (wt %)	Formation
CP–5	4806	396	1.39	1.83	0.4	Macabu
CP–5	4818	384	1.54	1.45	0.5	Macabu
CP–5	4824	378	1.64	1.48	0.6	Macabu
CP–5	4830	372	1.83	1.48	0.5	Macabu
CP–5	4836	366	2.67	1.47	0.6	Macabu
CP–5	4842	360	2.18	1.25	0.6	Macabu
CP–5	4848	354	1.71	1.42	0.8	Macabu
CP–5	4854	348	1.83	1.42	1.2	Macabu
CP–5	4860	342	1.57	1.35	1.2	Macabu
CP–5	4866	336	1.76	1.47	1.2	Macabu
CP–5	4872	330	2.02	1.15	0.8	Macabu
CP–5	4878	324	1.81	0.95	1.3	Macabu
CP–5	4884	318	2.05	1.08	0.6	Macabu
CP–5	4890	312	1.95	0.69	0.5	Macabu
CP–5	4902	300	0.69	0.59	0.4	Macabu
CP–5	4908	294	0.58	0.38	0.4	Macabu
CP–5	4914	288	1.21	0.85	0.3	Macabu
CP–5	4920	282	1.02	0.77	0.3	Macabu
CP–5	4926	276	1.09	0.82	0.3	Macabu
CP–5	4932	270	1.44	1.04	0.3	Macabu
CP–5	4938	264	1.47	1.18	0.3	Macabu
CP–5	4944	258	1.69	1.35	0.2	Macabu
CP–5	4950	252	1.65	1.21	0.2	Macabu
CP–5	4956	246	1.26	0.97	0.2	Macabu
CP–5	4962	240	1.30	1.00	0.1	Macabu
CP–5	4968	234	1.45	0.55	0.2	Macabu
CP–5	4974	228	2.71	1.10	0.2	Macabu
CP–5	4980	222	1.84	0.63	0.2	Macabu
CP–5	4986	216	1.86	0.40	0.2	Macabu
CP–5	4992	210	1.86	–0.15	2.0	Macabu
CP–5	4995	207	1.86	0.05	1.8	Macabu
CP–5	4998	204	2.08	–0.03	0.5	Macabu
CP–5	5001	201	1.91	–0.10	1.0	Macabu
CP–5	5004	198	2.14	0.13	1.0	Macabu
CP–5	5007	195	2.33	–0.03	0.7	Macabu
CP–5	5010	192	2.30	0.04	0.9	Macabu
CP–5	5013	189	2.59	0.02	1.2	Macabu
CP–5	5016	186	0.70	0.08	–	Coqueiros
CP–5	5034	168	–0.69	–1.97	–	Coqueiros
CP–5	5040	162	–0.22	–1.79	–	Coqueiros
CP–5	5046	156	0.03	–1.82	–	Coqueiros
CP–5	5052	150	0.12	–1.29	–	Coqueiros
CP–5	5058	144	0.02	–0.94	–	Coqueiros
CP–5	5064	138	–0.15	–0.70	–	Coqueiros
CP–5	5070	132	0.33	–0.16	–	Coqueiros
CP–5	5073	129	0.58	–0.36	–	Coqueiros
CP–5	5076	126	–0.12	–1.03	–	Coqueiros
CP–5	5079	123	0.63	–0.20	–	Coqueiros
CP–5	5082	120	0.26	–0.06	–	Coqueiros
CP–5	5088	114	–0.15	–0.73	–	Coqueiros
CP–5	5094	108	0.16	–0.45	–	Coqueiros
CP–5	5097	105	0.46	–0.21	–	Coqueiros

Well	Penetrated depth (m)	Relative thickness (m)	$\delta^{13}C_{carb}$ (‰)	$\delta^{18}O_{carb}$ (‰)	TOC (wt %)	Formation
CP–5	5103	99	–0.50	–0.34	–	Coqueiros
CP–5	5112	90	1.36	–0.35	–	Coqueiros
CP–5	5115	87	0.32	–0.12	–	Coqueiros
CP–5	5121	81	0.16	0.33	–	Coqueiros
CP–5	5127	75	0.12	0.28	–	Coqueiros
CP–5	5133	69	0.49	–0.35	–	Coqueiros
CP–5	5139	63	0.31	–0.02	–	Coqueiros
CP–5	5145	57	0.28	1.03	–	Coqueiros
CP–5	5151	51	–0.11	0.57	–	Coqueiros
CP–5	5157	45	–0.24	–0.88	–	Coqueiros
CP–5	5163	39	0.40	0.45	–	Coqueiros
CP–5	5166	36	0.24	–0.92	–	Coqueiros
CP–5	5172	30	–0.03	–0.72	–	Coqueiros
CP–5	5175	27	0.20	–0.66	–	Coqueiros
CP–5	5178	24	0.21	–0.65	–	Coqueiros
CP–5	5181	21	0.46	–0.55	–	Coqueiros
CP–5	5184	18	0.76	–0.41	–	Coqueiros
CP–5	5187	15	1.03	–0.22	–	Coqueiros
CP–5	5190	12	0.98	0.15	–	Coqueiros
CP–5	5196	6	–0.30	1.18	–	Coqueiros
CP–5	5199	3	–0.66	0.95	–	Coqueiros
CP–5	5202	0	–0.88	1.05	–	Coqueiros

Appendix B

Table 4.5 (Chapter 4)

Strontium–isotope ($^{87}Sr/^{86}Sr$) data of anhydrite from Petrobras Well A and post-evaporite shallow-marine carbonate samples from Petrobras Well CB-3 and calculate F_{sw} values of models 1 to 4 (see Chapter 4 for details).

Well	Depth (m)	Material	$^{87}Sr/^{86}Sr$	Model 1	Model 2	Model 3	Model 4
A	4833.6	Anhydrite	0.708780	60	74	68	80
		Anhydrite	0.708815	60	74	67	79
A	4834.0	Anhydrite	0.708800	60	74	67	80
		Anhydrite	0.708806	60	74	67	79
A	4834.4	Anhydrite	0.708772	61	74	68	80
		Anhydrite	0.708758	61	75	68	80
A	4841.1	Anhydrite	0.709523	43	63	49	68
		Anhydrite	0.709522	43	63	49	68
A	4841.5	Anhydrite	0.709728	39	60	43	64
		Anhydrite	0.709722	39	60	43	65
CB–3	2528.4	Limestone	0.707479	91	94	102	101
CB–3	2528.4	Limestone	0.707472	91	94	102	101
CB–3	2547.9	Limestone	0.707551	89	93	100	100
CB–3	2551.0	Limestone	0.707473	91	94	102	101
CB–3	2551.0	Limestone	0.707457	91	94	102	101
CB–3	2552.9	Limestone	0.707489	90	94	101	101
CB–3	2556.8	Limestone	0.707571	88	92	99	100
CB–3	2557.2	*Lenticulina*	0.707691	86	91	96	98
CB–3	2558.8	Limestone	0.707451	91	94	102	101
CB–3	2558.8	Limestone	0.707514	90	93	101	100
CB–3	2562.7	Limestone	0.707545	89	93	100	100
CB–3	2566.9	Limestone	0.707639	87	91	97	98
CB–3	2570.3	Limestone	0.707525	90	93	100	100
CB–3	2574.4	Limestone	0.707534	89	93	100	100
CB–3	2574.4	*Lenticulina*	0.707584	88	92	99	99
CB–3	2577.2	Limestone	0.707644	87	91	97	98
CB–3	2581.5	Limestone	0.707541	89	93	100	100
CB–3	2586.2	Limestone	0.707537	89	93	100	100
CB–3	2589.8	Limestone	0.707516	90	93	101	100
CB–3	2592.4	*Lenticulina*	0.707547	89	93	100	100
CB–3	2593.6	*Lenticulina*	0.707456	91	94	102	101
CB–3	2593.6	*Lenticulina*	0.707498	90	94	101	101
CB–3	2593.6	*Lenticulina*	0.707452	91	94	102	101
CB–3	2594.2	*Lenticulina*	0.707455	91	94	102	101
CB–3	2594.4	Limestone	0.707549	89	93	100	100
CB–3	2597.0	Limestone	0.707516	90	93	101	100

Well	Depth (m)	Material	$^{87}Sr/^{86}Sr$	Model 1	Model 2	Model 3	Model 4
CB–3	2598.0	Limestone	0.707612	88	92	98	99
CB–3	2603.2	Limestone	0.707536	89	93	100	100
CB–3	2607.3	Limestone	0.707481	91	94	102	101
CB–3	2610.8	Limestone	0.707553	89	93	100	100
CB–3	2614.4	Limestone	0.707510	90	93	101	100
CB–3	2618.2	Limestone	0.707652	87	91	97	98
CB–3	2622.9	Limestone	0.707602	88	92	98	99
CB–3	2625.9	Limestone	0.707593	88	92	99	99
CB–3	2630.3	Limestone	0.707533	89	93	100	100
CB–3	2634.2	Limestone	0.707555	89	93	100	100
CB–3	2637.6	Limestone	0.707550	89	93	100	100
CB–3	2641.4	Limestone	0.707555	89	93	100	100
CB–3	2644.2	Limestone	0.707560	89	93	99	100
CB–3	2644.2	Limestone	0.707543	89	93	100	100
CB–3	2647.6	Limestone	0.707681	86	91	96	98
CB–3	2650.6	Limestone	0.707618	87	92	98	99
CB–3	2651.0	Limestone	0.707561	89	93	99	100
CB–3	2654.2	Limestone	0.707520	90	93	101	100
CB–3	2656.4	Limestone	0.707557	89	93	100	100
CB–3	2658.6	Limestone	0.707555	89	93	100	100
CB–3	2661.8	Limestone	0.707783	84	89	94	96
CB–3	2670.7	Limestone	0.707636	87	92	98	98
CB–3	2671.7	Limestone	0.707567	89	93	99	100
CB–3	2672.7	Limestone	0.707622	87	92	98	99
CB–3	2677.5	Limestone	0.707605	88	92	98	99
CB–3	2681.3	Limestone	0.707611	88	92	98	99
CB–3	2685.4	Limestone	0.707617	87	92	98	99

Appendix C

Table 5.1 (Chapter 5)

S1, S2, S3 and Tmax parameters from Petrobras Well D.

Depth (m)	S1 (mg HC/g rock)	S2 (mg HC/g rock)	S3 (mg CO_2/g rock)	Tmax (°C)
77.80	0.02	0.13	0.44	418
78.70	0.01	0.02	0.16	415
79.70	0.03	0.13	0.30	417
87.60	0.01	0.43	1.05	426
87.60	0.02	0.39	0.95	431
90.38	0.00	0.04	0.19	417
93.55	0.05	0.31	0.53	419
96.65	0.05	0.19	0.43	407
99.70	0.05	0.23	0.66	417
103.63	0.03	0.46	0.69	424
105.20	0.02	0.44	0.45	426
105.70	0.02	0.21	0.45	426
108.60	0.02	0.21	0.49	419
112.68	0.02	0.24	0.46	424
113.60	0.03	0.09	0.41	417
116.02	0.02	0.19	0.43	418
118.25	0.04	0.36	0.68	417
122.36	0.03	0.64	0.75	421
124.10	0.06	1.38	0.59	428
126.73	0.03	0.28	0.30	421
130.72	0.03	0.09	0.28	417
132.96	0.03	0.20	0.51	422
133.61	0.01	0.05	0.25	418
138.22	0.00	0.00	0.00	416
138.22	0.00	0.01	0.03	418
139.64	0.01	0.02	0.07	414
145.83	0.10	3.51	1.02	421
147.25	0.03	0.13	0.66	420
148.72	0.03	0.14	0.41	412
152.94	0.28	10.09	1.71	404
154.63	0.03	0.19	0.30	418
156.31	0.54	18.93	1.41	409
159.12	0.05	0.87	0.51	430
160.63	0.02	0.12	0.25	418
162.41	0.03	0.21	0.52	417
164.29	0.01	0.04	0.48	406
166.17	0.02	0.07	0.30	402
167.74	0.12	0.70	0.41	428

Depth (m)	S1 (mg HC/g rock)	S2 (mg HC/g rock)	S3 (mg CO_2/g rock)	Tmax (°C)
168.55	0.08	0.81	0.59	422
171.11	0.01	0.04	0.15	418
171.82	0.29	4.27	0.31	415
173.06	0.07	0.40	0.18	402
175.40	0.13	0.71	0.38	424
177.91	0.15	2.16	0.56	400
180.81	0.02	0.14	0.20	418
180.81	0.07	0.20	0.19	385
183.67	0.08	0.29	0.32	398
184.97	0.01	0.08	0.52	350
186.97	0.07	0.64	0.21	418
189.56	0.02	0.18	0.49	403
191.80	0.07	0.76	0.23	419
192.48	0.03	0.26	0.62	419
195.08	0.04	0.44	0.68	429
197.85	0.10	0.79	1.00	415
198.84	0.02	0.48	0.39	434
201.43	0.24	8.51	0.97	426
202.90	0.12	2.70	0.60	424
203.77	0.25	1.49	0.37	420
204.79	0.22	1.17	0.41	413
206.44	0.01	0.17	0.42	418
208.32	0.05	0.32	0.53	418
214.70	0.09	1.01	0.34	427
215.56	0.10	1.07	1.29	412
217.20	0.18	5.10	0.94	425
218.10	0.06	2.01	0.88	428
218.10	0.06	2.17	0.81	430
218.40	0.08	2.64	1.13	427
220.92	0.09	1.41	0.37	423
222.61	0.16	1.52	0.51	425
224.08	0.27	3.48	0.75	428
227.08	0.04	0.91	0.67	427
228.26	0.07	1.64	0.42	425
230.63	0.07	3.28	1.16	427
233.17	0.04	0.46	0.81	417
235.87	0.04	0.63	1.04	423
238.23	0.04	0.70	0.69	422
239.66	0.08	1.25	0.66	425
241.80	0.08	0.85	0.66	423
243.16	0.02	0.26	0.81	415
244.45	0.09	0.94	0.96	427
247.09	0.22	0.78	0.73	421

Depth (m)	S1 (mg HC/g rock)	S2 (mg HC/g rock)	S3 (mg CO_2/g rock)	Tmax (°C)
249.35	0.66	13.96	0.56	419
251.08	0.42	1.20	0.82	415
253.60	0.13	2.83	0.50	422
263.63	0.29	11.45	1.07	432
265.05	0.15	3.29	0.54	427
267.16	0.02	0.18	2.93	516
267.24	0.17	4.15	0.21	431
269.18	0.08	1.86	0.18	426
271.78	0.33	5.14	0.55	432
275.43	0.23	7.26	1.03	433
277.80	0.04	1.35	0.29	435
279.66	0.08	2.77	0.51	436
281.47	0.10	3.43	0.42	436
282.78	0.12	4.95	0.58	431
283.63	0.30	13.51	2.23	434
289.55	0.10	6.40	1.25	435
294.91	0.03	0.71	1.89	435
295.88	0.05	2.24	0.74	432
296.54	0.16	7.30	1.64	433
305.95	0.07	3.20	0.57	430
307.69	0.11	5.94	1.07	432
309.10	0.58	9.35	1.42	429
311.60	0.47	4.70	0.58	429
313.33	0.44	5.58	0.71	430
314.98	0.07	3.96	0.87	431
316.71	0.13	7.05	1.66	435
317.12	0.05	2.81	0.59	432
320.45	0.07	3.01	0.80	433
322.38	0.04	1.27	0.57	431
325.20	0.05	1.81	0.38	434
329.36	0.04	1.10	0.96	436
331.80	0.07	2.88	0.34	430
334.02	0.02	0.16	0.92	415
336.00	0.09	2.70	0.44	429
337.92	0.12	8.23	0.26	444
344.86	0.02	0.15	0.32	374
346.35	0.14	7.32	0.29	441
348.26	0.11	4.11	0.23	437
354.90	0.09	2.86	1.21	431
355.94	0.01	0.14	0.46	416

Table 5.2 (Chapter 5)

Total organic and inorganic carbon (TOC and TIC) values from Petrobras Well D.

Depth (m)	TOC (wt %)	TIC (wt %)
77.80	0.59	0.83
78.70	0.06	2.70
79.70	0.38	0.62
87.60	1.53	0.49
87.60	1.37	0.45
90.38	0.10	8.09
93.55	1.23	0.89
96.65	0.34	3.64
99.70	0.69	1.09
103.63	0.84	6.96
105.20	0.63	6.45
105.70	0.17	6.69
108.60	0.71	1.58
112.68	0.60	4.35
113.60	0.19	7.63
116.02	0.53	1.31
118.25	0.94	0.45
122.36	1.05	1.35
124.10	1.15	2.04
126.73	0.42	1.67
130.72	0.25	1.56
132.96	0.91	0.37
133.61	0.08	10.40
138.22	0.02	3.07
138.22	0.04	3.09
139.64	0.04	4.85
145.83	2.13	0.47
147.25	0.32	10.38
148.72	0.33	10.23
152.94	4.11	0.20
154.63	0.47	9.07
156.31	4.26	0.98
159.12	0.33	7.87
160.63	0.15	9.24
162.41	0.26	5.69
164.29	0.15	4.06
166.17	0.10	3.14
167.74	0.53	10.24
168.55	0.71	8.62

Depth (m)	TOC (wt %)	TIC (wt %)
171.11	0.29	6.87
171.82	1.51	2.07
173.06	0.20	3.68
175.40	0.61	10.80
177.91	1.00	0.98
180.81	0.30	0.82
180.81	0.30	0.86
183.67	0.38	0.76
184.97	0.33	5.64
186.97	0.54	6.29
189.56	0.40	5.00
191.80	0.45	8.07
192.48	0.58	8.89
195.08	0.62	4.70
197.85	1.63	0.89
198.84	0.52	7.90
201.43	2.36	5.59
202.90	1.40	5.15
203.77	0.99	2.88
204.79	0.73	1.63
206.44	0.50	1.29
208.32	0.57	1.22
214.70	0.73	9.79
215.56	1.97	0.22
217.20	2.42	4.59
218.10	1.15	10.36
218.10	1.14	10.15
218.40	2.36	1.50
220.92	1.34	2.70
222.61	1.55	1.62
224.08	2.42	2.25
227.08	0.87	3.12
228.26	0.95	3.69
230.63	2.35	2.08
233.17	1.07	1.53
235.87	1.32	1.49
238.23	1.27	1.00
239.66	1.18	1.62
241.80	1.14	0.91
243.16	1.01	1.15
244.45	1.30	1.06
247.09	1.30	0.78
249.35	2.16	5.27

Depth (m)	TOC (wt %)	TIC (wt %)
251.08	1.68	0.92
253.60	1.59	2.75
263.63	2.55	9.29
265.05	1.42	5.43
267.16	0.14	4.72
267.24	1.22	2.55
269.18	0.61	1.57
271.78	1.94	4.91
275.43	3.09	1.02
277.80	0.58	5.61
279.66	1.00	4.63
281.47	1.00	0.65
282.78	1.51	2.10
283.63	5.22	0.98
289.55	1.62	5.17
294.91	1.07	1.98
295.88	0.81	1.84
296.54	2.64	2.83
305.95	1.14	3.60
307.69	2.03	1.19
309.10	3.49	1.34
311.60	1.55	1.92
313.33	2.03	0.97
314.98	1.43	2.15
316.71	2.77	1.03
317.12	1.07	0.93
320.45	0.84	3.64
322.38	0.44	4.45
325.20	0.54	1.83
329.36	0.64	2.78
331.80	0.62	1.38
334.02	0.24	3.25
336.00	0.70	0.75
337.92	1.21	0.23
344.86	0.11	0.20
346.35	1.08	0.40
348.26	0.79	0.18
354.90	1.41	1.62
355.94	0.58	0.05

Table 5.3 (Chapter 5)

$\delta^{13}C_{OM}$ values from Petrobras Well D. OU – Open University, UERJ – Universidade do Estado do Rio de Janeiro.

Depth (m)	$\delta^{13}C_{OM}$ OU (‰)	$\delta^{13}C_{OM}$ UERJ (‰)
77.80	–22.60	–
78.70	–23.46	–
79.70	–22.96	–
87.60	–	–21.61
87.60	–	–21.50
90.38	–24.41	–
93.55	–	–22.37
96.65	–23.24	–
103.63	–	–22.14
103.63	–	–22.20
105.20	–	–21.97
108.60	–22.44	–
112.68	–22.46	–
113.60	–24.65	–
116.02	–23.10	–
118.25	–	–22.91
122.36	–	–22.72
124.10	–	–23.13
126.73	–	–22.67
130.72	–23.26	–
132.96	–	–22.48
133.61	–24.75	–
138.22	–24.44	–
138.22	–24.72	–
139.64	–24.35	–
145.83	–	–22.87
147.25	–23.70	–
148.72	–24.23	–
152.94	–	–22.98
152.94	–	–23.08
154.63	–24.19	–
156.31	–	–24.18
159.12	–26.17	–
160.63	–25.97	–
162.41	–24.85	–
164.29	–25.53	–
166.17	–25.31	–

Depth (m)	$\delta^{13}C_{OM}$ OU (‰)	$\delta^{13}C_{OM}$ UERJ (‰)
167.74	–24.66	–
168.55	–23.60	–
171.11	–	–23.00
171.82	–	–24.28
173.06	–25.16	–
175.40	–24.68	–
177.91	–	–24.06
180.81	–23.03	–
180.81	–22.63	–
183.67	–23.93	–
184.97	–24.47	–
186.97	–25.18	–
189.56	–24.98	–
191.80	–24.28	–
192.48	–24.30	–
195.08	–24.82	–
197.85	–	–21.70
198.84	–23.94	–
201.43	–	–24.49
202.90	–	–23.51
203.77	–	–24.21
204.79	–25.20	–
206.44	–	–21.38
208.32	–22.08	–
214.70	–24.59	–
215.56	–	–21.62
217.20	–	–21.68
218.10	–	–21.30
218.10	–	–21.52
218.40	–	–21.37
220.92	–	–22.67
222.61	–	–21.81
222.61	–	–21.68
224.08	–	–22.01
227.08	–	–21.59
228.26	–	–22.68
230.63	–	–21.67
233.17	–	–22.02
235.87	–	–21.32
238.23	–	–22.26
239.66	–	–22.41
241.80	–	–22.20

Depth (m)	$\delta^{13}C_{OM}$ OU (‰)	$\delta^{13}C_{OM}$ UERJ (‰)
243.16	–	–21.59
244.45	–	–22.23
244.45	–	–22.11
247.09	–	–21.85
249.35	–	–25.47
251.08	–	–22.13
253.60	–	–23.57
263.63	–	–24.62
265.05	–	–22.49
267.16	–27.78	–
267.24	–	–24.54
267.24	–	–24.39
269.18	–25.72	–
271.78	–	–23.87
275.43	–	–22.75
277.80	–23.93	–
279.66	–	–23.55
281.47	–	–24.46
282.78	–	–23.69
283.63	–	–22.62
289.55	–	–26.50
294.91	–	–21.42
294.91	–	–21.39
295.88	–	–25.09
296.54	–	–23.83
305.95	–	–23.66
307.69	–	–23.40
309.10	–	–22.73
311.60	–	–23.60
313.33	–	–23.25
314.98	–	–23.53
316.71	–	–22.79
317.12	–	–24.87
317.12	–	–24.84
320.45	–	–25.59
322.38	–26.18	–
325.20	–26.18	–
329.36	–	–26.25
331.80	–26.62	–
334.02	–26.15	–
336.00	–	–25.74
337.92	–	–30.24

Depth (m)	$\delta^{13}C_{OM}$ OU (‰)	$\delta^{13}C_{OM}$ UERJ (‰)
344.86	–	–30.34
346.35	–	–29.06
346.35	–	–29.12
348.26	–	–27.51
354.90	–	–23.01
355.94	–21.41	–

Appendix D

Table 6.1 (Chapter 6)

TOC and S_{OM} values from DSDP Site 511. UO – University of Oxford, UERJ – Universidade do Estado do Rio de Janeiro, mbsf – metres below sea floor.

Core	Section	Interval (m)	Depth Top (mbsf)	S_{OM} LECO UERJ (wt %)	TOC LECO UERJ (wt %)	TOC Coulomat UO (wt %)	TOC Rock–Eval 6 UO (wt %)
49	5	10–11.5	428.81	0.13	0.07	0.02	–
49	5	38–42	429.09	0.13	0.08	0.13	–
49	5	70–71.5	429.41	0.18	0.06	0.09	–
49	5	98–101	429.69	0.13	0.05	1.21	–
49	5	130–131.5	430.01	0.13	0.05	0.06	–
49	6	10–11.5	430.31	0.13	0.07	0.08	–
49	6	40–42.5	430.61	0.12	0.06	0.16	–
50	1	10–11.5	432.6	0.12	0.05	0.54	–
50	1	40–43	432.9	0.13	0.05	0.53	–
50	1	68–69.5	433.18	0.13	0.06	0.13	–
50	1	101.5–103	433.515	0.13	0.05	0.00	–
50	1	130–131.5	433.8	0.32	0.05	0.40	–
50	2	11–12.5	434.11	0.14	0.05	0.25	–
50	2	40–42	434.4	0.14	0.07	0.06	–
50	2	70–71.5	434.7	0.13	0.05	0.14	–
50	2	102–103.5	435.02	0.19	0.05	0.12	–
50	2	130–131.5	435.3	0.13	0.06	0.18	–
50	3	9–10.5	435.59	0.15	0.07	0.20	–
50	3	40–42.5	435.9	0.14	0.07	0.19	–
50	3	68.5–70	436.185	0.14	0.03	0.13	–
50	3	101–102.5	436.51	0.14	0.04	0.11	–
50	3	130–131.5	436.8	0.13	0.03	0.20	–
50	4	20–22.5	437.08	0.13	0.02	0.15	–
50	4	47–50	437.35	0.17	0.04	0.16	–
50	5	5–6.5	437.56	0.13	0.02	0.13	–
51	1	10–13	442.1	0.14	0.05	0.15	–
51	1	40–41.5	442.4	0.13	0.04	0.00	–
51	1	70–71.5	442.7	0.13	0.06	0.00	–
51	1	100–101.5	443	0.14	0.03	0.12	–
51	1	128–129.5	443.28	0.13	0.03	0.12	–
51	2	10–11.5	443.6	0.13	0.04	0.33	–
51	2	40–41.5	443.9	0.13	0.05	0.20	–
51	2	71–72.5	444.21	0.13	0.07	0.13	–
51	2	100–101.5	444.5	0.13	0.06	0.25	–
51	2	130–132	444.8	0.13	0.11	0.29	–

Core	Section	Interval (m)	Depth Top (mbsf)	S_{OM} LECO UERJ (wt %)	TOC LECO UERJ (wt %)	TOC Coulomat UO (wt %)	TOC Rock–Eval 6 UO (wt %)
51	3	10–11.5	445.1	0.13	0.04	0.25	–
51	3	40–41.5	445.4	0.21	0.09	0.16	–
51	3	68.5–70	445.685	0.24	0.10	0.12	–
51	3	100–101.5	446	0.16	0.10	0.24	–
51	3	130–131.5	446.3	0.20	0.09	0.15	–
51	4	8.5–10	446.585	0.16	0.12	0.10	–
51	4	40–41.5	446.9	0.19	0.24	0.23	–
51	4	71–72.5	447.21	0.13	0.10	0.31	–
51	4	100–101.5	447.5	0.18	0.10	0.02	–
51	4	129–132	447.79	0.12	0.13	0.00	–
51	5	8–10	448.08	0.13	0.06	0.04	–
51	5	40–42	448.4	0.13	0.10	0.00	–
51	5	73–75	448.73	0.13	0.07	0.21	–
51	5	100–102	449	0.13	0.10	0.17	–
51	5	130–132	449.3	0.13	0.11	0.19	–
51	6	6–8	449.56	0.15	0.09	0.53	–
51	6	40–42	449.9	0.13	0.08	0.30	–
51	6	73–75	450.23	0.13	0.09	0.32	–
51	6	100–103	450.5	0.12	0.09	0.21	–
51	6	130–132	450.8	0.13	0.08	0.18	–
52	1	10–11.5	451.6	0.20	0.09	0.15	–
52	1	40–41.5	451.9	0.14	0.07	0.12	–
52	1	75–77	452.25	0.16	0.07	0.17	–
52	1	100–101.5	452.5	0.13	0.06	0.18	–
52	1	130–131.5	452.8	0.13	0.06	0.16	–
52	2	10–12	453.1	0.13	0.07	0.19	–
52	2	42–44	453.42	0.12	0.04	0.16	–
52	2	76–78	453.76	0.13	0.06	0.14	–
52	2	100–102	454	0.12	0.08	0.12	–
52	2	130–132	454.3	0.13	0.07	0.17	–
52	3	9–12	454.59	0.12	0.07	0.13	–
52	3	40–42	454.9	0.12	0.05	0.24	–
52	3	70–72	455.2	0.14	0.08	0.17	–
52	3	100–102	455.5	0.14	0.06	0.15	–
52	3	130–132	455.8	0.12	0.11	0.13	–
52	4	11–13	456.11	0.12	0.07	0.20	–
52	4	39–41	456.39	0.12	0.06	0.11	–
52	4	73–75	456.73	0.18	0.06	0.15	–
52	4	100–102	457	0.19	0.08	0.12	–
52	4	130–132	457.3	0.13	0.06	0.14	–
52	5	9–12	457.59	0.13	0.08	0.19	–
52	5	40–42	457.9	0.12	0.08	0.15	–

Core	Section	Interval (m)	Depth Top (mbsf)	S_{OM} LECO UERJ (wt %)	TOC LECO UERJ (wt %)	TOC Coulomat UO (wt %)	TOC Rock–Eval 6 UO (wt %)
52	5	70–72	458.2	0.13	0.07	0.16	–
52	5	100–101.5	458.5	0.14	0.11	0.16	–
52	6	10–12	458.81	0.12	0.07	0.17	–
52	6	40–41.5	459.11	0.12	0.08	0.20	–
52	6	70–72	459.41	0.12	0.09	0.15	–
52	6	101–103	459.72	0.13	0.07	0.27	–
52	6	130–132	460.01	0.13	0.08	0.23	–
52	7	9–12	460.3	0.13	0.09	0.25	–
52	7	40–42	460.61	0.12	0.07	0.22	–
52	8	3–5	460.91	0.12	0.08	0.21	–
53	1	37–38	461.37	0.05	0.00	0.13	–
53	1	83–84	461.83	0.05	0.02	0.23	–
53	1	118–119	462.18	0.06	0.02	0.20	–
53	2	46–47	462.96	0.04	0.01	0.12	–
53	2	84–85	463.34	0.05	0.00	0.15	–
53	2	118–120	463.68	0.09	0.03	0.16	–
53	3	39–40	464.39	0.10	0.18	0.15	–
53	3	72–73	464.72	0.11	0.03	0.21	–
53	3	121–122	465.21	0.06	0.01	0.17	–
53	4	26–27	465.76	0.09	0.01	0.12	–
53	4	78–79	466.28	0.13	0.03	0.12	–
53	4	78–79	466.28	–	–	0.19	–
53	4	121–122	466.71	0.12	0.04	0.19	–
53	5	37–38	467.37	–	–	0.37	–
53	5	37–38	467.37	–	–	0.25	–
53	5	70–71	467.7	0.07	0.02	0.19	–
53	5	106–107	468.06	0.10	0.03	0.16	–
53	6	26–27	468.76	0.12	0.04	0.24	–
53	6	70–71	469.2	0.08	0.02	0.24	–
53	6	94–95	469.44	–	–	0.17	–
53	7	19–20	470.19	0.09	0.04	0.21	–
54	1	33–35	470.83	0.08	0.03	0.21	–
54	1	69–70	471.19	0.10	0.02	0.10	–
54	1	120–121	471.7	0.08	0.00	0.13	–
54	2	41–42	472.41	–	–	0.11	–
54	2	80–81	472.8	0.08	0.11	0.30	–
54	2	116–117	473.16	0.07	0.05	0.10	–
54	3	38–39	473.88	0.51	0.00	0.21	–
54	3	38–39	473.88	–	–	0.25	–
54	3	81–82	474.31	0.15	0.00	0.16	–
54	3	81–82	474.31	–	–	0.19	–
54	3	127–128	474.77	0.14	0.02	0.19	–

Core	Section	Interval (m)	Depth Top (mbsf)	S_{OM} LECO UERJ (wt %)	TOC LECO UERJ (wt %)	TOC Coulomat UO (wt %)	TOC Rock–Eval 6 UO (wt %)
54	4	41–42	475.41	0.11	0.01	0.21	–
54	4	83–84	475.83	0.06	0.00	0.22	–
54	4	123–124	476.23	0.06	0.04	0.16	–
54	5	38–39	476.88	0.12	0.04	0.24	–
54	5	70–71	477.2	0.11	0.00	0.23	–
54	5	110–111	477.6	–	–	0.16	–
54	6	37–38	478.37	0.09	0.00	0.18	–
54	6	90–91	478.9	0.07	0.00	0.27	–
54	7	9–10	479.21	–	–	0.28	–
55	1	28–29	480.28	0.09	0.02	0.16	–
55	1	67–68	480.67	0.07	0.00	0.21	–
55	1	109–110	481.09	0.25	0.00	0.29	–
55	2	39–40	481.89	0.36	0.01	0.22	–
55	2	89–90	482.39	0.02	0.03	0.18	–
55	2	127–129	482.77	4.30	0.00	0.21	–
55	3	30–31	483.3	0.24	0.03	0.17	–
55	3	64–65	483.64	0.71	0.00	0.18	–
55	3	92–93	483.92	3.00	0.00	0.23	–
55	3	130–131	484.3	0.37	0.00	0.16	–
55	4	20–21	484.7	0.38	0.00	0.10	–
55	4	56–57	485.06	0.42	0.00	0.18	–
55	4	89–90	485.39	0.50	0.00	0.16	–
55	4	89–90	485.39	0.44	0.00	0.20	–
55	5	26–27	485.97	0.41	0.00	0.24	–
55	5	58–59	486.29	0.35	0.00	0.12	–
55	5	99–100	486.7	0.51	0.00	0.17	–
55	6	21–22	487.32	0.62	0.00	0.20	–
55	6	49–50	487.6	0.57	0.00	0.19	–
55	6	49–50	487.6	–	–	0.26	–
56	1	31–32	489.81	–	–	0.22	–
56	1	58–59	490.08	–	–	0.18	–
56	1	89–90	490.39	–	–	0.10	–
56	1	128–129	490.78	0.55	0.00	0.17	–
56	2	22–23	491.22	–	–	0.23	–
56	2	58–59	491.58	4.20	0.07	0.29	–
56	2	84–85	491.84	0.21	0.06	0.18	–
56	2	112–113	492.12	0.26	0.07	0.23	–
56	2	142–143	492.42	0.22	0.00	0.19	–
56	3	27–28	492.77	0.37	0.05	0.10	–
56	3	54–55	493.04	0.17	0.02	0.26	–
56	3	77–78	493.27	0.15	0.15	0.16	–
56	3	121–122	493.71	0.41	0.08	0.13	–

Core	Section	Interval (m)	Depth Top (mbsf)	S_{OM} LECO UERJ (wt %)	TOC LECO UERJ (wt %)	TOC Coulomat UO (wt %)	TOC Rock–Eval 6 UO (wt %)
56	3	147–148	493.97	–	–	0.11	–
56	4	22–23	494.22	0.13	0.39	0.38	–
56	4	50–51	494.5	0.15	0.30	0.17	–
56	4	81–82	494.81	0.12	0.16	0.19	–
56	4	107–108	495.07	0.13	0.14	0.18	–
56	4	107–108	495.07	0.12	0.15	–	–
56	4	135–136	495.35	0.15	0.16	0.17	–
56	5	14–15	495.64	0.13	0.32	0.37	–
56	5	38–39	495.88	0.12	0.35	0.37	–
56	5	63–64	496.13	0.13	0.54	0.57	–
56	5	88–89	496.38	0.15	0.36	0.36	–
56	5	119–120	496.69	0.22	0.69	0.77	–
57	1	19–20	499.19	0.15	0.37	0.38	–
57	1	43–44	499.43	0.14	0.43	0.41	–
57	1	74–75	499.74	0.19	0.51	0.48	–
57	1	101–102	500.01	0.23	0.23	0.24	–
57	1	125–126	500.25	0.46	0.63	0.64	–
57	1	146–147	500.46	0.35	0.90	1.06	–
57	1	146–147	500.46	–	–	1.04	–
57	2	5–6	500.55	0.22	0.66	0.66	–
57	2	25–26	500.75	0.21	0.58	0.58	–
57	2	49–50	500.99	0.69	2.57	2.88	–
57	2	49–50	500.99	–	–	2.81	–
57	2	71–72	501.21	0.43	1.29	1.32	–
57	2	95–96	501.45	0.59	1.79	1.86	–
57	2	122–123	501.72	0.31	0.62	0.77	–
57	2	122–123	501.72	0.30	0.63	0.69	–
57	2	140–141	501.9	0.36	0.73	0.93	–
57	2	140–141	501.9	–	–	0.84	–
57	3	24–25	502.24	–	–	0.72	–
57	3	24–25	502.24	–	–	0.65	–
57	3	49–50	502.49	0.36	0.90	1.03	–
57	3	49–50	502.49	–	–	0.97	–
57	3	69–70	502.69	0.29	0.33	0.35	–
57	3	89–90	502.89	–	–	0.17	–
57	3	110–111	503.1	0.32	0.52	0.57	–
57	3	137–138	503.37	0.39	0.55	0.63	–
57	4	22–23	503.72	0.33	0.16	0.27	–
57	4	39–40	503.89	–	–	0.55	–
57	4	39–40	503.89	–	–	0.62	–
57	4	65–66	504.15	0.53	1.13	1.16	–
57	4	97–98	504.47	0.53	1.51	1.56	–

Core	Section	Interval (m)	Depth Top (mbsf)	S_{OM} LECO UERJ (wt %)	TOC LECO UERJ (wt %)	TOC Coulomat UO (wt %)	TOC Rock–Eval 6 UO (wt %)
57	4	131–132	504.81	0.19	0.88	0.89	–
57	4	147–148	504.97	0.28	0.43	1.12	–
57	4	147–148	504.97	–	–	0.99	–
57	5	11–12	505.11	0.21	0.57	0.67	–
57	5	36–37	505.36	0.27	0.68	0.80	–
57	5	58–59	505.58	0.19	0.61	0.73	–
57	5	77–78	505.77	0.24	0.40	0.61	–
57	5	77–78	505.77	–	–	0.57	–
57	5	111–112	506.11	0.32	0.63	0.71	–
57	5	140–141	506.4	0.20	0.48	1.17	–
57	5	140–141	506.4	–	–	1.16	–
57	6	8–9	506.58	0.34	0.91	1.08	–
57	6	37–38	506.87	0.23	0.50	0.66	–
58	1	26–27	508.76	0.25	0.35	0.44	–
58	1	26–27	508.76	0.23	0.35	–	–
58	1	51–52	509.01	0.24	0.71	0.91	–
58	1	69–70	509.19	0.25	0.54	0.59	–
58	1	92–93	509.42	0.19	0.35	0.53	–
58	1	121–122	509.71	0.41	0.57	0.63	–
58	1	148–149	509.98	0.43	0.71	0.90	–
58	2	17–19	510.17	0.35	0.54	0.64	–
58	2	41–42	510.41	0.10	0.21	0.32	–
58	2	62–63	510.62	0.57	0.57	0.71	–
58	2	85–86	510.85	0.51	2.01	1.99	–
58	2	120–121	511.2	0.23	0.50	0.67	–
58	2	147–148	511.47	0.46	0.56	0.65	–
58	2	147–148	511.47	–	–	0.62	–
58	3	15–16	511.65	0.24	0.27	0.36	–
58	3	15–16	511.65	–	–	0.34	–
58	3	31–32	511.81	0.25	0.43	0.57	–
58	3	53–54	512.03	0.42	2.33	2.79	–
58	3	72–73	512.22	0.12	0.22	0.35	–
58	3	96–98	512.46	0.19	0.35	0.45	–
58	3	118–119	512.68	0.13	0.18	0.24	–
58	4	12–13	512.83	0.13	0.18	0.23	–
58	4	12–13	512.83	0.13	0.20	–	–
58	4	33–34	513.04	0.14	0.41	0.37	–
58	4	53–54	513.24	0.32	0.11	0.11	–
58	4	83–84	513.54	0.27	0.24	0.10	–
58	4	90–91	513.61	1.60	0.59	0.80	–
58	4	110–111	513.81	2.10	3.67	3.39	–
58	4	137–138	514.08	6.40	4.41	3.83	3.32

Core	Section	Interval (m)	Depth Top (mbsf)	S_{OM} LECO UERJ (wt %)	TOC LECO UERJ (wt %)	TOC Coulomat UO (wt %)	TOC Rock–Eval 6 UO (wt %)
58	4	147–148	514.18	1.60	4.42	3.98	4.04
58	5	10–11	514.31	2.50	7.78	5.32	5.44
59	1	17–18	518.17	0.72	7.77	6.01	6.19
59	1	39–40	518.39	0.69	8.07	6.63	6.49
59	1	60–61	518.6	0.44	7.32	5.88	5.75
59	1	90–91	518.9	1.20	3.79	4.56	4.50
59	1	123–124	519.23	1.90	2.27	2.63	–
59	1	146–147	519.46	1.50	11.40	9.20	8.86
59	2	20–21	519.7	–	–	2.12	2.01
59	2	20–21	519.7	–	–	–	2.05
59	2	20–21	519.7	–	–	–	2.02
59	2	43–44	519.93	–	–	4.27	4.32
59	2	61–62	520.11	–	–	4.01	3.78
59	2	105–106	520.55	0.59	3.94	3.94	–
59	2	132–133	520.82	0.84	2.03	2.36	1.96
59	3	26–27	521.26	0.81	5.28	5.23	5.22
59	3	26–27	521.26	0.83	5.47	–	–
59	3	49–51	521.49	1.00	4.90	5.24	5.36
59	3	65–66	521.65	0.73	7.82	6.70	6.57
59	3	94–95	521.94	0.88	5.65	5.55	5.88
59	3	123–124	522.23	2.90	5.57	5.64	6.02
59	4	6–8	522.56	0.18	0.41	0.58	–
59	4	26–27	522.76	1.30	3.77	4.17	4.27
59	4	71–73	523.21	1.00	1.79	2.31	
59	4	91–92	523.41	0.63	4.02	4.50	4.34
59	4	121–122	523.71	1.20	6.04	6.09	6.88
59	4	145–146	523.95	0.84	6.30	5.16	4.98
59	4	145–146	523.95	–	–	–	5.00
60	1	18–19	527.68	0.91	7.71	–	6.12
60	1	40–41	527.9	0.36	0.08	–	–
60	1	61–62	528.11	1.70	2.52	–	3.26
60	1	83–84	528.33	1.00	3.16	–	3.63
60	1	106–107	528.56	0.77	3.51	–	3.95
60	1	127–128	528.77	1.80	3.19	–	3.77
60	2	13–14	529.13	0.30	0.70	–	–
60	2	26–27	529.26	0.67	1.15	–	–
60	2	26–27	529.26	0.68	1.15	–	–
60	2	47–48	529.47	1.80	4.47	–	4.62
60	2	82–83	529.82	0.79	4.17	–	4.10
60	2	101–102	530.01	1.70	5.20	–	5.41
60	2	132–133	530.32	2.00	0.83	–	–

Core	Section	Interval (m)	Depth Top (mbsf)	S_{OM} LECO UERJ (wt %)	TOC LECO UERJ (wt %)	TOC Coulomat UO (wt %)	TOC Rock–Eval 6 UO (wt %)
60	3	16–17	530.66	2.90	5.09	–	–
60	3	38–39	530.88	1.00	5.07	–	4.95
60	3	56–57	531.06	1.10	5.50	–	5.49
60	3	61–63	531.11	1.60	3.83	–	4.04
60	3	88–89	531.38	1.10	4.42	–	4.38
60	3	115–116	531.65	1.10	2.82	–	2.87
60	3	132–133	531.82	0.84	5.10	–	4.75
60	4	26–27	532.26	1.60	4.62	–	4.47
60	4	58–59	532.58	1.60	5.03	–	4.95
60	4	81–82	532.81	1.30	4.46	–	4.34
60	4	106–107	533.06	1.50	4.19	–	4.19
60	4	135–136	533.35	1.60	4.37	–	4.28
60	5	18–20	533.56	1.80	5.32	–	5.35
60	5	18–20	533.56	–	–	–	5.29
60	5	18–20	533.56	–	–	–	5.3
60	5	40–41	533.78	1.10	2.85	–	2.81
60	5	40–41	533.78	1.10	2.83	–	–
60	5	66–67	534.04	1.00	1.81	–	2.41
60	5	90–91	534.28	2.20	3.46	–	4.74
60	5	118–119	534.56	1.10	3.74	–	3.41
60	6	19–20	534.78	0.68	3.31	–	3.04
60	6	37–38	534.96	0.87	3.96	–	–
60	7	8–9	535.25	1.10	5.18	–	4.62
61	1	5–6	537.05	0.62	4.62	–	4.18
61	1	5–6	537.05	–	–	–	4.21
61	1	5–6	537.05	–	–	–	4.19
61	1	32–33	537.32	0.58	3.36	–	3.04
61	1	71–72	537.71	0.81	6.25	–	–
61	1	94–95	537.94	0.97	7.10	–	–
61	1	115–116	538.15	1.50	6.40	–	5.59
61	1	148–149	538.48	1.10	4.60	–	–
61	2	16–17	538.66	1.10	7.19	–	–
61	2	35–36	538.85	0.94	5.73	–	–
61	2	60–62	539.1	1.60	4.85	–	–
61	2	92–93	539.42	1.60	4.19	–	–
61	2	118–120	539.68	1.80	5.31	–	–
61	2	147–148	539.97	1.10	3.81	–	–
61	2	147–148	539.97	1.10	3.77	–	–
61	3	15–16	540.15	0.83	5.59	–	–
61	3	35–36	540.35	1.50	4.94	–	–
61	3	71–72	540.71	0.79	4.56	–	–
61	3	102–103	541.02	1.90	5.96	–	–

Core	Section	Interval (m)	Depth Top (mbsf)	S_{OM} LECO UERJ (wt %)	TOC LECO UERJ (wt %)	TOC Coulomat UO (wt %)	TOC Rock–Eval 6 UO (wt %)
61	3	133–134	541.33	0.97	5.93	–	–
61	4	1–2	541.51	0.78	4.28	–	–
61	4	30–31	541.8	0.87	5.07	–	–
61	4	45–46	541.95	0.94	6.79	–	–
61	4	66–67	542.16	1.60	6.59	–	–
61	4	91–92	542.41	0.97	6.91	–	–
61	4	123–124	542.73	1.60	4.88	–	–
61	4	148–149	542.98	1.30	4.41	–	–
61	5	14–15	543.14	1.40	4.57	–	–
61	5	35–36	543.35	1.40	4.61	–	–
61	5	57–58	543.57	1.60	5.69	–	–
61	5	77–78	543.77	1.50	4.82	–	–
61	5	102–103	544.02	1.50	4.59	–	–
61	6	17–18	544.36	1.60	4.71	–	–
61	6	17–18	544.36	1.60	4.86	–	–
62	1	13–14	546.63	1.70	4.82	–	–
62	1	33–34	546.83	1.60	5.03	–	–
62	1	56–57	547.06	1.60	7.62	–	–
62	1	88–89	547.38	1.70	5.80	–	–
62	1	123–124	547.73	1.10	4.49	–	–
62	1	147–148	547.97	1.10	4.37	–	–
62	2	11–12	548.11	0.86	4.81	–	–
62	2	42–43	548.42	0.67	2.64	–	–
62	2	65–66	548.65	0.81	3.71	–	–
62	2	88–89	548.88	0.87	3.61	–	–
62	2	107–108	549.07	0.93	3.93	–	–
62	2	126–128	549.26	0.81	4.23	–	–
62	2	146–147	549.46	0.96	3.84	–	–
62	3	23–24	549.73	0.81	3.29	–	–
62	3	43–45	549.93	0.70	4.10	–	–
62	3	69–70	550.19	0.51	3.22	–	–
62	3	93–94	550.43	0.95	4.15	–	–
62	3	121–122	550.71	0.71	3.39	–	–
62	3	121–122	550.71	0.66	3.22	–	–
62	3	146–147	550.96	0.99	3.47	–	–
62	4	12–13	551.12	0.62	3.89	–	–
62	4	36–37	551.36	0.71	3.22	–	–
62	4	58–89	551.58	0.84	5.78	–	–
62	4	89–90	551.89	0.72	4.69	–	–
62	4	119–120	552.19	0.75	4.48	–	–
62	4	146–147	552.46	1.10	4.96	–	–
62	5	13–14	552.63	0.90	5.05	–	–

Core	Section	Interval (m)	Depth Top (mbsf)	S_{OM} LECO UERJ (wt %)	TOC LECO UERJ (wt %)	TOC Coulomat UO (wt %)	TOC Rock–Eval 6 UO (wt %)
62	5	31–32	552.81	0.75	4.59	–	–
62	5	58–59	553.08	1.90	6.76	–	–
62	5	92–93	553.42	0.79	4.98	–	–
62	5	115–116	553.65	0.97	4.79	–	–
62	6	14–15	553.84	1.10	4.67	–	–
62	7	2–3	553.87	2.40	6.79	–	–

Table 6.2 (Chapter 6)

S1, S2, S3 and Tmax parameters from DSDP Site 511. UO – University of Oxford, UERJ – Universidade do Estado do Rio de Janeiro, mbsf – metres below sea floor.

Core	Section	Interval (m)	Depth Top (mbsf)	S1 (mg HC/g rock) CENPES	S2 (mg HC/g rock) CENPES	S3 (mg CO_2/g rock) CENPES	Tmax (° C) CENPES	S1 (mg HC/ g rock) UO	S2 (mg HC/g rock) UO	S3 (mg CO_2/g rock) UO	Tmax (° C) UO
57	2	49–50	500.99	0.16	5.24	3.44	430	–	–	–	–
57	4	97–98	504.47	0.06	1.94	1.92	433	–	–	–	–
58	2	85–86	510.85	0.03	3.43	2.38	433	–	–	–	–
58	4	110–111	513.81	0.13	2.48	1.92	408	–	–	–	–
58	4	137–138	514.08	–	–	–	–	0.06	3.89	3.33	413
58	4	147–148	514.18	0.15	13.59	2.35	424	0.11	12.61	2.73	426
58	5	10–11	514.31	0.28	18.47	2.85	423	0.18	17.55	3.41	426
59	1	17–18	518.17	0.27	26.37	2.62	421	0.19	24.92	3.91	424
59	1	39–40	518.39	0.3	27.79	3.84	418	0.25	27.5	3.94	423
59	1	60–61	518.6	0.41	19.16	1.89	412	0.3	18.68	2.3	419
59	1	90–91	518.9	0.16	15	3.04	423	0.12	13.68	3.1	427
59	1	123–124	519.23	0.09	4.05	1.47	431	–	–	–	–
59	1	146–147	519.46	0.49	38.63	3.76	419	0.43	38.74	4.75	423
59	2	20–21	519.7	–	–	–	–	0.03	0.63	1.93	410
59	2	20–21	519.7	–	–	–	–	0.15	0.77	2.03	410
59	2	20–21	519.7	–	–	–	–	0.03	0.7	2	411
59	2	43–44	519.93	–	–	–	–	0.04	7.99	3.32	425
59	2	61–62	520.11	–	–	–	–	0.1	4.27	2.2	416
59	2	105–106	520.55	0.08	4.51	2.28	405	–	–	–	–
59	2	132–133	520.82	–	–	–	–	0.05	0.63	2.11	404

Core	Section	Interval (m)	Depth Top (mbsf)	S1 (mg HC/g rock) CENPES	S2 (mg HC/g rock) CENPES	S3 (mg CO_2/g rock) CENPES	Tmax (° C) CENPES	S1 (mg HC/ g rock) UO	S2 (mg HC/g rock) UO	S3 (mg CO_2/g rock) UO	Tmax (° C) UO
59	3	26–27	521.26	0.21	18.78	2.93	424	0.13	18.2	3.2	429
59	3	49–51	521.49	0.22	20.96	3.13	418	0.17	20.37	3.61	424
59	3	65–66	521.65	0.51	18.08	2.1	407	0.48	15.54	2.77	409
59	3	94–95	521.94	0.25	22.54	3.31	417	0.2	21.83	3.67	428
59	3	123–124	522.23	0.25	17.4	3.27	417	0.21	17.15	3.61	421
59	4	26–27	522.76	0.13	13.83	2.97	420	0.11	13.73	2.93	425
59	4	71–73	523.21	0.09	7.11	1.58	416	–	–	–	–
59	4	91–92	523.41	0.18	18.14	2.55	424	0.13	17.23	2.92	427
59	4	121–122	523.71	0.23	23.67	3.01	420	0.2	23.65	3.46	424
59	4	145–146	523.95	0.27	20.14	3.11	420	0.21	20.21	3.14	427
59	4	145–146	523.95	–	–	–	–	0.24	19.98	3.18	428
60	1	18–19	527.68	0.31	26.76	2.11	422	0.26	27.06	3.54	423
60	1	40–41	527.9	–	–	–	–	–	–	–	–
60	1	61–62	528.11	0.13	7.51	2.35	415	0.12	7.73	2.56	419
60	1	83–84	528.33	0.12	11.19	2.85	420	0.07	11.27	2.69	427
60	1	106–107	528.56	0.18	14.84	2.58	424	0.14	14.3	2.6	428
60	1	127–128	528.77	0.15	7.86	2.67	413	0.09	7.38	2.83	417
60	2	13–14	529.13	0.08	3.19	0.6	422	–	–	–	–
60	2	26–27	529.26	0.06	3.57	1.11	420	–	–	–	–
60	2	47–48	529.47	0.24	15.27	2.7	418	0.15	14.74	2.88	422
60	2	82–83	529.82	0.17	16.76	2.73	420	0.17	16.78	2.64	427
60	2	101–102	530.01	0.21	19.6	3.27	409	0.18	18.68	3.58	417
60	2	132–133	530.32	0.04	2.13	0.88	412	–	–	–	–
60	3	16–17	530.66	0.22	14.09	3.12	414	–	–	–	–

Core	Section	Interval (m)	Depth Top (mbsf)	S1 (mg HC/g rock) CENPES	S2 (mg HC/g rock) CENPES	S3 (mg CO_2/g rock) CENPES	Tmax (° C) CENPES	S1 (mg HC/ g rock) UO	S2 (mg HC/g rock) UO	S3 (mg CO_2/g rock) UO	Tmax (° C) UO
60	3	38–39	530.88	0.24	20.95	2.41	423	0.19	19.65	2.85	426
60	3	56–57	531.06	0.39	23.79	3.22	418	0.22	23.13	3.29	423
60	3	61–63	531.11	0.14	13.14	2.8	418	0.1	12.8	2.81	421
60	3	88–89	531.38	0.22	18.77	2.23	422	0.17	17.71	2.57	423
60	3	115–116	531.65	0.13	9.05	2.07	416	0.08	8.66	2.09	419
60	3	132–133	531.82	0.23	19.57	2.51	420	0.21	19.4	2.79	423
60	4	26–27	532.26	0.17	15.27	2.64	416	0.12	14.28	2.98	419
60	4	58–59	532.58	0.17	15.06	3.2	414	0.14	14.64	3.25	415
60	4	81–82	532.81	0.2	15.24	2.76	419	0.12	14.63	2.78	422
60	4	106–107	533.06	0.13	10.61	2.68	414	0.08	10.01	3.15	418
60	4	135–136	533.35	0.17	13.43	2.98	411	0.1	12.49	2.9	419
60	5	18–20	533.56	0.2	17.17	3.71	413	0.17	16.79	3.43	415
60	5	18–20	533.56	–	–	–	–	0.15	16.39	3.39	415
60	5	18–20	533.56	–	–	–	–	0.15	16.8	3.29	417
60	5	40–41	533.78	0.14	8.78	2.27	412	0.07	8.19	2.07	421
60	5	66–67	534.04	0.1	5.19	1.74	415	0.03	4.7	1.65	421
60	5	90–91	534.28	0.24	7.56	1.29	399	0.22	7.74	1.16	404
60	5	118–119	534.56	0.31	8.15	1.46	401	0.25	7.67	1.46	405
60	6	19–20	534.78	0.15	5.65	1.59	400	0.1	5.07	1.59	405
60	6	37–38	534.96	0.31	8.7	1.49	402	–	–	–	–
60	7	8–9	535.25	0.78	15.05	2.08	400	0.63	14.59	1.91	406
61	1	5–6	537.05	0.46	13.67	1.71	408	0.35	13.15	1.59	412
61	1	5–6	537.05	–	–	–	–	0.31	13.25	1.54	415
61	1	5–6	537.05	–	–	–	–	0.32	12.68	1.63	412

Core	Section	Interval (m)	Depth Top (mbsf)	S1 (mg HC/g rock) CENPES	S2 (mg HC/g rock) CENPES	S3 (mg CO_2/g rock) CENPES	Tmax (° C) CENPES	S1 (mg HC/ g rock) UO	S2 (mg HC/g rock) UO	S3 (mg CO_2/g rock) UO	Tmax (° C) UO
61	1	32–33	537.32	0.34	5.77	1.65	401	0.25	5.91	1.43	406
61	1	71–72	537.71	0.73	20.26	2.3	404	–	–	–	–
61	1	94–95	537.94	0.8	22.56	2.17	401	–	–	–	–
61	1	115–116	538.15	0.35	30.63	3.29	414	0.25	29.55	2.98	422
61	1	148–149	538.48	0.51	12.86	1.68	404	–	–	–	–
61	2	16–17	538.66	0.82	25.79	2.28	406	–	–	–	–
61	2	35–36	538.85	0.61	20.07	2.01	405	–	–	–	–
61	2	60–62	539.1	0.23	22.18	2.61	419	–	–	–	–
61	2	92–93	539.42	0.19	19.25	2.04	423	–	–	–	–
61	2	147–148	539.97	0.31	7.64	1.39	402	–	–	–	–
61	3	15–16	540.15	0.37	15.88	2	401	–	–	–	–
61	3	35–36	540.35	0.15	23.05	3.11	417	–	–	–	–
61	3	71–72	540.71	0.33	13.31	1.7	401	–	–	–	–
61	3	102–103	541.02	0.26	31.57	3.04	412	–	–	–	–
61	3	133–134	541.33	0.38	23.65	1.9	408	–	–	–	–
61	4	1–2	541.51	0.34	11.72	1.53	401	–	–	–	–
61	4	30–31	541.8	0.36	11.69	1.77	397	–	–	–	–
61	4	45–46	541.95	0.48	23.22	2.02	404	–	–	–	–
61	4	66–67	542.16	0.25	29.58	2.73	414	–	–	–	–
61	4	91–92	542.41	0.8	23.78	2.54	402	–	–	–	–
61	4	123–124	542.73	0.24	23.56	2.68	417	–	–	–	–
61	4	148–149	542.98	0.23	21.12	2.89	418	–	–	–	–
61	5	14–15	543.14	0.24	22.18	2.92	417	–	–	–	–
61	5	35–36	543.35	0.24	20.37	2.5	419	–	–	–	–

Core	Section	Interval (m)	Depth Top (mbsf)	S1 (mg HC/g rock) CENPES	S2 (mg HC/g rock) CENPES	S3 (mg CO_2/g rock) CENPES	Tmax (° C) CENPES	S1 (mg HC/ g rock) UO	S2 (mg HC/g rock) UO	S3 (mg CO_2/g rock) UO	Tmax (° C) UO
61	5	57–58	543.57	0.29	27.81	2.96	414	–	–	–	–
61	5	77–78	543.77	0.23	23.23	2.88	418	–	–	–	–
61	5	102–103	544.02	0.23	22.08	2.6	416	–	–	–	–
61	6	17–18	544.36	0.26	22.68	3.04	417	–	–	–	–
62	1	13–14	546.63	0.14	21.41	2.19	418	–	–	–	–
62	1	33–34	546.83	0.19	23.93	2.22	423	–	–	–	–
62	1	56–57	547.06	0.3	38.24	3.09	414	–	–	–	–
62	1	88–89	547.38	0.24	27.31	2.86	413	–	–	–	–
62	1	123–124	547.73	0.34	10.91	1.28	405	–	–	–	–
62	1	147–148	547.97	0.37	11.8	1.72	401	–	–	–	–
62	2	11–12	548.11	0.33	11.69	1.85	401	–	–	–	–
62	2	42–43	548.42	0.15	4.08	1.36	399	–	–	–	–
62	2	65–66	548.65	0.2	6.1	1.52	398	–	–	–	–
62	2	88–89	548.88	0.21	6.89	1.4	400	–	–	–	–
62	2	107–108	549.07	0.36	6.96	2.02	399	–	–	–	–
62	2	126–128	549.26	0.39	10.36	1.69	403	–	–	–	–
62	2	146–147	549.46	0.35	7.28	1.78	399	–	–	–	–
62	3	43–45	549.93	0.4	10.13	1.62	402	–	–	–	–
62	3	69–70	550.19	0.26	4.8	1.77	403	–	–	–	–
62	3	93–94	550.43	0.35	7.56	1.84	397	–	–	–	–
62	3	121–122	550.71	0.31	6.46	1.64	400	–	–	–	–
62	3	146–147	550.96	0.3	5.51	1.73	399	–	–	–	–
62	4	12–13	551.12	0.32	5.38	2.25	400	–	–	–	–
62	4	36–37	551.36	0.21	2.88	1.95	398	–	–	–	–

Core	Section	Interval (m)	Depth Top (mbsf)	S1 (mg HC/g rock) CENPES	S2 (mg HC/g rock) CENPES	S3 (mg CO_2/g rock) CENPES	Tmax (° C) CENPES	S1 (mg HC/ g rock) UO	S2 (mg HC/g rock) UO	S3 (mg CO_2/g rock) UO	Tmax (° C) UO
62	4	58–89	551.58	0.57	14.47	2.13	401	–	–	–	–
62	4	89–90	551.89	0.52	11.75	1.76	400	–	–	–	–
62	4	119–120	552.19	0.49	10.68	1.65	401	–	–	–	–
62	4	146–147	552.46	0.4	12.35	2.04	403	–	–	–	–
62	5	13–14	552.63	0.45	11.15	1.82	400	–	–	–	–
62	5	31–32	552.81	0.52	13.72	2.06	401	–	–	–	–
62	5	58–59	553.08	0.26	27.39	3.43	417	–	–	–	–
62	5	92–93	553.42	0.42	15.01	2.02	402	–	–	–	–
62	5	115–116	553.65	0.47	13.44	2.09	401	–	–	–	–
62	6	14–15	553.84	0.31	11.68	2.03	407	–	–	–	–
62	7	2–3	553.87	1.09	29.9	4.34	417	–	–	–	–

Table 6.3 (Chapter 6)

$\delta^{13}C_{OM}$ values from DSDP Site 511. OU – Open University, UERJ – Universidade do Estado do Rio de Janeiro, mbsf – metres below sea floor.

Core	Section	Interval (m)	Depth – top (mbsf)	$\delta^{13}C_{OM}$ – UERJ (‰)	$\delta^{13}C_{OM}$ – OU (‰)
49	5	10–11.5	428.81	–	–29.1
49	5	38–42	429.09	–	–28.6
49	5	70–71.5	429.41	–	–29.4
49	5	98–101	429.69	–	–26.4
49	5	98–101	429.69	–	–26.7
49	5	130–131.5	430.01	–	–27.7
49	6	10–11.5	430.31	–	–28.0
49	6	40–42.5	430.61	–	–27.8
50	1	10–11.5	432.6	–	–28.2
50	1	40–43	432.9	–	–27.4
50	1	68–69.5	433.18	–	–27.4
50	1	101.5–103	433.515	–	–26.5
50	1	130–131.5	433.8	–	–27.7
50	2	11–12.5	434.11	–	–27.0
50	2	40–42	434.4	–	–27.9
50	2	70–71.5	434.7	–	–28.1
50	2	102–103.5	435.02	–	–27.3
50	2	130–131.5	435.3	–	–27.3
50	3	9–10.5	435.59	–	–27.5
50	3	40–42.5	435.9	–	–26.9
50	3	68.5–70	436.185	–	–26.4
50	3	101–102.5	436.51	–	–27.8
50	3	130–131.5	436.8	–	–27.9
50	4	20–22.5	437.08	–	–28.2
50	4	47–50	437.35	–	–26.1
50	5	5–6.5	437.56	–	–26.6
51	1	10–13	442.1	–	–27.2
51	1	40–41.5	442.4	–	–27.2
51	1	70–71.5	442.7	–	–28.4
51	1	100–101.5	443	–	–28.0
51	1	128–129.5	443.28	–	–26.8
51	2	10–11.5	443.6	–	–28.4
51	2	40–41.5	443.9	–	–26.1
51	2	71–72.5	444.21	–	–26.5
51	2	100–101.5	444.5	–	–26.0
51	2	130–132	444.8	–	–26.7
51	3	10–11.5	445.1	–	–26.8
51	3	40–41.5	445.4	–	–27.8
51	3	68.5–70	445.685	–	–28.2

Core	Section	Interval (m)	Depth – top (mbsf)	$\delta^{13}C_{OM}$ – UERJ (‰)	$\delta^{13}C_{OM}$ – OU (‰)
51	3	100–101.5	446	–	–27.0
51	3	130–131.5	446.3	–	–27.3
51	4	8.5–10	446.585	–	–28.6
51	4	40–41.5	446.9	–	–28.3
51	4	71–72.5	447.21	–	–27.2
51	4	100–101.5	447.5	–	–28.3
51	4	129–132	447.79	–	–27.6
51	5	8–10	448.08	–	–27.9
51	5	40–42	448.4	–	–27.1
51	5	73–75	448.73	–	–27.5
51	5	100–102	449	–	–26.4
51	5	130–132	449.3	–	–26.4
51	6	6–8	449.56	–	–27.2
51	6	40–42	449.9	–	–26.8
51	6	73–75	450.23	–	–25.9
51	6	100–103	450.5	–	–26.9
51	6	130–132	450.8	–	–27.5
52	1	10–11.5	451.6	–	–26.7
52	1	40–41.5	451.9	–	–28.2
52	1	75–77	452.25	–	–26.1
52	1	100–101.5	452.5	–	–26.9
52	1	130–131.5	452.8	–	–27.0
52	2	10–12	453.1	–	–26.6
52	2	42–44	453.42	–	–26.7
52	2	76–78	453.76	–	–26.8
52	2	100–102	454	–	–27.0
52	2	130–132	454.3	–	–27.7
52	3	9–12	454.59	–	–25.5
52	3	40–42	454.9	–	–25.8
52	3	70–72	455.2	–	–26.2
52	3	100–102	455.5	–	–26.2
52	3	130–132	455.8	–	–25.6
52	4	11–13	456.11	–	–25.2
52	4	39–41	456.39	–	–25.8
52	4	73–75	456.73	–	–25.1
52	4	100–102	457	–	–25.1
52	4	130–132	457.3	–	–24.7
52	5	9–12	457.59	–	–24.7
52	5	40–42	457.9	–	–24.7
52	5	70–72	458.2	–	–24.9
52	5	100–101.5	458.5	–	–25.2
52	6	10–12	458.81	–	–25.3
52	6	40–41.5	459.11	–	–24.6

Core	Section	Interval (m)	Depth – top (mbsf)	$\delta^{13}C_{OM}$ – UERJ (‰)	$\delta^{13}C_{OM}$ – OU (‰)
52	6	70–72	459.41	–	–25.1
52	6	101–103	459.72	–	–24.7
52	6	130–132	460.01	–	–24.9
52	7	9–12	460.3	–	–24.5
52	7	40–42	460.61	–	–25.3
52	8	3–5	460.91	–	–25.8
53	1	37–38	461.37	–	–25.3
53	1	83–84	461.83	–	–26.7
53	1	118–119	462.18	–	–25.2
53	2	46–47	462.96	–	–25.9
53	2	84–85	463.34	–	–25.8
53	2	118–120	463.68	–	–26.3
53	3	39–40	464.39	–	–25.3
53	3	72–73	464.72	–	–24.7
53	3	121–122	465.21	–	–24.6
53	4	26–27	465.76	–	–25.0
53	4	78–79	466.28	–	–26.3
53	4	121–122	466.71	–	–25.6
53	5	37–38	467.37	–	–25.4
53	5	70–71	467.7	–	–24.9
53	5	106–107	468.06	–	–25.3
53	6	26–27	468.76	–	–24.0
53	6	70–71	469.2	–	–26.2
53	6	94–95	469.44	–	–25.4
53	7	19–20	470.19	–	–26.6
54	1	33–35	470.83	–	–25.8
54	1	69–70	471.19	–	–25.3
54	1	120–121	471.7	–	–25.2
54	2	41–42	472.41	–	–24.5
54	2	80–81	472.8	–	–26.0
54	2	116–117	473.16	–	–25.5
54	3	38–39	473.88	–	–26.6
54	3	81–82	474.31	–	–25.2
54	3	127–128	474.77	–	–25.9
54	4	41–42	475.41	–	–25.3
54	4	83–84	475.83	–	–25.4
54	4	123–124	476.23	–	–24.9
54	5	38–39	476.88	–	–24.5
54	5	70–71	477.2	–	–26.7
54	5	110–111	477.6	–	–26.2
54	6	37–38	478.37	–	–26.1
54	6	90–91	478.9	–	–25.6
55	1	28–29	480.28	–	–24.2

Core	Section	Interval (m)	Depth – top (mbsf)	$\delta^{13}C_{OM}$ – UERJ (‰)	$\delta^{13}C_{OM}$ – OU (‰)
55	1	67–68	480.67	–	–25.2
55	1	109–110	481.09	–	–24.7
55	2	39–40	481.89	–	–25.3
55	2	89–90	482.39	–	–25.2
55	2	127–129	482.77	–	–26.8
55	3	30–31	483.3	–	–26.2
55	3	64–65	483.64	–	–24.8
55	3	92–93	483.92	–	–23.8
55	3	130–131	484.3	–	–25.3
55	4	20–21	484.7	–	–23.5
55	4	56–57	485.06	–	–24.4
55	4	89–90	485.39	–	–27.2
55	5	26–27	485.97	–	–27.2
55	5	58–59	486.29	–	–25.0
55	5	99–100	486.7	–	–27.7
55	6	49–50	487.6	–	–26.2
56	1	31–32	489.81	–	–24.5
56	1	58–59	490.08	–	–25.8
56	1	89–90	490.39	–	–23.8
56	1	128–129	490.78	–	–27.7
56	2	22–23	491.22	–	–26.0
56	2	58–59	491.58	–	–27.9
56	2	84–85	491.84	–	–26.4
56	2	112–113	492.12	–	–24.1
56	2	142–143	492.42	–	–22.4
56	3	27–28	492.77	–	–31.3
56	3	54–55	493.04	–	–27.5
56	3	77–78	493.27	–	–22.0
56	3	121–122	493.71	–	–26.2
56	3	147–148	493.97	–	–25.5
56	4	22–23	494.22	–	–23.5
56	4	50–51	494.5	–	–21.5
56	4	81–82	494.81	–	–22.2
56	4	107–108	495.07	–	–23.4
56	4	135–136	495.35	–	–24.7
56	5	14–15	495.64	–	–22.5
56	5	38–39	495.88	–	–24.4
56	5	63–64	496.13	–	–24.4
56	5	88–89	496.38	–	–24.4
56	5	119–120	496.69	–	–23.2
57	1	19–20	499.19	–	–24.1
57	1	43–44	499.43	–	–24.4
57	1	74–75	499.74	–	–24.1

Core	Section	Interval (m)	Depth – top (mbsf)	$\delta^{13}C_{OM}$ – UERJ (‰)	$\delta^{13}C_{OM}$ – OU (‰)
57	1	101–102	500.01	–	–25.7
57	1	125–126	500.25	–	–25.3
57	1	146–147	500.46	–	–24.7
57	2	5–6	500.55	–	–23.7
57	2	25–26	500.75	–	–23.5
57	2	49–50	500.99	–25.9	–25.5
57	2	71–72	501.21	–25.3	–24.8
57	2	71–72	501.21	–	–24.6
57	2	95–96	501.45	–25.8	–22.6
57	2	122–123	501.72	–	–21.4
57	2	122–123	501.72	–	–23.8
57	2	140–141	501.9	–	–24.9
57	3	24–25	502.24	–	–24.8
57	3	49–50	502.49	–25.4	–24.9
57	3	69–70	502.69	–	–24.7
57	3	89–90	502.89	–	–25.9
57	3	110–111	503.1	–	–23.9
57	3	137–138	503.37	–	–25.4
57	4	22–23	503.72	–	–24.3
57	4	39–40	503.89	–	–24.8
57	4	65–66	504.15	–25.7	–24.8
57	4	65–66	504.15	–	–24.8
57	4	97–98	504.47	–26.1	–25.3
57	4	97–98	504.47	–	–25.1
57	4	131–132	504.81	–	–24.7
57	4	147–148	504.97	–	–23.8
57	5	11–12	505.11	–	–23.8
57	5	11–12	505.11	–	–23.7
57	5	36–37	505.36	–	–23.3
57	5	58–59	505.58	–	–22.1
57	5	77–78	505.77	–	–24.9
57	5	111–112	506.11	–	–24.2
57	5	140–141	506.4	–	–24.0
57	6	8–9	506.58	–	–24.9
57	6	37–38	506.87	–	–24.6
58	1	26–27	508.76	–	–24.0
58	1	51–52	509.01	–	–24.8
58	1	69–70	509.19	–	–23.8
58	1	92–93	509.42	–	–24.3
58	1	121–122	509.71	–	–23.1
58	1	148–149	509.98	–	–24.7
58	2	17–19	510.17	–	–24.5
58	2	41–42	510.41	–	–24.7

Core	Section	Interval (m)	Depth – top (mbsf)	$\delta^{13}C_{OM}$ – UERJ (‰)	$\delta^{13}C_{OM}$ – OU (‰)
58	2	62–63	510.62	–	–25.4
58	2	85–86	510.85	–27.1	–26.8
58	2	120–121	511.2	–	–25.1
58	2	147–148	511.47	–	–24.4
58	3	15–16	511.65	–	–23.2
58	3	31–32	511.81	–	–24.9
58	3	53–54	512.03	–25.7	–22.2
58	3	53–54	512.03	–	–25.5
58	3	53–54	512.03	–	–25.1
58	3	72–73	512.22	–	–24.7
58	3	96–98	512.46	–	–26.0
58	3	96–98	512.46	–	–25.2
58	3	118–119	512.68	–	–22.7
58	4	12–13	512.83	–	–24.1
58	4	33–34	513.04	–	–24.3
58	4	53–54	513.24	–	–25.9
58	4	83–84	513.54	–	–25.4
58	4	90–91	513.61	–	–28.1
58	4	110–111	513.81	–29.0	–27.0
58	4	137–138	514.08	–28.9	–
58	4	147–148	514.18	–29.7	–
58	5	10–11	514.31	–29.9	–29.9
59	1	17–18	518.17	–29.1	–29.1
59	1	39–40	518.39	–29.2	–28.7
59	1	39–40	518.39	–	–29.8
59	1	60–61	518.6	–28.9	–28.4
59	1	60–61	518.6	–	–28.0
59	1	90–91	518.9	–29.1	–28.8
59	1	123–124	519.23	–28.5	–28.0
59	1	146–147	519.46	–29.0	–28.4
59	2	43–44	519.93	–	–29.1
59	2	61–62	520.11	–	–28.1
59	2	105–106	520.55	–29.5	–29.1
59	2	105–106	520.55	–	–28.8
59	2	132–133	520.82	–29.8	–29.0
59	2	132–133	520.82	–	–29.0
59	2	132–133	520.82	–	–28.8
59	3	26–27	521.26	–30.3	–29.6
59	3	26–27	521.26	–	–30.5
59	3	49–51	521.49	–30.5	–29.7
59	3	49–51	521.49	–	–30.9
59	3	65–66	521.65	–29.6	–29.7
59	3	94–95	521.94	–30.1	–

Core	Section	Interval (m)	Depth – top (mbsf)	$\delta^{13}C_{OM}$ – UERJ (‰)	$\delta^{13}C_{OM}$ – OU (‰)
59	3	123–124	522.23	–29.6	–29.8
59	3	123–124	522.23	–	–30.8
59	4	6–8	522.56	–	–28.6
59	4	26–27	522.76	–30.0	–29.7
59	4	26–27	522.76	–	–29.2
59	4	71–73	523.21	–29.5	–29.4
59	4	91–92	523.41	–29.4	–29.1
59	4	91–92	523.41	–	–28.9
59	4	121–122	523.71	–29.4	–29.4
59	4	121–122	523.71	–	–28.7
59	4	145–146	523.95	–30.2	–29.5
59	4	145–146	523.95	–	–32.3
60	1	18–19	527.68	–30.0	–29.8
60	1	18–19	527.68	–	–30.7
60	1	40–41	527.9	–	–29.9
60	1	40–41	527.9	–	–29.7
60	1	40–41	527.9	–	–31.2
60	1	61–62	528.11	–30.1	–29.8
60	1	83–84	528.33	–30.2	–27.6
60	1	106–107	528.56	–29.9	–28.9
60	1	127–128	528.77	–29.6	–29.1
60	2	13–14	529.13	–	–29.1
60	2	13–14	529.13	–	–29.7
60	2	13–14	529.13	–	–30.6
60	2	26–27	529.26	–29.3	–28.4
60	2	47–48	529.47	–29.2	–32.0
60	2	82–83	529.82	–30.0	–30.5
60	2	101–102	530.01	–28.4	–
60	3	16–17	530.66	–29.0	–32.1
60	3	38–39	530.88	–29.5	–29.3
60	3	38–39	530.88	–	–29.1
60	3	56–57	531.06	–29.5	–29.5
60	3	61–63	531.11	–29.6	–29.5
60	3	88–89	531.38	–29.3	–
60	3	115–116	531.65	–28.9	–31.6
60	3	132–133	531.82	–29.3	–28.8
60	4	26–27	532.26	–29.6	–31.4
60	4	58–59	532.58	–29.3	–
60	4	81–82	532.81	–30.3	–29.5
60	4	106–107	533.06	–29.5	–29.0
60	4	135–136	533.35	–29.9	–30.6
60	5	18–20	533.56	–29.0	–28.5
60	5	40–41	533.78	–29.7	–

Core	Section	Interval (m)	Depth – top (mbsf)	$\delta^{13}C_{OM}$ – UERJ (‰)	$\delta^{13}C_{OM}$ – OU (‰)
60	5	66–67	534.04	–29.7	–
60	5	90–91	534.28	–29.3	–28.9
60	5	118–119	534.56	–30.6	–30.2
60	6	19–20	534.78	–29.9	–29.5
60	6	37–38	534.96	–30.4	–
60	7	8–9	535.25	–29.5	–29.4
61	1	5–6	537.05	–30.0	–29.8
61	1	32–33	537.32	–30.5	–29.8
61	1	71–72	537.71	–30.3	–
61	1	94–95	537.94	–30.1	–
61	1	115–116	538.15	–29.7	–30.7
61	1	148–149	538.48	–30.3	–
61	2	16–17	538.66	–29.6	–
61	2	35–36	538.85	–29.6	–29.6
61	2	60–62	539.1	–30.5	–30.0
61	2	92–93	539.42	–30.5	–29.8
61	2	118–120	539.68	–29.8	–
61	2	147–148	539.97	–30.4	–30.3
61	3	15–16	540.15	–30.8	–
61	3	35–36	540.35	–30.1	–
61	3	71–72	540.71	–30.1	–
61	3	102–103	541.02	–30.4	–
61	3	133–134	541.33	–29.8	–
61	4	1–2	541.51	–30.0	–
61	4	30–31	541.8	–30.4	–
61	4	45–46	541.95	–30.2	–
61	4	66–67	542.16	–29.8	–
61	4	91–92	542.41	–29.4	–
61	4	123–124	542.73	–28.8	–
61	4	148–149	542.98	–29.3	–
61	5	14–15	543.14	–29.7	–
61	5	35–36	543.35	–30.1	–
61	5	57–58	543.57	–30.3	–
61	5	77–78	543.77	–28.9	–
61	5	102–103	544.02	–29.9	–
61	6	17–18	544.36	–29.3	–
62	1	13–14	546.63	–30.3	–
62	1	33–34	546.83	–30.2	–
62	1	56–57	547.06	–29.6	–
62	1	88–89	547.38	–30.6	–
62	1	123–124	547.73	–29.6	–
62	1	147–148	547.97	–30.1	–
62	2	11–12	548.11	–30.0	–

Core	Section	Interval (m)	Depth – top (mbsf)	$\delta^{13}C_{OM}$ – UERJ (‰)	$\delta^{13}C_{OM}$ – OU (‰)
62	2	42–43	548.42	–30.2	–
62	2	65–66	548.65	–30.6	–
62	2	88–89	548.88	–30.3	–
62	2	107–108	549.07	–30.2	–
62	2	126–128	549.26	–30.2	–
62	2	146–147	549.46	–30.2	–
62	3	23–24	549.73	–30.4	–
62	3	43–45	549.93	–29.7	–
62	3	69–70	550.19	–30.2	–
62	3	93–94	550.43	–29.8	–
62	3	121–122	550.71	–30.6	–
62	3	146–147	550.96	–30.3	–
62	4	12–13	551.12	–30.0	–
62	4	36–37	551.36	–30.0	–
62	4	58–89	551.58	–29.7	–
62	4	89–90	551.89	–30.1	–
62	4	119–120	552.19	–29.2	–
62	4	146–147	552.46	–29.1	–
62	5	13–14	552.63	–29.1	–
62	5	31–32	552.81	–29.4	–
62	5	58–59	553.08	–28.4	–
62	5	92–93	553.42	–28.5	–
62	5	115–116	553.65	–28.4	–
62	6	14–15	553.84	–28.0	–
62	7	2–3	553.87	–27.6	–

Table 6.4 (Chapter 6)

Compilation of TIC, $\delta^{13}C_{carb}$, $\delta^{18}O_{carb}$, TOC, HI, OI and $\delta^{13}C_{OM}$ from DSDP Site 511 (Dias, 1998).

Depth (mbsf)	TIC (wt %)	$\delta^{13}C_{carb}$ (‰)	$\delta^{18}O_{carb}$ (‰)	TOC (wt %)	HI (mg HC/g TOC)	OI (mg CO_2/g TOC)	$\delta^{13}C_{OM}$ (‰)
501.46	0.06	–1.25	0.8	2.15	168	117	–28.1
503.57	0.00	4.06	–2.1	2.37	309	58	–18.5
506.04	1.08	3.72	–1.45	1.03	102	184	–26.8
506.56	0.30	3.54	–1.99	0.9	99	161	–28.2
508.87	0.00	–	–	0.41	80	90	–27.1
511.39	0.90	1.93	–1.87	0.99	88	97	–27.1
514.05	0.00	–	–	5.03	206	44	–29.5
518.26	3.00	0.01	–3.68	4.93	425	63	–29.2
520.31	0.00	–	–	2.52	44	67	–30.7
521.93	0.48	1.81	–2.88	4.54	283	58	–31.1
522.83	1.92	–0.22	–4.62	2.24	191	84	–29.2
527.51	3.84	1.07	–3.91	3.48	303	61	–29.7
529.52	2.52	1.6	–3.22	4.12	388	55	–29.6
531.07	2.22	0.85	–4.09	3.55	353	59	–30.6
533.13	3.00	0.59	–3.7	3.47	327	69	–
534.52	0.00	–	–	3.39	270	35	–
535.05	0.00	–	–	3.47	253	33	–31.0
537.49	0.00	–	–	4.28	293	36	–31.2
539.29	0.84	–8.7	–1.58	4.11	439	50	–29.7
540.59	0.00	–	–	4.66	409	36	–
542.42	1.20	–8.06	–2.44	4.81	503	52	–31.1
543.45	0.54	–0.29	–2.69	3.7	441	47	–31.1
547.62	0.00	–	–	5.98	403	33	–30.7
548.79	0.00	–	–	3.35	213	39	–
550.24	0.00	–	–	2.98	206	40	–
551.75	0.00	–	–	3.96	180	35	–30.4
553.19	0.78	–2.52	–1.92	5.25	421	41	–30.0
556.29	0.00	–1.08	–2.99	2.62	286	50	–30.2
559.69	0.00	2.06	–2.03	5.03	455	38	–29.3

Table 6.5 (Chapter 6)

Compilation of TOC, $\delta^{13}C_{carb}$ and $\delta^{18}O_{carb}$ from DSDP Site 511 (Azevedo, 2001).

Depth (mbsf)	TOC (wt %)	$\delta^{13}C_{carb}$ (‰)	$\delta^{18}O_{carb}$ (‰)
429.18	0.05	0.94	–1.1
429.39	0.07	1.01	–0.93
429.59	0.04	1.93	–0.08
429.8	0.04	2.15	0.07
430	0.04	2.23	0.03
430.2	0.03	2.07	–0.41
430.39	0.04	1.67	–0.71
430.69	0.03	1.63	–0.6
430.89	0.04	1.61	–0.33
432.7	0.03	1.27	–0.6
432.9	0.03	1.3	–0.42
433.1	0.03	1.23	–0.32
433.3	0.04	1.36	–0.05
433.49	0.03	1.02	–0.87
433.7	0.04	0.98	–0.11
433.9	0.03	1.51	–0.38
434.2	0.03	0.58	–0.61
434.4	0.05	0.89	–0.55
434.6	0.03	1.58	0.21
435.2	0.03	0.23	–0.73
435.4	0.06	0.96	–0.44
435.69	0.05	1.02	–0.24
435.9	0.04	1.18	–0.21
436.09	0.04	1.29	–0.41
436.3	0.04	0.95	–0.66
436.5	0.04	1.42	–0.21
436.7	0.07	1.38	–0.19
436.88	0.06	1.34	–0.37
437.2	0.04	1.14	–0.32
437.4	0.03	1.7	0.05
437.59	0.04	1.83	–0.02
442.2	–	1.58	–0.7
442.6	–	1.58	–0.7
443	–	1.55	–0.7
443.4	–	1.55	–0.7
443.9	–	2.15	–0.6
444.3	–	2.02	–0.5
444.69	–	2.35	–0.7
444.89	–	2.43	–0.3
445.2	–	2.21	–0.9

Depth (mbsf)	TOC (wt %)	$\delta^{13}C_{carb}$ (‰ – VPDB)	$\delta^{18}O_{carb}$ (‰ – VPDB)
445.4	–	1.84	–0.9
445.79	–	2.29	–0.2
446.2	–	1.98	–0.8
446.71	–	2.45	–0.2
447.1	–	2.3	–0.2
447.5	–	2.37	–0.3
447.9	–	1.95	–0.7
448.39	–	1.84	–0.8
448.8	–	1.77	–0.4
449.2	–	1.72	–0.9
449.7	–	1.81	–0.4
450.1	–	1.82	–1.4
450.5	–	2.03	–0.6
451.7	–	1.73	–0.2
452.1	–	1.8	–0.8
452.5	–	1.59	–0.2
452.71	–	1.58	–0.3
452.89	–	1.58	–0.7
453.39	–	2.26	–0.8
453.8	–	1.5	–0.5
454.2	–	1.82	–1.2
454.7	–	2.03	–0.5
455.1	–	2.21	–1
455.5	–	2.05	–0.5
455.9	–	2.06	–0.4
456.4	–	1.81	0.06
456.81	–	1.97	–1.1
457.2	–	1.78	0.02
459.19	–	2.26	–0.3
459.6	–	2.19	–0.4
460	–	2.34	0
460.38	–	2.34	–0.5
480.2	–	2.39	–0.6
480.59	–	1.67	–1
481	–	1.74	–0.8
481.38	–	2.21	–2
481.91	–	1.14	–1.2
482.29	–	1.92	–0.5
482.69	–	1.51	–0.9
483.19	–	1.68	–1.4
483.6	–	1.48	–1.3
483.99	–	1.67	–0.9
484.4	–	1.5	–1.2

Depth (mbsf)	TOC (wt %)	$\delta^{13}C_{carb}$ (‰ – VPDB)	$\delta^{18}O_{carb}$ (‰ – VPDB)
484.9	–	1.25	–1.1
485.3	–	0.75	–0.9
485.69	–	0.58	–1.3
486.19	–	0.01	–1.5
486.59	–	0.83	–1.9
486.99	–	1.72	–1.1
487.38	–	1.55	–1.1
487.89	–	1.8	–1
489.71	–	1.47	–1.4
490.1	–	0.87	–1.9
490.49	–	1.4	–2.5

Table 6.6 (Chapter 6)

Total inorganic carbon (TIC) values from DSDP Site 511. UO – University of Oxford, mbsf – metres below sea floor.

Core	Section	Interval (m)	Depth – top (mbsf)	TIC Coulomat – UO (wt %)	TIC Rock–Eval 6 –UO (wt %)
49	5	10–11.5	428.81	0.96	–
49	5	38–42	429.09	1.25	–
49	5	70–71.5	429.41	3.00	–
49	5	98–101	429.69	7.29	–
49	5	130–131.5	430.01	3.65	–
49	6	10–11.5	430.31	2.44	–
49	6	40–42.5	430.61	3.68	–
50	1	10–11.5	432.6	1.49	–
50	1	40–43	432.9	4.62	–
50	1	68–69.5	433.18	1.29	–
50	1	101.5–103	433.515	5.28	–
50	1	130–131.5	433.8	5.66	–
50	2	11–12.5	434.11	3.37	–
50	2	40–42	434.4	2.99	–
50	2	70–71.5	434.7	1.23	–
50	2	102–103.5	435.02	3.59	–
50	2	130–131.5	435.3	3.83	–
50	3	9–10.5	435.59	3.75	–
50	3	40–42.5	435.9	3.52	–
50	3	68.5–70	436.185	4.20	–
50	3	101–102.5	436.51	4.23	–
50	3	130–131.5	436.8	2.96	–
50	4	20–22.5	437.08	4.05	–
50	4	47–50	437.35	5.53	–
50	5	5–6.5	437.56	6.55	–
51	1	10–13	442.1	6.17	–
51	1	40–41.5	442.4	3.93	–
51	1	70–71.5	442.7	3.25	–
51	1	100–101.5	443	3.17	–
51	1	128–129.5	443.28	2.89	–
51	2	10–11.5	443.6	3.45	–
51	2	40–41.5	443.9	3.07	–
51	2	71–72.5	444.21	3.88	–
51	2	100–101.5	444.5	3.99	–
51	2	130–132	444.8	3.86	–
51	3	10–11.5	445.1	5.36	–
51	3	40–41.5	445.4	5.39	–
51	3	68.5–70	445.685	6.85	–

Core	Section	Interval (m)	Depth – top (mbsf)	TIC Coulomat – UO (wt %)	TIC Rock–Eval 6 –UO (wt %)
51	3	100–101.5	446	3.80	–
51	3	130–131.5	446.3	2.13	–
51	4	8.5–10	446.585	3.68	–
51	4	40–41.5	446.9	3.11	–
51	4	71–72.5	447.21	2.94	–
51	4	100–101.5	447.5	4.40	–
51	4	129–132	447.79	3.96	–
51	5	8–10	448.08	4.00	–
51	5	40–42	448.4	4.47	–
51	5	73–75	448.73	3.25	–
51	5	100–102	449	2.88	–
51	5	130–132	449.3	3.23	–
51	6	6–8	449.56	5.28	–
51	6	40–42	449.9	5.13	–
51	6	73–75	450.23	3.39	–
51	6	100–103	450.5	4.57	–
51	6	130–132	450.8	2.24	–
52	1	10–11.5	451.6	5.12	–
52	1	40–41.5	451.9	6.52	–
52	1	75–77	452.25	4.39	–
52	1	100–101.5	452.5	4.08	–
52	1	130–131.5	452.8	3.80	–
52	2	10–12	453.1	3.28	–
52	2	42–44	453.42	3.06	–
52	2	76–78	453.76	3.08	–
52	2	100–102	454	3.15	–
52	2	130–132	454.3	2.20	–
52	3	9–12	454.59	3.84	–
52	3	40–42	454.9	3.46	–
52	3	70–72	455.2	3.99	–
52	3	100–102	455.5	3.90	–
52	3	130–132	455.8	1.90	–
52	4	11–13	456.11	2.86	–
52	4	39–41	456.39	3.47	–
52	4	73–75	456.73	3.93	–
52	4	100–102	457	2.53	–
52	4	130–132	457.3	3.07	–
52	5	9–12	457.59	3.29	–
52	5	40–42	457.9	4.19	–
52	5	70–72	458.2	3.71	–
52	5	100–101.5	458.5	5.18	–
52	6	10–12	458.81	4.10	–

Core	Section	Interval (m)	Depth – top (mbsf)	TIC Coulomat – UO (wt %)	TIC Rock–Eval 6 –UO (wt %)
52	6	40–41.5	459.11	2.47	–
52	6	70–72	459.41	2.93	–
52	6	101–103	459.72	5.46	–
52	6	130–132	460.01	4.62	–
52	7	9–12	460.3	3.12	–
52	7	40–42	460.61	3.77	–
52	8	3–5	460.91	5.07	–
53	1	37–38	461.37	0.82	–
53	1	83–84	461.83	3.97	–
53	1	118–119	462.18	2.68	–
53	2	46–47	462.96	2.19	–
53	2	84–85	463.34	4.97	–
53	2	118–120	463.68	3.56	–
53	3	39–40	464.39	4.60	–
53	3	72–73	464.72	2.75	–
53	3	121–122	465.21	3.39	–
53	4	26–27	465.76	4.54	–
53	4	78–79	466.28	3.26	–
53	4	78–79	466.28	3.28	–
53	4	121–122	466.71	4.23	–
53	5	37–38	467.37	5.51	–
53	5	37–38	467.37	5.71	–
53	5	70–71	467.7	4.57	–
53	5	106–107	468.06	5.80	–
53	6	26–27	468.76	4.91	–
53	6	70–71	469.2	3.84	–
53	6	94–95	469.44	4.04	–
53	7	19–20	470.19	6.01	–
54	1	33–35	470.83	3.39	–
54	1	69–70	471.19	2.89	–
54	1	120–121	471.7	3.54	–
54	2	41–42	472.41	2.13	–
54	2	80–81	472.8	4.31	–
54	2	116–117	473.16	4.13	–
54	3	38–39	473.88	3.88	–
54	3	38–39	473.88	3.87	–
54	3	81–82	474.31	5.29	–
54	3	81–82	474.31	5.24	–
54	3	127–128	474.77	3.25	–
54	4	41–42	475.41	2.61	–
54	4	83–84	475.83	2.20	–
54	4	123–124	476.23	1.83	–

Core	Section	Interval (m)	Depth – top (mbsf)	TIC Coulomat – UO (wt %)	TIC Rock–Eval 6 –UO (wt %)
54	5	38–39	476.88	3.06	–
54	5	70–71	477.2	2.52	–
54	5	110–111	477.6	2.89	–
54	6	37–38	478.37	3.80	–
54	6	90–91	478.9	1.78	–
54	7	9–10	479.21	3.66	–
55	1	28–29	480.28	4.66	–
55	1	67–68	480.67	3.80	–
55	1	109–110	481.09	2.84	–
55	2	39–40	481.89	2.58	–
55	2	89–90	482.39	3.74	–
55	2	127–129	482.77	3.48	–
55	3	30–31	483.3	2.94	–
55	3	64–65	483.64	4.05	–
55	3	92–93	483.92	3.63	–
55	3	130–131	484.3	3.07	–
55	4	20–21	484.7	3.12	–
55	4	56–57	485.06	4.37	–
55	4	89–90	485.39	3.19	–
55	4	89–90	485.39	3.10	–
55	5	26–27	485.97	4.09	–
55	5	58–59	486.29	3.03	–
55	5	99–100	486.7	4.36	–
55	6	21–22	487.32	5.51	–
55	6	49–50	487.6	4.14	–
55	6	49–50	487.6	4.03	–
56	1	31–32	489.81	3.70	–
56	1	58–59	490.08	1.90	–
56	1	89–90	490.39	0.11	–
56	1	128–129	490.78	1.76	–
56	2	22–23	491.22	3.16	–
56	2	58–59	491.58	2.05	–
56	2	84–85	491.84	2.21	–
56	2	112–113	492.12	0.90	–
56	2	142–143	492.42	1.63	–
56	3	27–28	492.77	0.13	–
56	3	54–55	493.04	2.74	–
56	3	77–78	493.27	0.10	–
56	3	121–122	493.71	0.51	–
56	3	147–148	493.97	0.09	–
56	4	22–23	494.22	0.12	–
56	4	50–51	494.5	0.10	–

Core	Section	Interval (m)	Depth – top (mbsf)	TIC Coulomat – UO (wt %)	TIC Rock–Eval 6 –UO (wt %)
56	4	81–82	494.81	0.09	–
56	4	107–108	495.07	0.24	–
56	4	107–108	495.07	–	–
56	4	135–136	495.35	0.08	–
56	5	14–15	495.64	0.34	–
56	5	38–39	495.88	0.14	–
56	5	63–64	496.13	0.09	–
56	5	88–89	496.38	0.10	–
56	5	119–120	496.69	0.10	–
57	1	19–20	499.19	0.10	–
57	1	43–44	499.43	0.09	–
57	1	74–75	499.74	0.09	–
57	1	101–102	500.01	0.18	–
57	1	125–126	500.25	0.12	–
57	1	146–147	500.46	0.45	–
57	1	146–147	500.46	0.51	–
57	2	5–6	500.55	0.07	–
57	2	25–26	500.75	0.08	–
57	2	49–50	500.99	0.88	–
57	2	49–50	500.99	1.04	–
57	2	71–72	501.21	0.11	–
57	2	95–96	501.45	0.23	–
57	2	122–123	501.72	0.17	–
57	2	122–123	501.72	0.27	–
57	2	140–141	501.9	0.27	–
57	2	140–141	501.9	0.37	–
57	3	24–25	502.24	0.12	–
57	3	24–25	502.24	0.19	–
57	3	49–50	502.49	0.56	–
57	3	49–50	502.49	0.65	–
57	3	69–70	502.69	0.10	–
57	3	89–90	502.89	0.19	–
57	3	110–111	503.1	0.09	–
57	3	137–138	503.37	0.27	–
57	4	22–23	503.72	1.42	–
57	4	39–40	503.89	0.48	–
57	4	39–40	503.89	0.43	–
57	4	65–66	504.15	0.39	–
57	4	97–98	504.47	1.25	–
57	4	131–132	504.81	0.37	–
57	4	147–148	504.97	0.35	–
57	4	147–148	504.97	0.53	–

Core	Section	Interval (m)	Depth – top (mbsf)	TIC Coulomat – UO (wt %)	TIC Rock–Eval 6 –UO (wt %)
57	5	11–12	505.11	0.13	–
57	5	36–37	505.36	0.26	–
57	5	58–59	505.58	0.23	–
57	5	77–78	505.77	0.41	–
57	5	77–78	505.77	0.47	–
57	5	111–112	506.11	0.16	–
57	5	140–141	506.4	0.93	–
57	5	140–141	506.4	0.98	–
57	6	8–9	506.58	0.66	–
57	6	37–38	506.87	0.66	–
58	1	26–27	508.76	0.13	–
58	1	26–27	508.76	–	–
58	1	51–52	509.01	0.45	–
58	1	69–70	509.19	0.12	–
58	1	92–93	509.42	0.24	–
58	1	121–122	509.71	0.34	–
58	1	148–149	509.98	0.65	–
58	2	17–19	510.17	0.22	–
58	2	41–42	510.41	0.17	–
58	2	62–63	510.62	1.25	–
58	2	85–86	510.85	6.18	–
58	2	120–121	511.2	1.40	–
58	2	147–148	511.47	0.24	–
58	2	147–148	511.47	0.26	–
58	3	15–16	511.65	0.74	–
58	3	15–16	511.65	0.75	–
58	3	31–32	511.81	0.45	–
58	3	53–54	512.03	0.62	–
58	3	72–73	512.22	0.63	–
58	3	96–98	512.46	0.58	–
58	3	118–119	512.68	0.71	–
58	4	12–13	512.83	0.08	–
58	4	12–13	512.83	–	–
58	4	33–34	513.04	0.09	–
58	4	53–54	513.24	0.08	–
58	4	83–84	513.54	0.46	–
58	4	90–91	513.61	6.31	–
58	4	110–111	513.81	0.10	–
58	4	137–138	514.08	0.74	1.01
58	4	147–148	514.18	2.19	1.87
58	5	10–11	514.31	3.04	2.99
59	1	17–18	518.17	2.82	2.66

Core	Section	Interval (m)	Depth – top (mbsf)	TIC Coulomat – UO (wt %)	TIC Rock–Eval 6 –UO (wt %)
59	1	39–40	518.39	2.30	2.22
59	1	60–61	518.6	0.12	0.11
59	1	90–91	518.9	2.84	2.87
59	1	123–124	519.23	0.35	–
59	1	146–147	519.46	0.88	0.78
59	2	20–21	519.7	0.09	0.31
59	2	20–21	519.7	–	0.31
59	2	20–21	519.7	–	0.31
59	2	43–44	519.93	2.71	2.90
59	2	61–62	520.11	0.08	0.23
59	2	105–106	520.55	0.11	–
59	2	132–133	520.82	0.09	0.40
59	3	26–27	521.26	1.65	1.44
59	3	26–27	521.26	–	–
59	3	49–51	521.49	2.63	2.34
59	3	65–66	521.65	0.15	0.18
59	3	94–95	521.94	1.79	1.47
59	3	123–124	522.23	1.86	1.42
59	4	6–8	522.56	10.78	–
59	4	26–27	522.76	3.70	3.80
59	4	71–73	523.21	9.21	–
59	4	91–92	523.41	3.93	4.08
59	4	121–122	523.71	2.81	2.81
59	4	145–146	523.95	3.48	3.50
59	4	145–146	523.95	–	3.51
60	1	18–19	527.68	2.45	2.30
60	1	40–41	527.9	9.14	–
60	1	61–62	528.11	4.52	4.72
60	1	83–84	528.33	2.69	2.73
60	1	106–107	528.56	2.09	2.15
60	1	127–128	528.77	3.25	3.56
60	2	13–14	529.13	10.46	–
60	2	26–27	529.26	8.34	–
60	2	26–27	529.26	–	–
60	2	47–48	529.47	3.97	4.14
60	2	82–83	529.82	4.51	4.80
60	2	101–102	530.01	3.24	3.19
60	2	132–133	530.32	9.24	–
60	3	16–17	530.66	1.73	–
60	3	38–39	530.88	2.04	2.02
60	3	56–57	531.06	2.94	2.95
60	3	61–63	531.11	4.08	4.05

Core	Section	Interval (m)	Depth – top (mbsf)	TIC Coulomat – UO (wt %)	TIC Rock–Eval 6 –UO (wt %)
60	3	88–89	531.38	3.04	3.13
60	3	115–116	531.65	7.00	7.36
60	3	132–133	531.82	2.67	2.80
60	4	26–27	532.26	4.56	4.84
60	4	58–59	532.58	2.92	3.03
60	4	81–82	532.81	3.75	3.97
60	4	106–107	533.06	2.03	2.17
60	4	135–136	533.35	3.58	3.72
60	5	18–20	533.56	3.80	3.95
60	5	18–20	533.56	–	3.99
60	5	18–20	533.56	–	4.04
60	5	40–41	533.78	7.12	7.59
60	5	40–41	533.78	–	–
60	5	66–67	534.04	7.64	7.46
60	5	90–91	534.28	0.13	0.18
60	5	118–119	534.56	0.13	0.20
60	6	19–20	534.78	0.09	0.15
60	6	37–38	534.96	0.12	–
60	7	8–9	535.25	0.16	0.19
61	1	5–6	537.05	0.13	0.14
61	1	5–6	537.05	–	0.15
61	1	5–6	537.05	–	0.15
61	1	32–33	537.32	0.13	0.21
61	1	71–72	537.71	0.14	–
61	1	94–95	537.94	0.13	–
61	1	115–116	538.15	1.96	1.82
61	1	148–149	538.48	0.10	–
61	2	16–17	538.66	0.09	–
61	2	35–36	538.85	0.10	–
61	2	60–62	539.1	0.55	–
61	2	92–93	539.42	0.60	–
61	2	118–120	539.68	0.62	–
61	2	147–148	539.97	0.13	–
61	2	147–148	539.97	–	–
61	3	15–16	540.15	0.11	–
61	3	35–36	540.35	1.53	–
61	3	71–72	540.71	0.11	–
61	3	102–103	541.02	1.79	–
61	3	133–134	541.33	0.13	–
61	4	1–2	541.51	0.13	–
61	4	30–31	541.8	0.13	–
61	4	45–46	541.95	0.11	–

Core	Section	Interval (m)	Depth – top (mbsf)	TIC Coulomat – UO (wt %)	TIC Rock–Eval 6 –UO (wt %)
61	4	66–67	542.16	0.19	–
61	4	91–92	542.41	0.10	–
61	4	91–92	542.41	0.11	–
61	4	123–124	542.73	1.36	–
61	4	123–124	542.73	1.37	–
61	4	148–149	542.98	1.67	–
61	4	148–149	542.98	1.69	–
61	5	14–15	543.14	1.69	–
61	5	14–15	543.14	1.71	–
61	5	35–36	543.35	0.54	–
61	5	57–58	543.57	0.86	–
61	5	77–78	543.77	0.95	–
61	5	102–103	544.02	0.93	–
61	6	17–18	544.36	0.50	–
61	6	17–18	544.36	–	–
62	1	13–14	546.63	0.50	–
62	1	33–34	546.83	0.66	–
62	1	56–57	547.06	1.41	–
62	1	88–89	547.38	1.12	–
62	1	123–124	547.73	0.15	–
62	1	147–148	547.97	0.16	–
62	2	11–12	548.11	0.18	–
62	2	42–43	548.42	0.14	–
62	2	65–66	548.65	0.12	–
62	2	88–89	548.88	0.13	–
62	2	107–108	549.07	0.12	–
62	2	126–128	549.26	0.11	–
62	2	146–147	549.46	0.12	–
62	3	23–24	549.73	0.13	–
62	3	43–45	549.93	0.12	–
62	3	69–70	550.19	0.12	–
62	3	93–94	550.43	0.13	–
62	3	121–122	550.71	0.16	–
62	3	121–122	550.71	–	–
62	3	146–147	550.96	0.17	–
62	4	12–13	551.12	0.16	–
62	4	36–37	551.36	0.15	–
62	4	58–89	551.58	0.17	–
62	4	89–90	551.89	0.14	–
62	4	119–120	552.19	0.19	–
62	4	146–147	552.46	0.15	–
62	5	13–14	552.63	0.15	–

Core	Section	Interval (m)	Depth – top (mbsf)	TIC Coulomat – UO (wt %)	TIC Rock–Eval 6 –UO (wt %)
62	5	31–32	552.81	0.17	–
62	5	58–59	553.08	0.50	–
62	5	92–93	553.42	0.12	–
62	5	115–116	553.65	0.13	–
62	6	14–15	553.84	0.12	–
62	7	2–3	553.87	0.96	–

Table 6.7 (Chapter 6)

$\delta^{13}C_{carb}$ and $\delta^{18}O_{carb}$ values from DSDP Site 511.

Core	Section	Interval (m)	Depth – top (mbsf)	$\delta^{13}C_{carb}$ (‰)	$\delta^{18}C_{carb}$ (‰)
49	5	10–11.5	428.81	1.02	–1.13
49	5	38–42	429.09	1.12	–1.03
49	5	70–71.5	429.41	2.26	–0.08
49	5	98–101	429.69	2.22	–0.48
49	5	130–131.5	430.01	2.92	0.98
49	6	10–11.5	430.31	2.33	–0.57
49	6	40–42.5	430.61	1.61	–1.17
50	1	10–11.5	432.60	1.79	–0.59
50	1	40–43	432.90	2.67	1.37
50	1	68–69.5	433.18	1.76	–0.64
50	1	101.5–103	433.52	1.13	–0.13
50	1	130–131.5	433.80	1.66	0.59
50	2	11–12.5	434.11	1.36	–0.36
50	2	40–42	434.40	1.16	–0.52
50	2	70–71.5	434.70	0.99	–0.59
50	2	102–103.5	435.02	1.54	–0.52
50	2	130–131.5	435.30	0.60	–0.88
50	3	9–10.5	435.59	1.11	0.02
50	3	40–42.5	435.90	1.54	–0.30
50	3	68.5–70	436.19	1.76	–0.36
50	3	101–102.5	436.51	1.61	–0.33
50	3	130–131.5	436.80	1.41	–0.66
50	4	20–22.5	437.08	1.40	–0.22
50	4	47–50	437.35	1.83	0.18
50	5	5–6.5	437.56	1.88	0.07
51	1	10–13	442.10	1.61	0.19
51	1	40–41.5	442.40	1.59	0.80
51	1	70–71.5	442.70	1.54	–0.55
51	1	100–101.5	443.00	1.58	–0.45
51	1	128–129.5	443.28	1.55	–0.98
51	2	10–11.5	443.60	1.52	–0.53
51	2	40–41.5	443.90	1.86	–0.71
51	2	71–72.5	444.21	2.10	–0.24
51	2	100–101.5	444.50	2.01	–0.34
51	2	130–132	444.80	2.17	–0.57
51	3	10–11.5	445.10	2.27	0.46
51	3	40–41.5	445.40	2.30	–0.10
51	3	68.5–70	445.69	2.28	0.69
51	3	100–101.5	446.00	2.14	–0.61
51	3	130–131.5	446.30	2.00	–1.21

Core	Section	Interval (m)	Depth – top (mbsf)	$\delta^{13}C_{carb}$ (‰)	$\delta^{18}C_{carb}$ (‰)
51	4	8.5–10	446.59	2.08	0.71
51	4	40–41.5	446.90	2.06	0.17
51	4	71–72.5	447.21	2.18	–0.33
51	4	100–101.5	447.50	2.22	0.03
51	4	129–132	447.79	2.08	0.84
51	5	8–10	448.08	1.87	1.00
51	5	40–42	448.40	1.92	0.87
51	5	73–75	448.73	1.69	–0.43
51	5	100–102	449.00	1.49	–0.77
51	5	130–132	449.30	1.64	0.41
51	6	6–8	449.56	1.98	0.75
51	6	40–42	449.90	1.60	–0.35
51	6	73–75	450.23	1.38	–0.08
51	6	100–103	450.50	2.03	–0.40
51	6	130–132	450.80	2.25	–0.57
52	1	10–11.5	451.60	1.95	–0.21
52	1	40–41.5	451.90	1.82	–0.05
52	1	75–77	452.25	1.98	–0.05
52	1	100–101.5	452.50	1.63	–0.40
52	1	130–131.5	452.80	1.69	–0.71
52	2	10–12	453.10	2.03	–0.51
52	2	42–44	453.42	2.22	–0.64
52	2	76–78	453.76	1.76	–0.60
52	2	100–102	454.00	1.93	–0.56
52	2	130–132	454.30	1.89	–0.91
52	3	9–12	454.59	2.01	–0.32
52	3	40–42	454.90	2.30	–0.45
52	3	70–72	455.20	2.30	–0.34
52	3	100–102	455.50	2.19	–0.05
52	3	130–132	455.80	2.13	–0.97
52	4	11–13	456.11	1.76	–0.34
52	4	39–41	456.39	1.75	0.04
52	4	73–75	456.73	1.77	–0.58
52	4	100–102	457.00	2.04	–0.51
52	4	130–132	457.30	1.92	–0.57
52	5	9–12	457.59	1.75	–0.72
52	5	40–42	457.90	1.88	0.07
52	5	70–72	458.20	2.28	–0.48
52	5	100–101.5	458.50	2.15	–0.16
52	6	10–12	458.81	2.54	0.56
52	6	40–41.5	459.11	2.33	–0.65
52	6	70–72	459.41	2.34	–0.67
52	6	101–103	459.72	2.45	0.33

Core	Section	Interval (m)	Depth – top (mbsf)	$\delta^{13}C_{carb}$ (‰)	$\delta^{18}C_{carb}$ (‰)
52	6	130–132	460.01	2.37	0.37
52	7	9–12	460.30	2.13	–0.38
52	7	40–42	460.61	2.19	–0.21
52	8	3–5	460.91	2.09	0.37
53	1	37–38	461.37	2.46	–0.51
53	1	83–84	461.83	2.43	–0.48
53	1	118–119	462.18	3.11	0.58
53	2	46–47	462.96	1.93	–1.05
53	2	84–85	463.34	2.78	0.52
53	2	118–120	463.68	2.07	–0.80
53	3	39–40	464.39	2.24	0.14
53	3	72–73	464.72	2.49	–0.51
53	3	121–122	465.21	2.55	0.80
53	4	26–27	465.76	2.34	0.04
53	4	78–79	466.28	2.23	–0.70
53	4	121–122	466.71	2.50	0.92
53	5	37–38	467.37	2.36	–0.52
53	5	70–71	467.70	2.49	–0.60
53	5	106–107	468.06	2.42	–0.70
53	6	26–27	468.76	2.85	–0.35
53	6	70–71	469.20	2.83	–0.84
53	6	94–95	469.44	2.79	0.01
53	7	19–20	470.19	2.19	–0.05
54	1	33–35	470.83	2.54	–0.44
54	1	69–70	471.19	2.65	–0.46
54	1	120–121	471.70	2.84	–0.08
54	2	41–42	472.41	2.91	–0.29
54	2	80–81	472.80	3.16	–0.76
54	2	116–117	473.16	3.25	–0.89
54	3	38–39	473.88	2.66	–0.33
54	3	81–82	474.31	2.74	0.07
54	3	127–128	474.77	2.41	–0.84
54	4	41–42	475.41	2.25	–0.57
54	4	83–84	475.83	2.03	–0.54
54	4	123–124	476.23	2.76	–1.21
54	5	38–39	476.88	1.63	–0.55
54	5	70–71	477.20	2.11	–1.44
54	5	110–111	477.60	2.32	–0.86
54	6	37–38	478.37	2.39	–0.22
54	6	90–91	478.90	2.47	–0.66
54	7	9–10	479.21	2.29	–1.07
55	1	28–29	480.28	2.18	–0.24
55	1	67–68	480.67	2.32	–0.64

Core	Section	Interval (m)	Depth – top (mbsf)	$\delta^{13}C_{carb}$ (‰)	$\delta^{18}C_{carb}$ (‰)
55	1	109–110	481.09	1.68	–0.06
55	2	39–40	481.89	0.92	–1.37
55	2	89–90	482.39	2.02	0.07
55	2	127–129	482.77	0.93	–0.75
55	3	30–31	483.30	1.28	–1.77
55	3	64–65	483.64	1.58	–0.78
55	3	92–93	483.92	1.48	–1.03
55	3	130–131	484.30	–0.52	–1.58
55	4	20–21	484.70	1.57	–0.85
55	4	56–57	485.06	1.42	–0.87
55	4	89–90	485.39	–0.27	–1.50
55	5	26–27	485.97	–0.01	–1.43
55	5	58–59	486.29	0.92	–1.88
55	5	99–100	486.70	1.53	–1.43
55	6	21–22	487.32	1.93	–0.93
55	6	49–50	487.60	1.14	–1.65
56	1	31–32	489.81	1.79	–1.13
56	1	58–59	490.08	1.14	–1.92
56	1	128–129	490.78	0.88	–1.68
56	2	22–23	491.22	2.17	–1.25
56	2	58–59	491.58	1.58	–1.51
56	2	84–85	491.84	1.92	–1.72
56	2	112–113	492.12	1.22	–2.03
56	2	142–143	492.42	2.99	–1.49
56	3	54–55	493.04	2.48	–1.99
56	3	121–122	493.71	2.65	–1.03
56	4	50–51	494.50	–9.33	–0.28
56	4	107–108	495.07	0.22	–1.08
56	5	38–39	495.88	–2.35	–0.93
56	5	63–64	496.13	–7.06	–2.11
57	1	19–20	499.19	–8.03	–0.70
57	1	125–126	500.25	3.08	–1.59
57	1	146–147	500.46	–0.29	0.45
57	2	49–50	500.99	2.07	–0.39
57	2	95–96	501.45	5.57	–1.88
57	3	49–50	502.49	4.54	–1.39
57	3	69–70	502.69	1.07	–1.40
57	3	137–138	503.37	3.16	–2.12
57	4	22–23	503.72	3.53	–1.99
57	4	65–66	504.15	4.07	–1.12
57	4	97–98	504.47	3.00	–1.37
57	4	147–148	504.97	–2.18	0.81
57	5	11–12	505.11	3.08	–1.16

Core	Section	Interval (m)	Depth – top (mbsf)	$\delta^{13}C_{carb}$ (‰)	$\delta^{18}C_{carb}$ (‰)
57	5	36–37	505.36	3.99	–1.06
57	5	58–59	505.58	4.43	–1.33
57	5	77–78	505.77	2.74	–0.63
57	5	111–112	506.11	3.82	–2.04
57	5	140–141	506.40	–1.25	0.67
57	6	8–9	506.58	3.26	–1.84
57	6	37–38	506.87	3.22	–1.35
58	1	51–52	509.01	4.49	–1.80
58	1	92–93	509.42	–2.04	–0.63
58	1	148–149	509.98	3.77	–1.40
58	2	17–19	510.17	3.32	–1.46
58	2	62–63	510.62	3.57	–2.07
58	2	85–86	510.85	0.78	–2.35
58	2	120–121	511.20	2.27	–2.13
58	3	15–16	511.65	2.83	–2.28
58	3	31–32	511.81	3.13	–2.22
58	3	53–54	512.03	3.03	–2.15
58	3	72–73	512.22	2.18	–2.05
58	4	90–91	513.61	–16.73	–5.79
58	4	137–138	514.08	–8.30	–6.39
58	4	147–148	514.18	–2.82	–5.53
58	5	10–11	514.31	–1.56	–5.94
59	1	17–18	518.17	–0.98	–3.56
59	1	39–40	518.39	0.27	–3.89
59	1	90–91	518.90	–4.55	–4.20
59	1	123–124	519.23	–1.48	–4.12
59	1	146–147	519.46	1.30	–3.52
59	2	43–44	519.93	–1.94	–4.74
59	3	26–27	521.26	0.18	–3.53
59	3	49–51	521.49	–0.06	–4.34
59	3	94–95	521.94	1.34	–3.32
59	3	123–124	522.23	1.91	–3.73
59	4	6–8	522.56	–0.39	–2.47
59	4	26–27	522.76	0.61	–4.03
59	4	71–73	523.21	–4.20	–4.00
59	4	91–92	523.41	–0.14	–3.61
59	4	121–122	523.71	1.76	–2.91
59	4	145–146	523.95	1.66	–3.20
60	1	18–19	527.68	1.49	–3.29
60	1	40–41	527.90	–0.97	–4.74
60	1	61–62	528.11	–2.57	–4.18
60	1	83–84	528.33	0.01	–3.89
60	1	106–107	528.56	1.42	–2.51

Core	Section	Interval (m)	Depth – top (mbsf)	$\delta^{13}C_{carb}$ (‰)	$\delta^{18}C_{carb}$ (‰)
60	1	127–128	528.77	–0.96	–5.76
60	2	13–14	529.13	–6.33	–1.57
60	2	26–27	529.26	–2.02	–3.08
60	2	47–48	529.47	1.43	–4.26
60	2	82–83	529.82	0.89	–2.82
60	2	101–102	530.01	–0.94	–4.52
60	2	132–133	530.32	–8.67	–1.69
60	3	16–17	530.66	1.64	–3.31
60	3	38–39	530.88	1.73	–2.68
60	3	56–57	531.06	0.91	–3.46
60	3	61–63	531.11	–0.19	–3.24
60	3	88–89	531.38	1.13	–3.56
60	3	115–116	531.65	–2.01	–4.11
60	3	132–133	531.82	1.97	–0.85
60	4	26–27	532.26	–0.18	–3.33
60	4	58–59	532.58	–0.42	–3.19
60	4	81–82	532.81	–0.39	–5.49
60	4	106–107	533.06	0.24	–2.91
60	4	135–136	533.35	–2.03	–2.75
60	5	18–20	533.56	–0.96	–4.66
60	5	40–41	533.78	–2.63	–5.26
60	5	66–67	534.04	–4.79	–2.56
61	1	115–116	538.15	–4.73	–1.65
61	2	60–62	539.10	–5.38	–1.85
61	2	92–93	539.42	–4.66	–1.14
61	2	118–120	539.68	1.18	–1.94
61	3	35–36	540.35	–4.02	–2.22
61	3	102–103	541.02	–3.61	–1.82
61	4	123–124	542.73	–3.78	–2.07
61	4	148–149	542.98	–4.36	–2.73
61	5	14–15	543.14	–3.28	–3.45
61	5	35–36	543.35	–0.18	–2.75
61	5	57–58	543.57	–0.61	–2.94
61	5	77–78	543.77	–0.19	–2.74
61	5	102–103	544.02	–0.58	–2.05
61	6	17–18	544.36	–0.56	–2.78
62	1	13–14	546.63	–0.64	–2.68
62	1	33–34	546.83	–0.74	–2.59
62	1	56–57	547.06	–0.51	–2.54
62	5	58–59	553.08	–1.17	–1.80
62	7	2–3	553.87	–0.17	–2.77

Table 6.8 (Chapter 6)

Magnetic susceptibility (MS), characteristic remanent magnetization (ChRM) inclination (Inc), Maximum angular deviation (MAD) and palaeolatitude (Palaeo λ) values from DSDP Site 511. Data with MAD > 15° are in blue and diagrams where vectors were difficult to be interpreted in red.

Core	Section	Interval (m)	Depth* Top (m)	ChRM Inc (°)	MAD (°)	Palaeo λ	MS ($x10^{-8}$)
58	1	27–28	508.77	–74.7	10.9	–61.32	6.34
58	1	53–54	509.03	–65.9	12.6	–48.18	5.28
58	1	70–71	509.20	80.3	7.3	71.13	5.31
58	1	90–91	509.40	–67.4	6.5	–50.22	5.11
58	1	148–149	509.98	–65.2	14.7	–47.26	4.95
58	2	15–17	510.15	–43.7	18.7	–25.54	4.37
58	2	61–62	510.61	–49.3	12.6	–30.17	5.02
58	2	86–87	510.86	–69.5	26.6	–53.21	4.81
58	2	117–118	511.17	–68.0	6.0	–51.06	5.03
58	2	148–149	511.48	76.0	32.6	63.50	4.51
58	3	10–11	511.60	–62.0	13.6	–43.24	5.34
58	3	31–32	511.81	–62.2	5.8	–43.48	6.33
58	3	54–55	512.04	–51.2	7.6	–31.88	6.25
58	3	73–74	512.23	–76.9	8.2	–65.04	6.04
58	3	98–99	512.48	–64.4	9.0	–46.22	5.42
58	4	16–17	512.87	–61.2	5.3	–42.29	5.73
58	4	38–39	513.09	–50.3	7.6	–31.06	5.71
58	4	98–99	513.69	–63.4	20.1	–44.96	6.78
58	4	110–111	513.81	–35.6	7.2	–19.70	7.42
58	4	134–135	514.05	–44.2	30.9	–25.93	4.57
58	4	145–146	514.16	–63.3	27.6	–44.83	4.73
58	CC	7–8	514.28	–58.1	10.2	–38.77	4.13
59	1	16–17	518.16	88.2	17.4	86.40	4.12
59	1	40–41	518.40	64.1	2.4	45.84	5.93
59	1	60–61	518.60	–	–	–	–
59	1	90–91	518.90	73.0	8.4	58.56	5.62
59	1	123–124	519.23	–48.0	2.3	–29.04	3.09
59	2	61–62	520.11	–50.6	6.8	–31.33	6.07
59	2	104–105	520.54	–31.6	15.8	–17.10	4.94
59	2	131–132	520.81	–66.8	18.7	–49.40	11.3
59	3	24–25	521.24	–68.9	9.8	–52.34	4.30
59	3	47–48	521.47	–64.2	10.3	–45.97	3.46
59	3	65–66	521.65	–47.9	8.1	–28.96	4.06
59	3	95–96	521.95	–71.8	7.4	–56.67	4.87

Core	Section	Interval (m)	Depth* Top (m)	ChRM Inc (°)	MAD (°)	Paleo λ	MS – 1 ($x10^{-8}$)
59	3	124–125	522.24	–57.3	6.3	–37.91	2.00
59	4	7–8	522.57	–29.0	11.3	–15.49	2.83
59	4	25–26	522.75	–70.4	21.3	–54.54	3.47
59	4	70–71	523.20	–65.1	11.8	–47.13	3.07
59	4	90–91	523.40	–61.0	15.8	–42.05	2.93
59	4	120–121	523.70	–	–	–	–
59	4	144–145	523.94	–61.2	8.7	–42.29	2.94

Table 6.9 (Chapter 6)

Re-Os geochronology data from DSDP Site 511. $^{187}Os/^{188}Os_i$ – Initial ratio of $^{187}Os/^{188}Os_i$ calculated to 122, 125 and 130 Ma.

Core	Section	Interval (m)	Depth – top (mbsf)	Re (ppb)	±2σ	Os (ppt)	±2σ	$^{187}Re/^{188}Os$	±2σ	$^{187}Os/^{188}Os$	±2σ	rho	$^{187}Os/^{188}Os_i$ (122 Ma)	$^{187}Os/^{188}Os_i$ (125 Ma)	$^{187}Os/^{188}Os_i$ (130 Ma)
58	4	90–92	513.61	128.1	0.2	746.0	3.3	1127	3	2.904	0.011	0.7	0.61	0.55	0.40
58	4	95–97	513.66	184.0	0.3	1037	4	1184	3	3.081	0.008	0.7	0.67	0.61	0.45
58	4	100–102	513.71	113.8	0.2	967.5	3.3	709.0	1.7	2.053	0.006	0.6	0.61	0.57	0.48
58	4	111–113	513.82	68.37	0.13	864.9	2.4	440.4	1.0	1.323	0.003	0.7	0.43	0.40	0.35
58	4	115–117	513.86	150.2	0.3	1298	4	724.6	1.6	2.421	0.006	0.6	0.95	0.91	0.81
58	4	121–123	513.92	72.93	0.13	1015	3	400.0	0.9	1.320	0.003	0.6	0.51	0.49	0.43
58	4	125–127	513.96	41.03	0.08	787.1	2.1	283.6	0.7	1.118	0.003	0.6	0.54	0.53	0.49
58	4	129–132	514.00	271.9	0.5	1198	5	1672	4	4.182	0.012	0.6	0.78	0.70	0.47
58	4	135–137	514.06	535.9	1.0	1765	8	2583	6	5.996	0.017	0.6	0.74	0.61	0.27
59	1	101–103	519.01	108.6	0.2	1168	4	538.1	1.2	1.667	0.004	0.6	0.57	0.55	0.47
59	1	105–107	519.05	89.35	0.16	1090	3	466.9	1.0	1.522	0.004	0.6	0.57	0.55	0.49
59	1	110–112	519.10	45.68	0.09	831.2	2.3	301.8	0.7	1.198	0.003	0.6	0.58	0.57	0.53
59	1	115–117	519.15	55.41	0.10	837.6	2.8	366.7	1.0	1.279	0.005	0.6	0.53	0.51	0.47
59	1	120–122	519.20	28.76	0.06	981.0	2.4	153.9	0.4	0.816	0.002	0.6	0.50	0.50	0.47
59	1	125–127	519.25	371.7	0.7	1613	7	1674	4	4.019	0.010	0.6	0.61	0.53	0.31
59	1	129–131	519.29	245.6	0.4	1160	8	1489	6	3.650	0.025	0.6	0.62	0.55	0.35
59	1	135–137	519.35	91.69	0.17	1306	4	392.9	0.9	1.362	0.004	0.6	0.56	0.54	0.49
59	1	140–142	519.40	126.2	0.2	1674	5	424.0	0.9	1.410	0.003	0.6	0.55	0.53	0.47

Appendix E

Table 7.1 (Chapter 7)

$\delta^{13}C_{carb}$ and $\delta^{18}C_{carb}$ from Poggio le Guaine core.

Depth (m)	$\delta^{13}C_{carb}$ (‰)	$\delta^{18}C_{carb}$ (‰)
86.01	4.26	–2.61
86.12	4.55	–2.25
86.26	4.57	–2.14
86.26	4.43	–2.15
86.26	4.51	–1.93
86.26	4.55	–2.08
86.49	4.40	–2.33
86.64	4.64	–2.40
86.72	4.37	–3.04
86.83	4.34	–2.13
86.92	4.27	–2.41
86.92 (vein)	0.59	0.16
87.04	4.64	–2.16
87.04	4.64	–1.99
87.04	4.47	–2.44
87.16	4.50	–2.40
87.24	4.11	–2.00
87.38	4.54	–1.99
87.55	4.64	–1.88
87.64	4.34	–1.79
87.74	3.90	–2.23
87.74	3.90	–1.95
87.74	3.66	–2.32
88.68	4.22	–2.34
88.68	4.28	–2.50
88.68	4.33	–2.31
88.79	4.18	–2.63
89.11	4.43	–2.32
89.22	4.17	–2.92
89.22	3.85	–2.92
89.22	4.01	–2.98
89.29	3.59	–3.47
89.29	3.54	–3.46
89.29	3.62	–3.27
90.36	2.34	–2.19
90.67	1.77	–1.71
90.97	1.94	–2.94
90.97	1.69	–2.97
90.97	1.82	–2.72
91.17	2.88	–2.87
91.17	2.70	–3.25
91.17	2.76	–3.27
91.25	3.01	–2.62
91.33	3.02	–2.37
91.41	2.89	–2.50
91.53	3.25	–2.09

Depth (m)	$\delta^{13}C_{carb}$ (‰ – VPDB)	$\delta^{18}C_{carb}$ (‰ – VPDB)
91.53	3.23	–2.28
91.53	3.28	–2.29
91.63	3.14	–2.10
91.63 (vein)	2.70	–0.08
91.72	2.92	–1.78
91.83	2.90	–1.65
91.92	2.77	–2.08
92.09	2.78	–2.03
92.20	2.55	–1.84
92.20	2.79	–1.52
92.20	2.73	–1.67
92.34	2.63	–2.56
92.60	2.58	–2.34
92.71	2.53	–2.11
92.85	2.52	–2.23
93.05	2.82	–2.07
93.05	2.79	–2.06
93.05	2.77	–2.25
93.16	2.91	–2.21
93.25	2.79	–2.02
93.34	2.83	–2.12
93.43	2.66	–2.54
93.51	2.78	–1.76
93.62	3.18	–1.96
93.71	3.24	–2.32
93.71	3.34	–2.44
93.71	3.29	–2.47
93.81	2.72	–2.35
93.95	2.68	–2.09
94.06	2.66	–1.74
94.17	2.51	–1.71
94.28	2.43	–1.82
94.40	2.56	–1.72
94.50	2.54	–2.06
94.59	2.35	–1.68
94.68	2.30	–2.43
94.77	2.40	–2.32
94.90	2.34	–2.66
94.99	2.64	–2.38
95.10	2.46	–2.39
95.10	2.43	–2.35
95.10	2.24	–2.69
95.21	2.19	–2.75
95.29	2.18	–2.54
95.38	2.35	–2.46
95.48	2.43	–2.18
95.57	2.40	–2.14
95.71	2.38	–2.21
95.80	2.44	–2.33
95.90	2.45	–2.23
95.99	2.39	–2.38
95.99	2.69	–2.79
95.99	2.38	–2.50

Bibliography

Abrahão, D., and Warme, J. E., 1990. Lacustrine and Associated Deposits in a Rifted Continental Margin–Lower Cretaceous Lagoa Feia Formation, Campos Basin, Offshore Brazil. In: Katz, B. J. (Ed.), Lacustrine Basin Exploratiion – Case Studies and Modern Analogs. AAPG Memoir 56. The American Association of Petroleum Geologists, Tulsa USA, pp. 287–305.

Allègre, C. J., Louvat, P., Gaillardet, J., Meynadier, L., Rad, S., and Capmas, F., 2010. The fundamental role of island arc weathering in the oceanic Sr isotope budget. Earth and Planetary Science Letters, 292(1–2): 51–56.

Ando, A., 2015. Intersite discrepancy in the amplitude of marine negative $\delta^{13}C$ excursion at the onset of early Aptian oceanic anoxic event 1a: Reconciliation through Sr isotopic screening of peculiar diagenetic overprint on the Pacific reference section (Deep Sea Drilling Project Site 463). In: Neal, C. R., Sager, W. W., Sano, T., and Erba, E. (Eds.), Environmental consequences of Ontong Java Plateau and Kerguelen Plateau volcanism. Geological Society of America Special Paper 511. The Geological Society of America, Boulder, USA, pp. 329–339.

Ando, A., Huber, B. T., and Premoli Silva, I., 2013. *Paraticinella rohri* (Bolli, 1959) as the valid name for the latest Aptian zonal marker species of planktonic foraminifera traditionally called *bejaouaensis* or *eubejaouaensis*. Cretaceous Research, 45: 275–287.

Ando, A., Kaiho, K., Kawahata, H., and Kakegawa, T., 2008. Timing and magnitude of early Aptian extreme warming: Unraveling primary $\delta^{18}O$ variation in indurated pelagic carbonates at Deep Sea Drilling Project Site 463, central Pacific Ocean. Palaeogeography, Palaeoclimatology, Palaeoecology, 260(3–4): 463–476.

Ando, A., Kakegawa, T., Takashima, R., and Saito, T., 2002. New perspective on Aptian carbon isotope stratigraphy: Data from $\delta^{13}C$ records of terrestrial organic matter. Geology, 30(3): 227–230.

Arai, M., 2009. Paleogeografia do Atlântico Sul no Aptiano: um novo modelo a partir de dados micropaleontológicos recentes. Boletim de Geociências da Petrobras, 17(2): 331–351.

Arai, M., 2014. Aptian/Albian (Early Cretaceous) paleogeography of the South Atlantic: a paleontological perspective. Brazilian Journal of Geology, 44(2): 339–350.

Arthur, M. A., Brumsack, H.-J., Jenkyns, H. C., and Schlanger, S. O., 1990. Stratigraphy, geochemistry, and paleoceanography of organic-carbon-rich Cretaceous sequences. In: Ginsburg, R. N., and Beaudoin, B. (Eds.), Cretaceous Resources, Events, and Rhythms. Kluwer Academic Publishers, Dordrecht, Netherlands, pp. 75–119.

Azevedo, R. L. M., 2001, O Albiano no Atlântico sul: Estratigrafia, paleoceanografia e relações globais [PhD thesis]: Porto Alegre, Universidade Federal do Rio Grande do Sul, 265 p.

Azevedo, R. L. M., Gomide, J., Viviers, M. C., and Hashimoto, A. T., 1987. Bioestratigrafia do Cretáceo marinho da Bacia de Campos, Brasil. Revista Brasileira de Geociências, 17(2): 147–153.

Bailey, T. R., McArthur, J. M., Prince, H., and Thirlwall, M. F., 2000. Dissolution methods for strontium isotope stratigraphy: whole rock analysis. Chemical Geology, 167(3–4): 313–319.

Banner, J. L., 1995. Application of the trace element and isotope geochemistry of strontium to studies of carbonate diagenesis. Sedimentology, 42(5): 805–824.

Banner, J. L., 2004. Radiogenic isotopes: systematics and applications to earth surface processes and chemical stratigraphy. Earth-Science Reviews, 65(3–4): 141–194.

Barandas, A. P. M. G., Souza, C. F., and Duarte, M. A., 2011, Avaliação da presença de elementos traçadores isotópicos para monitoramento de fontes hidrominerais, XIII Congresso Brasileiro de Geoquímica - III Simpósio de Geoquímica dos Países do Mercosul: Gramado, Brazil, SBGq, Expanded abstract, p. 1199–1202.

Basov, I. A., and Krasheninnikov, V. A., 1983. Benthic Foraminifers in Mesozoic and Cenozoic Sediments of the Southwestern Atlantic as an Indicator of Paleoenvironment, Deep Sea Drilling Project Leg 71. In: Ludwig, W. J., Krasheninnikov, V. A., et al., M. (Eds.), Initial Reports of the Deep Sea Drilling Project covering Leg 71 of the cruises of the drilling vessel Glomar Challenger, Valparaiso, Chile to Santos, Brazil, January-February, 1980. Texas A & M University, Ocean Drilling Program, College Station, U. S. A., pp. 739–787.

Beerling, D. J., Lomas, M. R., and Gröcke, D. R., 2002. On the nature of methane gas-hydrate dissociation during the Toarcian and Aptian Oceanic anoxic events. American Journal of Science, 302(1): 28–49.

Behar, F., Beaumont, V., and Penteado, H. L. B., 2001. Technologie Rock-Eval 6: performances et développements. Revue d'Institut Français du Pétrole, 56(2): 111–134.

Bellanca, A., Erba, E., Neri, R., Premoli Silva, I., Sprovieri, M., Tremolada, F., and Verga, D., 2002. Palaeoceanographic significance of the Tethyan 'Livello Selli' (Early Aptian) from the Hybla Formation, northwestern Sicily: biostratigraphy and high-resolution chemostratigraphic records. Palaeogeography, Palaeoclimatology, Palaeoecology, 185(1–2): 175–196.

Bengston, P., Koutsoukos, E. A. M., Kakabadze, M. V., and Zucon, M. H., 2007, Ammonite and foraminiferal biogeography and the opening of the Equatorial Atlantic gateway, 1st International Palaeobiogeography Symposium: Paris, Université Pierre et Marie Curie Muséum national d'Histoire naturelle, Abstracts, p. 12.

Bergen, J. A., 2004. Calcareous nannofossils from ODP Leg 192, Ontong Java Plateau. In: Godfrey Fitton, J., Mahoney, J. J., Wallace, P. J., and Saunders, A. D. (Eds.), Origin and Evolution of the Ontong Java Plateau. Geological Society Special Publication 229. The Geological Society, London, UK, pp. 113–132.

Bernoulli, D., 1972. North Atlantic and Mediterranean Mesozoic facies: A comparison. In: Hollister, C. D., Ewing, J. I., Habib, et al., (Eds.), Initial Reports of the Deep Sea Drilling Project covering Leg 11 of the cruises of the drilling vessel Glomar Challenger, Miami, Florida to Hoboken, New Jersey, April–June, 1970. Texas A & M University, Ocean Drilling Program, College Station, USA, pp. 801–822.

Bernoulli, D., and Jenkyns, H. C., 1974. Alpine, Mediterranean, and Central Atlantic Mesozoic facies in relation to the early evolution of the Tethys. In: Dott, R. H., Jr., and Shaver, R. H. (Eds.), Modern and Ancient Geosynclinal Sedimentation. SEPM Special Publication No. 19. SEPM (Society for Sedimentary Geology), Tulsa, USA, pp. 129–160.

Bernoulli, D., and Jenkyns, H. C., 2009. Ancient oceans and continental margins of the Alpine-Mediterranean Tethys: deciphering clues from Mesozoic pelagic sediments and ophiolites. Sedimentology, 56(1): 149–190.

Bertani, R. T., and Carozzi, A. V., 1985a. Lagoa Feia Formation (Lower Cretaceous) Campos Basin, Offshore Brazil: Rift valley type lacustrine carbonate reservoirs – I. Journal of Petroleum Geology, 8(1): 37–58.

Bertani, R. T., and Carozzi, A. V., 1985b. Lagoa Feia Formation (Lower Cretaceous) Campos Basin, Offshore Brazil: Rift valley type lacustrine carbonate reservoirs – II. Journal of Petroleum Geology, 8(2): 199–220.

Bice, K. L., Huber, B. T., and Norris, R. D., 2003. Extreme polar warmth during the Cretaceous greenhouse? Paradox of the late Turonian $\delta^{18}O$ record at Deep Sea Drilling Project Site 511. Paleoceanography, 18(2): 1031.

Bischoff, G., and Mutterlose, J., 1998. Calcareous nannofossils of the Barremian/Aptian boundary interval in NW Europe: biostratigraphic and palaecologic implications of a high resolution study. Cretaceous Research, 19(5): 635–661.

Blaich, O. A., Faleide, J. I., and Tsikalas, F., 2011. Crustal breakup and continent-ocean transition at South Atlantic conjugate margins. Journal of Geophysical Research: Solid Earth, 116(B1): B01402.

Blättler, C. L., and Higgins, J. A., 2014. Calcium isotopes in evaporites record variations in Phanerozoic seawater SO_4 and Ca. Geology, 42(8): 711–714.

Bodin, S., Meissner, P., Janssen, N. M. M., Steuber, T., and Mutterlose, J., 2015. Large igneous provinces and organic carbon burial: Controls on global temperature and continental weathering during the Early Cretaceous. Global and Planetary Change, 133: 238–253.

Bosscher, H., and Schlager, W., 1993. Accumulation Rates of Carbonate Platforms. The Journal of Geology, 101: 345–355.

Bottini, C., Cohen, A. S., Erba, E., Jenkyns, H. C., and Coe, A. L., 2012. Osmium-isotope evidence for volcanism, weathering, and ocean mixing during the early Aptian OAE 1a. Geology, 40(7): 583–586.

Bottini, C., Erba, E., Tiraboschi, D., Jenkyns, H. C., Schouten, S., and Sinninghe Damsté, J. S., 2015. Climate variability and ocean fertility during the Aptian Stage. Climate of the Past, 11(3): 383–402.

Bottini, C., and Mutterlose, J., 2012. Integrated stratigraphy of Early Aptian black shales in the Boreal Realm: calcareous nannofossil and stable isotope evidence for global and regional processes. Newsletters on Stratigraphy, 45(2): 115–137.

Bown, P. R., Rutledge, D. C., Crux, J. A., and Gallagher, L. T., 1998. Lower Cretaceous. In: Bown, P. R. (Ed.), Calcareous Nannofossil Biostratigraphy. Chapman and Hall, Cambridge, pp. 86–102.

Bralower, T. J., Arthur, M. A., Leckie, R. M., Sliter, W. V., Allard, D. J., and Schlanger, S. O., 1994. Timing and Paleoceanography of Oceanic Dysoxia/Anoxia in the Late Barremian to Early Aptian (Early Cretaceous). Palaios, 9(4): 335–369.

Bralower, T. J., CoBabe, E., Clement, B., Sliter, W. V., Osburn, C. L., and Longoria, J., 1999. The record of global change in Mid-Cretaceous (Barremian-Albian) sections from the Sierra Madre, northeastern Mexico. The Journal of Foraminiferal Research, 29(4): 418–437.

Bralower, T. J., Fullagar, P. D., Paull, C. K., Dwyer, G. S., and Leckie, R. M., 1997. Mid-Cretaceous strontium-isotope stratigraphy of deep-sea sections. Geological Society of America Bulletin, 109(11): 1421–1442.

Bréhéret, J.-G., 1994. The Mid-Cretaceous Organic-Rich Sediments from the Vocontian Zone of the French Southeast Basin. In: Mascle, A. (Ed.), Hydrocarbon and petroleum geology of France. Special publication of the European Association of Petroleum Geoscientists No. 4. Springer, Berlin-Heidelberg-New York, pp. 295–320.

Brookes, S. T., and Belanger, C., 2005, Report of Analysis - IA-R041 - $^{15}N/^{13}C$ L-Alanine Laboratory Standard.

Burke, K., and Sengör, A. M. C., 1988. Ten metre global sea-level change associated with South Atlantic Aptian salt deposition. Marine Geology, 83(1–4): 309–312.

Burke, W. H., Denison, R. E., Hetherington, E. A., Koepnick, R. B., Nelson, H. F., and Otto, J. B., 1982. Variation of seawater $^{87}Sr/^{86}Sr$ throughout Phanerozoic time. Geology, 10(10): 516–519.

Campos Neto, O. P. d. A., Lima, W. S., and Cruz, F. E. G., 2007. Bacia de Sergipe-Alagoas. Boletim de Geociências da Petrobras, 15(2): 405–415.

Cande, S. C., and Kent, D. V., 1995. Revised calibration of the geomagnetic polarity timescale for the Late Cretaceous and Cenozoic. Journal of Geophysical Research: Solid Earth, 100(B4): 6093–6095.

Caron, M., 1978. Cretaceous planktonic foraminifers from DSDP leg 40, southeastern Atlantic Ocean. In: Bolli, H. M., Ryan, W. B. F., et al., (Eds.), Initial Reports of the Deep Sea Drilling Project covering Leg 40 of the cruises of the drilling vessel Glomar Challenger, Cape Town, South Africa to Abidjan, Ivory Coast, December 1974–February 1975. Texas A & M University, Ocean Drilling Program, College Station, USA, pp. 651–678.

Carvalho, M. A., Bengston, P., and Lana, C. C., 2016. Late Aptian (Cretaceous) paleoceanography of the South Atlantic Ocean inferred from dinocyst communities of the Sergipe Basin, Brazil. Paleoceanography, 31(1): 2–26.

Casellato, C. E., 2010. Calcareous nannofossil biostratigraphy of Upper Callovian–Lower Berriasian successions from the southern alps, North Italy. Rivista Italiana di Paleontologia e Stratigrafia, 116(3): 357–404.

Chaboureau, A.-C., Donnadieu, Y., Sepulchre, P., Robin, C., Guillocheau, F., and Rohais, S., 2012. The Aptian evaporites of the South Atlantic: a climatic paradox? Climate of the Past, 8(3): 1047–1058.

Chaboureau, A.-C., Guillocheau, F., Robin, C., Rohais, S., Moulin, M., and Aslanian, D., 2013. Paleogeographic evolution of the central segment of the South Atlantic during Early Cretaceous times: Paleotopographic and geodynamic implications. Tectonophysics, 604: 191–223.

Chambers, L. M., Pringle, M. S., and Fitton, J. G., Age and duration of magmatism on the Ontong Java Plateau: ^{40}Ar-^{39}Ar results from ODP Leg 192, *in* Proceedings American Geophysical Union, San Francico, USA, 2002, abstract #V71B-1271.

Chambers, L. M., Pringle, M. S., and Fitton, J. G., 2004. Phreatomagmatic eruptions on the Ontong Java Plateau: an Aptian $^{40}Ar/^{39}Ar$ age for volcaniclastic rocks at ODP Site 1184. In: Godfrey Fitton, J., Mahoney, J. J., Wallace, P. J., and Saunders, A. D. (Eds.), Origin and Evolution of the Ontong Java Plateau. Geological Society Special Publication 229. The Geological Society, London, UK, pp. 325–331.

Chandler, M. T., Wessel, P., Taylor, B., Seton, M., Kim, S.-S., and Hyeong, K., 2012. Reconstructing Ontong Java Nui: Implications for Pacific absolute plate motion, hotspot drift and true polar wander. Earth and Planetary Science Letters, 331–332: 140–151.

Channell, J. E. T., Erba, E., Muttoni, G., and Tremolada, F., 2000. Early Cretaceous magnetic stratigraphy in the APTICORE drill core and adjacent outcrop at Cismon (Southern Alps, Italy), and correlation to the proposed Barremian-Aptian boundary stratotype. Geological Society of America Bulletin, 112(9): 1430–1443.

Channell, J. E. T., Lowrie, W., and Medizza, F., 1979. Middle and early cretaceous magnetic stratigraphy from the Cismon section, northern Italy. Earth and Planetary Science Letters, 42(2): 153–166.

Charbonnier, G., and Föllmi, K. B., 2017. Mercury enrichments in lower Aptian sediments support the link between Ontong Java large igneous province activity and oceanic anoxic episode 1a. Geology, 45(1): 63–66.

Claypool, G. E., Holser, W. T., Kaplan, I. R., Sakai, H., and Zak, I., 1980. The age curves of sulfur and oxygen isotopes in marine sulfate and their mutual interpretation. Chemical Geology, 28: 199–260.

Coccioni, R., Erba, E., and Premoli-Silva, I., 1992. Barremian-Aptian calcareous plankton biostratigraphy from the Gorgo Cerbara section (Marche, central Italy) and implications for plankton evolution. Cretaceous Research, 13(5–6): 517–537.

Coccioni, R., Jovane, L., Bancalà, G., Bucci, C., Fauth, G., Frontalini, F., Janikian, L., Savian, J. F., Paes de Almeida, R., Mathias, G. L., and Trindade, R., 2012. Umbria-Marche Basin, Central Italy: A Reference Section for the Aptian-Albian Interval at Low Latitudes. Scientific Drilling, 13: 42–46.

Coccioni, R., Nesci, O., Tramontana, M., Wezel, F.-C., and Moretti, E., 1987. Descrizione di un livello–guida "radiolaritico–bituminoso–ittiolitico" alla base delle Marne a Fucoidi nell'Appennino Umbro–Marchigiano. Bollettino della Società Geologica Italiana, 106: 183–192.

Coccioni, R., Sabatino, N., Frontalini, F., Gardin, S., Sideri, M., and Sprovieri, M., 2014. The neglected history of Oceanic Anoxic Event 1b: insights and new data from the Poggio le Guaine section (Umbrial-Marche Basin). Stratigraphy, 11(3–4): 245–282.

Coccioni, R., Silva, I. P., Marsili, A., and Verga, D., 2007. First radiation of Cretaceous planktonic foraminifera with radially elongate chambers at Angles (Southeastern France) and biostratigraphic implications. Revue de Micropaléontologie, 50(3): 215–224.

Cohen, K. M., Finney, S. C., Gibbard, P. L., and Fan, J.-X., 2013; updated 2016. The ICS International Chronostratigraphic Chart. Episodes, 36(3): 199–204.

Coplen, T. B., Brand, W. A., Gehre, M., Gröning, M., Meijer, H. A. J., Toman, B., and Verkouteren, R. M., 2006. New Guidelines for $\delta^{13}C$ Measurements. Analytical Chemistry, 78(7): 2439–2441.

Crossey, L. J., Fischer, T. P., Patchett, P. J., Karlstrom, K. E., Hilton, D. R., Newell, D. L., Huntoon, P., Reynolds, A. C., and de Leeuw, G. A. M., 2006. Dissected hydrologic system at the Grand Canyon: Interaction between deeply derived fluids and plateau aquifer waters in modern springs and travertine. Geology, 34(1): 25–28.

Davison, I., 2007. Geology and tectonics of the South Atlantic Brazilian salt basins. In: Ries, A. C., Butler, R. W. H., and Graham, R. H. (Eds.), Deformation of the Continental Crust: The Legacy of Mike Coward. Geological Society Special Publication 272. The Geological Society, London, UK, pp. 345–359.

Davison, I., Anderson, L., and Nuttall, P., 2012. Salt deposition, loading and gravity drainage in the Campos and Santos salt basins. In: Alsop, G. I., Archer, S. G., Hartley, A. J., Grant, N. T., and Hodgkinson, R. (Eds.), Salt Tectonics, Sediments and Prospectivity. Geological Society Special Publication 363. The Geological Society, London, UK, pp. 159–174.

de Gea, G. A., Castro, J. M., Aguado, R., Ruiz-Ortiz, P. A., and Company, M., 2003. Lower Aptian carbon isotope stratigraphy from a distal carbonate shelf setting: the Cau section, Prebetic zone, SE Spain. Palaeogeography, Palaeoclimatology, Palaeoecology, 200(1–4): 207–219.

DeBond, N., Oakes, R. L., Paytan, A., and Wortmann, U. G., 2012. Early Aptian carbon and sulphur isotope signatures at ODP Site 765. Isotopes in Environmental and Health Studies, 48(1): 180–194.

Denison, R. E., Kirkland, D. W., and Evans, R., 1998. Using Strontium Isotopes to Determine the Age and Origin of Gypsum and Anhydrite Beds. The Journal of Geology, 106(1): 1–18.

Denison, R. E., Koepnick, R. B., Fletcher, A., Howell, M. W., and Callaway, W. S., 1994. Criteria for the retention of original seawater $^{87}Sr/^{86}Sr$ in ancient shelf limestones. Chemical Geology, 112(1): 131–143.

Deroo, G., Herbin, J. P., and Roucaché, J., 1983. Organic geochemistry of upper Jurassic-Cretaceous sediments from site 511, Leg 71, western South Atlantic. In: Ludwig, W. J., Krasheninnikov, V. A., et al., (Eds.), Initial Reports of the Deep Sea Drilling Project covering Leg 71 of the cruises of the drilling vessel Glomar Challenger, Valparaiso, Chile to Santos, Brazil, January-February, 1980. Texas A & M University, Ocean Drilling Program, College Station, USA, pp. 1001–1013.

Dias, J. L., 1998, Análise sedimentológica e estratigrafia do Andar Aptiano em parte da margem leste do Brasil e no platô das Malvinas - considerações sobre as primeiras incursões e ingressões marinhas do Oceano Atlântico Meridional [PhD thesis]: Porto Alegre, Universidade Federal do Rio Grande do Sul, 208 p.

Dias, J. L., 2005. Tectônica, estratigrafia e sedimentação no Andar Aptiano da margem leste brasileira. Boletim de Geociências da Petrobras, 13(1): 7–25.

Dias, J. L., Sad, A. R. E., Fontana, R. L., and Feijó, F. J., 1994. Bacia de Pelotas. Boletim de Geociências da Petrobras, 8(1): 235–245.

Dumitrescu, M., and Brassell, S. C., 2006. Compositional and isotopic characteristics of organic matter for the early Aptian Oceanic Anoxic Event at Shatsky Rise, ODP Leg 198. Palaeogeography, Palaeoclimatology, Palaeoecology, 235(1–3): 168–191.

Ehrlich, S., Gavrieli, I., Dor, L.-B., and Halicz, L., 2001. Direct high-precision measurements of the $^{87}Sr/^{86}Sr$ isotope ratio in natural water, carbonates and related materials by multiple collector inductively coupled plasma mass spectrometry (MC-ICP-MS). Journal of Analytical Atomic Spectrometry, 16(12): 1389–1392.

Erba, E., 1994. Nannofossils and superplumes: The Early Aptian “nannoconid crisis”. Paleoceanography, 9(3): 483–501.

Erba, E., 2004. Calcareous nannofossils and Mesozoic oceanic anoxic events. Marine Micropaleontology, 52(1–4): 85–106.

Erba, E., Bottini, C., Weissert, H. J., and Keller, C. E., 2010. Calcareous Nannoplankton Response to Surface-Water Acidification Around Oceanic Anoxic Event 1a. Science, 329(5990): 428–432.

Erba, E., Channell, J. E. T., Claps, M., Jones, C., Larson, R., Opdyke, B., Premoli Silva, I., Riva, A., Salvini, G., and Torricelli, S., 1999. Integrated stratigraphy of the Cismon Apticore (southern Alps, Italy); a "reference section" for the Barremian–Aptian interval at low latitudes. The Journal of Foraminiferal Research, 29(4): 371–391.

Erba, E., Duncan, R. A., Bottini, C., Tiraboschi, D., Weissert, H., Jenkyns, H. C., and Malinverno, A., 2015. Environmental consequences of Ontong Java Plateau and Kerguelen Plateau volcanism. In: Neal, C. R., Sager, W. W., Sano, T., and Erba, E. (Eds.), The Origin, Evolution, and Environmental Impact of Oceanic Large Igneous Provinces. Geological Society of America Special Paper 511. The Geological Society of America, Boulder, USA, pp. 271–303.

Erba, E., Premoli Silva, I., and Watkins, D. K., 1995. Cretaceous calcareous plankton biostratigraphy of sites 872 through 879. In: Haggerty, J. A., Premoli Silva, I., Rack, F., and McNutt, M. K. (Eds.), Proceedings of the Ocean Drilling Program, 144. A & M Texas University, Ocean Drilling Program, College Station, USA, pp. 157–169.

Erba, E., and Quadrio, B., 1987. Biostratigrafia a Nannofossili calcarei, Calpionellidi e Foraminiferi planctonici della Maiolica (Titoniano superiore–Aptiano) nelle Prealpi Bresciane (Italia settentrionalle). Rivista Italiana di Paleontologia e Stratigrafia, 93: 3–108.

Erbacher, J., Huber, B. T., Norris, R. D., and Markey, M., 2001. Increased thermohaline stratification as a possible cause for an ocean anoxic event in the Cretaceous period. Nature, 409(6818): 325–327.

Evain, M., Afilhado, A., Rigoti, C., Loureiro, A., Alves, D., Klingelhoefer, F., Schnurle, P., Feld, A., Fuck, R., Soares, J., de Lima, M. V., Corela, C., Matias, L., Benabdellouahed, M., Baltzer, A., Rabineau, M., Viana, A., Moulin, M., and Aslanian, D., 2015. Deep structure of the Santos Basin-São Paulo Plateau System, SE Brazil. Journal of Geophysical Research: Solid Earth, 120(8): 5401–5431.

Faure, G., and Mensing, T. M., 2005, Isotopes: principles and applications, Hoboken, USA, John Wiley & Sons, Inc., 897 p.

Fiet, N., Quidelleur, X., Parize, O., Bulot, L. G., and Gillot, P. Y., 2006. Lower Cretaceous stage durations combining radiometric data and orbital chronology: Towards a more stable relative time scale? Earth and Planetary Science Letters, 246(3–4): 407–417.

Florêncio, C. P., and Ribeiro Filho, E., 1998. Geoquímica do Bromo em Halitas da Sub-Bacia Evaporítica de Maceió-AL. Revista de Geologia USP, 11: 5–14.

Fodor, R. V., McKee, E. H., and Asmus, H. E., 1983. K-Ar ages and the opening of the South Atlantic Ocean: Basaltic rock from the Brazilian margin. Marine Geology, 54(1–2): M1–M8.

Föllmi, K. B., 2012. Early Cretaceous life, climate and anoxia. Cretaceous Research, 35: 230–257.

Fouke, B. W., Farmer, J. D., Des Marais, D. J., Pratt, L., Sturchio, N. C., Burns, P. C., and Discipulo, M. K., 2000. Depositional Facies and Aqueous-Solid Geochemistry of Travertine-Depositing Hot Springs (Angel Terrace, Mammoth Hot Springs, Yellowstone National Park, U.S.A.). Journal of Sedimentary Research, 70(3): 565–585.

França, R. L., Rey, A. C. D., Tagliari, C. V., Brandão, J. R., and Fontanelli, P. d. R., 2007. Bacia do Espírito Santo. Boletim de Geociências da Petrobras, 15(2): 501–509.

Freitas, J. T. R., 2006, Ciclos deposicionais evaporíticos da Bacia de Santos: Uma análise cicloestratigráfica a partir de dados de 2 poços e de traços de sísmica [PhD thesis]: Porto Alegre, Universidade Federal do Rio Grande do Sul, 160 p.

Fry, B., Silva, S. R., Kendall, C., and Anderson, R. K., 2002. Oxygen isotope corrections for online $\delta^{34}S$ analysis. Rapid Communications in Mass Spectrometry, 16(9): 1097–0231.

Gill, B. C., Lyons, T. W., and Jenkyns, H. C., 2011. A global perturbation to the sulfur cycle during the Toarcian Oceanic Anoxic Event. Earth and Planetary Science Letters, 312(3–4): 484–496.

Giorgioni, M., Weissert, H., Bernasconi, S. M., Hochuli, P. A., Coccioni, R., and Keller, C. E., 2012. Orbital control on carbon cycle and oceanography in the mid-Cretaceous greenhouse. Paleoceanography, 27(1): PA1204.

Gomes, M. L., Hurtgen, M. T., and Sageman, B. B., 2016. Biogeochemical sulfur cycling during Cretaceous oceanic anoxic events: A comparison of OAE1a and OAE2. Paleoceanography, 31(2): 233–251.

Gradstein, F. M., Ogg, J. G., and Smith, A. G., 2004, A Geologic Time Scale 2004, Cambridge, Cambridge University Press, 589 p.

Gröcke, D. R., Hesselbo, S. P., and Jenkyns, H. C., 1999. Carbon-isotope composition of Lower Cretaceous fossil wood: Ocean-atmosphere chemistry and relation to sea-level change. Geology, 27(2): 155–158.

Haq, B. U., 2014. Cretaceous eustasy revisited. Global and Planetary Change, 113: 44–58.

Hay, W. W., and Leslie, M. A., 1990. Could possible changes in global groundwater reservoir cause eustatic sealevel fluctuations? In: Sciences, T. N. A. o. (Ed.), Sea Level Change: Studies in Geophysics. National Academy Press, Washington D. C., pp. 161–170.

He, H., Pan, Y., Tauxe, L., Qin, H., and Zhu, R., 2008. Toward age determination of the M0r (Barremian–Aptian boundary) of the Early Cretaceous. Physics of the Earth and Planetary Interiors, 169(1–4): 41–48.

Heimhofer, U., Hochuli, P. A., Burla, S., Andersen, N., and Weissert, H., 2003. Terrestrial carbon-isotope records from coastal deposits (Algarve, Portugal): a tool for chemostratigraphic correlation on an intrabasinal and global scale. Terra Nova, 15(1): 8–13.

Heimhofer, U., Hochuli, P. A., Herrle, J. O., Andersen, N., and Weissert, H., 2004. Absence of major vegetation and palaeoatmospheric pCO_2 changes associated with oceanic anoxic event 1a (Early Aptian, SE France). Earth and Planetary Science Letters, 223(3–4): 303–318.

Helsley, C. E., and Steiner, M. B., 1968. Evidence for long intervals of normal polarity during the cretaceous period. Earth and Planetary Science Letters, 5: 325–332.

Herrle, J. O., Kößler, P., Friedrich, O., Erlenkeuser, H., and Hemleben, C., 2004. High-resolution carbon isotope records of the Aptian to Lower Albian from SE France and the Mazagan Plateau (DSDP Site 545): a stratigraphic tool for paleoceanographic and paleobiologic reconstruction. Earth and Planetary Science Letters, 218(1–2): 149–161.

Herrle, J. O., Pross, J., Friedrich, O., Kößler, P., and Hemleben, C., 2003. Forcing mechanisms for mid-Cretaceous black shale formation: evidence from the Upper Aptian and Lower Albian of the Vocontian Basin (SE France). Palaeogeography, Palaeoclimatology, Palaeoecology, 190: 399–426.

Herrle, J. O., Schröder-Adams, C. J., Davis, W., Pugh, A. T., Galloway, J. M., and Fath, J., 2015. Mid-Cretaceous High Arctic stratigraphy, climate, and Oceanic Anoxic Events. Geology, 43(5): 403–406.

Hesselbo, S. P., Robinson, S. A., and Surlyk, F., 2004. Sea-level change and facies development across potential Triassic–Jurassic boundary horizons, SW Britain. Journal of the Geological Society, 161(3): 365–379.

Hilgen, F. J., and Langereis, C. G., 1993. A critical re-evaluation of the Miocene/Pliocene boundary as defined in the Mediterranean. Earth and Planetary Science Letters, 118(1): 167–179.

Hochuli, P. A., Menegatti, A. P., Weissert, H., Riva, A., Erba, E., and Silva, I. P., 1999. Episodes of high productivity and cooling in the early Aptian Alpine Tethys. Geology, 27(7): 657–660.

Holmes, J. A., 1996. Trace-element and stable-isotope geochemistry of non-marine ostracod shells in Quaternary palaeoenvironmental reconstruction. Journal of Paleolimnology, 15(3): 223–235.

Hsü, K. J., Montadert, L., Bernoulli, D., Cita, M. B., Erickson, A., Garrison, R. E., Kidd, R. B., Melieres, F., Muller, C., and Wright, R., 1977. History of the Mediterranean salinity crisis. Nature, 267(5610): 399–403.

Hu, X., Scott, R. W., Cai, Y., Wang, C., and Melinte-Dobrinescu, M. C., 2012a. Cretaceous oceanic red beds (CORBs): Different time scales and models of origin. Earth-Science Reviews, 115(4): 217–248.

Hu, X., Zhao, K., Yilmaz, I. O., and Li, Y., 2012b. Stratigraphic transition and palaeoenvironmental changes from the Aptian oceanic anoxic event 1a (OAE1a) to the oceanic red bed 1 (ORB1) in the Yenicesihlar section, central Turkey. Cretaceous Research, 38: 40–51.

Huang, C., Hinnov, L., Fischer, A. G., Grippo, A., and Herbert, T., 2010. Astronomical tuning of the Aptian Stage from Italian reference sections. Geology, 38(10): 899–902.

Huber, B. T., Hodell, D. A., and Hamilton, C. P., 1995. Middle–Late Cretaceous climate of the southern high latitudes: Stable isotopic evidence for minimal equator-to-pole thermal gradients. Geological Society of America Bulletin, 107(10): 1164–1191.

Huber, B. T., and Leckie, R. M., 2011. Planktic foraminiferal species turnover across deep-sea Aptian/Albian boundary sections. The Journal of Foraminiferal Research, 41(1): 53–95.

Huber, B. T., Norris, R. D., and MacLeod, K. G., 2002. Deep-sea paleotemperature record of extreme warmth during the Cretaceous. Geology, 30(2): 123–126.

Hudson, J. D., 1977. Stable isotopes and limestone lithification. Journal of the Geological Society, 133(6): 637–660.

Irwin, H., Curtis, C., and Coleman, M., 1977. Isotopic evidence for source of diagenetic carbonates formed during burial of organic-rich sediments. Nature, 269(5625): 209–213.

Jacobsen, S. B., and Kaufman, A. J., 1999. The Sr, C and O isotopic evolution of Neoproterozoic seawater. Chemical Geology, 161(1–3): 37–57.

Jenkyns, H. C., 1980. Cretaceous anoxic events: from continents to oceans. Journal of the Geological Society, 137(2): 171–188.

Jenkyns, H. C., 1988. The early Toarcian (Jurassic) anoxic event; stratigraphic, sedimentary and geochemical evidence. American Journal of Science, 288(2): 101–151.

Jenkyns, H. C., 1995. Carbon-isotope stratigraphy and paleoceanographic significance of the Lower Cretaceous shallow-water carbonates of Resolution Guyot, Mid-Pacific Mountains. In: Winterer, E. L., Sager, W. W., Firth, J. V., and Sinton, J. M. (Eds.), Proceedings of the Ocean Drilling Program, Scientific Results, 143. Texas A & M University, Ocean Drilling Program, College Station, USA, pp. 99–104.

Jenkyns, H. C., 2010. Geochemistry of oceanic anoxic events. Geochemistry, Geophysics, Geosystems, 11(3): Q03004.

Jenkyns, H. C., Gale, A. S., and Corfield, R. M., 1994. Carbon- and oxygen-isotope stratigraphy of the English Chalk and Italian Scaglia and its palaeoclimatic significance. Geological Magazine, 131(1): 1–34.

Jenkyns, H. C., Paull, C. K., Cummins, D. I., and Fullagar, P. D., 1995. Strontium-isotope stratigraphy of Lower Cretaceous atoll carbonates in the Mid-Pacific Mountains. In: Winterer, E. L., Sager, W. W., Firth, J. V., and Sinton, J. M. (Eds.), Proceedings of the Ocean Drilling Program, Scientific Results, 143. Texas A & M University, Ocean Drilling Program, College Station, USA, pp. 89–97.

Jenkyns, H. C., Schouten-Huibers, L., Schouten, S., and Sinninghe Damsté, J. S., 2012. Warm Middle Jurassic–Early Cretaceous high-latitude sea-surface temperatures from the Southern Ocean. Climate of the Past, 8(1): 215–226.

Jenkyns, H. C., and Wilson, P. A., 1999. Stratigraphy, paleoceanography, and evolution of Cretaceous Pacific guyots: relics from a greenhouse Earth. American Journal of Science, 299(5): 341–392.

Jeremiah, J., 2001. A Lower Cretaceous nannofossil zonation for the North Sea Basin. Journal of Micropalaeontology, 20(1): 45–80.

Jones, C. E., and Jenkyns, H. C., 2001. Seawater Strontium Isotopes, Oceanic Anoxic Events, and Seafloor Hydrothermal Activity in the Jurassic and Cretaceous. American Journal of Science, 301(2): 112–149.

Keatings, K. W., Heaton, T. H. E., and Holmes, J. A., 2002. The effects of diagenesis on the trace element and stable isotope geochemistry of non-marine ostracod valves. Journal of Paleolimnology, 28(2): 245–252.

Kennedy, M. J., Gale, A. S., Lees, J. A., and Caron, M., 2004. The Global Boundary Stratotype Section and Point (GSSP) for the base of the Cenomanian Stage, Mont Risou, Hautes-Alpes, France. Episodes, 27(1): 21–32.

Kennedy, W. J., Gale, A. S., Huber, B. T., Petrizzo, M. R., Bown, P., Barchetta, A., and Jenkyns, H. C., 2014. Integrated stratigraphy across the Aptian/Albian boundary at Col de Pré-Guittard (southeast France): A candidate Global Boundary Stratotype Section. Cretaceous Research, 51: 248–259.

Kochhann, K. G. D., Koutsoukos, E. A. M., and Fauth, G., 2014. Aptian–Albian benthic foraminifera from DSDP Site 364 (offshore Angola): A paleoenvironmental and paleobiogeographic appraisal. Cretaceous Research, 48: 1–11.

Kochhann, K. G. D., Koutsoukos, E. A. M., Fauth, G., and Sial, A. N., 2013. Aptian–Albian Planktic Foraminifera from DSDP 364 (Offshore Angola): Biostratigraphy, Paleoecology, and Paleoanographic Significance. The Journal of Foraminiferal Research, 43(4): 443–463.

Koutsoukos, E. A. M., 1989, Mid- to late Cretaceous Microbiostratigraphy, Palaeo-ecology and Palaeogeography of the Sergipe Basin, northeastern Brazil [PhD thesis]: Southampton, Council for National Academic Awards/Polytechnic South West, 886 p.

Koutsoukos, E. A. M., 1992. Late Aptian to Maastrichtian foraminiferal biogeography and palaeoceanography of the Sergipe Basin, Brazil. Palaeogeography, Palaeoclimatology, Palaeoecology, 92(3): 295–324.

Koutsoukos, E. A. M., Destro, N., Azambuja Filho, N. C., and Spadini, A. R., 1993. Upper Aptian–Lower Coniacian Carbonate Sequences in the Sergipe Basin, Northeastern Brazil. In: Toni Simo, J. A., Scott, R. W., and Masse, J.-P. (Eds.), Cretaceous Carbonate Platforms. AAPG Memoir 56. The American Association of Petroleum Geologists, Tulsa, USA, pp. 127–144.

Koutsoukos, E. A. M., Mello, M. R., and de Azambuja Filho, N. C., 1991. Micropalaeontological and geochemical evidence of mid-Cretaceous dysoxic-anoxic palaeoenvironments in the Sergipe Basin, northeastern Brazil. In: Tyson, R. V., and Pearson, T. H. (Eds.) Modern and Ancient Continental Shelf Anoxia. The Geological Society Special Publication 58. The Geological Society, London, UK, Special Publications, pp. 427–447.

Krabbenhöft, A., Eisenhauer, A., Böhm, F., Vollstaedt, H., Fietzke, J., Liebetrau, V., Augustin, N., Peucker-Ehrenbrink, B., Müller, M. N., Horn, C., Hansen, B. T., Nolte, N., and Wallmann, K., 2010. Constraining the marine strontium budget with natural strontium isotope fractionations ($^{87}Sr/^{86}Sr*$, $\delta^{88/86}Sr$) of carbonates, hydrothermal solutions and river waters. Geochimica et Cosmochimica Acta, 74(14): 4097–4109.

Krijgsman, W., Hilgen, F. J., Raffi, I., Sierro, F. J., and Wilson, D. S., 1999. Chronology, causes and progression of the Messinian salinity crisis. Nature, 400(6745): 652–655.

Kuhnt, W., Holbourn, A., and Moullade, M., 2011. Transient global cooling at the onset of early Aptian oceanic anoxic event (OAE) 1a. Geology, 39(4): 323–326.

Kuiper, K. F., Deino, A., Hilgen, F. J., Krijgsman, W., Renne, P. R., and Wijbrans, J. R., 2008. Synchronizing Rock Clocks of Earth History. Science, 320(5875): 500–504.

Kushnir, J., 1982. The partitioning of seawater cations during the transformation of gypsum to anhydrite. Geochimica et Cosmochimica Acta, 46(3): 433–446.

Kuznetsov, A. B., Semikhatov, M. A., and Gorokhov, I. M., 2012. The Sr isotope composition of the world ocean, marginal and inland seas: Implications for the Sr isotope stratigraphy. Stratigraphy and Geological Correlation, 20(6): 501–515.

Laeter, J. R., Böhlke, J. K., De Bievre, P., Hidaka, H., Peiser, H. S., Rosman, J. R., and Taylor, P. D. P., 2003. Atomic weights of the elements. Review 2000 (IUPAC Technical Report). Pure and Applied Chemistry, 75(6): 683–800.

Lafargue, E., Marquis, F., and Pillot, D., 1998. Rock-Eval 6 Applications in Hydrocarbon Exploration, Production, and Soil Contamination Studies. Revue d'Institut Français du Pétrole, 53(4): 421–437.

Larson, R. L., 1991a. Latest pulse of Earth: Evidence for a mid-Cretaceous superplume. Geology, 19(6): 547–550.

Larson, R. L., 1991b. Geological consequences of superplumes. Geology, 19(10): 963–966.

Larson, R. L., and Erba, E., 1999. Onset of the Mid-Cretaceous greenhouse in the Barremian-Aptian: Igneous events and the biological, sedimentary, and geochemical responses. Paleoceanography, 14(6): 663–678.

Lawrenz, D., 2012, Certificate of Analysis – Soil Calibration Material – Part No: 502-308 – Lot No: 1016: LECO Corporation.

Leckie, R. M., Bralower, T. J., and Cashman, R., 2002. Oceanic anoxic events and plankton evolution: Biotic response to tectonic forcing during the mid-Cretaceous. Paleoceanography, 17(3): 13-11–13-29.

Li, X., Jenkyns, H. C., Zhang, C., Wang, Y. I. N., Liu, L., and Cao, K. E., 2014. Carbon isotope signatures of pedogenic carbonates from SE China: rapid atmospheric pCO_2 changes during middle–late Early Cretaceous time. Geological Magazine, 151(5): 830–849.

Li, Y.-X., Bralower, T. J., Montañez, I. P., Osleger, D. A., Arthur, M. A., Bice, D. M., Herbert, T. D., Erba, E., and Premoli Silva, I., 2008. Toward an orbital chronology for the early Aptian Oceanic Anoxic Event (OAE1a, ~120 Ma). Earth and Planetary Science Letters, 271(1–4): 88–100.

Lowrie, W., and Alvarez, W., 1984. Lower Cretaceous magnetic stratigraphy in Umbrian pelagic limestone sections. Earth and Planetary Science Letters, 71(2): 315–328.

Lowenstein, T. K., Kendall, B., and Anbar, A. D., 2014. Chapter 8.21 - The Geologic History of Seawater. In: Turekian, H. D. H. K. (Ed.), Treatise on Geochemistry (Second Edition). Elsevier, Oxford, pp. 569–622.

Lu, F. H., Meyers, W. J., and Schoonen, M. A., 2001. S and O (SO_4) isotopes, simultaneous modeling, and environmental significance of the Nijar messinian gypsum, Spain. Geochimica et Cosmochimica Acta, 65(18): 3081–3092.

Luciani, V., Cobianchi, M., and Jenkyns, H. C., 2001. Biotic and geochemical response to anoxic events: the Aptian pelagic succession of the Gargano Promontory (southern Italy). Geological Magazine, 138(3): 277–298.

Ludwig, W. J., Krasheninnikov, V. A., Basov, I. A., Bayer, U., Bloemendal, J., Bornhold, B., Ciesielski, P. F., Goldstein, E. H., Robert, C., Salloway, J., Usher, J. L., von der Dick, H., Weaver, F. M., and Wise Jr., S. W., 1983. Site 511. In: Ludwig, W. J., Krasheninnikov, V. A., et al., (Eds.), Initial Reports of the Deep Sea Drilling Project covering Leg 71 of the cruises of the drilling vessel Glomar Challenger, Valparaiso, Chile to Santos, Brazil, January-February, 1980. Texas A & M University, Ocean Drilling Program, College Station, USA, pp. 21–109.

Mahoney, J. J., Storey, M., Duncan, R. A., Spencer, K. J., and Pringle, M., 1993. Geochemistry and geochronology of leg 130 basement lavas: nature and origin of the Ontong Java Plateau. In: Berger, W. H., Kroenke, L. W., Mayer, L. A., et al., (Eds.), Proceedings of the Ocean Drilling Program, Scientific Results, 130. Texas A & M University, Ocean Drilling Program, College Station, USA, pp. 3–22.

Malinverno, A., Erba, E., and Herbert, T. D., 2010. Orbital tuning as an inverse problem: Chronology of the early Aptian oceanic anoxic event 1a (Selli Level) in the Cismon APTICORE. Paleoceanography, 25(2): PA2203.

Malinverno, A., Hildebrandt, J., Tominaga, M., and Channell, J. E. T., 2012. M-sequence geomagnetic polarity time scale (MHTC12) that steadies global spreading rates and incorporates astrochronology constraints. Journal of Geophysical Research: Solid Earth, 117(B6): B06104.

Marshall, J. D., 1992. Climatic and oceanographic isotopic signals from the carbonate rock record and their preservation. Geological Magazine, 129(2): 143–160.

McAnena, A., Flögel, S., Hofmann, P., Herrle, J. O., Griesand, A., Pross, J., Talbot, H. M., Rethemeyer, J., Wallmann, K., and Wagner, T., 2013. Atlantic cooling associated with a marine biotic crisis during the mid-Cretaceous period. Nature Geoscience, 6(7): 558–561.

McArthur, J. M., 1994. Recent trends in strontium isotope stratigraphy. Terra Nova, 6(4): 331–358.

McArthur, J. M., Howarth, R. J., and Shields, G. A., 2012. Chapter 7 - Strontium Isotope Stratigraphy. In: Gradstein, F. M., Ogg, J. G., Schmitz, M. D., and Ogg, G. M. (Eds.), The Geologic Time Scale. Elsevier, Boston, USA, pp. 127–144.

McCulloch, M. T., De Deckker, P., and Chivas, A. R., 1989. Strontium isotope variations in single ostracod valves from the Gulf of Carpentaria, Australia: A palaeoenvironmental indicator. Geochimica et Cosmochimica Acta, 53(7): 1703–1710.

Méhay, S., Keller, C. E., Bernasconi, S. M., Weissert, H., Erba, E., Bottini, C., and Hochuli, P. A., 2009. A volcanic CO_2 pulse triggered the Cretaceous Oceanic Anoxic Event 1a and a biocalcification crisis. Geology, 37(9): 819–822.

Menegatti, A. P., Weissert, H., Brown, R. S., Tyson, R. V., Farrimond, P., Strasser, A., and Caron, M., 1998. High-resolution $\delta^{13}C$ stratigraphy through the Early Aptian "Livello selli" of the Alpine tethys. Paleoceanography, 13(5): 530–545.

Mercer, C. M., and Hodges, K. V., 2016. ArAR — A software tool to promote the robust comparison of K–Ar and $^{40}Ar/^{39}Ar$ dates published using different decay, isotopic, and monitor-age parameters. Chemical Geology, 440: 148–163.

Meyers, S. R, 2008. Resolving Milankovitchian controversies: The Triassic Latemar Limestone and the Eocene Green River Formation. Geology, 36(4): 319–322.

Mizusaki, A. M. P., Petrini, R., Bellieni, P., Comin-Chiaramonti, P., Dias, J. L., De Min, A., and Piccirillo, E. M., 1992. Basalt magmatism along the passive continental margin of SE Brazil (Campos Basin). Contributions to Mineralogy and Petrology, 111(2): 143–160.

Mohriak, W. U., Szatmari, P., and Anjos, S., 2012. Salt: geology and tectonics of selected Brazilian basins in their global context. In: Alsop, G. I., Archer, S. G., Hartley, A. J., Grant, N. T., and Hodgkinson, R. (Eds.), Salt Tectonics, Sediments and Prospectivity. Geological Society Special Publication 363. The Geological Society, London, UK, pp. 131–158.

Moore, L. J., Murphy, T. J., Barnes, I. L., and Paulsen, P. J., 1982. Absolute Isotopic Abundance Ratios and Atomic Weight of a Reference Sample of Strontium. Journal of Research of the National Bureau of Standards, 87(1): 1–8.

Moreira, J. L. P., Madeira, C. V., Gil, J. A., and Machado, M. A. P., 2007. Bacia de Santos. Boletim de Geociências da Petrobras, 15(2): 531–549.

Moulin, M., Aslanian, D., and Unternehr, P., 2010. A new starting point for the South and Equatorial Atlantic Ocean. Earth-Science Reviews, 98(1–2): 1–37.

Moullade, M., Tronchetti, G., Granier, B., Bornemann, A., Kuhnt, W., and Lorenzen, J., 2015. High-resolution integrated stratigraphy of the OAE1a and enclosing strata from core drillings in the Bedoulian stratotype (Roquefort-La Bédoule, SE France). Cretaceous Research, 56: 119–140.

Müller, H., 1966, Palynological investigations of Cretaceous sediments in northeastern Brazil, Second West African Miropaleontological Colloquium: Ibadan, Proceedings, 123–136.

Mutterlose, J., 1989. Temperature-controlled migration of calcareous nannofloras in the north-west European Aptian. In: Crux, J. A., and van Heck, S. E. (Eds.), Nannofossils and their applications. Ellis Horwood, British Micropaleontology Society Series, pp. 122–142.

Mutterlose, J., Bottini, C., Schouten, S., and Sinninghe Damsté, J. S., 2014. High sea-surface temperatures during the early Aptian Oceanic Anoxic Event 1a in the Boreal Realm. Geology, 42(5): 439–442.

Mutterlose, J., Malkoc, M., Schouten, S., and Sinninghe Damsté, J. S., 2012. Reconstruction of vertical temperature gradients in past oceans — Proxy data from the Hauterivian–early Barremian (Early Cretaceous) of the Boreal Realm. Palaeogeography, Palaeoclimatology, Palaeoecology, 363–364: 135–143.

Naafs, B. D. A., Castro, J. M., De Gea, G. A., Quijano, M. L., Schmidt, D. N., and Pancost, R. D., 2016. Gradual and sustained carbon dioxide release during Aptian Oceanic Anoxic Event 1a. Nature Geoscience, 9(2): 135–139.

Naafs, B. D. A., and Pancost, R. D., 2014. Environmental conditions in the South Atlantic (Angola Basin) during the Early Cretaceous. Organic Geochemistry, 76: 184–193.

Naafs, B. D. A., and Pancost, R. D., 2016. Sea-surface temperature evolution across Aptian Oceanic Anoxic Event 1a. Geology, 44(11): 959–962.

Norton, I. O., Carruthers, D. T., and Hudec, M. R., 2016. Rift to drift transition in the South Atlantic salt basins: A new flavor of oceanic crust. Geology, 44(1): 55–58.

Nunn, J. A., and Harris, N. B., 2007. Subsurface seepage of seawater across a barrier: A source of water and salt to peripheral salt basins. Geological Society of America Bulletin, 119(9-10): 1201–1217.

Ogg, J. G., 2012. Chapter 5 - Geomagnetic Polarity Time Scale. In: Gradstein, F. M., Ogg, J. G., Schmitz, M. D., and Ogg, G. M. (Eds.), The Geologic Time Scale. Elsevier, Boston, USA, pp. 85–113.

Ogg, J. G., Hinnov, L. A., and Huang, C., 2012. Chapter 27 - Cretaceous. In: Gradstein, F. M., Ogg, J. G., Schmitz, M. D., and Ogg, G. M. (Eds.), The Geologic Time Scale. Elsevier, Boston, USA, pp. 793–853.

Owens, J. D., Gill, B. C., Jenkyns, H. C., Bates, S. M., Severmann, S., Kuypers, M. M. M., Woodfine, R. G., and Lyons, T. W., 2013. Sulfur isotopes track the global extent and dynamics of euxinia during Cretaceous Oceanic Anoxic Event 2. Proceedings of the National Academy of Sciences, 110(46): 18407–18412.

Parker, M. E., Arthur, M. A., Wise Jr., S. W., and Wenkam, C. R., 1983. Carbonate and Organic Carbon Cycles in Aptian–Albian Shales at Deep Sea Drilling Project Site 511, Falkland Plateau. In: Ludwig, W. J., Krasheninnikov, V. A., et al., (Eds.), Initial Reports of the Deep Sea Drilling Project covering Leg 71 of the cruises of the drilling vessel Glomar Challenger, Valparaiso, Chile to Santos, Brazil, January-February, 1980. Texas A & M University, Ocean Drilling Program, College Station, U. S. A., pp. 1051–1070.

Parkinson, I. J., Shaefer, B. F., scientist, O. L. s., and Arculus, R. J., 2002. A Lower mantle Origin for the World's Biggest LIP? A High Precision Os Isotope Isochron from Ontong Java Plateau Basalts Drilled on ODP Leg 192. Geochimica et Cosmochimica Acta, 66: A580.

Pauly, S., Mutterlose, J., and Wray, D. S., 2013. Palaeoceanography of Lower Cretaceous (Barremian–Lower Aptian) black shales from northwest Germany evidenced by calcareous nannofossils and geochemistry. Cretaceous Research, 42: 28-43.

Paytan, A., and Gray, E. T., 2012. Chapter 9 - Sulfur Isotope Stratigraphy In: Gradstein, F. M., Ogg, J. G., Schmitz, M. D., and Ogg, G. M. (Eds.), The Geological Time Scale. Elsevier, Boston, USA, pp. 167–180.

Paytan, A., Gray, E. T., Ma, Z., Erhardt, A., and Faul, K., 2011. Application of sulphur isotopes for stratigraphic correlation. Isotopes in Environmental and Health Studies, 48(1): 195–206.

Paytan, A., Kastner, M., Campbell, D., and Thiemens, M. H., 2004. Seawater Sulfur Isotope Fluctuations in the Cretaceous. Science, 304(5677): 1663–1665.

Pearson, P. N., Ditchfield, P. W., Singano, J., Harcourt-Brown, K. G., Nicholas, C. J., Olsson, R. K., Shackleton, N. J., and Hall, M. A., 2001. Warm tropical sea surface temperatures in the Late Cretaceous and Eocene epochs. Nature, 413(6855): 481–487.

Percival, L. M. E., Witt, M. L. I., Mather, T. A., Hermoso, M., Jenkyns, H. C., Hesselbo, S. P., Al-Suwaidi, A. H., Storm, M. S., Xu, W., and Ruhl, M., 2015. Globally enhanced mercury deposition during the end-Pliensbachian extinction and Toarcian OAE: A link to the Karoo–Ferrar Large Igneous Province. Earth and Planetary Science Letters, 428: 267–280.

Peterman, Z. E., Hedge, C. E., and Tourtelot, H. A., 1970. Isotopic composition of strontium in sea water throughout Phanerozoic time. Geochimica et Cosmochimica Acta, 34(1): 105–120.

Petrizzo, M. R., Huber, B. T., Gale, A. S., Barchetta, A., and Jenkyns, H. C., 2012. Abrupt planktic foraminiferal turnover across the Niveau Kilian at Col de Pré-Guittard (Vocontian Basin, southeast France): new criteria for defining the Aptian/Albian boundary. Newsletters on Stratigraphy, 45(1): 55–74.

Peucker-Ehrenbrink, B., and Ravizza, G., 2000. The marine osmium isotope record. Terra Nova, 12(5): 205–219.

Poropat, S. F., and Colin, J.-P., 2012a. Early Cretaceous ostracod biostratigraphy of eastern Brazil and western Africa: An overview. Gondwana Research, 22(3–4): 772–798.

Poropat, S. F., and Colin, J.-P., 2012b. Reassessment of the Early Cretaceous non-marine ostracod genera *Hourcqia* Krömmelbein, 1965 and *Pattersoncypris* Bate, 1972 with the description of a new genus, *Kroemmelbeincypris*'. Journal of Paleontology, 86(4): 699–719.

Premoli Silva, I., and Verga, D., 2004, Practical manual of Cretaceous planktonic foraminifera, Perugia, Italy, Tipografia Ponte Felcino, Universities of Perugia and Milan, Internationational School on Planktonic Foraminifera, 283 p.

Price, G. D., 2003. New constrains upon isotope variation during the early Cretaceous (Barremian–Cenomanian) from the Pacific Ocean. Geological Magazine, 140(5): 513–522.

Price, G. D., and Gröcke, D. R., 2002. Strontium-isotope stratigraphy and oxygen- and carbon-isotope variation during the Middle Jurassic–Early Cretaceous of the Falkland Plateau, South Atlantic. Palaeogeography, Palaeoclimatology, Palaeoecology, 183(3–4): 209–222.

Pringle, M., Chambers, L. M., and Ogg, J. G., Synchronicity of volcanism on Ontong Java and Manihiki Plateaux with global oceanographic events?, *in* Proceedings EGS-AGU-EUG Joint Assembly, Nice, France, April 6–11, 2003, abstract #13768.

Pringle, M. S., and Duncan, R. A., 1995. Radiometric ages of basement lavas recovered at Loen, Wodejebato, MIT, and Takuyo-Daisan Guyots, northwestern Pacific Ocean. In: Haggerty, J. A., Premoli Silva, I., Rack, F., and McNutt, M. K. (Eds.), Proceedings of the Ocean Drilling Program, Scientific Results, 144. A & M Texas University, Ocean Drilling Program, College Station, USA, pp. 547–557.

Prokoph, A., Shields, G. A., and Veizer, J., 2008. Compilation and time-series analysis of a marine carbonate $\delta^{18}O$, $\delta^{13}C$, $^{87}Sr/^{86}Sr$ and $\delta^{34}S$ database through Earth history. Earth-Science Reviews, 87(3–4): 113–133.

Quintaes, C. M. S. P., 2006, Aplicação da estratigrafia química e da estratigrafia de seqüências na seção albiana da porção sul da Bacia de Santos [Master thesis]: Rio de Janeiro, Universidade do Estado do Rio de Janeiro, 182 p.

Rabinowitz, P. D., and LaBrecque, J., 1979. The Mesozoic South Atlantic Ocean and evolution of its continental margins. Journal of Geophysical Research: Solid Earth, 84(B11): 5973–6002.

Raiswell, R., 1988. Chemical model for the origin of minor limestone-shale cycles by anaerobic methane oxidation. Geology, 16(7): 641–644.

Raiswell, R., and Fisher, Q. J., 2000. Mudrock-hosted carbonate concretions: a review of growth mechanisms and their influence on chemical and isotopic composition. Journal of the Geological Society, 157(1): 239–251.

Regali, M. S. P., 1989, *Complicatisaccus cearensis*: Uma palinozona do Eocretáceo do Brasil, XI Congresso Brasileiro de Paleontologia: Curitiba, Sociedade Brasileira de Paleontologia, Anais, 75–293.

Regali, M. S. P., and Viana, C. F., 1989, Late Jurassic-Early Cretaceous in Brazilian Sedimentary Basins: Correlation with the International Standard Scale, Rio de Janeiro, Editora Gávea, Petróleo Brasileiro S. A., 95 p.

Robinson, S. A., Clarke, L. J., Nederbragt, A., and Wood, I. G., 2008. Mid-Cretaceous oceanic anoxic events in the Pacific Ocean revealed by carbon-isotope stratigraphy of the Calera Limestone, California, USA. Geological Society of America Bulletin, 120(11–12): 1416–1426.

Robinson, S. A., and Hesselbo, S. P., 2004. Fossil-wood carbon-isotope stratigraphy of the non-marine Wealden Group (Lower Cretaceous, southern England). Journal of the Geological Society, 161(1): 133–145.

Rodrigues, R., 1995, A geoquímica na Bacia do Parnaíba [PhD thesis]: Porto Alegre, Universidade Federal do Rio Grande do Sul, 225 p.

Rodrigues, R., 2005. Chemostratigraphy. In: Koutsoukos, E. A. M. (Ed.), Applied Stratigraphy. Springer, Dordrecht, Netherlands, pp. 165–178.

Romaniello, S. J., Field, M. P., Smith, H. B., Gordon, G. W., Kim, M. H., and Anbar, A. D., 2015. Fully automated chromatographic purification of Sr and Ca for isotopic analysis. Journal of Analytical Atomic Spectrometry, 30(9): 1906–1912.

Ryan, W. B. F., Major, C. O., Lericolais, G., and Goldstein, S. L., 2003. Catastrophic flooding of the Black Sea Annual Review of Earth and Planetary Sciences, 31(1): 525–554.

Sabato Ceraldi, T., and Green, D., 2017. Evolution of the South Atlantic lacustrine deposits in response to Early Cretaceous rifting, subsidence and lake hydrology. In: Sabato Ceraldi, T., Hodgkinson, R., and Backe, G. (Eds.), Petroleum Geoscience of the West Africa Margin. Geological Society Special Publication 438. The Geological Society, London, UK, pp. 77–98.

Saller, A., Rushton, S., Buambua, L., Inman, K., NcNeil, R., and Dickson, J. A. D., 2016. Presalt stratigraphy and depositional systems in the Kwanza Basin, offshore Angola. The American Association of Petroleum Geologists Bulletin, 100(7): 1135–1164.

Salloway, J., 1983. Paleomagnetism of Sediments from Deep Sea Drilling Project Leg 71. In: Ludwig, W. J., Krasheninnikov, et al., (Eds.), Initial Reports of the Deep Sea Drilling Project covering Leg 71 of the cruises of the drilling vessel Glomar Challenger, Valparaiso, Chile to Santos, Brazil, January-February, 1980. Texas A & M University, Ocean Drilling Program, College Station, USA, pp. 1073–1091.

Saltzman, M. R., and Thomas, E., 2012. Chapter 11 - Carbon isotope stratigraphy. In: Gradstein, F. M., Ogg, J. G., Schmitz, M. D., and Ogg, G. M. (Eds.), The Geologic Time Scale. Elsevier, Boston, USA, pp. 207–232.

Sames, B., Wagreich, M., Wendler, J. E., Haq, B. U., Conrad, C. P., Melinte-Dobrinescu, M. C., Hu, X., Wendler, I., Wolfgring, E., Yilmaz, I. Ö., and Zorina, S. O., 2016. Review: Short-term sea-level changes in a greenhouse world — A view from the Cretaceous. Palaeogeography, Palaeoclimatology, Palaeoecology, 441(3): 393–411.

Sant'Anna, L. G., Riccomini, C., Rodrigues-Francisco, B. H., Sial, A. N., Carvalho, M. D., and Moura, C. A. V., 2004. The Paleocene travertine system of the Itaboraí basin, Southeastern Brazil. Journal of South American Earth Sciences, 18(1): 11–25.

Santantonio, M., 1993. Facies associations and evolution of pelagic carbonate platform/basin systems: examples from the Italian Jurassic. Sedimentology, 40(6): 1039–1067.

Santos Neto, E. V., Morais, E. T., Ferreira, A. A., and Torres, C. L., 2013, H_2S Risk in Presalt Reservoirs, OTC Brasil 2013: Rio de Janeiro, Brazil, Offshore Technology Conference, doi: 10.4043/24368-MS.

Sass, E., Bein, A., and Almogi-Labin, A., 1991. Oxygen-isotope composition of diagenetic calcite in organic-rich rocks: Evidence for ^{18}O depletion in marine anaerobic pore water. Geology, 19(8): 839–842.

Satolli, S., Besse, J., and Calamita, F., 2008. Paleomagnetism of Aptian–Albian sections from the Northern Apennines (Italy): Implications for the 150–100 Ma apparent polar wander of Adria and Africa. Earth and Planetary Science Letters, 276(1–2): 115–128.

Satolli, S., Besse, J., Speranza, F., and Calamita, F., 2007. The 125–150 Ma high-resolution Apparent Polar Wander Path for Adria from magnetostratigraphic sections in Umbria–Marche (Northern Apennines, Italy): Timing and duration of the global Jurassic–Cretaceous hairpin turn. Earth and Planetary Science Letters, 257(1–2): 329–342.

Savian, J. F., Trindade, R., Janikian, L., Jovane, L., Paes de Almeida, R., Coccioni, R., Frontalini, F., Sideri, M., Figueiredo, M., Tedeschi, L. R., and Jenkyns, H. C., 2016. The Barremian-Aptian boundary in the Poggio le Guaine core (central Italy): Evidence for magnetic polarity Chron M0r and oceanic anoxic event 1a. In: Menichetti, M., Coccioni, R., and Montanari, A. (Eds.), The Stratigraphic Record of Gubbio: Integrated Stratigraphy of the Late Cretaceous–Paleogene Umbria-Marche Pelagic Basin. Geological Society of America Special Paper 524. The Geological Society of America, Boulder, USA, pp. 57–78.

Schlanger, S. O., and Jenkyns, H. C., 1976. Cretaceous oceanic anoxic events: causes and consequences. Geologie en Mijnbouw, 55: 179–184.

Schlanger, S. O., Jenkyns, H. C., and Premoli-Silva, I., 1981. Volcanism and vertical tectonics in the Pacific Basin related to global Cretaceous transgressions. Earth and Planetary Science Letters, 52(2): 435–449.

Scholle, P. A., and Arthur, M. A., 1980. Carbon Isotope Fluctuations in Cretaceous Pelagic Limestones: Potential Stratigraphic and Petroleum Exploration Tool. The American Association of Petroleum Geologists Bulletin, 64(1): 67–87.

Schouten, S., Hopmans, E. C., Forster, A., van Breugel, Y., Kuypers, M. M. M., and Damsté, J. S. S., 2003. Extremely high sea-surface temperatures at low latitudes during the middle Cretaceous as revealed by archaeal membrane lipids. Geology, 31(12): 1069–1072.

Schreiber, B. C., and Hsü, K. J., 1980. Evaporites. In: Hobson, G. D. (Ed.), Developments in Petroleum Geology - 2. Applied Science Publishers Ltd., London, UK, pp. 87–138.

Selby, D., and Creaser, R. A., 2003. Re–Os geochronology of organic rich sediments: an evaluation of organic matter analysis methods. Chemical Geology, 200(3–4): 225–240.

Sharp, Z., 2007, Principles of Stable Isotope Geochemistry, Upper Saddle River, USA, Pearson Prentice Hall, 304 p.

Shimokawa, A., 2010, Zircon U-Pb Geochronology of the Great Valley Group: Recalibrating the Lower Cretaceous Time Scale [Master thesis]: Chapel Hill, University of North Caroline, 39 p.

Sikora, P. J., and Bergen, J. A., 2004. Lower Cretaceous planktonic foraminiferal and nannofossil biostratigraphy of Ontong Java Plateau sites from DSDP Leg 30 and ODP Leg 192. In: Godfrey Fitton, J., Mahoney, J. J., Wallace, P. J., and Saunders, A. D. (Eds.), Origin and Evolution of the Ontong Java Plateau. Geological Society Special Publication 229. The Geological Society, London, UK, pp. 83–111.

Silva-Telles Jr., A. C., 1996, Estatigrafia de sequências de alta resolução do Membro Coqueiros da Formação Lagoa Feia - (Barremiano/Aptiano da Bacia de Campos), Brasil. [Master thesis]: Porto Alegre, Universidadade Federal do Rio Grande do Sul, 268 p.

Silva-Telles Jr., A. C., Henz, G. I., and Arai, M., 1994. Evidences of the first marine ingressions during the east Braziliian margin rift phase. Boletim de Geociências da Petrobras, 8(2–4): 401–427.

Smoliar, M. I., Walker, R. J., and Morgan, J. W., 1996. Re-Os Ages of Group IIA, IIIA, IVA, and IVB Iron Meteorites. Science, 271(5252): 1099–1102.

Spigolon, A. L. D., 2003, Palynofacies and organic facies of Alagamar Formation (Aptian of Potiguar Basin, Brazil): Paleoenvironment and thermal maturation [Master thesis]: Brasília, Universidade de Brasília, 104 p.

Sprovieri, M., Bonanno, A., Barbieri, M., Bellanca, A., Neri, R., Patti, B., and Mazzola, S., 2004. $^{87}Sr/^{86}Sr$ variation in Tortanian Mediterranean sediments: a record of Milankovitch cyclicity. In: D'Argenio, B., Fischer, A. G., Premoli Silva, I., Weissert, H., and Ferreri, V. (Eds.), Cyclostratigraphy: approaches and case histories. SEPM Special Publication No. 81. SEPM (Society for Sedimentary Geology), Tulsa, USA, pp. 17–26.

Sprovieri, M., Coccioni, R., Lirer, F., Pelosi, N., Lozar, F., 2006. Orbital tuning of a lower Cretaceous composite record (Maiolica Formation, central Italy). Paleoceanography 21(4): PA4212.

Stampfli, G. M., Vavassis, I., De Bono, A., Rosselet, F., Matti, B., and Bellini, M., 2003. Remnants of the Paleotethys oceanic suture-zone in the western Tethyan area. Bollettino della Società Geologica Italiana, 2: 1–23.

Steiger, R. H., and Jäger, E., 1977. Subcommission on geochronology: Convention on the use of decay constants in geo- and cosmochronology. Earth and Planetary Science Letters, 36(3): 359–362.

Stein, M., Föllmi, K. B., Westermann, S., Godet, A., Adatte, T., Matera, V., Fleitmann, D., and Berner, Z., 2011. Progressive palaeoenvironmental change during the Late Barremian–Early Aptian as prelude to Oceanic Anoxic Event 1a: Evidence from the Gorgo a Cerbara section (Umbria-Marche basin, central Italy). Palaeogeography, Palaeoclimatology, Palaeoecology, 302(3–4): 396–406.

Steuber, T., and Veizer, J., 2002. Phanerozoic record of plate tectonic control of seawater chemistry and carbonate sedimentation. Geology, 30(12): 1123–1126.

Stichler, W., 1995, Interlaboratory comparison of new materials for carbon and oxygen isotope ratio measuraments: International Atomic Energy Agency: IAEA.

Swart, P. K., 2008. Global synchronous changes in the carbon isotopic composition of carbonate sediments unrelated to changes in the global carbon cycle. Proceedings of the National Academy of Sciences, 105(37): 13741–13745.

Swart, P. K., and Eberli, G., 2005. The nature of the $\delta^{13}C$ of periplatform sediments: Implications for stratigraphy and the global carbon cycle. Sedimentary Geology, 175(1–4): 115–129.

Tarduno, J. A., 1990. Brief reversed polarity interval during the Cretaceous Normal Polarity Superchron. Geology, 18(8): 683–686.

Taylor, B., 2006. The single largest oceanic plateau: Ontong Java–Manihiki–Hikurangi. Earth and Planetary Science Letters, 241(3–4): 372–380.

Tejada, M. L. G., Mahoney, J. J., Duncan, R. A., and Hawkins, M. P., 1996. Age and Geochemistry of Basement and Alkalic Rocks of Malaita and Santa Isabel, Solomon Islands, Southern Margin of Ontong Java Plateau. Journal of Petrology, 37(2): 361–394.

Tejada, M. L. G., Mahoney, J. J., Neal, C. R., Duncan, R. A., and Petterson, M. G., 2002. Basement Geochemistry and Geochronology of Central Malaita, Solomon Islands, with Implications for the Origin and Evolution of the Ontong Java Plateau. Journal of Petrology, 43(3): 449–484.

Tejada, M. L. G., Suzuki, K., Kuroda, J., Coccioni, R., Mahoney, J. J., Ohkouchi, N., Sakamoto, T., and Tatsumi, Y., 2009. Ontong Java Plateau eruption as a trigger for the early Aptian oceanic anoxic event. Geology, 37(9): 855–858.

Terra, G. J. S., Spadini, A. R., França, A. B., Sombra, C. L., Zambonato, E. E., Juschaks, L. C. S., Arienti, L. M., Erthal, M. M., Blauth, M., Franco, M. P., Matsuda, N. S., Silva, N. G. C., Moretti Jr., P. A., D'Ávila, R. S. F., Souza, R. S., Tonietto, S. N., Anjos, S. M. C., Campinho, V. S., and Winter, W. R., 2010. Classificação de rochas carbonáticas aplicável às bacias sedimentares brasileiras. Boletim de Geociências da Petrobras, 18(1): 9–29.

Thompson, D. L., Stilwell, J. D., and Hall, M., 2015. Lacustrine carbonate reservoirs from Early Cretaceous rift lakes of Western Gondwana: Pre-Salt coquinas of Brazil and West Africa. Gondwana Research, 28(1): 26–51.

Timofeeff, M. N., Lowenstein, T. K., da Silva, M. A. M., and Harris, N. B., 2006. Secular variation in the major-ion chemistry of seawater: Evidence from fluid inclusions in Cretaceous halites. Geochimica et Cosmochimica Acta, 70(8): 1977–1994.

Tiraboschi, D., Erba, E., and Jenkyns, H. C., 2009. Origin of rhythmic Albian black shales (Piobbico core, central Italy): Calcareous nannofossil quantitative and statistical analyses and paleoceanographic reconstructions. Paleoceanography, 24(2): PA2222.

Tissot, B. P., Pelet, R., and Ungerer, P., 1987. Thermal History of Sedimentary Basins, Maturation Indices, and Kinetics of Oil and Gas Generation. The American Association of Petroleum Geologists Bulletin, 71(12): 1445–1466.

Torsvik, T. H., Rousse, S., Labails, C., and Smethurst, M. A., 2009. A new scheme for the opening of the South Atlantic Ocean and the dissection of an Aptian salt basin. Geophysical Journal International, 177(3): 1315–1333.

Tosca, N. J., and Wright, V. P., 2015. Diagenetic pathways linked to labile Mg-clays in lacustrine carbonate reservoirs: a model for the origin of secondary porosity in the Cretaceous pre-salt Barra Velha Formation, offshore Brazil. In: Armitage, P. J., Butcher, A. R., Churchill, J. M., Csoma, A. E., Hollis, C., Lander, R. H., Omma, J. E., and Worden, R. H. (Eds.), Geological Society, London, Special Publications. Geological Society Special Publication 435. The Geological Society, London, UK, advance online publication. doi: 10.1144/SP435.1.

Trabucho Alexandre, J., Van Gilst, R. I., Rodríguez-López, J. P., and De Boer, P. L., 2011. The sedimentary expression of oceanic anoxic event 1b in the North Atlantic. Sedimentology, 58(5): 1217–1246.

Tupinambá, M., Heilbron, M., Valeriano, C., Júnior, R. P., de Dios, F. B., Machado, N., Silva, L. G. d. E., and de Almeida, J. C. H., 2012. Juvenile contribution of the Neoproterozoic Rio Negro Magmatic Arc (Ribeira Belt, Brazil): Implications for Western Gondwana amalgamation. Gondwana Research, 21(2–3): 422–438.

Turchyn, A. V., Schrag, D. P., Coccioni, R., and Montanari, A., 2009. Stable isotope analysis of the Cretaceous sulfur cycle. Earth and Planetary Science Letters, 285(1–2): 115–123.

Uesugui, N., 1979. Palinologia: técnicas de tratamento de amostras. Boletim Técnico Petrobras, 22: 229–240.

Uesugui, N., 1987. Posição estratigráfica dos evaporitos da Bacia Sergipe/Alagoas. Revista Brasileira de Geociências, 17(2): 131–134.

Vandenberg, J., Klootwijk, C. T., and Wonders, A. A. H., 1978. Late Mesozoic and Cenozoic movements of the Italian Peninsula: Further paleomagnetic data from the Umbrian sequence. Geological Society of America Bulletin, 89(1): 133–150.

Veizer, J., Ala, D., Azmy, K., Bruckschen, P., Buhl, D., Bruhn, F., Carden, G. A. F., Diener, A., Ebneth, S., Godderis, Y., Jasper, T., Korte, C., Pawellek, F., Podlaha, O. G., and Strauss, H., 1999. $^{87}Sr/^{86}Sr$, $\delta^{13}C$ and $\delta^{18}O$ evolution of Phanerozoic seawater. Chemical Geology, 161(1–3): 59–88.

Veizer, J., Buhl, D., Diener, A., Ebneth, S., Podlaha, O. G., Bruckschen, P., Jasper, T., Korte, C., Schaaf, M., Ala, D., and Azmy, K., 1997. Strontium isotope stratigraphy: potential resolution and event correlation. Palaeogeography, Palaeoclimatology, Palaeoecology, 132(1–4): 65–77.

Veizer, J., and Compston, W., 1974. $^{87}Sr/^{86}Sr$ composition of seawater during the Phanerozoic. Geochimica et Cosmochimica Acta, 38(9): 1461–1484.

Wang, C., Hu, X., Huang, Y., Scott, R. W., and Wegreich, M., 2009. Overview of Cretaceous oceanic red beds (CORBs): A window on global oceanic and climate change. In: Hu, X., Wang, C., Scott, R. W., Wagreich, M., and Jansa, L. (Eds.), Oceanic Red Beds: Stratigraphy, Composition, Origins, and Paleoceonographic and Paleoclimatic Significance. SEPM Special Publication No. 91. SEPM (Society for Sedimentary Geology), Tulsa, USA, pp. 13–33.

Wardlaw, N. C., 1972. Unusual Marine Evaporites with Salts of Calcium and Magnesium Chloride in Cretaceous basins of Sergipe, Brazil. Economic Geology, 67(2): 156–168.

Warren, J. K., 2010. Evaporites through time: Tectonic, climatic and eustatic controls in marine and nonmarine deposits. Earth-Science Reviews, 98(3–4): 217–268.

Weissert, H., and Lini, A., 1991. Ice age interludes during the time of Cretaceous Greenhouse climate? In: Müller, D. W., McKenzie, J. A., and Weissert, H. (Eds.), Controversies in Modern Geology: Evolution of Geological Theories in Sedimentology, Earth History and Tectonics. Academic Press, London, UK, pp. 173–191.

Wendler, J. E., and Wendler, I., 2016. What drove sea-level fluctuations during the mid-Cretaceous greenhouse climate? Palaeogeography, Palaeoclimatology, Palaeoecology, 441(3): 412–419.

Westermann, S., Stein, M., Matera, V., Fiet, N., Fleitmann, D., Adatte, T., and Föllmi, K. B., 2013. Rapid changes in the redox conditions of the western Tethys Ocean during the early Aptian oceanic anoxic event. Geochimica et Cosmochimica Acta, 121: 467–486.

Winter, W. R., Jahnert, R. J., and França, A. B., 2007. Bacia de Campos. Boletim de Geociências da Petrobras, 15(2): 511–529.

Wise, S., W. Jr., 1983. Mesozoic and Cenozoic Calcareous Nannofossils Recovered by Deep Sea Drilling Project Leg 71 in the Falkland Plateau Region, Southwest Atlantic Ocean. In: Ludwig, W. J., Krasheninnikov, et al., (Eds.), Initial Reports of the Deep Sea Drilling Project covering Leg 71 of the cruises of the drilling vessel Glomar Challenger, Valparaiso, Chile to Santos, Brazil, January-February, 1980. Texas A & M University, Ocean Drilling Program, College Station, U. S. A., pp. 481–550.

Wise, S. A., and Watters Jr., R. W., 2007, Report of Investigation – Reference Material 8573 – L-glutamic Acid USGS40 (Light Carbon and Nitrogen Isotopes in L-glutamic Acid): National Institute of Standards and Technology - USA.

Wissler, L., Funk, H., and Weissert, H., 2003. Response of Early Cretaceous carbonate platforms to changes in atmospheric carbon dioxide levels. Palaeogeography, Palaeoclimatology, Palaeoecology, 200(1–4): 187–205.

Wortmann, U. G., and Chernyavsky, B. M., 2007. Effect of evaporite deposition on Early Cretaceous carbon and sulphur cycling. Nature, 446(7136): 654–656.

Wortmann, U. G., and Paytan, A., 2012. Rapid Variability of Seawater Chemistry Over the Past 130 Million Years. Science, 337(6092): 334–336.

Wright, V. P., 2012. Lacustrine carbonates in rift settings: the interaction of volcanic and microbial processes on carbonate deposition. In: Garland, J., Neilson, J. E., Laubach, S. E., and Whidden, K. J. (Eds.), Advances in Carbonate Exploration and Reservoir Analysis. Geological Society Special Publication 370. The Geological Society, London, UK, pp. 39–47.

Wright, V. P., and Barnett, A. J., 2015. An abiotic model for the development of textures in some South Atlantic early Cretaceous lacustrine carbonates. In: Bosence, D. W. J., Gibbons, K. A., Le Heron, D. P., Morgan, W. A., Pritchard, T., and Vining, B. A. (Eds.), Microbial Carbonates in Space and Time: Implications for Global Exploration and Production. Geological Society Special Publication 418. The Geological Society, London, UK, pp. 209–219.

Xu, W., Ruhl, M., Jenkyns, H. C., Hesselbo, S. P., Riding, J. B., Selby, D., Naafs, B. D. A., Weijers, J. W. H., Pancost, R. D., Tegelaar, E. W., and Idiz, E. F., 2017. Carbon sequestration in an expanded lake system during the Toarcian oceanic anoxic event. Nature Geoscience: advance online publication, doi: 10.1038/ngeo2871.

Yamamoto, K., Ishibashi, M., Takayanagi, H., Asahara, Y., Sato, T., Nishi, H., and Iryu, Y., 2013. Early Aptian paleoenvironmental evolution of the Bab Basin at the southern Neo-Tethys margin: Response to global carbon-cycle perturbations across Ocean Anoxic Event 1a. Geochemistry, Geophysics, Geosystems, 14(4): 1104–1130.

Zakharov, Y. D., Baraboshkin, E. Y., Weissert, H., Michailova, I. A., Smyshlyaeva, O. P., and Safronov, P. P., 2013. Late Barremian–early Aptian climate of the northern middle latitudes: Stable isotope evidence from bivalve and cephalopod molluscs of the Russian Platform. Cretaceous Research, 44: 183–201.

Zijderveld, J. D. A., 1967. AC demagnetization of rocks: Analysis of results. In: Runcorn, S. K., Creer, K. M., and Collinson, D. W. (Eds.), Methods in Paleomagnetism. Elsevier, New York, USA, pp. 254–286.

Zimmerman, H. B., Boersma, A., and McCoy, F. W., 1987. Carbonaceous sediments and palaeoenvironment of the Cretaceous South Atlantic Ocean. In: Brooks, J., Fleet, A. J., (Eds.), Marine Petroleum Source Rocks. Geological Society Special Publication 26. The Geological Society, London, UK, pp. 271–286.